Quantum Mechanical Studies of Small Molecular Systems in Cryogenic Environments

Inaugural-Dissertation
to obtain the academic degree
Doctor Rerum Naturalium (Dr. rer. nat.)
Department of Biology, Chemistry and Pharmacy
Freie Universität Berlin

by
Antonio Accardi
from Wiesbaden

2012

Diese Arbeit wurde in der Zeit von Januar 2008 bis Dezember 2012 unter der Betreuung durch Herrn Prof. Dr. Jörn Manz am Fachbereich Chemie, Biologie, Pharmazie der Freien Universität Berlin, durch Herrn Prof. Dr. Oliver Kühn am Institut für Physik der Universität Rostock and durch Herrn Priv.-Doz. Dr. Burkhard Schmidt am Fachbereich Mathematik der Freien Universität Berlin durchgeführt.

Erst-Gutachter:	Prof. Dr. Beate Paulus
Zweit-Gutachter:	PD Dr. Burkhard Schmidt

Disputation am: 17.12.2012

Abstract

This thesis involves quantum mechanical studies of diatoms embedded in cryogenic environments. Computer simulations are performed on three molecular systems with the aim of disclosing the role of the interactions of the diatoms with their environment in the dynamical mechanisms of chemical reactions. It gives, therefore, a contribution to the transition of chemical reaction dynamics from the gas phase to the condensed phase. The complexity of such interactions increases along this work, from the elementary caging effect, until the active role of the environment in chemical reaction. The quantum mechanical treatment of many-body systems makes extensive use of the Born-Oppenheimer approach or even calls for going beyond it. Along this work a multi-stage hierarchical adiabatic separation scheme is applied in order to study different classes of degrees of freedom (DOF) of interest separately, even though approximately.

Two dimensional quantum dynamics simulations are carried out on the double proton transfer system embedded in the frozen scaffold of a porphine molecule. Starting from a non-equilibrium initial state a switch from synchronous (or concerted) to sequential (or stepwise or successive) breaking and forming of the two hydrogen bonds is observed. The wavepacket dynamics is analyzed in terms of the probability densities and flux densities. Quantitative results are inferred from the time evolutions of the populations in various regions of the potential energy surface (PES). The switch from the synchronous to the sequential mechanism is mediated by two effects: The wavepacket dispersion in time, and the relief reflections of the broadened wavepacket from the steep repulsive wall close to the minimum for the product. Both of them are directly connected to the landscape of the PES determined by the environment, i.e. the porphine scaffold.

The second study is concerned with the photo-dissociation dynamics of molecular bromine embedded in an Ar crystal upon laser excitations from the ground X to the electronically excited B state. Although the definitive internal bond breaking is prevented by caging effects of the environment, the investigation of the non-adiabatic transition (predissociation) between the bound B and the dissociative doubly degenerate C states is central for the understanding of the role of the matrix in the predissociation mechanism. The lattice is taken to be frozen with exception of the cage surrounding the impurity. The five dimensional model includes two anharmonic reaction coordinates, describing the Br-Br bond and a collective displacement of the caging atoms, and three additional vibrational modes of cage fragments. Laser control is performed with the aim to promote predissociation. Resonant vertical transitions from vibrationally preexcited eigenstates of the Br_2 coordinate in the X state are used to access different Franck-Condon windows in the B state. The largest predissociation yield is observed from the $v = 8$ vibrational eigenstate, since this supports formation of a wavepacket in the B state with energy close to the $B - C$ level crossing. Optimal control theory is used in order to achieve vibrational preexcitation via the C state. The ultra-short shaped light pulse is essentially constituted by four subpulses

triggering a pump-dump-type mechanism. The first and fourth subpulses are resonant to the vertical $C \leftarrow X(v = 0)$ and the $X(v = 8) \leftarrow C$ transitions, whereas the second and third subpulses have negative chirps covering the frequency range between the first and four subpulses.

In the third part of the thesis the structure and energetics of a Cl_2 molecule embedded in the parahydrogen crystal is investigated. The aim is the characterization of the initial state for $Cl + H_2 \rightarrow HCl + H$ chemical reaction, which has been experimentally observed upon simultaneous UV+IR laser irradiation. The role of the environment is fundamental for the understanding of the dynamical mechanism of the reaction, since it becomes a reactant itself. The many-body system is approximated in a pairwise fashion, neglecting three-body terms. The Cl_2-pH_2 and pH_2-pH_2 pair potentials are obtained by adiabatization of four-dimensional quantum chemistry potentials with respect to the rotational DOF of the hydrogen molecule(s) in a rigid rotor approximation. These potentials are used in order to grow the energetically lowest cluster sequence by means of classical simulations. A first-shell structure is found with the Cl_2 molecule occupying a single substitutional site of a fcc cluster pointing along the <001> crystallographic direction. The translational zero-point energies (ZPE) and wavefunctions of solvent and solute molecules in the matrix are calculated within the three dimensional Einstein model revealing large ZPEs compared to the well depths of the pair potentials, even for the heavier Cl_2 molecules. For the first time, relaxation of the cage around the pH_2 and Cl_2 molecules for the pure and doped crystals, respectively, is simulated in order to mimic the flexibility of translational quantum matrices. Comparison of the results obtained within the rigid and the non-rigid lattice approaches show that the translational time-scale of the individual hydrogen molecules is much shorter than the one needed by the surrounding molecules in order to relax, so that the rigid model more closely reproduces experimental data. The situation is reversed for Cl_2, since it translates more slowly due to its heavier mass, so that the simulation of a softer environment may be more adequate. The rotational energies and the rotational wavefunctions of the Cl_2 molecule in the matrix are evaluated within the Devonshire model disclosing that within both the rigid and non-rigid lattices the impurity cannot rotate freely, but actually librates around definite crystallographic directions implying librational ZPEs. Moreover, relaxation of the cage shows substantial changes on the landscapes of the rotational PESs, which favour librations around different crystallographic directions in the rigid and in the non-rigid lattices. A comparison with the pH_2 translational ZPEs suggest that the solvent molecules easily follow the Cl_2 rotations, so that the simulation of the non-rigid lattice may be required.

Kurzfassung

Die vorliegende Arbeit umfasst quantenmechanische Untersuchungen zweiatomiger Systeme, die in ultrakalte Umgebungen eingebettet sind. Für drei verschiedenen molekulare Systeme werden Computersimulationen durchgeführt mit dem Ziel, den Einfluss der Wechselwirkung der Diatome mit ihrer Umgebung auf die Dynamik chemischer Elementarschritte aufzudecken. Somit soll ein Beitrag zur chemischen Reaktionsdynamik beim Übergang von der Gasphase zur kondensierten Phase geleistet werden. Dabei steigt die Komplexität der Wechselwirkungen für die drei untersuchten Systeme, vom elementaren Käfigeffekt beim Bindungsbruch bis hin zur aktiven Rolle der Umgebung in einer chemischen Reaktion. Die quantenmechanische Behandlung der Vielkörper-Systeme basiert in weiten Teilen auf adiabatischen (Born-Oppenheimer) Näherungen oder geht sogar darüber hinaus. In dieser Arbeit wird eine mehrstufiges, hierarchisches adiabatische Approximationsverfahren entwickelt, das es uns näherungsweise erlaubt, verschiedene Klassen von Freiheitsgraden separat zu betrachten.

Das doppelte Protonentransfer-System im eingefrorenen Gerüst eines Porphin-Moleküls wird mit zweidimensionalen quantendynamische Simulationen modelliert. Ausgehend von einem Nicht-Gleichgewichtszustand kann ein Umschalten von synchronem (konzertiertem) zu sequentiellem (schrittweisem) Brechen und Neubilden der zwei Wasserstoffbrückenbindungen beobachtet werden. Die entsprechende Wellenpaketdynamik wird in Hinsicht auf Wahrscheinlichkeitsdichten und -flüsse analysiert. Quantitative Ergebnisse werden aus der Zeitentwicklung der Populationen in verschiedenen Bereichen der Potentialenergiefläche erschlossen. Der Wechsel vom synchronen zum sequentiellen Mechanismus wird durch zwei Effekte vermittelt: Zum einen die Dispersion des Wellenpaketes mit der Zeit, zum anderen die Reflektionen des verbreiterten Wellenpaketes an den repulsiven Wänden des Potentials in der Nähe des Minimums für das Produkt. Beide Effekte stehen in direktem Zusammenhang mit der Potentialenergie-Landschaft, die durch die Umgebung des Porphin-Gerüstes gegeben ist.

Die zweite Studie behandelt die Photodissoziations-Dynamik von Brom-Molekülen, die in einen Argon-Kristall eingebettet sind, nach Anregung vom Grundzustand (X) in den elektronisch angeregten B-Zustand. Auch wenn der endgültige Bindungsbruch von Käfigeffekt der Umgebung verhindert wird, ist die Untersuchung des nicht-adiabatischen Überganges (Prädissoziation) vom gebundenen B- zum dissoziativen und zweifach entarteten C-Zustand für das Verständnis des Einflusses der Matrix auf den Prädissoziations-Mechanismus von zentraler Bedeutung. Dabei wird das Gitter der Edelgas-Atome als starr angenommen, mit Ausnahme des Käfigs aus den Atomen, die die das Gastmolekül direkt umgeben. Das fünfdimensionale Modell umfasst zwei anharmonische Reaktionskoordinaten, die die Br-Br-Bindung und eine kollektive Auslenkung der Käfigatome beschreiben, sowie drei weitere Schwingungsmoden des Käfigfragmentes. Die Laser-Steuerung wird mit dem Ziel durchgeführt, Prädissoziation zu befördern. Resonante vertikale Übergänge werden verwendet, um verschiedene Franck-Condon-Fenster im B-Zustand zu erreichen, wobei die Schwingung des Br_2 Moleküls im X-Zustand vorher angeregt wird. Die größte Prädissoziations-Ausbeute wird vom v=8 Schwingungs-Eigenzustand aus beobachtetet, da dieser zu einem Wellenpaket im B-Zustand mit Energie nahe der B-C Durchschnei-

dung führt. Die Theorie der optimalen Steuerung wird verwendet, um die Schwingungs-Voranregung über den C-Zustand zu erreichen. Der ultraschnelle geformte Lichtpuls wird im wesentlichen aus vier Subpulsen gebildet, die einen Anregungs-Abregungs-Mechanismus auslösen. Der erste und vierte Subpuls sind resonant zu den vertikalen $C \leftarrow X(v = 0)$ und $X(v = 8) \leftarrow C$ Übergängen, während der zweite und dritte Subpuls mit ihren abfallenden Frequenzen den Bereich zwischen dem ersten und vierten Subpuls abdecken.

Im dritten Teil der vorliegenden Arbeit werden die Struktur und die Energetik von Cl_2 Molekülen untersucht, die in einen para-H_2 Kristall eingebettet sind. Das Ziel ist die Charakterisierung des Anfangszustands für die chemische Cl + H $_2$ $\rightarrow$ HCl + H Reaktion, die in Experimenten mit gleichzeitiger UV + IR Laserstrahlung beobachtet wurde. Dabei ist hier für das Verständnis der Reaktionsdynamik die Rolle der Umgebung von grundlegender Bedeutung, da sie selbst einen der Reaktanden darstellt. Die Vielkörper-Wechselwirkung wird durch die Summe aller paarweisen Wechselwirkungen approximiert, wobei Drei-Körper-Terme vernachlässigt werden. Die Cl_2-pH_2 und pH_2-pH_2 Paarpotentiale werden quantenchemisch in vier Dimensionen berechnet und dann bezüglich der Rotation des/der Wasserstoff-Moleküle(n) adiabatisiert, wobei die Näherung der starren Rotoren verwendet wird. Die resultierenden Potentiale werden verwendet, um zunächst das Wachstum kleiner Cluster an Hand der energetisch niedrigsten Cluster-Sequenz mit Hilfe klassischer Simulationen zu untersuchen. Als erste komplette Solvatationshülle ergibt sich eine fcc-ähnliche Struktur, bei der das Cl_2 Molekül einen mono-substitutionellen Platz einnimmt und entlang der kristallographischen <001> Richtung ausgerichtet ist. Die translatorischen Nullpunktsenergien und die zugehörigen Wellenfunktionen der Gastmoleküle und der Moleküle des Wirtskristalles werden im Rahmen eines dreidimensionalen Einstein-Modells berechnet. Dabei zeigt sich, dass die Nullpunktsenergien im Vergleich zu den Topftiefen der Paarpotentiale großsind, sogar für die schwereren Cl_2 Moleküle. Zum ersten Mal wird auch die Relaxation des Käfigs um die pH_2 und Cl_2 Moleküle für die reinen bzw. dotierten Kristallen simuliert, um die Flexibilität der translatorischen Quanten-Matrizen zu modellieren. Ein Vergleich der Ergebnisse für die starren und nicht-starren Gitter zeigt, dass die translatorische Zeitskala der einzelnen Wasserstoffmoleküle viel kürzer ist als die Zeit, die die umgebenden Moleküle zu ihrer Relaxation benütigen, so dass die starren Modelle die experimentellen Daten besser wiedergeben. Die Situation für Cl_2 Moleküle ist umgekehrt, da sie sich aufgrund ihrer höheren Masse langsamer bewegen, so dass die Simulation mit einer flexiblen Umgebung angemessener erscheint. Die Rotations-Energien und -Wellenfunktionen des Cl_2 Moleküls in der pH_2 Matrix werden im Rahmen eines Devonshire Modells berechnet, wobei sich zeigt, dass sich die Gastmoleküle weder in den starren noch in den nicht-starren Gittern frei drehen können, sondern tatsächlich Librations-Schwingungen um bestimmte kristallographische Richtungen ausführen, was insbesondere auch eine Nullpunktsenergie impliziert. Darüber hinaus führt die Relaxation des Käfigs zu wesentlichen Änderungen in den Landschaften der Rotationsenergieflächen, die Librationen um verschiedene kristallographische Richtungen in den starren und in den nicht-starre Gittern favorisieren. Ein Vergleich mit den Energien der pH_2 Translation legt nahe, dass die Umgebungsmoleküle den Cl_2 Drehungen leicht folgen können, so dass die Simulation mit nicht-starren Gitter nötig ist.

Acronyms

AHR	Adiabatic Hindered Rotor
AO	Atomic Orbital
APF	Atomic Packing Factor
AS	Adiabatic Separation
ATM	Axilrod-Teller-Muto
BO	Born-Oppenheimer
BSSE	Basis-Set Superposition Error
CBS	Complete Basis Set
CC	Coupled-Cluster
CCD	Coupled-Cluster Double
CCSD	Coupled-Cluster Single Double
CCSDT	Coupled-Cluster Single Double Triple
CGTO	COntracted Gaussian Type Orbital
CI	Configuration Interaction
CIS	Configuration Interaction Single
CISD	Configuration Interaction Single Double
CISDT	Configuration Interaction Single Double Triple
CMF	Constant Mean-Field
COM	Center Of Mass
CP	Counterpoise
CPU	Central Processing Unit
CRS	Cartesian Reaction Surface
CT	Charge Transfer
CFT	Crystal Field Theory
DIC	Double Icosahedron
DIM	Diatomics-in-Molecules
DM	Devonshire Model
DOF	Degree of Freedom
DPT	Double Proton Transfer
DTD	Domain-To-Domain
DVR	Discrete Variable Representation

EM	Einstein Model
EOM	Equation of Motion
FBR	Finite Basis Representation
FCI	Full Configuration Interaction
FROG	Frequency Resolved Optical Gating
FWHM	Full Width at Half Maximum
GP	Grid Point
GTO	Gaussian Type Orbital
GQ	Gaussian Quadrature
HF	Hartree-Fock
HFD	Hartree-Fock Dispersion
LAC	Large Amplitude Coordinate
LCAO	Linear Combination of Atomic Orbitals
LEPS	London-Eyring-Polanyi-Sato
LJ	Lennard-Jones
LLR	Li-LeRoy-Roy
LP	Legendre Polynomials
MBPT	Many-Body Perturbation Theory
MCTDH	Multi-Configuration Time-Dependent Hartree
MD	Molecular Dynamics
MO	Molecular Orbital
MP	Møller-Plesset
NACT	Non Adiabatic Coupling Term
NN	Nearest-Neighbour
NNd	Nearest-Neighbour distance
NWB	Norman-Watts-Buck
OCT	Optimal Control Theory
PD	Probability Density
PES	Potential Energy Surface
PGTO	Primitive Gaussian Type Orbital
PT	Perturbation Theory
QC	Quantum Chemistry
QM	Quantum Mechanics
QQ	Quadrupole-Quadrupole
RA	Rotationally Adiabatic

RAS Rotational Adiabatic Separation
RG Rare Gas
RS Rayleigh Schrödinger
RSVC Reaction Surface-Vibronic Coupling
RTC Rotational-Translational Coupling
SAD Small Amplitude Displacement
SCF Self Consistent Field
SE Schrödinger Equation
SG Silvera-Goldmann
SH Spherical Harmonics
SPF Single Particle Function
TD Time-Dependent
TI Time-Independent
TDSE Time-Dependent Schrödinger Equation
TISE Time-Independent Schrödinger Equation
TS Transition State
UC Unit Cell
VCH Vibronic Coupling Hamiltonian
VDW van der Waals
VMF Variable Mean-Field
ZPE Zero Point Energy
pH_2 para Hydrogen
oH_2 ortho Hydrogen
pD_2 para Deuterium
oD_2 ortho Deuterium

Contents

1 Introduction

Understanding the dynamical mechanisms of chemical reactions is central in physical chemistry. Characterization of energetic states of particles in reactive collisions relies in general upon spectroscopic techniques, because of the uniqueness of atomic and molecular spectra. In the gas-phase, information about the initial conditions of reactants and products, such as the kinetic energy or the angle of orientation, at the moment of the collision are lost, since they are eventually averaged. Spectroscopic investigations have been therefore proposed in solid-matrices, where the reactant molecules are fixed in well-defined positions. In the last decades matrix isolation techniques developed ideal conditions for such spectroscopic and also for photochemical investigations [1–7]. The molecular system of interest is trapped in an unreactive matrix, i.e. the host-guest interactions are weak or even negligible. Natural candidates for such host matrices are therefore inert species, such as close-shell rare gas atoms [1–4] or hydrogen molecules [5–7], which present crystalline structures with a broad optical transparency in their solid state at low temperatures. Thus, their very low melting points call for a spectroscopy at cryogenic temperature, where the system lies preferably in its ground state and information about the initial conditions are known. Moreover, the solvent first electronic excitations are found at much higher energies (10-12 eV [2, 8]) than the solute electronic transitions which allows for recording their spectral responses upon light interrogation similarly as in the gas-phase. Even more interesting in the field of quantum reaction dynamics has been the development of ultra-fast lasers, which permits to excite specific modes in the system with the aim of controlling the dynamics of the hosting molecules [4], as for example, the excitation of specific lattice phonon modes. In this case the weak solute-solvent interactions are actually of interest and present even a major challenge.

The above-mentioned experimental conditions are also suitable for theoretical treatments such as quantum chemistry and quantum dynamics, since they generally rely on the validity of the Born-Oppenheimer approximation [9–12] for the study of the molecular system and approximate low-dimensional models. Quantum calculations are in fact expensive, and simulations are mostly carried out in reduced dimensionality. Finally, cryogenic temperatures are the closest phenomenon to an ideal frozen environment, which allows to focus on the subpart of interest of the system, i.e. the solute or guest molecules. Furthermore, the calculation of the multi-dimensional matrix interaction potentials is also simplified by the approximate pairwise additivity of two-body forces, which accounts for 90-95% of the total

solvent-solvent interaction energy. In particular, the isotropic solvent-solvent pair potentials are known to high precision from experiment. Finally, the three-body interactions are in general well approximated by the Axilrod-Teller-Muto potentials, which contain triple-dipole polarization terms [2]. The use of hydrogen as hosting species poses some more challenges to the theoreticians, since one has to deal with additional degrees of freedom, such as molecular rotations and vibrations, which where absent in the case of noble gas atoms, and which are connected to many quantum effects because of the lighter mass, such as partial flexibility of the quantum crystal [13,14].

The present thesis comprehends quantum dynamical studies of three different molecular systems at cryogenic temperatures. One entire chapter is devoted to each of three topics, which deserve their own introduction and conclusion. Therefore, only a short survey is provided here on the topics themselves emphasizing the common aspects. Since the investigations are carried out in the same quantum mechanical framework, the second chapter contains the whole theoretical background required along the thesis. The first part is consecrated to the Born-Oppenheimer approach, which pervades the entire thesis, even though it aims at the observation of different phenomena depending on the molecular system. Adiabatic separation is a useful tool, which simplifies the study of a molecular system by considering its degrees of freedom to be independent, so that they may be treated separately. This assumption is not always valid, but has permitted several generations of scientists to gain insights in the molecular systems observed. An adiabatic separation relies essentially on different masses and different contents of energy of the dynamical degrees of freedom, thus the larger the difference between such contents of energy is, the safer is the corresponding adiabatic separation. On the one hand, the motion of the degrees of freedom showing fast dynamics. i.e. the light particles, can be averaged, so that the system is then described by its quantum mechanically properties. On the other hand, the degrees of freedom showing a slow dynamics, i.e. the heavy particles, can be considered frozen, so that a classical approximation is then applied by considering fixed particle positions instead of distribution functions. Since a system formed by N particles has $3N$ degrees of freedom, when trying to isolate the ones of interest, several consecutive adiabatic separations may be applied to the system. This is addressed in chapter two as "multi-stage adiabatic separation" and has been in particular adapted to the hydrogen matrix system. The second part of the chapter two is a review of the quantum chemistry and quantum dynamics methods involved in the research. Afterwards, the three topics are presented individually.

In the first topic quantum dynamics of the double proton transfer reaction of the biological system porphine is investigated, where the molecular scaffold can be seen as the matrix embedding the two-proton subsystem. Attention is focused on the long-standing debate, whether the two proton exchange their equivalent positions synchronously or sequentially. Despite of the many approximations involved, the two dimensional analytical

potential taking into account just the linear motions of the two protons and their coupling, and ignoring therefore the scaffold-matrix dynamics, served well for the proof of principle disclosed there.

The second and third topics investigate the two halogen molecules Br_2 and Cl_2 embedded respectively in a Ar and H_2 matrices, even though with two different purposes. In the fourth chapter laser-driven quantum dynamical reactions are simulated on the Br_2@Ar system. Attention is focused on controlling the predissociation dynamics of Br_2 through electronic excited states by using ultra-fast laser pulses. The quantum simulations involve therefore non-adiabatic vibronic coupling terms between electronic states, which are included in the diabatic multi-dimensional potential energy surface obtained within the Diatomics-In-Molecule (diabatic) approximation. Thus, by means of a Group Born-Oppenheimer approximation [10,11] we select the relevant subgroup of electronic states, even though by treating non-adiabatic coupling terms within that group we are actually going beyond the Born-Oppenheimer approximation [10–12].

In the fifth chapter the Cl_2@pH_2 system is studied prior to laser excitations. Attentions is focused on the structure and the energetics of the doped quantum crystal in the electronic ground state in order to prepare the system to form HCl *in situ* upon combined UV/IR irradiation [15,16]. Intuitive, low-dimensional models are applied for taking into account the quantum effects such as the rotations and the large and strong anharmonic translational zero-point energy typical for solid hydrogen, as well as the the rotations of the solute, which could be simply hindered by matrix or even reduced to librations involving therefore again a zero-point energy. All degrees of freedom of the reactants play a role in the system, so that one has to consider them all. The validity of the many adiabatic separations involved is discussed both when calculating the pH_2-Cl_2 and pH_2-pH_2 pair potentials needed for the evaluation of the matrix interaction potential energy surfaces in terms of two-body forces, and when treating the solvent translational and solute translational and rotational degrees of freedom within the matrix.

Thus, even though we investigate three different systems, the common aim is to describe chemical processes of small molecules embedded in an environment quantum mechanically. Molecular spectroscopy as well as reaction dynamics of three body systems are well understood in the gas phase and full quantum mechanical models are straightforward. It is the aim of this thesis to move towards the understanding of physical chemical processes of molecular systems in the condensed phase. This poses more challenges because of the interactions with the environments, so that crystallized systems or frozen environments at cryogenic temperatures are still simplified prototypes. Nevertheless, the interactions with the environment must be included when developing theoretical models, which in principle means to account for all possible degrees of freedom of hosting and guest molecules, i.e. rotational, translational, vibrational, electronic motions. Thus, it becomes difficult to have a full quantum mechanical description of these systems and one has to focus just on

certain aspects. For this reason mixed classical-quantum mechanical approximate models are often applied and/or are commonly based on the Born-Oppenheimer approximation, generally called also adiabatic separation, where two or more molecular degrees of freedom with rather low energies are taken into account individually.

2 Theoretical Concepts

2.1 Overview

The investigation carried out throughout this work is based on time-independent (TI) and time-dependent (TD) Quantum Mechanics (QM). In this chapter the reader will be introduced to the theoretical concepts underlying the methods employed. In section 2.2 the Born-Oppenheimer approach is presented and the Schrödinger Equation in its adiabatic picture is derived. The second section 2.3 is an introductory review about the different Quantum Chemistry methods used throughout this work. Finally, in the third section 2.4 the Multi-Configurational Time-Dependent Hartree (MCTDH) method used in order to carry out the numerical Quantum Dynamics simulations, is discussed.

2.2 The Born-Oppenheimer Approach

2.2.1 The Born-Oppenheimer Approximation

QM is a branch of physics born in the early 1900's, after a number of experimental observations, such as for example the emission of discrete quantities of energy (quanta) from the black body by Planck or the photoelectric effect could not be interpreted within the classical mechanics picture anymore. A new paradigm was developed in physics which was well supported by de Broglie in the wave-particle duality at the atom-scale: on the one hand, particle-like properties were recognized to the waves (photons) by Einstein, on the other hand, wave-like properties were recognized to the particles (electrons) by Compton. Thus, at the microscopic scale Newton's laws give way to the Time-Independent (TISE) and Time-Dependent Schrödinger Equation (TDSE), respectively,

$$\left.\begin{array}{l} E_{\mathrm{tot}}|\Psi_{\mathrm{tot}}\rangle \\ i\hbar\frac{\partial}{\partial t}|\Psi_{\mathrm{tot}}(t)\rangle \end{array}\right\} = \hat{\mathbf{H}}_{\mathrm{tot}} \left\{\begin{array}{l} |\Psi_{\mathrm{tot}}\rangle \\ |\Psi_{\mathrm{tot}}(t)\rangle \end{array}\right. , \tag{2.1}$$

where $\hat{\mathbf{H}}_{\mathrm{tot}}$ is the total Hamiltonian, the operator corresponding to the total energy E_{tot} of the system, and $|\Psi_{\mathrm{tot}}\rangle$ and $|\Psi_{\mathrm{tot}}(t)\rangle$ are, respectively, the time-independent and time-dependent full particle wavefunctions expressed in the Dirac notation. In the TISE the total Hamiltonian and the wavefunction are always time-independent. In the TDSE the

wavefunction is strictly time-dependent, however, the total Hamiltonian can be both independent of, or dependent on, time according to the system and/or the phenomenon to be described. For example, the 2-dimensional model system of Porphine presented in Chap. 3, it is assumed to not exchange energy with the ambient, which implies conservation of the total energy of the system, so that the Quantum Dynamics simulations are carried out by solving the TDSE for a time-independent total Hamiltonian. In turn, in Chap. 4 the Br_2@Ar system is excited by an external electromagnetic field changing in time, implying a non-conservation of the total energy of the system and the total Hamiltonian being time-dependent.

The TISE is an eigenvalue equation, E_{tot} and $|\Psi_{\text{tot}}\rangle$ being its eigenvalues and eigenfunctions, respectively. It is widely used in the first part of Chap. 5, since its solution allows for the calculation of the Cl_2-H_2 2-dimensional potential energy surface and of the pH_2-pH_2 1-dimensional potential energy curve, in terms of which the energetics of a chlorine molecule embedded in a para-hydrogen crystal (Cl_2@pH_2) at cryogenic temperatures is described.

The wavefunction is a mathematical function providing information about the probability amplitude of position and momentum of the particles. Thus, the Schrödinger equations give the most complete non-relativistic description to a physical system[1], since they describe both its microscopic and macroscopic properties, but at the same time they are very difficult equations to deal with.

The Born-Oppenheimer (BO) approximation [9], also known as adiabatic separation, is a well-known concept in theoretical chemistry and physics, based on the very general separation of the particles into heavy and light ones, under the assumption the mass ratio $\frac{M}{m}$, whose inverse squared, $\left(\frac{m}{M}\right)^{\frac{1}{2}}$, is often called adiabatical parameter, to be large enough. The mass of the heavy and light particles are M and m, respectively. The idea is, in fact, to try to separate the total Hamiltonian $\hat{\mathbf{H}}_{\text{tot}}(\vec{\nabla}_R, \vec{R}, \vec{\nabla}_r, \vec{r})$ of the system in Eq. 2.1 into two contributions: a heavy particle Hamilton operator $\hat{\mathbf{H}}_{\text{heavy}}(\vec{\nabla}_R, \vec{R})$ containing the kinetic energy of the heavy particles, with coordinates $\vec{R}$ and gradient with respect to them, $\vec{\nabla}_R$, as well as the interactions between the heavy particles, and a light Hamilton operator $\hat{\mathbf{H}}_{\text{light}}(\vec{\nabla}_r, \vec{r}; \vec{R})$ containing the kinetic energy of the light particles with coordinates $\vec{r}$ and gradient with respect to them, $\vec{\nabla}_r$, the interactions between the light particles as well as the interactions between heavy and light particles.

$$\hat{\mathbf{H}}_{\text{tot}}(\vec{\nabla}_R, \vec{R}, \vec{\nabla}_r, \vec{r}) = \hat{\mathbf{H}}_{\text{heavy}}(\vec{\nabla}_R, \vec{R}) + \hat{\mathbf{H}}_{\text{light}}(\vec{\nabla}_r, \vec{r}; \vec{R}) \ , \tag{2.2}$$

$$\hat{\mathbf{H}}_{\text{heavy}}(\vec{\nabla}_R, \vec{R}) = \hat{\mathbf{T}}_{\text{heavy}}(\vec{\nabla}_R) + \hat{\mathbf{V}}_{\text{heavy,heavy}}(\vec{R}) \ , \tag{2.3}$$

$$\hat{\mathbf{H}}_{\text{light}}(\vec{\nabla}_r, \vec{r}; \vec{R}) = \hat{\mathbf{T}}_{\text{light}}(\vec{\nabla}_r) + \hat{\mathbf{V}}_{\text{light,light}}(\vec{r}; \vec{R}) + \hat{\mathbf{V}}_{\text{light,heavy}}(\vec{r}; \vec{R}) \ , \tag{2.4}$$

[1] In the more particular case of molecular systems, the description of bosons and fermions, in q accordance with the Pauli principle, is not directly covered by the Schrödinger equation and must be introduced as a constraint when representing the wavefunction, Ψ

where the kinetic energy operators are expressed in terms of the momentum operators in QM, $\vec{P} = -i\hbar\vec{\nabla}_R$ and $\vec{p} = -i\hbar\vec{\nabla}_r$ [2]:

$$\hat{T}_{\text{heavy}}(\vec{\nabla}_R) = -\frac{\hbar^2}{2M}\Delta_R \ , \tag{2.5}$$

$$\hat{T}_{\text{light}}(\vec{\nabla}_r) = -\frac{\hbar^2}{2m}\Delta_r \ . \tag{2.6}$$

In order to solve the TISE and TDSE, Born and Oppenheimer proposed to expand the total wavefunction in terms of the light wavefunction. The so-called BO-expansion reads

$$|\Psi_{\text{tot}}(\vec{R},\vec{r},t)\rangle = \sum_{q=0}^{\infty} |\Psi^{(q)}_{\text{heavy}}(\vec{R}_1,\vec{R}_2,...\vec{R}_N,t)\rangle \times |\Psi^{(q)}_{\text{light}}(\vec{r}_1,\vec{r}_2,...,\vec{r}_n;\vec{R}_1,\vec{R}_2,...\vec{R}_N)\rangle \ , \tag{2.7}$$

where, in the case of the TISE, one just has to drop the time-dependence in the equation. N and n are the total numbers of heavy and light particles, respectively, and q is a quantum number running, in general, from zero to infinity. The heavy wavefunctions $\Psi^{(q)}_{\text{heavy}}$ depend only on the set of coordinates $\vec{R} = \vec{R}_1,\vec{R}_2,...\vec{R}_N$, whereas the light wavefunctions $\Psi^{(q)}_{\text{light}}$ depend on the set of coordinates $\vec{r} = \vec{r}_1,\vec{r}_2,...,\vec{r}_n$ as well as parametrically on the set of coordinates $\vec{R}$. Moreover, the complete set of light wavefunctions is orthonormal:

$$\langle \Psi^{(q)}_{\text{light}} | \Psi^{(q')}_{\text{light}} \rangle = \delta_{qq'} \ . \tag{2.8}$$

The light TISE is defined as

$$(\hat{\mathbf{H}}_{\text{light}}(\vec{\nabla}_r,\vec{r};\vec{R}) - E^{(q)}_{\text{light}}(\vec{R}))|\Psi^{(q)}_{\text{light}}(\vec{r};\vec{R})\rangle = 0 \ , \tag{2.9}$$

where the set of eigenvalues, $E^{(q)}_{\text{light}}(\vec{R})$, define the so-called adiabatic energies of the light particles. Please note that the coordinates $\vec{r}$ are averaged out by solving the light TISE. Hence, the heavy particles feel only an interaction with the light ones, which is averaged

[2] The choice to express the total energy in terms of kinetic energy depending only on the derivative with respect to the position coordinates, the $\vec{\nabla}$ operators, and the interactions, or rather the potential energies, depending only on the position coordinates themselves, is not the most general one. For example, the use of non-Cartesian coordinates, which might be a better choice for describing certain systems, would make the kinetic energy to become coordinate-dependent. In turn, the presence of a magnetic field would make the potential to depend, classically speaking, on the velocity of the particles and hence on the momentum operators, $\vec{\nabla}$. As a final remark, it is mentioned that in general the form of the momentum operator could be conveniently rethought case by case. This notation used here is anyway preferred since the approximation will be later applied to molecular systems without involving any magnetic field.

over all their possible positions since they move much more rapidly.

$$\langle \Psi^{(q)}_{\rm light}(\vec{r};\vec{R})|\hat{\mathbf{H}}_{\rm light}(\vec{\nabla}_r,\vec{r};\vec{R})|\Psi^{(q)}_{\rm light}(\vec{r};\vec{R})\rangle_r = E^{(q)}_{\rm light}(\vec{R}) \ . \tag{2.10}$$

In the following it shall be useful to consider

$$W^{(q)}_{\rm light}(\vec{R}) = E^{(q)}_{\rm light}(\vec{R}) + \hat{\mathbf{V}}_{\rm heavy,heavy}(\vec{R}) \ , \tag{2.11}$$

which defines the potential energies governing the dynamics of the heavy particles. In order to derive the coupled equations for the expansion coefficients $|\Psi^{(q)}_{\rm heavy}(\vec{R},t)\rangle$, the BO-expansions of Eq. 2.7, are now inserted in Eq. 2.1. Multiplication from the left by $\langle\Psi^{(q')}_{\rm light}(\vec{r};\vec{R})|$ with $q' \neq q$ and integration over the light coordinates finally leads to

$$\begin{aligned} \left.\begin{array}{r} E^{(q)}_{\rm heavy}|\Psi^{(q)}_{\rm heavy}(\vec{R})\rangle \\ i\hbar\frac{\partial}{\partial t}|\Psi^{(q)}_{\rm heavy}(\vec{R},t)\rangle \end{array}\right\} &= \sum_{q'=0}^{\infty}\Bigg[-\frac{\hbar^2}{2M}\Delta_R\ \delta_{q'q} + W^{(q')}_{\rm light}(\vec{R})\ \delta_{q'q} - \\ &- \frac{\hbar^2}{2M}\left(2\vec{\tau}_1^{(q'q)}\cdot\vec{\nabla}_R + \vec{\tau}_2^{(q'q)}\right)\Bigg] \left\{\begin{array}{l} |\Psi^{(q')}_{\rm heavy}(\vec{R})\rangle \\ |\Psi^{(q')}_{\rm heavy}(\vec{R},t)\rangle \end{array}\right. \end{aligned} \ , \tag{2.12}$$

where the explicit form for the kinetic operator for the heavy particles given in Eq. 2.5 was used. Eqs. 2.12 are the TISE and TDSE within the adiabatic representation. The first two terms are diagonal matrices, with the $W^{(q')}_{\rm light}(\vec{R})$ being the sum of the interactions between the heavy particles and the adiabatic potential energies resulting from the average of the light particle Hamiltonian with respect to the light densities, as already mentioned above for Eq. 2.11. The third term couples the motions of electrons and nuclei through the two matrices, $\vec{\tau}_1^{(q'q)}$ and $\vec{\tau}_2^{(q'q)}$, which are, therefore, called the first and second order Non Adiabatic Coupling Terms (NACT), and is inversely proportional to the mass, M, of the heavy particles. The definitions of the NACTs are

$$\vec{\tau}_1^{(q'q)}(\vec{R}) = \langle \Psi^{(q')}_{\rm light}(\vec{r};\vec{R})|\vec{\nabla}_R|\Psi^{(q)}_{\rm light}(\vec{r};\vec{R})\rangle_r \ , \tag{2.13}$$

$$\vec{\tau}_2^{(q'q)}(\vec{R}) = \langle \Psi^{(q')}_{\rm light}(\vec{r};\vec{R})|\Delta_R|\Psi^{(q)}_{\rm light}(\vec{r};\vec{R})\rangle_r \ , \tag{2.14}$$

so that they are matrix representations of the gradient and the Laplacian operator in the basis of the light wavefunctions, respectively. The $\vec{\tau}_1^{(q'q)}$ is an off-diagonal matrix, whereas $\vec{\tau}_2^{(q'q)}$ is a full matrix. They also have the following interesting properties [10, 12]:

$$(\vec{\tau}_1^{(q'q)})^* = -\vec{\tau}_1^{(qq')} \ , \tag{2.15}$$

$$\vec{\tau}_2^{(q'q)} = \nabla_R\cdot\vec{\tau}_1^{(q'q)} + \vec{\tau}_1^{(q'q)}\cdot\vec{\tau}_1^{(qq')} \ , \tag{2.16}$$

where $\tau_2^{(\vec{q'q})}$, is rewritten in terms of $\tau_1^{(\vec{q'q})}$. Moreover, by using the extended Hellmann-Feynman theorem, the first order NACT can be otherwise expressed as [10, 12]

$$\vec{\tau}_1^{(q'q)}(\vec{R}) = \frac{\langle \Psi_{\text{light}}^{(q')}(\vec{r};\vec{R})| \left(\vec{\nabla}_R \hat{\mathbf{H}}_{\text{light}}(\vec{\nabla}_r,\vec{r};\vec{R})\right) |\Psi_{\text{light}}^{(q)}(\vec{r};\vec{R})\rangle_r}{E_{\text{light}}^{(q)}(\vec{R}) - E_{\text{light}}^{(q')}(\vec{R})} \ , \tag{2.17}$$

where, instead of the diagonal elements, as in the traditional Hellmann-Feynman theorem, the off-diagonal elements with $q' \neq q$, are taken. Eq. 2.17 shows that the magnitude of $\tau_1^{(\vec{q'q})}$ is inversely proportional to the energy gap between the two states, q' and q, considered. In the traditional Hellmann-Feynman theorem, derivation of the Hamiltonian with respect to the positions of the particles results in the averaged forces acting on them. Thus, the numerator in Eq. 2.17 has also the unit of a force. Moreover, this equation highlights the link between the first order NACTs and the topography of the eigenstates, since $\vec{\tau_1}^{(q'q)}$ shows a singularity whenever two eigenstates are degenerate.

2.2.2 Adiabatic Separation (AS)

For the while being, no approximations have been introduced, since the BO-expansion in Eq. 2.7 is assumed to be complete. However, the solution of the heavy TISE and TDSE in Eq. 2.12 requires the infinite set of eigenvalues $E_{\text{light}}^{(q')}(\vec{R})$ in order to calculate the adiabatic potential energies $W_{\text{light}}^{(q')}(\vec{R})$ and eigenfunctions $\Psi_{\text{light}}^{(q')}(\vec{r};\vec{R})$ from the light TISE in Eq. 2.10, since they are needed for the calculation of the NACTs of first and second order.

The BO-approximation enters the discussions at this point by simply neglecting the third (coupling) term of Eq. 2.12, which reduces the number of eigenvalues to be calculated. The new TISE and TDSE read:

$$\left.\begin{array}{l} \tilde{E}_{\text{heavy}}^{(q)} |\tilde{\Psi}_{\text{heavy}}^{(q)}(\vec{R})\rangle \\ i\hbar\frac{\partial}{\partial t}|\tilde{\Psi}_{\text{heavy}}^{(q)}(\vec{R},t)\rangle \end{array}\right\} = \left(-\frac{\hbar^2}{2M}\Delta_R + W_{\text{light}}^{(q)}(\vec{R})\right) \left\{\begin{array}{l} |\tilde{\Psi}_{\text{heavy}}^{(q)}(\vec{R})\rangle \\ |\tilde{\Psi}_{\text{heavy}}^{(q)}(\vec{R},t)\rangle \end{array}\right. \ , \tag{2.18}$$

where the motions of the heavy and light particles are now decoupled from each other, but, due to the adiabatic approximation, the eigenvalues $\tilde{E}_{\text{heavy}}^{(q)}$ are different from $E_{\text{heavy}}^{(q)}$ in Eqs. 2.12. The same applies to the wavefunctions, i.e. $|\tilde{\Psi}_{\text{heavy}}^{(q)}(\vec{R})\rangle \neq |\Psi_{\text{heavy}}^{(q)}(\vec{R})\rangle$ and $|\tilde{\Psi}_{\text{heavy}}^{(q)}(\vec{R},t)\rangle \neq |\Psi_{\text{heavy}}^{(q)}(\vec{R},t)\rangle$.

Since the neglected coupling term is inversely proportional to the mass, M, of the heavy particles, its magnitude is proportional to the adiabatic parameter $(\frac{m}{M})^{\frac{1}{2}}$, which indeed dictate the limits of applicability of the BO-approximation. Additionally, the magnitude of the coupling term depends on the magnitude of the NACTs themselves and on the action

of the nabla operator dot-multiplying $\vec{\tau}_1^{(q'q)}$ (that is the momentum operator $-i\frac{\hbar}{M}\vec{\nabla}_R$) on the heavy wavefunctions. For the NACTs to be small enough, the light wavefunctions have to change as little as possible when varying the position of the heavy particles (see Eq. 2.13 and Eq. 2.14), whereas the effect of the nabla operator is the smaller, the slower the heavy particles move. The last condition connects the use of the words adiabatic and diabatic in the BO-approach to the concept of "adiabatic process" in thermodynamics, where the terminology actually comes from, where systems are said to behave "adiabatically" or "diabatically" when e.g. the temperature changes slowly or rapidly, respectively. Recalling Eqs. 2.17, one can equivalently state that $\vec{\tau}_1^{(q'q)}$ is small whenever the energy gap between two eigenvalues, $E_{\text{light}}^{(q')}(\vec{R})$ and $E_{\text{light}}^{(q)}(\vec{R})$, and subsequently also between the corresponding adiabatic potential energies, $W_{\text{light}}^{(q')}(\vec{R})$ and $W_{\text{light}}^{(q)}(\vec{R})$ (see Eqs. 2.11 and 2.17), is large enough. Therefore, the following corollary can be additionally drawn: "The slower the heavy particles move and the larger the energy gap between the adiabatic potential energies is, for which the TISE is solved, and the rest of them, the more accurate the adiabatic separation of the motions of heavy and light particles is". Thus, the BO-approximation fails whenever two eigenvalues approach each other at some set of $\vec{R}$, since the $\vec{\tau}_1^{(q'q)}$ becomes very large (infinite at singularities), even if the heavy particles move very slowly. These points of degeneracies between the adiabatic potential energies are known as avoided crossings (one dimension) or conical intersections (more than one dimension).

Whenever the BO-approximation fails, an accurate description of the system under investigation calls for the explicit treatment of the NACTs. However, their calculation is not straightforward since their dependence on the heavy particle coordinate generally presents singularities. Therefore, it is usually preferred to switch to the so called diabatic representation, in which the equation of motion for the heavy particles is formulated in a set of diabatic (light) wavefunctions, generally obtained by an orthogonal transformation in a small subset of (light) adiabatic wavefunctions, chosen such that the off-diagonal coupling term in the kinetic energy operator becomes small (ideally vanishes). As a consequence, in this new representation, the motions are not coupled via the momenta, but via the potentials, namely the potential energy matrix becomes off-diagonal. Thus, avoiding the calculation of the NACTs, one eventually has to deal with these off-diagonal elements in the new potential energy matrix, which, however, often behave smoothly. Finally, since the new diabatic set of states is obtained from a subset of the adiabatic wavefunctions, diabatic representations are also approximated, so that one speaks of "quasi-diabatic" representation [10]. This domain is usually called as going "beyond the BO-approximation" and will not be treated explicitly here. A in depth discussion can be found for example in the book of Baer [12] or in the book of Domcke *et al.* [10]. Please note that even though the Br_2@Ar system in Chap. 4 is treated in the diabatic picture, still the so called Group-Born-Oppenheimer Approximation [10] is applied in order to separate a subgroup

of adiabatic electronic potential surfaces (the ground state and three excited states) from the higher lying ones.

The Born-Oppenheimer approach presented in this section is a very powerful tool and can be applied whenever the total Hamiltonian of the system can be separated into the heavy (or slow) and light (or fast) parts and the DOFs involved satisfy the above mentioned conditions. In the particular case of molecular systems, one could even think to iteratively apply adiabatic separations in a multi-stage process with the aim of separating motions of different nature like the electronic, vibrational, rotational and translational DOFs, which may have different effective masses and/or lie in different energy scales, two of the conditions seen in the last paragraph for having negligible coupling terms. Such procedures are common in QM and can be generally repeated until the desired level is reached (if possible), which the molecular system is studied at. The study of the Cl_2@pH_2 system in Chap. 5, for example, involves electronic, vibrational, rotational and translational motions of the Cl_2 and H_2 molecules, so that such an iterative application of the Born-Oppenheimer approach is performed. Therefore, in the next section, the multi-stage adiabatic separation tool is presented.

2.2.3 AS of Nuclear from Electronic Molecular Degrees of Freedom (DOF)

The first stage of the multi-stage adiabatic separation tool is the separation of the electronic and nuclear motions. The BO-approximation is tailored to the description of molecular systems in the electronic ground state. The TISE and TDSE, in fact, can not be solved exactly for systems larger than H_2^+ (a three particle problem!). Since the ratio between the mass of a proton and an electron is about 1836, the electrons move much faster than the nuclei and it seems obvious to consider the electronic and nuclear Hamiltonians as the light (or fast) and heavy (or slow) Hamiltonians of the adiabatic separation, respectively

$$\hat{\mathbf{H}}_{\text{heavy}} = \hat{\mathbf{H}}_{\text{nuc}}(\vec{\nabla}_{nuc}, \vec{R}_{nuc}) \ , \tag{2.19}$$

$$\hat{\mathbf{H}}_{\text{light}} = \hat{\mathbf{H}}_{\text{el}}(\vec{\nabla}_{el}, \vec{R}_{el}; \vec{R}_{nuc}) \ , \tag{2.20}$$

$$\hat{\mathbf{H}}_{\text{tot}} = \hat{\mathbf{H}}_{\text{mol}}(\vec{\nabla}_{nuc}, \vec{R}_{nuc}, \vec{\nabla}_{el}, \vec{R}_{el}) = \hat{\mathbf{H}}_{\text{heavy}} + \hat{\mathbf{H}}_{\text{light}} \ , \tag{2.21}$$

where $\vec{R}_{nuc}$ and $\vec{R}_{el}$ are the coordinates of the nuclei($= nuc$) and of the electrons($= el$), respectively, and $\vec{\nabla}_{nuc}$ and $\vec{\nabla}_{el}$ are the corresponding gradient vectors [3]. Consider a molecule composed of N_{nuc} nuclei with masses M_k, momenta $\vec{P}_k$ and nuclear charges $Z_k e$ at Cartesian coordinates $\vec{R}_{nuc,k}$, with $k = 1, ..., N_{\text{nuc}}$ surrounded by n_{el} electrons with masses m_e, momenta $\vec{p_j}$ and charge e at Cartesian coordinates $\vec{R}_{el,j}$, with $j = 1, ..., n_{\text{el}}$. The light

[3] Please note that from now on in order to keep the notation compact, the gradient vectors will carry a subscript indicating only the kind of Degree Of Freedom (DOF) involved, $\vec{\Delta}_{DOF}$, instead of $\vec{\Delta}_{R_{DOF}}$

electronic and heavy nuclear Hamiltonians are, respectively

$$\hat{\mathbf{H}}_{\mathrm{nuc}}(\vec{\nabla}_{nuc}, \vec{R}_{nuc}) = \hat{\mathbf{T}}_{\mathrm{nuc}}(\vec{\nabla}_{nuc}) + \hat{\mathbf{V}}_{\mathrm{nuc,nuc}}(\vec{R}_{nuc}) \ , \tag{2.22}$$

$$\hat{\mathbf{H}}_{\mathrm{el}}(\vec{\nabla}_{el}, \vec{R}_{el}; \vec{R}_{nuc}) = \hat{\mathbf{T}}_{\mathrm{el}}(\vec{\nabla}_{el}) + \hat{\mathbf{V}}_{\mathrm{el,el}}(\vec{R}_{el}; \vec{R}_{nuc}) + \hat{\mathbf{V}}_{\mathrm{el,nuc}}(\vec{R}_{el}; \vec{R}_{nuc}) \ , \tag{2.23}$$

with

$$\hat{\mathbf{T}}_{\mathrm{nuc}} = \sum_{k=1}^{N_{\mathrm{nuc}}} \frac{\vec{P}_k^2}{2M_k} \ , \tag{2.24}$$

$$\hat{\mathbf{V}}_{\mathrm{nuc,nuc}} = \sum_{k<l}^{N_{\mathrm{nuc}}} \frac{Z_k Z_l e^2}{|\vec{R}_{nuc,k} - \vec{R}_{nuc,l}|} \ , \tag{2.25}$$

$$\hat{\mathbf{T}}_{\mathrm{el}} = \sum_{j=1}^{n_{\mathrm{el}}} \frac{\vec{p}_j^2}{2m_e} \ , \tag{2.26}$$

$$\hat{\mathbf{V}}_{\mathrm{el,el}} = \sum_{i<j}^{n_{\mathrm{el}}} \frac{e^2}{|\vec{r}_{el,i} - \vec{r}_{el,j}|} \ , \tag{2.27}$$

$$\hat{\mathbf{V}}_{\mathrm{el,nuc}} = -\sum_{k=1}^{N_{\mathrm{nuc}}} \sum_{j=1}^{n_{\mathrm{el}}} \frac{Z_k e^2}{|\vec{r}_{el,j} - \vec{R}_{nuc,k}|} \ . \tag{2.28}$$

By following the adiabatic separation procedure, the total wavefunctions will be now expanded in the electronic wavefunctions

$$|\Psi_{\mathrm{tot}}(\vec{R}_{nuc}, \vec{R}_{el}, t)\rangle = \sum_{n}^{\infty} |\Psi_{\mathrm{nuc}}^{(n)}(\vec{R}_{nuc}, t)\rangle \times |\Psi_{\mathrm{el}}^{(n)}(\vec{R}_{el}; \vec{R}_{nuc})\rangle \ , \tag{2.29}$$

where n is the first or principal or main quantum number, not to be confused with the total number of electrons in the system, n_{el} [4]. Similarly, the TISE for the electronic part is:

$$(\hat{\mathbf{H}}_{\mathrm{el}}(\vec{\nabla}_{el}, \vec{R}_{el}; \vec{R}_{nuc}) - E_{\mathrm{el}}^{(n)}(\vec{R}_{nuc}))|\Psi_{\mathrm{el}}^{(n)}(\vec{R}_{el}; \vec{R}_{nuc})\rangle = 0 \ , \tag{2.30}$$

where, the eigenvalues, $E_{\mathrm{el}}^{(n)}(\vec{R}_{nuc})$, are obtained by multiplying Eq. 2.30 by $\langle\Psi_{\mathrm{el}}^{(n)}(\vec{R}_{el}; \vec{R}_{nuc})|$, which means to average the electronic Hamiltonian with respect to the electronic wavefunctions. The electronic adiabatic energies $E_{\mathrm{el}}^{(n)}(\vec{R}_{nuc})$ and the nuclear repulsion

[4] Please note that in this and in the next sections the BO-expansion is always presented in its time-dependent form and that in the case of the TISE, one just has to drop the time-dependence.

term, $\hat{\mathbf{V}}_{\mathrm{nuc,nuc}}(\vec{R}_{nuc})$, together form the potential energy surface (PES) of the molecular system along the nuclear coordinates, $\vec{R}_{nuc}$, namely:

$$W_{\mathrm{el}}^{(n)}(\vec{R}_{nuc}) = E_{\mathrm{el}}^{(n)}(\vec{R}_{nuc}) + \hat{\mathbf{V}}_{\mathrm{nuc,nuc}}(\vec{R}_{nuc}) \ . \tag{2.31}$$

Finally, the coupled TISE and TDSE for the nuclear Degree Of Freedom (DOF) reads

$$\begin{aligned} \left.\begin{array}{l} E_{\mathrm{nuc}}^{(n)}|\Psi_{\mathrm{nuc}}^{(n)}(\vec{R}_{nuc})\rangle \\ i\hbar\frac{\partial}{\partial t}|\Psi_{\mathrm{nuc}}^{(n)}(\vec{R}_{nuc},t)\rangle \end{array}\right\} &= \sum_{n'=0}^{\infty}\Bigg[-\frac{\hbar^2}{2M}\Delta_{nuc}\ \delta_{n'n} + W_{\mathrm{el}}^{(n')}(\vec{R}_{nuc})\ \delta_{n'n} - \\ &- \frac{\hbar^2}{2M}\left(2\vec{\tau}_1^{(n'n)}\cdot\vec{\nabla}_{nuc} + \vec{\tau}_2^{(n'n)}\right)\Bigg] \left\{\begin{array}{l} |\Psi_{\mathrm{nuc}}^{(n')}(\vec{R}_{nuc})\rangle \\ |\Psi_{\mathrm{nuc}}^{(n')}(\vec{R}_{nuc},t)\rangle \end{array}\right. \end{aligned} \tag{2.32}$$

where the first two terms in square brackets are diagonal matrices describing the kinetic energy of the nuclei and the PES governing their dynamics, respectively, while the third term is an off-diagonal matrix coupling the nuclear and electronic DOFs. By applying the BO-approximation, this latter term is neglected, which reduces the number of eigenvalues $E_{\mathrm{el}}^{(n)}(\vec{R}_{nuc})$ to be calculated from infinite to just one (or few in the Group-BO-Approximation mentioned in the previous section). Finally, the TISE and TDSE become:

$$\left.\begin{array}{l} \tilde{E}_{\mathrm{nuc}}^{(n)}|\tilde{\Psi}_{\mathrm{nuc}}^{(n)}(\vec{R}_{nuc})\rangle \\ i\hbar\frac{\partial}{\partial t}|\tilde{\Psi}_{\mathrm{nuc}}^{(n)}(\vec{R}_{nuc},t)\rangle \end{array}\right\} = \left(-\frac{\hbar^2}{2M}\Delta_{nuc} + W_{\mathrm{el}}^{(n)}(\vec{R}_{nuc})\right)\left\{\begin{array}{l} |\tilde{\Psi}_{\mathrm{nuc}}^{(n)}(\vec{R}_{nuc})\rangle \\ |\tilde{\Psi}_{\mathrm{nuc}}^{(n)}(\vec{R}_{nuc},t)\rangle \end{array}\right. , \tag{2.33}$$

where the motions of nuclei and electrons are now decoupled from each other, but, due to the adiabatic approximation, the eigenvalues $\tilde{E}_{\mathrm{nuc}}^{(n)}$ are different from $E_{\mathrm{nuc}}^{(n)}$ in Eq. 2.32. The same applies to the wavefunctions, i.e. $|\tilde{\Psi}_{\mathrm{nuc}}^{(n)}(\vec{R}_{nuc})\rangle \neq |\Psi_{\mathrm{nuc}}^{(n)}(\vec{R}_{nuc})\rangle$ and $|\tilde{\Psi}_{\mathrm{nuc}}^{(n)}(\vec{R}_{nuc},t)\rangle \neq |\Psi_{\mathrm{nuc}}^{(n)}(\vec{R}_{nuc},t)\rangle$.

The discussion about the validity of the BO-approximation in Sec. 2.2.2 is now transferred to the adiabatic separation of the electronic and nuclear DOFs. In this case, in fact, the adiabatical parameter appearing as a prefactor in the coupling term in Eq. 2.32 is often small enough to decouple them safely (for the hydrogen atom, for instance, this ratio is approximately $(\frac{1}{1822})^{\frac{1}{2}}$). Additionally, since the magnitude of the coupling term is directly proportional both to the effect of the nabla operator $\vec{\nabla}_{nuc}$ acting on the nuclear wavefunction and to the magnitude of the NACTs $\vec{\tau}_1^{(n'n)}$ and $\vec{\tau}_2^{(n'n)}$, the BO-approximation is the more accurate, the slower the nuclei move and the smaller the NACTs are. This last condition is satisfied when the electronic wavefunction does not change dramatically, during the motion of the nuclei, or, equivalently, if the energy difference between two PESs, n and n', is large enough. This is shown in the next three equations:

$$
\begin{aligned}
\vec{\tau}_1^{(n'n)}(\vec{R}_{nuc}) &= \langle \Psi_{\mathrm{el}}^{(n')}(\vec{R}_{el};\vec{R}_{nuc})|\vec{\nabla}_{nuc}|\Psi_{\mathrm{el}}^{(n)}(\vec{R}_{el};\vec{R}_{nuc})\rangle_{el} \ , \\
\vec{\tau}_1^{(n'n)}(\vec{R}_{nuc}) &= \frac{\langle \Psi_{\mathrm{el}}^{(n')}(\vec{R}_{el};\vec{R}_{nuc})|\left(\vec{\nabla}_{nuc}\hat{\mathbf{H}}_{\mathrm{el}}(\vec{\nabla}_{el},\vec{R}_{el};\vec{R}_{nuc})\right)|\Psi_{\mathrm{el}}^{(n)}(\vec{R}_{el};\vec{R}_{nuc})\rangle_{el}}{E_{\mathrm{el}}^{(n)}(\vec{R}_{nuc}) - E_{\mathrm{el}}^{(n')}(\vec{R}_{nuc})} \ , \\
\vec{\tau}_2^{(n'n)}(\vec{R}_{nuc}) &= \langle \Psi_{\mathrm{el}}^{(n')}(\vec{R}_{el};\vec{R}_{nuc})|\Delta_{nuc}|\Psi_{\mathrm{el}}^{(n)}(\vec{R}_{el};\vec{R}_{nuc})\rangle_{el} \ . \qquad (2.34)
\end{aligned}
$$

In turn, the faster the nuclei move and/or the bigger the NACTs are, the less accurate Eq. 2.33 will be, implying the failure of the BO-approximation. Thus, on the one hand, the BO-approximation critically fails whenever two or more PESs approach one another forming the so-called avoided crossing (1 dimension) or conical intersection (more than 1 dimension). In those cases, in fact, the NACTs become very large (infinite at the contact points), so that the BO-approximation fails even if the nuclei move slowly. On the other hand, although the energy gap between two adiabatic potentials may be large enough, the BO-approximation might still fail if the heavy nuclei move too fast.

The failure of the BO-approximation was found for more and more systems during the last decades, but nevertheless this approximation and the underlying idea have been a milestone in the theory of molecules, basic to all molecular QM and remains therefore the reference to which we compare and in term of which we discuss different quantum systems [10, 11].

The separation of electronic and nuclear DOFs is just the first stage of the multi-stage AS tool mentioned above. Since in the next section the nuclear DOFs will be further separated, the counter m indicating the number of consecutive ASs applied is introduced. The consecutive ASs performed are depicted in the tree diagram in Fig. 2.1 together with the counter m, the quantum numbers and the corresponding nomenclature used at each stage. Eventually, the positions of the three molecular systems investigated along this thesis in the tree diagram are also indicated. The Br_2@Ar system investigated in Chap. 4, is treated at the present stage, $m = 1$, of the multi-stage adiabatic separation. The model involves four PESs (Group-BO-Approximation), but actually, since the NACTs between them are treated explicitly, we even go beyond the BO-approximation. The PES were obtained by Borowski [17] by using the Diatomics-In-Molecule (DIM), which is a suitable model for the calculation of electronic PESs in their diabatic picture and for the treatment of the relative diabatic nuclear equation of motion within the vibronic coupling theory. In this context the NACTs are called "vibronic couplings", since they measure the coupling between vibrational and electronic motions. In particular, after population is transferred from the electronic ground state to the first excited state via an electromagnetic field, the

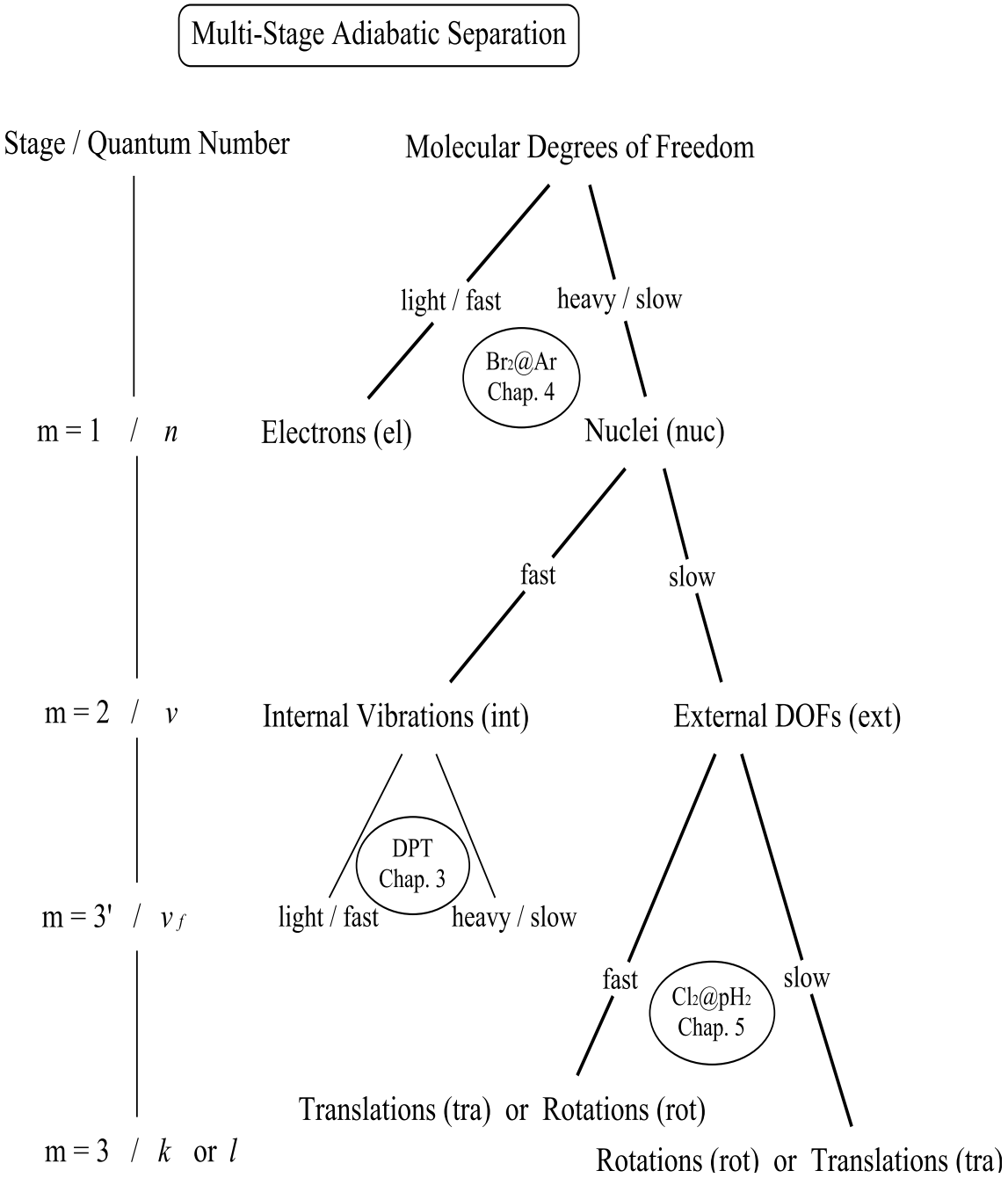

Figure 2.1: Tree diagram of the multi-stage adiabatic separation applied along the thesis. The counter m indicates the number of subsequent adiabatic separations. In Chap. 4 the Br_2@Ar system is treated at the stage, $m = 1$ (actually we go beyond Born-Oppenheimer). In Chap. 5 the Cl_2@pH_2 system is studied at the stage, $m = 3$. In Chap. 3 the investigation of the Double Proton Transfer (DPT) also involve three subsequent ASs, but the stage is indicated as $m = 3'$, since the path in the tree diagram differs from the path for the Cl_2@pH_2 system and, moreover, the vibrationally-fast DOFs are treated in a time-dependent picture. Quantum numbers and labels used along the thesis are also reported.

role of two vibronic couplings in the non-adiabatic population transfer (predissociation) between the first and two additional electronically excited PESs is investigated.

It is also mentioned here that the PES for the DPT is not calculated by solving the TISE for the electronic part in Eq. 2.30. Instead, the ground state adiabatic PES is an analytical function fitted to both experimental and *ab-initio* parameters from the literature. Non-adiabatic transitions to electronically excited states and NACTs are completely neglected, even if this approximation is very critical.

2.2.4 AS of External and Internal Molecular DOFs

So far the general adiabatic separation between the DOFs of heavy (or slow) and light (or fast) particles has been applied to electronic and nuclear motions. The subsequent stage, $m = 2$, involves the AS of external and internal DOFs (see Fig. 2.1), where the former ones are the three translational and two rotational motions (three in the more general cases of non linear molecules), which are indeed defined with respect to an external coordinate system of reference (space-fixed frame), whereas the latter ones are the $3N-5$ ($3N-6$ for non linear molecules) vibrational motions, which are indeed defined with respect to an internal coordinate system of reference with origin at the center of mass (COM) of the molecule (body-fixed frame). In particular, it should be verified whether the adiabatic parameter is small enough to separate internal and external DOFs and whether the molecules involved are vibrating faster enough than translating or rotating, that is whether the Cl_2, Br_2 and H_2 molecules possess higher vibrational than translational or rotational frequencies. The comparison of rotational and vibrational effective masses is difficult, since rotations imply the moment of inertia of the molecules instead of just their masses. The moment of inertia is defined in general as $I = \sum_p^{n_p} m_p r_p^2$, where n_p is the total number of particles and m_p and r_p are the mass of the particle and its distance from the rotational axis, which goes through the COM of the system, respectively. Since the moment of inertia is directly proportional to both these quantities, the heavier and/or the more extended a molecular system is, the greater the momentum of inertia will be and the better will vibrational and rotational DOFs separate. Translational and vibrational effective masses are, in contrast, easily compared. In the case of linear homonuclear diatomic molecules, the vibrational effective masses corresponds to the reduced masses $\mu_{X_2} = \frac{m_X}{2}$, that is half of the mass of the atom X, and the effective mass of the translational motions is the total mass of the molecule, $M_{X_2} = 2m_X$. As a consequence, the adiabatic parameter when separating vibrational and translational DOFs is $\frac{1}{2}$. Since all linear homonuclear molecules present the same adiabatic parameter, the separation of vibrational and translational motions is principally based on different frequency scales (fast vs slow) rather than on mass differences (light vs heavy), see also Fig. 2.1. For more general molecular systems, different reduced masses allow also for an AS of vibrations of light and heavy nuclei [18–20], as mentioned above.

In principle, the procedure in the first stage, where the motions of electrons and nuclei were separated, is now repeated by splitting the nuclear coordinates into a set of external and internal coordinates, $\vec{R}_{nuc} = \{\vec{R}_{ext}, \vec{R}_{int}\}$, assigned to the heavy and light particle Hamiltonian, respectively.

$$\hat{\mathbf{H}}_{\text{tot}} = \hat{\mathbf{H}}_{\text{nuc}}(\vec{\nabla}_{nuc}, \vec{R}_{nuc}) = \hat{\mathbf{H}}_{\text{ext}}(\vec{\nabla}_{ext}, \vec{R}_{ext}) + \hat{\mathbf{H}}_{\text{int}}(\vec{\nabla}_{int}, \vec{R}_{int}; \vec{R}_{ext}) \quad (2.35)$$

$$\hat{\mathbf{H}}_{\text{heavy}} = \hat{\mathbf{H}}_{\text{ext}}(\vec{\nabla}_{ext}, \vec{R}_{ext}) = \hat{\mathbf{T}}_{\text{ext}}(\vec{\nabla}_{ext}) + \hat{\mathbf{V}}_{\text{ext}}(\vec{R}_{ext}) \ , \quad (2.36)$$

$$\hat{\mathbf{H}}_{\text{light}} = \hat{\mathbf{H}}_{\text{int}}(\vec{\nabla}_{int}, \vec{R}_{int}; \vec{R}_{ext}) = \hat{\mathbf{T}}_{\text{int}}(\vec{\nabla}_{int}) + \hat{\mathbf{V}}_{\text{int}}(\vec{R}_{int}; \vec{R}_{ext}) \ . \quad (2.37)$$

With the purpose of giving an explicit expression for the corresponding kinetic and potential energy operators in terms of linear diatomic molecules, the very general external coordinates are split into translational and rotational ones. Whereas the former ones are still expressed in Cartesian coordinates, $\vec{R}_{tra}$, describing the COM position of the molecules, the latter ones are better expressed in spherical coordinates, r, θ and ϕ, describing the rotations around the COM. The Laplacian in the new coordinates becomes

$$\Delta_{rot-vib} = \frac{1}{r^2}\nabla_r\left(r^2\nabla_r\right) + \frac{1}{r^2\sin\theta}\nabla_\theta\left(\sin\theta\nabla_\theta\right) + \frac{1}{r^2\sin^2\theta}\Delta_\varphi \ , \quad (2.38)$$

where, since r refers to the internuclear bond distance, one has

$$\Delta_{int} = \frac{1}{r^2}\nabla_r\left(r^2\nabla_r\right) \quad (2.39)$$

$$\Delta_{rot} = \frac{1}{r^2\sin\theta}\nabla_\theta\left(\sin\theta\nabla_\theta\right) + \frac{1}{r^2\sin^2\theta}\Delta_\varphi \ . \quad (2.40)$$

Even though Eq. 2.40 shows a dependence of the rotational operator on the internuclear distance, in the present work the molecular bonds will be considered fixed at their equilibrium position, r_{eq}. For the internal DOFs, this implies a further classical approximation (on top of the adiabatic separation otherwise the right-hand side of Eq. 2.39 would vanish), i.e. an infinitely narrow delta distribution function centered at the ground state vibrational equilibrium distance is used instead of the quantum mechanical distribution. For the rotational DOFs, it implies neglecting the centrifugal distortion of the bond due to rotation. Finally, the external and internal kinetic energy operators are

$$\hat{\mathbf{T}}_{\text{ext}}(\vec{\nabla}_{ext}) = -\frac{\hbar^2}{2M}\left[\Delta_{tra} + \frac{1}{r_{eq}^2\sin\theta}\nabla_\theta\left(\sin\theta\nabla_\theta\right) + \frac{1}{r_{eq}^2\sin^2\theta}\Delta_\varphi\right] \ , \quad (2.41)$$

$$\hat{\mathbf{T}}_{\text{int}}(\vec{\nabla}_{int}) = -\frac{\hbar^2}{2\mu}\Delta_{int} \ , \quad (2.42)$$

where $\vec{R}_{ext} = \{\vec{R}_{tra}, \theta, \varphi\}$ and $\vec{\nabla}_{ext} = \{\vec{\nabla}_{tra}, \nabla_\theta, \nabla_\varphi\}$. Moreover, μ is the reduced mass of the molecule and $\vec{\nabla}_{int}$ is a $(3N-5)$-dimensional vector ($(3N-6)$-dimensional in the general case of polyatomic molecules). Regarding the potential energy operators in Eqs. 2.36 and 2.37, $\hat{\mathbf{V}}_{\text{ext}}(\vec{R}_{ext})$ is the PES obtained by solving the respective light TISE of the present AS stage $m = 2$, whereas $\hat{\mathbf{V}}_{\text{int}}(\vec{R}_{int})$ is the PES obtained by solving the respective heavy TISE from the previous AS stage $m = 1$, that is

$$\hat{\mathbf{V}}_{\text{ext}}(\vec{R}_{ext}) = \quad W_{\text{int}}^{(n,v)}(\vec{R}_{ext}) \quad = W_{\text{int}}^{(n,v)}(\vec{R}_{tra}, \theta, \varphi) \ , \tag{2.43}$$

$$\hat{\mathbf{V}}_{\text{int}}(\vec{R}_{int}; \vec{R}_{ext}) = \quad W_{\text{nuc}}^{(n)}(\vec{R}_{nuc}) \quad = W_{\text{nuc}}^{(n)}(\vec{R}_{int}; \vec{R}_{tra}, \theta, \varphi) \ , \tag{2.44}$$

It is worth to note at this point, that the potential, $W_{\text{el}}^{(n)}(\vec{R}_{nuc})$, governing the dynamics of the heavy particles, in the first stage $m = 1$, is obtained by averaging the light particle Hamiltonian, $\hat{\mathbf{H}}_{\text{el}}(\vec{\nabla}_{el}, \vec{R}_{el}; \vec{R}_{nuc})$, with respect to the light particle wavefunctions, $\Psi_{\text{el}}^{(n)}(\vec{R}_{el}; \vec{R}_{nuc})$; in turn the potential, $W_{\text{nuc}}^{(n)}(\vec{R}_{nuc}) = W_{\text{nuc}}^{(n)}(\vec{R}_{tra}, \theta, \varphi)$, governing the light particle dynamics of this stage $m = 2$ are the eigenvalues, $E_{\text{nuc}}^{(n)}(\vec{R}_{nuc})$ obtained by solving the heavy TISE in Eq. 2.33 for the heavy Hamiltonian, $\hat{\mathbf{H}}_{\text{nuc}}(\vec{\nabla}_{nuc}, \vec{R}_{nuc})$, with respect to the heavy particle wavefunctions, $\Psi_{\text{nuc}}^{(n)}(\vec{R}_{nuc})$ of stage $m = 1$. In close analogy, the potential, $W_{\text{int}}^{(n,v)}(\vec{R}_{tra}, \theta, \varphi)$, governing the dynamics of the heavy particles in this stage $m = 2$, is obtained by averaging $\hat{\mathbf{H}}_{\text{int}}(\vec{\nabla}_{int}, \vec{R}_{int}; \vec{R}_{ext})$ with respect to the vibrational wavefunctions and so on. Please refer to Fig. 2.1 for an overview of which DOFs are assigned to the light (or fast) and heavy (or slow) parts of the system from one stage to the next one. Please note also that the iterative application of the adiabatic separations causes the list of quantum numbers to increase in order to completely specify an adiabatic state.

In order to solve the TISE for the vibrational Hamiltonian, the nuclear wavefunction, $\tilde{\Psi}_{\text{nuc}}^{(n)}(\vec{R}_{nuc})$, is now expanded in the internal wavefunctions, $\Psi_{\text{int}}^{(n,v)}(\vec{R}_{int}; \vec{R}_{ext})$

$$|\tilde{\Psi}_{\text{nuc}}^{(n)}(\vec{R}_{nuc}, t)\rangle = \sum_v |\Psi_{\text{ext}}^{(n,\ v)}(\vec{R}_{ext}, t)\rangle \times |\Psi_{\text{int}}^{(n,\ v)}(\vec{R}_{int}; \vec{R}_{ext})\rangle \ , \tag{2.45}$$

with v being a new set of $(3N_{nuc} - 5)$ vibrational quantum numbers [5].

Finally, the internal TISE reads

[5] Along this work the electronic adiabatic separation in stage $m = 1$ is always assumed to be valid, i.e. we consider only the $n = 0$ electronic ground state and forget about vibrational, rotational and translational NACTs to the $n > 0$ excited electronic states.

$$(\hat{\mathbf{H}}_{\text{int}}(\vec{\nabla}_{int}, \vec{R}_{int}; \vec{R}_{ext}) - E_{\text{int}}^{(n,v)}(\vec{R}_{ext}))|\Psi_{\text{int}}^{(n,v)}(\vec{R}_{int}; \vec{R}_{ext})\rangle = 0 \ , \tag{2.46}$$

which is solved by multiplying it by $\langle\Psi_{\text{int}}^{(n,v)}(\vec{R}_{int}; \vec{R}_{ext})|$, namely by averaging the internal Hamiltonian with respect to the internal wavefunctions. The resulting eigenvalues, $E_{\text{int}}^{(n,v)}(\vec{R}_{ext})$, finally correspond to the vibrational adiabatic PES, $W_{\text{int}}^{(n,v)}(\vec{R}_{ext})$, of the electronic state n and vibrational states v, governing the external DOFs, namely translations and rotations.

It is briefly mentioned that in the particular case of diatomic molecules, the nuclear PES, $W_{\text{nuc}}^{(n)}(\vec{R}_{int}; \vec{R}_{ext})$, can be approximated by the simple Morse oscillator model, which also includes anharmonicity effects. The Morse potential is defined as

$$M(r) = D_e(1 - e^{-a(r-r_e)})^2 \ , \tag{2.47}$$

where D_e is the dissociation energy, a is a range parameter controlling the width of the potential, and r_{eq} the equilibrium bond distance of the molecule considered, and the resulting vibrational eigenvalues are

$$E^{(n,v)} = \hbar\omega_e\left(v + \frac{1}{2}\right) - \hbar\omega_e x_e\left(v + \frac{1}{2}\right)^2 \ , \tag{2.48}$$

where $\omega_e = a\sqrt{\frac{2D_e}{\mu}}$ is the harmonic vibrational frequency and $\omega_e x_e = \frac{\hbar\omega_e^2}{4D_e}$ is the anharmonicity constant.

The coupled TISE and TDSE for the external DOFs finally reads

$$\left.\begin{array}{l} E_{\text{ext}}^{(n,v)}|\Psi_{\text{ext}}^{(n,v)}(\vec{R}_{ext})\rangle \\ i\hbar\frac{\partial}{\partial t}|\Psi_{\text{ext}}^{(n,v)}(\vec{R}_{ext}, t)\rangle \end{array}\right\} = \sum_{v'}^{\infty} -\frac{\hbar^2}{2M}\left[\Delta_{tra} + \frac{1}{r_{eq}^2}\left(\Delta_\theta + \cot\theta\ \nabla_\theta + \frac{1}{\sin^2\theta}\Delta_\varphi\right)\right]\ \delta_{v'v} +$$
$$+ \ W_{\text{int}}^{(n,v')}(\vec{R}_{ext})\ \delta_{v'v} + C\left\{\begin{array}{l} |\Psi_{\text{ext}}^{(n,v')}(\vec{R}_{ext})\rangle \\ |\Psi_{\text{ext}}^{(n,v')}(\vec{R}_{ext}, t)\rangle \end{array}\right. \ , \tag{2.49}$$

with C being the coupling term

$$C = -\frac{\hbar^2}{2M}\left[2\vec{\tau}_{1,tra}^{(n,\ v'v)}\cdot\vec{\nabla}_{tra}+\vec{\tau}_{2,tra}^{(n,\ v'v)}+\frac{1}{r_{eq}^2}\left(2\vec{\tau}_{1,\theta}^{(n,\ v'v)}\cdot\nabla_\theta+\vec{\tau}_{2,\theta}^{(n,\ v'v)}+\right.\right.$$
$$\left.\left.+\ \cot\theta\ \vec{\tau}_{1,\theta}^{(n,\ v'v)}\right)+\frac{1}{r_{eq}^2\sin^2\theta}\left(2\vec{\tau}_{1,\varphi}^{(n,\ v'v)}\cdot\Delta_\varphi+\vec{\tau}_{2,\varphi}^{(n,\ v'v)}\right)\right]\ . \tag{2.50}$$

The parts in Eqs. 2.49 and 2.50 referring to the translational DOFs are very similar to the corresponding equations in the previous sections. The same is true for the terms referring to the coordinate φ, except for the prefactor, $\frac{1}{r_{eq}^2\sin^2\theta}$, multiplying them. The parts referring to the polar angle θ, in contrast, present two new terms, that is the diagonal and off-diagonal matrices $\cot\theta\ \nabla_\theta$ and $\cot\theta\ \vec{\tau}_{1,\theta}^{(n,v'v)}$, respectively.

Within the adiabatic approximation, the coupling term C in Eq. 2.50 is neglected and Eq. 2.49 simplifies to

$$\left.\begin{array}{l}\tilde{E}_{\rm ext}^{(n,v)}|\tilde{\Psi}_{\rm ext}^{(n,v)}(\vec{R}_{ext})\rangle\\ i\hbar\frac{\partial}{\partial t}|\tilde{\Psi}_{\rm ext}^{(n,v)}(\vec{R}_{ext},t)\rangle\end{array}\right\} = -\frac{\hbar^2}{2M}\left[\Delta_{tra}+\frac{1}{r_{eq}^2}\left(\Delta_\theta+\cot\theta\ \nabla_\theta+\frac{1}{\sin^2\theta}\Delta_\varphi\right)\right]+$$
$$+\ W_{\rm int}^{(n,v)}(\vec{R}_{ext}))\left\{\begin{array}{l}|\tilde{\Psi}_{\rm ext}^{(n,v)}(\vec{R}_{ext})\rangle\\ |\tilde{\Psi}_{\rm ext}^{(n,v)}(\vec{R}_{ext},t)\rangle\end{array}\right. , \tag{2.51}$$

where the motions of external and internal DOFs are now decoupled from each other, but, due to the adiabatic approximation, the eigenvalues $\tilde{E}_{\rm ext}^{(n,v)}$ are different from $E_{\rm ext}^{(n,v)}$ in Eq. 2.49. The same applies to the wavefunctions, i.e. $|\tilde{\Psi}_{\rm ext}^{(n,v)}(\vec{R}_{ext})\rangle \neq |\Psi_{\rm ext}^{(n,v)}(\vec{R}_{ext})\rangle$ and $|\tilde{\Psi}_{\rm ext}^{(n,v)}(\vec{R}_{ext},t)\rangle \neq |\Psi_{\rm ext}^{(n,v)}(\vec{R}_{ext},t)\rangle$.

The neglected NACTs are expressed in the following equations

$$\vec{\tau}_{1,a}^{(n,\ v'v)}(\vec{R}_{ext}) = \langle\Psi_{\rm int}^{(n,v')}(\vec{R}_{int};\vec{R}_{ext})|\vec{\nabla}_a|\Psi_{\rm int}^{(n,v)}(\vec{R}_{int};\vec{R}_{ext})\rangle_{int}\ ,$$

$$\vec{\tau}_{1,a}^{(n,\ v'v)}(\vec{R}_{ext}) = \frac{\langle\Psi_{\rm int}^{(n,v')}(\vec{R}_{int};\vec{R}_{ext})|\left(\vec{\nabla}_a\hat{\mathbf{H}}_{\rm int}(\vec{\nabla}_{int},\vec{R}_{int};\vec{R}_{ext})\right)|\Psi_{\rm int}^{(n,v)}(\vec{R}_{int};\vec{R}_{ext})\rangle_{int}}{W_{\rm int}^{(n,v)}(\vec{R}_{ext})-W_{\rm int}^{(n,v')}(\vec{R}_{ext})}\ ,$$

$$\vec{\tau}_{2,a}^{(n,\ v'v)}(\vec{R}_{ext}) = \langle\Psi_{\rm int}^{(n,v')}(\vec{R}_{int};\vec{R}_{ext})|\Delta_a|\Psi_{\rm int}^{(n,v)}(\vec{R}_{int};\vec{R}_{ext})\rangle_{int}\ , \tag{2.52}$$

where, by cyclically substituting the subscript a by tra, θ and φ, the different NACTs in Eq. 2.50 are obtained.

Similarly to the previous stages of the ASs, the magnitude of the coupling term in Eq. 2.50 is directly proportional to the adiabatic parameter, which mainly dictates the applicability of the BO-approximation. Additionally, two more factors influence the magnitude of the coupling term, the velocity at which the molecules rotate and translate, which is expressed by the nabla operators, $\vec{\nabla}_{tra}$, ∇_θ and ∇_φ acting on the external wavefunction, and the magnitude of the NACTs, themselves, which depends on how much the internal wavefunction, $\Psi_{\text{int}}^{(n,v)}(\vec{R}_{int};\vec{R}_{ext})$, change when varying the parameters $\vec{R}_{tra}$ or θ or φ (see Eqs. 2.52 and 2.52).

These two factors becomes important for example in molecular collisions, where translational and/or rotational energy is transferred to the vibrational DOFs, so that the higher the collision energies are, the higher the non-adiabatic effects will be, since under a faster motion (consequence of an higher frequency/energy) of the external DOFs, the vibrational (internal) wavefunctions undergo drastic changes.

A second equivalent way to interpret the first order NACTs is shown in Eq. 2.52, that is non-adiabatic couplings are the smaller, the larger the energy gaps between the vibrational eigenstates, $W_{\text{int}}^{(n,v)}(\vec{R}_{ext})$ are. Correspondingly, if the internal vibrational motions in a molecule occur at a much higher frequency-range than the rotational and translational ones, one condition for the validity of the approximation is fulfilled. However, the adiabatic separation could still fail, if the external DOFs move too fast.

Before we continue to the next stage $m = 3$, it should be mentioned that the adiabatic separation can also be applied in order to decouple the motions of heavy (or slow) and light (or fast) vibrations within the internal DOFs, see for example [18–20]. This permits for example to combine classical and quantum dynamics simulations, by treating light/fast particles, such as hydrogen, quantum mechanically, and the heavy rest of the molecular system classically [21–23]. This is actually done in Chap. 3, where the DPT mechanism of the porphine molecule is investigated. The relative equations are not included in this chapter, since their derivation involves an extension of the Born-Oppenheimer approach to time-dependent solutions for the light (or fast) DOFs, in close analogy to the field of attosecond chemistry [24], where the nuclei are still clamped, but the electronic SE in solved in a time-dependent picture[6]. Nevertheless, three ASs are consecutively applied on the DPT system, so that in the tree diagram of Fig. 2.1 this stage is numbered $m = 3'$, where the prime serves to distinguish between the two series of ASs applied to the DPT and to the Cl_2@pH_2 systems, respectively. A new quantum number v_f is therefore also defined, which stays for vibrationally-fast DOFs.

[6] Please note that this is never foreseen for the Br_2@Ar and the Cl_2@pH_2 systems, but the multi-stage adiabatic separation tool could be generalized to include the time-dependent solution of the light or fast DOFs.

2.2.5 AS of Translational and Rotational Molecular DOFs

In the stage $m = 3$ of the multistage AS the separation of translational and rotational DOFs is presented. This stage is applied only on the Cl_2@pH_2 system treated in Chap. 5. At stage $m = 1$ electronic and nuclear DOFs have been separated. The electronic pair potentials for the Cl_2-H_2 (2D) and pH_2-pH_2 (1D) systems are obtained by means of the Quantum Chemistry methods presented later in this chapter, that is, by solving the electronic TISE in Eq. 2.30. In this case, electronic transitions will be neglected, since no electromagnetic fields are applied and, at the cryogenic temperatures considered, the system has not enough energy to reach the electronic excited states, which lie energetically well above. At stage $m = 2$ the nuclear ones are separated into internal (vibrational) and external (rotational and translational) DOFs. The AS of translations and rotations is, in general, more severe, since the conditions for its validity are not always fulfilled by molecular systems. Translational motions of the molecules around their nominal position in the crystal, could for example take place at similar frequency as rotations, [7] so that assignment of rotational and translational DOFs to the fast and or slow parts of the Hamiltonian has to be considered case by case. Therefore, differently from the previous sections, both cases will be considered. In the worse case, if rotations and translation can not be treated separately, they must be treated simultaneously.

Let us split the external coordinates in rotational and translational ones, $\vec{R}_{ext} = \{\vec{R}_{tra}, \theta, \varphi\}$, and assign first the rotations to the light Hamiltonian. Hence,

$$\hat{\mathbf{H}}_{\text{tot}} = \hat{\mathbf{H}}_{\text{ext}}(\vec{\nabla}_{ext}, \vec{R}_{ext}) = \hat{\mathbf{H}}_{\text{tra}}(\vec{\nabla}_{tra}, \vec{R}_{tra}) + \hat{\mathbf{H}}_{\text{rot}}(\nabla_\theta, \nabla_\varphi, \theta, \varphi; \vec{R}_{tra}) \quad (2.53)$$

$$\hat{\mathbf{H}}_{\text{heavy}} = \hat{\mathbf{H}}_{\text{tra}}(\vec{\nabla}_{tra}, \vec{R}_{tra}) = \hat{\mathbf{T}}_{\text{tra}}(\vec{\nabla}_{tra}) + \hat{\mathbf{V}}_{\text{tra}}(\vec{R}_{tra}) \ , \quad (2.54)$$

$$\hat{\mathbf{H}}_{\text{light}} = \hat{\mathbf{H}}_{\text{rot}}(\nabla_\theta, \nabla_\varphi, \theta, \varphi; \vec{R}_{tra}) = \hat{\mathbf{T}}_{\text{rot}}(\nabla_\theta, \nabla_\varphi) + \hat{\mathbf{V}}_{\text{rot}}(\theta, \varphi; \vec{R}_{tra}) \ , \quad (2.55)$$

with

$$\hat{\mathbf{T}}_{\text{tra}}(\vec{\nabla}_{tra}) = -\frac{\hbar^2}{2M}\Delta_{tra} \ , \quad (2.56)$$

$$\hat{\mathbf{V}}_{\text{tra}}(\vec{R}_{tra}) = W_{\text{rot}}^{(n,v,l)}(\vec{R}_{tra}) \ , \quad (2.57)$$

$$\hat{\mathbf{T}}_{\text{rot}}(\nabla_\theta, \nabla_\varphi) = B\left[\frac{1}{\sin\theta}\nabla_\theta\left(\sin\theta\ \nabla_\theta\right) + \frac{1}{\sin^2\theta}\Delta_\varphi\right] \ , \quad (2.58)$$

$$\hat{\mathbf{V}}_{\text{rot}}(\theta, \varphi; \vec{R}_{tra}) = W_{\text{ext}}^{(n,v)}(\vec{R}_{ext}) = W_{\text{ext}}^{(n,v)}(\theta, \varphi, \vec{R}_{tra}) \ , \quad (2.59)$$

[7] In this context, it must be also remarked that in two of the systems studied here, Br_2@Ar and Cl_2@pH_2, since the single molecules or atoms in the matrix are surrounded by the other ones, which behave as a cage around them, the translational motions will be called "external" vibrational motions, in contrast to the "internal" one, in the sense that the COM of the molecules or of the atoms is oscillating forth and back around their nominal positions.

where M is the total mass of the molecular system, $B = -\frac{\hbar^2}{2I}$ is the well-known rotational constant of the specific molecule with $I = Mr_{eq}^2$ being the moment of inertia mentioned above. Moreover, θ and φ are the same spherical coordinates as in the previous section, $W_{\text{rot}}^{(n,v,l)}(\vec{R}_{tra})$ is the rotationally adiabatic PES governing the dynamics of the translational DOFs obtained by solving the rotational TISE in Eq. 2.61 in the present stage $m = 3$ and $W_{\text{ext}}^{(n,v)}(\vec{R}_{ext}) = E_{\text{ext}}^{(n,v)}(\vec{R}_{ext})$ are the eigenvalues obtained by solving the external TISE in Eq. 2.51, that is the external PES from the previous stage with $m = 2$, governing the dynamics of the DOFs defined as "light" in this third stage with $m = 3$.

The external wavefunction, $\tilde{\Psi}_{\text{ext}}^{(n,v)}(\vec{R}_{\text{ext}})$, is now expanded in the rotational wavefunctions, $\Psi_{\text{rot}}^{(n,v,l)}(\theta, \varphi; \vec{R}_{tra})$

$$|\tilde{\Psi}_{\text{ext}}^{(n,v)}(\vec{R}_{ext}, t)\rangle = \sum_{l} |\Psi_{\text{tra}}^{(n,v,l)}(\vec{R}_{tra}, t)\rangle \times |\Psi_{\text{rot}}^{(n,v,l)}(\theta, \varphi; \vec{R}_{tra})\rangle \ , \tag{2.60}$$

where l is an index collecting the two rotational quantum numbers for linear molecules in a three dimensional Cartesian space[8].

The TISE for the rotational DOFs reads

$$(\hat{\mathbf{H}}_{\text{rot}}(\vec{\nabla}_{rot}, \theta, \varphi; \vec{R}_{tra}) - E_{\text{rot}}^{(n,v,l)}(\vec{R}_{tra}))|\Psi_{\text{rot}}^{(n,v,l)}(\theta, \varphi; \vec{R}_{tra})\rangle = 0 \ , \tag{2.61}$$

where the eigenvalues, $E_{\text{rot}}^{(n,v,l)}(\vec{R}_{tra})$ are obtained by multiplying Eq. 2.61 by $\langle\Psi_{\text{rot}}^{(n,v,l)}(\theta, \varphi; \vec{R}_{tra})|$, that is by averaging the rotational Hamiltonian with respect to the rotational wavefunctions. The rotationally adiabatic energies, $E_{\text{rot}}^{(n,v,l)}(\vec{R}_{tra})$, finally correspond to the rotational adiabatic PES, $W_{\text{rot}}^{(n,v,l)}(\vec{R}_{tra})$, of the electronic state n, vibrational state v and rotational state l governing the translational DOFs.

Finally, the coupled TISE and TDSE for the translational DOFs become

$$\left.\begin{array}{ll} E_{\text{tra}}^{(n,v,l)} & |\Psi_{\text{tra}}^{(n,v,l)}(\vec{R}_{tra})\rangle \\ i\hbar\frac{\partial}{\partial t} & |\Psi_{\text{tra}}^{(n,v,l)}(\vec{R}_{tra}, t)\rangle \end{array}\right\} = \sum_{l'=0}^{\infty} -\frac{\hbar^2}{2M}\Delta_{tra}\ \delta_{l'l} + W_{\text{rot}}^{(n,v,l')}(\vec{R}_{tra})\ \delta_{l'l} - \tag{2.62}$$

$$- \ \frac{\hbar^2}{2M}\left(2\vec{\nabla}_{tra} \cdot \vec{\tau}_1^{(n,v,l'l)} + \vec{\tau}_2^{(n,v,l'l)}\right) \left\{\begin{array}{l} |\Psi_{\text{tra}}^{(n,v,l')}(\vec{R}_{tra})\rangle \\ |\Psi_{\text{tra}}^{(n,v,l')}(\vec{R}_{tra}, t)\rangle \end{array}\right. ,$$

[8] Again it is assumed the electronic and internal adiabatic separations in the previous stages with $m = 1$ and 2, respectively, to be valid, i.e. we consider only the electronic and vibrational ground state, $n = v = 0$ and forget therefore about rotational and translational NACTs to the $v > 0$ excited vibrational states.

and neglecting the coupling part of these equations, the TISE and TDSE within the adiabatic approximation are obtained, namely

$$\left.\begin{array}{ll} \tilde{E}_{\mathrm{tra}}^{(n,v,l)} & |\tilde{\Psi}_{\mathrm{tra}}^{(n,v,l)}(\vec{R}_{tra})\rangle \\ i\hbar\frac{\partial}{\partial t} & |\tilde{\Psi}_{\mathrm{tra}}^{(n,v,l)}(\vec{R}_{tra},t)\rangle \end{array}\right\} = \hat{\mathbf{T}}_{\mathrm{tra}}(\vec{R}_{tra}) + W_{\mathrm{rot}}^{(n,v,l)}(\vec{R}_{tra})) \left\{\begin{array}{l} |\tilde{\Psi}_{\mathrm{tra}}^{(n,v,l)}(\vec{R}_{tra})\rangle \\ |\tilde{\Psi}_{\mathrm{tra}}^{(n,v,l)}(\vec{R}_{tra},t)\rangle \end{array}\right. , \quad (2.63)$$

where the motions of the translational and rotational DOFs are now decoupled from each other, but, due to the adiabatic approximation, the eigenvalues $\tilde{E}_{\mathrm{tra}}^{(n,v,l)}$ are different from $E_{\mathrm{tra}}^{(n,v,l)}$ in Eq. 2.71. The same applies to the wavefunctions, i.e. $|\tilde{\Psi}_{\mathrm{tra}}^{(n,v,l)}(\vec{R}_{tra})\rangle \neq |\Psi_{\mathrm{tra}}^{(n,v,l)}(\vec{R}_{tra})\rangle$ and $|\tilde{\Psi}_{\mathrm{tra}}^{(n,v,l)}(\vec{R}_{tra},t)\rangle \neq |\Psi_{\mathrm{tra}}^{(n,v,l)}(\vec{R}_{tra},t)\rangle$.

Let us now briefly consider the second case where the translational motions are assign to the light Hamiltonian instead. Hence, the two Hamiltonians become

$$\hat{\mathbf{H}}_{\mathrm{tot}} = \hat{\mathbf{H}}_{\mathrm{ext}}(\vec{\nabla}_{ext},\vec{R}_{ext}) = \hat{\mathbf{H}}_{\mathrm{rot}}(\nabla_\theta,\nabla_\varphi,\theta,\varphi) + \hat{\mathbf{H}}_{\mathrm{tra}}(\vec{\nabla}_{tra},\vec{R}_{tra};\theta,\varphi) \quad (2.64)$$

$$\hat{\mathbf{H}}_{\mathrm{heavy}} = \hat{\mathbf{H}}_{\mathrm{rot}}(\nabla_\theta,\nabla_\varphi,\theta,\varphi) = \hat{\mathbf{T}}_{\mathrm{rot}}(\nabla_\theta,\nabla_\varphi) + \hat{\mathbf{V}}_{\mathrm{rot}}(\theta,\varphi) \ , \quad (2.65)$$

$$\hat{\mathbf{H}}_{\mathrm{light}} = \hat{\mathbf{H}}_{\mathrm{tra}}(\vec{\nabla}_{tra},\vec{R}_{tra};\theta,\varphi) = \hat{\mathbf{T}}_{\mathrm{tra}}(\vec{\nabla}_{tra}) + \hat{\mathbf{V}}_{\mathrm{tra}}(\vec{R}_{tra};\theta,\varphi) \ , \quad (2.66)$$

where the kinetic energy operators are those of Eqs. 2.59 and 2.57, but the potential energy operators are

$$\hat{\mathbf{V}}_{\mathrm{rot}}(\theta,\varphi) = W_{\mathrm{tra}}^{(n,v,k)}(\theta,\varphi) \ , \quad (2.67)$$

$$\hat{\mathbf{V}}_{\mathrm{tra}}(\vec{R}_{tra};\theta,\varphi) = W_{\mathrm{ext}}^{(n,v)}(\vec{R}_{ext}) \ , \quad (2.68)$$

with $W_{\mathrm{tra}}^{(n,v,k)}(\theta,\varphi)$ being the translationally adiabatic PES governing the dynamics of the rotational DOFs obtained by solving the translational TISE in Eq. 2.70 in the present stage $m = 3$. With this aim, the external wavefunction, $\tilde{\Psi}_{\mathrm{ext}}^{(n,v)}(\vec{R}_{ext})$ is expanded this time in the translational wavefunctions, $\Psi_{\mathrm{tra}}^{(n,v,k)}(\vec{R}_{tra};\theta,\varphi)$

$$|\tilde{\Psi}_{\mathrm{ext}}^{(n,v)}(\vec{R}_{\mathrm{ext}},t)\rangle = \sum_k |\Psi_{\mathrm{rot}}^{(n,v,k)}(\theta,\varphi,t)\rangle \times |\Psi_{\mathrm{tra}}^{(n,v,k)}(\vec{R}_{tra};\theta,\varphi)\rangle \ , \quad (2.69)$$

where k is an index, which collects the three new translational quantum numbers for a molecule with its COM translating in the three-dimensional space. The TISE for the translational DOFs reads

$$(\hat{\mathbf{H}}_{\mathrm{tra}}(\vec{\nabla}_{tra}, \vec{R}_{tra}; \theta, \varphi) - E_{\mathrm{tra}}^{(n,v,k)}(\theta, \varphi))|\Psi_{\mathrm{tra}}^{(n,v,k)}(\vec{R}_{tra}; \theta, \varphi)\rangle = 0 \ , \tag{2.70}$$

where the eigenvalues, $E_{\mathrm{tra}}^{(n,v,k)}(\theta, \varphi)$ are found by multiplying Eq. 2.70 by $\langle\Psi_{\mathrm{tra}}^{(n,v,k)}(\vec{R}_{tra}; \theta, \varphi|$, that is by averaging the translational Hamiltonian with respect to the corresponding wavefunctions. The rotationally adiabatic energies, $E_{\mathrm{tra}}^{(n,v,k)}(\theta, \varphi)$, finally correspond to the rotational adiabatic PES, $W_{\mathrm{tra}}^{(n,v,k)}(\theta, \varphi)$, of the electronic state n, vibrational state v and translational state k governing the rotational DOFs. Finally, the coupled TISE and TDSE for the rotational DOFs become

$$\begin{aligned} \left.\begin{array}{ll} E_{\mathrm{rot}}^{(n,v,k)} & |\Psi_{\mathrm{rot}}^{(n,v,k)}(\theta, \varphi)\rangle \\ i\hbar\frac{\partial}{\partial t} & |\Psi_{\mathrm{rot}}^{(n,v,k)}(\theta, \varphi, t)\rangle \end{array}\right\} &= \sum_{k'=0}^{\infty} B\left(\Delta_\theta + \cot\theta\nabla_\theta + \frac{1}{\sin^2\theta}\Delta_\varphi\right)\ \delta_{k'k} + \\ &+ W_{\mathrm{tra}}^{(n,v,k')}(\theta, \varphi)\ \delta_{k'k} + C\left\{\begin{array}{l} |\Psi_{\mathrm{rot}}^{(n,v,k')}(\theta, \varphi)\rangle \\ |\Psi_{\mathrm{rot}}^{(n,v,k')}(\theta, \varphi, t)\rangle \end{array}\right. \end{aligned} \tag{2.71}$$

with

$$C = B\left[2\vec{\tau}_{1,\theta}^{(n,v,k'k)} \cdot \nabla_\theta + \vec{\tau}_{2,\theta}^{(n,v,k'k)} + \cot\theta\vec{\tau}_{1,\theta}^{(n,v,k'k)} + \frac{1}{\sin^2\theta}\left(2\vec{\tau}_{1,\varphi}^{(n,v,k'k)} \cdot \Delta_\varphi + \vec{\tau}_{2,\varphi}^{(n,v,k'k)}\right)\right].$$

Please note that the sum of the coupling terms in Eqs. 2.71 and 2.63 corresponds to the term coupling the external and internal DOFs in Eq. 2.49. Finally, by neglecting the coupling term in Eq. 2.72, the TISE and TDSE within the adiabatic approximation are obtained, namely

$$\left.\begin{array}{ll} \tilde{E}_{\mathrm{rot}}^{(n,v,k)} & |\tilde{\Psi}_{\mathrm{rot}}^{(n,v,k)}(\theta, \varphi)\rangle \\ i\hbar\frac{\partial}{\partial t} & |\tilde{\Psi}_{\mathrm{rot}}^{(n,v,k)}(\theta, \varphi, t)\rangle \end{array}\right\} = \hat{\mathbf{T}}_{\mathrm{rot}}(\theta, \varphi) + W_{\mathrm{tra}}^{(n,v,k)}(\theta, \varphi))\left\{\begin{array}{l} |\tilde{\Psi}_{\mathrm{rot}}^{(n,v,k)}(\theta, \varphi)\rangle \\ |\tilde{\Psi}_{\mathrm{rot}}^{(n,v,k)}(\theta, \varphi, t)\rangle \end{array}\right. \ , \tag{2.72}$$

where the motions of the rotational and translational DOFs are now decoupled from each other, but, due to the adiabatic approximation, the eigenvalues $\tilde{E}_{\mathrm{rot}}^{(n,v,k)}$ are different from $E_{\mathrm{rot}}^{(n,v,k)}$ in Eq. 2.63. The same applies to the wavefunctions, i.e. $|\tilde{\Psi}_{\mathrm{rot}}^{(n,v,k)}(\vec{R}_{rot})\rangle \neq |\Psi_{\mathrm{rot}}^{(n,v,k)}(\vec{R}_{rot})\rangle$ and $|\tilde{\Psi}_{\mathrm{rot}}^{(n,v,k)}(\vec{R}_{rot}, t)\rangle \neq |\Psi_{\mathrm{rot}}^{(n,v,k)}(\vec{R}_{rot}, t)\rangle$.

It is briefly mentioned here that in the trivial case of $W_{\mathrm{tra}}^{(n,v,k)}(\theta, \varphi) = 0$ the solution of the rotational TISE, $E_{\mathrm{rot}}^{(n,v,k)}$ are just the eigenvalues of the rigid rotor, that is

$$E_{\mathrm{rot}}^{(n,v,k)}(J) = BJ(J+1) \ , \tag{2.73}$$

where J is the rotational quantum number, and $Y_{J,M}(\theta,\varphi)$ are the corresponding eigenfunctions (spherical harmonics) and $B = \frac{\hbar^2}{2\mu r_{eq}^2}$ is the rotational constant of the rigid rotor. In the case of diatomic molecules in vacuum, where translational and rotational DOFs are separable (no collisions), the rovibrational spectra can be interpreted within the non-rigid rotor model, which is an extension of the rigid rotor including the centrifugal distortion of the molecular bond due to rotations. In this sense, it is a simple model for approximating the rovibrational operator in Eq. 2.38. The non-rigid rotor approximation give the following eigenvalues

$$E_{rot-vib}^{(n,v)}(J_v) = B_v \ J_v(J_v+1) + D_v \ J_v^2(J_v+1)^2 \ , \tag{2.74}$$

where $B_v = \frac{\hbar^2}{2\mu r_v^2}$ and $D_v = \frac{\hbar^4}{2k\mu^2 r_v^6}$ (in the harmonic oscillator approximation [25]) are the rotational and centrifugal distortion constants, which depend on the vibrational eigenstate v the molecules are vibrating at, since the higher is the vibrational frequency, the larger is the expectation value of the bond distance r_v, the smaller are B_v and D_v.

The equations for the first order NACTs for the two cases exposed above, namely, when assigning either the rotational (case 1) or the translational (case 2) DOFs to the light part of the Hamiltonian, are now given below.

Case 1:

$$\begin{aligned}
\vec{\tau}_1^{(n,v,l'l)}(\vec{R}_{tra}) &= \langle \Psi_{\mathrm{rot}}^{(n,v,l')}(\theta,\varphi;\vec{R}_{tra}) | \vec{\nabla}_{tra} | \Psi_{\mathrm{rot}}^{(n,v,l)}(\theta,\varphi;\vec{R}_{tra}) \rangle_{rot} \ , \\
\vec{\tau}_1^{(n,v,l'l)}(\vec{R}_{tra}) &= \frac{\langle \Psi_{\mathrm{rot}}^{(n,v,l')}(\theta,\varphi;\vec{R}_{tra}) | \left(\vec{\nabla}_{tra} \hat{\mathbf{H}}_{\mathrm{rot}}(\vec{\nabla}_{rot},\theta,\varphi;\vec{R}_{tra}) \right) | \Psi_{\mathrm{rot}}^{(n,v,l)}(\theta,\varphi;\vec{R}_{tra}) \rangle_{rot}}{W_{\mathrm{rot}}^{(n,v,l)}(\vec{R}_{tra}) - W_{\mathrm{rot}}^{(n,v,l')}(\vec{R}_{tra})} \ , \\
\vec{\tau}_2^{(n,v,l'l)}(\vec{R}_{tra}) &= \langle \Psi_{\mathrm{rot}}^{(n,v,l')}(\theta,\varphi;\vec{R}_{tra}) | \Delta_{tra} | \Psi_{\mathrm{rot}}^{(n,v,l)}(\theta,\varphi;\vec{R}_{tra}) \rangle_{rot} \ .
\end{aligned} \tag{2.75}$$

Case 2:

$$\begin{aligned}
\vec{\tau}_1^{(n,v,k'k)}(\theta,\varphi) &= \langle \Psi_{\text{tra}}^{(n,v,k')}(\vec{R}_{tra};\theta,\varphi)|\vec{\nabla}_{rot}|\Psi_{\text{tra}}^{(n,v,k)}(\vec{R}_{tra};\theta,\varphi)\rangle_{tra} \ , \\
\vec{\tau}_1^{(n,v,k'k)}(\theta,\varphi) &= \frac{\langle \Psi_{\text{tra}}^{(n,v,k')}(\vec{R}_{tra};\theta,\varphi)|\left(\vec{\nabla}_{rot}\hat{\mathbf{H}}_{\text{tra}}(\vec{\nabla}_{tra},\vec{R}_{tra};\theta,\varphi)\right)|\Psi_{\text{tra}}^{(n,v,k)}(\vec{R}_{tra};\theta,\varphi)\rangle_{tra}}{W_{\text{tra}}^{(n,v,k)}(\theta,\varphi)-W_{\text{tra}}^{(n,v,k')}(\theta,\varphi)} \ , \\
\vec{\tau}_2^{(n,v,k'k)}(\theta,\varphi) &= \langle \Psi_{\text{tra}}^{(n,v,k')}(\vec{R}_{tra};\theta,\varphi)|\Delta_{rot}|\Psi_{\text{tra}}^{(n,v,k)}(\vec{R}_{tra};\theta,\varphi)\rangle_{tra} \ . \qquad (2.76)
\end{aligned}$$

Thus, as already discussed for the previous stages, the AS separation is the more accurate, the smaller the adiabatic parameter is, since the coupling terms are directly proportional to it. However, the magnitude of the coupling term is also proportional to the magnitude of the NACTs and to the velocity, or momentum, at which the heavy components move relative to their light counterparts, depending on the cases 1 and 2, because of the gradient multiplying the heavy wavefunctions in Eqs. 2.63 and 2.71. Finally, the NACTs are negligible if and only if upon variation of the heavy particle coordinates, the respective light wavefunctions do not change drastically (see Eqs. 2.75, 2.75, 2.76 and 2.76). Equivalently, the extended Feynman-Hellman theory allows us to state that the first order NACTs are inversely proportional to the energy gaps between two considered PESs, as shown in Eqs. 2.75 and 2.76.

When for the molecular system considered, translational and rotational DOFs do not separate, the NACTs have to be treated explicitly. Referring to the present work for example, $\vec{\tau}_1^{(n,v,l'l)}(\vec{R}_{tra})$ could be calculated by quantifying the changes in the rotational states of Cl_2 or H_2, when translating their COM in the crystal. Correspondingly, $\vec{\tau}_1^{(n,v,k'k)}(\theta,\varphi)$ could be calculated by quantifying the changes in the translational states when the orientation of Cl_2 or H_2 is changed (rotation). This field of research is established since many years, see for example [26], and is still actual, see for example [27]. Afterwards, the SE for the system has to be solved, which is, in the case of a linear molecule, a five-dimensional coupled equation (3 translational and 2 rotational DOFs) and can be nowadays treated, by using the Discrete Variable Representations (DVR) [28–30], also implemented in the Multi Configurational Time-Dependent Hartree program package [31–37] used for the Br_2@Ar system in Chap. 4 and exposed later in this chapter.

2.3 Quantum Chemistry Methods

In this section it will be focused on the Quantum Chemistry (QC) methods used during this investigation for solving the TISE in Eq. 2.30. In the first subsection the Hartree Fock (HF) method will be introduced, whereas in the next ones the so-called post-HF or correlation methods will be exposed. The subscript el indicating electronic wavefunction

will be dropped from now on, and instead the method will be indicated in order to highlight the connections between the HF method in section 2.3.1 and the correlated methods in Sec. 2.3.3, 2.3.4 and 2.3.5, which improve the results upon the HF approximation. Hence, $\Psi^{\text{method}} = \Psi_{\text{el}}$ (where "method" may be "HF", "CI", "MP", etc.) and $\hat{\mathbf{H}} = \hat{\mathbf{H}}_{\text{el}}$. Please note that the different QC techniques are adapted from various sources including Refs.38 and 39.

2.3.1 Hartree Fock (HF) Method

Solution of the TISE for atoms and molecules containing many electrons is not a trivial task. Most of the calculations rely on the Hartree-Fock method, which is equivalent to the molecular orbital (MO) approximation, in which a determinant of one-electron functions is constructed so that the total electronic wavefunction results antisymmetric with respect to the exchange of any two electrons (Pauli exclusion principle) and then optimized [38]. For an n_{el}-electron system the HF wavefunction can be expressed by means of a Slater determinant:

$$|\Psi^{\text{HF}}\rangle = \frac{1}{\sqrt{n_{\text{el}}!}} \begin{vmatrix} \chi_1(\vec{q}_1) & \chi_2(\vec{q}_1) & \cdots & \chi_{n_{\text{el}}}(\vec{q}_1) \\ \chi_1(\vec{q}_2) & \chi_2(\vec{q}_2) & \cdots & \chi_{n_{\text{el}}}(\vec{q}_2) \\ \cdots & \cdots & \cdots & \cdots \\ \chi_1(\vec{q}_{n_{\text{el}}}) & \chi_2(\vec{q}_{n_{\text{el}}}) & \cdots & \chi_{n_{\text{el}}}(\vec{q}_{n_{\text{el}}}) \end{vmatrix} . \tag{2.77}$$

The multiplying prefactor in Eq. 2.77 is the normalization factor and the $\chi_i(\vec{q}_i)$ are a set of orthonormal spin-orbitals describing each electron. They are a product of a spatial part, $\psi_i(\vec{r}_i)$, which depends on the position of the electron, and a spin orbital, $\alpha(\omega)$ or $\beta(\omega)$, which depends only on its spin coordinate:

$$\chi_i(\vec{q}_i) = \psi_i(\vec{r}_i) \cdot \begin{cases} \alpha(\omega) \\ \beta(\omega) \end{cases} . \tag{2.78}$$

In order to determine the best spin-orbitals, the variational method is applied to minimize the electronic Hamiltonian operator:

$$\langle \Psi^{\text{HF}} | \hat{\mathbf{H}} | \Psi^{\text{HF}} \rangle = min \ . \tag{2.79}$$

Finally, the variation results in the following eigenvalue problem [38]:

$$\hat{\mathbf{f}}(\vec{q}_i)\chi(\vec{q}_i) = \epsilon_i \chi(\vec{q}_i) \ . \tag{2.80}$$

Eqs. 2.80 are called Hartree-Fock equations. ϵ_i are the eigenvalues and $\hat{\mathbf{f}}(\vec{q}_i)$ is an effective one-electron operator called Fock operator with the form,

$$\hat{\mathbf{f}}(\vec{q}_i) = \hat{\mathbf{h}}(\vec{q}_i) + \langle \hat{\mathbf{V}}^{\mathrm{HF}}(\vec{q}_i) \rangle = \hat{\mathbf{h}}(\vec{q}_i) + \sum_{j=1}^{n_{\mathrm{el}}} \Big(\hat{\mathbf{J}}_j(\vec{q}_i) - \hat{\mathbf{K}}_j(\vec{q}_i) \Big) \ . \tag{2.81}$$

The first term is the one-electron Hamiltonian for the ith electron

$$\hat{\mathbf{h}}(\vec{q}_i) = -\frac{\hbar^2}{2m_e}\nabla_i^2 - \sum_{k=1}^{N_{\mathrm{nuc}}} \frac{Z_k e^2}{|\vec{r}_i - \vec{R}_k|} \ . \tag{2.82}$$

It describes the motion of a single electron i in the field of the nuclear frame. Indeed the two terms are the kinetic energy and the potential energy for the attraction between the ith electron and each of the nuclei. $\langle \hat{\mathbf{V}}^{\mathrm{HF}}(\vec{q}_i) \rangle$ is the so-called one-electron effective HF potential, describing the interaction of each electron in the mean-field of all the other electrons. In turn, $\langle \hat{\mathbf{V}}^{\mathrm{HF}}(\vec{q}_i) \rangle$ is composed of the one-electron Coulomb operator

$$\hat{\mathbf{J}}_j(\vec{q}_i)\chi_i(\vec{q}_i) = \Big[\int dq_j \chi_j^*(\vec{q}_j) \frac{1}{|\vec{r}_i - \vec{r}_j|} \chi_j(\vec{q}_j) \Big] \chi_i(\vec{q}_i) \ , \tag{2.83}$$

which specifies the classical interaction of an electron with coordinate $\vec{q}_i$ in the average field arising from the remaining $n_{\mathrm{el}} - 1$ electrons, and the exchange operator

$$\hat{\mathbf{K}}_j(\vec{q}_i)\chi_i(\vec{q}_i) = \Big[\int dq_j \chi_j^*(\vec{q}_j) \frac{1}{|\vec{r}_i - \vec{r}_j|} \chi_i(\vec{q}_j) \Big] \chi_j(\vec{q}_i) \ , \tag{2.84}$$

which arise from the antisymmetric nature of the Slater-determinant and does not have a classical interpretation like the Coulomb operator [38]. The last two expressions show that the Fock equations in 2.80 are not independent, since the Fock operator, $\hat{\mathbf{f}}(\vec{q}_i)$, acting on a spin orbital, $\chi_i(\vec{q}_i)$, depends itself on all other spin-orbitals via the Hartree Fock potential operator, $\langle \hat{\mathbf{V}}^{\mathrm{HF}}(\vec{q}_i) \rangle$. Thus, the problem has to be solved iteratively: an initial guess for the spin-orbitals, $\chi_j(\vec{q}_j)$, is used to calculate $\hat{\mathbf{J}}$ and $\hat{\mathbf{K}}$ and, hence, the Fock operator $\hat{\mathbf{f}}$. Then the Hartree Fock equations are solved yielding new $\chi_i(\vec{q}_i)$ which are again used to calculate a new Fock operator. This iteration step is repeated until convergence is reached and it is known as the *Self Consistent Field* method (SCF) [38].

In general, if the spatial part of the spin-orbital is expanded in an infinite basis set (see Sec. 2.3.2 for an introduction to the basis set used in this work; for a more detailed review of basis sets, see instead Ref. 39) ensures the HF energy $E^{\mathrm{HF}}(=E_{\mathrm{el}}^{(0)})$ to reach the

Hartree-Fock limit.

$$E^{\mathrm{HF}} = \langle \Psi^{\mathrm{HF}} | \hat{\mathbf{H}} | \Psi^{\mathrm{HF}} \rangle \ , \tag{2.85}$$

where $\Psi^{\mathrm{HF}} = \Psi_{\mathrm{el}}^{(0)}$, is the HF ground state wavefunction. The difference between the exact non-relativistic energy within the BO approximation, E^{exact}, and the HF energy E^{HF} at the basis set limit is called correlation energy

$$E^{\mathrm{corr}} = E^{\mathrm{exact}} - E^{\mathrm{HF}} \ . \tag{2.86}$$

Please note that, since the E^{HF} is an upper bound to the exact energy, the correlation energy is always negative. Correlation energy arises since the motion of the electrons with the same spin (called *Fermi correlation* [39]) is treated approximately and the motion of electrons with opposite spin (called *Coulomb correlation* [39]), which is the largest contribution to the correlation energy, is not treated at all within the Hartree-Fock approach. Since the HF method gives the best wavefunction for a single Slater determinant, the obvious way to improve on this result is to start from a trial wavefunction containing more than one Slater determinant,

$$\Phi_0 = c_0 \Psi^{\mathrm{HF}} + \sum_{d=1}^{\infty} c_d \Psi_d \ , \tag{2.87}$$

where c_0 is usually close to 1 and the subscript d stays for determinant. Several methods, called electron correlation methods, were developed in order to recover the correlation energy upon the HF approximation and they actually differ in how the coefficients c_d in Eq. 2.87 are calculated [39].

Before some of those methods will be exposed, in the next section the Roothaan Equation are derived by introducing the set of function (basis set) used in order to represent the atomic orbitals (AO) before the SCF procedure is applied.

2.3.2 Basis Set and Roothaan Equation (MO-LCAO)

The spatial part $\psi_i(\vec{r}_i)$ of the spin-orbital $\chi_i(\vec{q}_i)$, that is, the Molecular Orbitals (MO), is generally expanded in a set of known K spatial basis functions $\theta_\mu(\vec{r}), \mu = 1, 2, ..., K$, representing the atomic orbitals (AO).

$$\psi_i(\vec{r}_i) = \sum_{\mu} c_{\mu i}\theta_\mu(\vec{r}_i) \qquad i = 1, 2, ..., n_{\text{el}} \ . \tag{2.88}$$

The $c_{\mu i}$ are the coefficients for the linear combination of atomic orbitals (LCAO), to be iteratively found by using the SCF method mentioned above, which minimize the electronic energy. The set of known functions θ_μ is in general finite, because of practical computational limits, and K is therefore chosen such that a good compromise between accuracy and computer resources is achieved. Substitution of Eq. 2.88 in the Fock equations 2.80 leads to the so-called Roothaan-Hall equations [40, 41].

$$\mathbf{FC} = \mathbf{SC}\boldsymbol{\epsilon} \ , \tag{2.89}$$

with $\mathbf{F}$ being the Fock matrix with elements

$$\mathbf{F}_{ij} = \langle\theta_i(\vec{r})|\hat{\mathbf{f}}(\vec{q})|\theta_j(\vec{r})\rangle \tag{2.90}$$

and $\mathbf{S}$ the overlap matrix with elements

$$\mathbf{S}_{ij} = \langle\theta_i(\vec{r})|\theta_j(\vec{r})\rangle \ . \tag{2.91}$$

Across this work, the MO were expanded by using the Polarized Correlation Consistent (cc-p) basis set [42] and the discussion will therefore be restricted just to them. For a more general knowledge refer to Ref. 39. The cc-p are a widely used type of basis set developed by Dunning and co-workers [42], which was especially designed to converge systematically to the Complete Basis Set (CBS) limit using extrapolation techniques, see Eq. 2.94. The cc-p basis set are based on the Gaussian Type Orbitals (GTO), which in polar or Cartesian coordinates can be written as

$$GTO_{\zeta,n,l,m}(r,\theta,\varphi) = NY_{l,m}(\theta,\varphi)r^{(2n-2-l)}e^{-\zeta r^2} \ , \tag{2.92}$$

$$GTO_{\zeta,l_x,l_y,l_z}(x,y,z) = Nx^{l_x}y^{l_y}z^{l_z}e^{-\zeta r^2} \ . \tag{2.93}$$

Since the number of GTO functions increases very rapidly with the complexity of the system to be described, it is of common use to fix, in a reasonable manner, some of the variational coefficients, $c_{\mu i}$, of the MO expansion creating fixed linear combination of basis functions, called contracted GTOs (CGTO). Therefore, in contrast, the initial basis functions are generally denoted primitive GTOs (PGTO). In Table 2.1 the total number of contracted Gaussian functions used in order to represent the MOs is shown. The red colour code highlights the cases occurring in this work. The CGTO functions used in the cc-p type basis sets and in the aug-cc-p type basis sets are listed in the upper and

Table 2.1: The number of contracted Gaussian functions (CGTO) used for each basis set are listed for the first and third rows of the periodic table containing the H atom and, the Cl and Ar atoms, respectively. The red colour highlights the cases occurred in this work. VDZ, VTZ, VQZ, ect. stay for Valence Double, Triple, Quadruple, and so on, Zeta and means that a n-tuple set of CGTOs is used for describing the valence Atomic Orbitals (AO) of an atom. For the H-He row a VDZ basis set contains 2 CGTOs for the s-AO indicated by [2s]. cc-p stays for Polarized Correlation Consistent basis set and means, for the H and He elements, that 1 set of CGTOs is taken for the p AOs (indicated by [1p]), which accounts for polarization effects of the electronic cloud. Since the p-AOs are triply degenerate, the total number of CGTOs is 5. Aug- stays for augmented and means that for each of the AOs, 1 more CGTO is taken, which accounts for dispersion effects. For the H and He elements 1 GCTO must be added for each of the AOs, i.e. [1s1p]. This finally means to add to the 5 functions in the cc-pVDZ basis set four more CGTOs for a total of 9.

	$H - H_e$	$Na - Ar$
$cc-pVDZ$	$[2s + 1p] \rightarrow 5$	$[4s3p2d + 1f] \rightarrow 30$
$cc-pVTZ$	$[3s2p + 1d] \rightarrow 14$	$[5s4p3d2f + 1g] \rightarrow 55$
$cc-pVQZ$	$[4s3p + 2d1f] \rightarrow 30$	$[6s5p4d3f + 2g1h] \rightarrow 91$
$cc-pV5Z$	$[5s4p + 3d2f1g] \rightarrow 55$	$[7s6p5d4f + 3g2h1i] \rightarrow 140$
$cc-pV6Z$	$[6s5p + 4d3f2g1h] \rightarrow 91$	$[8s7p6d5f + 4g3h2i1l] \rightarrow 204$
$aug-cc-pVDZ$	$[2s1p + 1s1p] \rightarrow 9$	$[4s3p2d1f + 1s1p1d1f] \rightarrow 46$
$aug-cc-pVTZ$	$[3s2p1d + 1s1p1d] \rightarrow 23$	$[5s4p3d2f1g + 1s1p1d1f1g] \rightarrow 80$
$aug-cc-pVQZ$	$[4s3p2d1f + 1s1p1d1f] \rightarrow 46$	$[6s5p4d3f2g1h + 1s1p1d1f1g1h] \rightarrow 91$
$aug-cc-pV5Z$	$[5s4p...2f1g + 1s1p1d1f1g] \rightarrow 80$	$[7s6p...2h1i + 1s1p1d1f1g1h1i] \rightarrow 189$
$aug-cc-pV6Z$	$[6s5p...2g1h + 1s1p1d1f1g1h] \rightarrow 91$	$[8s7p...2i1l + 1s1p1d1f1g1h1i1l] \rightarrow 268$

lower part of the table, respectively. The keywords *DZ* (Double Zeta), *TZ* (Triple Zeta), *QZ* (Quadruple Zeta), ect., mean that the CGTOs are doubled, tripled, quadrupled and so on. The term zeta stems from the exponent used above in the GTO equations. The addition of the keyword *V*, specifies that only the valence AOs are doubled, tripled, ect.. Finally, the cc-p basis sets include already a set of CGTOs, generally called polarization or correlation functions, which take into account for polarization effects on the AOs and are indispensable for the calculation of the correlation energy. In the second part of the table *aug*, stays for augmented and refers to the addition of diffuse functions, which are indispensable for calculating long-range interactions like for example Van der Waals forces. They are, indeed, very large CGTOs with small exponent coefficients.

As already mentioned, the use of p-cc basis sets allows the extrapolation of the PES values to the complete basis set limit by using the following formula [43]

$$E_{XY} = \frac{X^3 E_X - Y^3 E_Y}{X^3 - Y^3} \ , \tag{2.94}$$

where X and Y represent the cardinal numbers in the basis sets used.

2.3.3 Configuration Interaction (CI) Method

The CI method can be seen as an extension of the HF method in the sense that the new ansatz is constructed starting from the n-electron Slater determinant of the HF ground state wavefunction

$$\Psi^{\mathrm{HF}} = |\chi_1 \chi_2 \cdots \chi_a \chi_b \cdots \chi_{n_{\mathrm{el}}}\rangle \ , \tag{2.95}$$

which contains all occupied spin-orbitals. The latter will be labelled with the first letters of the alphabet, whereas the unoccupied or virtual ones will be labeled with the later letters of the alphabet $r, s, ...$ If one now moves one electron from one occupied to an unoccupied spin-orbital, a new wavefunction describing a single excited Slater determinant would be created.

$$\Psi_a^r = |\chi_1 \chi_2 \cdots \chi_r \chi_b \cdots \chi_{n_{\mathrm{el}}}\rangle \ . \tag{2.96}$$

At the same way exciting two electrons from two occupied to two unoccupied spin-orbitals one would end up with a wavefunction describing double excited Slater determinant.

$$\Psi_{ab}^{rs} = |\chi_1 \chi_2 \cdots \chi_r \chi_s \cdots \chi_{n_{\mathrm{el}}}\rangle \ . \tag{2.97}$$

In general, this procedure could be repeated until all electrons have been excited from all occupied to unoccupied spin-orbitals, obtaining all possible Slater determinants describing all possible electronic configurations of the system. The CI Ansatz consists in writing the exact electronic wavefunction for any state of the system as an expansion of all these configuration state functions [38].

$$\Phi_0^{\mathrm{CI}} = c_0|\Psi^{\mathrm{HF}}\rangle + \sum_{ra} c_a^r|\Psi_a^r\rangle + \sum_{\substack{a<b\\r<s}} c_{ab}^{rs}|\Psi_{ab}^{rs}\rangle + \sum_{\substack{a<b<c\\r<s<t}} c_{abc}^{rst}|\Psi_{abc}^{rst}\rangle + \ldots\,, \tag{2.98}$$

which is the exact wavefunction for the electronic ground state. It is very interesting to examine the structure of the full CI matrix, obtained by solving variationally the SE. For this purpose it is more convenient to rewrite the Eq. 2.98 as

$$\Phi_0 = c_0|\Psi^{\mathrm{HF}}\rangle + \sum_S c_S|S\rangle + \sum_D c_D|D\rangle + \sum_T c_T|T\rangle + \sum_Q c_Q|Q\rangle + \ldots \tag{2.99}$$

By virtue of the Brillouin's theorem (see Sec. 3.3.2 in Ref. 38) and because the matrix elements of 2 electrons operator vanish if two Slater determinants differ for more than 2 spin-orbital, the final Full CI matrix reads:

$$\begin{bmatrix}
\langle\Psi^{\mathrm{HF}}|\hat{\mathbf{H}}_{\mathrm{el}}|\Psi^{\mathrm{HF}}\rangle & 0 & \langle\Psi^{\mathrm{HF}}|\hat{\mathbf{H}}_{\mathrm{el}}|D\rangle & 0 & 0 & \ldots \\
 & \langle S|\hat{\mathbf{H}}_{\mathrm{el}}|S\rangle & \langle S|\hat{\mathbf{H}}_{\mathrm{el}}|D\rangle & \langle S|\hat{\mathbf{H}}_{\mathrm{el}}|T\rangle & 0 & \ldots \\
 & & \langle D|\hat{\mathbf{H}}_{\mathrm{el}}|D\rangle & \langle D|\hat{\mathbf{H}}_{\mathrm{el}}|T\rangle & \langle D|\hat{\mathbf{H}}_{\mathrm{el}}|Q\rangle & \ldots \\
 & & & \langle T|\hat{\mathbf{H}}_{\mathrm{el}}|T\rangle & \langle T|\hat{\mathbf{H}}_{\mathrm{el}}|Q\rangle & \ldots \\
 & & & & \langle Q|\hat{\mathbf{H}}_{\mathrm{el}}|Q\rangle & \ldots \\
\ldots & \ldots & \ldots & \ldots & \ldots & \ldots
\end{bmatrix}. \tag{2.100}$$

The Brillouin's theorem is based on the use of the canonical HF equations. In this case, in fact, the Fock matrix of Eq. 2.90 is diagonal and the off-diagonal (or mixing) elements, $\langle\chi_i(\vec{r})|\hat{\mathbf{f}}(\vec{q})|\chi_j(\vec{r})\rangle$, with $j = i \pm 1$ vanish. Since the singly excited Slater determinants $\langle\Psi^{\mathrm{HF}}|\hat{\mathbf{H}}|S\rangle$ correspond to such mixing terms, the first conclusion to be drawn is that they only mix indirectly with $|\Psi^{\mathrm{HF}}\rangle$ through the doubly excited determinants and have consequently a very small effect on the ground state energy. On the contrary the doubly excited determinants are the first important term, since they directly mix with the ground state. Finally the more highly excited determinants only interact with the ground state indirectly.

At this point the CI expansion of Eq. 2.98 is conveniently rewritten in its *intermediately normalized* form

$$|\Phi_0^{\mathrm{CI}}\rangle = |\Psi^{\mathrm{HF}}\rangle + \sum_{ra} \tilde{c}_a^r |\Psi_a^r\rangle + \sum_{\substack{a<b \\ r<s}} \tilde{c}_{ab}^{rs} |\Psi_{ab}^{rs}\rangle + \sum_{\substack{a<b<c \\ r<s<t}} \tilde{c}_{abc}^{rst} |\Psi_{abc}^{rst}\rangle + \ldots \,, \tag{2.101}$$

which involves the reasonable approximation that the coefficient c_0 is much larger than all other coefficients and that c_0^2 must be really close to 1. Multiplying the SE for the correlation energy by $\langle\Psi^{\mathrm{HF}}|$ from the left one obtains

$$\langle\Psi^{\mathrm{HF}}|(\hat{\mathbf{H}} - E_{HF})|\Phi_0^{\mathrm{CI}}\rangle = (E_{exact} - E_{HF})\langle\Psi^{\mathrm{HF}}|\Phi_0^{\mathrm{CI}}\rangle = E_{corr}\langle\Psi^{\mathrm{HF}}|\Phi_0^{\mathrm{CI}}\rangle = E_{corr} \,, \tag{2.102}$$

since for the intermediately normalized wavefunction condition $\langle\Psi^{\mathrm{HF}}|\Phi_0^{\mathrm{CI}}\rangle = 1$. Substituting the expansion in Eq. 2.101 in the left-hand side of the last equation, an explicit equation for the calculation of the correlation energy E_{corr} is obtained:

$$E_{corr} = \sum_{\substack{a<b \\ r<s}} \tilde{c}_{ab}^{rs} \langle\Psi^{\mathrm{HF}}|\hat{\mathbf{H}}|\Psi_{ab}^{rs}\rangle \,. \tag{2.103}$$

By using the intermediately normalized wavefunction, the correlation energy seems to depend only on the coefficients of the double excitations, but in reality those coefficients are affected by the presence of other excitations, as demonstrable by multiplying the SE for the correlation energy by $\langle\Psi_a^r|$, $\langle\Psi_{ab}^{rs}|$, $\langle\Psi_{abc}^{rst}|$, etc.. By doing it, a large number of equations involving higher excitations would be generated. Those equations have to be solved simultaneously and show how CI is not a feasible method.

In the case that all n_{el}-electron determinants for the molecular system are included the method is called "full CI" (FCI). If, additionally, an infinite number of basis functions are used with FCI, ideally the non-relativistic solution of the SE within the BO-approximation would be obtained. Unfortunately, the number of the n_{el}-electron determinants increases exponentially with the number of electrons of the system, so that the method becomes unrealistic from the computational point of view. Therefore, the CI expansion is often truncated including only determinants with single (CIS), single/double (CISD), single/double/triple (CISDT) excitations and so on. In opposition to the FCI, the truncated CI methods do not fulfill the *Size Consistency* requirement. The size consistency is an important property, which can be explained, considering for example the interaction potential between two H_2 molecules as a function of their distance. Imagine the two H_2 molecules at a very large

distance, at which the two molecules do not interact. Physically, the energy of the dimer should be twice the energy of the monomer, namely $E(H_4) = 2E(H_2)$. If the approximation scheme considered, fulfill such a requirement, then the method is size consistent. This is the case for the HF method, since only closed-shell monomers are considered and the interaction between the monomers is automatically not included. In turn, at the CISD level, single and double excited determinants will be created for each of the monomers, and multiplying this by two would generate quadruply excited determinants. Since the method is restricted to doubly excited determinants, the size consistency is lost, or simply $E(H_4) \neq 2E(H_2)$. Briefly, it must be mentioned that if the two monomers interact (in the previous example for short distances) an additional property has to be in general fulfilled, the *Size Extensivity*. In this case the method must scale properly with the number of particles, or in other terms the energy of a many-particle system, must be proportional to the number of particles n in the limit $n \to \infty$ [38]. These two properties are all but modest requirements. For the study of molecular dissociation evidently a method is needed which is able to treat the molecule and its fragments at the same level. In general, the CI methods have the advantage to be variational, but the disadvantage to be computationally unreliable (FCI) and to not be size consistent (CIS,CID,CISD,...,etc.). In the next sections new correlation methods are introduced, which unfortunately are not variational, but are size consistent and in the case of the Møller-Plesset (MP) method shows considerable calculating time advantages.

2.3.4 Møller-Plesset (MP) Method

The MP method is based on the more general theoretical framework called the Many-body Perturbation Theory (MBPT) or simply Perturbation Theory (PT). The idea behind all perturbation methods is to treat a system being only slightly different from a reference one, which has an exactly known solution. Mathematically, it means that the electronic Hamilton operator is separated into two parts:

$$\hat{\mathbf{H}} = \hat{\mathbf{H}}_0 + \lambda \hat{\mathbf{H}}' \ , \tag{2.104}$$

a reference Hamiltonian $\hat{\mathbf{H}}_0$ and a perturbation Hamiltonian $\hat{\mathbf{H}}'$, which should be very small compared to $\hat{\mathbf{H}}_0$. λ is a continuous parameter (Lagrange multiplier), which is in the range $[0, 1]$ and switches on and off the perturbation. The general perturbed SE reads:

$$\hat{\mathbf{H}}|\Psi^{\mathrm{PT}}\rangle = (\hat{\mathbf{H}}_0 + \lambda \hat{\mathbf{H}}')|\Psi^{\mathrm{PT}}\rangle = E^{\mathrm{PT}}|\Psi^{\mathrm{PT}}\rangle \ . \tag{2.105}$$

The eigenfunctions and eigenvalues of the unperturbed Hamiltonian fulfill the unperturbed SE,

$$\hat{\mathbf{H}}_0|\Phi_i\rangle = E_i|\Phi_i\rangle \ . \tag{2.106}$$

If $\lambda = 0$, one simply has the SE for the unperturbed Hamiltonian, so that $\hat{\mathbf{H}} = \hat{\mathbf{H}}_0$, $|\Psi^{\mathrm{PT}}\rangle = |\Phi_0\rangle$ and $E^{\mathrm{PT}} = E_0$. As the perturbation increases continuously, the new energy and wavefunction also change continuously and can be written as an expansion in powers of the perturbation parameter λ [39]

$$\begin{aligned} E^{\mathrm{PT}} &= \lambda^0 E_0^{\mathrm{PT}} + \lambda^1 E_1^{\mathrm{PT}} + \lambda^2 E_2^{\mathrm{PT}} + \lambda^3 E_3^{\mathrm{PT}} + ..., \\ \Psi^{\mathrm{PT}} &= \lambda^0 \Psi_0^{\mathrm{PT}} + \lambda^1 \Psi_1^{\mathrm{PT}} + \lambda^2 \Psi_2^{\mathrm{PT}} + \lambda^3 \Psi_3^{\mathrm{PT}} + ... \ , \end{aligned} \tag{2.107}$$

where the Ψ_n^{PT} and E_n^{PT} are the nth-order corrections to the wavefunction and the energy, respectively.

Again to work with *intermediately normalized* wavefunction is useful. This implies that the corrections to the wavefunction are orthogonal to the unperturbed wavefunction.

$$\langle \Psi_{n\neq 0}^{\mathrm{PT}} | \Phi_0 \rangle = 0 \ . \tag{2.108}$$

Thus, by using the expansions of Eqs. 2.107 the SE becomes

$$(\hat{\mathbf{H}}_0 + \lambda^1 \hat{\mathbf{H}}' - \lambda^0 E_0^{\mathrm{PT}} - \lambda^1 E_1^{\mathrm{PT}} - \lambda^2 E_2^{\mathrm{PT}} - ...)(\lambda^0 \Psi_0^{\mathrm{PT}} + \lambda^1 \Psi_1^{\mathrm{PT}} + \lambda^2 \Psi_2^{\mathrm{PT}} + ...) = 0 \tag{2.109}$$

and by sorting the terms with the same power of λ, the nth-order perturbation equations are obtained

$$\begin{aligned} \lambda^0 &: \ \hat{\mathbf{H}}_0|\Psi_0^{\mathrm{PT}}\rangle = E_0^{\mathrm{PT}}|\Psi_0^{\mathrm{PT}}\rangle \\ \lambda^1 &: \ \hat{\mathbf{H}}_0|\Psi_1^{\mathrm{PT}}\rangle + \hat{\mathbf{H}}'|\Psi_0^{\mathrm{PT}}\rangle = E_0^{\mathrm{PT}}|\Psi_1^{\mathrm{PT}}\rangle + E_1^{\mathrm{PT}}|\Psi_0^{\mathrm{PT}}\rangle \\ \lambda^2 &: \ \hat{\mathbf{H}}_0|\Psi_2^{\mathrm{PT}}\rangle + \hat{\mathbf{H}}'|\Psi_1^{\mathrm{PT}}\rangle = E_0^{\mathrm{PT}}|\Psi_2^{\mathrm{PT}}\rangle + E_1^{\mathrm{PT}}|\Psi_1^{\mathrm{PT}}\rangle + E_2^{\mathrm{PT}}|\Psi_0^{\mathrm{PT}}\rangle \\ \lambda^n &: \ \hat{\mathbf{H}}_0|\Psi_n^{\mathrm{PT}}\rangle + \hat{\mathbf{H}}'|\Psi_{n-1}^{\mathrm{PT}}\rangle = \sum_{i=0}^{n} E_i^{\mathrm{PT}} \Psi_{n-i}^{\mathrm{PT}} \ . \end{aligned} \tag{2.110}$$

The *zero*-order equation is just the unperturbed problem for the ground state, i.e. $\hat{\mathbf{H}}_0|\Phi_0\rangle = E_0|\Phi_0\rangle$. The *higher*-order perturbation equations in turn contains unknowns. The energy correction to the nth-order can be easily calculated by multiplying the nth-oder equation from the left by $\langle\Phi_0|$ and using the intermediate normalization property.

$$E_n^{\mathrm{PT}} = \langle\Phi_0|\hat{\mathbf{H}}'|\Psi_{n-1}^{\mathrm{PT}}\rangle \ . \tag{2.111}$$

It appears that for the calculation of the nth-order corrections to the energy, E_n, the *(n-1)*th-order correction to the wavefunction is required, but in reality by using the equations 2.110 it can be shown that actually the nth-order correction to the wavefunction allows the calculation of energies up to the *(2n+1)*th-order [39].

At this point an expedient for the solution of the perturbation equations is needed. Rayleigh and Schrödinger (RS) proposed to expand the unknown nth-order corrections to the wavefunction, $|\Psi_n^{\mathrm{PT-RS}}\rangle$, in the unperturbed wavefunctions, $|\Phi_i\rangle$.

$$|\Psi_n^{\mathrm{PT-RS}}\rangle = \sum_i c_{n,i}|\Phi_i\rangle \ , \tag{2.112}$$

Thus, the *first*-order perturbation equation becomes

$$(\hat{\mathbf{H}}_0 - E_0^{\mathrm{PT-RS}})(\sum_i c_{1,i}\Phi_i) + (\hat{\mathbf{H}}' - E_1^{\mathrm{PT-RS}})\Phi_0 = 0. \tag{2.113}$$

Multiplying from the left by $\langle\Phi_0|$ and integrating yields the first correction to the energy

$$E_1^{\mathrm{PT-RS}} = \langle\Phi_0|\hat{\mathbf{H}}'|\Phi_0\rangle \ , \tag{2.114}$$

which is the average of the perturbation operator over the unperturbed wavefunctions. Otherwise, multiplying from the left by $\langle\Phi_j|$ and integrating, the first correction to the wavefunction is obtained

$$c_{1,j} = \frac{\langle\Phi_j|\hat{\mathbf{H}}'|\Phi_0\rangle}{E_0 - E_j} \ . \tag{2.115}$$

Solving the *second*-order perturbation equation, leads to the following two equations

$$E_2^{\mathrm{PT-RS}} = \sum_i c_{1,i}\langle\Phi_0|\hat{\mathbf{H}}'|\Phi_i\rangle = \sum_{i\neq 0}\frac{\langle\Phi_0|\hat{\mathbf{H}}'|\Phi_i\rangle\langle\Phi_i|\hat{\mathbf{H}}'|\Phi_0\rangle}{E_0 - E_i} \ , \tag{2.116}$$

$$c_{2,j} = \sum_{i\neq 0}\frac{\langle\Phi_j|\hat{\mathbf{H}}'|\Phi_i\rangle\langle\Phi_i|\hat{\mathbf{H}}'|\Phi_0\rangle}{(E_0 - E_j)(E_0 - E_i)} - \frac{\langle\Phi_j|\hat{\mathbf{H}}'|\Phi_0\rangle\langle\Phi_0|\hat{\mathbf{H}}'|\Phi_0\rangle}{(E_0 - E_j)^2} \ , \tag{2.117}$$

for the *second*-order correction to the energy and to the wavefunction, respectively. Comparing, Eqs. 2.113, 2.115, 2.116 and 2.117, it becomes already clear how complicated the formulas for the *higher*-order corrections must become. Please note, however, that all corrections can be expressed in terms of unperturbed energies and wavefunctions.

In the Møller Plesset theory the unperturbed Hamiltonian is expressed as a sum of Fock operators,

$$\hat{\mathbf{H}}_0 = \sum_{i=1}^{n_{\mathrm{el}}}\hat{\mathbf{f}}_i = \sum_{i=1}^{n_{\mathrm{el}}}\hat{\mathbf{h}}_i + 2\langle\hat{\mathbf{V}}_{\mathrm{ee}}\rangle \ , \tag{2.118}$$

where, $\langle\hat{\mathbf{V}}_{\mathrm{ee}}\rangle = \sum_{i=1}^{n_{\mathrm{el}}}\langle\hat{\mathbf{V}}_i^{\mathrm{HF}}\rangle$, is just the sum of the one-electron mean-field of Eq. 2.81 over all electrons and the factor 2 arises because the interaction between pairs of electrons is counted twice. Thus, the *zero*-order wavefunction is just the HF wavefunction, i.e. $|\Psi_0^{\mathrm{MP}}\rangle = |\Psi^{\mathrm{HF}}\rangle$, and E_0 is just the sum of the MO energies. This is what makes MP so attractive, the method, in fact, becomes size consistent. The inconvenient is that for this choice the perturbation is not so small, as the MBPT requires. In principle, by solving the total Hamiltonian, $\hat{\mathbf{H}}$, the total interaction potential, $\hat{\mathbf{V}}_{\mathrm{ee}}$, between the electrons is recovered. The perturbation Hamiltonian $\hat{\mathbf{H}}'$, if expressed as the difference between the total Hamiltonian, $\hat{\mathbf{H}}$ and the unperturbed Hamiltonian $\hat{\mathbf{H}}_0$, can be rewritten as

$$\hat{\mathbf{H}}' = \hat{\mathbf{H}} - \hat{\mathbf{H}}_0 = \hat{\mathbf{V}}_{\mathrm{ee}} - 2\langle\hat{\mathbf{V}}_{\mathrm{ee}}\rangle \ . \tag{2.119}$$

Recalling the first order correction to the energy in Eq. 2.113, since the *first*-order correction is the average of the perturbation operator over the *zero*-order wavefunction, one obtains:

$$E_1^{\mathrm{MP}} = \langle\Phi_0|\hat{\mathbf{H}}'|\Phi_0\rangle = \langle\hat{\mathbf{V}}_{\mathrm{ee}}\rangle - 2\langle\hat{\mathbf{V}}_{\mathrm{ee}}\rangle = -\langle\hat{\mathbf{V}}_{\mathrm{ee}}\rangle \ . \tag{2.120}$$

Please note that in the Møller Plesset theory, the *zero-* and *first*-order corrections to the energy correspond to the Hartree-Fock energy, where E_1^{MP} is just the correction for the overcounting of the electron-electron repulsion, so that the first evaluation of the correlation energy is the *second*-order energy, e.i. MP2, followed by the *higher*-order terms. Therefore, the correlation energy in Eq. 2.86 is defined in MP terms as

$$E_{corr} = \sum_{i=2}^{\infty} E_i^{\mathrm{MP}} \ . \tag{2.121}$$

Since in the MP theory, the *zero*-order wavefunction is just the HF wavefunction, the various equations derived above could be now discussed in terms of CI determinants. Recalling Eq. 2.115, from the Brillouin theorem, it is known that $c_{1,j}$ will not vanish, only if $|\Phi_j\rangle$ is a doubly excited determinant. Therefore, since with the *first*-order correction to the wavefunction, $|\Psi_1^{\mathrm{MP}}\rangle$, it is possible to calculate the *second* and *third*-order corrections to the energy, then E_2^{MP} and E_3^{MP} contain contributions only from doubly excited determinants. In Eq. 2.117 the coefficients $c2, j$ will not vanish, only if the $|\Phi_j\rangle$ in the second term and the $|\Phi_i\rangle$ in the first one, are again doubly excited determinants, whereas the $\langle\Phi_j|$ of first term may be either singly, doubly, triply or quadruply excited determinants, see Eq. 2.100. Hence, since with the *second*-order correction to the wavefunction, $|\Psi_2^{\mathrm{MP}}\rangle$, it is possible to calculate the *fourth* and *fifth*-order corrections to the energy, then E_4^{MP} and E_5^{MP} contain contributions from singly, doubly, triply and quadruply excited determinants.

Size consistency and greater computational reliability make MPn methods a good alternative to the variational but not size consistent truncated CI methods. Furthermore, even if the energy could be overestimated, this is rarely a problem, since the basis set imposes even more severe limitations [39].

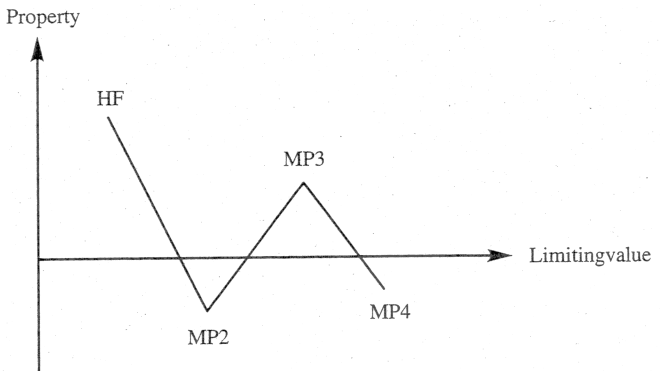

Figure 2.2: Typically oscillating convergence behaviour of energy results obtained with the MPn methods. The Limiting value is the exact non-relativistic electronic energy in the Born-Oppenheimer approximation. (Adapted from [39])

Probably the main disadvantage of MPn methods is that the HF reference Hamiltonian is not really consistent with the premise of the perturbation theory, the perturbation to be small enough. It is indeed known that in such a case the MP2, MP3 and MP4 methods show oscillatory convergence, as shown in Fig. 2.2 overshooting in some case the exact energy. This behaviour becomes more drastic if big basis sets are used, as for example basis sets with augmented functions. In such a case the MP3 method gives certainly wrong, whereas MP2 often gives surprisingly good results [39] and is considered to be then the best choice.

2.3.5 Coupled-Cluster (CC) Method

Coupled Cluster (CC) methods form another popular approach to the problem of constructing correlated wavefunctions. CC theory was born in the physics community in particular in the area of nuclear physics, but since over 30 years it found an always increasing application in Quantum Chemistry, where perhaps the most reliable computational method for the calculation of electronic structures and for the prediction of molecular properties has been developed. Like the MPn methods, the CC is size consistent, but non-variational.

The intermediate normalized coupled cluster wavefunction is written as

$$|\Psi^{\mathrm{CC}}\rangle = e^{\hat{\mathbf{T}}}|\Phi_0\rangle \ , \tag{2.122}$$

where $|\Phi_0\rangle$ is the HF reference wavefunction and $\hat{\mathbf{T}}$ is the cluster operator, given by

$$\hat{\mathbf{T}} = \hat{\mathbf{T}}_1 + \hat{\mathbf{T}}_2 + \hat{\mathbf{T}}_3 + ... + \hat{\mathbf{T}}_N \ . \tag{2.123}$$

Moreover, the $e^{\hat{\mathbf{T}}}$ term can be expanded as follows:

$$e^{\hat{\mathbf{T}}} = 1 + \hat{\mathbf{T}} + \frac{1}{2}\hat{\mathbf{T}}^2 + \frac{1}{6}\hat{\mathbf{T}}^3 + ... = \sum_{k=0}^{\infty} \frac{1}{k!}\hat{\mathbf{T}}^k \ . \tag{2.124}$$

When the $\hat{\mathbf{T}}_i$ operator acts on the HF wavefunction $|\Phi_0\rangle$, the nth-ply excited Slater determinants are created,

$$|\Psi^{\mathrm{CC}}\rangle = |\Phi_0\rangle + \sum_{ra} t_a^r |\Psi_a^r\rangle + \sum_{\substack{a<b \\ r<s}} t_{ab}^{rs} |\Psi_{ab}^{rs}\rangle + \sum_{\substack{a<b<c \\ r<s<t}} t_{abc}^{rst} |\Psi_{abc}^{rst}\rangle + ... \ . \tag{2.125}$$

where

$$\hat{\mathbf{T}}_1|\Phi_0\rangle = \sum_{ra} t_a^r|\Psi_a^r\rangle \tag{2.126}$$

$$\hat{\mathbf{T}}_2|\Phi_0\rangle = \sum_{\substack{a<b\\r<s}} t_{ab}^{rs}|\Psi_{ab}^{rs}\rangle \tag{2.127}$$

$$\cdots \quad \cdots \quad \cdots \quad .$$

and t are called amplitudes. Substitution of Eq. 2.123 into 2.124 leads to the explicit form of the exponential operator:

$$\begin{aligned} e^{\hat{\mathbf{T}}} &= 1 + \hat{\mathbf{T}}_1 + \left(\hat{\mathbf{T}}_2 + \frac{1}{2}\hat{\mathbf{T}}_1^2\right) + \left(\hat{\mathbf{T}}_3 + \hat{\mathbf{T}}_2\hat{\mathbf{T}}_1 + \frac{1}{6}\hat{\mathbf{T}}_1^3\right) + \\ &+ \left(\hat{\mathbf{T}}_4 + \hat{\mathbf{T}}_3\hat{\mathbf{T}}_1 + \frac{1}{2}\hat{\mathbf{T}}_2^2 + \frac{1}{2}\hat{\mathbf{T}}_2\hat{\mathbf{T}}_1^2 + \frac{1}{24}\hat{\mathbf{T}}_1^4\right) + ... \end{aligned} \tag{2.128}$$

The last expression already gives an idea of the advantages of truncated CC over truncated CI methods, since it shows the size consistent nature of the CC ansatz. The first term is the reference wavefunction, the second term generates the single excited Slater determinants, the first parenthesis includes all doubly excited configurations, both the so called connected ($\hat{\mathbf{T}}_2$) and disconnected ($\hat{\mathbf{T}}_1^2$), whereas the second parenthesis includes all connected and disconnected triply excited determinants, and so on. The size consistent property of the truncated CC methods arises from the presence of those disconnected terms. For example the CISD method does not include the term $\hat{\mathbf{T}}_1^2$ and at the same way the CISDT method does not include the terms $\hat{\mathbf{T}}_1^3$ and $\hat{\mathbf{T}}_2\hat{\mathbf{T}}_1$ and so on. By using the CC wavefunction the SE reads

$$\hat{\mathbf{H}}e^{\hat{\mathbf{T}}}|\Phi_0\rangle = E^{\mathrm{CC}}e^{\hat{\mathbf{T}}}|\Phi_0\rangle \ . \tag{2.129}$$

Similarly to the Eqs. 2.113, 2.115, 2.116 and 2.117, if one multiplies the SE from the left by $\langle\Phi_0|$ or by one of the nth-ply excited determinants and integrates the expressions the CC energy or the nth amplitudes are attained, respectively.

$$\begin{aligned} E^{\mathrm{CC}}\underbrace{\langle\Phi_0|e^{\hat{\mathbf{T}}}\Phi_0\rangle}_{=1} &= \langle\Phi_0|\hat{\mathbf{H}}e^{\hat{\mathbf{T}}}|\Phi_0\rangle \ , \\ E^{\mathrm{CC}} &= \langle\Phi_0|\hat{\mathbf{H}}e^{\hat{\mathbf{T}}}|\Phi_0\rangle \ , \\ E^{\mathrm{CC}} &= E^{\mathrm{HF}} + \underbrace{\sum_{ra} t_a^r\langle\Phi_0|\hat{\mathbf{H}}|\Psi_a^r\rangle}_{=0} + \sum_{\substack{a<b\\r<s}}(t_{ab}^{rs} + t_a^r t_b^s - t_b^r t_a^s)\langle\Phi_0|\hat{\mathbf{H}}|\Psi_{ab}^{rs}\rangle + ... \ , \end{aligned} \tag{2.130}$$

and

$$E^{\mathrm{CC}}\langle\Phi_a^r|e^{\hat{\mathbf{T}}_1}\Phi_0\rangle = \langle\Phi_a^r|\hat{\mathbf{H}}e^{\hat{\mathbf{T}}}|\Phi_0\rangle \ , \tag{2.131}$$

$$E^{\mathrm{CC}}\langle\Phi_a^r|\hat{\mathbf{T}}_1\Phi_0\rangle = \langle\Phi_a^r|\hat{\mathbf{H}}|\Phi_0\rangle + \underbrace{\sum_{ra} t_a^r\langle\Phi_a^r|\hat{\mathbf{H}}|\Psi_a^r\rangle}_{=0} + \sum_{\substack{a<b\\r<s}}(t_{ab}^{rs} + t_a^r t_b^s - t_b^r t_a^s)\langle\Phi_0|\hat{\mathbf{H}}|\Psi_{ab}^{rs}\rangle + ...$$

The last expression only shows the amplitudes of the singly excited determinants, as an example. In both equations the matrix elements of the singly excited determinants are zero because of the Brillouins Theorem.

If all possible operators are included in Eq. 2.128 up to the order $N = \infty$, the CC- and FCI-ansatz become equivalent and equivalently the method becomes computationally unreliable. The CC operator has to be truncated at some excitation level, and like CI, Coupled Cluster Double (CCD), Single Double (CCSD) are generally used and the only applicable ones. The CCSDT and the higher methods are, in fact, computationally too demanding. Unfortunately the contributions from the double and triple excitations, $\hat{\mathbf{T}}_2$ and $\hat{\mathbf{T}}_3$, respectively, in the CC operator expansions are the dominant terms, so that a relevant part of the correlation energy is therefore not included. It is possible to avoid the obstacle and add the triple excitations calculating them by mean of perturbation theory at a same level of approximation. The MP4 methods for example includes the correlation energy given by the triple excitations and is usually added to the CCSD energy. In this case the method is called CCSD+T(CCSD). Addition of more terms arising from MP5 and describing the coupling between singles and triples leads to the CCSD(T) method. The CCSD(T) method is often called "the gold standard of quantum chemistry" for its excellent compromise between the accuracy and the computational cost for the molecules near equilibrium geometries. One could go on and add other terms from the MP5 or even from higher MPn methods, but again the procedure would become computationally too demanding. Please note that in those hybrid MPn-CC methods for the calculations of the MPn energy correction the CCSD-wavefunctions (amplitudes) are used.

2.4 Quantum Dynamics Method

2.4.1 Multi-Configuration Time-Dependent Hartree Method (MCTDH)

The multi-configuration time-dependent Hartree (MCTDH) method [31–37] is probably one of the most powerful numerical implementations for propagating wavepackets, i.e. for solving the TDSE in Eq. 2.33.

$$i\hbar\frac{\partial}{\partial t}\Psi_{\mathrm{nuc}}(t) = \hat{H}\Psi_{\mathrm{nuc}}(t) \ . \tag{2.132}$$

The method is particularly advantageous in case of multi-dimensional systems. In order to appreciate this point let us consider first the standard wavepacket propagation approach, before the basic concepts behind the MCTDH method will be illustrated. Consider a system with f nuclear degrees of freedom k, which may be represented by a set of generalized coordinates $\{q_k\}$, being different kinds of coordinates, the standard expansion in term of a time-independent basis for representing a multi-dimensional wavepacket reads

$$\Psi_{\rm nuc}(\{q_k\};t) = \sum_{j_1=1}^{N_1} \cdots \sum_{j_f=1}^{N_f} A_{j_1 \cdots j_f}(t) \prod_{k=1}^{f} \chi_{j_k}^{(k)}(q_k) \equiv \sum_J A_J(t) X_J(\{q_k\}) \ , \tag{2.133}$$

where N_k denotes the number of basis functions $\chi_{j_k}^{(k)}(q_k)$ required for representing the kth DOF; $A_J(t) = A_{j_1 \cdots j_f}(t)$ are the time-dependent expansion coefficients with J collecting all the j_k indices; $X_J(\{q_k\}) = \prod_{k=1}^{f} \chi_{j_k}^{(k)}(q_k)$ is a time independent Hartree product expansion of the one dimensional basis set. By solving the TDSE the basis functions $\chi_{j_k}^{(k)}(q_k)$ are often chosen by using a Discrete Variable Representation (DVR)/Finite Basis Representation (FBR) on a grid, [28, 29, 44, 45]. For more detailed information on DVR techniques refer to the reviews in Refs. [36] and [30]. By using the ansatz in Eq. 2.133 and applying the Dirac-Frenkel variational principle to Eq. 2.132

$$\langle \delta\Psi_{\rm nuc}(\{q_k\};t) | \hat{H} - i\hbar \frac{\partial}{\partial t} | \Psi_{\rm nuc}(\{q_k\};t) \rangle \quad = \quad 0 \ , \tag{2.134}$$

the following equations of motion (EOM) for the expansion coefficients $A_J(t)$ can be obtained:

$$i\hbar \dot{A}_J(t) \quad = \quad \sum_L H_{JL} A_L(t) \ , \tag{2.135}$$

where $H_{JL} = \langle X_J(\{q_k\}) | \hat{H} | X_L(\{q_k\}) \rangle$ denote the matrix elements of the Hamiltonian in the above product basis set. If for simplicity the same number $N_k = N$ of grid points is chosen for all k, the numerical effort in evaluating the EOMs is proportional to fN^{f+1}. This exponential scaling restricts the applicability of standard methods to quantum problems with only few nuclear DOFs. In the MCDTH method a new ansatz is proposed for the wavefunction $\Psi_{\rm nuc}(\{q_k\},t)$ [46]:

$$\Psi_{\rm nuc}(\{q_k\},t) = \sum_{j_1=1}^{n_1} \cdots \sum_{j_f=1}^{n_f} \tilde{A}_{j_1 \cdots j_f}(t) \prod_{k=1}^{f} \tilde{\chi}_{j_k}^{(k)}(q_k,t) \equiv \sum_J \tilde{A}_J(t) \tilde{X}_J(\{q_k\},t) \tag{2.136}$$

The main difference is that the configurations $\tilde{X}_J(\{q_k\},t)$ are time-dependent, since they are represented by f-dimensional *Hartree products* of now time-dependent *single-particle functions* (SPFs) $\tilde{\chi}_{j_k}^{(k)}(q_k,t)$, as they are called in the MCTDH frame. The single particle functions are now able to follow the propagation of the system (imagine a moving grid), decreasing substantially the number n of SPFs needed for representing the different nuclear DOFs. Considering s expansion terms, the total effort now scales as $sfn(N^2+fn^f)$, which is advantageous over fN^{f+1}, as long as $n \ll N$ [36]. Numerically, each SPF is represented by a linear combination of time-independent basis (grid) functions $g_{i_k}^{(k)}(q_k)$:

$$\tilde{\chi}_{j_k}^{(k)}(q_k,t) \;=\; \sum_{i_k=1}^{N_k} c_{j_k,i_k}(t) g_{i_k}^{(k)}(q_k) \;. \tag{2.137}$$

The limiting case $n_k = N_k$ corresponds again to the numerically exact expansion of the wavefunction in Eq. 2.133. Since both, the expansion coefficients and SPFs are time-dependent, Eq. 2.136 also introduces some redundancies in the representation of the wavefunction, which can be avoided applying additional constraints to the SPFs, e.g.:

$$\langle \tilde{\chi}_{j_k}^{(k)}(q_k,t=0) | \tilde{\chi}_{l_k}^{(k)}(q_k,t=0)\rangle \;=\; \delta_{j_k l_k} \;, \tag{2.138}$$

$$\langle \tilde{\chi}_{j_k}^{(k)}(q_k,t) | \dot{\tilde{\chi}}_{l_k}^{(k)}(q_k,t)\rangle \;=\; 0 \;. \tag{2.139}$$

In particular, Eq. 2.138 ensures the SPFs to be orthonormal at $t = 0$. Eq. 2.139 in turn ensures orthonormality for $t > 0$ and moreover minimizes the motions of the SPFs.

It is helpful to introduce the *single-hole functions*

$$\Psi_{l_k}^{(k)}(\{q_1,q_{k-1},q_{k+1},q_f\},t) \;=\; \langle \tilde{\chi}_{l_k}^{(k)}(q_k,t) | \Psi_{\mathrm{nuc}}(\{q_k\},t)\rangle \;. \tag{2.140}$$

which is a linear combination of Hartree products of $(f-1)$ SPFs, which does not contain the SPF for the kth-DOF. The single-hole functions permit the following alternative expression for Eq. 2.136

$$\Psi_{\mathrm{nuc}}(\{q_k\},t) \;=\; \sum_{l_k} \tilde{\chi}_{l_k}^{(k)}(q_k,t) \Psi_{l_k}^{(k)}(\{q_1,q_{k-1},q_{k+1},q_f\},t) \;, \tag{2.141}$$

and *density matrices* as well as *mean field* matrix elements, which act on a kth-DOF only, can be expressed respectively in an easier way:

$$\rho^{(k)}_{j_k l_k}(\{q_1,q_{k-1},q_{k+1},q_f\},t) = \langle \Psi^{(k)}_{j_k}(\{q_1,q_{k-1},q_{k+1},q_f\},t)|\Psi^{(k)}_{l_k}(\{q_1,q_{k-1},q_{k+1},q_f\},t)\rangle \ , \tag{2.142}$$

$$\langle \hat{H}\rangle^{(k)}_{j_k l_k} = \langle \Psi^{(k)}_{j_k}(\{q_1,q_{k-1},q_{k+1},q_f\},t)|\hat{H}|\Psi^{(k)}_{l_k}(\{q_1,q_{k-1},q_{k+1},q_f\},t)\rangle \ . \tag{2.143}$$

Finally, after defining the *single-particle projector* onto the space of the SPFs

$$P^{(k)} = \sum_{j_k=1}^{n_k} |\tilde{\chi}^{(k)}_{j_k}(q_k,t)\rangle\langle\tilde{\chi}^{(k)}_{j_k}(q_k,t)| \tag{2.144}$$

and employing Eqs. 2.142-2.144, the MCTDH coefficients and single-particle functions can be optimized by using the Dirac-Frenkel variational principle in Eq. 2.134. The following EOMs can thus be derived [36,37]:

$$i\hbar\dot{\tilde{A}}_J(t) = \sum_L \langle \tilde{X}_J(\{q_k\},t)|\hat{H}|\tilde{X}_L(\{q_k\},t)\rangle \tilde{A}_L(t) \ , \tag{2.145}$$

$$i\hbar\dot{\tilde{\chi}}^{(k)}(q_k,t) = \left(1-P^{(k)}\right)\left(\boldsymbol{\rho}^{(k)}(\{q_1,q_{k-1},q_{k+1},q_f\},t)\right)^{-1}\langle\mathbf{H}\rangle^{(k)}\tilde{\chi}^{(k)}(q_k,t) \ , \tag{2.146}$$

where the constraints Eq. 2.138 and 2.139 were used. $\tilde{\chi}^{(k)}(q_k,t) = (\tilde{\chi}^{(k)}_1,\ldots,\tilde{\chi}^{(k)}_{n_k})^T$ refers to a column vector of the individual SPFs $\tilde{\chi}^{(k)}_{j_k}$, and $\boldsymbol{\rho}^{(k)}(\{q_1,q_{k-1},q_{k+1},q_f\},t)$ and $\langle\mathbf{H}\rangle^{(k)}$ to the respective density and mean field matrices defined by Eqs. 2.142 and 2.143, respectively.

It is worth to highlight that the eigenvectors and eigenvalues of the density matrix $\boldsymbol{\rho}^{(k)}(\{q_1,q_{k-1},q_{k+1},q_f\},t)$, the so-called *natural orbitals* and *natural populations*, are unique quantities with respect to the chosen SPFs, such that the population of the highest natural orbital provides a measure for the convergence of a MCTDH calculation.

The most CPU expensive part in solving the EOMs is the direct evaluation of the f- and $f-1$-dimensional integrals of the Hamilton matrix elements mean fields, Eqs. 2.145 and 2.146, respectively. A way to avoid the problem is to utilize a separate representation of the Hamiltonian in terms of sums over products of one-dimensional operators, similar to the MCTDH ansatz of Eq. 2.136. Unfortunately, the PES in general does not have this form. For this reason the additional internal algorithm Potfit [47,48] was implemented in order to fit PESs in such a form.

Since the TDSE is an initial value problem, an initial guess, namely $\Psi_{\text{nuc}}(t=0)$, is required. The ground state wavefunction of a coupled Hamiltonian can be provided by

propagating an initial Hartree product of 1D-eigenfunctions of uncoupled Hamiltonians, in imaginary time $t \rightarrow -i\tau$ [49]. In this case the new TDSE reads:

$$-\hbar\frac{\partial}{\partial\tau}\Psi_{\mathrm{nuc}}(\tau) \;=\; \hat{H}\Psi_{\mathrm{nuc}}(\tau) \tag{2.147}$$

and the general formal solution for the wavefunction becomes

$$\Psi_{\mathrm{nuc}}(\tau) = e^{-\frac{\hat{\mathbf{H}}\tau}{\hbar}}\Psi_{\mathrm{nuc}}(0)\ . \tag{2.148}$$

Finally, expanding the initial wavefunction in eigenfunctions θ_n of the Hamiltonian the following equation is obtained

$$\Psi_{\mathrm{nuc}}(\tau) = \sum_n a_n e^{-\frac{E_n\tau}{\hbar}}\theta_n(0)\ . \tag{2.149}$$

which shows how each eigenfunction relaxes to zero at a rate proportional to its eigenvalue. Therefore, after a time τ the eigenfunction n is reduced relative to the ground state by the ratio $e^{-(E_n-E_0)\tau}$. This means that the ground state relaxes most slowly persisting over all other ones, such that after sufficient time and by preserving the norm of the wavefunction only the pure ground state is left.

The MCTDH program package is capable to treat non adiabatic systems using the built-in *multi-set formalism* [34–37, 50–52]. Different sets of SPFs are employed for each electronic state considered. The expansion of the Hamiltonian H as well as the wavefunction Ψ_{nuc} has therefore to be expanded into a set $\{|a\rangle\}$ of electronic states:

$$|\Psi_{\mathrm{nuc}}(\{q_k\};t)\rangle \;=\; \sum_a \Psi^{(a)}_{\mathrm{nuc}}(\{q_k\};t)|a\rangle\ , \tag{2.150}$$

$$\hat{H} \;=\; \sum_a\sum_b |a\rangle\hat{H}^{(ab)}\langle b|\ , \tag{2.151}$$

where each wavefunction $\Psi^{(a)}_{\mathrm{nuc}}(\{q_k\};t)$ has the MCTDH form in Eq. 2.136. The new EOMs read now [34, 36, 51]:

$$i\hbar\dot{\tilde{A}}_J^{(a)}(t) = \sum_b \sum_L \langle \tilde{X}_J^{(a)}(\{q_k^{(a)}\},t)|H^{(ab)}|\tilde{X}_L^{(b)}(\{q_k^{(b)}\},t)\rangle \tilde{A}_L^{(b)}(t) \ , \quad (2.152)$$

$$i\hbar\dot{\tilde{\chi}}^{(a,k)}(q_k^{(a)},t) = \left(1-P^{(a,k)}\right)\left(\boldsymbol{\rho}^{(a,k)}(\{q_1^{(a)},q_{k-1}^{(a)},q_{k+1}^{(a)},q_f^{(a)}\},t)\right)^{-1} \cdot \cdot \sum_b \langle \mathbf{H}\rangle^{(ab,k)} \tilde{\chi}^{(b,k)}(q_k^{(b)},t) \ , \quad (2.153)$$

Finally, a brief discussion must be carried out about the integration schemes the MCTDH package provides. The EOMs both in the single and multi-set formalism are systems of coupled non-linear equations of first-order. The standard predictor-corrector methods are available under the name *variable mean-field* (VF) [36]. Alternatively another scheme is provided, which was specifically developed for the numerically efficient solution of the MCTDH-EOMs, called *constant mean-field* (CF) [53]. The name refers to the fact, that Hamiltonian matrix elements $\langle \tilde{X}_J(\{q_k\},t)|\hat{H}|\tilde{X}_L(\{q_k\},t)\rangle$, as well as the products of the inverse density and mean field matrices, respectively $\left(\boldsymbol{\rho}^{(k)}(\{q_1^{(a)},q_{k-1}^{(a)},q_{k+1}^{(a)},q_f^{(a)}\},t)\right)^{-1}$ and $\langle \mathbf{H}\rangle^{(k)}$, change much slower in time than the MCTDH coefficients and single-particle functions, such that the former matrix elements can be kept constant over some time. In this case the differential equation for the A-vector in Eq. 2.145, becomes a set of linear equations with constant coefficients, most efficiently solved by using the short iterative Lanczos (SILE) or Lanczos-Arnoldi integrators implemented. Similarly, the differential equation for the single-particle functions in Eq. 2.146 splits up into each subsets of uncoupled, but still non-linear equations, which can be integrated using the implemented Bulirsch-Stoer (BS) extrapolation method.

2.4.2 Optimal Control Theory (OCT)

Optimal Control Theory (OCT) is a mathematical discipline with numerous applications in science, engineering and even in economy. The method is sometimes called quantum optimal control theory in the particular case of quantum systems. The idea is to vary a properly defined functional in order to shape specially tailored laser pulses, which are able to control the quantum dynamics of the system under consideration, as for example to coherently control product ratios of chemical reactions. Thus, the OCT method has an own history, which is independent from the MCTDH framework (see for example Refs. 54,55).

Since the OCT method must be solved iteratively after an initial laser pulse has been given as a guess, it turns to be very expensive from the CPU point of view. As it will be shown in this section, two wavefunctions have to be propagated forward and backward in a time interval T numerous times, in order to reach the chosen target, restricting the

use of the method to system with few degrees of freedom. Thus, the combination of OCT and MCTDH appears to be a natural choice for controlling multi-dimensional systems [56, 57]. Moreover, Brown et al. implemented the possibility to perform forward and backward propagation at the same time and also saving the time-dependent wavefunction is not required anymore. The expedient speeds up the MCTDH-OCT implementation considerably [57].

The OCT method was implemented in the MCTDH package by May et al. [56] within the electric dipole approximation. Later Brown et al. [57] even moved on allowing the use of arbitrary dipole operators.

Assuming that the interaction between a system and an electromagnetic field can be treated semi-classically, the TDSE can be rewritten as

$$\frac{\partial}{\partial t}|\Psi_{\mathrm{nuc}}(t)\rangle = -\frac{i}{\hbar}\Big(\hat{\mathbf{H}}_0 - \hat{\mu}\epsilon(t)\Big)|\Psi_{\mathrm{nuc}}(t)\rangle \ , \tag{2.154}$$

where $\Psi_{\mathrm{nuc}}(t)$ is the nuclear wavefunction as in the MCTDH expansion, $\hat{\mu}$ denotes the dipole operator in S.I. units of [Cm] and atomic units of $[ea_0]$, $\epsilon(t)$ is the electric field in S.I. units of $\left[\frac{\mathrm{V}}{\mathrm{m}}\right]$ and atomic units of $\left[\frac{E_h}{ea_0}\right]$, so that the product $\hat{\mu}\epsilon(t)$ finally has units of energy as well as the time independent Hamiltonian of the unperturbed system, $\hat{\mathbf{H}}_0$ in the initial state $|\Psi_{\mathrm{nuc}}(0)\rangle$.

There are different ways to define the OCT functional J. The one implemented in MCTDH and used in this work is given by [58]

$$\begin{aligned} J(\epsilon,T) &= \langle\Psi_{\mathrm{nuc}}(T)|\hat{O}|\Psi_{\mathrm{nuc}}(T)\rangle \\ &+ 2Re\left\{\int_0^T dt\ \langle\Theta_{\mathrm{nuc}}(t)|\left(-\frac{\partial}{\partial t}+\frac{H}{i\hbar}\right)|\Psi_{\mathrm{nuc}}(t)\rangle\right\} - \int_0^T dt\ \alpha(t)|\epsilon(t)|^2 \ , \end{aligned} \tag{2.155}$$

where $\hat{O}$ is associated with an observable, or in other words denotes the control target, whose expectation value has to be maximized at the final propagation time T. The operator $\hat{O}$ could be, for example, a projector operator $\hat{O} = |\Phi\rangle\langle\Phi|$, where $|\Phi\rangle$ can be a target state or a target wavepacket. Please note that in all cases every term in Eq. 2.156 has to be dimensionless. Therefore, α_0 has S.I. units of $\left[\frac{\mathrm{m}^2}{\mathrm{V}^2\mathrm{s}}\right]$ and atomic units of $\left[\frac{e^2a_0^2}{\hbar E_h}\right]$. The second term in Eq. 2.156, ensures that Eq. 2.154 is fulfilled and introduces the Lagrangian multiplier $\langle\Theta_{\mathrm{nuc}}(t)|$. Moreover, $\Theta_{\mathrm{nuc}}(t)$ and $\Psi_{\mathrm{nuc}}(t)$ obey the TDSE. The third term in Eq. 2.156, guarantees strong fields to be penalized, in order to avoid, for example, the ionization of the system. $\alpha(t)$ is a time-dependent constraint function, which ensures the

pulse to be switched on and off smoothly, namely [59]

$$\alpha(t) = \begin{cases} \frac{\alpha_0}{s(t)} & \text{if t} \leq \text{T} \\ 0 & \text{otherwise} \end{cases} , \tag{2.156}$$

with α_0 being the constant constraint controlling the intensity of the pulse. Finally, $s(t)$ within the MCTDH package is simply defined as:

$$s(t) = \sin^2(\pi t/T) \ . \tag{2.157}$$

Variation of the functional J with respect to the laser pulse $\epsilon(t)$ leads to the expression for the optimal electric field [56]

$$\epsilon(t) = -\frac{\sin^2(\pi t/T)}{\hbar\alpha_0} Im\langle\Theta_{\text{nuc}}(t)|\hat{\mu}|\Psi_{\text{nuc}}(t)\rangle \ , \tag{2.158}$$

where $\Theta_{\text{nuc}}(t)$ is propagated back in time and is, initially, $\Theta_{\text{nuc}}(T) = \hat{O}\Psi_{\text{nuc}}(T) = |\Phi\rangle\langle\Phi|\Psi_{\text{nuc}}(T)\rangle$. The wavefunction $\Theta_{\text{nuc}}(t)$ evolves according to the TDSE.

$$\frac{\partial}{\partial t}|\Theta_{\text{nuc}}(t)\rangle = -\frac{i}{\hbar}\Big(\hat{\mathbf{H}}_{\text{mol}} - \hat{\mu}\epsilon(t)\Big)|\Theta_{\text{nuc}}(t)\rangle \tag{2.159}$$

The general OCT scheme presented above exhibits a quadratic and monotonic convergence behaviour as demonstrated by different authors (see Refs. 27-29 of Ref.56). Since the MCTDH-ansatz in Eq. 2.133 results in coupled nonlinear EOMs for the SPFs and expansion coefficients, a direct check of the convergence behaviour is not possible [53] and convergence has to be proved within the course of the numerical calculations. However, this above-mentioned OCT scheme can not be implemented in the existing MCTDH code, since solution of the noni-linear TDSEs obtained when the left-hand side of Eq. 2.158 for the electric field $\epsilon^{(n)}$ is substituted in Eqs. 2.154 and 2.159, is not possible [56]. May *et al.* proposed to approximate the optimal pulse via a quadratic extrapolation [56]. The field at time $t - \Delta t$ is evaluated within the n-th iteration by using $\Theta_{\text{nuc}}^{(n-1)}(t - \Delta t)$ of the previous, $(n-1)$-th iteration.

$$\epsilon^{(n)}(t - \Delta t) = -\frac{\sin^2(\pi t/T)}{\hbar\alpha_0} Im\langle\Theta_{\text{nuc}}^{(n-1)}(t - \Delta t)|\hat{\mu}|\Psi_{\text{nuc}}^{(n)}(t - \Delta t)\rangle \ . \tag{2.160}$$

$\Theta_{\text{nuc}}^{(n)}(t - \Delta t)$ is, in fact, not yet available, since it should be obtained after backward propagation of Eq. 2.159 by using $\epsilon^{(n)}$.

For the calculation of the electric field for the n-th iteration at time t, $\epsilon^{(n)}(t)$, the two following auxiliary fields are necessary

$$\epsilon_{aux}^{(1)} = \frac{1}{2}(\epsilon^{(n)}(t-3\Delta t) - 4\epsilon^{(n)}(t-2\Delta t) + 3\epsilon^{(n)}(t-\Delta t) \ , \tag{2.161}$$

$$\epsilon_{aux}^{(2)} = \frac{1}{2}(\epsilon^{(n)}(t-3\Delta t) - 2\epsilon^{(n)}(t-2\Delta t) + \epsilon^{(n)}(t-\Delta t) \ . \tag{2.162}$$

The extrapolated field strengths at t and $t+\Delta t$ are finally obtained as follows

$$\epsilon^{(n)}(t) = \epsilon^{(n)}(t-\Delta t) + E_{aux}^{(1)} + E_{aux}^{(2)} \ , \tag{2.163}$$

$$\epsilon^{(n)}(t+\Delta t) = \epsilon^{(n)}(t-\Delta t) + 2\epsilon_{aux}^{(1)} + 4\epsilon_{aux}^{(2)} \ . \tag{2.164}$$

The stability of this numerical strategy is proved in Appendix B of Ref. 56.

3 From Synchronous to Sequential Double Proton Transfer: Quantum Dynamics Simulations for the Model Porphine [60]

3.1 Introduction

Porphyrins and metalloporphyrins are a wide class of organic compounds known as well as the "pigment of life", since they play important roles in several biological processes, such as photosynthesis (*chlorins*), oxygen transport (*hemoglobin and myoglobin*) and oxygen activation (*cytochromes*). Their characteristics are utilized in many fields as for example in medicine for phototherapeutic treatments, as well as for many advanced materials as for example artificial photosynthetic systems or molecular memories. Therefore, these kind of systems are object of a wide research in both basic and applied sciences, which consequently drove to a systematic development of synthetic procedures in order to obtain them [60].

All porphyrins show a second, but biologically not less important process: the Double Proton Transfer (DPT) mechanism. For example its dysfunction in the DNA base pairs may cause irreversible mutations. Moreover, DPT mechanism has been observed for many reactions such as cycloadditions [61–66] or three-body dissociations [67]. To those systems the same question was addressed, whether the DPT shows a synchronous (or concerted) or sequential (or stepwise or successive) mechanism. In this chapter the DPT mechanism of porphine will be inquired entering a hot debate of the last decades [60, 68–85].

The research carried out here aims at a proof of principle, showing that the question addressed till now was wrong, since it implied a restricted classification of the mechanism either as concerted or stepwise. Both mechanisms in fact may occur simultaneously, albeit with different probabilities, or even a switch from one to the other mechanism may be observed. Moreover, the classification of the DPT may depend on the definition of the two mechanisms themselves. On the side of quantum chemistry (QC), the classification was essentially based on the discussion of the saddle points [61, 65, 68] of the PES for a given system. In other words, the system will prefer the mechanism with the lower energy barrier. In the same fashion sometimes the decision is based on consideration of the reaction path: if it leads from the reactant to the product via a quasi-bound reaction

intermediate which is characterized by a local minimum on the PES, then the mechanism is classified as stepwise, otherwise as concerted, see e.g. Refs. 80,81. Accordingly, constrained dynamics simulations along specific paths *a priori* classify a mechanism as either stepwise or concerted. In contrast, unconstrained classical Molecular Dynamics(MD) simulations carried out by Ushiyama and Takatsuka [73], discovered, for example, that the DPT in the formic acid dimer shows a sequential mechanism, even though the second hydrogen is transferred only 8 fs later. This result contradicts previous studies based on exclusively energetic considerations, which favour the synchronous mechanism. Their counter-intuitive result is supported by an in-depths-discussion of the underlying properties of the system, which induce the sequential events [73]. A new and very interesting definition of concerted and stepwise mechanisms has been recently given by Houk et al. [66], see also Refs. 65,84,85, who carried out MD simulation of 1,3-dipolar cycloadditions. They classify the mechanism as synchronous, if the two new bonds in the reaction are formed within a time gap below a characteristic period of vibration. In particular, the reactions between nitrous oxide, fulminic acid and methylene nitrone with acetylene occurs in a time scale below 30 fs, which is the vibrational period of the characteristic bending mode of the three linear molecules. Since this bending mode distorts the reactants, supporting the formation of the precursors of the respective transition states (TS), the phenomenon can also be described in terms of Polanyi rules [86], where the excitation of the vibrational mode can be seen as a typical late barrier reaction. In this new definition, however, the formic acid dimer DPT should be regarded as synchronous again, in contrast with the assignment as sequential given by Ushiyama and Takatsuka [73]. Apparently, different definitions based on MD simulations may yield different classifications.

In contrast with the previous MD simulations [65,66,73], and with the previous quantum dynamics simulations along a selective reaction coordinate [80–83], in the present approach quantum dynamics simulations are carried out for the DPT reaction of a model porphine, which involves the breaking of two NH bonds and the formation of two alternative NH bonds, in the electronic ground state. The purpose of this work is on the one hand to demonstrate a proof of principle, the scenario of competing synchronous and sequential mechanisms via alternative reaction to be possible, and on the other hand to answer the question about synchronous or sequential mechanism within a quantum time-dependent approach, since, as it will be seen later, the quantum effects play a major role for a switch from a synchronous to a sequential mechanism. Moreover another important aspect disregarded in the previous approaches is considered here, namely the initial preparation of the reactants, which effects the mechanism. Unfortunately, performance of quantum instead of classical dynamics simulations is much more demanding, so that a dimensionally reduced model of porhine is used. In the next section the model of porphine designed by Smedarchina, Siebrand, and Fernández-Ramos [69] is adapted. This model has also been used in a recent quantum model simulation of laser driven double proton transfer [87].

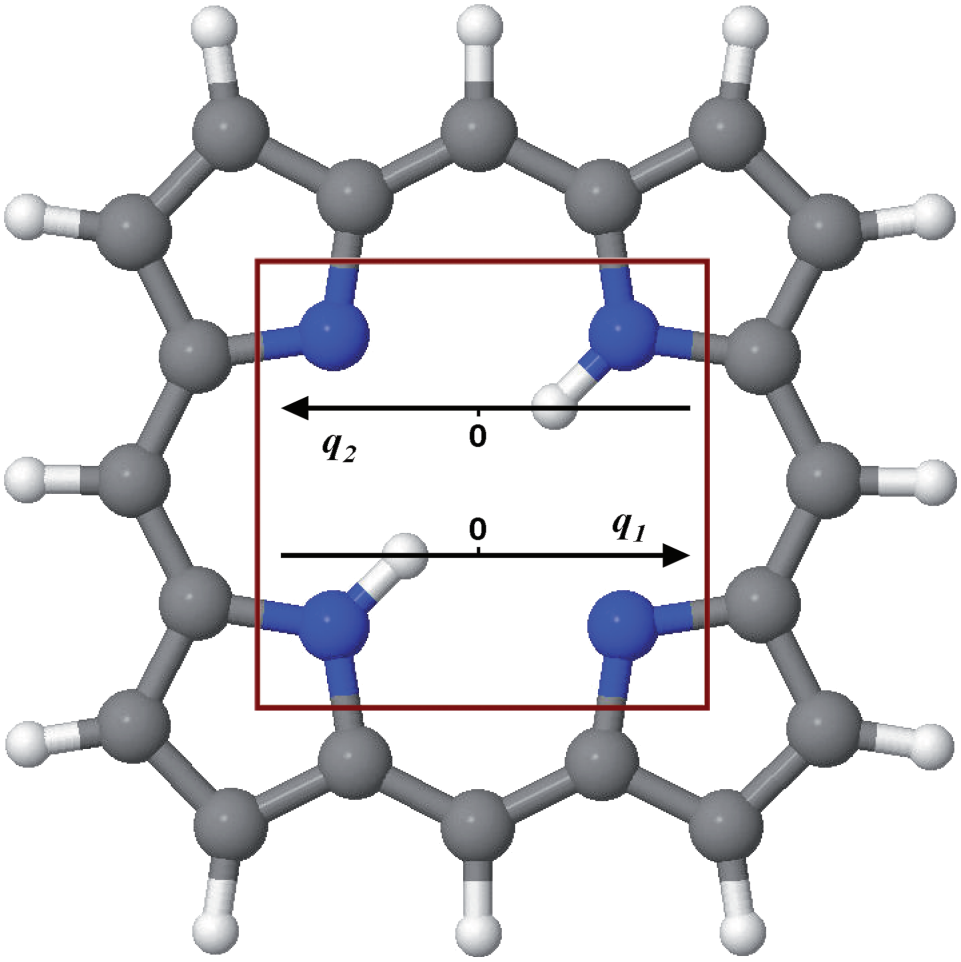

Figure 3.1: Double proton transfer of the model porphine, adapted from Smedarchina et al. [69]. The protons move along coordinates q_1, q_2. The snapshot shows the configuration of the minimum of the model PES, see Eq. 3.1, corresponding to the reactant.

3.2 Model

The simple two-dimensional model of porphine [69] adopted in this work takes into account only the constrained dynamics of the two protons of the DPT reaction and clearly involves many approximations. Recalling the multi-stage adiabatic separation tool in Chap. 2, at the first stage the electronic and nuclear motions are adiabatically separated. Afterwards the fast vibrational DOFs of the light protons is adiabatically separated from the slow motions of the heavy molecular scaffold, which is therefore considered frozen (see also Fig. 2.1). It should also be recalled that the light DOFs, i.e. the motion of the two protons, is treated in a time-dependent picture in close analogy to the attosecond chemistry [24], where the position of the electrons in time is investigated. In contrast, in Chaps. 4 and 5, the light DOFs are exclusively treated in a time-independent picture. Obviously, excitation of the other vibrational DOFs can have a dramatic influence on the DPT dynamics, as

recently shown by Waluk and coworkers [88] on the related porphycene molecule, but in the time scale of a few tens of femtoseconds investigated here, the adiabatic separation of the two fast proton from the scaffold can be considered a valid assumption, as supported in a paper by Limbach [89], based on the Rice-Ramsperger-Kassel-Marcus (RRKM) theory, which states that the molecule shows a slow intramolecular vibrational relaxation (IVR). Finally, with respect to the first chapter, the resulting two-dimensional PES for the motion of the two hydrogens refers to the light adiabatic potential of Eq. 2.11, which is here obtained by using the analytical model by Smedarchina et al. [69] fitted to experimental and calculated parameters.

The model is illustrated in Fig. 3.1. The two protons are labeled 1 and 2 and move parallel along the coordinates q_1 and q_2, respectively. A DPT reaction is always completed when the two protons have moved from the domain of the reactant close to $q_1 = q_2 = -\Delta q_{min}$ to the product domain near to $q_1 = \Delta q_{min}$ and $q_2 = \Delta q_{min}$, or back from the product to the reactant domain. The analytical function for modelling the PES is given by

$$W_{\mathrm{nuc}}^{(n=0)}(q_1, q_2) = \frac{U_0}{\Delta q_0^4}\left[\left(q_1^2 - \Delta q_0^2\right)^2 + \left(q_2^2 - \Delta q_0^2\right)^2 - 4G\Delta q_0^2 q_1 q_2\right] + 2G(2+G)U_0 \ . \quad (3.1)$$

where $W_{\mathrm{nuc}}^{(n=0)}(q_1, q_2)$ uses the nomenclature of Chap. 2 with the quantum number, $n = 0$, indicating the adiabatic electronic ground state. The function represents a quartic potential and can be thought of as a two-dimensional quadruple-well potential, with an additional bilinear coupling between the transfers of the two single hydrogens. The parameter $U_0 = 0.473$ eV has been fitted in Ref. 69 considering the experimental results of nuclear magnetic resonance (NMR) and laser-induced fluorescene (LIF) measurements of Refs. 90–92 and represents the barrier height for the transfer of one single decoupled hydrogen, i.e $G = 0$. The parameters $\Delta q_0 = 1.251\, a_0$ and $G = 0.063$ are based on density functional theory (DFT) calculations of Smedarchina et al. [93] at the B3LYP/6-31G* level. Finally the constant term $2G(2+G)U_0$ is added in order to shift the PES, such that the two equivalent global minima for the reactant (R, cf. 3.1) and the product (P) are set to zero, $W_{\mathrm{nuc}}^{(n=0)}(-\Delta q_{\mathrm{min}}, -\Delta q_{\mathrm{min}}) = W_{\mathrm{nuc}}^{(n=0)}(\Delta q_{\mathrm{min}}, \Delta q_{\mathrm{min}}) = 0\,\mathrm{eV}$, where $\Delta q_{\mathrm{min}} = \Delta q_0\sqrt{1+G} = 1.290\,\mathrm{a_0} \approx \Delta q_0$. Note that the nomenclature has been simplified and the first quantum number "n =0" is just indicated with its value "0".

The PES resulting from the analytical functions is shown in Fig. 3.2, where new features are now visible: the two equivalent local potential minima, $W_{\mathrm{nuc}}^{(n=0)}(\Delta q_{\mathrm{I}}, -\Delta q_{\mathrm{I}}) = W_{\mathrm{nuc}}^{(n=0)}(-\Delta q_{\mathrm{I}}, \Delta q_{\mathrm{I}}) = 8GU_0 = 0.238\,\mathrm{eV}$, which support two reaction intermediates, labeled respectively, I_1 and I_2, with $\Delta q_{\mathrm{I}} = \Delta q_0\sqrt{1-G} = 1.211\, a_0 \approx \Delta q_0$; the four equivalent barriers between reactant or product and the intermediates, $W_{\mathrm{nuc}}^{(n=0)}(-\Delta q_{\mathrm{TS}}^{+}, \Delta q_{\mathrm{TS}}^{-}) = W_{\mathrm{nuc}}^{(n=0)}(\Delta q_{\mathrm{TS}}^{+}, -\Delta q_{\mathrm{TS}}^{-}) = W_{\mathrm{nuc}}^{(n=0)}(\Delta q_{\mathrm{TS}}^{-}, -\Delta q_{\mathrm{TS}}^{+}) = W_{\mathrm{nuc}}^{(n=0)}(-\Delta q_{\mathrm{TS}}^{-}, \Delta q_{\mathrm{TS}}^{+}) = (1+2G)^2U_0 =$

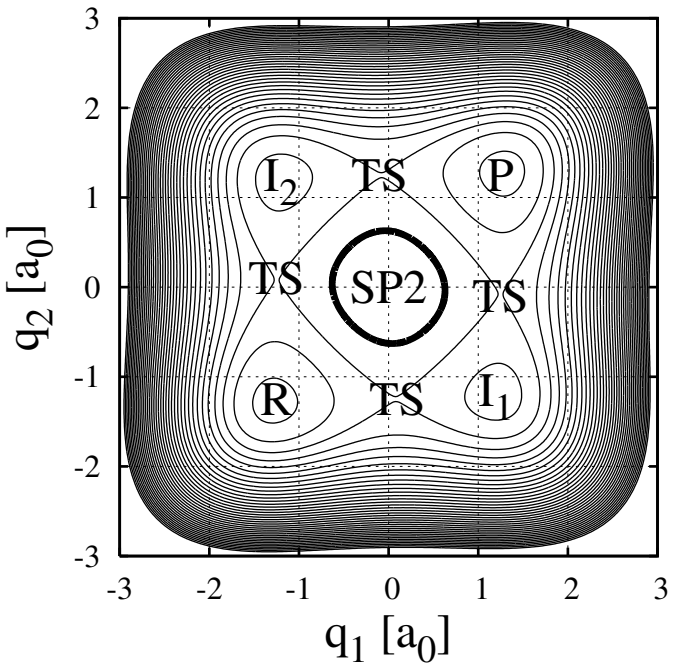

Figure 3.2: Potential energy surface for double proton transfer of the model porphine, see Eq. 3.1, adapted from Ref. 69. The equidistant values of the contours range from 0 eV for the potential minima for the reactant (R) and product (P) configurations, to 9.7 eV. The corresponding energies of the local minima for the intermediates I_1, I_2, of the four barriers labeled TS, and of the saddle point SP2 are 0.238, 0.600 and 1.069 eV, respectively. Synchronous double proton transfer leads via the domain which is encircled by the thick contour; its energy is 0.860 eV, and it passes through the point $(-\Delta q_0/2, 0)$ and three other equivalent points, half way between SP2 and TS.

0.600 eV, where $\Delta q^{\pm}_{\rm TS} = (\Delta q_0/\sqrt{2})\sqrt{1 \pm \sqrt{1-4G^2}}$, hence $\Delta q^{+}_{\rm TS} = 1.249\, a_0 \approx \Delta q_0$ and $\Delta q^{-}_{\rm TS} = 0.079\, a_0$. Please, note how the small displacements, $\Delta q^{-}_{\rm TS}$, can be discovered in Fig. 3.2. The label TS of the four barrier reminds of "transition states" for two alternative sequential reaction mechanisms, which are illustrated schematically in Fig. 3.3. The forward reactions can lead from the reactant R to the intermediate I_1 and I_2 via two alternative TSs and subsequently via the other two alternative TSs to the product P. Equivalently, the back reaction is also shown in Fig. 3.3. Additionally, Fig. 3.2 shows a saddle point, $W^{(n=0)}_{\rm nuc}(0,0) = 2(1+G)^2 U_0 = 1.069$ eV, labeled SP2, since it is a saddle point of second order with two imaginary frequencies corresponding, in two dimensions, to a maximum. Thus, the synchronous mechanism leads from the reactant R to the product P via the SP2, as schematically illustrated in Fig. 3.4.

In order to analyse the dynamics of the DPT, the PES was schematically divided in different domains (D), as illustrated in Fig. 3.5. The different domains are D = R, P, SP2, I_1 and I_2. In both Figs 3.2 and 3.5 the SP2 domain is encircled by the equi-potential-contour $W^{(n=0)}_{\rm nuc}(q_1, q_2) = 0.860$ eV, which passes through the four points half way ("equal

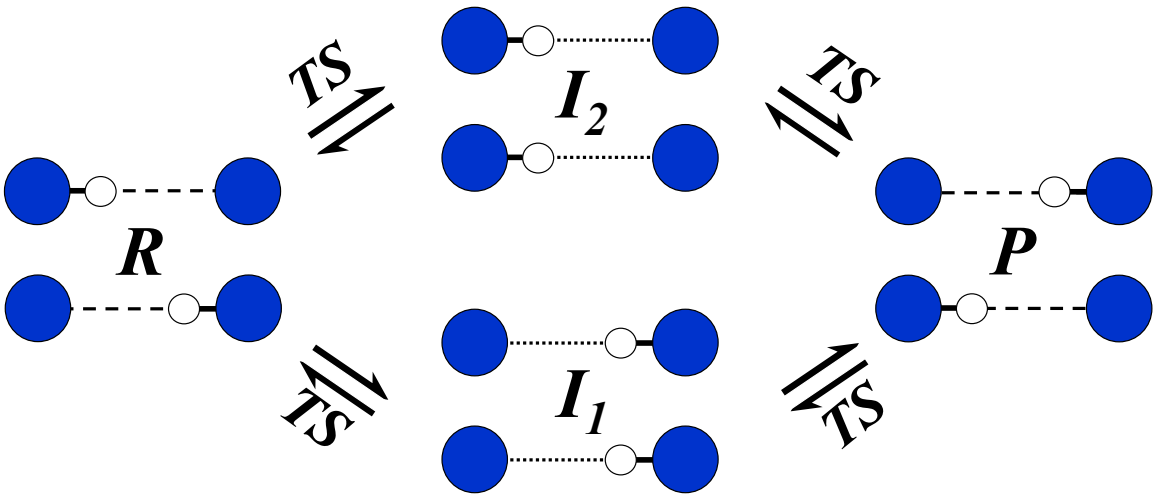

Figure 3.3: Two equivalent mechanisms for sequential double proton transfer of the model porphine, from the reactant R via alternative barriers or transition states TS to intermediates I_1 or I_2, and subsequently via the other two TS to the product P, and back (schematic). The path via I_1 corresponds to initial motion of proton 1 along q_1, followed by the motion of proton 2 along q_2, from the reactant to the product configurations. The path via I_2 has the reverse order of the sequential steps, first transfer of proton 2, then 1. Compare with Figs 3.1 and 3.2.

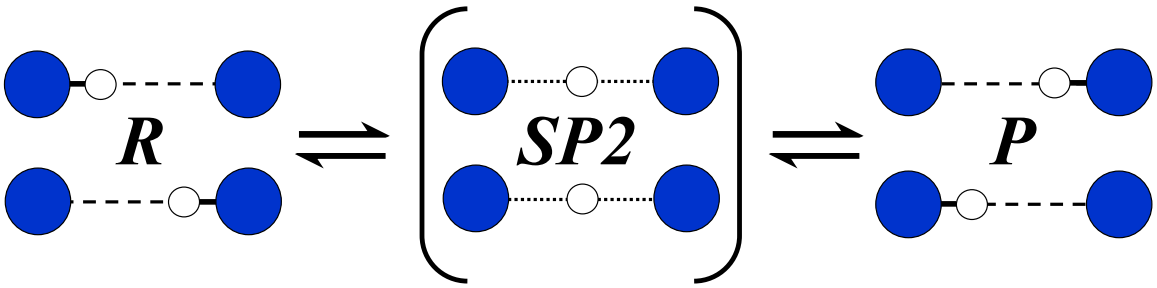

Figure 3.4: Synchronous double proton transfer of the model porphine, from the reactant R via the saddle point SP2 to the product P, and back (schematic). Compare with Figs 3.1 and 3.2.

share") between the saddle point SP2 and the four barriers TS, e.g. $(q_1 = -\Delta q_0/2, q_2 = 0)$. Finally, Fig. 3.5 also shows the domain boundaries (DB), which will be labeled using the same notation, DB = R, P, SP2, I_1, I_2. The straight lines DB(R,I_1), DB(I_1,P), DB(P,I_2), DB(I_2,R), separating the neighbouring domains R and I_1, I_1 and P, P and I_2 as well as I_2 and R from each other, extend to infinity and are connected by quarter circle. This ensures closed loops for each of the domains R, I_1, P, I_2. However, these extensions are physically irrelevant, since the representative wavefunction never penetrates outside the region which is shown in Fig. 3.2, since the potential energy goes to infinity for q_1 and $q_2 = \pm\infty$. This means the corresponding densities are negligible, beyond the domain boundaries which

are shown in Fig. 3.5. The definition of these domains and their boundaries is, of course, somewhat arbitrary, but reasonable. Other reasonable definitions, e.g. slightly smaller or larger domains SP2, possibly with different shapes of the boundaries, yield equivalent results and conclusions.

The potential provided by Eq. 3.1 is symmetric with respect to the diagonal $q_1 = \pm q_2$, since reactants and products are identical, according to experimental results by Limbach and coworkers for various similar environments [89–92]. Consequently, the corresponding eigenstates of the PES must be near-degenerate doublets, namely $\Psi_{\text{light}}^{(n=0,\ v_f+)}(q_1, q_2)$ and $\Psi_{\text{light}}^{(n=0,\ v_f-)}(q_1, q_2)$, with respective energies $E_{\text{light}}^{n=0,\ v_f+}(q_1, q_2)$ and $E_{\text{light}}^{n=0,\ v_f-}(q_1, q_2)$, delocalized, either preferably in the R and P, or I_1 and I_2. The heavy model Hamiltonian for the DPT is defined as

$$\hat{\mathbf{H}}_{\text{light}}(q_1, q_2) = \frac{\hat{\mathbf{P}}_\mathbf{1}^2}{2M} + \frac{\hat{\mathbf{P}}_\mathbf{2}^2}{2M} + W_{\text{nuc}}^{(n=0)}(q_1, q_2) \tag{3.2}$$

where

$$\begin{pmatrix} \hat{\mathbf{P}}_\mathbf{1} \\ \hat{\mathbf{P}}_\mathbf{2} \end{pmatrix} = -i\hbar \begin{pmatrix} \partial/\partial q_1 \\ \partial/\partial q_2 \end{pmatrix} \tag{3.3}$$

are the momentum operators conjugate to q_1, q_2, and $M = m_p$ is the proton mass. The symmetry of the PES in Eq. 3.1, implies that the Hamiltonian in Eq. 3.2, is symmetric with respect to exchange of protons 1 and 2, namely

$$\hat{\mathbf{H}}_{\text{light}}(q_1, q_2) = \hat{\mathbf{H}}_{\text{light}}(q_2, q_1). \tag{3.4}$$

The initial ($t = 0$) state $\Psi_{\text{light}}(q_1, q_2, t = 0)$ is determined by propagating in imaginary time an initial two-dimensional wavefunction in the domain of the reactant by using Eq. 2.147 and the MCTDH method [36, 53]. This initial guess is a Hartree product (see Eq. 2.77, but for generalized DOFs) of one dimensional ground state eigenfunctions, obtained by diagonalizing two one-dimensional operators [53] for two respective one-dimensional cuts of the two-dimensional PES, $W_{\text{nuc}}^{(n=0)}(q_1, q_2)$, along the relative DOFs, q_1 and q_2 at the minimum of the reactant well R. At the initial time, $\tau = 0$, of the relaxation, the two-dimensional Hartree product is represented in MCTDH as a linear combination in the doublet eigenstates, see Eq. 2.149, calculated by solving the TDSE of Eq. 2.18 for $W_{\text{nuc}}^{(n=0)}(q_1, q_2)$,

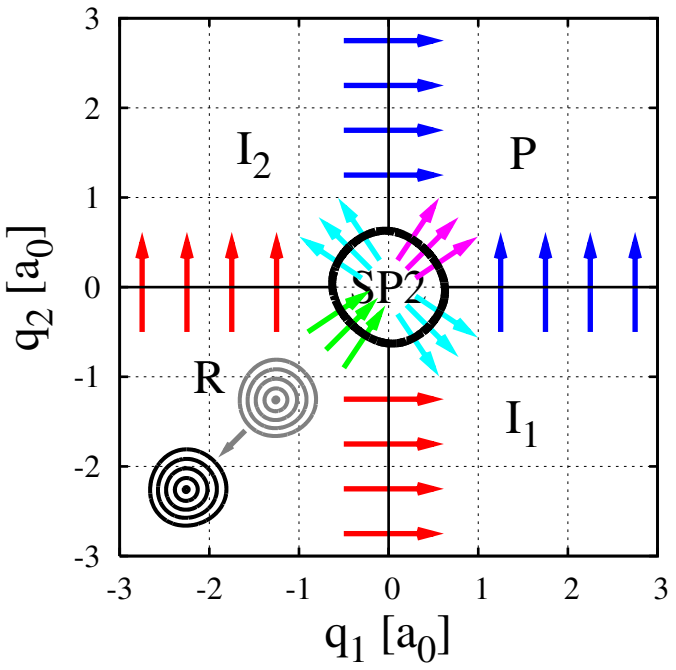

Figure 3.5: Domains of reactant (R), product (P), two intermediates (I_1, I_2), and the saddle point (SP2), together with their boundaries. Horizontal and vertical red arrows indicate the flux densities of protons 1 and 2 from the domain of the reactant R to the intermediates I_1 and I_2, respectively, corresponding to the first step of the two alternative routes of the sequential reaction mechanism, cf. 3.3. Likewise, vertical and horizontal blue arrows symbolize the flux densities of protons 2 and 1, from domains I_1 or I_2 to the product P, respectively, corresponding to the second step of the sequential reaction mechanism (schematic). Moreover, green and magenta arrows indicate the flux densities at the boundaries between domains R and SP2 as well as SP2 and P, respectively, corresponding to synchronous double proton transfer, see 3.4. Furthermore, cyan arrows indicate the flux densities at the boundaries between SP2 and intermediates I_1, I_2. Also shown by equi-density contours is the ground state wavefunction $\Psi_{\text{light,R}}^{(n=v_f=0)}(q_1, q_2, t = 0)$ (gray), 3.6, which is localized close to the potential minimum in the domain of the reactant (R), together with the initial wavefunction $\Psi_{\text{light}}(q_1, q_2, t = 0)$ (black), 3.7, which is obtained by a shift (gray arrow) of $\Psi_{\text{light,R}}^{(n=v_f=0)}(q_1, q_2, t = 0)$ along the diagonal $q_1 = q_2$, see text.

$$\hat{\mathbf{H}}_{\text{light}} \Psi_{\text{light}}^{(n=0,\ v_f\pm)}(q_1, q_2, t = 0) = E_{\text{light}}^{(n=0,\ v_f\pm)} \Psi_{\text{light}}^{(n=0,\ v_f\pm)}(q_1, q_2, t = 0). \tag{3.5}$$

Finally, after a relaxation time of $\tau_{rel} = 28$ fs the corresponding localized ground state is obtained, which is the superposition of the ground state doublet

$$\Psi_{\text{light,R}}^{(n=v_f=0)}(q_1, q_2, t = 0) = \frac{1}{\sqrt{2}}[\Psi_{\text{light}}^{(n=0,\ v_f=0+)}(q_1, q_2) + \Psi_{\text{light}}^{(n=0,\ v_f=0-)}(q_1, q_2)] \tag{3.6}$$

with mean energy $E_{\text{light,R}}^{(n=v_f=0)} = (E_{\text{light}}^{(n=0,\ v_f=0+)} + E_{\text{light}}^{(n=0,\ v_f=0-)})/2 = 0.194$ eV. The localized wavefunction is rigorously non-stationary, since it tunnels from the reactant to the product with tunneling time $\tau_0 = h/\Delta E_0$, where $\Delta E_0 = E_{\text{light}}^{(n=0,\ v_f=0-)} - E_{\text{light}}^{(n=0,\ v_f=0+)}$ is the tunneling splitting. ΔE_0 is a very small number: the four barriers TS in fact ensure both $E_{\text{light}}^{(n=0,\ v_f=0+)}$ and $E_{\text{light}}^{(n=0,\ v_f=0-)}$ to be below the TS barrier height $W_{\text{nuc}}^{(n=0)}(-\Delta q_{\text{TS}}^{+}, \Delta q_{\text{TS}}^{-}) = 0.600$ eV and, therefore, their difference to be even smaller. Consequently, the tunneling time τ_0 is very long compared both with the relaxation time τ_{rel} and with the final time of propagation of approximately $T = 40$ fs and is therefore negligible. From the experimental point of view, such a localized ground state may be created by symmetry breaking, namely by deuteration of the C_4N rings. The slightly heavier mass in fact does not change the PES, but induces a localization of the reactant wavefunction. For reference, in harmonic approximation, each of the two global potential minima supports two normal modes, one for symmetric vibration along the diagonal $Q_1 = Q_2$, with vibrational period $t_{sym} = 21.2$ fs, and the other one for perpendicular antisymmetric vibration, $t_{asym} = 20.6$ fs.

As mentioned above, the dynamics crucially depends on the preparation of the initial wavefunction. In this study the following scenario is chosen, where the localized wavefunction, $\Psi_{\text{light,R}}^{(n=v_f=0)}(q_1, q_2, t = 0)$, is displaced along the diagonal $q_1 = q_2$ to a non-equilibrium position

$$\Psi_{\text{light}}(q_1, q_2, t = 0) = \Psi_{\text{light,R}}^{(n=v_f=0)}(q_1 + \Delta q, q_2 + \Delta q, t = 0) \tag{3.7}$$

as shown in Fig. 3.5, where $\Delta q = -1\, a_0$. Such a shift can be induced, for example, by means of pump-dump laser pulse control, as designed by Tannor and Rice [94–97]. Shortly, the first ultra-short pump pulse transfers the wavepacket to the excited electronic state, where it evolves until it is shifted to the target position. At this point the dunp pulse transfers the wavepacket back to the electronic ground state. A similar shift has been shown recently by means of laser pulse control, by Kapteyn, Murnane and coworkers [98]. The displaced wavefunction has now a new mean energy $E_0 = 4.885$ eV. The wavefunction at later time $t > 0$ is evaluated by solving the TDSE of Eq. 2.18 using again the MCTDH method [36,53].

3.3 Fluxes and Flux Densities

The quantitative analysis of the dynamics of the DPT was done by evaluating the fluxes and flux densities flowing from a domain to the neighbouring ones through the boundaries defined in the previous section. The net fluxes can be calculated by deriving the population in each of the domains with respect to the time:

$$F_{\mathrm{D}}(t) = \frac{d}{dt} P_{\mathrm{D}}(t) = \dot{P}_{\mathrm{D}}(t) \ , \tag{3.8}$$

where the population is obtained by integration of the densities in the domains D = R,P,SP,I_1 or I_2 with respect to the two coordinates q_1 and q_2 for each time step

$$P_{\mathrm{D}}(t) = \int \int_{\mathrm{D}} \rho(q_1, q_2, t)\, dq_1 dq_2 \ . \tag{3.9}$$

and the density is obtained from the propagated wavefunction as

$$\rho(q_1, q_2, t) = |\Psi_{\mathrm{light}}(q_1, q_2, t)|^2, \tag{3.10}$$

Please note that for the present 2D model, the density in Eq. 3.10 has units of 1/area, analogous to the units of 1/volume of the densities in the 3D world. Similarly, the fluxes can be calculated by integrating the flux densities along the domain boundaries DB = R,P,SP,I_1 or I_2

$$F_{\mathrm{D}}(t) = -\int_{\mathrm{DB}} \vec{j}(q_1, q_2, t) \cdot d\vec{S}(q_1, q_2) \ , \tag{3.11}$$

where $|d\vec{S}(q_1, q_2)|$ represents the infinitesimal part of the boundaries at (q_1, q_2) and $d\vec{S}(q_1, q_2)$ denotes the corresponding infinitesimal vectors perpendicular to the boundaries, pointing out of the domains. The Gauss's theorem, known as the divergence theorem, allows to rewrite the integrals of Eq. 3.11 as corresponding 2D ("surface") integrals of the divergence, $\nabla = (\partial/\partial q_1, \partial/\partial q_2)^{\mathrm{T}}$, of the flux densities in the domains D,

$$F_{\mathrm{D}}(t) = -\int \int_{\mathrm{D}} \vec{\nabla} \cdot \vec{j}(q_1, q_2, t)\, dq_1 dq_2. \tag{3.12}$$

The continuity equation for the considered model

$$\dot{\rho}(q_1, q_2, t) + \vec{\nabla} \cdot \vec{j}(q_1, q_2, t) = 0 \tag{3.13}$$

yields finally,

$$F_{\mathrm{D}}(t) = \int\int_{\mathrm{D}} \dot{\rho}(q_1, q_2, t)\, dq_1 dq_2 \ . \tag{3.14}$$

Please note that by substituting Eq. 3.9 in Eq. 3.14, Eq. 3.8 is obtained.

The symmetry of the system and its Hamiltonian, as well as the symmetry of the initial condition implies the probabilities and the fluxes for the domains of the two intermediates to be equal,

$$P_{\mathrm{I}_1}(t) = P_{\mathrm{I}_2}(t) = \frac{1}{2} P_{\mathrm{I}}(t) \tag{3.15}$$

and

$$F_{\mathrm{I}_1}(t) = F_{\mathrm{I}_2}(t) = \frac{1}{2} F_{\mathrm{I}}(t) \ , \tag{3.16}$$

so that from now on $P_{\mathrm{I}}(t)$ and $F_{\mathrm{I}}(t)$ denote the overall population and fluxes of the domain of both intermediates, $\mathrm{I} = \mathrm{I}_1 + \mathrm{I}_2$, respectively. This means that the two possible routes from the reactant to the product, $\mathrm{R} \rightarrow \mathrm{I}_1 \rightarrow \mathrm{P}$ or $\mathrm{R} \rightarrow \mathrm{I}_2 \rightarrow \mathrm{P}$, have the same probabilities at any time.

The population present in the different domains during the propagation of the initial wavepacket is used to indicate whether the synchronous or sequential DPT mechanism is preferred by the system, as discussed in the next section. If the population in the SP2 domain, $P_{\mathrm{SP2}}(t)$, is larger than the population in the I domain, $P_{\mathrm{I}}(t)$, then the system prefers a synchronous mechanism, and vice versa. In order to analyse even more deeply the DPT reaction, it would be interesting to evaluate not only the whole population flowing out from each of the domains to its neighbor ones (net fluxes), but to evaluate the so-called domain-to-domain (DTD) fluxes from one domain (say D1) to only one of the neighboring ones (say D2), as well. These new fluxes will be denoted as $F_{\mathrm{D1,D2}}(t)$. The DTD fluxes can be obtained by using Eq. 3.11 after the two-proton flux density has been calculated from the wavefunction as

$$\vec{j}(q_1, q_2, t) = \frac{1}{2M} \left(\Psi^*_{\mathrm{light}}(q_1, q_2, t) \hat{\mathbf{P}}\, \Psi_{\mathrm{light}}(q_1, q_2, t) - \Psi_{\mathrm{light}}(q_1, q_2, t) \hat{\mathbf{P}}\, \Psi^*_{\mathrm{light}}(q_1, q_2, t) \right) \tag{3.17}$$

where the two components $j_1(q_1, q_2, t)$, $j_2(q_1, q_2, t)$ correspond to the one-proton flux densities of protons 1 and 2, respectively. Please note that the components of the flux density have units of $1/(\mathrm{time} \cdot \mathrm{length})$, analogous to the units of $1/(\mathrm{time} \cdot \mathrm{area})$ of the familiar flux

density in the 3D space. Due to the momentum operator in Eq. 3.17, the first derivative of the wavefunction has been evaluated numerically using finite difference approximations for representations of the wavefunction on the non-equidistant grids used in the MCTDH propagations. For example the DTD flux between the domain of the reactant R and the specific intermediate I_1 is evaluated as

$$F_{\mathrm{R,I_1}}(t) = -\int_{\mathrm{DB(R,I_1)}} \vec{j}(q_1, q_2, t) \cdot d\vec{S}(q_1, q_2) = -\int_{-\infty}^{-\Delta q_0/2} j_1(q_1 = 0, q_2, t)\, dq_2 \ , \quad (3.18)$$

where DB(R,I_1) is the straight line boundary between domains R and I_1, see Fig. 3.5. The integral is evaluated by using the midpoint rectangle rule applied to the fluxes density representation on the non-equidistant grid employed for the MCTDH propagation of the wavefunction in principle between $-\infty$ and $-\Delta q_0/2$, which corresponds to the boundary between the two domains. Equally, the DTD flux between the domain I_1 and the product P can be calculated as

$$F_{\mathrm{I_1,P}}(t) = -\int_{\mathrm{DB(I_1,P)}} \vec{j}(q_1, q_2, t) \cdot d\vec{S}(q_1, q_2) = -\int_{\Delta q_0/2}^{\infty} j_2(q_1, q_2 = 0, t)\, dq_1 \ . \quad (3.19)$$

For symmetry reasons, the DTD fluxes between R and I_1 and R and I_2, as well as between P and I_1 and P and I_2 are again equal,

$$F_{\mathrm{R,I_2}}(t) = F_{\mathrm{R,I_1}}(t) = \frac{1}{2} F_{\mathrm{R,I}}(t) \ , \quad (3.20)$$

and

$$F_{\mathrm{I_2,P}}(t) = F_{\mathrm{I_1,P}}(t) = \frac{1}{2} F_{\mathrm{I,P}}(t) \ , \quad (3.21)$$

where $F_{\mathrm{R,I}}(t)$ and $F_{\mathrm{I,P}}(t)$ denote the overall DTD flux between R and the domain of the two alternative intermediates, I = I_1 + I_2, and between the domain of the two alternative intermediates, I = I_1 + I_2, and P, respectively. In general, the infinitesimal vectors $d\vec{S}(q_1, q_2)$ for the DTD fluxes $F_{\mathrm{D1,D2}}(t)$ are perpendicular to the boundaries DB(D1,D2) and point from D1 to D2. Consequently, the DTD flux $F_{\mathrm{D1,D2}}(t)$ is negative for the proton transfer from D1 to D2 and vice versa.

Moreover, microscopic reversibility implies

$$F_{\mathrm{D1,D2}}(t) = -F_{\mathrm{D2,D1}}(t). \quad (3.22)$$

Finally, the balance equations are employed for the net fluxes, Eq. 3.8, for all domains D = R, P, SP2, I = I_1 + I_2, in terms of all the DTD fluxes, specifically

$$
\begin{aligned}
F_{\mathrm{R}}(t) &= F_{\mathrm{R,I}}(t) + F_{\mathrm{R,SP2}}(t) && (3.23)\\
F_{\mathrm{P}}(t) &= F_{\mathrm{P,I}}(t) + F_{\mathrm{P,SP2}}(t) && (3.24)\\
F_{\mathrm{SP2}}(t) &= F_{\mathrm{SP2,R}}(t) + F_{\mathrm{SP2,P}}(t) + F_{\mathrm{SP2,I}}(t). && (3.25)\\
F_{\mathrm{I}}(t) &= F_{\mathrm{I,R}}(t) + F_{\mathrm{I,P}}(t) + F_{\mathrm{I,SP2}}(t) && (3.26)\\
0 &= F_{\mathrm{R}}(t) + F_{\mathrm{P}}(t) + F_{\mathrm{SP2}}(t) + F_{\mathrm{I}}(t)\ . && (3.27)
\end{aligned}
$$

where the Eq. 3.27 is the conservation of fluxes obtained by summing up all net fluxes. The last five equations allow the indirect calculation of the DTD fluxes between the domains SP2 and R and P, $F_{\mathrm{R,SP2}}(t)$ and $F_{\mathrm{P,SP2}}(t)$, respectively, which are used in order to measure the DTD fluxes associated with the synchronous mechanism, as well as the DTD fluxes between the domains SP2 and I. Please note that direct integration of the flux density in the partially circular boundaries of the SP2 domain would have been a more difficult task. To the best of our knowledge, the complete DTD fluxes between neighbouring domains have not been calculated previously, with the exception of special cases where the overall fluxes from R to P were evaluated, see, for example, Refs. 83, 99.

3.4 Results

The populations in all the domains versus time are shown in Fig. 3.6a. The net fluxes together with their decomposition in the DTD fluxes are shown in Figs 3.6b-e. Finally, in Fig. 3.7 the densities and flux densities are shown with snapshots of the salient moments (identified by t_a, t_b, t_c, ... , t_l corresponding to the events **a**,**b**,**c**, ... ,**l** shown both in Figs 3.6a and 3.7) of the wavepacket propagation. Analysis of this detailed documentation yields, as a proof of principle, a switch of the reaction mechanism of the DPT reaction of the model porphine from synchronous to sequential. In principle, at any time the $P_{\mathrm{D}}(t)$ curves represent the probabilities of the different species D on the PES. In general, higher or smaller $P_{\mathrm{D}}(t)$ values corresponds to more and less important population and processes, respectively. Specifically, dominance of $P_{\mathrm{SP2}}(t)$ or $P_{\mathrm{I}}(t)$ documents a mechanism which is preferably (not exclusively!) synchronous or sequential. The discovery of simultaneous occurrence of more than one species on the PES, reflects the non-deterministic quantum description of the process and, as a consequence, makes the reaction never either synchronous or sequential. Instead, it may proceed at the same time both synchronously and sequentially, albeit with different probabilities. Consider first the populations in Fig. 3.6a. At time $t_a = 0$ the whole population resides in the reactant domains R, since it corresponds to the prepared initial state (see Eq. 3.6 in sec. 3.2). At time $t_b = 3$ fs, the reactant is still dominant with probability $P_{\mathrm{R}}(t_b) > 0.99$. Afterwards, the two protons of the model

porphine are transferred preferably with a synchronous mechanism during the first forward reaction from R to P. The transfer from the reactant region to the SP2 domain is evident from the loss of $P_{\mathrm{R}}(t)$, which starts soon after 5 fs, and from the increase of $P_{\mathrm{SP2}}(t)$, e.g. $P_{\mathrm{SP2}}(t_c) = 0.264$, $P_{\mathrm{SP2}}(t_d) = 0.657$, $P_{\mathrm{SP2}}(t_e) = 0.475$ at $t_c = 5.65\,\mathrm{fs}$, $t_d = 6.75\,\mathrm{fs}$, $t_e = 7.75\,\mathrm{fs}$, respectively. Subsequently, the population flows to the product region P and reaches its maximum value $P_{\mathrm{P}}(t_f) = 0.959$ at $t_f = 14.85$ fs. Soon after, the first back propagation to the product starts and, in fact, the population in the domain P at $t_g = 17.8$ fs already decreases to $P_{\mathrm{P}}(t_g) = 0.756$. This time the population flows back to the reactant preferably via the I domains, namely following the sequential mechanism: the maximum population $P_{\mathrm{I}}(t_h) = 0.390$ is reached at $t_h = 21.20$. Finally, the reactant rises again to its second maximum population, $P_{\mathrm{R}}(t_j) = 0.793$ at $t_j = 27.75$ fs ending the first back propagation. At this point, the second forward propagation starts which again is dominantly sequential, $P_{\mathrm{I}}(t_k) = 0.326$ at $t_k = 34.90\,\mathrm{fs}$. The second maximum for the product is reached at $t_l = 40.90\,\mathrm{fs}$, $P_{\mathrm{P}}(t_l) = 0.618$. Fig. 3.6a shows that the maximum probabilities for R and P never reach 1 again, but decreases continuously in favour of SP2 and in particular of I. This behaviour is linked to well-known quantum effects of wavepackets, which are composed of faster and slower parts. The faster parts, in fact, run away, whereas the slower parts lack behind causing an increasing "wash-out" effect of the dominant population to the benefit of others. Summarizing Fig. 3.6a, the two protons of the model porphine are transferred preferably concertedly during the first forward propagation, but stepwise during the first back and second forward propagations, which provides the proof of principle. The subsequent analysis of the fluxes gives more detailed information of the underlying effects.

The flux dynamics shown in Figs 3.6b-e may be divided into two different periods: the initial one corresponding to the first forward propagation, where the concerted process dominates, and a second one corresponding to the first back and second forward propagations, where both mechanisms are present, but nevertheless, the sequential process is dominant, as seen in Fig. 3.6a for the population analysis. Moreover, a second distinction must be done between the panels b and c, regarding the fluxes of R and P, and the panels d and e regarding the fluxes of SP2 and I. The former, in fact, show unidirectional processes from R to P and vice versa, whereas the latter show unidirectional as well as antagonist processes, which in some case compensate. The second panel in Fig. 3.6 shows the net and DTD fluxes relative to the reactant: $F_{\mathrm{R}}(t)$, $F_{\mathrm{R,SP2}}(t)$ and $F_{\mathrm{R,I}}(t)$. In the first 10 fs $F_{\mathrm{R,SP2}}(t)$ dominantly participates to $F_{\mathrm{R}}(t)$ resulting in a concerted process during the first forward propagation. Later the first back and the second forward propagations is supported by both DTD components with slightly larger contribution from $F_{\mathrm{R,I}}(t)$. Likewise, in Fig. 3.6c, the net flux $F_{\mathrm{P}}(t)$ is, clearly, dominated by a the DTD fluxes from the SP2 to the P domains, $F_{\mathrm{SP2,P}}(t)$. The contribution of $F_{\mathrm{I,P}}(t)$ to $F_{\mathrm{P}}(t)$ increases, however, with respect to the contribution of $F_{\mathrm{R,I}}(t)$ to $F_{\mathrm{R}}(t)$. Subsequently, both mechanisms contribute

unidirectionally, with slightly larger losses of $F_{\mathrm{P,I}}(t)$ with respect to $F_{\mathrm{SP2,I}}(t)$ during the first back propagation, followed by more or less equal contributions during the second forward propagation. The forth panel in Fig. 3.6 shows the net and DTD fluxes relative to the saddle point domain representing the synchronous DPT. Two rather sharp opposite peaks can be noted during the first forward propagation corresponding to $F_{\mathrm{SP2}}(t)$. Its decomposition in DTD fluxes readily shows that the two peaks are due to the slightly delayed (circa 3 fs) decay of the reactant ($F_{\mathrm{SP2,R}(t)}$) and formation of the product ($F_{\mathrm{SP2,P}}(t)$) by the synchronous mechanism. Moreover, a direct switch from synchronous to the sequential mechanism is visible ($F_{\mathrm{SP2,I}}(t)$). This corresponds to the two sets of opposite arrows, from the SP2 to the I domain shown in Fig. 3.5. Pictorially speaking, they represent a switch from initial concerted motions of protons 1 and 2, corresponding to the beginning of synchronous double proton transfer, to the repulsion of one of the protons, either 2 or 1, back towards its position at the reactant, while the other one that means 1 or 2, respectively, continues its paths to the product geometry, implying formation of one of the intermediates, I_1 or I_2, respectively. Ultimately, this repulsion of the two protons from each other may be interpreted as consequence of their Coulomb interaction. Afterwards, the two contributions, $F_{\mathrm{SP2,R}}(t)$ and $F_{\mathrm{SP2,P}}(t)$ form again pairs of opposite and slightly delayed peaks which are now broader (circa 5 fs) than their delay (circa 2 fs) and have smaller amplitudes. They are reversed during each propagation from or to the P, but their effects compensate more and more, so that the initial two opposite sharp peaks become a strongly damped oscillation of $F_{\mathrm{SP2}(t)}$ around the mean value zero (note that the DTD $F_{\mathrm{SP2,I}}(t)$ does not play any role in the second part of the propagation).

The synchronous mechanism is thus dominant only during the first forward propagation ($P_{\mathrm{SP2}}(t_d) = 0.657$ and $P_{\mathrm{SP2}}(t_h) = 0.182$). The major source for this "wash-out" effect is due to several partial waves with different momenta, which lower and broadens the amplitudes of the peaks of the DTD fluxes, resulting in the suppression of the concerted mechanism. The fifth and last panel of Fig. 3.6 shows the flux dynamics of the intermediate domains I_1 and I_2 representing the sequential process. The net flux $F_{\mathrm{I}}(t)$ results from the contributions of $F_{\mathrm{I,R}}(t)$, $F_{\mathrm{I,P}}(t)$ and $F_{\mathrm{I,SP2}}(t)$. This picture appears more complex than the others, but in reality there are no prominent large amplitude peaks, which becomes clear when looking at the blow-up of the scale of the fluxes in this panel. Nevertheless, $F_{\mathrm{I}}(t)$ and its components show al least three minor effects taking place during the first part of the propagation: first the DTD flux $F_{\mathrm{I,R}}(t)$, which accompanies the dominant DTD flux $F_{\mathrm{SP2,R}}(t)$ from R to SP2 as discussed before in Figs 3.6b,d; second about 2 fs later comes the direct switch from SP2 to I given by $F_{\mathrm{I,SP2}}(t)$, discussed previously in Fig. 3.6d. Moreover, these two contribution are unidirectional and have equally large contributions. Third, the contribution $F_{\mathrm{I,P}}(t)$, which has opposite sign and slightly smaller amplitude with respect to the previous contributions, arises circa 1-2 fs after $F_{\mathrm{I,R}}(t)$ showing that the small gain of the intermediate is almost instantaneously transformed into the products P.

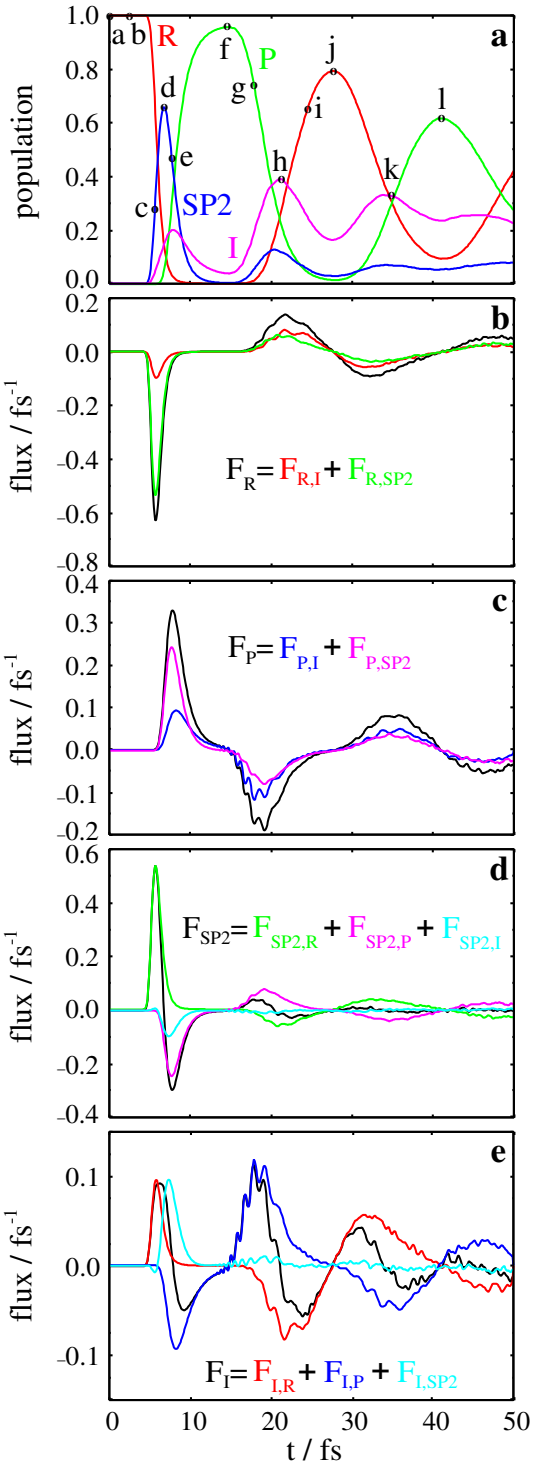

Figure 3.6: Population and flux dynamics of double proton transfer in the model porphine, starting from the initial state, Eq. 3.7. (a) Populations $P_{\mathrm{D}}(t)$ of the domains D = R, P, SP2 and I = I_1 + I_2 of the reactant, product as well as the saddle point and the two intermediates, for the synchronous and sequential reactions, respectively. The events labeled a, b, c, etc are discussed in the text. (b), (c), (d), (e) Net fluxes $F_{\mathrm{D}}(t)$ out of, or into the domains D, and domain-to-domain (DTD) fluxes $F_{\mathrm{D1,D2}}(t)$ for the domains D1 = D = R, P, SP2 and I = I_1 + I_2 and neighboring domains D2, respectively. The colors for the DTD fluxes correspond to the domain boundaries DB(D1,D2), see Fig. 3.5.

This results in the maximum population $P_{\mathrm{I}}(t)$ for the sequential mechanism for the first concerted forward propagation, close to $t = t_d$. In the following backward and second forward propagations the direct switch component $F_{\mathrm{I,SP2}}(t)$ becomes zero, as seen already in Fig. 3.6d and the net flux is the result of the superposition of the two left components, with alternate gains and losses of $F_{\mathrm{I,P}}(t)$ and $F_{\mathrm{I,R}}(t)$ in the first backward propagation and of $F_{\mathrm{I,R}}(t)$ and $F_{\mathrm{I,P}}(t)$ in the second forward propagation, respectively. Their behaviours are similar to the behaviour of $F_{\mathrm{SP2,R}}(t)$ and $F_{\mathrm{SP2,P}}(t)$ seen in panel d of Fig. 3.6. In particular, the peaks are broader (circa 5 fs) than their time delay (circa 2 fs), so that they overlap. The more and more efficient compensation ends with the damped oscillation around the mean value zero of the net flux F_{I}. The largest amplitude peak is given by $F_{\mathrm{I,P}}(t)$ at the first backward propagation and causes the population $P_{\mathrm{I}}(t_h)$ to be the dominant peak in Fig. 3.6a. Moreover, their amplitudes decrease systematically due to the "wash-out" effect. The main difference between the net flux $F_{\mathrm{I}}(t)$ and the previously discussed $F_{\mathrm{SP2}}(t)$ is the mean value around which the populations oscillate because of the damped oscillation of the respective net fluxes, which is larger for $P_{\mathrm{I}}(t)$, confirming that after the mechanism switches from concerted to sequential, it will not return.

More detailed information about the quantum nature of the underlying effects for the switch of the mechanism from concerted to sequential are illustrated in Fig. 3.7, by using snapshots of the density of the wavefunction together with the flux density which corresponds to the events **a**,**b**,**c**, ... ,**l**. In panel **a** the initial wavefunction at $t_a = 0$ fs is shown, when the flux density is still zero. During the first 3 fs the wavefunction propagate towards the global minimum of the reactant region R, driven by the L-shaped parts of the steep walls of the PES close to the reactant which impose various momenta on different part of the initial wavefunction. In panel **b** at $t_b = 3$ fs a fascinating quantum effect is visible, namely the wavepacket is squeezed into the minimum well, since the forces by the PES walls impose a "lensing" effect, such that the wavefunction is narrowed in the "focus". Similar effects are described for example in Refs. 58, 100. Subsequently, the wavefunction is driven forward and climbs the saddle point reaching the top at $t_d = 6.75$ fs. Afterwards it runs towards the product well ($t_e = 07.75$ fs), see panel e. The "lensing" effect seen before is suddenly converted into a strong dispersion of the wavefunction with several consequences. In particular, the minor DTD flux $F_{\mathrm{R,I}}(t)$, which accompanies the dominant $F_{\mathrm{R,SP2}}(t)$ at $t_c = 5.65$ fs discussed in Fig. 3.6b, is due to the wings of the wavepacket, which slightly penetrate into the domains of the two intermediates I_1 and I_2. Moreover, the dispersion causes also the small DTD flux, $F_{\mathrm{SP2,I}}(t)$, for the direct switch from concerted to sequential mechanism, seen above in Figs 3.6d,e. At $t_f = 14.85$ fs the wavepacket is already in the product domain P. This is visible in Fig. 3.7f which corresponds to the first maximum of population $P_{\mathrm{P}}(t_f) = 0.959$ of Fig. 3.6a. From now on, the wavepacket dispersion has the most decisive consequences for inducing the switch of the mechanism from synchronous to sequential. Specifically, the wavefunction crashes against the inverse L-shaped part of the

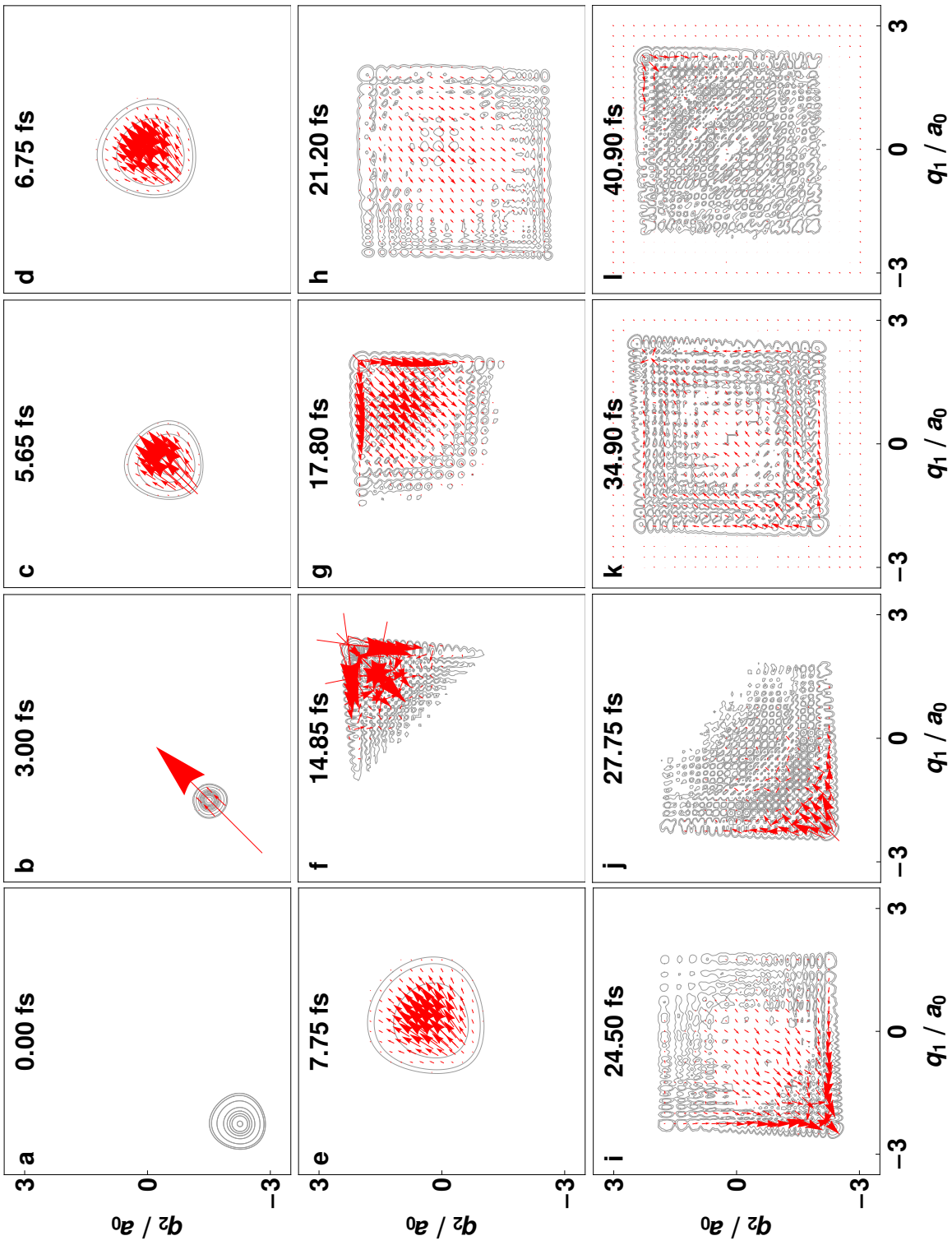

Figure 3.7: Density (equi-contours) and flux density (arrows) dynamics of the wavefunction representing double proton transfer in the model porphine, starting from the initial state, Eq. 3.7. The snapshots labeled a, b, c, etc correspond to the events a, b, c etc which are marked in 3.6a. The vectors have common logarithmic scales for panels (a)-(j), with a blow-up for panels (k), (l).

steep walls close to the minimum for the product, covering a much broader range compared with the part of the opposite L-shaped steep potential close to the reactants, covered by the initial wavepacket at $t_a = 0$ fs. Consequently, so-called relief reflections of the different parts of the wavefunction into different directions is induced [101,102]. Thus, at $t_g = 17.80$ fs in Fig. 3.7g, the wavepacket takes three major different directions: one part is scattered back towards the SP2 domain and two prominent equivalent parts are scattered towards the two intermediates domains I_1 and I_2. Therefore, it can be concluded that the present switch of the mechanism from synchronous to sequential has to be attributed to the dispersion of the wavepacket and to the relief reflections from the walls of the PES. This switch could be called "indirect" in contrast with the "direct" switch due to the DTD flux $F_{I,SP2}(t)$ seen above in Figs 3.6d,e. A last relevant consequence of the dispersion of the wavefunction is the rich interferences patterns of the wavepacket, whose faster parts have already been scattered by the wall, whereas the slower parts are still running towards it. The Figs 3.7g-j show the first back reaction. At $t_h = 21.20$ the majority of the wavefunction is in the domains of the intermediates I_1 and I_2. This corresponds to the maximum population $P_I(t_h) = 0.390$ of Fig. 3.6a. The preference for the sequential mechanism is even more evident in Fig. 3.7i at $t_i = 24.50$ fs. In panel j at $t_j = 27.75$ the population of the reactant achieves its second maximum, $P_R(t_j) = 0.793$, see Fig. 3.6a. This snapshot confirms the conjecture which has been made during the discussions of the probabilities $P_R(t_j)$ and $P_I(t_h)$, that is, the time dilatation of the wavefunction is so large that even though most parts of the wavepacket are back to the domain R of the reactant, there are still some other slower parts which lack behind in domain I. The two last panels, k and l, of Fig. 3.7 at $t_k = 34.90$ fs and $t_l = 40.90$ fs confirm the dominance of the sequential mechanism, as well as the time dilatation supported by continuous wavepacket dispersion, during the second forward reaction.

3.5 Conclusion

The proof of principle for the switch of the DPT mechanism of porhine from synchronous to sequential has been demonstrated within a simple two dimensional model, starting from the symmetric non-equilibrium position of the initial wavepacket. This is schematically depicted in Fig. 3.8, where the synchronous first forward reaction through the saddle point SP2 is followed by the sequential first backward reaction through the intermediate domains I_1 and I_2. The subsequent second forward reaction is not shown. Admittedly, the chosen scenario may be considered as somewhat extraordinary, but it is just fine for a proof of principle.

The effects for the switch of the mechanism are analyzed within quantum reaction dynamics methods starting from the qualitative patterns of densities and flux densities and from the quantitative fluxes and populations probabilities in the different domains of the

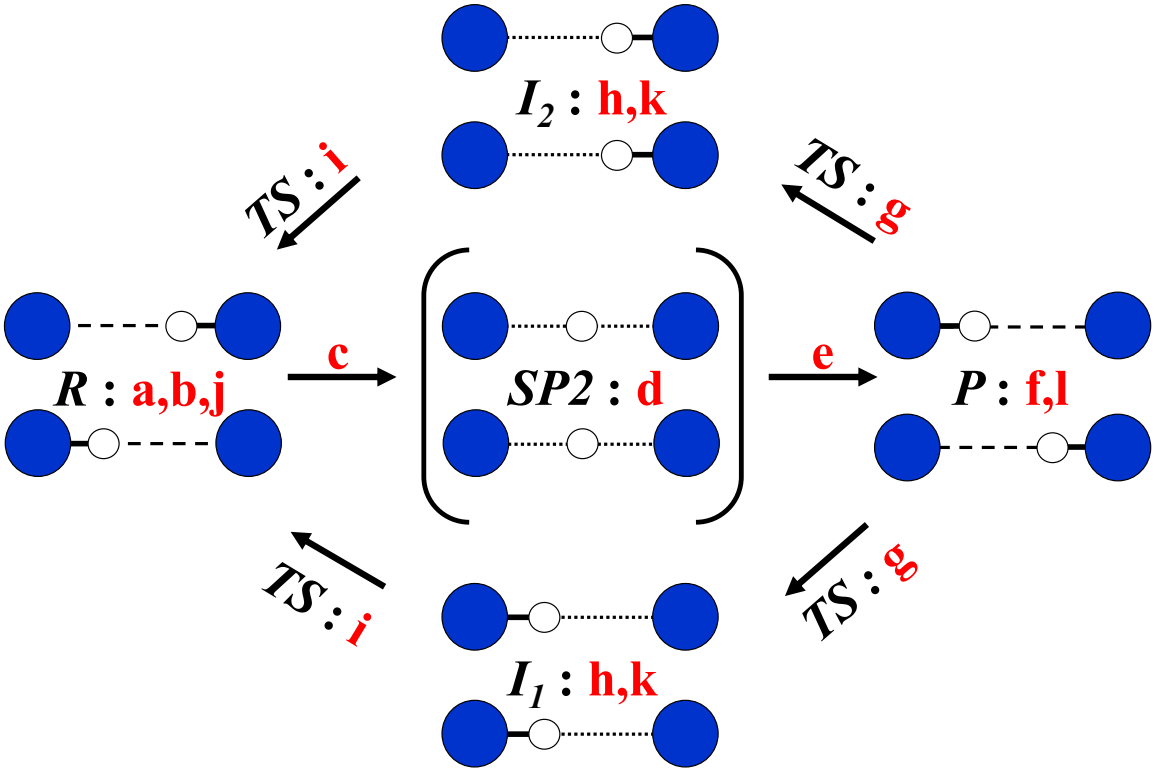

Figure 3.8: Switch from synchronous double proton transfer (DPT) of the model porphine, during the first forward reaction from the reactant (R) to the product (P) via the saddle point domain (SP2) (horizontal arrows), to two sequential DPTs during the first back reactions via two intermediates I_1 and I_2 (other arrows, schematic). The events a, b, c, etc correspond to those of Figs. 3.6 and 3.7. After the first back reaction, the second forward reaction is also sequential (not shown).

PES during the propagation of the initial wavefunction during the first 40 fs. The net fluxes were decomposed into the DTD fluxes providing additional interesting information about the causes for the switch of the mechanism. Thus, the present definition of synchronous and sequential mechanism is based on the populations flowing through the synchronous and sequential regions, SP2 and I, respectively, and may be considered as a quantum mechanical extension of the definition of Ushiyama and Takatsuka based on classical MD simulation [73]. The transfer of the protons one-after-the-other corresponds to the representative wavepacket flowing mainly through the intermediates domains I_1 and I_2 ($P_I(t) > P_{SP2}(t)$) from R to P or vice versa, whereas the both-at-the-time transfer of the two protons corresponds to the representative wavepacket flowing mainly through the SP2 domain($P_{SP2}(t) > P_I(t)$). Alternatively, within the recent quantification of synchronicity by Houk and coworkers [66], since the wavepacket always resides in the I or in the SP2 domains less than 10 fs and the characteristic vibrational periods are $\tau_{sym} = 21.2$ fs and $\tau_{asym} = 20.6$ fs for the symmetric and asymmetric stretching modes, respectively, the DPT mechanism of the model porphine would be classified as synchronous. Apparently,

the different assignments depend on the specific definitions of synchronous and sequential mechanisms. Moreover, by joining these two quantum extension of the classical definition by Ushiyama and Takatsuka [73] and by Houk and coworkers [66], the present results could be summarized as follows: during the first forward reaction both protons are transferred via the saddle point SP2, whereas during the first backward and second forward propagations the two protons are transferred preferably one-after-the-other via the intermediates domains; all forward and backward reactions are ultra-fast and occur within less than the characteristic periods of vibrations.

The central point of the results presented here, is that the switch of the mechanism is supported essentially by the quantum effect of the dispersion of the wavepacket during the propagation and by the relief reflections from the corner and the two arms of the rather steep, inverse L-shaped repulsive walls of the PES near the product P. Minor effects are also discovered as for example the direct switch from synchronous to sequential or the partially compensating processes of the reformation and decay of the reactant during the sequential first back and second forward reactions.

Explicit considerations of flux densities and domain-to-domain fluxes are still innovative tools for the analysis of reaction processes, beyond the investigations based only on densities and probabilities analyses. Similar analyses can be found for the interpretations of electronic flux densities and fluxes [100, 103, 104].

The present study should stimulate systematic investigations for switches of mechanism from concerted to sequential or from sequential to concerted, or even multiple switches for more realistic models and for different non-equilibrium initial conditions. For example, a break of the symmetry of the two intermediates of the initial condition could induce switch from synchronous mechanism to clockwise or anticlockwise sequential reactions via the intermediates I_1 first and I_2 second, or in the reverse order. Ultimately, these types of switches of the reaction mechanism should be induced and observed experimentally. The design of laser pulse for driving clockwise or anticlockwise electronic ring currents [105, 106], or nuclear currents [107] (or see the review [108]), or molecular rotors [109] are very encouraging examples for such quantum controls.

4 Non-adiabatic Quantum Dynamics Simulations and Laser Control of Br_2 in Solid Argon

4.1 Introduction

Dihalogen and interhalogen systems embedded in cryogenic rare gas matrices are very suitable prototypes for detailed spectroscopic studies of condensed-phase systems. On the one hand, the dihalogen chromophores show a rich set of bound, repulsive, and crossing electronic states. On the other hand, the inertness and spectroscopic al transparency of rare gas matrices allow for a deep investigation of the energetics, as well non-radiative and coherent dynamics processes. Moreover, both the dihalogens and the rare gases have been studied in great detail in the past decades, both theoretically and experimentally, so that a very well characterized set of spectroscopic constants for simulations is available in the literature [3, 4, 25, 110–113].

Pump-probe spectroscopy has been mainly used for the investigation of these systems, since it allows for a systematic collection of information about the electronic population and nuclear wavepacket evolution on one electronic state. First, an ultra-fast pump pulse vertically excites the chromophore from the electronic ground state to the Franck-Condon region of an electronic excited state, where a coherent superposition of vibrational states is created. Such superposition is a vibrational wavepacket evolving in time, which can be interrogated by a probe pulse at the delay time Δt and excited, in turn, to higher lying Charge Transfer (CT) states. The fluorescence from CT states can be finally recorded as a function of the delay time, tracking the time evolution of the wavepacket. These experiments have permitted to observe a large number of interesting phenomena, as for example, vibrational energy relaxation effects for Br_2 in Ar, for which an effective chromophore potential could be deduced [114]. Due to the presence of non-adiabatic electronic transitions (see Sec. 2.2.1 in Chap. 2), ultra-fast spin-flip [115–117] takes place. For instance, for ClF molecules in Ar matrices a time scale of 0.5 ps has been reported, which is a rather fast intersystem crossing process from a singlet to a triplet state. The wavepacket simulation for this system using a one-dimensional model (bond coordinate) gave an even lower limit of 60 fs [116], whereas for HF in Ar a 1 fs spin-flip time has been predicted on the basis of non-adiabatic trajectory simulations [118]. For the heavier dihalogens Br_2 and I_2,

a classification of the electronic states according to the Hund case c is preferred to the case a, due to the enhanced spin-orbit coupling [17]. For those systems the most studied non-adiabatic transition is the predissociation from 0_u^+ to the doubly degenerate 1_u states, usually called B and C states, respectively [119, 120]. The B state is attractive, whereas the C state is repulsive in the gas-phase. The predissociation yield in the gas-phase is extremely low [121], but it is considerably enhanced in the rare gas environment due to the non-adiabatic couplings to the lattice modes (vibronic coupling). This has been shown in particular for I_2 in Ar at different pressures [122]. For Br_2 in Ar the predissociation probability has been experimentally estimated from the broadening of the zero-phonon lines to be 5% per vibrational round-trip [123].

The cage effects are probably the most dramatic manifestations of the interaction between chromophore and matrix and have been demonstrated, for example, for F_2 in a Ar_{54} cluster host comprising the first four shells of an fcc crystal structure [124]. The collision with the matrix transfers energy to the cage, which excites specific collective vibrational motions. This has been seen, for instance, in Cl_2 in Ar [125]. Moreover, the electronic transition induce coherent phonon motion in the host, which display a dynamics mostly decoupled from the dihalogen's bond vibration, as seen for I_2 in Kr and Cl_2 and Br_2 in Ar [126, 127]. The respective oscillations persist during several picoseconds with a frequency corresponding to the zone boundary phonon mode of the host crystal.

These results stimulated several new experiments aiming at the investigation of electronic and vibrational coherences. The former have been investigated by using Phase-Locked Pulse Pairs (PLPP). Two pulses excite a population from the electronic ground to the excited state within a delay time $\Delta\tau$. Population can be transferred by the second pulse in a constructive or destructive way, by tuning the relative phase ϕ between the PLPP. As in the pump-probe scheme seen above, the vibrational wavepacket is probed by a third pulse at time Δt to a CT state. The vibrational recurrences on the excited state have been registered on an interferogram and can be related to the electronic coherence, which persist for more than 660 fs for Cl_2 in Ar and 300 fs for Br_2 in Ar [128, 129]. With the same technique, it has been shown that the chromophore-matrix interaction can even be tuned by generating a frequency comb able to excite a wave packet composed of either zero-phonon lines or phonon side bands [130]. Ultimately, vibrational coherence has been investigated by means of shaped laser pulses. In particular, chirped pulses have been used for Br_2 in Ar in order to compensate for the wavepacket dispersion on the B state due to the anharmonicity of the potential and to measure the time scale of vibrational decoherence due to the interaction with the environment [129].

On the theoretical side, a great effort has been made in order to treat those systems and carry out classical trajectory and quantum dynamics simulations. The first challenge for theoreticians has been the calculation of the PESs, which may describe the manifold of the dihalogen (at least valence) states and take into account the very large number of nuclear

DOFs of the considered crystal. Moreover, since the nuclear motions are coupled to the electronic ones (see Sec. 2.2.3), the electronic states mix and non-adiabatic transitions have to be treated as well. The semi-empirical method Diatomics-In-Molecules (DIM) was able to match all these criteria: the many-body nature of these systems, the valence electronic states of the dihalogen molecules (the extended Diatomics-in-Ionic-System method, DIIS, actually includes also CT states [131, 132]) as well as the easy calculation of forces and NACTs (see Sec. 2.2.1). The method was initially worked out by Ellison [133, 134] for the calculation of electronic structures of polyatomic molecules from diatomic and atomic potentials avoiding, thus, the calculation of interaction integrals. It was adapted later by Tully for studying molecular collision dynamics within the surface hopping approach [135–137], since it efficiently allows for the calculation of the PES "on-the-fly". The basic idea of the DIM method is to approximate the polyatomic PES by a sum of all diatomic interactions and it is, therefore, closely related to the *valence bond* theory of pairs of electrons forming bonds between atoms. Finally, the pair potentials are simple analytical functions fitted to experimental and/or calculated data. Despite its semi-empirical nature, the DIM method was widely used for classical trajectory simulations, revealing itself as an optimal compromise between accuracy and numerical feasibility, in particular for halogen-rare gas systems [138–151].

Although classical and semi-classical methods treat these systems in their full dimensionality, the description of coherent dynamics as well as the laser-matter interaction clearly call for quantum dynamical simulations. Unfortunately, the dimensionality of the problems must be drastically decreased, restricting the model systems to a subset of relevant electronic states and nuclear DOFs. In this respect, quantum dynamics profits from classical simulations, which have shown a reduced effective dimensionality, at least in the early time window [144–146].

Quantum dynamics simulations have been carried out in particular by Manz and coworkers, who developed models based on the DIM-PES including one or two nuclear DOFs. Quantum dynamics has been performed in order to simulate cage exit dynamics of F_2 in Ar including a collective cage coordinate next to the bond distance [101, 152, 153]. It was also shown that the inter-system crossing process for Cl_2 [154, 155] and ClF [116, 117, 156, 157] in Ar systems can be controlled by laser pulses on ultra-fast time scales. Specifically, a case was studied where two wave packets are excited, respectively, from the third preexcited vibrational state in the electronic ground to the singlet B-state and from the vibrational and electronic ground to the triplet C-state, so that the populations in the excited states are about equal. The constructive or destructive interferences of the associated wavepackets in the region of strong spin-orbit coupling can favour the triplet or the singlet components depending on their initial preparation. Moreover, 4D [119, 120, 158] and 5D [120] dimensional models including 4 electronic states have been developed for the Br_2 in Ar system by combining concepts from the Cartesian Reaction Surface (CRS) and the Vibronic Coupling

Hamiltonian (VCH) approaches. Within the CRS concept [31,159–161], two mass-weighted large amplitude coordinates (LAC) have been chosen for simulating excitation from the ground X- to the B-state. The first is just the dihalogen internal bond and the second is a collective matrix coordinate obtained from the coordinate shift between the configurations at the minima of the X- and B-state PES. Within the VCH concept [162–164], two more harmonic coupling modes are included in the 4D-model [119, 120, 158], which are involved in the non-adiabatic transition, and a supplementary harmonic tuning mode is included in the 5D-model [120], which modulates the energies of the electronic excited states [10, 11]. Specifically, Ref. 119,120,158 considered those modes, which are important for the B to C transition, since the role of the cage matrix in the predissociation has been investigated. The quantum dynamics of the dimension-adapted Reaction Surface-Vibronic Coupling (RSVC) Hamiltonian has been conveniently treated using the MCTDH package (see Sec. 2.4.1), after the PES and NACTs were calculated by using the DIM method, as outlined on Ref. 17. In the present contribution the B-C predissociation mechanism is investigated further from the perspective of optimal laser control by using the OCT method implemented in the MCTDH package (see Sec. 2.4.2). In fact, the simulations carried out by using the 4D and 5D models were not able to reproduce the experimental predissociation yield mentioned above (about 5% per vibrational round-trip). One straightforward way to enhance such yield is to add more (in principle all) of the remaining vibronic coupling and tuning modes (in other words, to take into account all possible NACTs). This way will be not pursued here, since the 5D model from [119, 120, 158] is not further developed in the present work. Instead, a second way to enhance such yield is presented in the following sections and is based on changing the Frack-Condon window of the B $\leftarrow$ X excitation by using OCT, so that the wavepacket created on the electronically excited bound B-state spends as much time as possible at the crossing seam with the other two electronically excited dissociative C and C' states, where predissociation actually takes place.

4.2 Theory and Model [119, 120, 158]

The RSVC Hamiltonian has been derived in Ref. 158 and takes into account four electronic states: X, B and the doubly degenerate C and C' states. Two large-amplitude coordinates, ζ_R and ζ_{X-B}, account for the Br-Br bond elongation and for the displacements of the cage atoms upon excitation from the X-ground state to the B-excited state, respectively. The two large-amplitude coordinates are depicted in panels (c) and (d) of Fig. 4.1: Upon elongation of the Br-Br distance, the four belt atoms invade the space emptied by the chromophore, whereas the 8 (4+4) atoms forming the 2 windows, toward which the Br atoms are moving, are pushed outward. Fig. 4.1b shows the X-state PES along these two coordinates by taking all other DOFs frozen at the minimum configuration, whereas Fig. 4.1a shows the quasi-adiabatic PES obtained by following the lowest energy path along

the B and C states. Both large-amplitude coordinates preserve the overall D_{2h} symmetry of the cage and are of A_g symmetry. Therefore, they form a crossing seam along the intersection of the B and C states, as indicated by the solid line in Fig. 4.1, which is almost parallel to the ζ_{X-B} coordinate. Finally, the filled circle marks the energetic minimum along the seam.

Within the CRS approach, the two large-amplitude coordinates account for the full anharmonicity of this PES cut [120]. In order to represent the DOFs of the remaining part of the system, vibronic coupling theory is applied. In particular, the two LACs are

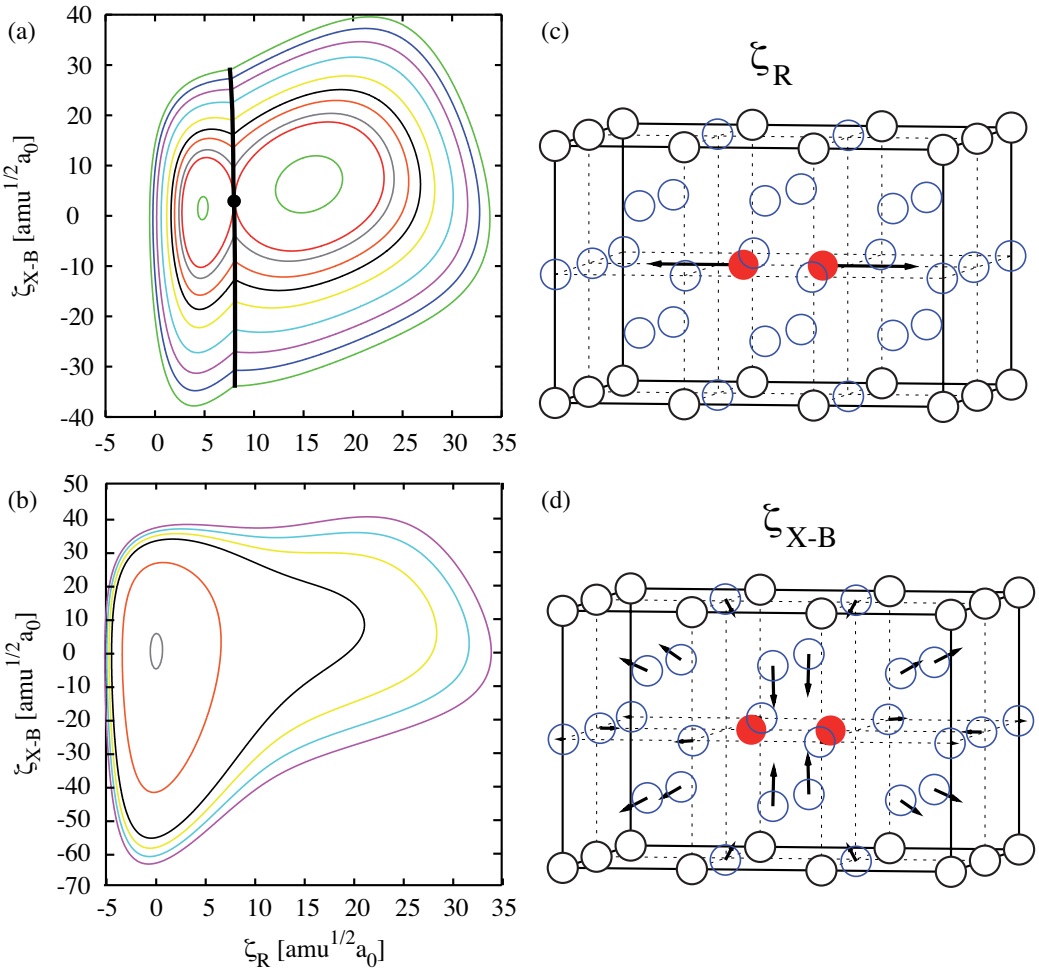

Figure 4.1: PES along the two large-amplitude coordinates for the (X) ground (panel (b), contour lines at 0.001, 0.035, 0.069, 0.080, 0.090, and 0.100 E_h) and quasi-diabatic (B-C) first excited state (panel (a), contour lines at 0.069, 0.072, 0.073, 0.075, 0.077, 0.080, 0.085, 0.090, 0.095 and 0.100 E_h). In panel (a), the crossing seam is included as a black line. The minimum along this seam is at $\zeta_R \approx 8$ and $\zeta_{X-B} \approx 3$ amu$^{1/2}a_0$. Panels (c) and (d) show the mass-weighted atomic displacement vectors for the two large-amplitude coordinates. The four panels are adapted from Ref. 120

projected out and the Hessian matrix is diagonalized at the minimum of the electronic ground state, in order to obtain normal modes, which are orthogonal to the LACs.

Within the VCH approach [162], the normal mode coordinates, $\{q_i\}$, are treated in harmonic approximation and are added to the model, giving the following RSVC Hamiltonian matrix in diabatic representation [119, 120, 158]:

$$\mathbf{H} = \begin{pmatrix} T+V_X & 0 & 0 & 0 \\ 0 & T+V_B & -V_{BC}^* & V_{BC'} \\ 0 & -V_{BC} & T+V_C & 0 \\ 0 & V_{BC'}^* & 0 & T+V_{C'} \end{pmatrix}. \tag{4.1}$$

Since the $\{q_i\}$ normal modes are taken to be dimensionless, the kinetic energy is simply defined as

$$T = -\frac{\hbar^2}{2}\left(\frac{\partial^2}{\partial\zeta_R^2} + \frac{\partial^2}{\partial\zeta_{X-B}^2}\right) - \frac{\hbar}{2}\sum_i \omega_i \frac{\partial^2}{\partial q_i^2}. \tag{4.2}$$

Finally, the diagonal and off-diagonal elements of the potential energy operator are given by (a,b = X,B,C,C')

$$V_a = U_a(\zeta_R, \zeta_{X-B}) + \frac{\hbar}{2}\sum_i \omega_i q_i^2 + \sum_i F_{a,i}(\zeta_R, \zeta_{X-B}) q_i \tag{4.3}$$

and

$$V_{ab} = \sum_i F_{ab,i}(\zeta_R, \zeta_{X-B}) q_i \ . \tag{4.4}$$

In Eq. 4.3, U_a denotes the potential energy of the Cartesian reaction surface spanned by the two LACs (see Fig. 4.1a and Fig. 4.1b). The second term is the potential energy of the bath oscillators. The last term in Eq. 4.3 is, in terms of vibronic coupling theory, the sum over the *intra-state* couplings (tuning modes), where $F_{a,i}$ are the gradients along the $\{q_i\}$ modes. The gradients are taken here in linear approximation with respect to the LACs,

$$F_a(\zeta_R, \zeta_{X-B}) \approx F_a(\zeta_R = 0, \zeta_{X-B} = 0) + \frac{\partial F_a}{\partial \zeta_R}\zeta_R + \frac{\partial F_a}{\partial \zeta_{X-B}}\zeta_{X-B} \ , \tag{4.5}$$

with $F_B(\zeta_R = 0, \zeta_{X-B} = 0)$ = -4.101, $F_C(\zeta_R = 0, \zeta_{X-B} = 0)$ = -25.96 (in $10^{-5}E_h$),

$\partial F_B/\partial\zeta_R$ = -2.325, $\partial F_B/\partial\zeta_{X-B}$ = 3.828, $\partial F_C/\partial\zeta_R$ = -2.025, and $\partial F_C/\partial\zeta_{X-B}$ = 3.603 (in $10^{-5}E_h/a_0(amu)^{-1/2}$). Notice, that such quantities can be calculated analytically within the DIM approach. Moreover, since the C and C' PESs are degenerate, all quantities referring to them are the same.

The off-diagonal potential energy matrix elements of Eq. 4.4 are the *inter-state* interactions mediated by the coupling modes and are taken to be the Taylor expansion of the gradient with respect to ζ_{X-B} up to the fourth term. In fact, since they are calculated at the energetic minimum of the crossing seam (called below c), the derivative with respect to ζ_R practically vanishes.

$$F_{ab,i}(\zeta_{X-B}) \approx F_{ab,i}(\zeta_{X-B}=c) + \sum_{j=1}^{4} \frac{\partial^j F_{ab,i}}{\partial\zeta_{X-B}^j}\zeta_{X-B}^j \ , \tag{4.6}$$

with

$$\begin{aligned}
F_{BC,1}(\zeta_{X-B}=c) &= 3.56\cdot10^{-06}\,E_h \ , \\
F_{BC,2}(\zeta_{X-B}=c) &= 1.91\cdot10^{-05}\,E_h \ , \\
\frac{\partial F_{ab,1}}{\partial\zeta_{X-B}}\zeta_{X-B} &= 1.16\cdot10^{-06}E_h/a_0(amu)^{-1/2} \ , \\
\frac{\partial F_{ab,2}}{\partial\zeta_{X-B}}\zeta_{X-B} &= 1.69\cdot10^{-06}E_h/a_0(amu)^{-1/2} \ , \\
\frac{\partial^2 F_{ab,1}}{\partial\zeta_{X-B}^2}\zeta_{X-B}^2 &= 3.46\cdot10^{-08}E_h/(a_0(amu)^{-1/2})^2 \ , \\
\frac{\partial^2 F_{ab,2}}{\partial\zeta_{X-B}^2}\zeta_{X-B}^2 &= 8.17\cdot10^{-08}E_h/(a_0(amu)^{-1/2})^2 \ , \\
\frac{\partial^3 F_{ab,1}}{\partial\zeta_{X-B}^3}\zeta_{X-B}^3 &= 1.53\cdot10^{-09}E_h/(a_0(amu)^{-1/2})^3 \ , \\
\frac{\partial^3 F_{ab,2}}{\partial\zeta_{X-B}^3}\zeta_{X-B}^3 &= 2.15\cdot10^{-09}E_h/(a_0(amu)^{-1/2})^3 \ , \\
\frac{\partial^4 F_{ab,1}}{\partial\zeta_{X-B}^4}\zeta_{X-B}^4 &= 1.20\cdot10^{-11}E_h/(a_0(amu)^{-1/2})^4 \ , \\
\frac{\partial^4 F_{ab,2}}{\partial\zeta_{X-B}^4}\zeta_{X-B}^4 &= 2.33\cdot10^{-11}E_h/(a_0(amu)^{-1/2})^4 \ ,
\end{aligned}$$

Where again, these gradients have been calculated analytically within the DIM model. Moreover, projecting them on the normal modes is a useful way to identify the strongest coupled modes. In the 4D-model in Ref. 158, two coupling modes are identified by projecting the F_{BC} gradients taken at the minimum of the crossing seam, c, onto the normal modes. These modes have been selected because they show, within the approximations employed here, the strongest non-adiabatic effects. They are here denoted as q_1

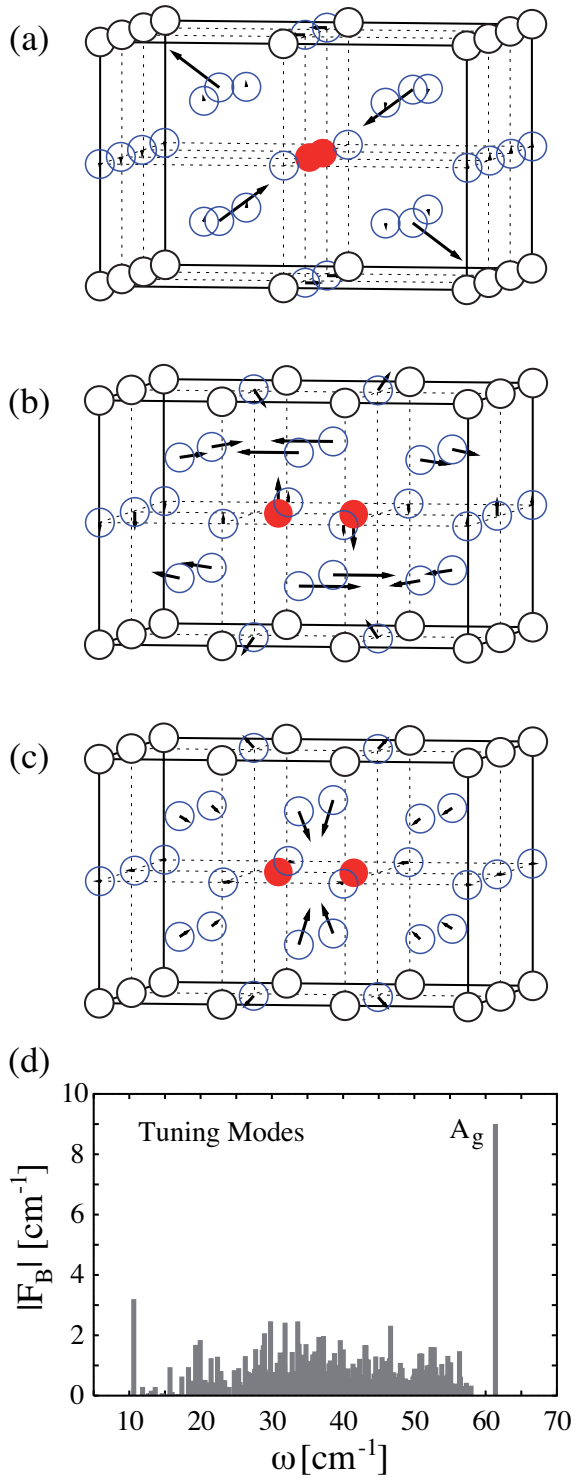

Figure 4.2: Mass-weighted atomic displacement vectors for the vibronic coupling modes q_1 (B_{3g}) in panel (a) and q_2 (B_{2g}) in panel (b) and the tuning mode q_3 (A_g) in panel (c). In panel (d) the coupling of the ground state normal modes to the X to B transition upon vertical excitation is shown. The four panels are adapted from Ref. 120

($\hbar\omega_1 = 60cm^{-1}$ of B_{3_g} symmetry) and q_2 ($\hbar\omega_2 = 63cm^{-1}$ of B_{2_g} symmetry) and are shown in Fig. 4.2a and Fig. 4.2b. Displacements along these two modes lead to conical intersections (not shown, see Ref. 119,120,158). The coupling of the ground state normal modes to the B $\leftarrow$ X transition upon vertical excitation (Franck-Condon), is depicted in Fig. 4.2d and has been obtained by projecting the F_B gradients onto the normal modes [120]. The coupled tuning mode included in the 5D-model [119,120] is denoted here as q_3 ($\hbar\omega_3 = 61cm^{-1}$ of A_g symmetry). This mode has been selected because it shows, within the approximations employed here, the strongest displacement upon laser excitation. The respective displacement vectors are shown in Fig. 4.2c.

The interaction with the laser field is included in the model by means of the following interaction Hamiltonian

$$H_{\text{field}}(t) = -\mu\mathcal{E}(t) \ , \tag{4.7}$$

where the laser field $\mathcal{E}(t)$ is linearly polarized along the Br-Br bond and the dipole operator μ allows for transitions between the X ground and the B and C excited states. The dipole gradient with respect to ζ_R [119] is also included in the model and has been adapted from Ref. 165. The transition dipole moment operators are given by (a = B,C,C')

$$\mu_{Xa} = \mu_{Xa}^{(0)} + \frac{\partial\mu_{Xa}}{\partial\zeta_R}\zeta_R \ , \tag{4.8}$$

with $\mu_{XC}^{(0)} = 0.1953ea_0$, $\partial\mu_{XC}/\partial\zeta_R = -0.01047e(amu)^{-1/2}$, $\mu_{XB}^{(0)} = 0.15ea_0$, $\partial\mu_{XB}/\partial\zeta_R = 0.01e(amu)^{-1/2}$.

For the electric field the following form is assumed

$$\mathcal{E}(t) = E_0 \exp(-t^2/2\sigma^2)\cos(\omega t), \tag{4.9}$$

with amplitude E_0, carrier frequency ω, and width σ.

These 4D and 5D models developed in Refs. 119, 120, 158, have been used to perform quantum dynamics simulations by using the multi-set formulation within the MCTDH package (see Sec. 2.4.1) and the harmonic oscillator DVR (see Refs. 28–30, 44, 45). Tests for the convergence of the number of grid points N_k as well as the number of SPFs (Single Particle Functions, see 2.4.1) used, have been carried out in the corresponding Refs. 119, 120. In particular, the wavepacket dynamics on the excited B state and the relative nonadiabatic population transfer (predissociation) from the B to the doubly degenerate

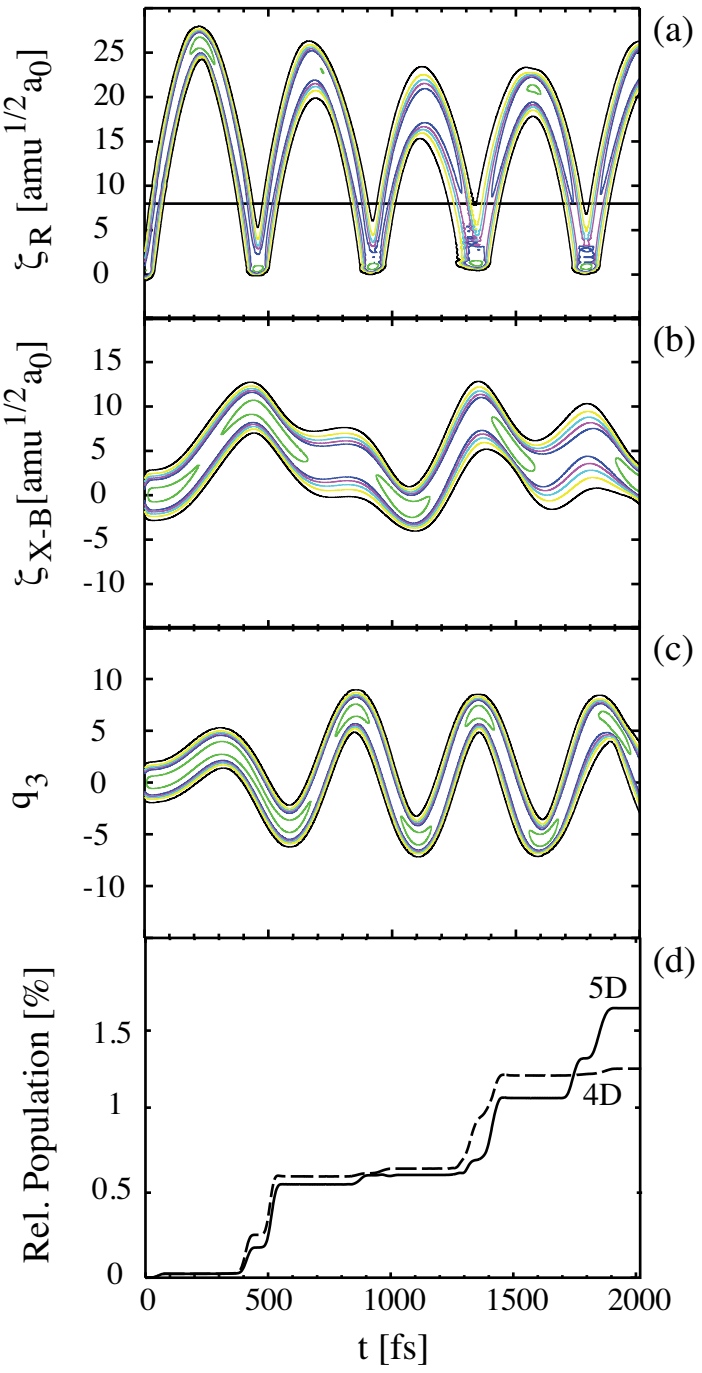

Figure 4.3: Time-dependent reduced B-state densities for (a) the Bromine coordinate $\rho^{(B)}(\zeta_R, t)$ (isodensity values of 0.001, 0.003, 0.005, 0.007, 0.01, and 0.03), (b) the matrix coordinate $\rho^{(B)}(\zeta_{X-B}, t)$ (isodensity values of 0.002, 0.004, 0.006, 0.008, 0.01, and 0.02), and (c) the tuning mode $\rho^{(B)}(q_3, t)$ (isodensity values of 0.001, 0.003, 0.005, 0.007, 0.01, and 0.03). Panel (d) compares the relative C-state population, Eq. 4.11, of the present 5D to that of the former 4D model [119], which did not include the tuning mode. The four panels are adapted from Ref. 120

C state have been investigated. The vertical excitation from the vibrational ground state $v = 0$ of the X state to the Franck-Condon region of the B state has been performed by using the analytical laser pulse in Eq. 4.9 with resonant frequency $\omega = 0.092 E_h/\hbar$, width $\sigma = 18 fs$ and amplitude $E_0 = 0.005 E_h/(e a_0)$, which corresponds to an intensity I of about $1.8 \cdot 10^{12} W cm^{-2}$, calculated with the following formula:

$$I = c\epsilon_0 E_0^2 \tag{4.10}$$

With these conditions, about 8% of the total population is transferred onto the excited bound state, where the wavepacket is propagated during 2 ps. In order to focus on the predissociation yield versus propagation time t, the following quantity has been defined:

$$P(t) = \frac{P_C(t) + P_{C'}(t)}{1 - P_X(t)} \ , \tag{4.11}$$

where $P_a(t)$ is the population of the diabatic a = X,C,C' states and $1 - P_X(t)$ is the population excited from the X state by the laser pulse, so that finally $P(t)$ is the relative population transferred non-adiabatically from the bound to the dissociative in the gas-phase states. This quantity is shown in Fig. 4.3d for the 4D (dashed line) [119, 120] and 5D model (solid line) [120]. Both curves show a step-wise behaviour with different predissociation dynamics at different propagation times. The reason for this behaviour can be understood from panels (a), (b) and (c) of Fig. 4.3, which show 1D reduced densities of the wavepacket with respect to the coordinates ζ_R, ζ_{X-B} and q_3, respectively. In the first panel the reason for the step-wise predissociation mechanism is disclosed. Each time the wavepacket passes the crossing seam, nonadiabatic population transfer occurs. A comparison with panel (b) shows that the predissociation yield is enhanced whenever the wavepacket passes the crossing seam and at the same time the matrix coordinate ζ_{X-B} is maximally elongated, showing that compression of the cage is a prerequisite for predissociation, since the B and C states are brought in resonance. Note that the interaction with the two coupling modes is a function of the ζ_{X-B} elongation (not shown, see Refs. 119, 120), that is, the coupling to the asymmetric cage deformation is enhanced by symmetric compression of the matrix LAC, favouring predissociation. Finally, comparing panels (b) and (c), the role of the tuning mode is discovered. With respect to the 4D model, which did not include the q_3 mode, the final predissociation yield increases. The tuning mode involves a breathing of the 4 belt-atoms of the cage, as well as the collective matrix coordinate ζ_{X-B}, so that they exchange energy. When the two coordinates are out of phase (t=750fs and t = 1700fs), ζ_{X-B} is decelerated by the tuning mode and the predissociation yield is lowered. When the two coordinates are in-phase (t between 1300 and 1400 fs and t = 1800 fs), ζ_{X-B} is accelerated by the tuning mode and the predissociation yield is, in

Table 4.1: Parameters used for the MCTDH propagation. All coordinates were represented by a harmonic oscillator discrete variable representation using N_k grid points; the numbers of SPFs per DOF for the multi-set formulation are given in the last columns for the respective electronic states (number of SPFs for the non converged result of Fig. 4.7 in parentheses).

Mode	N_k	X	B	C	C'
ζ_R	160	12(6)	12(6)	12(4)	12(4)
ζ_{X-B}	160	12(6)	12(6)	12(4)	12(4)
q_1	10	4(2)	4(2)	4(2)	4(2)
q_2	10	4(2)	4(2)	4(2)	4(2)
q_3	65	12(6)	12(6)	12(4)	12(4)

Table 4.2: The first and second columns show the vibrational quantum number v from 0 to 10 and the corresponding energy values within the direct product approximation (see text) representing the vibrationally preexcited initial states. In the third column the respective laser frequencies for excitation from these vibrational states to the electronically excited B-state are listed. They have been taken to be the frequencies matching the resonance condition.

Eigenstate v	Eigenvalue $E^{(n=0,\ v)}[E_h]$	Excitation frequency $\omega[E_h/\hbar]$
0	0.001182	0.0920
1	0.002612	0.0825
2	0.004029	0.0775
3	0.005437	0.0740
4	0.006837	0.0704
5	0.008225	0.0676
6	0.009605	0.0651
7	0.010973	0.0630
8	0.012331	0.0606
9	0.013679	0.0586
10	0.015017	0.0567

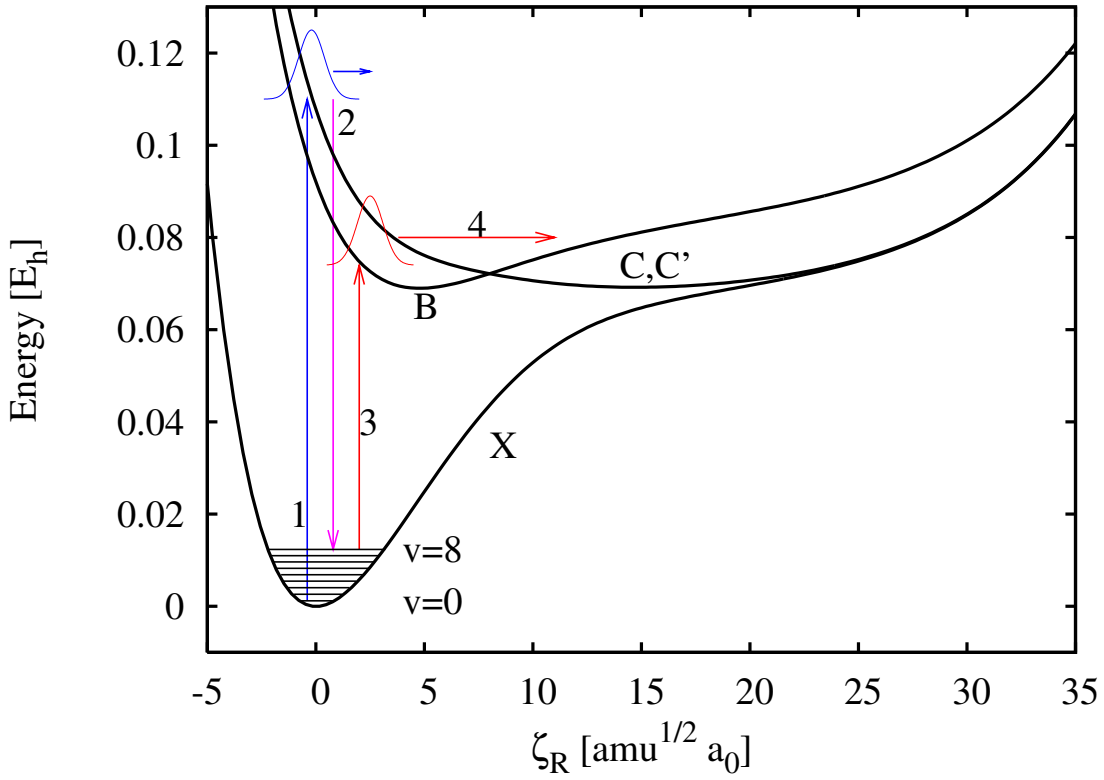

Figure 4.4: The strategy for the enhancement of the population transfer from the B- to the C-state (predissociation) is shown. The first 8 vibrational levels of the X-state potential are depicted. Their energy values are listed in the second column of Tab. 4.2. Steps 1 and 2 (blue and violet arrows) refer to the Tannor's pump-dump scheme used in order to populate the vibrational level $v = 8$ starting from $v = 0$. This part is accomplished by the OCT scheme. Steps 3 and 4 (red arrows), respectively, refer to the excitation of the wavepacket created by the OCT pulse to the B-state and to the subsequent propagation on it.

turn, higher. In particular, at $t = 1800$ fs, the energy gap between the B and C states, modulated by the tuning mode, becomes very small (not shown, see Ref. 120) showing a decisive enhancement of the predissociation yield with respect to the 4D-model.

Upon vertical Franck-Condon excitation from the vibrational ground state $v = 0$, the wavepacket on the B state is energetically about $0.016E_h$ above the crossing seam at the first passage, so that deformation of the cage matrix is needed in order to bring the B and C states in resonance and have an efficient nonadiabatic population transfer, as seen above in Fig. 4.3. Another way for establishing resonance would be the excitation of a wavepacket to a lower energy region of the B state. Using a vertical Franck-Condon excitation, this is possible only by starting from preexcited vibrational states of the electronic ground state.

The next section can be split into three subparts. In the first part, the dependence of the predissociation yield on the starting vibrational levels $v = 1-8$ in the X state is investigated ($v = 1$ has been already investigated in Refs. 119, 120). The starting vibrational levels

are drawn in Fig. 4.4 and their corresponding values are listed in Tab. 4.2. Enhanced predissociation is disclosed for excitation from the preexcited vibrational eigenstate $v = 8$, motivating the subsequent study. In the second part, the OCT method is applied for the preparation of the vibrational level $v = 8$ in the X state. The strategy presented involves the C state and is labeled in Fig. 4.4 by 1 and 2 and corresponds to the blue (pump) and violet (dump) arrows. In the third part, the state obtained by the OCT pulse, is used as the initial state for further investigation of the B-C predissociation, labeled in Fig. 4.4 by 3 and 4, and corresponding to the two red arrows, respectively.

The number of grid points N_k as well as the number of SPFs used in MCTDH for carrying out all quantum dynamics calculations are listed in Tab. 4.1. The VMF (Variable Mean-Field, see Sec. 2.4.1) scheme has been used in combination with an eight-order Burlisch-Stoer integrator. The maximum of the lowest natural orbital population was well below 10^{-10}.

4.3 Results

4.3.1 Vibrational Preexcitation-Dependent Dynamics

The first ten vibrationally excited (stationary) states, from 1 to 10, along the ζ_R coordinate have been chosen as the initial states for the investigation of the B-C predissociation, upon vertical excitation to the B state. They are approximated as direct products of vibrational eigenfunctions of one-dimensional cuts of the PES along the five coordinates,

$$\begin{aligned} \Psi^{(n=0,\ v=0)}(\zeta_R,\zeta_{X-B},q_1,q_2,q_3;t=0) &\approx \psi^{\tilde{v}_{\zeta_R}}(\zeta_R)\,\psi^{\tilde{v}_{\zeta_{X-B}}}(\zeta_{X-B})\,\psi^{\tilde{v}_{q_1}}(q_1)\,\psi^{\tilde{v}_{q_2}}(q_2)\,\psi^{\tilde{v}_{q_3}}(q_3) \\ &\text{or} \\ &\approx |\tilde{v}_{\zeta_R},\tilde{v}_{\zeta_{X-B}},\tilde{v}_{q_1},\tilde{v}_{q_2},\tilde{v}_{q_3}\rangle \end{aligned} \tag{4.12}$$

Thus, the ground state $\Psi^{(n=0,\ v=0)}(\zeta_R,\zeta_{X-B},q_1,q_2,q_3;t=0) = |0,0,0,0,0\rangle$ in the direct product approximation has all quantum numbers equal to zero. The first excited state $\Psi^{n=0,\ v=1}(\zeta_R,\zeta_{X-B},q_1,q_2,q_3;t=0) = |1,0,0,0,0\rangle$ has all quantum numbers equal to zero except for $\tilde{v}_{\zeta_R}$, and so on. Please note that $\tilde{v}_{\zeta_R}$ is the only quantum number changed from 0 to 8, whereas the other four ones are always zero, so that from now on, the quantum number $v = \tilde{v}_{\zeta_R}$ will be used in order to refer to the vibrational states obtained in the direct product approximation. The validity of this last approximation was checked only for the ground state, $\Psi^{n=0,\ v=0}(\zeta_R,\zeta_{X-B},q_1,q_2,q_3;t=0)$ which has been relaxed on the 5 dimensional PES. The eigenvalue for the ground state before and after relaxation does not change within the first 6 digits. In Tab. 4.2 the vibrational quantum numbers v and the energy values $E^{(n=0,\ v)}$ of the corresponding vibrational states are listed from 0 to 10 in

the first and second columns, respectively. In the third column the corresponding carrier frequencies of the laser fields are listed, which has been used for vertically excite a wavepacket from those 10 vibrationally states in the electronically ground state X, to the B-state. They have been taken to be the frequencies matching the resonance condition for vertical excitation. For all cases the width of the pulse has been $\sigma = 18$ fs, the amplitude $E_0 = 0.005\ E_h/(ea_0)$ and the population transfer to the B state about 8%.

Fig. 4.5 shows the relative nonadiabatic transfer population $P(t)$ in Eq. 4.11 from the B to the C and C' states for four chosen initial conditions: $v = 0$, 1, 8 and 10, labeled cases I, II, III, and IV, respectively. The black curve for case I was already shown in Fig. 4.3 for the 5D model [120] and is now drawn for comparison with the other cases. First, the predissociation yield decreases as a function of v until $v = 5$, but then increases to reach a maximum at $v = 8$ (case III), after which it decreases again (case IV). The reason for the decrease of the population yield in case II has already been explained in Refs. 119,120. Excitation to a lower region of the B-state corresponds to a shorter round-trip for the wavepacket, so that the matrix cage compression and, consequently, the coupling to the q_1 and q_2 asymmetric compressions are reduced, causing a decrease of the predissociation yield [119,120]. Moreover, the kinetic energy of the wavepacket upon passing the crossing seam is still too high and can not compensate for the reduced coupling by having better resonance. This behaviour can be explained in terms of Landau-Zener formula [166–168],

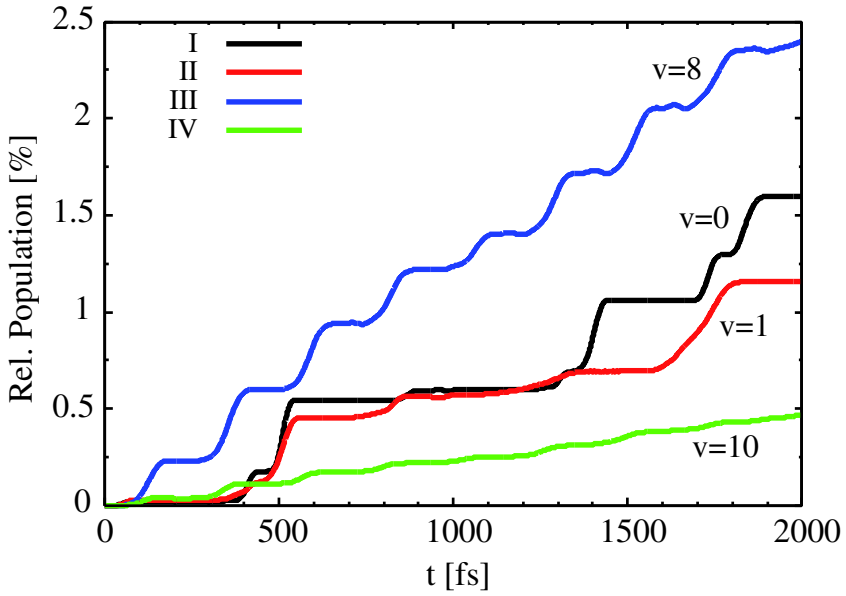

Figure 4.5: Population dynamics (relative C-state population, Eq. 4.11), for excitation from different vibrational states in the electronic ground state, (I) $v = 0$, (II) $v = 1$, (III) $v = 8$, (IV) $v = 10$. The pulse parameter of the Gaussian pulse have been set to $\sigma = 18$ fs, and $E_0 = 0.005 E_h/(ea_0)$. The respective frequencies matching the resonance condition are listed in Tab. 4.2 in the text.

$$P_{LZ} = 1 - e^{-\gamma} \quad \text{with} \quad \gamma = \frac{2\pi\lambda^2}{v\Delta F} \tag{4.13}$$

where λ is the coupling matrix element in the diabatic representation, v is the classical velocity at the crossing point and ΔF is the difference in the slopes of the two crossing diabatic PESs taken to be linear at the crossing point.Thus, the nonadiabatic transfer probability is proportional to the coupling and inversely proportional to the velocity and to the slopes at the crossing point. Starting from $v = 5$, this situation changes and for $v = 8$ (case III in Fig. 4.3), the energy of the wavepacket is close to the energy of the crossing seam of $0.074E_h$, corresponding to the fourth vibrational level in the B state. The energy of the $v = 8$ level is, in fact, $0.0123E_h$, which together with the excitation energy, $0.0606E_h$ (see Tab. 4.2) approximately matches the energy of the crossing seam along the ζ_R coordinate close to its minimum. The step-like increase of the predissociation yield results from the small-amplitude vibration of the Br_2 coordinate in the B state. The turning point of the wavepacket propagation is located approximately at the crossing seam, so that for each round-trip population is transferred to the repulsive states. Finally, by exciting even closer to the potential minimum, the wavepacket does not reach the crossing seam anymore and predissociation through the barrier would be possible only by tunneling, which is, due to the high mass of Br_2, practically impossible. Thus, the predissociation yield dramatically drops.

4.3.2 OCT Preparation of a Vibrationally Excited Ground State

Motivated by these results, the preparation of the vibrationally excited ground state $v = 8$ is now attempted. Experimentally, vibrational preexcitation of matrix-isolated heterodimers has been demonstrated, for example, for HCl in Kr [169], by direct IR excitation. However, since Br_2 is a homodimer, excitation strategies involving excited electronic states have to be used in analogy to Tannor's pump-dump scheme [95]. This stimulated Raman type of excitation has been carried out in experiments on K_2 in the gas-phase, where the ground state wavepackets could be generated with mean quantum numbers ranging from 4 to 18 depending on the laser pulse parameters, such as wavelength and pulse delay [170]. From the theoretical point of view, non-equilibrium ground state distributions have been generated by vibrational hole burning mechanism in the strong field regime [171, 172]. In contrast, in Refs. [154, 155], the goal has been to selectively excite a single vibrational state in the electronic ground state. This was achieved by means of narrow bandwidth lasers with durations of picoseconds, which are state-selective within an effective one-dimensional model of Cl_2 in Ar.

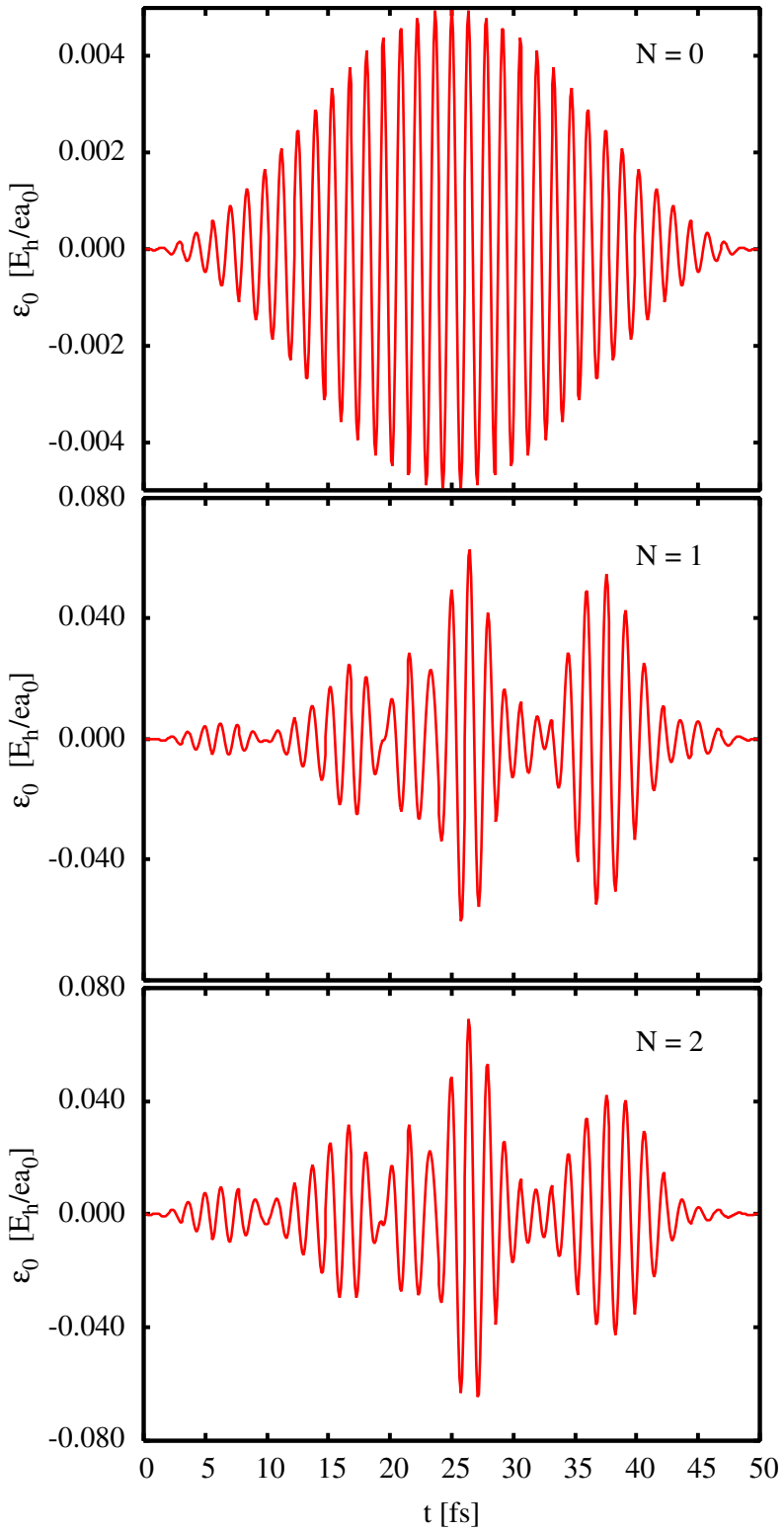

Figure 4.6: Guess field ($N = 0$) and fields from the first two OCT iterations, $N = 1$, and $N = 2$.

In this work, the preparation of the vibrational level $v = 8$ in the electronic ground state was achieved by using the OCT method. For this purpose, the operator $\hat{O}$ in Eq. 2.156 of Sec. 2.4.2 has been defined as the projection operator $\hat{O} = |X, v = 8\rangle\langle X, v = 8|$ on the target state. Since in the next step the wave function from the OCT pulse will be used as the initial state for further investigations of the B-C predissociation mechanism, the B state as intermediate state for the pump-dump strategy is immediately excluded. Thus, the choice is reduced to one of the two repulsive C and C' states included in the already-developed model Hamiltonian used along this work. Note that any other electronic optically bright state would have been equally well-suited for the present purpose. For the present choice, however one still has to deal with the part of the wavepacket eventually left on the C or C' state by the OCT-Pulse. The round-trip of the wavepacket on the dissociative state is, in fact, approximately 300 fs, which is much shorter than the time interval of 500 fs chosen below for the B-C predissociation, so that in order to avoid interferences with the predissociation mechanism to be studied, the population on the C state is neglected after the OCT pulse is over and the wavepacket in the X-state is re-normalized. Re-normalization does not affect the results presented, since only relative nonadiabatic population transfer from the B- to the C-state are considered (see Eq. 4.11).

In the Franck-Condon region, the C-state PES is repulsive, and the wavepacket moves rapidly out of the region where it overlaps with the $v = 8$ eigenstate. For this reason, the final time T for the OCT pulse, in Eq. 2.156 of Sec. 2.4.2, is chosen to be only 50 fs. The time step is chosen to be $\Delta t = 0.1$ fs. The initial guess field has been chosen as $\mathcal{E}(t) = E_0 \sin^2(\pi t/T)\cos(\omega_0(t - T/2))$, with $E_0 = 0.005 E_h/ea_0$ and $\omega_0 = 0.1099 E_h/\hbar$, which corresponds to the vertical transition energy at the minimum of the X state, and is shown in Fig. 4.6a. In order to obtain a J functional different from 0, a very small penalty factor (see Eq. 2.156 of Sec. 2.4.2), $\alpha_0 = 0.000025\, e^2 a_o^2/E_h^2$, was used for the first iteration. Immediately, upon starting the OCT iteration, the amplitude E_0 of the pulse increases from 0.005 to 0.08 E_h/ea_0, and the relative intensity from about 1.8 $\cdot 10^{12}$ W cm^{-2} to about 4.5 $\cdot 10^{14}$ W cm^{-2} entering the strong field regime (compare panel (a) and (b) of Fig. 4.6). The penalty factor is increased to $\alpha_0 = 0.08\, e^2 a_o^2/E_h^2$ for the second iteration and subsequently kept constant at a value of $\alpha_0 = 0.1\, e^2 a_o^2/E_h^2$ until the final iteration N = 200. The laser pulses after the second and the final iterations are shown in Fig. 4.6c and Fig. 4.8a, respectively. After one iteration the laser field already shows a four pulses envelope, which does not change appreciably along the 200 OCT iterations, except for their relative amplitudes.

A convergence study with respect to the number of SPFs is shown in Fig. 4.7. First, the number of SPFs listed in parentheses in Tab. 4.1 were used. The resulting OCT yield (dashed line in Fig. 4.7) does not show any monotonic or quadratic behaviour, as expected from the general scheme of OCT implemented in the MCTDH package (see Sec. 2.4.2). In contrast, the solid line in Fig. 4.7 shows a monotonic convergence behaviour

and corresponds to the use of the larger number of SPFs listed in Tab. 4.1. After 200 iterations the change in the J functional becomes rather small.

Fig. 4.8c shows that about 17% of the population is transferred into the target state $v = 8$ and about one third of the population remains on the C state. This amount of population left on the C state is neglected later as detailed above. The rest of the population is distributed over vibrational levels $v \neq 8$ as demonstrated in Fig. 4.9. The dashed and solid black lines refer to the population left on the vibrational ground state and the one transferred on to the target state $v = 8$, respectively, which has been maximized with respect to all other vibrationally excited states. An appreciable percentage of populations (above 5%) are distributed on vibrational levels around the target state; in decreasing order: v =7, 9, 6, 1, 10, 5 and 11.

Finally, the optimized OCT-pulse generates a vibrational wavepacket in the X state, whose distribution is, at the final time T, centered around the target state $v = 8$, as confirmed by the average occupation number calculated with respect to t,

$$\langle v(t) \rangle = \sum_{v=1}^{12} v P_v(t) \ , \tag{4.14}$$

and plotted in Fig. 4.9c (solid black line).

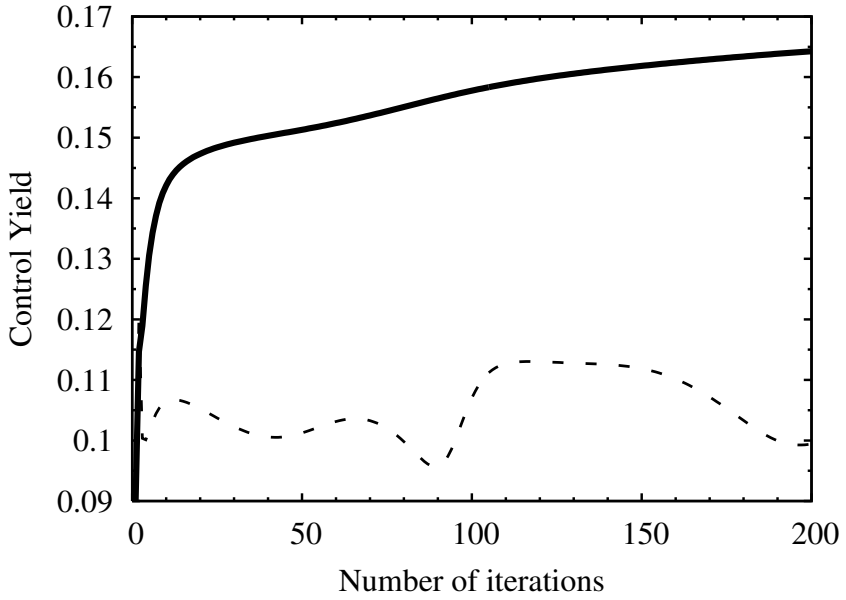

Figure 4.7: Convergence of the Yield Control versus the number of OCT iterations. The solid line corresponds to the large SPF basis used with MCTDH in order to obtain all the presented results. The dashed line shows the non-monotonic behaviour obtained for a smaller set of SPF functions as given in Tab. 4.1.

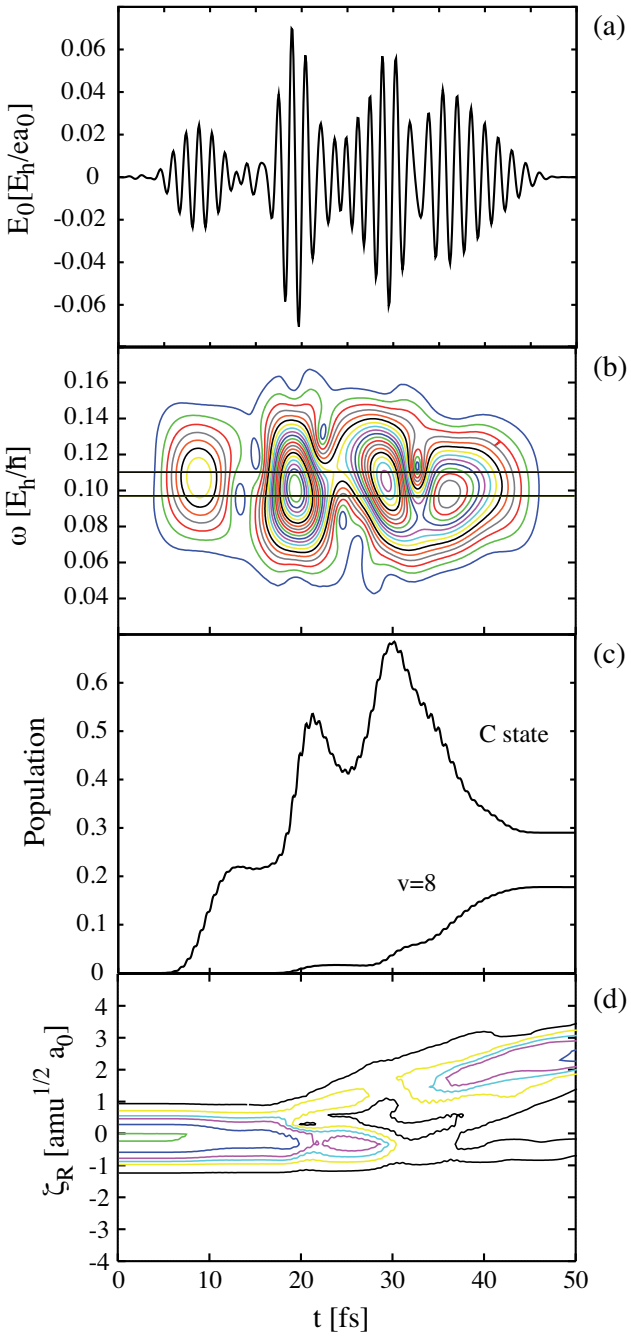

Figure 4.8: (a) OCT pulse after 200 iterations (see text). (b) XFROG trace of the OCT pulse (contours from 0.2 to 4 in steps of 0.2). The gate function in Eq. 4.15 is a rectangle of width $41\hbar/E_h$ with Gaussian tails of the same width; see Ref. 57. The two horizontal lines correspond to the vertical transitions from the $v = 0$ and 8 vibrational states in the X state to the C state. (c) Population of the C state and of the target state $v = 8$ in the electronic ground state. (d) Time-dependent reduced 1D X-state density for the Bromine coordinate $\rho^{(B)}(\zeta_R, t)$ (isodensity values of 0.05, 0.15, 0.25, 0.35, 0.55, and 0.85) during the OCT pulse.

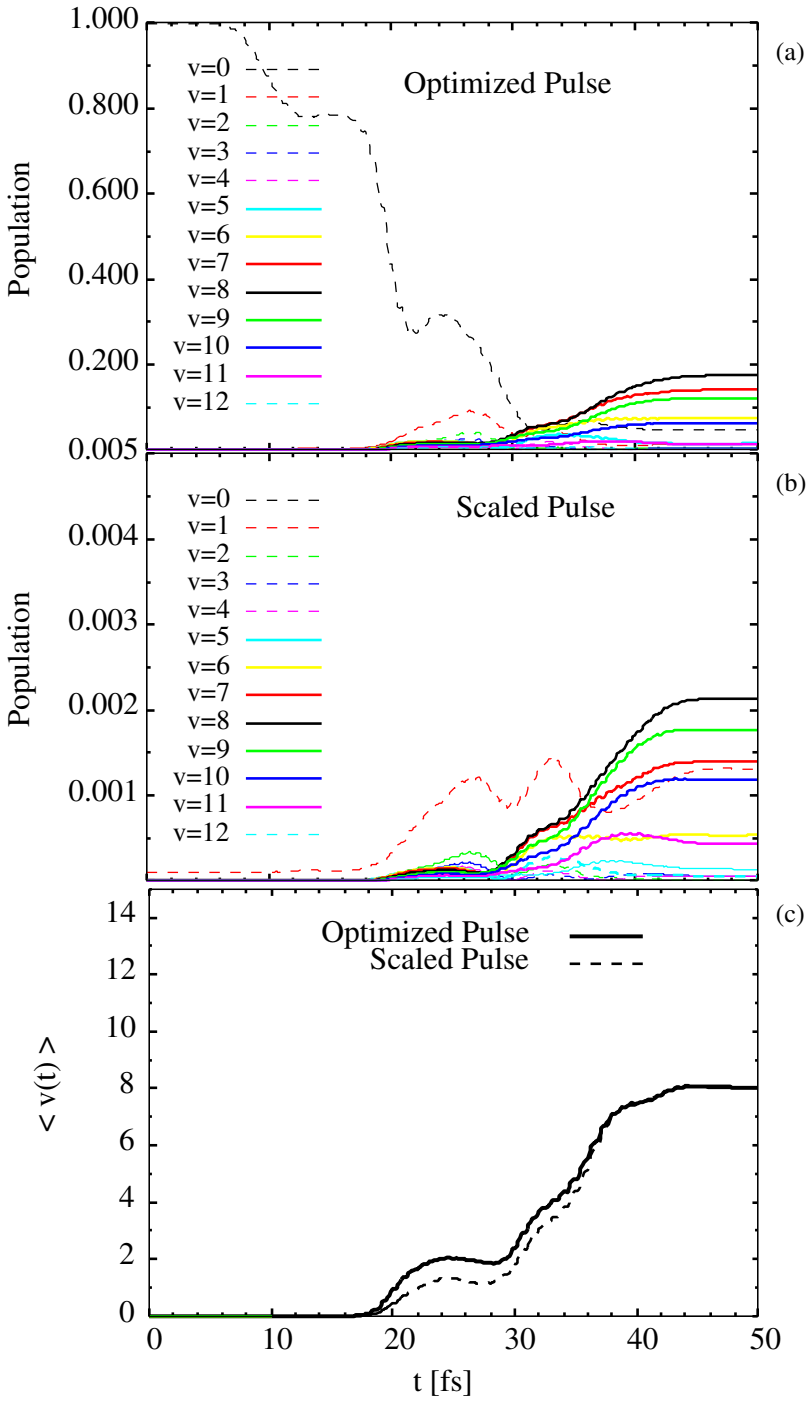

Figure 4.9: The population distribution on the vibrational levels $v = 0-12$ of the electronic ground state X upon the OCT optimized laser pulse after 200 iterations (see Fig. 4.8a) is depicted in panel a). The population distribution obtained by scaling the intensity of the same OCT-pulse by a factor 4 is shown in panel b) for comparison. Panel c) compares the average occupation versus time, <v(t)>, of the corresponding wavepackets created on the electronic X-state.

The reduced 1D-density of the generated wavepacket is shown in Fig. 4.8d. In Fig. 4.8c the changes of population on the target state and on the C state are plotted together. Fig. 4.8b shows the XFROG trace (see Ref. 57) of the respective OCT-pulse of panel (a). The XFROG trace is calculated as

$$I_{XFROG}(\omega,\tau) = \left| \int dt \mathcal{E}(t) G(t-\tau) \exp(-\omega t) \right|^2 \tag{4.15}$$

where, $G(t)$ is a rectangular gate function with Gaussian tails, as in Ref. 57. Comparing panels (b) and (c) the action of the laser pulse can be rationalized. The first subpulse is resonant to the vertical excitation C $\leftarrow$ X($v = 0$), whose frequency, $\omega_0 = 0.1099 E_h/\hbar$, is shown by the upper horizontal black line in Fig. 4.8b. It populates the C state by about 20%, but there is no population of the target state. The second subpulse has a negative chirp; it excites the C state and stimulates population down to the X state at the same time. The chirp brings the center frequency down to accomodate the transition energy from the C to the $v = 8$ state, whose frequency, $\omega_0 = 0.0966 E_h/\hbar$, is shown by the lower horizontal black line in Fig. 4.8b. The action of the third subpulse is rather similar to that of the second one. Finally, a fourth subpulse being resonant to the X($v = 8$)$\leftarrow C$ transition captures part of the propagating C-state wavepacket and dumps it down to the X state.

One should notice that the peak intensity of the OCT field of about 4.5 $\cdot 10^{14}$ W cm^{-2} is about 2 orders of magnitude larger than the estimated damage threshold for Br_2 in solid Ar (N. Schwentner, private communication). An attempt to reduce the intensity of the shaped OCT-field by a factor 4 also reduced the control yield, as shown in Fig. 4.9b. The populations distributed on the vibrational states $v \neq 0$ dramatically drop (about 2 orders of magnitudes) and the distribution is clearly dominated by the $v = 0$ level. However, the pump-dump-like scheme is not appreciably modified: Still a wavepacket on the X-state is produced, whose averaged occupation number still corresponds to the target state $v = 8$, as shown in Fig. 4.9c by the black dashed line. In other words, the mechanistic aspects of the proposed control pathway do carry to the regime of lower intensities, as well.

4.3.3 Predissociation Starting From the OCT ground state Wavepacket

The propagation of the ground state wavepacket during the next 500 fs is depicted in Fig. 4.10a. After the OCT-pulse is over, the wavepacket begins to regularly oscillate with a period of circa 100 fs. Hence, the ground state wavepacket needs to be promoted to the B state. The most simple scheme appears to be its excitation whenever the outer turning points are reached and this for two reasons: First, it is rather compact, and second,

its maximal displacement allows for the energetically lowest excitation onto the B-state potential.

This was achieved by a short Gaussian laser pulse, Eq. 4.9, of width $\sigma = 18fs$, amplitude $E_0 = 0.005E_h/ea_0$ and frequency $\omega = 0.0606\ E_h/\hbar$, which matches the resonance condition giving the maximum of population of again about 8%. The pulse is centered at 185 fs, as shown in Fig. 4.10b. The predissociation yield obtained, is finally shown in Fig. 4.10c (black solid line) and compared to the case of excitation from the vibrational preexcited stationary eigenstate $v = 8$ (solid blue line), see also Fig. 4.5, within the first 500 fs. The predissociation dynamics looks rather similar, that is, one observes steps whenever the wavepacket arrives at the crossing seam region. Two points should be emphasized. First, it is surprising that the predissociation yield after 550 fs is almost the same in both simulations. After all, one compares excitations from rather different initial states, and optimization of the pulse parameters of the second pulse were not even attempted. Second, one could, in principle, envisage a simple extension of this control scheme, which consists of a train of pulses acting each time the wavepacket is located at its outer point.

4.4 Conclusion

The five-dimensional RSVC-Hamiltonian model, based on the DIM theory and developed in Refs. 119, 120, 158, was used here in order to get more insights into the nonadiabatic population transfer mechanism (predissociation) from the B- to the C-state of the dihalogen molecule Br_2 embedded in a Ar matrix. All nonadiabatic laser-driven quantum dynamics simulations were based on the MCTDH wavepacket propagation.

In this work a new strategy has been applied for studying the predissociation mechanism, which could be resumed in the following three stages. In the first stage, it has been proved that excitation to the energetically lower region of the B-state potential permits to create a wavepacket energetically closer to the B-C crossing seam, which slightly increases the predissociation yield with respect to the previous studies, Refs. 119,120,158. A systematic study of the dependence of the predissociation yield on the starting vibrationally preexcited (stationary) states $v = 1 - 10$ has shown that this resonance condition to the B-C crossing seam is matched by promoting a wavepacket into the B state from the preexcited vibrational level $v = 8$. The energy values of the first eight vibrational states are listed in Tab. 4.2 and are additionally drawn in Fig. 4.4. In the second stage, population on the vibrationally state $v = 8$ is achieved by using Optimal Control Theory. The shaped pulse actually prepares a wave packet in the electronic ground state with dominating $v = 8$ character, via a multiple pump-dump-like mechanism involving the electronic C state. This is schematically depicted by the blue and violet arrows, labeled 1 and 2, in Fig. 4.4. The created wavepacket oscillates in the X state and is, in the third stage, excited by a simple Gaussian pulse to the B state. This stage is represented in Fig. 4.4 by the two red arrows, numbered 3 and

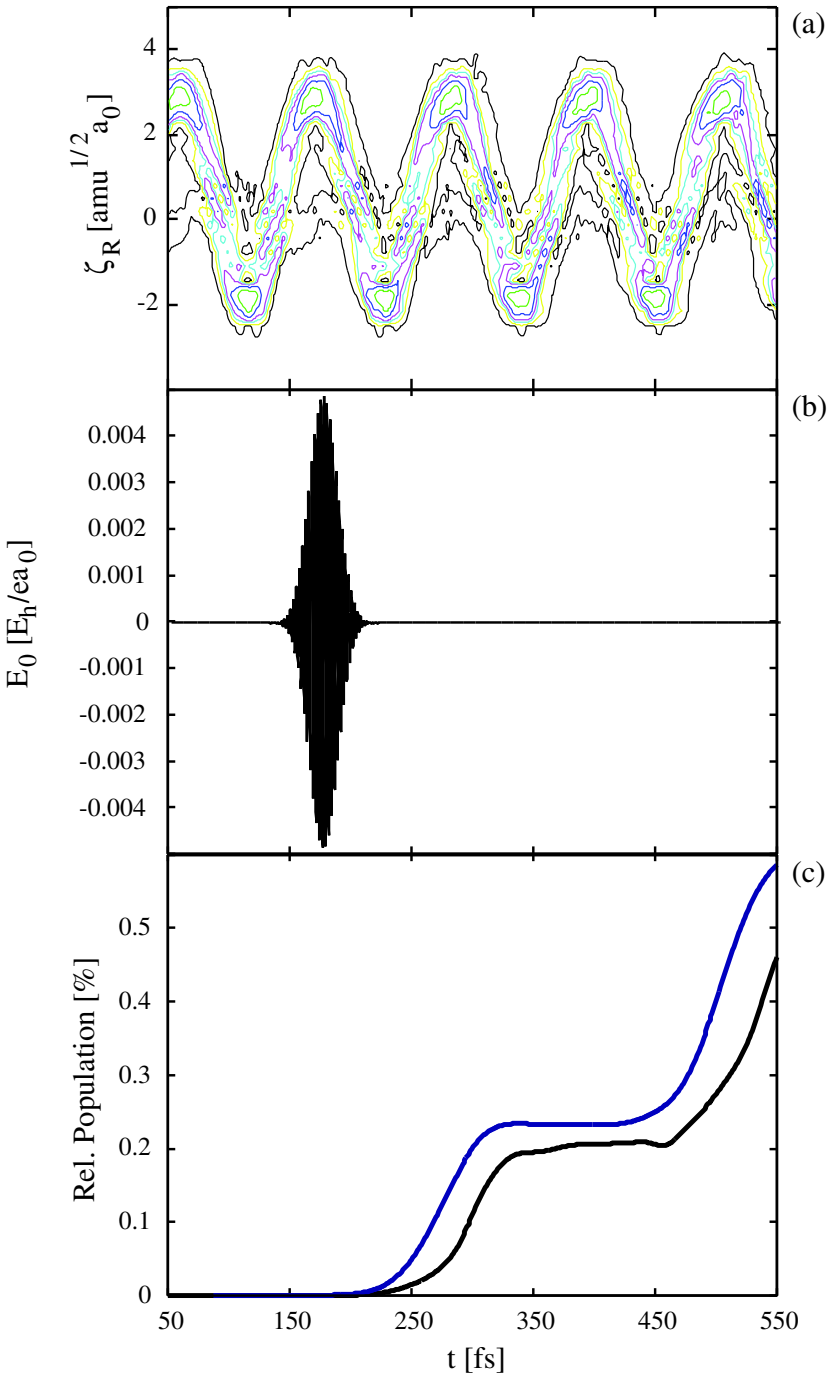

Figure 4.10: (a) Time-dependent reduced X-state density for the Bromine coordinate $\rho^{(B)}(\zeta_R, t)$ (isodensity values of 0.05, 0.15, 0.25, 0.35, 0.55, and 0.85) after the OCT pulse is over. (b) Gaussian pulse (σ = 18 fs, $E_0 = 0.005 E_h/ea_0$, $\omega = 0.0606 E_h/\hbar$) promoting part of the ground state wavepacket to the B state. (c) Predissociation yields (C-state relative populations, Eq. 4.11) are compared when starting from the stationary eigenstate $v = 8$ (blue solid line), see also Fig. 4.5, and when taking the OCT wavepacket in the X-state as the initial state (black solid line), within the first 500 fs.

4. Approximately, the same predissociation yield was obtained as for the idealized case when the stationary vibrational preexcited eigenstate $v = 8$ is taken as the initial state.

Even though the new strategy enhances the nonadiabatic transfer process, the increasing of the predissociation yield still does not reach the threshold of 5% per round-trip estimated experimentally from the broadening of zero-phonon lines mentioned in the introduction. One source of error in the model could be the Br-Ar interaction potential used for calculating the DIM-PESs, which has been extracted from photoelectron spectroscopy. A further inconvenience in the present strategy lies on the OCT method used in the second stage, which involves a very intense pulse, not reproducible in a real experiment.

Finally, in more general terms, it must be emphasized that dihalogens in rare gas matrices lend themselves as laboratories for testing new concepts. They are versatile simplified models for disclosing basic quantum mechanics phenomena as shown throughout this work.

5 Structure and Quantum Dynamics of Cl_2 Embedded in Solid H_2

5.1 Introduction

The main purpose of this chapter is to get insights on the structure and energetics of a Cl_2 molecule trapped in solid hydrogen. In the previous chapter, a Br_2 molecule embedded in an Ar matrix was investigated. In general, cold and well-ordered crystalline systems such as RG matrices permit to study a wide range of interesting chemical processes, such as photodissociation of the guest molecules, in detail both in experiment and in theory. At cryogenic temperatures solid hydrogen shares many properties with the RG matrices. For example, the individual molecules rotate in their rotational ground state wavefunctions, which is indeed almost spherical, closely mimicking the RG atoms. Moreover, the interactions between the hydrogen molecules and with doping molecules are also in the van der Waals regime. However, solid hydrogen shows many quantum effects connected to its lighter mass, such as the high zero-point energy, which make the crystal to be less rigid. Additionally, under certain conditions, chemical reactions can be observed *in situ*.

At the end of this chapter, we try to hand over the information needed for future quantum dynamics simulations of the Cl + H_2 -> HCl + H reaction observed *in situ* by Anderson and Raston in Ref. 15 when irradiating the system with UV and IR light at the same time. From the theoretical point of view, this implies many challenges, since practically all possible degrees of freedom of the reactants have to be considered, i.e. rotations, translations and vibrations of the hosting hydrogen molecules, and also rotations (or librations), vibrations and translations of the guest molecules. In order to treat this complicated system, the multi-stage adiabatic separation tool developed in Chap. 2 is applied, which essentially permits to separate most of these DOFs and study them individually at least in an approximate way.

In the first part of this introduction, a review is given about the fascinating features of pure solid hydrogen. Afterwards, since the many-body system is described in terms of pair interactions, the second part is dedicated to the H_2-H_2 pair potential, which has been widely investigated in the past decades. Finally, in the third part, a review is given about the use of doped solid hydrogen for matrix isolation spectroscopy.

In Sec. 5.2, the multi-stage adiabatic separation tool is applied in order to calculate the H_2-H_2, D_2-D_2, H_2-Cl_2 and D_2-Cl_2 pair potentials. The theoretical model is detailed and the corresponding equations for the rotational adiabatization of the H_2 molecule in the rigid-rotor approximation are derived.

In Sec. 5.3, the results are presented. This section is subdivided into three main parts. In the first one, the quantum chemistry calculations are performed. On the way, the pair interactions are discussed in terms of quadrupole-quadrupole electrostatic interactions. The resulting rotationally adiabatic pair potentials are finally fitted to HFD-functions. In the second part, the pair potentials are used in order to grow pure and doped clusters by means of classical dynamics. The obtained growth sequences are therefore discussed before building up the crystal. In the third part, the study on the translational and rotational DOFs of guest and hosting molecules in the pure and doped matrices within the Einstein [173] and the Devonshire [174] models are presented. In Sec. 5.4, the main results are summarized.

5.1.1 H_2 Solid Crystal

Molecular hydrogen and its different isotopes form the simplest of all molecular species. Intensive experimental and theoretical investigation of solid molecular hydrogen only began in the early 1960s (see for example the review [13]), whereas solid He, the smallest stable atom of similar mass, has already been studied since the 1930s. One possible reason for this is that the theoretical treatment of molecular H_2 poses more difficulties than that of atomic He, owing to the rotational and vibrational DOFs of the diatomic molecule.

In the solid phase molecular hydrogen presents many fascinating features mostly connected with its quantum nature. The light mass, in fact, heavily influences the condensed phase properties, as for example its low melting and boiling temperatures of 14.01 and 20.28 K, respectively, at normal pressure. Its phase diagram is rather complicated and supersolid and metastable metallic phases are expected at high pressures. Nevertheless, since we are only interested in low pressure properties, all simulations carried out do not involve pressure.

In the solid state the H_2 molecules rotate almost freely, even at T=0 K [13]. The reasons for this particular behaviour are, on the one hand, the small moment of inertia corresponding to a large molecular rotational constant, on the other hand the weak anisotropic forces due to the almost spherical distribution of the electronic density. Moreover, because of the light mass and the weak intermolecular interaction, the system possesses a large translational Zero Point Energy (ZPE), which conferred to solid H_2 (and He) the attribute of "translational quantum" solid. The large ZPE is also accompanied by a large anharmonicity which explains why the quasi-harmonic theory of lattice dynamics can not be applied to translational quantum solids [13]. A further consequence of the large ZPE and strong anharmonicity is the large nearest-neighbour distance (NNd), which becomes 0.3789 nm in

the limit of 0 K. Based on a hard-sphere model with van der Waals radius of 0.12 nm [175] for atomic hydrogen and considering the experimental minimum equilibrium distance of circa 0.074 nm for molecular hydrogen, one may guess the NNd to be around 0.314 nm, which is about 17% less than the experimental value. Thus, due to the ZPE, solid hydrogen undergoes a great expansion in each direction. The same model applied on Ar, gives an expected NNd around 0.376 nm, (0.379 nm within the extended Einstein model of Manz *et al.* [176]), with the difference that effectively the experimental NNd has been measured to be 0.376 nm [177].

The total wavefunction of an isolated hydrogen molecule may be approximated by the product of the vibrational, rotational and nuclear spin wavefunctions. Molecular hydrogen is formed by two indistinguishable protons with nuclear spin $I_N = \frac{1}{2}\hbar$, that is two fermion particles. Thus, they are subject to the Pauli's principle and the total wavefunction must be antisymmetric under exchange of the two nuclei. Seeing that the vibrational wavefunction is symmetric, either the nuclear spin wave function is antisymmetric (anti-parallel spins) and the rotational one is symmetric (the rotational quantum number J assumes even values) or vice versa. In the first case the species is termed para-H_2 (pH_2), whereas in the second case ortho-H_2 (oH_2). For the boson deuterium, the situation is simply reversed since the total wave function has to be symmetric under exchange of the nuclei. Thus, the rotational quantum number J assumes even and odd values for the ortho-D_2 (oD_2) and para-D_2 (pD_2) species, respectively.

Para and ortho-hydrogen as well as ortho and para-deuterium should be regarded as different species with different properties. Conversion between them is forbidden in the case of isolated molecules and very slow in general, because of the small spin coupling term. In the solid phase at zero pressure, conversion takes place with a constant rate of 1.9%/h and 0.06%/h for H_2 and D_2, respectively. Thus, pure samples of them can be prepared up to a concentration of 99.98% [13], which remain metastable for long enough to permit suitable experimental investigations.

5.1.2 The $(pH_2)_2$ Interaction Potential

Theoretical study of the intermolecular interactions in solids has been and still is a challenge for scientists. The total interaction energy of a solid can be subdivided in sums over the n-body interactions as

$$E_{\mathrm{tot}}(N) = \sum_n E_n(N) = \sum_{i<j} E_{ij}(2) + \sum_{i<j<k} E_{ijk}(3) + ... \tag{5.1}$$

where N is the number of closed-shell particles and n runs from 2 to N. The importance of the terms in the expansion decreases with the number n of body interactions involved, whereas the difficulties in calculating them remarkably increases, so that the expansion is truncated at some value of n where hopefully the results are a good compromise between

computational feasibility and a reasonable value of the total interaction energy. For certain systems the three-body interactions can already be neglected, whereas, for example for RG crystals, they are indispensable in order to find the equilibrium fcc structure [3]. The three-body interactions can be divided in two contributions, the exchange terms, which are operative at short-distance and have to be considered only in liquid-phase or high density solids, and the dispersion terms, which are operative at long-distances and whose leading term is the interaction between the induced-dipoles of three particles, generally evaluated by the Axilrod-Teller-Muto (ATM) potential [178]. Thus, in the zero-temperature limit, eventually, the ATM approximately describes the three-body interactions and can therefore be considered an estimation of the error introduced by neglecting the three-body term in Eq. 5.1. In the case of Ar, Kr and Xe crystals, the ATM contribution amounts to 7%, 9% and 10% of the cohesive energy [179] and in the case of solid hydrogen it amounts to 10% of the pure pair interactions [13]. Finally, even though the importance of three-body terms has been largely demonstrated, they have been normally neglected and the total interaction energy approximated just by the sum over the two-body interactions. By all means, the study of the $(pH_2)_2$ pair potential has been a milestone for the understanding of the properties of solid pH_2 and many efforts have been made in the last decades by both the theoretical [180–191] and experimental [13, 192, 193] communities.

Please note that in Chap. 4, in the spirit of the DIM model used for calculating the PES of the Br_2@Ar system only two-body interactions have been considered, as well.

Two of the most famous and widely used semi-empirical $(pH_2)_2$ pair potentials in the past decades as well as in this study are the experimental potentials of Silvera-Goldmann (SG) [13, 192] and Norman-Watts-Buck *et al.* (NWB) [193]. Both potentials are fitted to the Hartree-Fock-dispersion (HFD) potential family developed by Ahlrichs *et al.* [194], which consists of the sum of an attractive and a replies part

$$V = V_{\text{rep}} + V_{\text{attr}} = \exp[f(R)] + \sum_{i=6,8,\ldots} \frac{C_i}{R^i} \times S(R) \ . \tag{5.2}$$

V_{rep} describes the short-range interaction and has in general an exponential form, so that the energy goes to infinity when the nuclei approach each other, as expected from Pauli's principle forbidding two different electrons to occupy the same spin-orbital. V_{attr} accounts for the long-range interactions and behaves as some inverse power of the distance R between the centers of mass. The attractive part is, additionally, multiplied by the switch function $S(R)$, which attenuates the asymptotic van der Waals (VDW) attraction at short distances. Both the repulsive and attractive parts arise mainly from the electrostatic interactions between the molecules and are well established in theory (see for example [195]). V_{attr} reflects the multipole expansion, which is a valid assumption as long as the distance between two molecules is large compared to the dimension of the molecule (or more precisely to the dimension of the multi-particle charge-distribution). Moreover, the multipole expansion

terms become infinite at the origin, so that the switch function also has the role to cut them off at shorter distances. Within this theory, the C_i coefficients assume a physical meaning and quantify the contributions from the electrostatic, induction and dispersion effects. Its leading term with $n = 6$ is the induced dipole -induced dipole interaction.

Neutral, homonuclear molecules, with $D_{\infty h}$ symmetry, like H_2, D_2 and Cl_2 (treated in the next sections) do not possess a monopole or dipole so that the lowest order of electrostatic interaction between two of these molecules is the quadrupole-quadrupole interaction, which has a R^{-5} dependence. Since the next symmetry allowed multipole is the hexadecapole, the next two ones are the quadrupole-hexadecapole and hexadecapole-hexadecapole interactions, which have R^{-7} and R^{-9} dependencies, respectively. Their orders of magnitude have been guessed here to be never greater than 10^{-3} kJ/mol. However, the C_5/R^5, C_7/R^7 and C_9/R^9 terms do not appear in the HFD fitting function by Norman-Watts-Buck (NWB) and Silvera-Goldmann (SG), since all electrostatic moments vanish in the case of isolated para-hydrogen and ortho-deuterium molecules in their lowest rotational state, $J = 0$. Please note that the C_9/R^9 term in the HFD fitting function of Silvera-Goldmann term refers to the three-body interaction and not to the hexadecapole-hexadecapole interaction. In the rotational ground state, the average static multipolar field outside the molecule vanishes because all the multiple moments of a spherical charge distribution are zero, whereas in the state $J = 1$ the molecule is surrounded by a relatively strong field of mainly quadrupolar nature [14], as shown also in App. 6.3, where such quadrupole moments have been calculated. As a consequence, electrostatic contributions are expected to be important only for oH_2 (and pD_2), whereas for pH_2 (and oD_2) only induction and dispersion effects play a role. The isotropic part of the $(pH_2)_2$ pair potential, almost exclusively arises from dispersion effects (of quantum-mechanical nature), and the leading terms are the C_6/R^6, C_8/R^8 and C_{10}/R^{10}, namely, the induced dipole-induced dipole, induced dipole-induced quadrupole and induced quadrupole-induced quadrupole interactions, respectively. These coefficients have been determined by Meyer by means of perturbation theory [196].

The SG and NBW potentials are compared later in Fig. 5.14 and show very similar shapes independently of the inclusion of the three-body term C_9, which is approximated as αC_6, with α being the polarizability of pH_2. This coefficient has been determined so that the effective pair interactions, when summed over the lattice, give the same energy as the true ATM forces [13]. This approach has been recently criticized by Hinde in Ref. [191], where high level quantum chemistry calculations demonstrate that three-body exchange (non-ATM) interactions can not be neglected at high densities. The author justifies the very good agreement to the experiments to a fortuitous error cancellation of the neglected non-ATM effects and the fit of the repulsive part of the potential to very low level calculations. Operetto and Pederiva recently computed the pressure-volume curve at $T = 0$ K by using the diffusion quantum Monte Carlo method and reported a poor

agreement with the experimental curve when using the SG potential, whereas a better agreement is achieved by using the NWB potential when the ATM triple-dipole term is included explicitly.

From the theoretical point of view the interaction between four nuclei and four electrons is in principle calculable to high precision from *ab-initio* approaches. However, since the interactions are of VDW nature, a very high level of calculation is needed. Thus, from the first calculations of Gallup in 1976 [180], to the first accurate 4-dimensional potential of Deep and Johnson in 1999 [186] about 2 decades passed. In 2008 an even more accurate 4-dimensional potential has been calculated by Patkowski *et al.* [188], which accurately reproduces measured thermodynamic properties. In about the same period Hinde published a 6-dimensional potential at nearly the same level of calculation as Diep and Johnson, including the intramolecular vibrational DOFs of the two monomers. The agreement of the rotational and rovibrational infrared spectra with those obtained experimentally, is impressive. Recently, Hinde also recalculated the isotropic dispersion coefficients C_6, C_8 and C_{10} of the parahydrogen dimer by averaging them over the monomer vibrations [197]. They are compared later in Tab. 5.6 of Sec. 5.3.5 to the ones calculated by Meyer [196] and along this work.

5.1.3 Doped pH_2 Solid Crystal

The many peculiar properties mentioned above make pH_2 crystal a very interesting medium for matrix isolation spectroscopy, as well as for hosting chemical reactions. Matrix isolation spectroscopy was initiated in the 40's by Lewis [198] and found many interesting applications in physical chemistry. Because of their chemical inertness and weak perturbation, Rare Gas (RG) atoms have been mostly used in this field (see Chap. 4 or for example [199]). However, the resolution in RG matrices is limited due to both homogeneous and inhomogeneous line broadening, which could, as a consequence, hide some information in the spectra [6]. Moreover, the rigidity of such matrices limits the study of chemical reactions at cryogenic temperatures, as strong interactions from the surrounding lattice may distort the reaction potential surface significantly with respect to those in gas-phase [6]. After Oka in the 80's demonstrated that enriched pH_2 can be used as matrix for IR spectroscopy with high resolution of $\Delta v/v < 10^{-6}$ [5], many investigations started on pH_2 doped with several molecules [6, 7, 15, 200–206]. The IR spectra of molecules embedded in pH_2-crystal present very sharp linewidths, indicating that the dopants are in well-defined rotational and vibrational quantum states [7]. Moreover, due to the large ZPE, pH_2 results in a "soft" crystal (that is in a high compressibility [176, 207]), so that cage effects are practically absent and chemical reactions upon photolysis can be observed *in situ*, opening a way for the investigation of chemical processes in condensed-phase and at cryogenic temperatures [7], as for example, pure tunneling reactions. Isolated hydrogen molecules as well as solid pH_2 do not show IR activity, in contrast, absorption is observed in the presence of impurities

as for example oH_2 or other molecules. The interaction with the hosted species, in fact, induces dipole moments in the neighbouring pH_2 molecules, so that the resulting spectra contain information about the response of the pH_2 matrix [7].

Since pH_2 in the condensed-phase retain good vibrational and rotational quantum numbers, v and J, respectively, the IR spectrum features correlate with well-defined rovibrational transitions [7]. Upon absorption due to an impurity, a vibrational coupling based mechanism delocalised the $v = 1$ vibrational state, so that the vibrational excitation can "hop" between neighbouring pH_2 molecules. The $v = 1$ vibrational state is therefore broadened (4 cm^{-1}) and the vibrational exciton is termed vibron after van Kranendonk [14]. Analogously, delocalized rotational excitations are called rotons (see for example [208]. Finally, this vibrational bond energy can be used to induce reactions with reactive species stabilised in solid para-hydrogen. Solid pH_2 possesses, in fact, a property not yet mentioned: a thermal conductivity of 50 W m^{-1} K^{-1} [6], which is comparable with that of Cu and is almost one order of magnitude larger than the conductivity of RG crystals [1]. Thus, solid pH_2 stabilises photofragments resulting from photodissociation processes through a very efficient dissipation of the excess of energy [6].

Several molecules have been used to dope pH_2 for experimental investigations in the past years. Momose *et al.* studied the photochemistry of methyl iodide, CH_3I, in pH_2 [6], showing that methylradicals and iodine atoms can be stabilised and that upon a new irradiation, formation of methane is induced via a three-step reaction mechanism. They also observed the same chemical reaction via quantum tunneling. Yoshioka *et al.* [7] investigated pH_2 doped with CH_3F, CH_3Cl and CH_3Br, showing that the residual oH_2 molecules in the crystal cluster around the dopant species due to electrostatic interactions between the non-vanishing quadrupole moment of oH_2 and the dipole moment of the dopant. Similar clustering effects were observed when doping with N_2O. Clustering of oH_2 molecules around trans-formic acid embedded in pH_2, instead, has been shown by Paulson and Anderson [205]. Anderson *et al.* for the first time demonstrated a cooperative transition in pH_2 matrices doped with HCl: A single photon excites the rotational motion of the dopant molecules and the vibrational coordinate of an adjacent pH_2 molecule, which are the condensed-phase analogs of combination bands in VDW clusters [202]. Cyclic water hexamer have been observed in solid para-hydrogen by Fajardo *et al.* [209], who also recorded spectra of H_2O, D_2O and HDO molecules in pH_2 2 years later [203]. Infrared spectroscopy of carbon clusters trapped in solid para-hydrogen have been presented by Miki *et al.* [201]. Several atomic species embedded in solid para-hydrogen have been also studied and literature can be found on H, Li, B, C, N, O, Mg, Al, see, for example, the small review Ref. 210.

Many of the mentioned experiments were stimulated by, or conversely went on to stimulate theoretical investigations, including the present one. Theoretical investigation has been found in the literature on OCS [211–213], on HF [214–220], on CO [221, 222], on

O_2 [223] as well as on NO_2 [224] molecules and on Li [225–230], on Li^+ [231,232] as well as on B [233] and on O [234] atoms.

The present work was inspired by the experiments carried out in the group of Anderson on solid pH_2 doped with Cl_2 molecules [15,204]. In particular, they photolysed the dopant species and monitored the formation of HCl *in situ* under different experimental conditions. In the first instance, they irradiated the sample by using a 355 nm UV source exciting the Cl_2 molecules to the dissociative C, $^2\Pi_u$ state and generating Cl* atoms almost exclusively in their spin-orbit ground state $^2P_{3/2}$. Conservation of energy gives the translational energy of the photofragments with respect to the laboratory frame

$$E_{\mathrm{T}} = \frac{m_{\mathrm{Cl}}}{m_{\mathrm{Cl_2}}}[E_{\mathrm{ph}} - D_0] = 48.93\,kJ/mol \tag{5.3}$$

where E_{ph}=337.02 kJ/mol is the photon energy and D_0 = 239.22 kJ/mol is the dissociation energy of Cl_2 ($X\ ^1\Sigma_g$).

For this experimental set up, referred to as "only UV", formation of the product HCl was not observed. It is known from previous theoretical and experimental studies [235,236] that in the gas phase the Cl + H_2(v=0) -> HCl(v=0) + H reaction is endothermic by about 4.31 kJ/mol. However, even though the translational energy for the Anderson experiment in H_2 crystal is far above the reaction barrier, formation of the product is negligible and has a probability of P_{UV} = 0.006.

In a second experiment, the sample is simultaneously irradiated by UV + IR sources. The authors refer to this experimental set up as "UV+IR", in which production of HCl is observed with a probability P_{UV+IR} = 0.15. They state that excitation to at least the first vibrational level v=1 of the pH_2 matrix is necessary in order to induce reaction, since the PES presents a late barrier, hence explaining the mechanism in terms of Polanyi rules [86]. In a third experiment, to which they refer as "IR" only, the IR source is used to irradiate the sample after the UV source is turned off. Again no significant amount of HCl was produced, demonstrating that the translational energy of the Cl* atoms after photolysis is rapidly dissipated by the crystal thanks to the high thermal conductivity mentioned above.

Finally, the results for the three experiments can be summarized by the following respective reactions

$$\begin{aligned}
1 \ &: \ Cl^* + H_2(v=0) \nrightarrow HCl + H \\
2 \ &: \ Cl^* + H_2(v=1) \rightarrow HCl + H \\
3 \ &: \ Cl^* + H_2(v=0) \xrightarrow{\Delta t} Cl + H_2(v=0) \xrightarrow{IR} Cl + H_2(v=1) \nrightarrow HCl + H
\end{aligned} \tag{5.4}$$

where Cl* and Cl are the photofragments produced upon UV photolysis with high translational energy and after the translational energy has been dissipated, respectively.

Quantum dynamics simulations corresponding to reactions 1 and 2 have been carried out in the Manz group [16]. Reaction 3 is more difficult to simulate, since the time needed by the Cl* atoms to relax in the pH_2 matrix is too long with respect to the approximation for which the environment is considered frozen during the first 100 fs. Admittedly, the model involves many approximations. For example, it assumes a single vibrationally excited H_2 molecule, instead of a delocalized vibron. Moreover, such H_2 is positioned in the first shell of molecules surrounding the dopant, so that the direction of the Cl_2 bond is directly pointing to it. As a consequence, the probability found for the reaction resulted in an upper limit of the real one. A second approximation lies in the description of the wavefunction of the reactant H_2 molecules in terms of the Einstein model (EM), which is for the first time applied to a "translational quantum crystal" [176]. For this purpose the classical EM has been extended including anharmonicity effects. The effective potential has been evaluated by moving the COM of the H_2 molecule along three important crystallographic directions. The three 1-dimensional cuts of the effective potential have been found to be approximately harmonic within the width of the 1-dimensional wavefunction of H_2. Moreover, this all is assumed to be valid also for the dopant molecule, so that the width of the wavefunction of the Cl_2 molecule is calculated within the harmonic oscillator model from that of the H_2 molecule, to be proportional to the fourth-root of the ratio between the masses of the two molecules. Additionally, the dimensionality of the problem is reduced to 2 and the reaction is considered to start from the electronic ground state instead of from the $C^2\Pi_u$ state. Finally, a London-Eyring-Polanyi-Sato (LEPS) PES is used with parameters fitted to the ab-initio PES of Capecchi and Werner [236] and the total wavefunction entering the LEPS represented simply by a product of the Cl and H_2 wavefunctions.

Nevertheless, this simplified model already elucidates some of the most important and interesting features of the reaction mechanism involved in the experiment of Anderson. In particular, reactions 1 and 2 have been explained as consequences of energetic and dynamical effects. From the energetic point of view, if one considers the "only UV" experiment, only about 5.4% of the kinetic energy of the photodissociated Cl atoms are converted into translational energy available for reaction, whereas the rest is "wasted" as energy of the COM of the reactive system. This is shown in App. 6.1 and published in Ref. [16], where the three-body collision kinematic is treated in detail for the special case of photodissociation. Finally, the main energy of the system, which only consists of this small fraction of the kinetic energy, is below the reaction barrier height. The "UV +IR" experiment, in contrast, supplies additional vibrational energy, making the reaction endothermic. From the dynamical point of view, the experimental results can be explained within an extended theory of the Polanyi rules, called "interpolated Polanyi rules". Manz *et al.*, in fact, found the barrier of the LEPS PES to be neither "early" nor "late", but actually in between, at "high noon", as they termed it. In other words, in order to efficiently overcome the barrier

and obtain the products, the total energy must be adequately partitioned in translational + vibrational energy, which seems to be the case for the experimental setup in reaction 2.

The present work aims to prepare the ground for the quantum reaction dynamical treatment of the Cl_2@pH_2 system, i.e. the mechanism of the UV/IR driven reactions observed in situ by Anderson *et al.*. It critically reviews some of the assumptions made in Ref. 16 in order to gain a deeper knowledge of the structure and the energetics of the reactants in the matrix.

The crystal is described in terms of only pair interactions, so that the first step involves the calculation of the $(H_2)_2$ and H_2-Cl_2 pair potentials by means of quantum chemistry in Sec. 5.3.2. In order to have a compact description of them, the multi-stage AS tool developed in Chap. 2 is going to be applied, since electronic, vibrational and rotational DOFs of both molecules have to be in principle considered simultaneously. Finally, the quantum chemistry PESs are further averaged with respect the hydrogen molecule rotations (rotational adiabatization), which allows for the calculation of the $(pH_2)_2$ and pH_2-Cl_2 as well as of the oH_2-Cl_2, oD_2-Cl_2, pD_2-Cl_2 and (in principle also $(oD_2)_2$) pair potentials in Sec. 5.3.3.

The first question addressed is which of the close-packed structures is energetically favoured in the pure and doped crystal, fcc or hcp? It is known that the pure crystal can be grown both in fcc and hcp symmetries depending on the experimental conditions, so that near degenerate energies are expected from theoretical simulations. However, the structure of the crystal in the presence of the impurity has to be thoroughly investigated. Comparing the magnitude of the dopant molecule and the particularly large NNd of solid para-H_2, the Cl_2 molecule is expected to occupy only a single substitutional lattice site, but no theoretical simulations were still performed to confirm it. In contrast, Br_2 for example is found to occupy a double substitutional site in the Ar matrix, see Chap. 4. Moreover, Br_2 is found to undergo only small librations around the <110> fcc crystallographic direction: On the other hand the Ar atoms are heavy to be pushed away and Br_2 has even a smaller rotational constant than Cl_2. Immediately, another question arises: Along which crystallographic direction does Cl_2 align? Since hydrogen molecules are very light and the crystal very soft, is the impurity librating or even rotating in the matrix? One step in this direction, is the investigation of the growth sequences of pure and doped clusters in Sec. 5.3.6.

In order to perform quantum reaction dynamics on a translational quantum crystal, sophisticated models must be developed for the calculation of realistic initial wavefunctions for the reactants H_2 and Cl_2. The models have to take into account the anharmonicity originating from the large excursions (translations or external vibrations) from the nominal lattice position and the rotations of the H_2 molecules and, eventually the rotations or librations (rotational oscillations around a main crystallographic direction) of a solute molecule. This clearly calls for a quantum mechanical treatment in order to properly

describe the position of the molecule in terms of distribution functions. Moreover, due to the high ZPE and to the large lattice constant, translational quantum crystals are highly compressible [176, 207] and therefore considered to be "soft" matrices. Finally, the high dimensionality of condensed systems unfortunately makes it difficult to include all those properties in an unique model. Anharmonicity was included by Manz *et al.* in Ref. 16 within the "anharmonic Einstein model", but the lattice is still treated classically, i.e. with the nuclei frozen at their nominal lattice positions. Distribution functions for the nuclei of the lattice are instead included by Rościszewski and Paulus in Ref. 237, within the "quantum Einstein model", which, on the contrary, does not include anharmonicity. In the present work we try to include the softness of translational quantum crystals by simulating a less rigid environment. This is achieved by extending the anharmonic Einstein model, so that for the first time anharmonicity and high compressibility of solid hydrogen are considered at the same time.

Investigation of the Cl_2 rotations also involves approximate models, which closely recall the EMs just discussed. The rotational potential felt by the guest molecule in the matrix are calculated within the Devonshire model (DM) [174] by considering both fcc and hcp rigid lattices. Similarly to the EMs, the DM is also extended to include a non-rigid environments. Dynamics of the molecules in the matrix is treated in Sec. 5.3.8, which also includes a discussion on the validity of the fourth and last AS of translational and rotational DOFs.

5.2 Multi-Stage Adiabatic Separation for Pure and Doped pH_2 Crystals.

Description of the pure pH_2 and doped Cl_2@pH_2 crystals in terms of (at least) the pair interactions involves the calculation of the $(pH_2)_2$ and pH_2-Cl_2 pair potentials, which is the aim of this section. Such pair potentials are calculated within the multi-stage AS tool presented in Chap. 2, so that the many DOFs involved in the pair interactions will be separated and the validity of the critical AS-stages discussed.

The application of the multi-stage AS tool calls, therefore, for the comparison of the energy (or frequency) or time scales, in which the different DOFs of the involved species lie. These data are listed in Tab. 5.1 together with the diatomic constants, where the time scales are calculated as

$$T_{\mathrm{DOF}} = \frac{h}{\Delta E_{\mathrm{DOF}}} \tag{5.5}$$

with ΔE_{DOF} being the energy difference between first excited and ground states.

In general, the first stage, i.e. the nuclear and electronic AS in Sec. 2.2.3, is considered to be valid for all species, since the first electronic excited states lie well above their respective

ground states (last three rows in Tab. 5.1) and no electronic laser-driven excitations are foreseen[1]. For the subsequent stages, only vibrational and rotational energy scales are compared, since the translational DOFs enter the model only when considering both species in the matrix. Moreover, the application of the multi-stage AS must be separately discussed for the "homomolecular" $(pH_2)_2$ and the "heteromolecular" pH_2-Cl_2 pair potentials. In order to compare vibrational and rotational energy scales, one also may compare the ratios between them. These ratios are defined as $\frac{\Delta E_{DOF1=f\leftarrow i}(mol1)}{\Delta E_{DOF2=f\leftarrow i}(mol2)}$, where DOF1 and DOF2 can be either a vibrational or a rotational DOF, and $mol1$ and $mol2$ refer to one of the species considered. Finally, i and f refer to the quantum numbers of the initial and final states. Please note that for para and ortho molecules, since they are two different species, the ground and first excited rotational states are, respectively, $J = 0$ and $J = 2$ for pH_2 and oD_2, and $J = 1$ and $J = 3$ for oH_2 and pD_2. For instance, the energy scale ratio between the vibrational DOF of Cl_2 and the rotational DOF of pH_2 is defined as $\frac{\Delta E_{v=1\leftarrow 0}(Cl_2)}{\Delta E_{J=2\leftarrow 0}(pH_2)}$. Thus, the bigger the ratio between energy (or frequency, or time) scales, the safer is the corresponding AS.

Vibrational and rotational frequencies are compared first for the isolated molecules. By analysing the Tab. 5.1, one notes that for Cl_2 they are safely separable: The respective energy scale ratio is 1230, that is a frequency difference of more than three orders of magnitude. In turn, for the four species, pH_2, oH_2, oD_2 and pD_2, such separation is less accurate, since the corresponding ratios lie between 7.3 and 17, which means that the frequencies, at which each of those molecules rotates and vibrates, differ only about one order of magnitude. Nevertheless, in all cases we apply the adiabatic separation and consider only the vibrational ground state $v = 0$. Additionally, the corresponding probability density function, $|\Psi_{\text{int}}^{(n,v=0)}|^2$ (see Sec. 2.2.4), e.g. Gaussian function, is approximated to an infinitely narrow delta distribution centered at the $v = 0$ vibrationally averaged equilibrium distances, $\tilde{r}_{Cl_2} = \langle r_{Cl_2}\rangle_{v=0} = 0.2032$ nm, $\tilde{r}_{pH_2} = \langle r_{pH_2}\rangle_{v=0} = 0.0757$ nm and $\tilde{r}_{oD_2} = \langle r_{oD_2}\rangle_{v=0} = 0.0753$ nm. At the low temperature of few Kelvin, in fact, only the vibrational ground state is populated, the probability density distribution of which has its maximum at the equilibrium distance[2]. The ground state probability densities were calculated resulting in nearly Gaussian shapes and the corresponding FWHM are respectively 0.0208, 0.0175 and 0.0103 nm for H_2, D_2 and Cl_2 molecules, that is the 13.5%, 11.5% and 2.5% of the vibrationally averaged equilibrium distances. Thus, the Cl_2 vibrational density function is effectively narrow, whereas at a first glance the classical approximation may appear not to be valid for the solvent molecules. However, when separating the vibrational and rotational DOFs, this corresponds to describe the molecules in the rigid rotor approximation, for which the centrifugal distortion constants are found to be 5 orders of

[1] This was not the case for the Br_2@Ar system in Chap. 4, where we instead went beyond the Born-Oppenheimer approximation, since non-adiabatic laser-driven processes were investigated.

[2] Please note that this is exactly the opposite for classical oscillators, where the maximal probability to find the molecule is at the minimum and maximum elongation of the bond.

Table 5.1: Diatomic constants of H_2, D_2 and Cl_2 are listed in order to compare energy, ΔE_{DOF}, and time scales, T_{DOF} (see Eq. 5.5), of the different DOFs involved.

DOF	Species	Diatomic Constants$[kJ/mol]$	$\Delta \mathrm{E}_{\mathrm{DOF}}[kJ/mol]$	$\mathrm{T}_{\mathrm{DOF}}[fs]$
Rotational	pH_2	$B_e = 0.6812$	$\Delta \mathrm{E}_{\mathrm{J=2\leftarrow 0}} = 4.087$	97
	oH_2	$B_e = 0.6812$	$\Delta \mathrm{E}_{\mathrm{J=3\leftarrow 1}} = 6.812$	59
	oD_2	$B_e = 0.3498$	$\Delta \mathrm{E}_{\mathrm{J=2\leftarrow 0}} = 2.099$	190
	pD_2	$B_e = 0.3498$	$\Delta \mathrm{E}_{\mathrm{J=3\leftarrow 1}} = 3.498$	114
	Cl_2	$B_e = 2.733 \times 10^{-3}$	$\Delta \mathrm{E}_{\mathrm{J=1\leftarrow 0}} = 5.4 \times 10^{-3}$	72×10^3
Vibrational	H_2	$\omega_e = 52.65$ [8] $\omega_e x_e = 1.451$ [8]	$\Delta \mathrm{E}_{\nu=1\leftarrow 0} = 49.75$	8
	D_2	$\omega_e = 37.27$ [8] $\omega_e x_e = 7.397 \times 10^{-1}$ [8]	$\Delta \mathrm{E}_{\nu=1\leftarrow 0} = 35.79$	11
	Cl_2	$\omega_e = 6.695$ [8] $\omega_e x_e = 3.194 \times 10^{-2}$ [8]	$\Delta \mathrm{E}_{\nu=1\leftarrow 0} = 6.632$	60
Electronic	H_2		$\Delta \mathrm{E}_{\mathrm{n=1\leftarrow 0}} = 1096.97$ [8]	0.36
	D_2		$\Delta \mathrm{E}_{\mathrm{n=1\leftarrow 0}} = 1096.94$ [8]	0.36
	Cl_2		$\Delta \mathrm{E}_{\mathrm{n=1\leftarrow 0}} = 205.28$ [8]	1.94

magnitude smaller than the respective rotational constants for H_2 and D_2 and 8 orders of magnitude for Cl_2 [8].

Comparison between the vibrational as well as rotational frequencies of H_2 (para and ortho) and D_2 (ortho and para) is not mentioned here, since only solvent-pure crystals are considered. Moreover, the ratio between their fundamental vibrational frequencies as well as between the anharmonicity corrections to them are already known from the solutions to the Morse potential given in Eq. 2.48, that is $\frac{\omega_e(H_2)}{\omega_e(D_2)} = \sqrt{2}$ and $\frac{\omega_e x_e(H_2)}{\omega_e x_e(D_2)} = 2$.

In the case of the pH_2-Cl_2 dimer the situation is further complicated, since the DOFs of Cl_2 and pH_2 have to be considered at the same time, but the idea behind the multi-stage AS discussed in Chap. 2 remains essentially the same. Solute and solvents rotational energy scales lie in very different ranges because of the particularly large rotational constant of H_2 and D_2. The vibrational energy scales instead only differ less than one order of magnitude. However, the most critical point is the adiabatic separation of solute vibrations and the solvent rotations, since their motions happen in a very similar time scale. Thus, even though the Cl_2 vibrational ground state wavefunction is narrow (classical approximation), the NACTs may be still large due to the very fast H_2 and D_2 rotations (see Eqs. 2.49 and 2.52 in Sec. 2.2.4)), so that this is, *a priori*, probably the weakest point in the application of the multi-stage AS on the H_2-Cl_2 and D_2-Cl_2 dimer systems. The error introduced by rotational adiabatization will be estimated later in Sec. 5.3.4. In order to avoid such error an average with respect to the vibrational ground state of Cl_2, should be considered as well, but implies excessive CPU-time, which we cannot afford, since the *ab-initio* PES should be calculated at different Cl_2 bond distances. This has been done for example on the $(H_2)_2$ dimer at a high level of theory by Hinde [197]. Summarizing, specifically for the pH_2-Cl_2 and oD_2-Cl_2 dimers, the sequence of ASs can be represented in terms of the energy scales of the different DOFs as follows:

$$\begin{aligned} \Delta E_{\mathrm{n=1\leftarrow 0}}(\mathrm{H_2/D_2}) \;&>>\; \Delta E_{\mathrm{n=1\leftarrow 0}}(\mathrm{Cl_2}) >> \Delta \mathrm{E_{v=1\leftarrow 0}}(\mathrm{pH_2/oD_2}) \approx \\ &\approx\; \Delta E_{v=1\leftarrow 0}(\mathrm{Cl_2}) \approx \Delta \mathrm{E_{J=2\leftarrow 0}}(\mathrm{pH_2/oD_2}) >> \Delta \mathrm{E_{J=1\leftarrow 0}}(\mathrm{Cl_2}) \end{aligned} \tag{5.6}$$

At this point, one can proceed to the rotational adiabatization of the H_2 (and D_2) molecules for the calculation of the pair potentials. Since at the temperature of liquid Helium (less than 4 K), only the rotational ground state is thermally populated, in a first assumption, one expects all pH_2 (and oD_2) molecules to behave almost isotropically in solid hydrogen, like in solid Helium. In contrast, anisotropic interactions are expected for oH_2 (and pD_2). Consideration of the shape of the pH_2 molecules as perfectly spherically shaped, in fact, notably reduces the computational effort of, e.g., dynamical simulations, since the molecules are then treated as He-like atoms. Under these assumptions, the

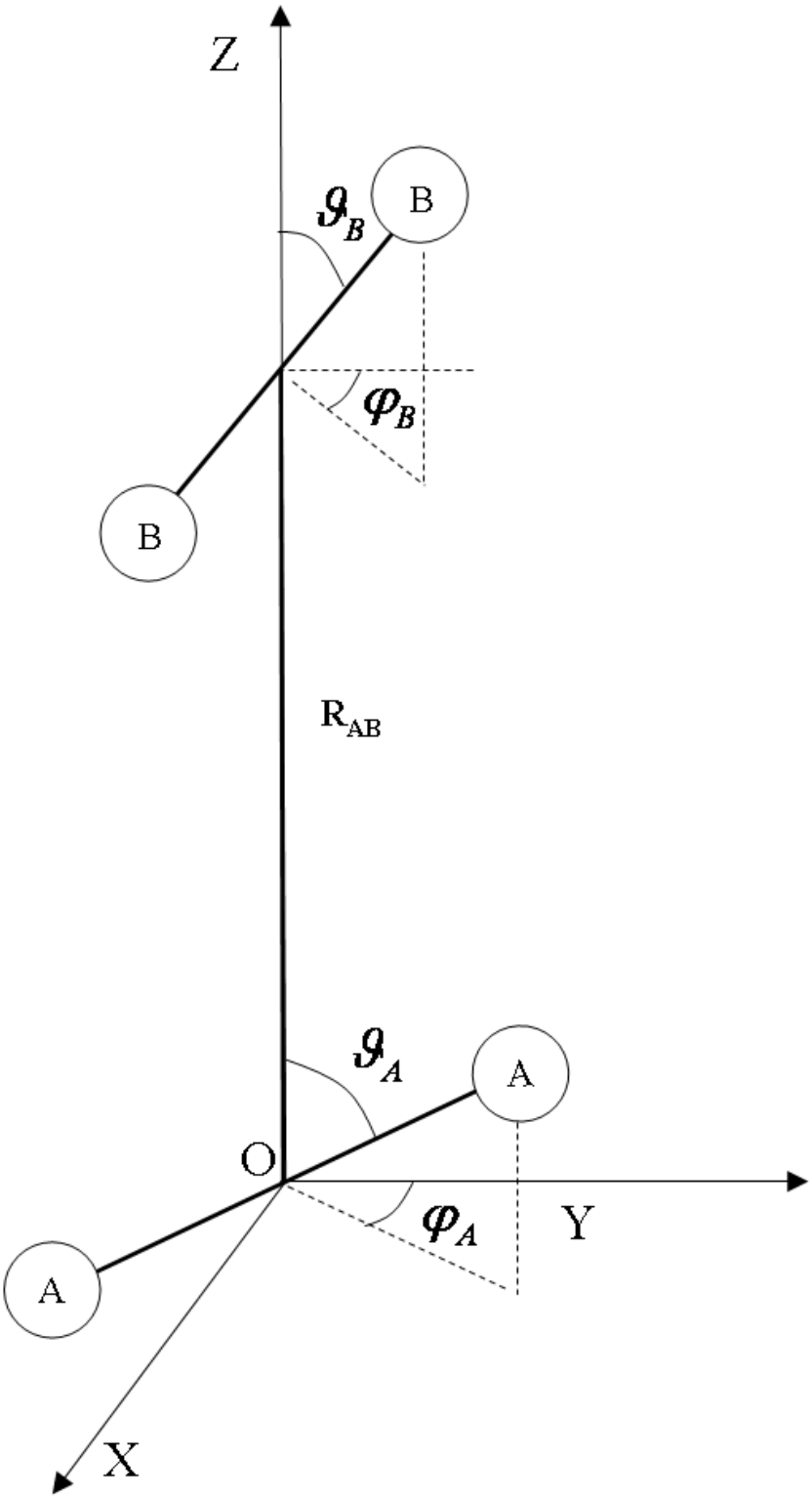

Figure 5.1: The figure shows the Cartesian coordinate system in the laboratory frame used in order to carry out the quantum chemistry calculations.

respective angular distribution functions become those of the free rotor, that is the spherical harmonics with angular and directional quantum numbers $J = 0$ and $M = 0$ (s-like spherical distribution) and $J = 1$ and $M = -1$, 0, 1 (p-like distributions), respectively, and the pair potential can be obtained by a crude spherical average of the PES on a surface of a sphere, that is the absolute value of the lowest spherical harmonics function, $|Y_{J=0,M=0}|^2$ when considering only pH_2. This approximation is called here Spherical-Average-Approximation (SAA) and has been applied in the past in several works, see for example [221, 224, 234, 238, 239]. Recently Le Roy *et al*, [240], compared the results obtained within the SAA to those obtained within an "adiabatic-hindered-rotor" (AHR) approximation, when applying them to the hydrogen molecule in the case of the pH_2-CO_2, pH_2-CO and $(pH_2)_2$ dimer systems (and on the deuterium molecule for the corresponding systems with oD_2) finding slightly more accurate PESs. In contrast to the SAA, the AHR approximation consists in the average of the PES with respect to a basis-set of SHs, which is complete, in principle, so that it describes also the distortion due to the presence of the field of a second molecule (pair potential). Actually, the different results between the two methods can be considered as measure of the degree of distortion undergone by the system. Thus, the more similar are the AHR wavefunctions to the SHs, the more decoupled are the rotational DOFs. Please note that the AHR approximation is completely equivalent to the rotational adiabatization applied in the present work within the multi-stage AS.

The pH_2-Cl_2 and $(pH_2)_2$ *ab-initio* PESs have been calculated referring to the coordinate system shown in Fig. 5.1. The molecule labeled by A can either be the chlorine or the hydrogen (or deuterium) molecules, whereas the molecule labeled by B is always hydrogen (or deuterium). In both cases the position of the four atoms is defined by the four angles θ_A, θ_B, ϕ_A and ϕ_B and the distance R_{AB} between the COM's of the two molecules. The internal bonds R_A and R_B of the two molecules are considered rigid and fixed at the quantum mechanical average values for the respective vibrational ground states (classical approximation). Consequently, R_A can either be $\tilde{r}_{Cl_2}$ or $\tilde{r}_{H_2}$, wheres $R_B = \tilde{r}_{H_2}$ always. Nevertheless, for both dimer systems, the *ab-initio* PESs are four dimensional because of their respective $C_{\infty v}$ and $D_{\infty h}$ global symmetries, which make them to be dependent only on the mutual orientations of the planes on which the two monomers lie, which is indeed expressed by $\phi_B - \phi_A$. Hence, the *ab-initio* PESs are defined as $W^{(n=0)}_{\mathrm{A-B}}(R_{AB}, \theta_A, \theta_B, \phi_B - \phi_A)$. Please note that in order to obtain the final pair potentials, different procedures are applied for the two molecular systems: In the case of the H_2-Cl_2 dimer, the hydrogen molecule is rotationally adiabatized with respect to fixed values of the parameters R_{AB}, θ_A and ϕ_A, whereas in the $(H_2)_2$ molecular system both the monomers are rotationally adiabatized with respect to fixed values of the intermolecular distance, R_{AB}.

Let us now derive the equations for the rotational adiabatization of H_2 in the H_2-Cl_2 dimer system. Please note that the H_2-Cl_2 pair potential is independent of the variable ϕ_A, that is a two dimensional potential is obtained upon adiabatization, but the following

equations are given in a more general formulation in view of the calculation of rotational PESs of Cl_2 embedded in the crystal, where θ_A and ϕ_A define indeed its orientation. In the most general formulation the R_A and R_B parameters should be also included in such equations, but they are skipped here, since their values are just kept fixed, within the rigid rotor approximation applied here.

The four-dimensional intermolecular translational-rotational Hamiltonian, in terms of the notation used in Eq. 2.55 in Sec. 2.2.5, has the following form

$$\begin{aligned} \hat{\mathbf{H}}_{\text{tot}} &= -\frac{\hbar^2}{2\mu_{AB}}\frac{\partial^2}{\partial R_{AB}^2} + \frac{(\hat{J}-\hat{j}_A-\hat{j_B})^2}{2\mu_{AB}R_{AB}^2} + B^A\hat{j}_A^2 \\ &+ \hat{\mathbf{H}}_{\text{rot}}(\nabla_{\theta_B},\nabla_{\phi_B},\theta_B,\phi_B;R_{AB},\theta_A,\phi_A)\ , \end{aligned} \tag{5.7}$$

where A and B are Cl_2 and H_2, respectively. The first and the second term in the former equation are the translational and the rotational Hamiltonians with respect to the COM of the dimer. μ_{AB} is the reduced mass of the dimer, $(\hat{J}-\hat{j}_A-\hat{j}_B)^2=\hat{\lambda}^2$ is the angular momentum operator for the rotation of the dimer with respect to the intermolecular axis, R_{AB}. $\hat{J}$ is the total angular momentum operator and $\hat{j}_A$ and $\hat{j}_B$ are the angular momentum operators of the two single molecules. The third term finally is the rotational Hamiltonian of the hydrogen molecule, the solution of which will give us the rotationally adiabatic H_2-Cl_2 pair potential. Please note that by splitting the Hamiltonian in two parts, i.e. the translational and rotational DOFs with respect to the dimer COM from the rotational DOFs of the H_2 molecule, an AS has been applied to the system, where, recalling Sec. 2.2.5, the first three terms of Eq. 5.7 represent the heavy or slow Hamiltonian depending only on R_{AB}, θ_A and ϕ_A, and Eq. 5.8 represent the light or fast Hamiltonian depending on θ_B and ϕ_B, but parametrically also on R_{AB}, θ_A and ϕ_A. Following the notation in Sec. 2.2.5, the rotational Hamiltonian is defined as

$$\hat{\mathbf{H}}_{\text{rot}}(\nabla_{\theta_B},\nabla_{\phi_B},\theta_B,\phi_B;R_{AB},\theta_A,\phi_A) = B^B\hat{j}_B^2 + W^{(n=v=0)}_{\text{H}_2-\text{Cl}_2}(R_{AB},\theta_A,\theta_B,\phi_B-\phi_A)\ , \tag{5.8}$$

where the parameters $\{R_{AB},\theta_A,\phi_A\}$, the variables $\{\theta_B,\phi_B\}$ and the potential $W^{(n=v=0)}_{\text{H}_2-\text{Cl}_2}$ $(R_{AB},\theta_A,\theta_B,\phi_B-\phi_A)$ correspond respectively to the parameter $\vec{R}_{\text{tra}}$, the variables $\{\theta,\phi\}$ and the potential $\hat{V}_{\text{rot}}(\theta,\phi;\vec{R}_{\text{tra}}) = W^{(n,v)}_{\text{ext}}(\vec{R}_{\text{ext}})$ in Eq. 2.59. The quantum numbers $(n = v = 0)$ specify that the system is in its electronic and vibrational ground state. The validity of this AS has to be still proved along this work and will tell us how strongly coupled those DOFs eventually are. Finally, a two-dimensional (light) TISE for the rotational Hamilton operator in Eq. 5.8 is solved for every (R_{AB}, θ_A, ϕ_A)-configuration averaging out θ_B and

ϕ_B, namely

$$\begin{aligned}(\hat{\mathbf{H}}_{\rm rot}(\nabla_{\theta_B},\nabla_{\phi_B},\theta_B,\phi_B;R_{AB},\theta_A,\phi_A) &- E_{\rm rot}^{(n=v=0,\,l)}(R_{AB},\theta_A,\phi_A))\times \\ &\times \psi_{\rm H_2-Cl_2}^{(n=v=0,\,l)}(\theta_B,\phi_B;R_{AB},\theta_A,\phi_A)=0\end{aligned} \tag{5.9}$$

where l is the rotational quantum number. The rotational wavefunction in Eq. 5.10 is hence expanded in terms of spherical harmonics

$$\psi_{\rm H_2-Cl_2}^{(n=v=0,\,l)}(\theta_B,\phi_B;R_{AB},\theta_A,\phi_A)=\sum_{J=0}^{J_{\rm max}}\sum_{M=-J}^{J} c_{J,M}^{(l)}(R_{AB},\theta_A,\phi_A)\,Y_{J,M}(\theta_B,\phi_B) \tag{5.10}$$

with [241],

$$Y_{JM}(\theta_B,\phi_B)=\sqrt{(2J+1)\frac{(J-M)!}{(J+M)!}}\,P_J^M(\cos\theta_B)\,e^{iM\phi_B} \qquad \text{for M } \geq 0 \tag{5.11}$$

where $P_J^M(\cos\theta_B)$ is an associated Legendre polynomial. It is interesting to show that the SHs obey the following symmetry-law [241]:

$$Y_{J(-M)}(\theta_B,\phi_B)=-\sqrt{(2J+1)\frac{(J-M)!}{(J+M)!}}\,P_J^M(\cos\theta_B)\,e^{-iM\phi_B}=-Y_{JM}(\theta_B,\phi_B)\;. \tag{5.12}$$

In order to solve the two-dimensional TISE, let us multiply Eq. 5.8 by the left by $\psi_{\rm H_2-Cl_2}^{*(n=v=0,\,l)}(\theta_B,\phi_B;R_{AB},\theta_A,\phi_A)$, so to obtain the matrix, $\hat{\mathbf{H}}_{\rm rot}^{J',M',J,M}(\theta_B,\phi_B;R_{AB},\theta_A,\phi_A)$, which is the sum of a diagonal matrix from the kinetic energy operator of the free rotor (see Eq. 2.73) and a full potential energy matrix with elements

$$\begin{aligned}W_{\rm H_2-Cl_2}^{(J',M',J,M)}(R_{AB},\theta_A,\phi_A) &= \frac{1}{4\pi}\int_0^{\pi}\sin\theta_B d\theta_B\int_0^{2\pi}d\phi_B\times \\ &\times W_{\rm H_2-Cl_2}^{(n=v=0)}(R_{AB},\theta_A,\theta_B,\phi_B-\phi_A)\times \\ &\times Y_{J'M'}^{*}(\theta_B,\phi_B)\,Y_{JM}(\theta_B,\phi_B)\end{aligned} \tag{5.13}$$

$\sin\theta_B\,d\theta_B\,d\phi_B$ representing the infinitesimal surface element of a sphere. Since $\frac{d\cos\theta_B}{d\theta_B}=\sin\theta_B$, this integration can be conveniently rewritten in terms of $\cos\theta_B$,

$$W^{(J'M'JM)}_{H_2-Cl_2}(R_{AB},\theta_A,\phi_A) = N\int_{-1}^{1} d\cos\theta_B \int_0^{2\pi} d\phi_B \; W^{(n=v=0)}_{H_2-Cl_2}(R_{AB},\theta_A,\theta_B,\phi_B-\phi_A)\times \\ \times P^{M'}_{J'}(\cos\theta_B)\, P^{M}_{J}(\cos\theta_B)\, e^{i(M-M')\phi_B} \tag{5.14}$$

with

$$N = \frac{1}{4\pi}\sqrt{2J+1\frac{(J-M)!}{(J+M)!}}\sqrt{2J'+1\frac{(J'-M')!}{(J'+M')!}} \tag{5.15}$$

Since Eq. 5.10 will be solved separately for the para and ortho species of molecular hydrogen, two different matrices are diagonalized, that is $\hat{\mathbf{H}}^{(J',M',J,M)}_{pH_2-Cl_2}(R_{AB},\theta_A,\phi_A)$ and $\hat{\mathbf{H}}^{(J',M',J,M)}_{oH_2-Cl_2}(R_{AB},\theta_A,\phi_A)$, respectively for even and odd values of J. The eigenvalues $E^{(n=v=0,\,l)}_{rot}(R_{AB},\theta_A,\phi_A)$ for each of the (R_{AB},θ_A,ϕ_A) configurations define the adiabatic PES, $W^{(n=v=0,\,l)}_{H_2-Cl_2}(R_{AB},\theta_A,\phi_A)$, describing the interaction of pH_2 and oH_2 with the Cl_2 molecule, respectively, and l defines a new quantum number, running over the resulting rotationally adiabatic PESs. The resulting potentials are grouped with respect to their asymptotic limits, given by the free rotor kinetic energies (in units of B), 0, 2, 6, 12, etc., which are one-, three-, five-, seven-fold, etc., degenerate. Thus, the energetically lowest PES, $W^{(n=v=0,\,l=0)}_{H_2-Cl_2}(R_{AB},\theta_A,\phi_A)$ (resulting from the diagonalization of $\hat{\mathbf{H}}^{(J',M',J,M)}_{pH_2-Cl_2}$) describes the interaction between chlorine molecule and the pH_2 species in its rotational ground state and the first three PESs $W^{(n=v=0,\,l=1,2,3)}_{H_2-Cl_2}(R_{AB},\theta_A,\phi_A)$ (resulting from the diagonalization of $\hat{\mathbf{H}}^{(J',M',J,M)}_{oH_2-Cl_2}$) describe the interactions between the chlorine molecules and the oH_2 species in its lowest three states. Please note that the same applies to the D_2-Cl_2 system, except for the different masses involved, so that $W^{(n=v=0,\,l=0)}_{D_2-Cl_2}(R_{AB},\theta_A,\phi_A)$ describes the interaction between chlorine molecule and the oD_2 species in its rotational ground state and the first three PESs $W^{(n=v=0,\,l=1,2,3)}_{D_2-Cl_2}(R_{AB},\theta_A,\phi_A)$ describe the interactions between the chlorine molecules and the pD_2 species in the three lowest states.

After the rotational adiabatization, the Hamiltonian in Eq. 5.7 is effectively reduced to

$$\hat{\mathbf{H}}^{(l)} \approx -\frac{\hbar^2}{2\mu_{AB}}\frac{\partial^2}{\partial R^2_{AB}} + \frac{(\hat{J}-\hat{j_A})^2}{2\mu_{AB}R^2_{AB}} + B^A\hat{j}^2_A + W^{(n=v=0,\,l)}_{H_2-Cl_2}(R_{AB},\theta_A,\phi_A)\;. \tag{5.16}$$

The equations relative to the rotational adiabatization of H_2 in the $(H_2)_2$ dimer system are just an extension of the previous ones, since simultaneous adiabatization of the two monomers is involved. The total rotational-translational Hamiltonian is now

$$\begin{aligned}\hat{\mathbf{H}}_{\rm tot} &= -\frac{\hbar^2}{2\mu_{AB}}\frac{\partial^2}{\partial R_{AB}^2} + \frac{\hat{\lambda}^2}{2\mu_{AB}R_{AB}^2} + \\ &+ \hat{\mathbf{H}}_{\rm rot}(\nabla_{\theta_A},\theta_A,\nabla_{\phi_A},\phi_A,\nabla_{\theta_B},\theta_B,\nabla_{\phi_B},\phi_B;R_{AB})\end{aligned} \tag{5.17}$$

where again the first two terms build up the slow (or heavy) Hamiltonian, and the third term the fast (or light) Hamiltonian, so that following the notation in Sec. 2.2.5 the rotational Hamiltonian reads:

$$\begin{aligned}\hat{\mathbf{H}}_{\rm rot}(\nabla_{\theta_A},\theta_A,\nabla_{\phi_A},\phi_A,\nabla_{\theta_B},\theta_B,\nabla_{\phi_B},\phi_B;R_{AB}) &= B^A\hat{j}_A^2 + B^B\hat{j}_B^2 + \\ &+ W_{(\mathrm{H_2})_2}^{(n=v=0)}(\theta_A,\theta_B,\phi_B-\phi_A;R_{AB})\end{aligned} \tag{5.18}$$

where the parameter R_{AB} and the potential $W_{(\mathrm{H_2})_2}^{(n=v=0)}(\theta_A,\theta_B,\phi_B-\phi_A;R_{AB})$ correspond respectively to $\vec{R}_{\rm tra}$ and $W_{\rm ext}^{(n,v)}(\vec{R}_{\rm ext})$ in Eq. 2.55.

The TISE to be solved is now four-dimensional and will average out the couples of polar angles of the hydrogen molecules.

$$\begin{aligned}(\hat{\mathbf{H}}_{\rm rot}(\nabla_{\theta_A},\theta_A,\nabla_{\phi_A},\phi_A,\nabla_{\theta_B},\theta_B,\nabla_{\phi_B},\phi_B;R_{AB}) &- E_{\rm rot}^{(n=v=0,\,l)}(R_{AB}))\times \\ &\times \psi_{(\mathrm{H_2})_2}^{(n=v=0,\,l)}(\theta_A,\phi_A,\theta_B,\phi_B;R_{AB}) = 0\end{aligned} \tag{5.19}$$

The adiabatic wavefunction is expanded by using the product of two sets of SHs, namely

$$\begin{aligned}\psi_{(\mathrm{H_2})_2}^{(n=v=0,\,l)}(\theta_A,\phi_A,\theta_B,\phi_B;R_{AB}) &= \sum_{J_A=0}^{J_{\max}}\sum_{M_A=-J_A}^{J_A}\sum_{J_B=0}^{J_{\max}}\sum_{M_B=-J_B}^{J_B} \\ c_{J_A,M_A,J_B,M_B}^{(l)}(R_{AB}) &\times Y_{J_A,M_A}(\theta_A,\phi_A)\times Y_{J_B,M_B}(\theta_B,\phi_B)\end{aligned} \tag{5.20}$$

so that the full potential energy matrix involves the four pairs of quantum numbers J'_A, M'_A, J_A, M_A, J'_B, M'_B, J_B, M_B:

$$\begin{aligned}W_{(\mathrm{H_2})_2}^{\binom{J'_AM'_AJ'_BM'_B}{J_AM_AJ_BM_B}}(R_{AB}) &= N_A\times N_B\int_{-1}^{1}d\cos\theta_A\int_{-1}^{1}d\cos\theta_B\int_0^{2\pi}d\phi_A\int_0^{2\pi}d\phi_B \\ &W_{(\mathrm{H_2})_2}^{(n=v=0)}(R_{AB},\theta_A,\theta_B,\phi_B-\phi_A) \\ &P_{J'_A}^{M'_A}(\cos\theta_A)\,P_{J'_B}^{M'_B}(\cos\theta_B)\,P_{J_A}^{M_A}(\cos\theta_A)\,P_{J_B}^{M_B}(\cos\theta_B) \\ &e^{i(M_A-M'_A)\phi_A}\,e^{i(M_B-M'_B)\phi_B}\end{aligned} \tag{5.21}$$

Thus, for the case of two para-Hydrogen molecules, the initial rotational-translational Hamiltonian of Eq. 5.18 is now reduced to just one dimension.

$$\hat{\mathbf{H}}^{(l)} \approx -\frac{\hbar^2}{2\mu_{AB}}\frac{\partial^2}{\partial R_{AB}^2} + \frac{\hat{l^2}}{2\mu_{AB}R_{AB}^2} + W_{(\mathrm{H_2})_2}^{(n=v=0,\,l)}(R_{AB}) \tag{5.22}$$

Once the TISE is solved for each of the R_{AB} distances, the lowest eigenvalue, $l = 0$, defines the one-dimensional isotropic interaction potential between two para-hydrogen molecules in their rotationally adiabatic ground state. Please note again that, except for the different masses involved, the same applies to the $(\mathrm{oD_2})_2$ system.

In general, the weaker the NACTs are, the more the rotationally adiabatic ground state wavefunctions will resemble the first spherical harmonic $Y_{J=0,M=0}$, which is independent of θ and ϕ, or a product of two of them, $Y_{J_A=0,M_A=0} \cdot Y_{J_B=0,M_B=0}$, respectively for the $\mathrm{pH_2}$-$\mathrm{Cl_2}$ and $(\mathrm{pH_2})_2$ systems. This is expected to be the case for the $\mathrm{pH_2}$ dimer, since the interaction at the minimum of the pair potential of approximately 0.28 kJ/mol is very weak compared to the rotational energy spacing of 4.087 kJ/mol (see also Tab. 5.1):

$$\psi_{(\mathrm{H_2})_2}^{(n=v=0,\,l=0)}(\theta_A, \phi_A, \theta_B, \phi_B; R_{AB}) \propto Y_{J_A=0,M_A=0}(\theta_A, \phi_A) \cdot Y_{J_B=0,M_B=0}(\theta_B, \phi_B) \tag{5.23}$$

for each of the R_{AB} distances. In contrast, in the SAA the ground state wavefunctions are taken just to be the first spherical harmonic or the respective product of two of them, ignoring the couplings to higher SHs, as already mentioned above.

5.3 Results

All quantum chemistry calculations have been carried out by using the quantum chemistry methods presented in Chap. 2.3 by means of the MOLPRO program package [242–252]. The bond distances of the two molecules were fixed at the quantum mechanical average values for the respective vibrational ground states: $\tilde{r}_{\mathrm{Cl_2}} = \langle r_{\mathrm{Cl_2}} \rangle_{v=0} = 0.2032$ nm, $\tilde{r}_{\mathrm{pH_2}} = \langle r_{\mathrm{pH_2}} \rangle_{v=0} = 0.0757$ nm and $\tilde{r}_{\mathrm{oD_2}} = \langle r_{\mathrm{oD_2}} \rangle_{v=0} = 0.0753$ nm. The electronic ground state curves have been calculated at the CCSD(T):aug-cc-pV5Z and Full-CI:aug-cc-pV6Z levels of theory, respectively. [3]

For all calculations, the Basis-Set Superposition Error (BSSE) was handled by using the *a posteriori* counterpoise (CP) method introduced in the famous paper by Boys and

[3] Please note the notation "METHOD:BASIS-SET" adopted from now on.

Bernardi [253]. The BSSE becomes significant for systems bound through hydrogen bond or VDW interactions, like in the systems investigated here. Interaction energies between two atoms or molecules A and B are typically calculated as the energy difference between the product complex AB and its components A and B:

$$E_{\text{interaction}} = E(AB, r_c) - E(A, r_a) - E(B, r_b) \tag{5.24}$$

where the label r_c indicates the geometry of the product complex AB, while r_a and r_b indicate the geometries of the separated reactants. The BSSE originates from the fact that the wavefunction of the monomer is typically expanded in much fewer basis functions than the wavefunction of the complex. Strictly speaking, the use of an infinite basis-set would prevent such an error, so that the BSSE in more general terms originates from the use of a finite basis-set. The CP interaction energy is therefore computed as:

$$E_{\text{interaction}} = E(AB, r_c)^{AB} - E(A, r_a)^{AB} - E(B, r_b)^{AB} \tag{5.25}$$

where the superscript AB indicates that the complex as well as the separate components are calculated in the absolute basis.

5.3.1 Basis-set Convergence

The basis-set convergence test has been carried out only on six particular highly symmetric geometries of the H_2-Cl_2 complex, which are shown in Fig. 5.2. For each of these configurations, the PES curve has been calculated by using the following basis-sets: The aug-cc-pVTZ, cc-pVQZ, aug-cc-pVQZ, cc-pV5Z and aug-cc-pV5Z. Single point calculations with the aug-cc-pV6Z basis-set were carried out, but they appeared to be prohibitive for complete scans of the surfaces.

Fig. 5.3 shows the curves calculated at two different levels of theory, the CCSD (dashed-line) and the CCSD(T) (solid-line) methods. For all configurations, the curves obtained with the CCSD method underestimate the binding energy and lie well separated above the corresponding CCSD(T)-curves independently of the basis-set used. Moreover, the use of the augmented basis-set is found to be essential for an accurate description of the VDW interactions involved, so that only those curves are shown. The aug-cc-pV5Z almost converge to the extrapolated complete basis-set limit, with respect to which the relative errors are also given in Fig. 5.3. Errors between 2.7% and 4.3% occur depending on the configuration considered.

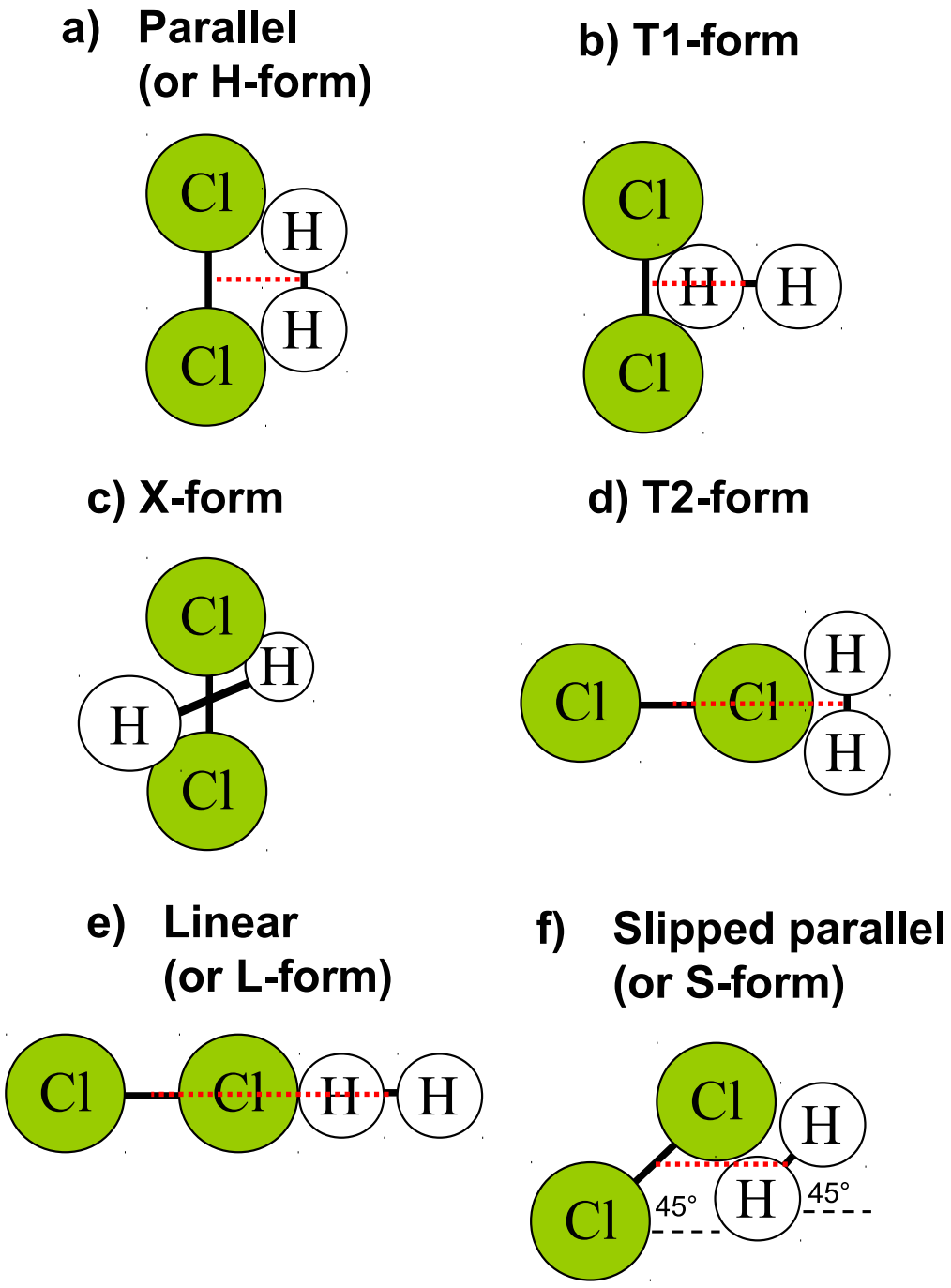

Figure 5.2: The six highly symmetric geometries taken into account for the first calculation of the H_2-Cl_2 pair interaction. Four of them, namely the H-, T1-, T2- and X-configurations take their names from their geometrical dispositions in the space, whereas the other two take the names from the word used to name them, L-form comes from "Linear"and S-form comes from "Slipped", respectively.

Table 5.2: The two pairs of angles corresponding to each of the six highly symmetric configurations are listed referring to the Cartesian coordinate system depicted in Fig. 5.1.

Configuration	θ_A	ϕ_A	θ_B	ϕ_B	$G(\theta_A, \theta_B, \phi_B - \phi_A)$
Parallel or H	90°	0°	90°	0°	$+\frac{9}{4}$
T	90°	0°	0°	0°	-3
X	90°	0°	90°	90°	$+\frac{3}{4}$
Linear or L	0°	0°	0°	0°	$+6$
Slipped or S	45°	0°	45°	0°	$-2\frac{7}{16}$

A similar trend is discovered in Fig. 5.3 (see also Fig. 5.4 top-left for an overlook) for the H-, T1-, and X-configurations, respectively. They have similar binding energies between -1.58 and -1.29 kJ/mol and similar equilibrium distances of approximately 0.35 nm. In contrast, the T2- and L-configurations exhibit very different behaviour: the L-configuration is much less bounded and has a minimum geometry at a larger distance of 0.44 nm, whereas the T2-one is the most stable complex at a distance of 0.40 nm. A partial explanation lies in the symmetry of these 5 configurations, which can be divided in two main groups: the "Collinear", where the Cl-Cl bond lies on the line connecting the two centres of mass and the H_2 molecule essentially interacts only with one Cl atom, and the "Non-Collinear" symmetry group where the Cl-Cl bond is perpendicular to the same line. The Slipped configuration can be placed in between the two groups, even though, the equilibrium distance is more similar to those of the "Collinear" group.

The same calculations have been carried out for the $(H_2)_2$ complex at the CCSD(T):aug-cc-pV5Z level, but only for five different highly symmetric configurations, since now T1 and T2 are degenerate and the configuration is simply called T. These curves are shown all together in the top-right panel of Fig. 5.4. A comparison of the two top panels highlights two different energy scales for the two dimers. The H_2-Cl_2 potential depths are about five times deeper than the corresponding $(H_2)_2$ ones. Moreover, the equilibrium distances are much more homogeneous in the second system confirming almost spherical electronic density. Only for the $(H_2)_2$ linear configuration a slightly shorter equilibrium distance is observed.

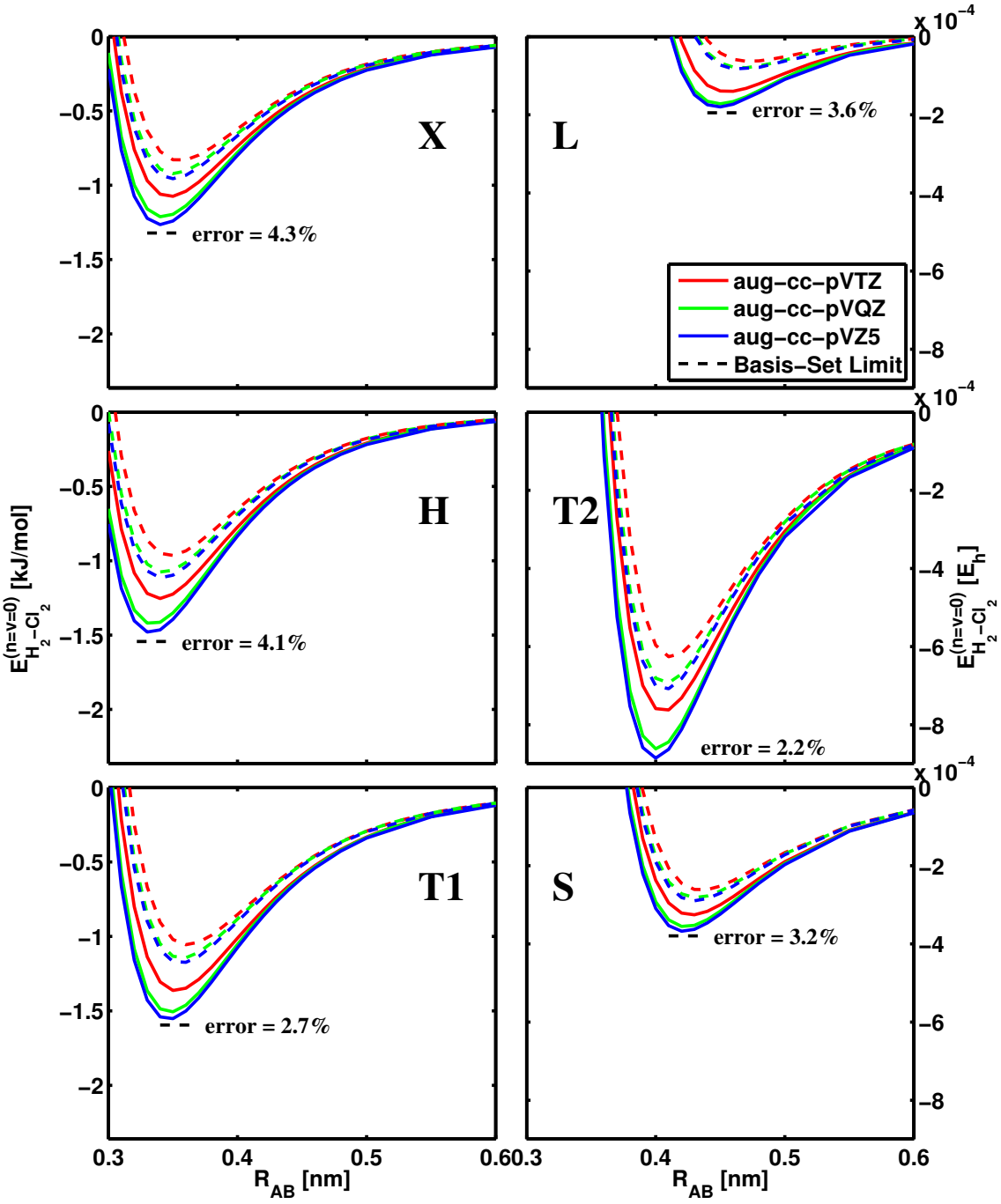

Figure 5.3: H_2-Cl_2 *ab-initio* potential energy curves in the electronic ground state calculated within the CCSD (dashed lines) and CCSD(T) (solid lines) methods for the highly symmetric configurations X, H and T1 (top/middle/bottom left) and L, T2 and S (top/middle/bottom right) with internal bond distances fixed at $\tilde{r}_{H_2} = \langle r_{H_2} \rangle_{v=0} = 0.0757$ nm and $\tilde{r}_{Cl_2} = \langle r_{Cl_2} \rangle_{v=0} = 0.2032$ nm. The colour code denotes the use of three different basis-sets. The basis-set limit was calculated for the CCSD(T) curves at the equilibrium distances by using Eq. 2.94.

Most of the features in Fig. 5.4 can be interpreted in terms of quadrupole-quadrupole (QQ) electrostatic interactions typical between linear neutral homonuclear molecules. Since they are simple to calculate, let us compare them to the already calculated *ab-initio* PES curves. The formula for the calculation of the QQ interaction is found in literature [195] and reads:

$$U_{\mathrm{Q_A Q_B}} = \frac{Q_A Q_B}{4\pi\epsilon_0 R^5} \times G(\theta_A, \theta_B, \phi_B - \phi_A) \tag{5.26}$$

with the angular-dependent function $G(\theta_A, \theta_B, \phi_B - \phi_A)$ being

$$\begin{aligned} G(\theta_A, \theta_B, \phi_B - \phi_A) &= \frac{3}{4}[1 - 5\cos^2\theta_A - 5\cos^2\theta_B - 15\cos^2\theta_A\cos^2\theta_B + \\ &+ 2(4\cos\theta_A\cos\theta_B - \sin\theta_A\sin\theta_B\cos(\phi_B - \phi_A))^2] \end{aligned}$$

Q_A and Q_B are the z-components (along the bond axis) of the quadrupole tensors of the molecules involved, hence, $Q_{\mathrm{H_2}} = 0.4252ea_0^2$ or $Q_{\mathrm{Cl_2}} = 2.4704ea_0^2$, which have been calculated at the CCSD(T) level of theory and using the very large basis-set aug-cc-pV6Z at the equilibrium bond distances $\tilde{r}_{\mathrm{H_2}} = \langle r_{\mathrm{H_2}}\rangle_{v=0}$ and $\tilde{r}_{\mathrm{Cl_2}} = \langle r_{\mathrm{Cl_2}}\rangle_{v=0}$, defined above. The two couples of polar angles refer to the Cartesian system shown in Fig. 5.1 and their values are given in Tab. 5.2 for the five particular configurations. By substituting them into Eq. 5.26, five different values are obtained for the angular-dependent function, $G(\theta_A, \theta_B, \phi_B - \phi_A)$, which are listed in the last column of the same table (see also [195]).

The QQ electrostatic interactions for the two systems, $(H_2)_2$ and H_2-Cl_2, are plotted in the bottom-left and bottom-right panels of Fig. 5.4, respectively, together with the respective *ab-initio* curves (top-left and top-right, respectively). The QQ-interaction curves all start from a minimum distance, which has been calculated on the base of a very simple model, here called hard-sphere. Consider the atoms involved to be hard spheres with the VDW radii tabulated in Ref. 175. These minimum distances correspond to the R_{AB} separations, when the hard spheres are brought into contact. They are therefore called VDW minimum distances and compared with the equilibrium distances from the *ab-initio* curves. The VDW minimum distances are depicted in Fig. 5.2 by the red dashed lines. Below this distance, since the hard spheres cannot overlap, the energy goes to infinity.

In spite of its simplicity, this model already correctly reproduces many of the trends obtained with the *ab-initio* methods. First of all, since both molecules have a positive quadrupole moment along the internuclear axis, the energetic order of the QQ-interactions for the different configurations remains the same for H_2-Cl_2 and $(H_2)_2$. Please note that under consideration of the QQ-interaction only, QQ(T_1) and QQ(T_2) are completely de-

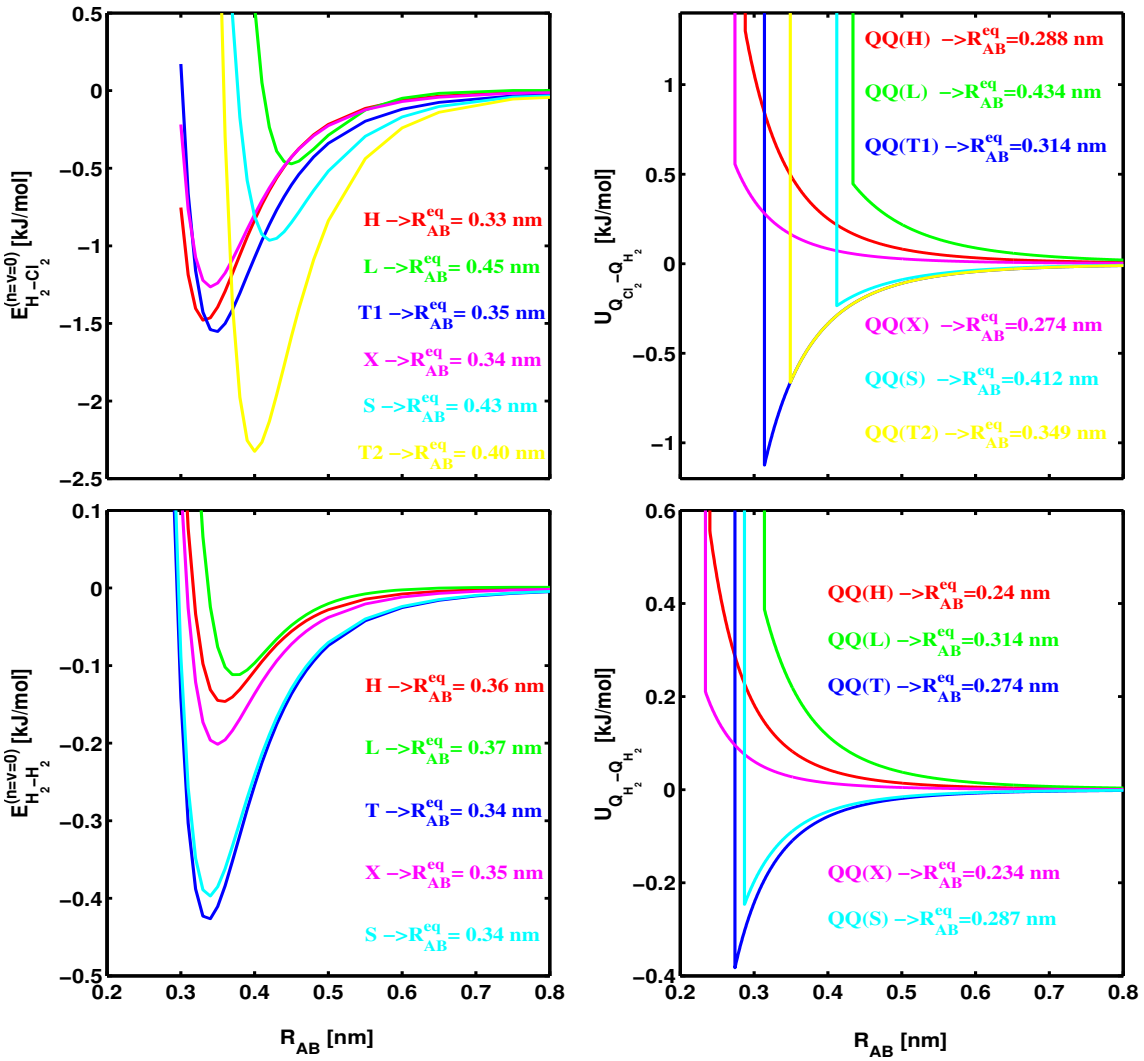

Figure 5.4: H_2-Cl_2 (top-left) and $(H_2)_2$ (bottom-left) *ab-initio* potential energy curves calculated respectively for the 6 and 5 highly symmetric configurations shown in Fig. 5.2 at the CCSD(T):aug-cc-pV5Z level of theory, are compared to the corresponding QQ-interactions (top-right and bottom-right). The intermolecular distances R_{AB}^{eq} from which the QQ-interactions are calculated are based on the simple hard-sphere model.

generate. Moreover, this order is well conserved also in the *ab-initio* curves, even if for the H_2-Cl_2 dimer it is necessary to zoom in close to the asymptotic limit, where quantum mechanical effects (or dispersion effects) are still negligible. The order of the VDW minima are also very well predicted for the L-, S-, and T- (T1- and T2-) configurations, whereas for both dimers, the H- and X-configurations are not. Those configurations can definitely get closer in the hard-sphere picture, than in the Quantum Mechanical one. The binding energies for the X-,H- and L- configurations all exclusively originate from dispersion effects, since the QQ-interaction is repulsive. Finally, the dispersion effects are definitely much more important for the complex involving the chlorine molecule, which is much more

polarizable, as disclosed when comparing the difference between the energy scale of the QQ- and of the *ab-initio*-curves separately for each dimer.

5.3.2 Calculation of the Multi-Dimensional PESs

The two four-dimensional H_2-Cl_2 and $(H_2)_2$ PESs have been calculated at 36 and 37 different R_{AB} distances between 0.17 and 0.95 and 0.27 and 0.95 nm, respectively. Additionally, 19 equidistant angles between 0° and 90° have been chosen to represent θ_A in the former case. The sets of angles corresponding to the rotation of one H_2 monomer have been taken to be the Gaussian-Legendre Discrete Variable Representation (DVR) grid points, so that the average of the PESs with respect to the rotational states of each hydrogen monomer was evaluated with a Gaussian-Quadrature (GQ), see App. 6.2. In particular, the grid consists of 8×16 points along the $\cos\theta_B$ and ϕ_B angle, as well as along $\cos\theta_A$ and ϕ_A in the case of two hydrogen molecules, which run from 1 to -1 and from 0° to 360°, respectively. In total, the electronic SE has to be solved for $36 \times 19 \times 8 \times 16$=87552 and $37 \times 8 \times 16 \times 8 \times 16$=606208 different geometrical configurations for the H_2-Cl_2 and $(H_2)_2$ molecular systems, respectively. Additionally, in view of calculating counterpoise energy points, for each of those geometrical configurations the SE has to be solved three times. Even though the number of configurations to be calculated for the homomolecular dimer system is almost 10 times greater than for the other one, it only involves four electrons, so that the high level of theory CCSD(T) could be chosen and the results extrapolated to the complete basis-set from the large aug-cc-pVTZ and aug-cc-pVQZ by using Eq. 2.94 in Sec. 2.3.2. In contrast, for the pH_2-Cl_2 dimer a lower level of theory has been used, since now the dimer system has 34 electrons and the CCSD(T) method revealed itself to be highly CPU consuming. With four Intel(R) Xeon(R) CPU's (2.33GHz) running in parallel, the calculation of the PES at each of the geometrical configurations, (R_{AB},θ_A), takes about 1.5 h and 2.5 h when using the aug-cc-pVQZ and aug-cc-pV5Z basis-sets, respectively, so that circa 15 and 25 years would be needed in order to calculate the entire surface when using only one of such machines. For this reason, the previous highly symmetric pair potential curves have been recalculated by using the MP2 method with different basis-sets and then compared with them calculated at the CCSD(T):aug-cc-pV5Z as well as with at the CCSD(T):extrapolated level of theory. It is known from literature that the Møller-Plasset method of 2^{nd} order (MP2) based on the perturbation theory (see Sec. 5.3.2) gives good results and is very competitive from the CPU-time point of view (0.28 h for one point on the PES). Fig. 5.5 compares the PES curves obtained with the CCSD(T):aug-cc-pV5Z method with the MP2:aug-cc-pVQZ as well as the MP2:aug-cc-pV5Z methods. The basis-set limits at the minima of the curves calculated in the previous section are also re-shown and the errors are given in percent with respect to them. The errors lie between -9.7% and 9.5%, depending on the basis-set used and the configuration considered. Negative or positive values correspond to an over- or underestimation of the binding energies, re-

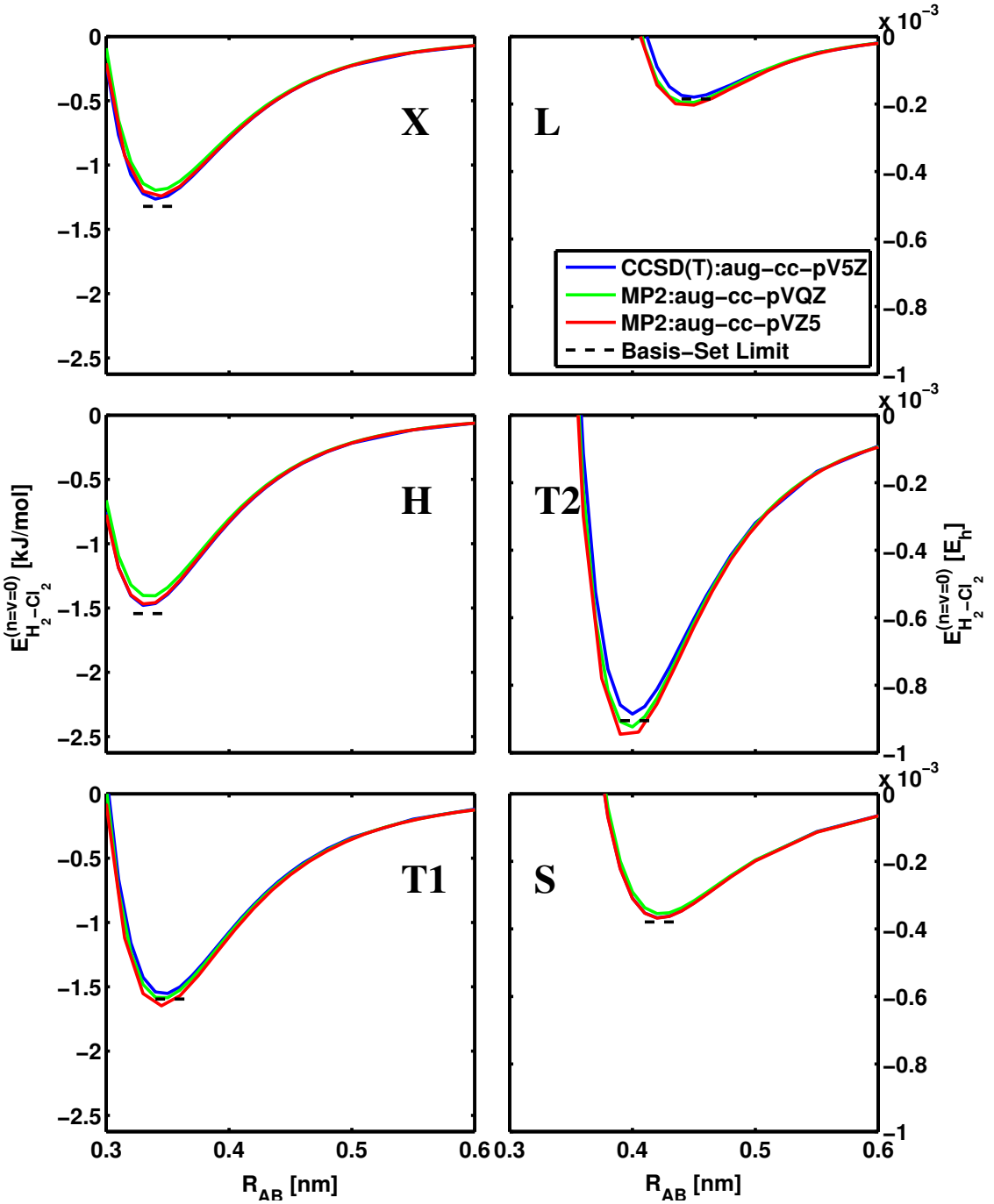

Figure 5.5: H_2-Cl_2 *ab-initio* potential energy curves in the electronic ground state calculated within the MP2:aug-cc-pVQZ and MP2:aug-cc-pV5Z methods are compared to the CCSD(T):aug-cc-pV5Z curves for the highly symmetric configurations X, H and T1 (top/middle/bottom left) and L, T2 and S (top/middle/bottom right) with internal bond distances fixed at $\tilde{r}_{H_2} = \langle r_{H_2} \rangle_{v=0} = 0.0757$ nm and $\tilde{r}_{Cl_2} = \langle r_{Cl_2} \rangle_{v=0} = 0.2032$ nm. The error with respect to the basis set limit extrapolated within the CCSD(T) method is given in percent.

spectively. Both the MP2:aug-cc-pVQZ and MP2:aug-cc-pV5Z curves in all cases lie very close to those calculated with CCSD(T):aug-cc-pV5Z, so that finally the smaller basis set has been chosen, as the CPU time will also be considerably shorter. Furthermore, the MP2:aug-cc-pVQZ curves are almost equally distributed around the CCSDT:aug-cc-pV5Z ones through the configurations, so that one could argue a cancellation of the error after rotational adiabatization. Later in this work, a counter check of our choice of the basis-set is provided for the H_2-Cl_2 complex at $\theta_A = 0°$, 45°, and 90° (see Sec. 5.13).

5.3.3 Rotational Adiabatic Separation: Numerical Treatment

Once the *ab-initio* PES has been computed at the Gauss-Legendre DVR points, the GQ scheme is applied and Eqs. 5.14 and 5.21 are numerically integrated:

$$\begin{aligned} W^{\binom{J'M'}{JM}}_{\mathrm{H_2-Cl_2}}(R_{AB},\theta_A,\phi_A) \quad &\approx N \sum_{k=1}^{G_{\theta_B}=8} w_k \sum_{j=1}^{G_{\phi_B}=16} w_j \times \\ \times \quad & W^{(n=v=0)}_{\mathrm{H_2-Cl_2}}(R_{AB},\, \theta_A,\, \phi_A = 0\,,\, \cos\theta_{B,k},\, \phi_{B,j}) \times \\ & \times P^{M'}_{J'}(\cos\theta_{B,k}) P^{M}_{J}(\cos\theta_{B,k})\, e^{i(M-M')\phi_{B,j}} \end{aligned} \tag{5.27}$$

and

$$\begin{aligned} W^{\binom{J'_A M'_A J'_B M'_B}{J_A M_A J_B M_B}}_{(\mathrm{H_2})_2}(R_{AB}) \quad &\approx N \sum_{p=1}^{G_\theta=8} w_p \sum_{q=1}^{G_\phi=16} w_q \sum_{k=1}^{G_\theta=8} w_k \sum_{j=1}^{G_\phi=16} w_j \times \\ & \times W^{(n=v=0)}_{(\mathrm{H_2})_2}(R_{AB},\, \cos\theta_{A,p},\, \cos\theta_{B,k},\, \phi_{A,q},\, \phi_{B,j}) \times \\ & \times P^{M'_A}_{J'_A}(\cos\theta_{A,p})\, P^{M'_B}_{J'_B}(\cos\theta_{B,k})\, P^{M_A}_{J_A}(\cos\theta_{A,p})\, P^{M_B}_{J_B}(\cos\theta_{B,k}) \times \\ & \times e^{i(M_A - M'_A)\phi_{A,k}}\, e^{i(M_B - M'_B)\phi_{B,j}} \end{aligned} \tag{5.28}$$

The precision of the numerical integration through the GQ scheme depends on several factors. First of all, the accuracy of the *ab-initio* energies at the Gauss-Legendre DVR grid points. The default energy error threshold in the MOLPRO program package is $\Delta E = 1\times10^{-8}$ E_h, which is already enough for the calculation of van der Waals interactions in the order of 10^{-4} E_h.

The most severe limitation for the integration of Eqs. 5.27 and 5.28 lies, however, in the precision attainable within the chosen size of the DVR grid. In fact, the higher the quantum numbers J and M are, the more numerous the nodes of the corresponding SH functions and the less accurate the integration becomes. Since the integral also includes the PES (with its nodes), a numerical convergence test is needed in order to find out for which maximum angular momentum $J_{\max}$ the GQ is still accurate.

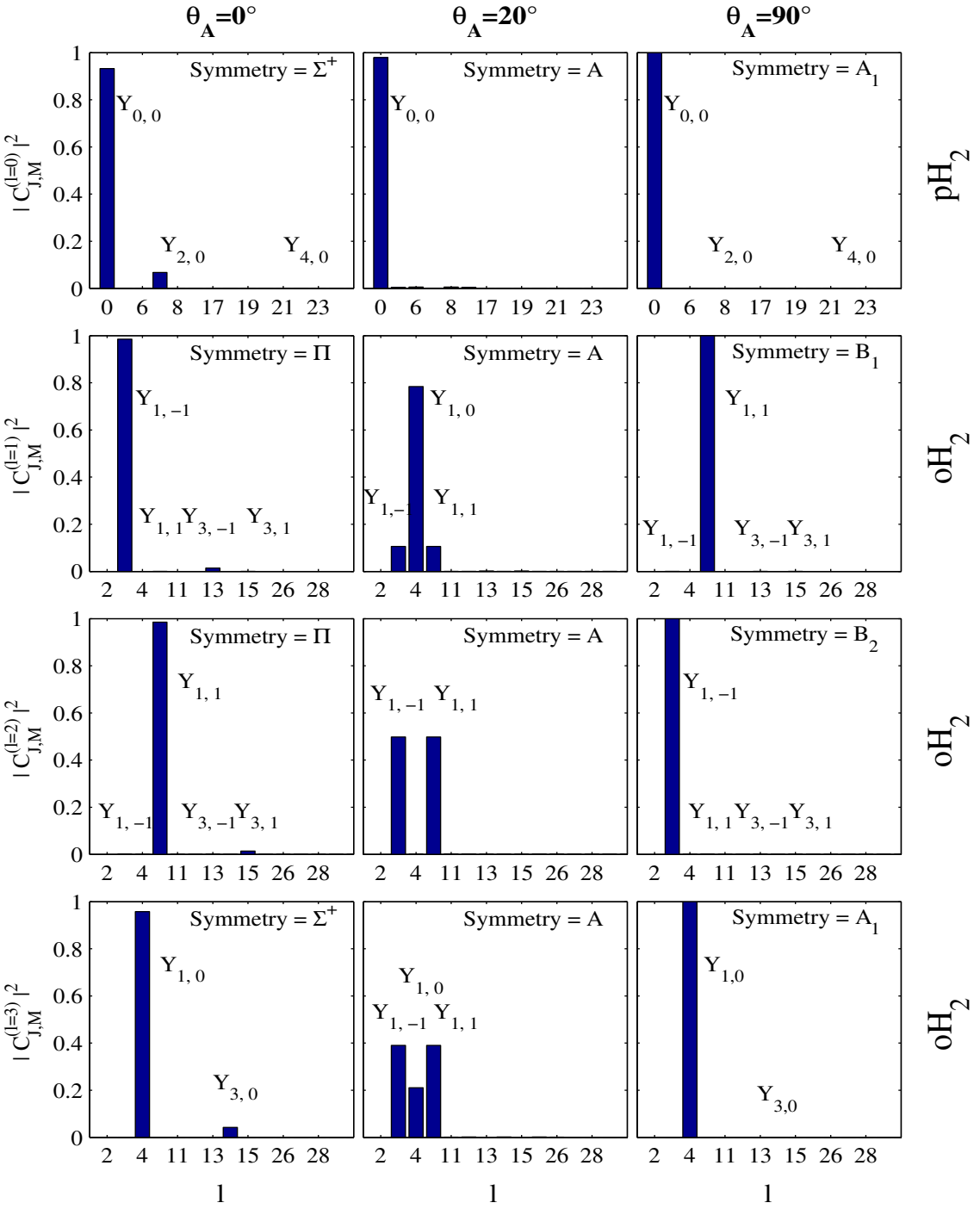

Figure 5.6: Squared value of the expansion coefficients $c^{(l)}_{J,M}$ in Eqs. 5.10 are plotted revealing the linear combinations of spherical harmonics, $Y_{J,M}$, building the rotationally adiabatic wavefunctions $\psi^{(n=v=0,\,l)}_{H_2-Cl_2}(R_{AB},\theta_A)$ of the pH_2-Cl_2 ($l=0$, see first row of panels) and of the oH_2-Cl_2 dimers ($l=1,2,3$, see second, third and fourth rows of panels, respectively). The three columns of panels refer to the three configurations with ($R_{AB}=0.36$ nm; $\theta_A=0°, 20°, 90°$)

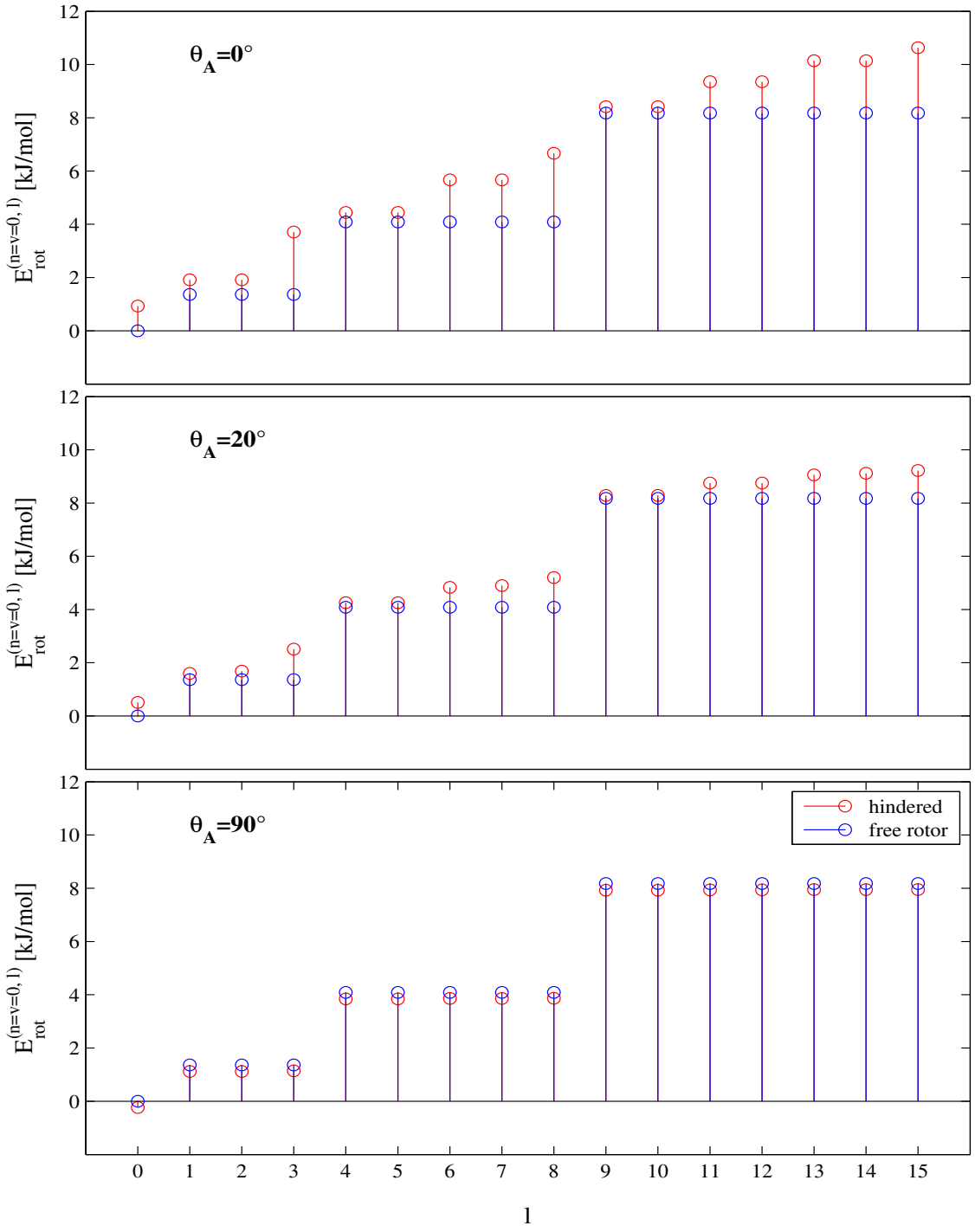

Figure 5.7: H_2-Cl_2 eigenvalues, $E_{\text{rot}}^{(n=v=0,\,l)}(R_{AB}, \theta_A)$ (red circles), with quantum numbers $l = 0, ..., 15$ obtained by solving the two-dimensional TISE of Eq. 5.10 for the three configurations with ($R_{AB} = 0.36$ nm; $\theta_A = 0°, 20°, 90°$) are compared to the eigenvalues of the free rotor model in Eq. 2.73 (blue circles).

Eq. 5.27 has been integrated at three different configurations with $\theta_A = 0°, 20°$ and $90°$ and $\phi_A = 0$ on a 25×25 DVR grid to make sure the integration scheme is accurate even for relatively high values of $J_{\max}$. For these three configurations the system assumes $C_{\infty v}$, C_1 and C_{2v} symmetries, respectively. Contributions from the SHs to the eigenvectors $\psi^{(n=v=0,\,l)}_{\mathrm{H_2-Cl_2}}(R_{AB}, \theta_A, \phi_A = 0)$ are obtained by projecting out the expansion coefficients $c^{(l)}_{J,M} = \langle JM|l\rangle$. The corresponding results are plotted in Fig. 5.6. The three columns correspond to the three chosen configurations with $\theta_A = 0°$, $20°$, $90°$, whereas the rows correspond to the eigenvectors with quantum numbers $l = 0, 1, 2, 3$, which are the ground state wavefunction describing the pH_2-Cl_2 ($l = 0$) and the three lowest ones describing the oH_2-Cl_2 (l=1,2,3) molecular systems, respectively. Please note that the irreducible representations under which the eigenvectors $\psi^{(n=v=0,\,l)}_{\mathrm{H_2-Cl_2}}(R_{AB}, \theta_A, \phi_A = 0)$ transform have also been given in Fig. 5.6.

Many comments arise from this figure. First of all, it is well-known that for $\theta_A = 0°$ and $90°$ only higher SHs with the same symmetry contribute to a given eigenvector. Moreover, the contributions to the eigenvectors from SHs with high quantum numbers J and M are limited just to the SHs with quantum numbers $J' = J + 1$ (and $M' = M$), which reflects a weak coupling due to the interaction potential. Additionally, these contributions become smaller when θ_A increases from $0°$ to $90°$ and, correspondingly, the rotationally adiabatic (RA) wavefunction $\psi^{(n=v=0,\,l=0)}_{\mathrm{H_2-Cl_2}}(R_{AB}, \theta_A, \phi_A = 0)$ becomes more similar to the corresponding SHs of the free rotor, that is $Y_{J=0,M=0}$. Finally, since the SH with the highest quantum numbers, which significantly contributes to the adiabatic wavefunctions, is $Y_{J=4,M=0}$, $J_{\max}$ has been set to 5, involving therefore two basis-sets of 15 and 21 spherical harmonics for the para and ortho species, respectively.

In Fig. 5.7 the RA-energies, corresponding to the same chosen configurations as in Fig. 5.6, are depicted by red circles and are compared to the energy levels obtained within the free rotor, which have already been defined in Eq. 2.73. The first free rotor energy levels are $0B^{\mathrm{pH_2}}, 2B^{\mathrm{oH_2}}, 6B^{\mathrm{pH_2}}, 12B^{\mathrm{oH_2}}, ...$, and are depicted by blue circles in Fig. 5.7. Whereas the free rotor eigenvalues are $2J + 1$-fold degenerate, such degeneracy is lifted within the rotational adiabatic separation (RAS), due to the potential energy interaction. Thus, at distances, $R_{AB} \to \infty$, where the interaction potential between the two molecules vanishes, the eigenvalues $E^{(n=v=0,\,l)}_{\mathrm{rot}}$ tend to the energy values of the free rotor, $E^{(J)}$, themselves. In other words, the energy levels of the free rotors are the asymptotic limits of the RA-PESs calculated later in this chapter (see for instance Fig. 5.8).

Since the interaction is weak, it is still easy in Fig. 5.7 to assign the free rotor energy levels, $E^{(J)}$, with even and odd values of J, to the respective eigenvalues $E^{(n=v=0,\,l)}_{\mathrm{rot}}(R_{AB} = 0.36, \theta_A = 90°, \phi_A = 0)$ to the values of $l = 0, 4, 5, 6, 7, 8$ corresponding to pH_2, and those with $l = 1, 2, 3, 9, 10, 11, 12, 13, 14, 15$ corresponding to oH_2. They in fact do not differ much in general. For $\theta_A = 90°$, the pH_2 rotor in its ground state, $l = 0$, is practically unperturbed by the Cl_2 molecule. This can be traced back to the results obtained above in Sec. 5.3.1,

when the H_2-Cl_2 pair potentials have been calculated for the six highly symmetric H-, L-, X-, T_1, T_2 and S-configurations. The T_2- and L-configurations were subgrouped in the "Collinear" symmetry group, since they present higher bonding energies and larger equilibrium bond distances, whereas the H-, X- and T_1-configurations were subgrouped in the "Non-Collinear" symmetry group, since they present in turn lower bonding energies and shorter equilibrium bond distances. For symmetry reasons only configurations from the "Non-Collinear" subgroup (the COM of H_2 is always perpendicular to the Cl_2 bond) contribute to the RA-eigenvalues $E_{\rm rot}^{(n=v=0,\,l)}(R_{AB}=0.36,\theta_A=90°,\phi_A=0)$, which are indeed weakly bound. As a consequence, the RA-wavefunction is only slightly distorted.

For the same value of $J_{\rm max}=5$, the RAS has been carried out on different grids and the results then compared. Convergence for the RA ground state potential, $W_{\rm H_2-Cl_2}^{(n=v=0,\,l=0)}(R_{AB}$, $\theta_A,\phi_A=0)$ is already reached for a 8×4 grid. Convergence up to $W_{\rm H_2-Cl_2}^{(n=v=0,\,l=8)}(R_{AB},\theta_A$, $\phi_A=0)$ is instead reached for a 14×8 grid. Finally, the more safe 16×8 grid has been chosen. The rather good accuracy reached despite such small grids is explained by the fact that within the chosen basis-functions, those with $M>1$, which are the ones calculated with less precision because of the increased number of nodes along ϕ_B, play no role, i.e. they do not contribute to the building of the RA-eigenvectors, $\psi_{\rm H_2-Cl_2}^{(n=v=0,\,l)}(R_{AB},\theta_A,\phi_A=0)$ at $\theta_A=0°$.

5.3.4 The H_2-Cl_2 and D_2-Cl_2 RA-PESs

In the previous section, all needed convergence tests have been carried out for the calculation of the RA-PESs of the H_2-Cl_2 and D_2-Cl_2 systems. The calculation of the RA-eigenvalues $E_{\rm rot}^{(n=v=0,l)}(R_{AB}=0.36$ nm,$\theta_A,\phi_A=0)$ with $\theta_A=0°$, 20° and 90° and of the expansion coefficients of the first RA-eigenvectors, $\psi_{\rm H_2-Cl_2}^{(n=v=0,\,l)}(R_{AB},\theta_A,\phi_A=0)$, with $\theta_A=0°$, 20° and 90° and $l=0,1,2,3$, already gave us physical insights in the system under investigations. In particular, the very small contributions from SHs with high values of J to the RA-eigenvectors and the small differences between the free rotor energy levels and the RA-eigenvalues, already tell us that, at least at the distance, $R_{AB}=0.36$ nm, the pair interaction is very weak and, hence, that the hydrogen behaves almost like a free rotor. Moreover, considering the NNd in the para-hydrogen crystal of 0.3798 nm, and assuming that the Cl_2 molecule occupies a single substitutional site, the convergence test is probably a close example of the changes the solute molecule induces to each of the hydrogen molecules in its first shell environment when embedded into the crystal (within the two-body interaction approximation).

In order to gain some more insight, let us now investigate the resulting RA-PESs, $W_{\rm H_2-Cl_2}^{(n=v=0,l)}(R_{AB},\theta_A,\phi_A=0)$ and $W_{\rm D_2-Cl_2}^{(n=v=0,l)}(R_{AB},\theta_A,\phi_A=0)$, for the four lowest quantum number $l=0,1,2,3$, where $l=0$ corresponds to the potential interaction of pH_2 or oD_2 with Cl_2 and $l=1,2,3$ corresponds to the interaction potential of oH_2 or pD_2 with Cl_2. Please note that the *ab-initio* PESs have been calculated at the quantum mechanical

Table 5.3: The values of the dissociation energies at three one-dimensional cuts of the RA-PESs along $\theta_A = 0°$, 45° and 90° for the H_2-Cl_2 and D_2-Cl_2 molecular dimers with four different values of the quantum number $l = 0$ (pH_2/oD_2) and $l = 1, 2, 3$ (oH_2/pD_2) are listed together and compared to those of the SAA-PES for the first four spherical harmonics with $J, M = (0,0), (1,-1), (1,1), (1,0)$. In brackets the deviations of the dissociation energies for the SAA-model from those of the more accurate RA-model.

PES	$\theta_A = 0°$	$\theta_A = 45°$	$\theta_A = 90°$	Asymptotic Limits
		H_2-Molecule		
RA ($l = 0$)	1.8790	0.7361	1.4169	$0 \times B_e^{H_2}$
SAA ($J = 0, M = 0$)	1.7648 (−6%)	0.7278 (−1%)	1.4132 (−0.3%)	$0 \times B_e^{H_2}$
RA ($l = 1$)	2.1324	0.8870	1.5110	$2 \times B_e^{H_2}$
SAA ($J = 1, M = -1$)	2.0916 (−2%)	0.7249 (−18%)	1.4144 (−6%)	$2 \times B_e^{H_2}$
RA ($l = 2$)	2.1324	0.6955	1.4119	$2 \times B_e^{H_2}$
SAA ($J = 1, M = 1$)	2.0916 (−2%)	0.7249 (+4%)	1.4144 (+0.2%)	$2 \times B_e^{H_2}$
RA ($l = 3$)	1.2435	0.6069	1.3209	$2 \times B_e^{H_2}$
SAA ($J = 1, M = 0$)	1.1989 (−4%)	0.7335 (+20%)	1.4109 (+7%)	$2 \times B_e^{H_2}$
		D_2-Molecule		
RA ($l = 0$)	1.9593	0.7442	1.4202	$0 \times B_e^{D_2}$
SAA ($J = 0, M = 0$)	1.7648 (−10%)	0.7278 (−2%)	1.4132 (−0.5%)	$0 \times B_e^{D_2}$
RA ($l = 1$)	2.1709	0.8905	1.5123	$2 \times B_e^{D_2}$
SAA ($J = 1, M = -1$)	2.0916 (−4%)	0.7255 (−19%)	1.4144 (−6%)	$2 \times B_e^{D_2}$
RA ($l = 2$)	2.1709	0.6976	1.4109	$2 \times B_e^{D_2}$
SAA ($J = 1, M = 1$)	2.0916 (−4%)	0.7249 (+4%)	1.4144 (+0.2%)	$2 \times B_e^{D_2}$
RA ($l = 3$)	1.2867	0.6126	1.3273	$2 \times B_e^{D_2}$
SAA ($J = 1, M = 0$)	1.1989 (−7%)	0.7335 (+20%)	1.4108 (+6%)	$2 \times B_e^{D_2}$

average value of the H_2 bond distance, but used also for applying the RAS to the D_2-Cl_2 molecular system. Since the difference between the two bond distances is circa 1%, and the potentials are not averaged with respect to the vibrational DOF, the systematic error is expected to be very small with respect to the systematic error introduced by all previous assumptions.

The two-dimensional contour-plots of the RA-PESs with respect to R_{AB} and θ_A for the H_2-Cl_2 and D_2-Cl_2 systems are presented in the next section. For the moment, in order to better understand the topology of the PESs and disclose some more physical insights, let us look at Fig. 5.8, where one-dimensional cuts of the RA-PESs (solid lines) along $\theta_A = 0°, 45°, 90°$ (first, second and third column of panels) are depicted and compared with the SAA-PESs (dashed lines) for the four lowest rotationally adiabatic states of the H_2-Cl_2 ($l = 0$) and D_2-Cl_2 ($l = 1, 2, 3$) systems, and in Tab. 5.3, where the values of the dissociation energies of the different RA-PES and SAA-PES cuts are collected and the relative discrepancies given in percent.

Topologically, for all PESs shown two minima have been found at $\theta_A = 0°$ and $\theta_A = 90°$, the global one always at $\theta_A = 0°$, except for $W^{(n=v=0,l=3)}_{H_2-Cl_2}(R_{AB}, \theta_A, \phi_A = 0)$. The position of the saddle points is discussed later after fitting the PESs to continuous functions. Focusing on the $W^{(n=v=0,l=0)}_{H_2-Cl_2}(R_{AB}, \theta_A, \phi_A = 0)$ cuts (first row of panels), one notes that the magnitude of the energy discrepancy between the RA- and SAA-models increases with stronger interaction with maximum value at $\theta_A = 0°$ and that this dependence is enhanced for the oD_2-Cl_2 molecular system. These two conclusions have already been drawn by Le Roy *et al.* in [240] and are confirmed here. However, only the second conclusion applies to all RA-PESs, since for $l = 1$ and 3 the greatest discrepancy is found at $\theta_A = 45°$. Such discrepancies may not be large in absolute terms, but in relative terms the RA-PESs deviate up to a ± 20% from the SAA-PESs in particular in the region close to the saddle points. This justifies the application of the RAS model on the present system.

In Tab. 5.3 the rotational constants for H_2 and D_2 molecules have different values due to the different masses of the two molecules and therefore $B_e^{D_2} < B_e^{H_2}$. Thus, the PES cuts with $l = 0$ (first row of panels) have the same asymptotic limit, since the rotational constants are both multiplied by 0, but for $l \neq 0$ the asymptotic limits for the two systems are shifted by $2(B_e^{H_2} - B_e^{D_2})$, such that the H_2-Cl_2 PESs are always located above the D_2-Cl_2 ones. Apart from this shift, the RA-PESs with $l > 0$ (second, third and fourth row of panels) are rather similar in the two molecular systems as in the $l = 0$ case. Please note that within the SAA model, apart from the $B_e^{H_2} - B_e^{D_2}$ shift, the potentials are identical. This also is a reason for using the RAS model instead of the SAA model.

Even more interesting is the fact that both molecular systems, H_2-Cl_2 and D_2-Cl_2, present deeper minima, i.e. the complex is more stable, when the chlorine molecule forms complexes with oH_2 and pD_2 ($l = 1$ and 2) instead of with pH_2 and oD_2 ($l = 0$), respectively. This happens quite often: At $\theta_A = 0°$ and $l = 1$ and 2, at $\theta_A = 45°$ and 90° for

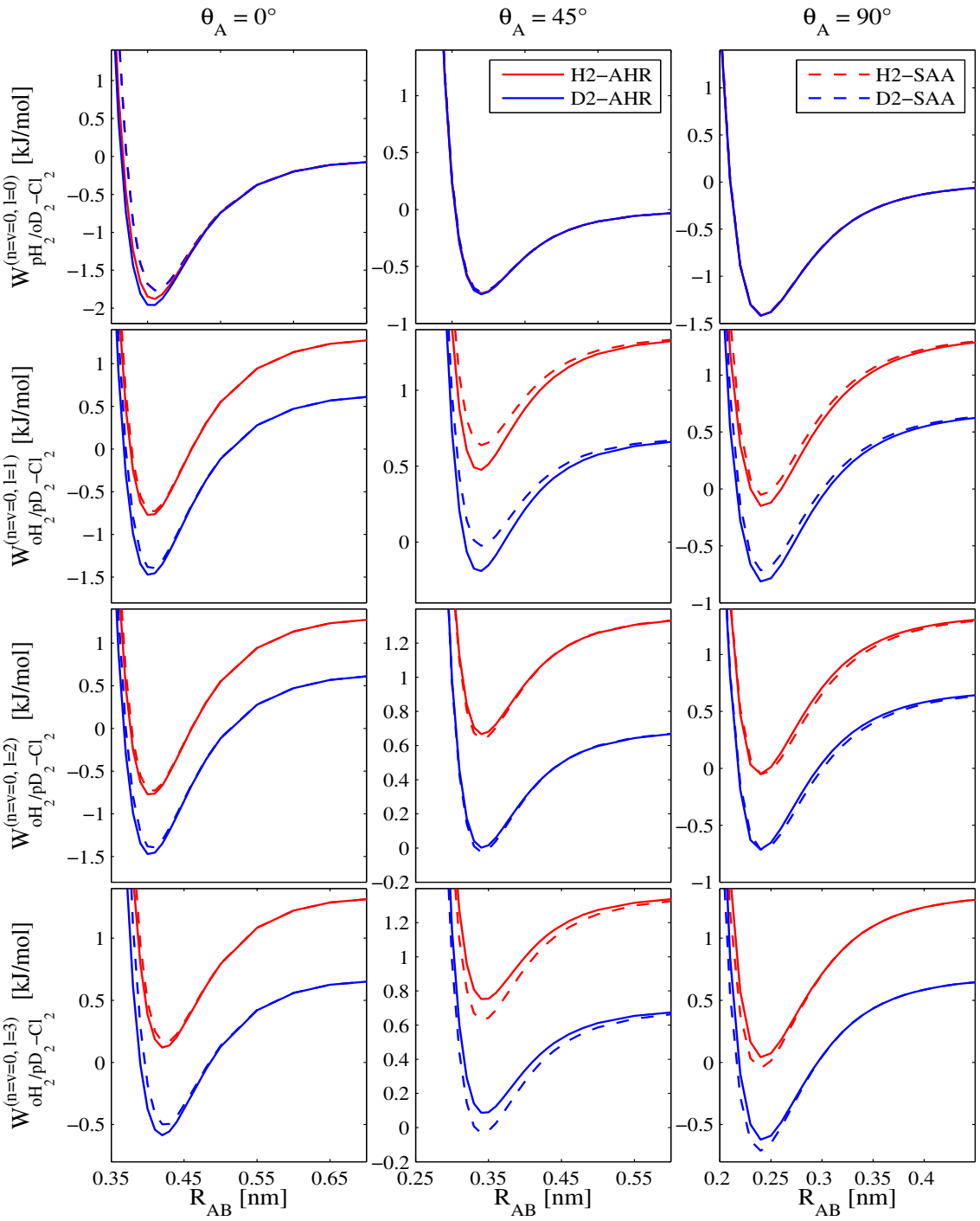

Figure 5.8: Four H_2-Cl_2 (red-solid lines) and four D_2-Cl_2 (blue-solid lines) one-dimensional cuts of the 2D RA-PESs with quantum numbers $l = 0$ (pH_2/oD_2) and $l = 1, 2, 3$ (oH_2/pD_2), are compared to the corresponding cuts of the SAA-PESs with quantum numbers $J, M = (0, 0)$ (red-dashed lines) and $J, M = (1, -1), (1, 1), (1, 0)$ (blue-dashed lines).

$l = 1$. Additionally, for many of the remaining cases the values in Tab. 5.3 eventually only differ by less than 0.1 kJ/mol. The increase in stability of such complexes is due to the interaction between the quadrupolar moment of the chlorine molecule and the non-vanishing quadrupolar moment of the rotating oH_2 and pD_2 molecules (see Appendix 6.3) and is expected to increase further in complexes with molecules possessing electrostatic moments lower than the quadrupolar one. Thus, molecular impurities embedded in H_2 and D_2 crystals, which have a dipole moment or even a charge, interact more strongly with oH_2 and pD_2 than with pH_2 and oD_2, respectively, since the latter ones do not have any electrostatic moments. This would confirm the conclusion drawn by Yoshioka *et al.* [7] and by Paulson and Anderson [205] from their experiments on CH_3F, CH_3Cl, CH_3Br, NO_2 and trans-formic acid molecules embedded in a para-hydrogen crystal, that the observed clustering effects of oH_2 molecules around the impurities is mainly due to the interaction with the dipole moment possessed by those impurities.

Fit of the H_2-Cl_2 and D_2-Cl_2 RA-PESs

The fit of molecular PESs is the starting point for the definition of a PES to be used in molecular dynamical calculations. The use of a parametrized continuous functions provides the energy values on the global PES and not only at the *ab-initio* energy values. In this section the 8 RA-PESs obtained for the two molecular systems, H_2-Cl_2 and D_2-Cl_2, are fitted by including an angular dependence to the analytical HFD-function, invented by Ahlrichs *et al.* [194] and used for instance by Goldmann and Silvera, and Norman, Watts and Buck, for fitting their semi-empirical $(pH_2)_2$ pair potentials. In the present work the latter one is used, so the attractive part does not contain the C_9 coefficient. The function reads:

$$\begin{aligned} V_{AB}^{(l)}(R_{AB},\theta_A) &= a(\theta_A)\times\exp[-b(\theta_A)\times R_{AB} - c(\theta_A)\times R_{AB}^2] \\ &\quad -\left(\frac{C_6(\theta_A)}{R_{AB}^6}+\frac{C_8(\theta_A)}{R_{AB}^8}+\frac{C_{10}(\theta_A)}{R_{AB}^{10}}\right)\times B(R_{AB},\theta_A) \end{aligned} \tag{5.29}$$

$$B(R_{AB},\theta_A) = \begin{cases} \exp[-p(\theta_A)(R_p(\theta_A)/R_{AB}-1)^2], & \text{if } R_{AB}\le R_p \\ 1, & \text{if } R_{AB}\ge R_p \end{cases}, \tag{5.30}$$

where $R_p(\theta_A)$, $p(\theta_A)$, $a(\theta_A)$, $b(\theta_A)$, $c(\theta_A)$, $C_6(\theta_A)$, $C_8(\theta_A)$ and $C_{10}(\theta_A)$ are angle dependent fitting parameters expanded in terms of the first three even Legendre Polynomials (LP)

$$X(\theta_A) = X_0\cdot P_0(\theta_A) + X_2\cdot P_2(\theta_A) + X_4\cdot P_4(\theta_A)\ . \tag{5.31}$$

where $X(\theta_A)$ represents each of the fitting parameters and X_0, X_2 and X_4 are the coefficients of the LP expansion[4]. On the one hand, expansion of the fitting parameters in the first three even LPs makes this analytical function dependent on 24 parameters, hence to be very flexible. On the other hand, the computational costs for fitting the RA-PESs are expected to be very high. For this reason, it is important to have already reasonable initial values as input for the fitting code. This has been achieved, by fitting three one-dimensional cuts of the RA-PESs along $\theta_A = 0°$, 45°, 90° for each of the four values of l. In other words, the angular dependent fitting function of Eq. 5.29 is used for fixed values of the angle θ_A. Thus, three values, $X(0°)$, $X(45°)$ and $X(90°)$, are obtained for each of the 8 fitting parameters, which can be used in order to solve 8 different systems of linear equations (for each value of the quantum number l) of the type given below:

$$P_0(0°) \times X_0 + P_2(0°) \times X_2 + P_4(0°) \times X_4 = X(0°) \quad (5.32)$$

$$P_0(45°) \times X_0 + P_2(45°) \times X_2 + P_4(45°) \times X_4 = X(45°) \quad (5.33)$$

$$P_0(90°) \times X_0 + P_2(90°) \times X_2 + P_4(90°) \times X_4 = X(90°) \quad (5.34)$$

where the matrix of LPs is known, the LP expansion coefficients X for each of the 8 fitting parameters have to be determined and will be the initial values of the 24 fitting parameters for fitting each of the two-dimensional RA-PESs using Eq. 5.29, as mentioned above.

The two-dimensional fitted RA-PESs of the H_2-Cl_2 and D_2-Cl_2 systems are shown in Figs. 5.9, 5.10, 5.11 and 5.12 and the corresponding fitting parameters can be found in Appendix 6.4. The positions of the two minima R_{min1} and R_{min2} (always at $\theta_A = 0°$ and 90°, respectively) and of the saddle point R_{sp}, and the corresponding dissociation energies, D_e, are collected in Tab. 5.4. A comparison with the dissociation energies given in Tab. 5.3 at $\theta_A = 0°$ and 90°, which came from the quantum chemistry raw data, shows some small discrepancy, in particular for the PESs with $l > 0$, but, nevertheless, their topologies have been maintained. The dissociation energies given in Tab. 5.3 at $\theta_A = 45°$ can not be directly compared, since within the analytically fitted RA-PESs they are given in correspondence of the saddle points, the location of which depends on the potential considered hence on the quantum number l and are indeed always located at $\theta_A > 45°$. Please note that all the dissociation energies given in the Tab. 5.4 are now subject to the accuracy of the fitting procedure.

The large change in the equilibrium distances when going from the L- to the T-shaped configurations makes the PESs to depend strongly on θ_A, hence on the Legendre expansion of the fitting parameters. Such a high anisotropic character is also seen in the PESs of

[4]Please note that from now on the new notation $V^{(l)}_{H_2-Cl_2}(R_{AB}, \theta_A)$ and $V^{(l)}_{(H_2)_2}(R_{AB})$ will be used to indicate the now fitted pair potentials, see Eq. 5.29

Table 5.4: For each of the two species, H_2 and D_2, the positions of the two minima, R_{min1} and R_{min2} and of the saddle point R_{sp}, and the corresponding dissociation energy values, D_e, are tabulated for the first four lowest fitted RA-PESs with l =0, 1, 2 and 3. Distances are given in nm, angles in degrees and energies in kJ/mol.

PES	Minimum1			Saddle Point			Minimum2			Asymptotic Limits
	θ_A	R_{min1}	D_e	θ_A	R_{sp}	D_e	θ_A	R_{min2}	D_e	
H_2-Molecule										
RA ($l=0$)	0°	0.408	1.876	46.6°	0.341	0.734	90°	0.241	1.415	$0 \times B_e^{H_2}$
RA ($l=1$)	0°	0.408	2.116	45.9°	0.338	0.847	90°	0.244	1.515	$2 \times B_e^{H_2}$
RA ($l=2$)	0°	0.409	2.107	48.7°	0.332	0.686	90°	0.242	1.434	$2 \times B_e^{H_2}$
RA ($l=3$)	0°	0.428	1.262	45.4°	0.346	0.624	90°	0.244	1.368	$2 \times B_e^{H_2}$
D_2-Molecule										
RA ($l=0$)	0°	0.407	1.967	46.6°	0.339	0.716	90°	0.243	1.427	$0 \times B_e^{D_2}$
RA ($l=1$)	0°	0.406	2.171	46.2°	0.337	0.852	90°	0.243	1.561	$2 \times B_e^{D_2}$
RA ($l=2$)	0°	0.404	2.176	55.5°	0.312	0.765	90°	0.241	1.394	$2 \times B_e^{D_2}$
RA ($l=3$)	0°	0.424	1.285	46.1°	0.344	0.608	90°	0.244	1.343	$2 \times B_e^{D_2}$

other RG-Cl_2 systems, even if the change on the equilibrium distances between linear and T-shaped minima are not so large. For example, for the linear and T-shape configurations in the He-Cl_2 and Ar-Cl_2 systems they are respectively 0.420 against 0.345 nm and 0.447 against 0.374 nm [254] (see also Tab. 5.11). In a similar way, the equilibrium distance between Cl_2 and the other three molecules is always shorter at $\theta_A = 90°$ than at $\theta_A = 0°$ because of the linear shape of Cl_2, as already seen in Sec. 5.3.1 when comparing Collinear against Non-Collinear spacial configurations.

Validity of Previous Assumptions

At this point, as already mentioned above in Secs. 5.2 and 5.3.2, respectively, two significant *a posteriori* tests are carried out in order to validate two important assumptions made throughout this work: 1) the choice of the Quantum Chemistry method and of the basis-set

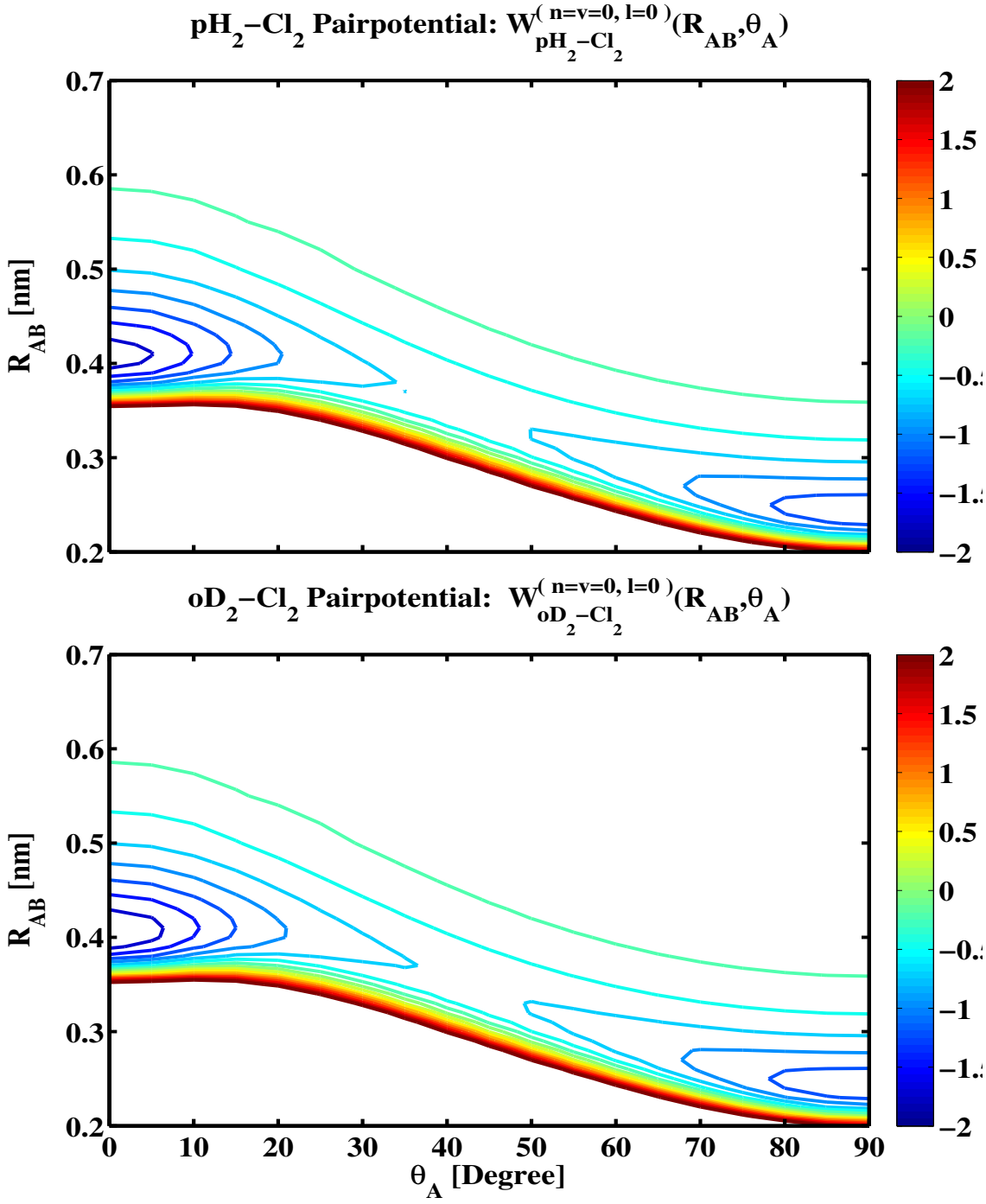

Figure 5.9: pH_2-Cl_2 (top) and oD_2-Cl_2 (bottom) 2D RA-PES contourplots with quantum number $l = 0$ obtained by solving Eq. 5.10. The contour levels are given at -1.75, -1.50, -1.25, -1.00, -0.75, -0.50, -0.25, 0, 0.25, 0.50, 0.75, 1.00, 1.25, 1.50, 1.75, 2.00. For the positions and energies of the minima and the saddle points refer to Tab. 5.4. The zero is defined as the BSSE-corrected energy value at $R_{AB} = 0.95$ nm.

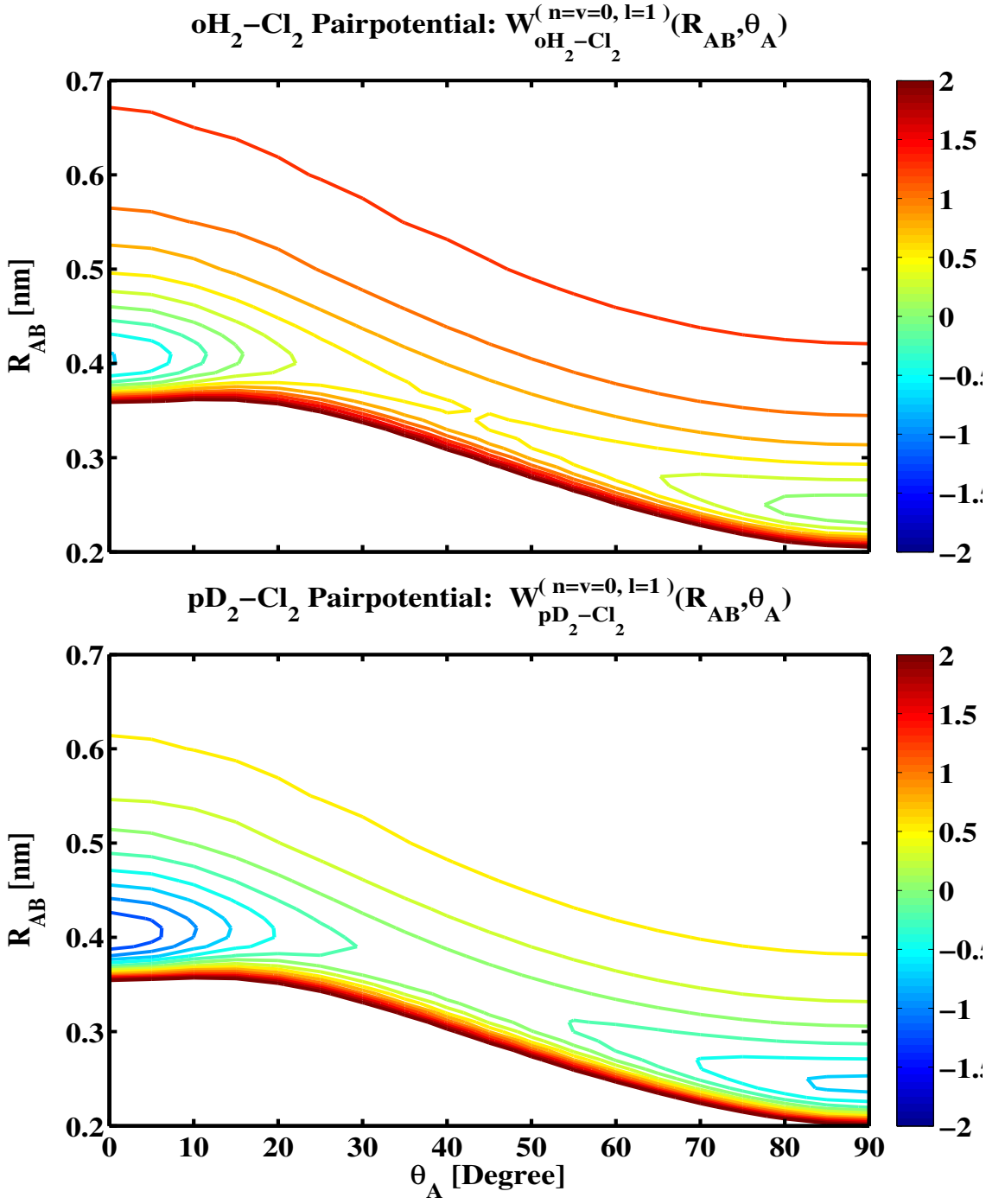

Figure 5.10: oH_2-Cl_2 (top) and pD_2-Cl_2 (bottom) 2D RA-PES contourplots with quantum number $l = 1$ obtained by solving Eq. 5.10. The contour levels are given at -0.75, -0.50, -0.25, 0, 0.25, 0.50, 0.75, 1.00, 1.25, 1.50, 1.75, 2.00 for the top-panel and at -1.25, -1.00, -0.75, -0.50, -0.25, 0, 0.25, 0.50, 0.75, 1.00, 1.25, 1.50, 1.75, 2.00 for the bottom-panel. For the positions and energies of the minima and the saddle points refer to Tab. 5.4. The zero is defined as the BSSE-corrected energy value at $R_{AB} = 0.95$ nm.

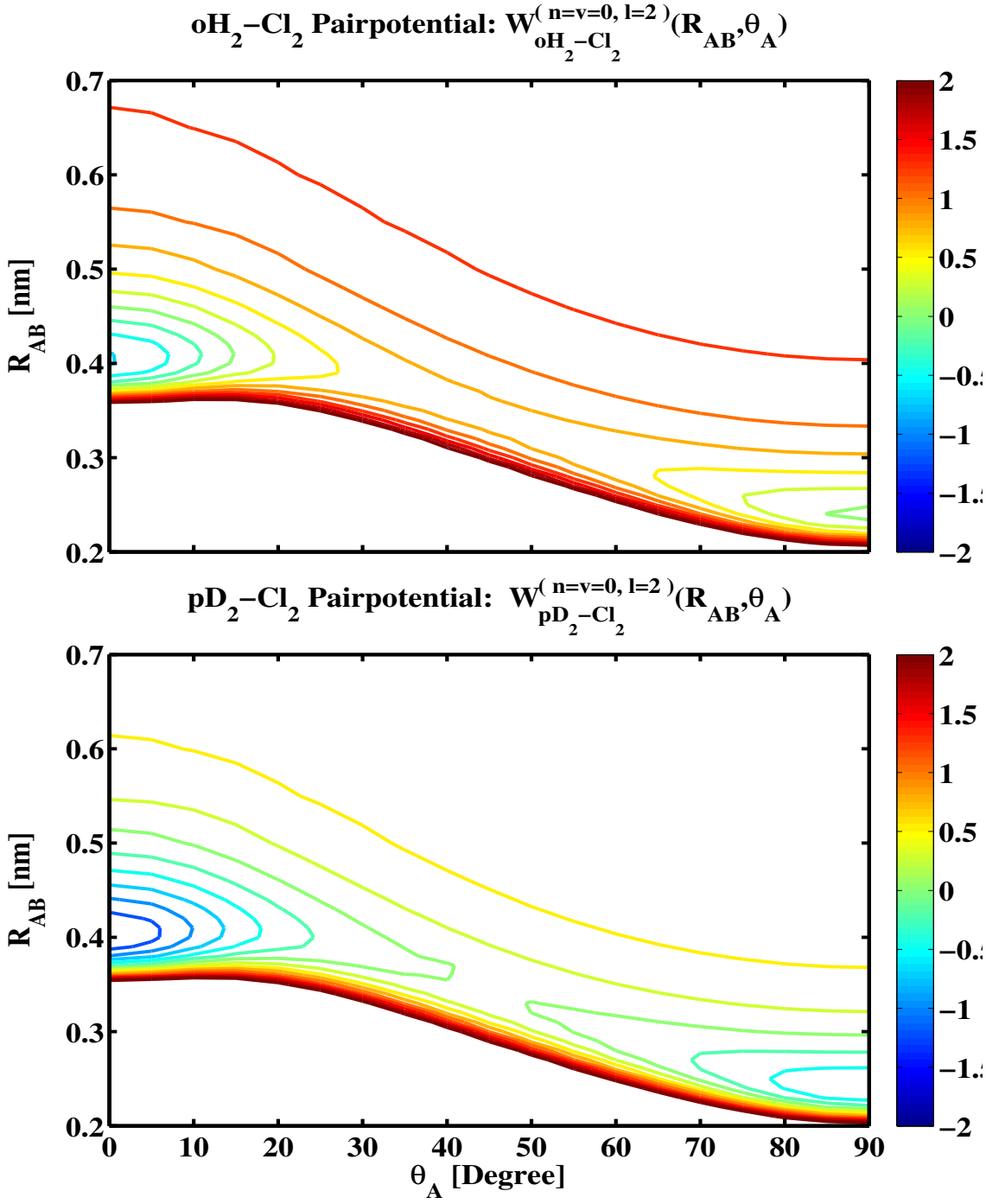

Figure 5.11: oH_2-Cl_2 (top) and pD_2-Cl_2 (bottom) 2D RA-PES contourplots with quantum number $l = 2$ obtained by solving Eq. 5.10. The contour levels are given at -0.75, -0.50, -0.25, 0, 0.25, 0.50, 0.75, 1.00, 1.25, 1.50, 1.75, 2.00 for the top-panel and at -1.25, -1.00, -0.75, -0.50, -0.25, 0, 0.25, 0.50, 0.75, 1.00, 1.25, 1.50, 1.75, 2.00 for the bottom-panel. For the positions and energies of the minima saddle points refer to Tab. 5.4. The zero is defined as the BSSE-corrected energy value at $R_{AB} = 0.95$ nm.

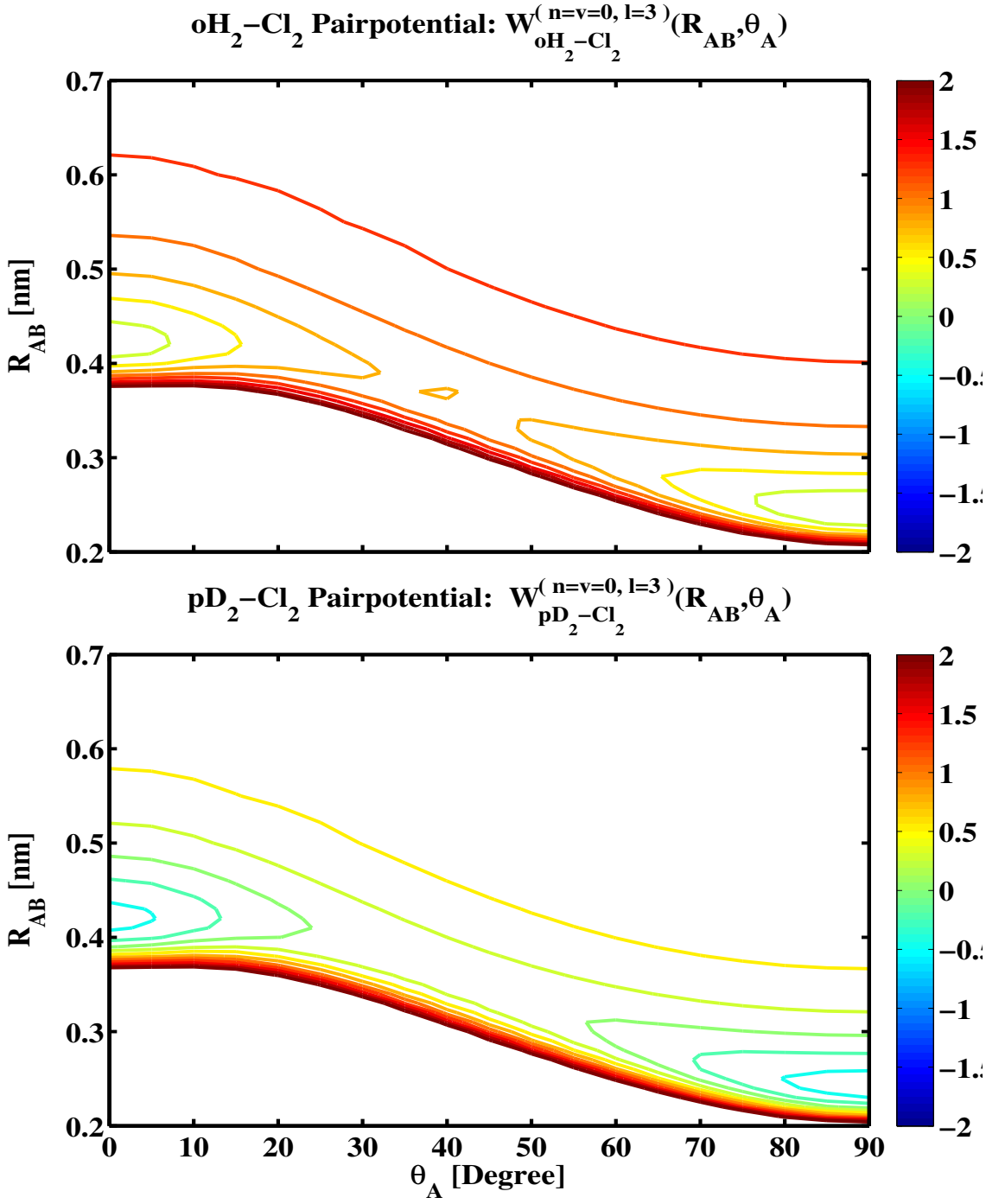

Figure 5.12: oH_2-Cl_2 (top) and pD_2-Cl_2 (bottom) 2D RA-PES contourplots with quantum number $l = 3$ obtained by solving Eq. 5.10. The contour levels are given at -0.75, -0.50, -0.25, 0, 0.25, 0.50, 0.75, 1.00, 1.25, 1.50, 1.75, 2.00 for the top-panel and at -1.25, -1.00, -0.75, -0.50, -0.25, 0, 0.25, 0.50, 0.75, 1.00, 1.25, 1.50, 1.75, 2.00 for the bottom-panel. For the positions and energies of the minima saddle points refer to Tab. 5.4. The zero is defined as the BSSE-corrected energy value at $R_{AB} = 0.95$ nm.

used in the evaluation of the *ab-initio* PESs, and 2) the validity of the RA approximation upon the vibrational motion of the Cl_2 molecule. Again only the three one-dimensional cuts of the RA-PESs at $\theta_A = 0°$, 45° and 90°, are considered.

Recall that the Quantum Chemical calculations have been carried out at the MP2:aug-cc-pVQZ level of theory. The results obtained after adiabatization with respect to the rotational DOFs of the hydrogen or deuterium molecules are now compared with data produced at a higher level of theory. The one-dimensional cuts along $\theta_A = 45°$ and 90° have been reproduced at the CCSD(T):aug-cc-pVQZ level of theory, whereas the one-dimensional cut along $\theta_A = 0°$ has been reproduced using the CCSD(T) method, but extrapolating the results to the complete basis-set from the aug-cc-pVQZ and aug-cc-pV5Z basis-sets (CCSD(T):extrapolated), see Eq. 2.94. This last configuration is in fact CPU-time saving for symmetry reasons, since the rotational adiabatization of the H_2 molecule becomes independent of ϕ_B.

These two counter-checks are depicted in the left and right panels of Fig. 5.13 only for the H_2-Cl_2 molecular system, but all conclusions drawn in this section are valid for the D_2-Cl_2 molecular system as well. The top-, middle- and bottom-panels are the respective cuts along $\theta_A = 0°$, 45° and 90°. Moreover, the relative errors with respect to the dissociation energies are given in percent in Tab. 5.5, which is also divided in a left and right part for the validity of the chosen *ab-initio* level of theory and of the adiabatic separation. In the table, the relative errors are given for both molecular systems.

Let us focus first on the *ab-initio* level of theory counter-check. With respect to the energy differences observable in Fig. 5.5 between the interaction potential curves for the H, L, X, T1, T2 and S configurations (hence before adiabatization!), the energy differences between the RA-PESs (hence after adiabatization!) obtained from the two different levels of theory almost vanish for $\theta_A = 45°$ and $\theta_A = 90°$ and all relative errors are below or equal to 4%. Greater discrepancy is found at $\theta_A = 0°$ (top-panel), where the cyan colour has been used instead of blue, since the comparison is now done with respect to the CCSD(T):extrapolated level of theory. The dissociation energies are overestimated between a 5% and 8%. A reason for this larger discrepancy can be found in the strength of the interaction between the two molecules in a collinear configuration, which means that the MP2 method is less accurate in evaluating the correlation energy at the collinear geometries.

The magnitude of the error introduced by considering the Cl_2 bond length fixed at the $v = 0$ vibrationally averaged values (classical approximation) has been estimated by recalculating the RA at two additional values of the Cl_2 bond distances, which have been chosen to be the distances corresponding to the Full Width at Half of the Maximum (FWHM) of the vibrational ground state wavefunction, namely $\tilde{r}^- = (\tilde{r}_{Cl_2} - \Delta r) = 0.1959$ nm and $\tilde{r}^+ = (\tilde{r}_{Cl_2} + \Delta r) = 0.2107$ nm. The changes of the dissociation energies for the

Table 5.5: The difference between the values of the dissociation energies at three one-dimensional cuts of the RA-PESs along $\theta_A = 0°$, 45° and 90° for the H_2-Cl_2 and D_2-Cl_2 molecular dimers with four different values of the quantum number $l = 0$ (pH_2/oD_2) and $l = 1, 2, 3$ (oH_2/pD_2) and the dissociation energies obtained when using the higher level of theory CCSD(T):aug-cc-pV5Z (CCSD(T):extrapolated in the case of $\theta_A = 0°$) (left part of the table) and the dissociation energies obtained when using the new values r^- and r^+ for the Cl_2 bond distance (right part of the table) are given in percent.

	Counter-check					
	ab-initio Level of Theory			Adiabatic Separation		
PES	$\theta_A = 0°$	$\theta_A = 45°$	$\theta_A = 90°$	$\theta_A = 0°$	$\theta_A = 45°$	$\theta_A = 90°$
			H_2			
RA ($l = 0$)	+5%	−1%	+2%	−7%/ + 8%	−1%/ + 1%	+4%/ − 3%
RA ($l = 1$)	+5%	+0.6%	+4%	−7%/ + 7%	−2%/ + 2%	+2%/ − 1%
RA ($l = 2$)	+5%	−2%	+1%	−6%/ + 7%	−1%/ + 1%	+5%/ − 4%
RA ($l = 3$)	+8%	−3%	+0.8%	−6%/ + 7%	−0.1%/ + 0.6%	+4%/ − 3%
			D_2			
RA ($l = 0$)	+5%	−0.9%	+2%	−7%/ + 8%	−1%/ + 1%	+3%/ − 3%
RA ($l = 1$)	+5%	+0.6%	+4%	−7%/ + 8%	−2%/ + 2%	+2%/ − 1%
RA ($l = 2$)	+5%	−2%	+1%	−6%/ + 8%	−1%/ + 1%	+5%/ − 4%
RA ($l = 3$)	+7%	−3%	+0.9%	−6%/ + 7%	−0.2%/ + 0.6%	+4%/ − 3%

molecular complexes at the Cl_2 bond distances $\tilde{r}^-$ and $\tilde{r}^+$ with respect to the equilibrium position $\tilde{r}_{Cl_2}$ are given in percent on the last three columns of Tab. 5.5.

Once more the differences between the energy curves are more pronounced for configurations close to the collinear one. As expected, the potential energy is very sensitive to the Cl_2 internuclear distance at $\theta_A = 0°$, since in this case the chlorine vibrations are along the axis pointing to the hydrogen or deuterium molecule. The relative errors are below 6% for the PES-cuts along $\theta_A = 45°$ and 90°,but lie between 6% and 8% for the PES-cut along $\theta_A = 0°$. Since the quantum mechanical probability to find the molecule at its equilibrium

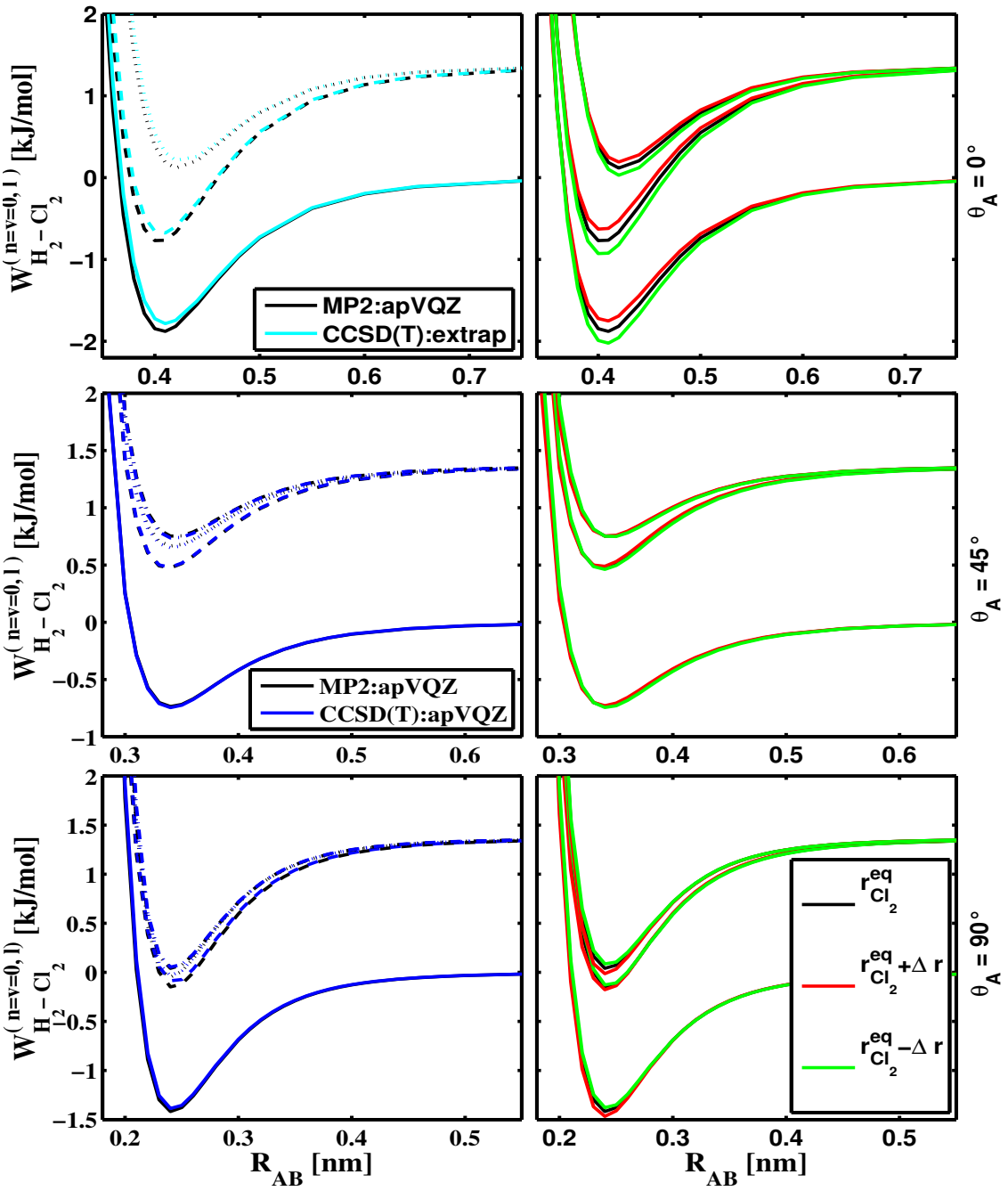

Figure 5.13: Two *a posteriori* checks are shown: The level of theory chosen for the *ab-initio* calculations (left column) and the separability of the H_2 rotations and from the Cl_2 vibrations (right column). Three different cuts of the 2D RA-PESs, $W^{(n=v=0,l)}_{H_2-Cl_2}(R_{AB}, \theta_A)$ for quantum numbers $l = 0, 1, 2, 3$ are depicted at three configurations ($\theta_A = 0°, 45°$ and $90°$ (top-, middle- and bottom-row, respectively). Colour-code: The black curves refer to the RA-PESs calculated at the MP2:aug-cc-pVQZ level of theory with $\tilde{r}_{Cl_2} = \langle r_{Cl_2} \rangle_{v=0} = 0.2033$ nm. The colours red and green refer to the same RA-PESs with $\tilde{r}^+ = (\tilde{r}_{Cl_2} + \Delta r) = 0.2107$ nm and $\tilde{r}^- = (\tilde{r}_{Cl_2} - \Delta r) = 0.1959$ nm, respectively.

distance is maximal, we believe that neglecting the Cl_2 vibrational DOF does not affect the present results for more than 10%.

5.3.5 The $(pH_2)_2$ RA-Pair Potential

In the calculation of the ground state of the $(pH_2)_2$ RA-pair potential, $W_{(pH_2)_2}^{(n=v=0,\ l=0)}(R_{AB})$, the size of the DVR-grid 8×16 is taken to be the same without any further convergence test, since the interaction potential energy is weaker and almost isotropic compared to the pH_2-Cl_2 molecular system. Moreover, only the rotational ground state is calculated, since no applications are foreseen, which imply mixed ortho/para or pure ortho/ortho crystals.

The $(pH_2)_2$ and $(oD_2)_2$ pair interaction are expressed in this work by the same curve. Strictly speaking the quantum chemistry PES should have been recalculated with the two D_2 monomer bond length fixed at the $\tilde{r}_{D_2}$ distance, instead of $\tilde{r}_{H_2}$, but within all above mentioned approximation we believe that the systematic error introduced may be negligible.

The $(pH_2)_2$ RA-pair potential pair potential is fitted to the $V_{(pH_2)_2}^{(l=0)}(R_{AB})$ HFD-function in Eq. 5.29, where the angular dependence is now dropped. The resulting curve is compared in Fig. 5.14 (red solid line) to the semi-empirical potential curves by Norman, Watts and Buck [193], by Silvera-Goldmann [13] and to the Lennard-Jones potential based on Michels' results [255] (black lines) as well as to the pair potentials calculated by Li, Le Roy and Roy (LLR) [240] within the AHR model (blue solid line) and to the one calculated by Hinde [189] (green solid line). The LLR curve is based on the *ab-initio* PES calculated by Patkowski *et al.* [188] at a higher level of theory than in this work (they extrapolated the energies from the QC to the basis-set limit from CCSD(T):aug-cc-pVQZ and CCSD(T):aug-cc-pV5Z), however also in the rigid-rotor approximation, whereas the calculations by Hinde are based on an *ab-initio* PES at a very similar level of theory as in the present work (CCSD(T):aug-cc-pVQZ supplemented with a set of $3s3p2d$ bond functions at the dimer's COM), but include also the vibrational average of the hydrogen monomers, so that comparison to the curve from the present work can be considered as direct measurement of the error introduced by fixing the molecular internal bond distance (classical approximation).

The HFD fitting parameters are listed in Tab. 5.6 except for the curve by Hinde, since none have been found in the literature. Nevertheless, the vibrationally averaged dispersion coefficients C_6, C_8 and C_{10} were recently calculated by Lillistolen and Hinde [197] (LH) at the high CCSD:d-aug-cc-pV5Z level of theory and are, therefore, listed in Tab. 5.6 for comparison. Finally, the equilibrium distances and the dissociation energies are summarized in Tab. 5.7. In general, all pair potentials present very similar shapes, equilibrium distances and dissociation energies. Nevertheless, the curves from *ab-initio* present slightly larger equilibrium bond distances and dissociation energies than the semi-empirical ones. It is also interesting to note that the potential curves by Hinde and from the present work have a softer repulsive part than the LLR curve. As already mentioned in the introduction

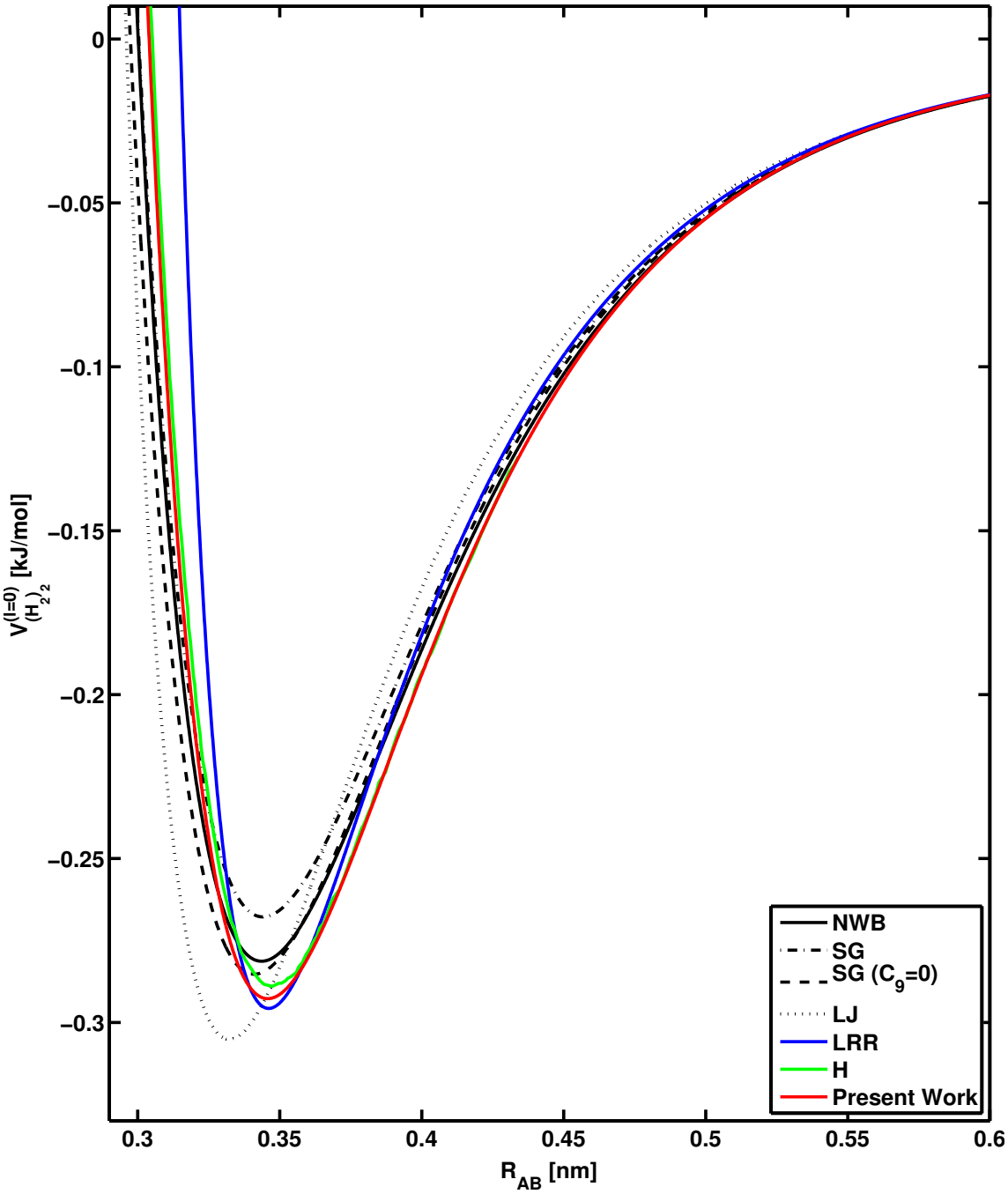

Figure 5.14: The $(pH_2)_2$ RA-pair potential, $V^{(l=0)}_{(pH_2)_2}(R_{AB})$ from the present work is compared to the semi-empirical curves by Norman-Watts-Buck (NWB) [193], by Silvera-Goldmann (SG) with and without the C_9 coefficient [13], to the Lennard-Jones (LJ) potential [255], to the $(pH_2)_2$ AHR-pair potential curve calculated by Le Roy *et al.* [240] (based on an *ab-initio* PES calculated by Patkowski *et al.* [188] at a higher level of theory than in the present work) and to the vibrationally averaged pair potential by Hinde (H) [190] (based on an *ab-initio* PES calculated at a similar level of theory).

Table 5.6: HFD-parameters fitting the one-dimensional isotropic $(pH_2)_2$ RA-PES, $V^{(l=0)}_{(pH_2)_2}(R_{AB})$, from the present work and the semi-empirical pair potentials by Norman, Watts and Buck (NWB) [193] and by Silvera-Goldmann (SG) [13]. The vibrationally averaged dispersion coefficients by Lillestolen and Hinde [197] are also listed both for the $(pH_2)_2$ and the $(oD_2)_2$ dimers. All values are given in au.

pair potential	Unit	Present Work	NWB	SG	LH (H_2)	LH (D_2)
R_p	$[a_0]$	9.7410	9.641	–	–	–
R_m	$[a_0]$	–	–	0.341	–	–
p		1.0	1.0	–	–	–
$log(a) \equiv \alpha$		1.4414	1.3154	1.713	–	–
$b \equiv \beta$	$[a_0^{-1}]$	1.3706	1.47058	1.5671	–	–
$c \equiv \gamma$	$[a_0^{-2}]$	0.0419	0.02240	0.00993	–	–
C_6	$[E_h \times a_0^6]$	11.6812	12.14	12.14	12.073	11.865
C_8	$[E_h \times a_0^8]$	235.2	215.2	215.2	212.7	207.4
C_9	$[E_h \times a_0^9]$	–	–	143.1	–	–
C_{10}	$[E_h \times a_0^{10}]$	4813.9	4813.9	4813.9	4783	4630

to this chapter, the *ab-initio* methods give in general more repulsive energies at short bond distances than the semi-empirical methods. In fact, inclusion of the three-body interactions has been proved to soften the repulsive wall [191]. Nevertheless, for our purpose it is more important to compare the attractive parts of the potentials. Since at larger distances, the curves converge to each other, similar results are expected when using any of those curves. This becomes also evident by comparing the dispersion coefficients in Tab. 5.6. No drastic deviations are indeed disclosed, neither upon vibrational average, nor between the LH (H_2) and LH (D_2) coefficients, so that on one hand the classical approximation seems to introduce only negligible errors in the pair potential, on the other hand the $(pH_2)_2$ can be used to express also the $(oD_2)_2$ interaction.

5.3.6 From Clusters to Crystals

In the next sections solid state aggregation is investigated starting from the growth of small clusters and arriving at the building of infinite crystals. All simulations are based on the two-body interaction potentials calculated in the previous sections within the multi-stage adiabatic separation, so that all conclusions drawn on the pair potentials are transferred to the multi-body simulations. The solvent-solvent pair potential showed a very low interaction energy confirming that the pH_2 molecules rotate almost freely. In the solvent-solute

Table 5.7: The positions of the minima, $R_{\min}$, and the dissociation energies of different one-dimensional isotropic $(pH_2)_2$ pair potentials are listed. The semi-empirical potentials by Norman, Watts and Buck (NWB) [193] and by Silvera-Goldmann (SG) [13] (with and without the C_9 parameter), the Lennard-Jones potential by Michels (LJ) [255] and those from *ab-initio* by Li-Le Roy-Roy (LLR) [240] and by Hinde(H) [190] are compared to the fitted RA-PES, $V^{(l=0)}_{(pH_2)_2}(R_{AB})$, from the present work. Distances are given in nm and energies kJ/mol.

Potential		$R_{\min}$[nm]	D_e[kJ/mmol]
NWB		0.344	0.281
SG		0.344	0.268
SG	$(C_9 = 0)$	0.341	0.285
LJ		0.332	0.305
LLR		0.346	0.296
H		0.347	0.289
Present Work		0.346	0.286

pair potentials the solvent rotations were found to be slightly dependent on the Cl_2 internal vibrations, but the error was evaluated to be less or equal to 8%. Consequently, it is now assumed in the aggregates that the rotational DOFs of the single pH_2 molecules are practically decoupled from those in their neighbourhood as well as from the Cl_2 vibrations, even though this introduces a systematic error in the simulations (see Sec. 5.3.4).

In the next section the structures of the closest packed crystals, the hexagonal close-packed (hcp) and the face-centered cubic (fcc), and of the icosahedral (ico) quasi-crystal are introduced as a background for the subsequent sections. Afterwards, small pure and doped clusters are grown by means of classical simulations with the aim of investigating which structure is energetically favoured when describing the N-dimensional PESs just by a sum of pair interactions of HFD type. Secondly, since the three structures, fcc, hcp and ico, all have 12 molecules in their first coordination shell, the total energies of these first-shell pure $(pH_2)_{13}$ and doped $Cl_2(pH_2)_{12}$ clusters, are calculated as a function of the NNd and compared. Thirdly, the (in principle infinite) pure and doped crystal structures, hcp and fcc, are discussed, which will be used later when applying the non-rigid anharmonic EM for calculating the translational energies of H_2 and Cl_2 and the rotational PES of the Cl_2 in the crystal.

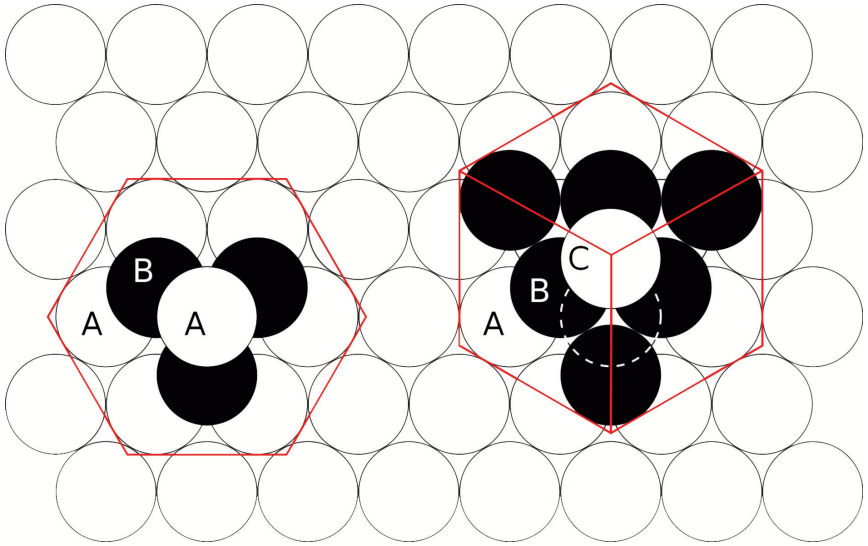

Figure 5.15: The two different ways of stacking sheets of spheres are shown, from which the hcp (ABA..) and fcc (ABC...) structures originate, in the left and right part of the figure, respectively. The red honeycomb-like hexagon typical for closed-packed lattices is shown in the left part of the figure, whereas in the right part the cubic form of the fcc unit cell is highlighted. The figure has been adapted from Wikipedia.

Close Packing of Spheres

In nature, atoms, ions or molecules aggregate in several different crystal structures depending on the magnitude of the particles involved and on the kind of interactions between them, ionic, covalent, hydrogen bonds or VDW. Since the particles in the solid state attract each other, the denser the arrangements in the space are, the more stable the structures will be. For this reason, two of the most common crystallographic structures found in nature are the hcp and fcc ones, which are based on the closest way of packing spheres. This means that within these arrangements the particles occupy the largest fraction of space which is achievable in a regular lattice. Both structures are based on sheets of touching spheres disposed at the vertices of equilateral triangles. They just differ in the way how subsequent sheets are stacked on each other as depicted in Fig. 5.15. First a sheet of spheres is created, such that each triad of contiguous spheres forms a triangle. This sheet is called A. The second sheet of spheres called B (black triangle), is stacked on top of the first one, leaning the spheres at the centers of the triangles of sheet A. Please note that in the top-left part of the figure (hcp ABA-stacking), there are two possible ways of leaning the new black triangle: The one shown in the figure, which forms the B-sheet, and a second one (not shown) where the black triangle is rotated by 60° around the axis perpendicular to the sheet and passing through the center of the black triangle, which is called C-sheet. Finally, if the third sheet put in top of the second is again an A sheet, then the hcp packing

originates, whereas if the sheet is a C sheet, the fcc crystal arises, as shown in the left and right part of Fig. 5.15, respectively.

The two structures also reach the same highest average density possible in nature, which is called, generally, the atomic packing factor (APF). This quantity is obtained by dividing the volume occupied by the spheres contained in the unit cell of a crystal by the total volume of such unit cell. The calculation of these quantities can be easily done looking at the two different unit cells (UC), which are the hexagonal prism and the external cube represented in the top and middle parts of Fig. 5.16. The hcp and fcc UCs contain 6 and 4 spheres, so that the volumes occupied by such spheres are

$$V_{\text{sphere}}^{\text{hcp}} = 6 \times \frac{4\pi}{3}(r)^3 \tag{5.35}$$

$$V_{\text{sphere}}^{\text{fcc}} = 4 \times \frac{4\pi}{3}(r)^3 \ , \tag{5.36}$$

whereas the volumes of the UCs are

$$V_{\text{uc}}^{\text{hcp}} = 6 \times \sqrt{3}r^2 \times 2c = 24\sqrt{2}r^3 \tag{5.37}$$

$$V_{\text{uc}}^{\text{fcc}} = \left(2\sqrt{2}r\right)^3 = 16\sqrt{2}r^3 \ , \tag{5.38}$$

respectively, where r is the radius of a sphere. Since the diameter corresponds to the distance between the centers of two touching spheres the diameter is indeed the NNd, $R_d = 2r$, where the subscript d stays for diameter[5]. Finally, the fcc lattice constant is $a = 2\sqrt{2}\ r = \sqrt{2}\ R_d$, whereas for the hcp lattice a second lattice constant $c = \sqrt{6} \times \frac{2r}{3}$ has to be considered along the z-axis stacking direction, being half of the height of the hexagonal prism forming the hcp unit cell. Finally, the APF of both crystal structures is

$$APF = \frac{V_{\text{sphere}}^{\text{hcp}}}{V_{\text{uc}}^{\text{hcp}}} = \frac{V_{\text{sphere}}^{\text{fcc}}}{V_{\text{uc}}^{\text{fcc}}} = \frac{\pi}{3\sqrt{2}} \approx 0.74048... \tag{5.39}$$

Please note that the fcc UC is a face-centered cube, and its edges are usually taken to be the Cartesian system of coordinates of references for it, whereas for the hcp, each of the sheet lies on the xy plane, and the sheets are stacked in the z-direction.

The hcp and fcc UCs are depicted in the top and middle panels of Fig. 5.16. For the fcc crystal, a primitive cell is defined within the UC by the following so-called primitive

[5] The nearest-neighbour distance will be indicated by R_d through the entire thesis.

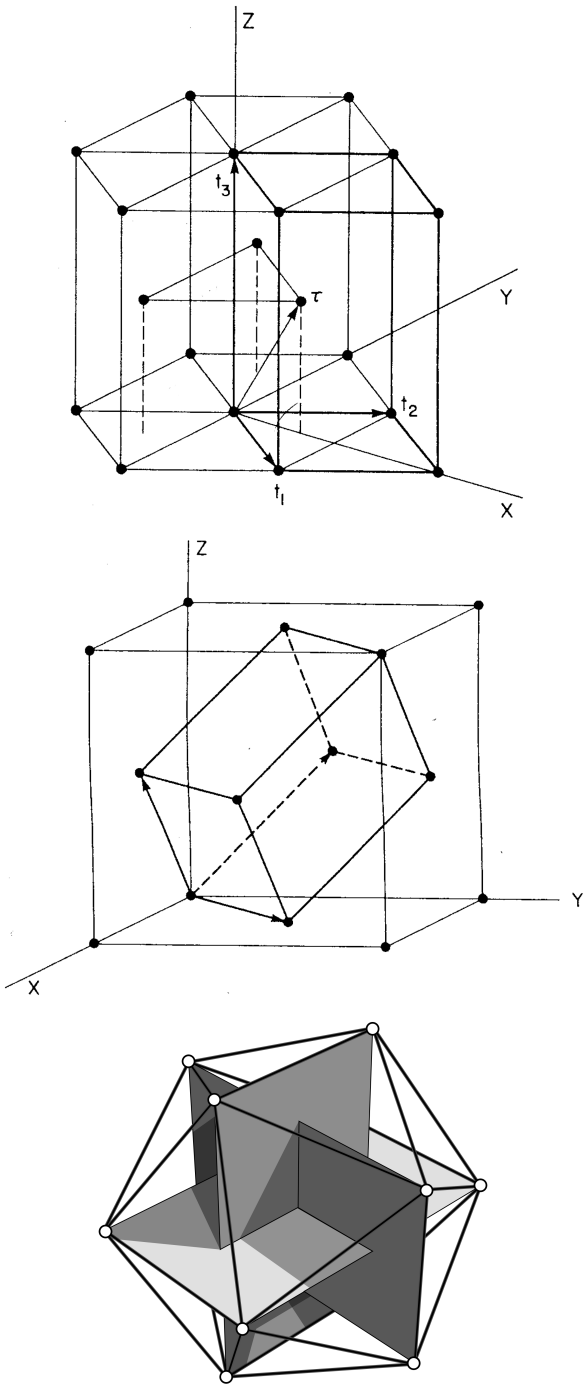

Figure 5.16: The UCs and the primitive cells together with the primitive vectors for the hcp (top panel) and the fcc (middle panel) lattices. These two pictures have been adapted from [14]. In the bottom panel, a regular icosahedron is constructed by three concentric, mutually orthogonal rectangles, the two sides of which define the golden formula (Paciolo construction 15^{th} century [256]).

vectors

$$\vec{t}_1 = \frac{a}{\sqrt{2}}(\vec{i}+\vec{j}) \quad (5.40)$$

$$\vec{t}_2 = \frac{a}{\sqrt{2}}(\vec{j}+\vec{k}) \quad (5.41)$$

$$\vec{t}_3 = \frac{a}{\sqrt{2}}(\vec{k}+\vec{i}) \ , \quad (5.42)$$

where $\vec{i}$, $\vec{j}$ and $\vec{k}$ are the unitary vectors in the x, y and z directions as defined in the middle panel of Fig. 5.16, where also the primitive cell is shown, that is the smaller inclined cube inside the UC. It contains one sphere per cell and when translated along the three dimensional space generates an infinite lattice without overlapping itself or leaving voids (translational symmetry). This is expressed mathematically by the Bravais vector [257],

$$\vec{T} = n_1\vec{t}_1 + n_2\vec{t}_2 + n_3\vec{t}_3 \quad (5.43)$$

where n_l, with $l = 1, 2, 3$, can be any integer number. These regular lattices are indeed called Bravais-lattice [257].

The primitive cell for an hcp lattice can be defined by the following three vectors

$$\vec{t}_1 = \frac{1}{2}a(\sqrt{3}\,\vec{i} - \vec{j}) \quad (5.44)$$

$$\vec{t}_2 = \frac{1}{2}a(\sqrt{3}\,\vec{i} + \vec{j}) \quad (5.45)$$

$$\vec{t}_3 = 2c\,\vec{k} \quad (5.46)$$

where $\vec{i}$, $\vec{j}$ and $\vec{k}$ are the unitary vectors in the x, y and z directions as defined in the top panel of Fig. 5.16. The hcp lattice contains two spheres per primitive cell and the position of this second sphere is given by the non-primitive vector

$$\vec{\tau} = \frac{1}{3}(\vec{t}_1 + \vec{t}_2) + \frac{1}{2}\vec{t}_3 \ . \quad (5.47)$$

also shown in Fig. 5.16.

Icosahedral Structure

The use of mass spectroscopy has revealed that when growing large RG clusters particularly stable sizes constituted by N particles appear [258]. These particular cluster sizes, N, form a sequence of so-called magic numbers, which are closely connected to the mechanism of cluster formation and growing. In the case of noble gases, the magic clusters mainly have size $N = \frac{1}{3}(2S+1)(5S^2+5S+3)$, which is the analytical formula counting the number of particles required to build icosahedral clusters with $S = 1, 2, 3, 4, 5, ...$, etc. complete coordination shells. Since icosahedral structures are crystal-like ordered, but do not present translational symmetry, they have been called quasi-crystal after Shachtman [259], who has been awarded the Nobel Prize in chemistry in 2011 for having observed them experimentally for the first time in 1982.

Since pH_2 molecules have almost a spherical shape and the binding energy is also in the range of VDW interactions, the growth sequence is expected to be similar. Experimentally, only one investigation has been found in the literature based on Raman spectroscopy of small pH_2 clusters formed in cryogenic free jets [260], where the authors were able to resolve Raman peaks for the first clusters with $N = 2, ..., 8$ molecules, whereas broad maxima were observed at $N \approx 13, 33, 55$, and connected to icosahedral structures. In turn, theoretical studies are numerous, most of them based on Monte Carlo methods [261–266]. They all observe formation of the so called Mackay clusters [267], which is a series of global minimum structures of icosahedral symmetry typical for RGs when the pair potential interaction is approximated by a Lennard-Jones (LJ) potential [268–270], which has a R^{-6} dependence for the attractive part, or also by Morse potentials [270]. The similar results obtained for molecular hydrogen clusters are easily explained by the use of the NWB or the SG pair potentials fitted to HFD-functions having the same dependence on the intermolecular distance in their leading term C_6/R^{-6}. In the paper by Doye *et al.* [269] a very interesting structural phase diagram for general LJ clusters is found, which predict that at $T = 0$ K icosahedral structures are stable up to a maximum number of particles (critical number) of about 2000. Afterwards a switch is expected to the decahedral phase and finally, to the fcc phase. RGs certainly switch at same point to the fcc symmetry as experimentally observed [258], whereas para hydrogen has been experimentally observed to form fcc or hcp crystals depending on the growing conditions [13].

For the above mentioned reasons, the icosahedral structure is also presented in the following. The formation of icosahedral clusters should not astonish for two simply reasons: all three structures, fcc, hcp and ico show the same coordination number 12 in the first shell and, moreover, the surface over volume ratio is of 5.163 against 5.7195 of the hcp or fcc first shells clusters [271]. Mackay showed in 1962 [267] that the icosahedral structures are a dense non-crystallographic packing of spheres with a very large APF. The number of spheres contained in an icosahedron, as well as the APF, changes depending on the number S of shells forming it. Each of the spheres at the vertex counts 0.20965, at the edges 0.38386

and at the faces 0.5. The number of spheres within an icosahedral shell has been calculated by Mackay to be $C_S = \frac{10}{3r^3} + 0.15183r$ and the APF to be $P_S = 0.68818 + 0.03767r^{-2}$ [267], where r is the radius of the icosahedron, that is the centre-vertex distance. Finally, the APF for the first shell is 0.72585, for the second shell already 0.69769 and decreases continuously for increasing number of shells tending to the value 0.68818, if the number of shells tends to infinity.

The regular icosahedron is formed by 20 identical equilateral triangular faces, 30 edges and 12 vertices. The Platonic body can be partitioned into 20 equal distorted tetrahedra sharing the common vertex at the center of the icosahedron. For this reason the edges are 1.05 times longer than the radius r, and the vertex-center-vertex angle is 63.43° instead of 60° (as for the regular tetrahedron), so that the spheres on the faces of the icosahedron can not be densely packed. A regular icosahedron is shown in the bottom panel of Fig. 5.16, where it is created by three concentric, mutually orthogonal golden rectangles (Paciolo construction 15th century [256]), which have a ratio between the two edges corresponding to the golden ratio, that is, if the shorter side is long a, the NNdistance, the longer side will be $a \times \frac{\sqrt{5}+1}{2}$. From this, the Cartesian coordinates of the 12 spheres at the vertices of the regular icosahedron can be easily found.

The icosahedral clusters are closely related to the fcc and hcp crystals and, in fact, each of the spheres is 12 coordinated: Those at the vertices in pentagonal pyramidal prisms (I_h icosahedral symmetry), those in the edges in anti-cuboctahedra (D_{3h} hcp symmetry) and those at the faces in cuboctahedra (O_h, fcc symmetry), where anti-cuboctahedron and cuboctahedron are the polyhedra formed by hcp and fcc complete coordination shells, respectively, as shown in the top and middle panels of Fig. 5.20 for their first coordination shells. The anti-cuboctahedra and the cuboctahedra are slightly distorted, which helps in understanding why above the critical number, icosahedral structure switch to the fcc one. The first reason is certainly the APF, but the second is that the number of sphere at the faces of the icosahedron, which are almost fcc-packed, at some point is overwhelming with respect to the others, in particular the number of vertices, which is constant from shell to shell, so that a fault in the stacking of layers parallel to the faces easily prevent the icosahedral clusters to grow further [267].

Growing Small Clusters

When growing small clusters, the aim is generally to find the global minimum structure out of the N dimensional PES. Those global minima are equilibrium structures at $T =$ 0 K and are normally considered as good starting points for the structures at higher temperatures [269]. The degree of difficulty for these global optimizations increases with the size of the clusters, N, since the number of local minima increases exponentially. Moreover, optimization of some cluster sizes may be even more difficult because of an unfavourable topography of the PES (see for example Ref. 272, 273).

In this section, small pure $(pH_2)_N$ and doped $Cl_2(pH_2)_N$ clusters are grown within a size-range from 2 to 65, and from 2 to 60 molecules, respectively. The growth process does not involve the temperature. The total binding energy was calculated by minimizing the cohesive energy of the clusters with respect the two-body distances

$$E_{\rm tot} = \min \left\{ \sum_{i=1}^{N_p-1} \sum_{j>i}^{N_p} V^{(l=0)}_{(\rm pH_2)_2}(R_{ij}) \right\} \tag{5.48}$$

and

$$E_{\rm tot} = \min \left\{ \sum_{i=2}^{N_p-1} \sum_{j>i}^{N_p} V^{(l=0)}_{(\rm pH_2)_2}(R_{ij}) + \sum_{j=2}^{N_p} V^{(l=0)}_{\rm pH_2-Cl_2}(R_{1j}, \theta_A, \phi_A) \right\} \tag{5.49}$$

for the pure and doped clusters, respectively. In Eq. 5.49 the first and second terms are respectively the sum over the solvent-solvent interactions, $E_{\rm pH_2-pH_2}$, and over the solute-solvent interactions, $E_{\rm pH_2-Cl_2}$. The interaction between each pair of pH_2 molecules in the clusters is approximated by the NWB pair potential (the pair potential from the present work had not been yet calculated, but the results are expected to be very similar), whereas for describing the interaction between each of the pH_2 molecules and the Cl_2 molecule the RA-pair potential $V^{(l=0)}_{pH_2-Cl_2}(R_{AB}, \theta_A, \phi_A)$ from the present work is used. For each cluster size many independent optimizations with random initial conditions have been run by using the TrajLab software [274], which means that, when the size of the clusters increases, the probability to get the most stable structure (i.e. the global minimum) fast decreases and the number of calculations to be performed must be notably increased. The most stable cluster configuration (or cluster isomer) of size N has been taking as starting configuration for the simulations involving the cluster with size $N+1$.

The binding energy per molecule with respect to the size N of the clusters in general decreases monotonically, that is the clusters become more stable during the growth process, but particularly drops for certain values of N, referred to as magic numbers, which are peculiar to the structures formed. For the icosahedral structure the following analytical formula, $N = \frac{1}{3}(2S+1)(5S^2+5S+3)$ with $S = 1, 2, 3, 4, \ldots$ ect. being the number of concentric icosahedra, has been found for the calculation of the magic numbers. Thus, at each of these magic numbers the clusters assume the form of an icosahedron. This formula, however, does not take into account other particularly magic numbers occurring when growing clusters and corresponding to stable substructures between two different concentric icosahedra S and $S+1$. Please note that no simple formulas have been found for the calculation of the magic numbers in the case of fcc and hcp structures, but they can be calculated by using a slightly more complicated method treated elsewhere [275].

In the following, the total binding energies (or chemical potentials) of the clusters, $E_{\mathrm{tot}}(N)$ and the "first derivative" (or incremental binding energies) $\Delta E_{\mathrm{tot}}(N) = E_{\mathrm{tot}}(N) - E_{\mathrm{tot}}(N-1)$, are listed in Tabs. 5.8 and 5.9, respectively, together with the sizes N and the corresponding point group symmetries. Moreover, the series of magic numbers, both for the pure and the doped clusters, are highlighted instead by plotting the "second derivative" of the total binding energy, $\Delta^2 E_{\mathrm{tot}}(N) = E_{\mathrm{tot}}(N-1) - 2E_{\mathrm{tot}}(N) + E_{\mathrm{tot}}(N+1)$, in the lower parts of Figs. 5.17 and 5.19, respectively. In the upper parts of the same figures the most important/symmetric cluster structures are also shown.

Pure $(pH_2)_N$ Clusters

The total binding energies, $E_{\mathrm{tot}}(N)$ of the $(pH_2)_N$ clusters shown in the first column of Tab. 5.8, decrease stepwise while the cluster size N increases. The magnitude of such steps, that is $\Delta E_{\mathrm{tot}}(N)$, when going from N to $N+1$, is not constant and present minima at $N = 7$, 13, 19, 23, 26, 29, 32, 34, 37, 41, 43, 45, ..., ect., showing that such structures are magic clusters. Moreover, next to these minima always a maximum of $\Delta E_{\mathrm{tot}}(N)$, that is at $N+1$ is found, since the next molecule is placed at the surface of a complete coordination shell, or subshell, such to have a smaller number of nearest neighbours to interact with. The magic numbers are also highlighted by plotting the "second derivative", $\Delta^2 E_{\mathrm{tot}}(N)$, in the lower part of Fig. 5.17, which, inversely to $\Delta E_{\mathrm{tot}}(N)$, shows a maximum at the magic sizes. Additionally, Tab. 5.8 also shows the corresponding symmetries of the grown clusters, some of which can be recognized in the upper part of Fig. 5.17. The two smallest clusters with sizes $N = 2$ and 3 have not been shown since they have the trivial linear and equitriangular shapes with point group symmetries $D_{\infty h}$ and D_{3h}, respectively. The first cluster visualized in panel a of Fig. 5.17 has size $N = 4$ and the shape of a tetrahedron with point group symmetry T_d. In panel b, the cluster with $N = 5$ forms a trigonal bipyramide of D_{3h} symmetry, for which, $\Delta^2 E_{\mathrm{tot}}(N)$, shows a minimum, since the two molecules above and under the triangular plane do not touch each other. The next cluster with $N = 6$ forms an octahedral and belongs therefore to the O_h point group. At $N = 7$ the second maximum of $\Delta^2 E_{\mathrm{tot}}(N)$ is reached, which together with the clusters of size $N = 19$ and 34 (panels d, j and l of Fig. 5.17, respectively) present a D_{5h} symmetry typical for some of the substructures between consecutive complete icosahedral shells. At $N = 13$ the first icosahedral shell with $S = 1$ is completed (see panel h and/or i of Fig. 5.17). This is the most stable structure (highest maximum in bottom panel of Fig. 5.17), since it has maximum APF as already mentioned in Sec. 5.3.6. The remaining clusters do not present elements of symmetry other than the identity.

The magic numbers $N = 13$, 19, 23, 26, 29, 32, 34, 37, 43, 49 highlighted by the maxima of $\Delta^2 E_{\mathrm{tot}}(N)$ in the bottom part of Fig. 5.17 are a typical series of magic clusters, which follows the growth process model made of interpenetrating icosahedron units proposed in Ref. 268. Starting from the first-shell cluster with size $N = 13$, shown in panel h and i of

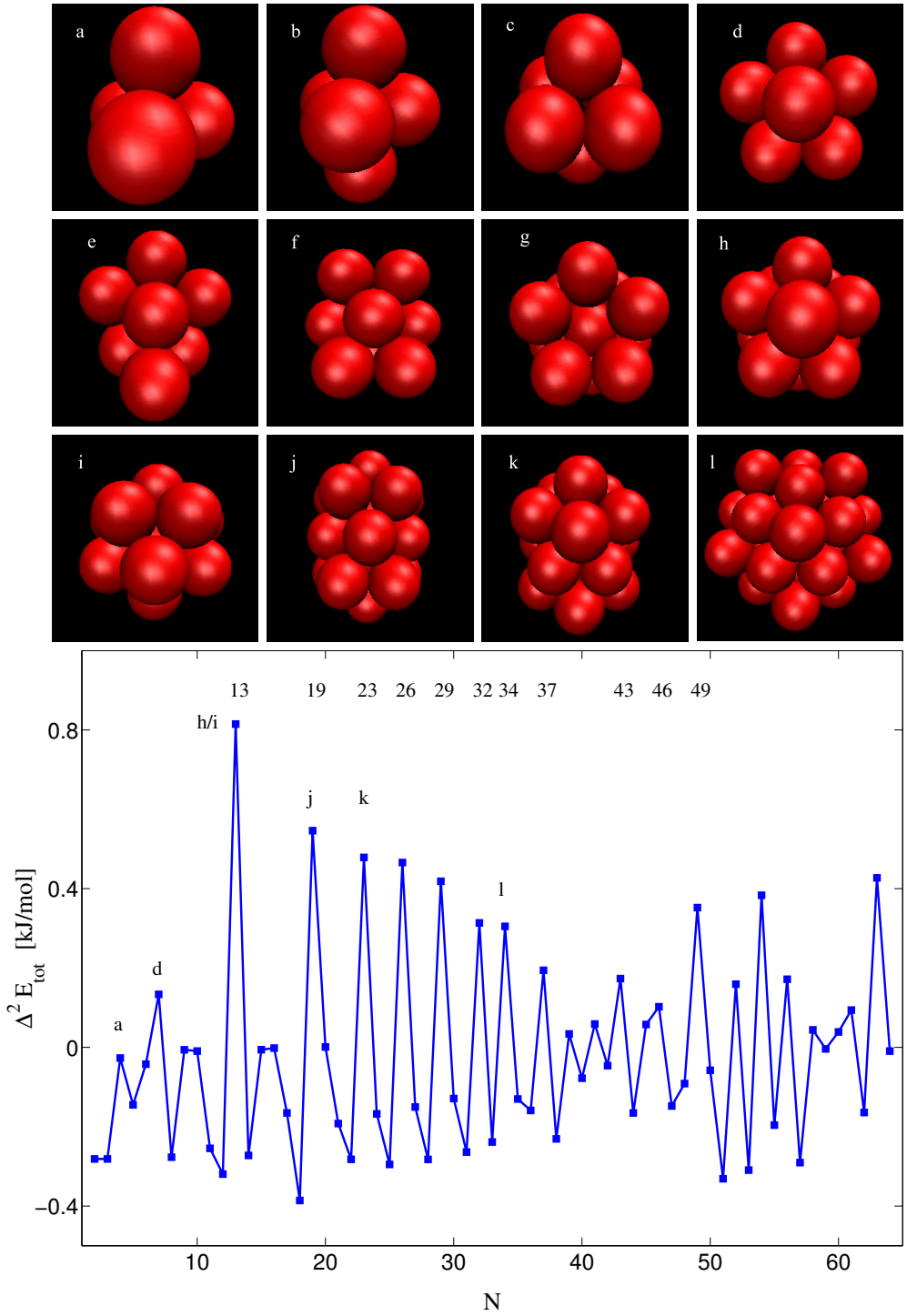

Figure 5.17: The most symmetric and/or significant cluster structures from the growing sequence with number of pH_2 molecules $N = 4, 5, 6, 7, 8, 9, 12, 13, 19, 23, 34$ are shown in the top part of the figures in panels *a-l*. In the bottom part, the "second derivative" of the cohesive energy, $\Delta^2 E_{\mathrm{tot}}(N) = E_{\mathrm{tot}}(N-1) - 2E_{\mathrm{tot}}(N) + E_{\mathrm{tot}}(N+1)$, is plotted against the cluster size N in order to discriminate particularly stable structures (maxima).

Table 5.8: The total binding energies of the pure $(pH_2)_N$ clusters obtained by using the NWB pair potential are shown together with their sizes N and their corresponding point group symmetries. Energies are given in kJ/mol.

N	$E_{tot}(N)$	$\Delta E_{tot}(N)$	Point Group	N	$E_{tot}(N)$	$\Delta E_{tot}(N)$	Point Group
1	0	–	–	33	−40.5489	−1.3478	C_1
2	−0.28132	−0.28132	$D_{\infty h}$	34	−42.1354	−1.5865	D_{5h}
3	−0.84396	−0.56264	D_{3h}	35	−43.4170	−1.2816	C_1
4	−1.68790	−0.84396	T_d	36	−44.8289	−1.4119	C_1
5	−2.55880	−0.87089	D_{3h}	37	−46.3999	−1.5710	C_1
6	−3.57470	−1.0159	O_h	38	−47.7767	−1.3768	C_1
7	−4.63310	−1.0584	D_{5h}	39	−49.3841	−1.6074	C_1
8	−5.55820	−0.92502	C_1	40	−50.9579	−1.5738	C_1
9	−6.76000	−1.2018	C_1	41	−52.6096	−1.6517	C_1
10	−7.96790	−1.2079	C_1	42	−54.2025	−1.5928	C_1
11	−9.18510	−1.2172	C_1	43	−55.8415	−1.6390	C_1
12	−10.6570	−1.4719	C_{5v}	44	−57.3072	−1.4657	C_1
13	−12.4484	−1.7914	I_h	45	−58.9382	−1.6310	C_1
14	−13.4249	−0.97653	C_1	46	−60.5116	−1.5734	C_1
15	−14.6738	−1.2489	C_1	47	−61.9827	−1.4711	C_1
16	−15.9285	−1.2547	C_1	48	−63.6015	−1.6188	C_1
17	−17.1852	−1.2567	C_1	49	−65.3117	−1.7102	C_1
18	−18.6074	−1.4222	C_1	50	−66.6696	−1.3580	C_1
19	−20.4156	−1.8082	D_{5h}	51	−68.0854	−1.4157	C_1
20	−21.6776	−1.2620	C_{2v}	52	−69.8325	−1.7471	C_1
21	−22.9387	−1.2611	C_{2v}	53	−71.4203	−1.5878	C_1
22	−24.3919	−1.4532	C_S	54	−73.3175	−1.8972	C_1
23	−26.1273	−1.7354	C_{2v}	55	−74.8314	−1.5139	C_1
24	−27.3840	−1.2567	C_1	56	−76.5415	−1.7101	C_1
25	−28.8085	−1.4245	C_1	57	−78.0800	−1.5386	C_1
26	−30.5283	−1.7198	C_{2v}	58	−79.9090	−1.8290	C_1
27	−31.7823	−1.2540	C_1	59	−81.6940	−1.7850	C_1
28	−33.1868	−1.4045	C_1	60	−83.4829	−1.7889	C_1
29	−34.8738	−1.6870	C_{2v}	61	−85.2330	−1.7500	C_1
30	−36.1422	−1.2684	C_{2v}	62	−86.8891	−1.6562	C_1
31	−37.5396	−1.3974	C_1	63	−88.7096	−1.8204	C_1
32	−39.2011	−1.6614	C_{2v}	64	−90.1028	−1.3933	C_1
–	–	–	–	65	−91.5054	−1.4026	C_1

Fig. 5.17 (top and side views, respectively), a double icosahedron (DIC) can be obtained by completing the first-shell coordination of one of the vertices. The DIC is constituted by 19 molecules, which is, indeed, the second magic number, and is shown in panel j of Fig. 5.17. The DIC is now a prolate structure of three pentagonal rings and four atoms lying on the five-fold axis (two of them being the vertices). If one now takes one of the molecules of the central ring and completes its first-shell coordination a new icosahedron interpenetrates the DIC and the new cluster has in total 23 molecules, which is the third magic number. The corresponding cluster is shown in panel k of Fig. 5.17 (top view). If the same is done for the other molecules of the same ring, e.g. the neighbouring one in clock-wise direction, only 3 more molecules are now required to complete its first-shell coordination. The new cluster has now size $N = 26$, the fourth magic number. Following the clock-wise direction the procedure can be repeated 2 more times adding always 3 molecules and a third and last time adding 2 molecules only, forming the now oblate cluster shown in panel l of Fig. 5.17 (top view), and the corresponding magic sizes are therefore 29, 32, 34 and 37. The cluster structures for $N = 43$, 46 and 49 are not shown, but they also continue the interpenetrating model just explained. Starting from $N = 50$ this pathway is lost and the next magic number 55, corresponding to the complete second icosahedral shell has been not found, at least within the number of runs simulated.

The growth process discovered in the present investigation at $T = 0$ K, is in close agreement with most of the results obtained by others theoretical groups, who use Quantum Monte Carlo methods [261–264]. A small comment is worth about the investigation by Cuervo and Roy in Ref. 265, who compared the magic number sequence obtained by using the SG and the NWB potentials finding only magic clusters with $N = 13$, 19, 23, 26, 30, 36 and $N = 13$, 26 and 33, respectively. These results are definitely in contrast to the present ones, since we found all magic clusters (except the one of size $N = 55$) by using indeed the NWB pair potential, for which they found fewer magic clusters.

As already mentioned above, the attractive part of the HFD-potentials presented along this work all present an R^{-6} dependence in their leading term. This is shared by the Lennard-Jones (LJ) potential as seen in the next equation

$$LJ(R) = 4\epsilon \left[\left(\frac{\sigma}{R} \right)^{12} - \left(\frac{\sigma}{R} \right)^{6} \right] \tag{5.50}$$

where ϵ is the depth of the potential well, σ is the distance at which the potential is zero, and R is the internuclear distance. The LJ-potential has been widely used for growing clusters, so that it could be very interesting to compare the total binding energies, $E_{\mathrm{tot}}(N)$, listed in Tab. 5.8, with those of so-called LJ-clusters. A very easy way of calculating such energies is to make use of the disconnectivity graphs [276], which have been suggested as an intuitive

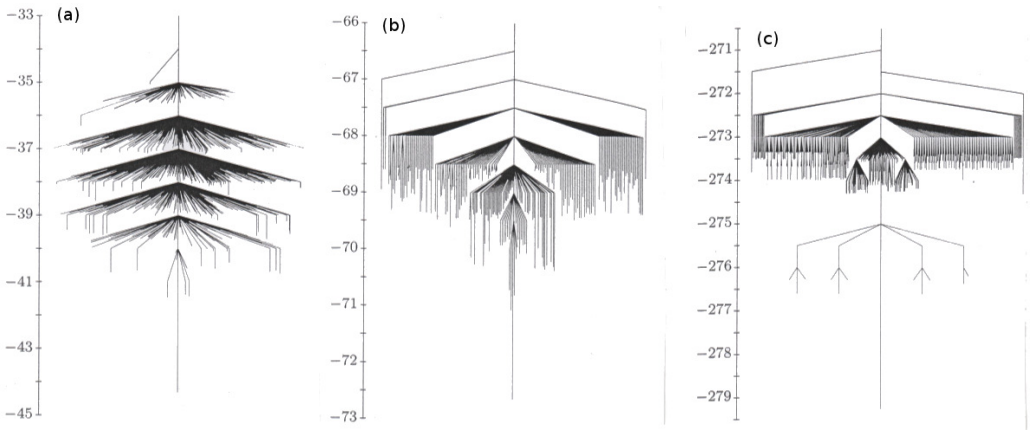

Figure 5.18: Disconnectivity graphs for (a) LJ_{13}, (b) LJ_{19} and (c) LJ_{55}. In (a) all minima are included, whereas in (b) and (c) only the branches leading to the 250 and 900 lowest minima are shown. The figures have been adapted from Ref. 276.

and simple way for visualizing multi-dimensional energy landscapes of systems in just two dimensions. The idea is to connect the local minima (isomers) and the transition states between them in a tree-like graphic. In particular, given an energy, E, the minima can be grouped in subsets, termed "superbasins", if they are mutually accessible via transition states lying below E. Two minima are instead in different superbasins if the pathway between them exceeds this energy. By raising the energy threshold, new local minima become accessible and more superbasins appear. Construction of disconnectivity graphs for LJ-clusters results in a further advantage: they can be given in units of ϵ and become independent of the molecular system under investigation, as shown in Fig. 5.18a, b and c for the LJ-clusters of size $N = 13$, 19 and 55, which have been adapted from Ref. 276. The Disconnectivity graph for the LJ-cluster of size $N = 13$ is complete and shows 1467 local minima, whereas the other two only show their lower parts. The global minimum in the first graph corresponds to the first Mackay icosahedron with 12 vertices and one particle at the center. The next three lowest isomers correspond instead to "defect" structures, where one particle is moved from the vertex to one of the three possible so-called "capping" sites, for example at one of the faces of the icosahedron. The energy gaps between the global minima and the first lowest isomers are 2.85ϵ and 2.64ϵ for the complete Mackay icosahedra at $N = 13$ and 55, which are quite large since the icosahedral structures are very stable. By taking ϵ to be the depth of the NWB potential used to grow the clusters in the present work, i.e. 0.2813 kJ/mol (see Tab. 5.7), the binding energies of the corresponding 13-, 19- and 55-LJ-clusters can be calculated from the graphs by multiplying the energy of the global minimum by ϵ. By doing so, one obtains approximately -12.52, -20.45 and -78.62 kJ/mol. The first two values are very similar to the corresponding ones in Tab. 5.8, which demonstrates that HFD-cluster closely follow the growth process of LJ-clusters. The third value instead is, as expected, in disagreement (5%), since in the present work the

global minimum structure at $N = 55$ has not been found. For the capped 55-LJ-cluster an approximate energy of -77.88 kJ/mol is expected from the disconnectivity graph in Fig. 5.18c, which is still much lower than the energies of the 55-isomers found in the present work. Nevertheless, the disconnectivity graph could be used, inversely, to predict the superbasin of belonging of our local minimum structure. In this case, its energy is divided by ϵ, and results -266.02, which is unfortunately outside of the partial graph given in Fig. 5.18c.

Doped $Cl_2(pH_2)_N$ Clusters

Similar to the growth process of the pure clusters, the total binding energies $E_{\mathrm{tot}}(N)$ of the now doped $Cl_2(pH_2)_N$ clusters also decrease in a stepwise fashion while the cluster size N increases, as shown in the fourth column of Tab. 5.9. The magnitudes of such steps, $\Delta E_{\mathrm{tot}}(N)$, are shown in the second column and define the "first derivatives" of $E_{\mathrm{tot}}(N)$, that is the gain in energetic stability when going from the N to the $N+1$ cluster. The minima of $\Delta E_{\mathrm{tot}}(N)$ show magic numbers at $N = 6, 9, 14, 18, 23, 26, 29, 31, 36, 39, 42, 46, 49, 52, 54, 57$, ..., etc., which correspond to maxima of the "second derivative", $\Delta^2 E_{\mathrm{tot}}(N)$, plotted in the lower part of Fig. 5.19. Tab. 5.9 also lists the corresponding symmetries of the grown clusters, some of which are depicted in the upper part of Fig. 5.17. The first cluster with $N = 1$ has two minima (see also PES in top Fig. 5.9): the global one has a linear (L) $C_{\infty v}$ symmetry with the only pH_2 molecule in a head-on position, and is shown in panel *a* of Fig. 5.19; the local one is instead T-shaped and has, therefore a C_{2v} symmetry (not shown). The clusters of sizes $N = 2, 3, 4$ have even three different minima, the global ones are shown in panel *b*, *c* and *d* and have $D_{\infty h}$, C_{2v} and C_{2v} symmetry, respectively. The corresponding other two isomers are obtained by moving one or both the molecules from L-position to the T-position, respectively. Thus, as long as the ring around the Cl_2-bond has less than three molecules, the head-on positions (L-shaped) are favoured with respect to the equatorial ones (T-shaped), which is a consequence of the high anisotropy of the pH_2-Cl_2 pair potential from this work, that is an appreciable energy difference between the L- and T-shape configurations (about 0.45 kJ/mol). The situation changes in panel *e* where the cluster of size $N = 5$ with C_{4v} symmetry is depicted. Since the four-fold ring is now closed, the T-configurations are stabilized and the cluster structure has only one molecule in the L-configuration. The cluster with $N = 6$ in panel *f* is an elongated octahedral of D_{4h} symmetry (a subgroup of the O_h point group) and is the first magic number of the growing sequence. The other clusters up to $N = 11$ do not present any symmetry elements, so that the cluster at $N = 9$ is not shown in Fig. 5.19, even if it is a magic number. The cluster with size $N = 14$ in panel *g* shows a distorted fcc structure with D_{4h} symmetry. This is easily recognised by comparison with the next panel *h*, where an fcc slab is depicted with the corresponding 14 solvent molecules highlighted in blue. Since the molecules of the two non-equatorial ring around Cl_2 are now the least bound,

the two structures with $N = 12$ and 13 simply have one or both the rings incomplete (not shown). Since the fcc symmetry is slightly distorted and the L-configuration has the shortest equilibrium distance, the first-shell around the Cl_2 is first complete at $N = 14$ whereas at $N = 12$ no magic cluster is found, as one would expect when considering the first coordination shell in an fcc crystal when the doping molecule occupies a single substitutional site. Moreover, no cluster structures are found for larger values of N with the impurity occupying a double substitutional site and pointing along the <001> or along another typical fcc (nor hcp) crystallographic direction. On the contrary, the fcc "cage" slightly distorts in order to better accommodate the dopant molecule, so that Cl_2 occupies a single substitutional site, as it has been correctly assumed by Manz *et al.* in Ref. 16, and after completion of the first shell, i.e. starting from $N = 15$, the growth process is dominated by the solvent-solute interactions and the new solvent molecules prefer to stack on each other forming an icosahedral phase, instead of building a second coordination shell around Cl_2, see second and third columns of Tab. 5.9. This leaves the doping molecule and the distorted fcc-structure at the surface of the larger clusters (not shown) implying an optimal shield of the Cl_2 attraction when the latter occupies a single substitutional site and points along the <001> fcc crystallographic direction, and, therefore, an energetically favourable structure.

Unfortunately, no literature has been found about Cl_2 impurity clustered by pH_2 molecules to compare with. Theoretical investigations based on Quantum Monte Carlo simulations have been carried out on $(pH_2)_N$ clusters doped by the two isotopomers, oH_2 [278] and oD_2 [279], which form icosahedral structures as in the case of pure pH_2. Clusters doped with OCS [280], CO_2 [281], CO [221] and N_2O [282] have been also studied, but the sizes only ranged between N = 1-19 depending on the molecular system considered. However, clusters doped by triatomic molecules are expected to show a different sequence of magic numbers. The system $CO(pH_2)_N$, which is already more similar to ours, even if less symmetric, has a very stable structure at the cluster size $N = 12$, for which the first shell is completed. A second less stable minimum of the cohesive energy is found at $N = 14$, but unfortunately, such structure and their symmetries are not shown.

Other cluster growth sequences to compare with are naturally doped RG systems, since they are also closed-shell systems interacting in the VDW regime. Here, results are reported for Cl_2He_N [283] and Cl_2Ar_N [284]. The Cl_2Ar_N clusters have magic numbers at $N = 8$, 11, 13, 15, 17, 21 and 23, which correspond to icosahedral structures ascribable to the corresponding pure Ar_{N+2} ones, but distorted by the presence of the dopant molecule, which occupies a double substitutional site in an icosahedral quasi-crystal, so that the first coordination shell is completed at $N = 17$, that is the DIC structure seen above in Fig. 5.17j as well as in other Dihalide-RG system as for example I_2Kr_{17} [285]. In Ref. 283, Cl_2He_N clusters are investigated, but only for $N = 1$, 6 and 20, so that no sequence of magic numbers is given. At $N = 6$, the solvent molecules form a six-fold ring around the

Table 5.9: The solvent-solvent, the solvent-solute, the total and the relative binding energies of the doped $Cl_2(pH_2)_N$ clusters are listed respectively in the second, third, fourth and fifth columns with respect to the cluster size N (first column) together with their corresponding point group symmetries (last column). Energies are given in kJ/mol.

N	$E_{pH_2-pH_2}(N)$	$E_{pH_2-Cl_2}(N)$	$E_{tot}(N)$	$\Delta E_{tot}(N)$	Point Group
0	0	0	0	–	$D_{\infty h}$
1	0	−1.8348	−1.8348	0	$C_{\infty v}$
2	−0.0025515	−3.6697	−3.6722	−1.8374	$D_{\infty h}$
3	−0.15827	−5.1047	−5.263	−1.5908	C_{2v}
4	−0.59829	−6.5383	−7.1366	−1.8736	C_{2v}
5	−1.5782	−7.5759	−9.1541	−2.0175	C_{4v}
6	−1.8806	−9.4097	−11.2903	−2.1362	D_{4h}
7	−3.1036	−9.8416	−12.9452	−1.6548	C_1
8	−3.9917	−10.7498	−14.7415	−1.7963	C_1
9	−5.1645	−11.721	−16.8855	−2.144	C_1
10	−6.5669	−12.0726	−18.6396	−1.7541	C_1
11	−7.2811	−12.9858	−20.267	−1.6274	C_1
12	−8.9206	−12.8203	−21.7409	−1.4739	C_1
13	−9.8726	−13.38	−23.2525	−1.5116	C_1
14	−10.7965	−14.0878	−24.8843	−1.6318	D_{4h}
15	−12.0532	−14.1284	−26.1816	−1.2973	C_1
16	−13.3159	−14.1721	−27.488	−1.3064	C_1
17	−15.0961	−13.6872	−28.7833	−1.2953	C_1
18	−16.3639	−13.969	−30.3329	−1.5497	C_1
19	−17.5407	−14.2601	−31.8008	−1.4679	C_1
20	−18.8106	−14.4474	−33.258	−1.4571	C_1
21	−20.0558	−14.6482	−34.7039	−1.4459	C_1
22	−21.8295	−14.4352	−36.2647	−1.5608	C_1
23	−23.0247	−14.7403	−37.765	−1.5003	C_1
24	−24.4706	−14.7019	−39.1725	−1.4075	C_1
25	−25.902	−14.7571	−40.6591	−1.4865	C_1
26	−27.5675	−14.7677	−42.3352	−1.6761	C_1
27	−28.9619	−14.7776	−43.7395	−1.4043	C_1
28	−30.4867	−14.8117	−45.2984	−1.5589	C_1
29	−32.0854	−14.8225	−46.9078	−1.6094	C_1
30	−33.4789	−14.8936	−48.3725	−1.4647	C_1
31	−35.1684	−14.8979	−50.0663	−1.6938	C_1
32	−36.8045	−14.8427	−51.6471	−1.5808	C_1
33	−38.2205	−14.9187	−53.1392	−1.4921	C_1

continued in the next page

Table 5.10: Continued from previous page.

N	$E_{(pH_2)_2}(N)$	$E_{pH_2-Cl_2}(N)$	$E_{tot}(N)$	$\Delta E_{tot}(N)$	Point Group
34	−39.5352	−15.083	−54.6182	−1.4789	C_1
35	−40.9438	−15.2685	−56.2123	−1.5941	C_1
36	−42.5808	−15.2774	−57.8582	−1.6459	C_1
37	−44.1862	−15.1819	−59.368	−1.5099	C_1
38	−45.2277	−15.7158	−60.9435	−1.5755	C_1
39	−47.0886	−15.6055	−62.6942	−1.7506	C_1
40	−48.4195	−15.5693	−63.9888	−1.2947	C_1
41	−49.9658	−15.4471	−65.4129	−1.424	C_1
42	−51.6973	−15.37	−67.0673	−1.6544	C_1
43	−53.141	−15.437	−68.578	−1.5106	C_1
44	−54.7321	−15.487	−70.219	−1.6411	C_1
45	−56.3826	−15.5769	−71.9595	−1.7405	C_1
46	−58.2686	−15.5434	−73.812	−1.8525	C_1
47	−60.1383	−15.1796	−75.3178	−1.5058	C_1
48	−61.8862	−14.948	−76.8342	−1.5164	C_1
49	−63.5199	−14.9582	−78.4781	−1.6439	C_1
50	−65.1236	−14.9749	−80.0986	−1.6204	C_1
51	−66.9477	−14.9362	−81.8839	−1.7854	C_1
52	−67.9766	−15.6279	−83.6045	−1.7206	C_1
53	−69.5734	−15.678	−85.2514	−1.6469	C_1
54	−71.7259	−15.1743	−86.9002	−1.6488	C_1
55	−73.2058	−15.2122	−88.418	−1.5178	C_1
56	−74.3714	−15.4815	−89.8529	−1.4349	C_1
57	−76.351	−15.5547	−91.9057	−2.0528	C_1
58	−78.1162	−15.5193	−93.6355	−1.7297	C_1
59	−79.5479	−15.6229	−95.1708	−1.5353	C_1
60	−81.4042	−15.4162	−96.8204	−1.6496	C_1

Cl_2 bond. A six-fold ring structure is also found for OCS embedded in liquid ^{4}He droplets with a complete first shell at $N = 17$ in Ref. 286. The OCS-He and Cl_2-He pair potentials present indeed similar anisotropies [286].

Since the optimized growth sequences for the Cl_2He_N, Cl_2Ar_N and $Cl_2(pH_2)_N$ systems are based on two-body interactions, a further comparison shall focus on the equilibrium distance and on the energetics, that is the well depth, of the solvent-solvent and solvent-solute pair potentials listed in Tab. 5.11. The solute-solvent PESs for the three systems have a similar topography, since all present one global and one local minimum in the L- and T-shaped configurations, respectively. Let us now define a new quantity for measuring

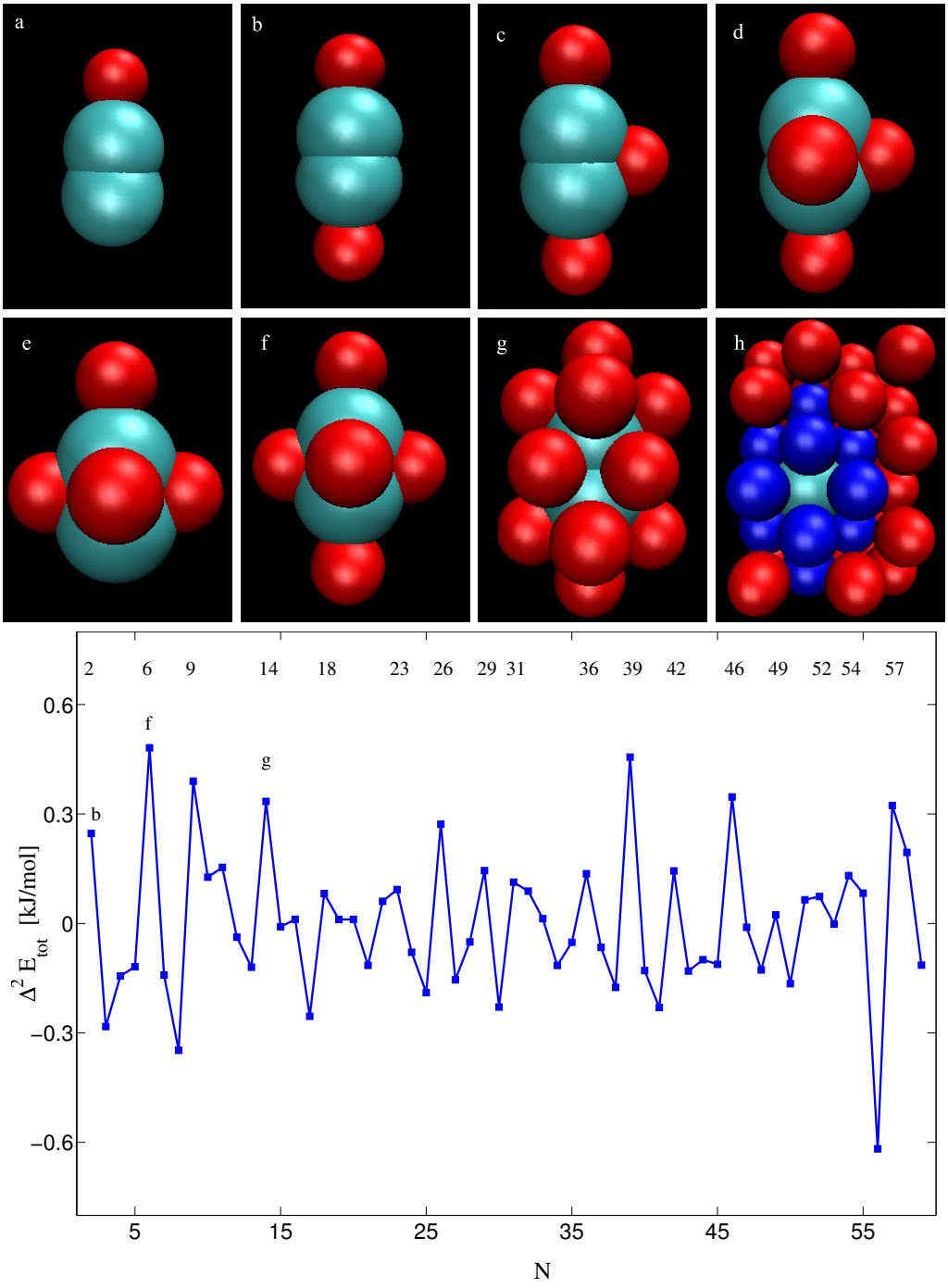

Figure 5.19: The most symmetric and/or significant $Cl_2(pH_2)_N$ cluster structures from the growing sequence with number of pH_2 molecules $N = 1, 2, 3, 4, 5, 6, 14$ are shown in the top part of the figures in panels *a*-*g*. Panel *h* depicts a small slab of fcc crystal, where the blue spheres correspond to the pH_2 molecules in panel *g*. In the bottom part, the second derivative of the cohesive energy, $\Delta^2 E_{tot}(N) = E_{tot}(N-1) - 2E_{tot}(N) + E_{tot}(N+1)$, is plotted against the cluster size N in order to discriminate particularly stable structures (maxima).

Table 5.11: The equilibrium distances and the respective well depths of the He-He, $(pH_2)_2$, Ar-Ar, He-Cl_2, pH_2-Cl_2 and Ar-Cl_2 pair potentials are compared. For the mixed pair potential the energy difference between the L- and T-shape minima relative to their mean energy is also given as a measure of anisotropy. All entries are given in nm and kJ/mol.

Pair Potential	R_{eq}(nm)	D_e(kJ/mol)	$\frac{2\Delta_{L-T}}{E^L+E^T}$
He-He [277]	0.296	0.090	–
$(pH_2)_2$	0.344	0.281	–
Ar-Ar [120]	0.374	1.190	–
He-$Cl_2^{(L)}$ [254]	0.420	0.481	0.076
He-$Cl_2^{(T)}$ [254]	0.345	0.446	
pH_2-$Cl_2^{(L)}$	0.405	1.879	0.280
pH_2-$Cl_2^{(T)}$	0.242	1.417	
Ar-$Cl_2^{(L)}$ [254]	0.447	2.573	0.013
Ar-$Cl_2^{(T)}$ [254]	0.374	2.540	

their relative anisotropy as follows:

$$A = \frac{2\Delta_{L-T}}{E^L + E^T} \tag{5.51}$$

where $\Delta_{L-T} = E^L - E^T$ is the absolute energy differences between the global and local minima, i.e. 0.4621, 0.035 and 0.033 kJ/mol for the pH_2-Cl_2, He-Cl_2 and Ar-Cl_2 dimers, respectively, and $0.5(E^L + E^T)$ is in turn the corresponding mean energy. The results are listed in Tab. 5.11 and mirror the higher anisotropy of the pH_2-Cl_2 system with respect to the RG ones. Thus, the preference in occupying the head-on positions in the $Cl_2(pH_2)_N$ growing sequence and the in contrast formation of the six-fold ring in the $Cl_2(He)_6$ cluster are a consequence of the different anisotropies in the pair potentials. This is further confirmed in [254], where it is stated that, even if the linear minimum of the He-Cl_2 PES is deeper, experiments show that the T-shape configuration is favoured because of the ZPE

energies associated with the minima. Finally, the formation of the six-fold ring around the Cl_2 bond is instead related to the shorter He-He equilibrium distance.

The second interesting feature is the relation between the solvent-solute and the solvent-solvent pair potential well depths, which strongly influences the growth processes. In the pH_2-Cl_2 and He-Cl_2 systems their ratio is about 5, whereas in the Ar-Cl_2 system the ratio is circa 2 (with respect to the T-shape configuration), which could explain why the Ar-Cl_{2N} clusters form icosahedral structures, that is the growing sequence is dominated by the solvent-solvent interaction already from the beginning.

Finally, it seems counter-intuitive that the Ar atoms form a five-fold ring around the Cl_2, whereas in the present work the ring is four-fold, even if the equilibrium distance is larger for the Ar-Ar system than for the $(pH_2)_2$. However, this proves that both the energetics and the equilibrium distances play a role in growing process of cluster systems and the Ar prefers a growing process based on icosahedral structures because of five-fold rings.

First-Shell Clusters

On the way to build the infinite crystal, pure and doped first-shell clusters are investigated in order to disclose the energetics of fcc, hcp and icosahedral structures when imposing those symmetries onto the clusters. For this purpose cohesive energies are calculated as a function of the NNd and compared. First-shell clusters represent the closest environment to the solvent or the solute in the crystal. They are responsible for the most part of its cohesive energy (per molecule) and strongly influence the growth process of the crystal in the first stages when surface effects play a dominant role. In fact, whereas the central molecule is 12 coordinated, the surface coordination number is always smaller. Thus, it is interesting to guess to which of the closest packed crystal structures the pure cluster may switch because of the missing translational symmetry in the icosahedral quasi-crystals. Even more interesting are the first-shell doped clusters, since they can be seen as the precursors of larger rigid crystals in contrast to the optimized cluster structures which can be seen as distorted local symmetries induced by an impurity in a non-rigid lattice (as for example translational quantum crystals) of different global symmetry. Actually, in Sec. 5.3.8 rotational and translational DOFs of solvent and solute are investigated in the matrix and the first two shells (see Fig. 5.24) around them will be relaxed so that such local distorted symmetries may occur.

The first coordination shells of fcc, hcp and icosahedral symmetry are all constituted by 12 molecules. They differ just in how those molecules are distributed in the space, as shown in Fig. 5.20. They form three solid polyhedra: the anti-cuboctahedron (hcp), the cuboctahedron (fcc) and the icosahedron (ico), respectively from the top. The Miller indices,

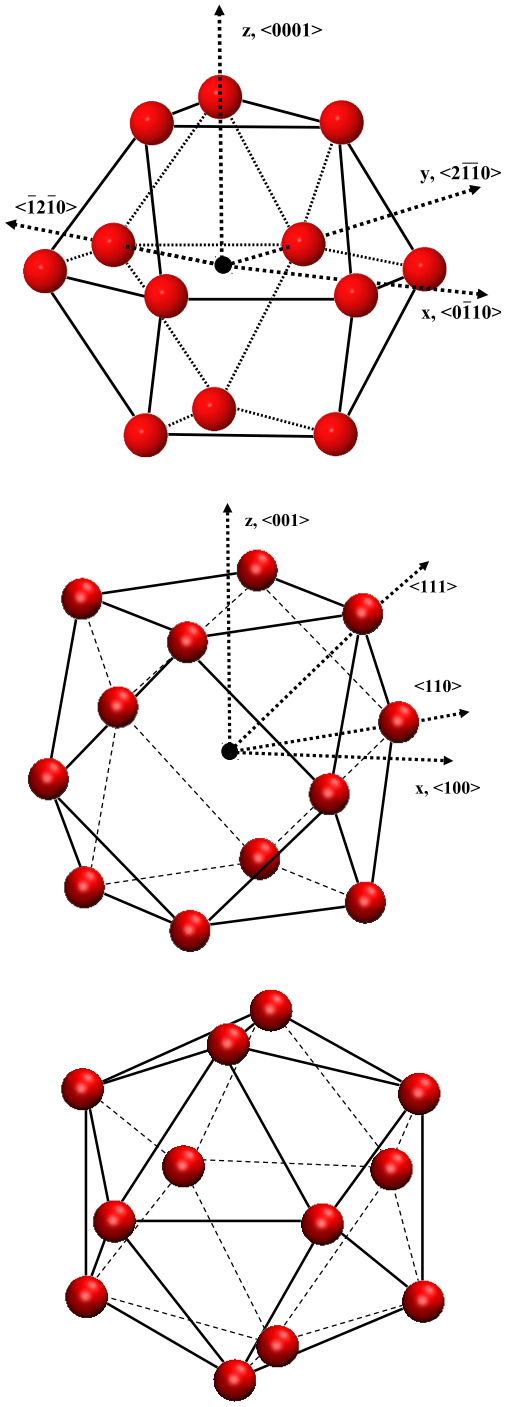

Figure 5.20: The first-shell of nearest-neighbour molecules for the hcp (top), fcc (middle) crystals and for the icosahedral structure (bottom) are shown. All of them are formed by 12 molecules placed at the vertices of three regular platonic polyhedra, the anti-cuboctahedron, the cuboctahedron and the icosahedron, respectively. The Miller indices [287] are also shown.

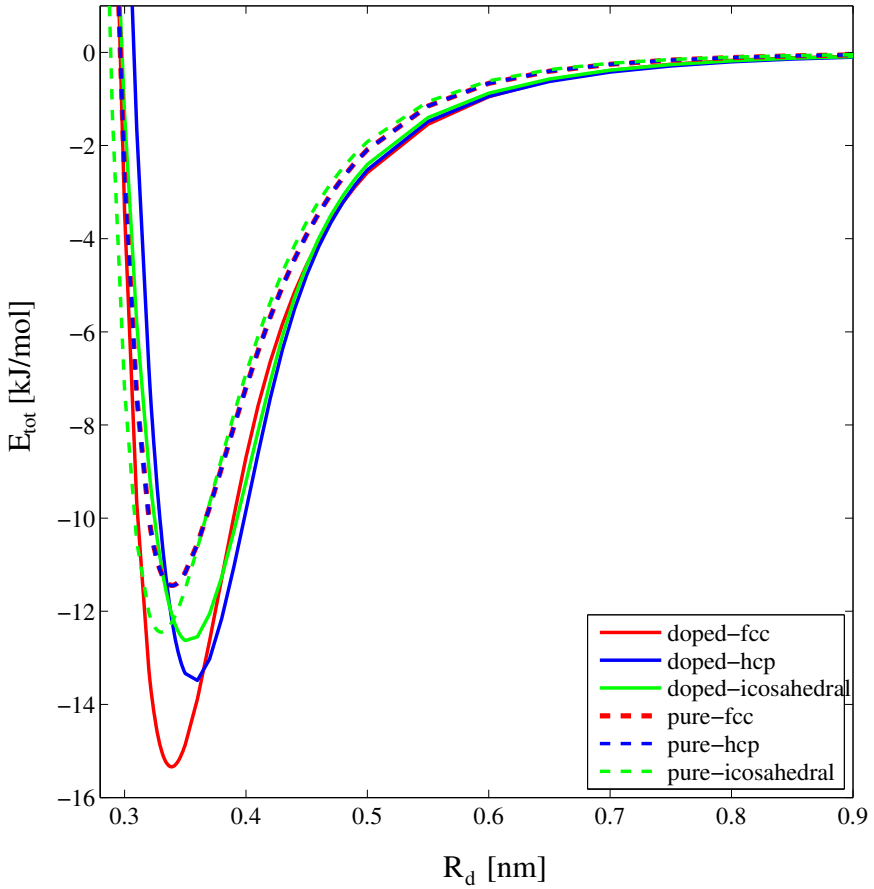

Figure 5.21: The total energies, $E_{\mathrm{tot}}(R_d)$ and $E_{\mathrm{tot}}(R_d, \theta_A, \phi_A)$ in Eqs. 5.52 and 5.53, respectively of pure and doped first shell clusters with fcc (red curve), hcp (blue curve) and ico (green curve) symmetry, are plotted with respect to the NNdistance, R_d.

which define the crystallographic directions of Bravais lattices are also given (however not for ico)[6].

The binding energies of the clusters have been calculated as the sum of the contributions of all distinct pairs for the pure and doped first-shell clusters, respectively:

$$E_{\mathrm{tot}}(R_d) = \sum_{i=1}^{N_p-1} \sum_{j>i}^{N_p} V_{(\mathrm{pH_2})_2}^{(l=0)}(R_{ij}; R_d) \tag{5.52}$$

[6]Please note that when using the Miller indices for the crystallographic directions, the convention is to indicate sets of equivalent directions [hkl] by <hkl>, whereas sets of equivalent plane (hkl) are indicate by curly brackets {hkl}. Moreover, for the hcp lattice it is possible to use four Miller indices <hkil>, as in the present work. For the equivalence to the three indices convention please refer to [287].

Table 5.12: Nearest-neighbour equilibrium distances, R_d^{min} and the corresponding binding energies, E_{tot} of pure $(pH_2)_{13}$ and doped $Cl_2(pH_2)_{12}$ clusters with fcc, hcp and icosahedral symmetries are listed. All entries are given in nm and kJ/mol.

Molecular System	Symmetry	R_d^{min}(nm)	$E_{tot}(R_d)$(kJ/mol)
$(pH_2)_{13}$	fcc	0.339	−11.44
	hcp	0.339	−11.45
	ico	0.330/0.3465	−12.45
Molecular System	Symmetry	R_d^{min}(nm)	$E_{tot}(R_d, \theta_A, \phi_A)$(kJ/mol)
$Cl_2(pH_2)_{12}$	fcc	0.339	−15.34
	hcp	0.360	−13.49
	ico	0.350/0.3675	−12.63

and

$$E_{\text{tot}}(R_d, \theta_A, \phi_A) = \sum_{i=2}^{N_p-1} \sum_{j>i}^{N_p} V^{(l=0)}_{(\text{pH}_2)_2}(R_{ij}; R_d) + \sum_{j=2}^{N_p} V^{(l=0)}_{\text{pH}_2-\text{Cl}_2}(R_{1j}; R_d, \theta_A, \phi_A) \qquad (5.53)$$

which is the usual formula for calculating the cohesive energy of a crystal with N_p particles at their lattice positions, $\vec{R}_i$, with $\vec{R}_i$ depending on the Nearest-Neighbour (NN) distance, R_d. R_d is changed from 0.25 to 0.9 nm and the resulting curves are shown in Fig. 5.21. All curves tend to zero at their asymptotic limits, since the interaction energy vanishes, when the molecules are taken apart. In the case of the pure $(pH_2)_{13}$ clusters, the hcp and fcc structures present nearly identical curves (dashed blue and red lines), since the two clusters count the same numbers of NN interactions: 12 between the central molecule and those of the shell and 24 between these latter ones, which correspond to the number of edges of the cuboctahedron and of the anti-cuboctahedron (see Fig. 5.21). Thus, they present almost the same binding energies, -11.44 and -11.45 kJ/mol for fcc and hcp, respectively, at the minimum of the curves with NNd, $R_d^{min} = 0.339$ nm, as shown in Tab. 5.12. This is not surprising, since the two polyhedra are interchangeable just by halving the polyhedron with a plane parallel to one of the triangular faces and rejoining them after rotation of 60° [267]. The icosahedral structure is the most stable in the case of pure first-shell clusters, since the icosahedron possesses now 30 edges, and the molecules at the surface are therefore 5,

instead of 4 coordinated as in the two previous polyhedra (see also Tab. 5.8). Its energy at the minimum of the green dashed line is -12.45 kJ/mol and has the same energy as the optimized $(pH_2)_{13}$ cluster structure in Fig. 5.17*h* and 5.17*i*, see Tab. 5.8. It must be recalled, however, that the distance between the molecules at the surface is 1.05 times the NNd, $R_d^{\min} = 0.330$ (center-vertex distance), which increases the weight of surface effects for larger crystals (see also Sec. 5.3.6). Finally, large icosahedral cluster may switch either to an hcp or an fcc structure confirming the many experimental founding of pure hcp, fcc or mixed hcp/fcc hydrogen crystals [13].

The total binding energy of the doped first-shell clusters strongly depend on the orientation of the Cl_2 molecule inside the cluster. Since the growth sequence in the previous section brought to a complete first coordination shell with a distorted fcc symmetry with the Cl_2 oriented along the z-direction, that is the <001> crystallographic direction, the calculations have been limited to this direction. The direction of the impurity in the hcp crystal is arbitrarily chosen to be also the z-direction, that is the <0001> crystallographic direction. Finally, in the case of the icosahedral quasi-crystal, the Cl_2 molecule lies along one of the C_5 symmetry axis. Later in Sec. 5.3.8 the rotational DOF of the Cl_2 in the crystal is going to be studied giving more insights about the relative distribution function of Cl_2 along the crystallographic directions. Relatively to the z-direction, the Cl_2-doped first-shell clusters favour the fcc structure with a binding energy of -15.34 kJ/mol at the bottom of the solid red curve with $R_d^{\min} = 0.339$ nm. This cohesive energy rather deviate from the energy of the $Cl_2(pH_2)_{12}$ in Tab. 5.9 because of the imposed fcc symmetry. In fact, the optimized cluster $Cl_2(pH_2)_{14}$ in Fig. 5.19*g* presents an elongated D_{4h} symmetry instead of O_h. Please note, however, that the pure and doped first-shell cluster in Fig. 5.21 present the same NNds at the bottom of the fcc curves (solid and dotted red curves) with $R_d^{\min} = 0.339$ nm, which means that the Cl_2 molecules has enough space to accommodate in the single substitutional site, so that the deviation from the fcc symmetry disclosed for the optimized $Cl_2(pH_2)_{14}$ cluster exclusively depend on the anisotropy of the Cl_2-pH_2 pair potential, i.e. $R_{\text{eq}}^{(T)} < R_d^{\min} < R_{\text{eq}}^{(L)}$. The icosahedral structure is the least stable (solid green line) with an energy of -12.63 kJ/mol at $R_d^{\min} = 0.350$ nm, which is slightly larger than in the pure cluster meaning that the cluster need to expand to accommodate the impurity. The hcp curve lies energetically in between the other two curves and has the largest NNd, $R_d^{\min} = 0.360$ nm, so that again the cluster need to expand to leave place to the Cl_2 molecule, at least when directed along the z-direction.

5.3.7 Simulation Boxes for fcc and hcp Crystals

In this section, the sizes of the simulation boxes for the hcp and fcc crystals are converged by calculating the cohesive energy per molecule with respect to the number of primitive cells, n_c, in each direction, hence, with respect to the number of molecules N_p constituting the box. Since a primitive cell contains 4 molecules, the total number of molecules in the

simulation box is simply $N_p = 4 \times (n_c)^3$. The cohesive energy per molecule is calculated by dividing the total binding energy $E_{\mathrm{tot}}(R_d)$ from Eqs. 5.52 and 5.53 by the total number of molecules, N_p.

$$E_{\mathrm{c}}(R_d) = \frac{E_{\mathrm{tot}}(R_d)}{N_p} \tag{5.54}$$

for the pure and doped crystals. The subscript c stays for classical and its meaning will become clear at the end of this section. Periodic boundary conditions are applied onto the simulation boxes, which practically corresponds to modelling the crystal by the infinite repetition of a small part of it. This small part is normally taken to be a slab of lattice for which the central particle feel no surface effects. Since all other particles in this slab still suffer surface effects, the minimum image convention is additionally applied, which is a stratagem ensuring that each molecule in the simulation box should feel the same environment as it would be at the center. This is achieved by letting each individual particle in the lattice slab interact with the closest image of the remaining particles in one of the repeated neighbour slabs. Periodic boundary conditions is only applicable to Bravais lattices, so that it was not used for the icosahedral quasi-crystal. Upon application of the minimum image convention Eq. 5.54 can be rewritten respectively for the pure and doped crystals as

$$E_{\mathrm{c}}(R_d) = \sum_{j=2}^{N_p} V^{(l=0)}_{(\mathrm{pH_2})_2}(R_{1j}; R_d) \tag{5.55}$$

where the molecule number 1 is always the central molecule, and

$$E_{\mathrm{c}}(R_d, \theta_A, \phi_A) = \frac{N_p - 1}{N_p} \sum_{j=2}^{N_p} V^{(l=0)}_{(\mathrm{pH_2})_2}(R_{1j}; R_d) + \frac{1}{N_p} \sum_{j=2}^{N_p} V^{(l=0)}_{\mathrm{pH_2-Cl_2}}(R_{1j}; R_d, \theta_A, \phi_A) \tag{5.56}$$

with $\theta_A = \phi_A = 0°$ independently of the crystal symmetry considered.

The results of the convergences of the simulation boxes made of pure pH_2 and doped Cl_2@pH_2 crystal are shown in Figs. 5.22 and 5.23, respectively, and are practically identical. The top panels show the crystal cohesive energy per molecule with respect to the NNd. The fcc and hcp crystals are constituted by 4000 molecules ($n_c = 10$) and the ico quasi-crystal by 3870 molecules (10 concentric icosahedral shells). Because of the surface effects the icosahedral quasi-crystal has the lowest cohesive energy per molecule. The fcc and hcp crystals show almost identical curves. At $N_p = 4000$, the cohesive energy per molecule of pure pH_2 fcc and hcp crystals are approximately -2.36 kJ/mol, which is slightly above

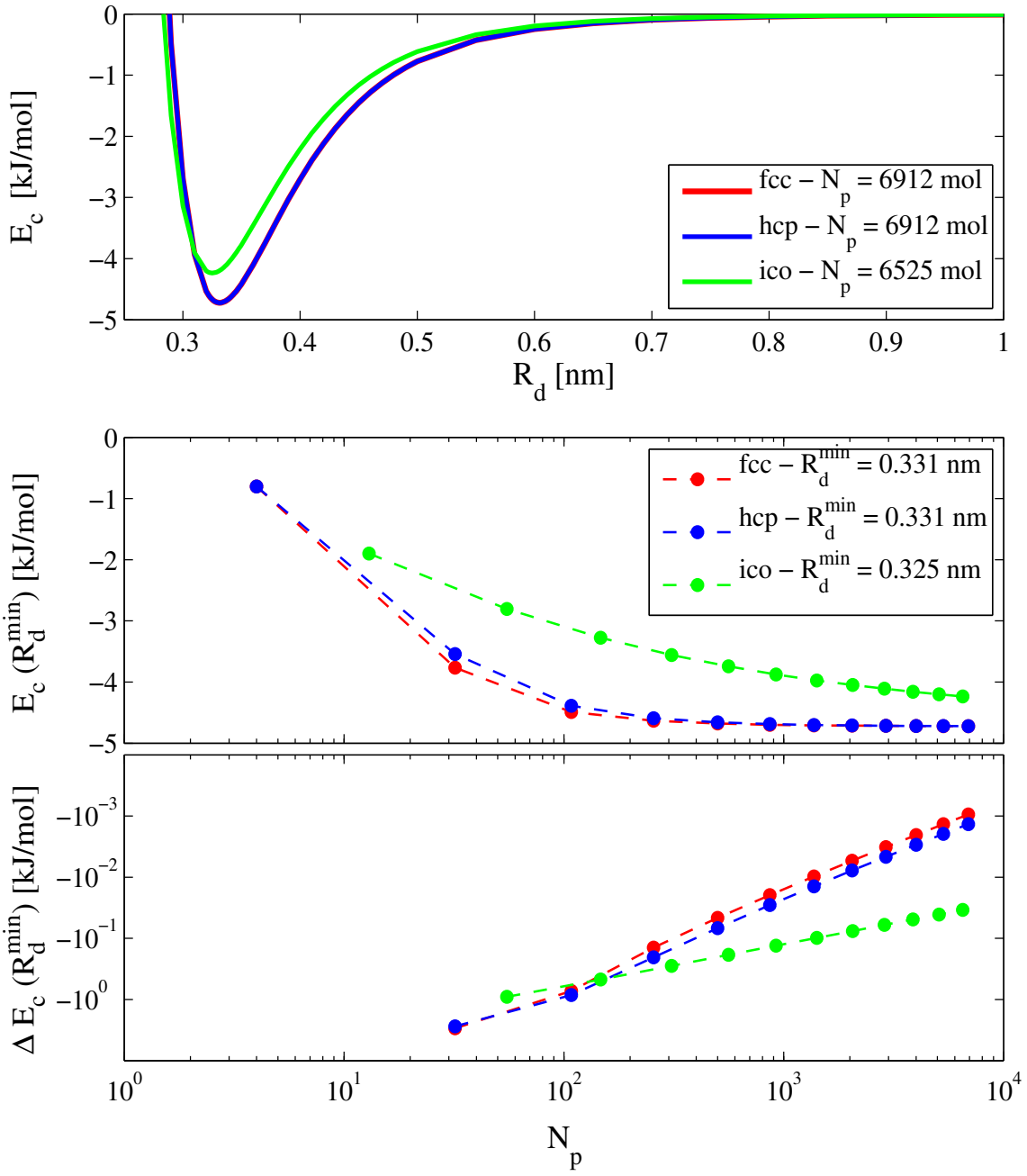

Figure 5.22: The cohesive energies per molecule, $E_c(R_d)$, from Eq. 5.55 is converged with respect to the magnitude of the simulation boxes, i.e. the number of molecules, N_p, constituting the pH_2-pure crystals with fcc (blue curves), hcp (red curves) and ico (green curves) symmetries. The top panel shows the cohesive energies vs the NNdistance, R_d, for a simulation box made of $n_c = 10$ primitive cells per direction. The middle panel shows the convergence of the cohesive energies at the minimum NNdistance, R_d^{min}, from the top panel vs N_p. The bottom panel shows the changes in the cohesive energies when increasing the magnitude of the simulation box, i.e. of number of primitive cells per direction, n_c, by steps of one unit.

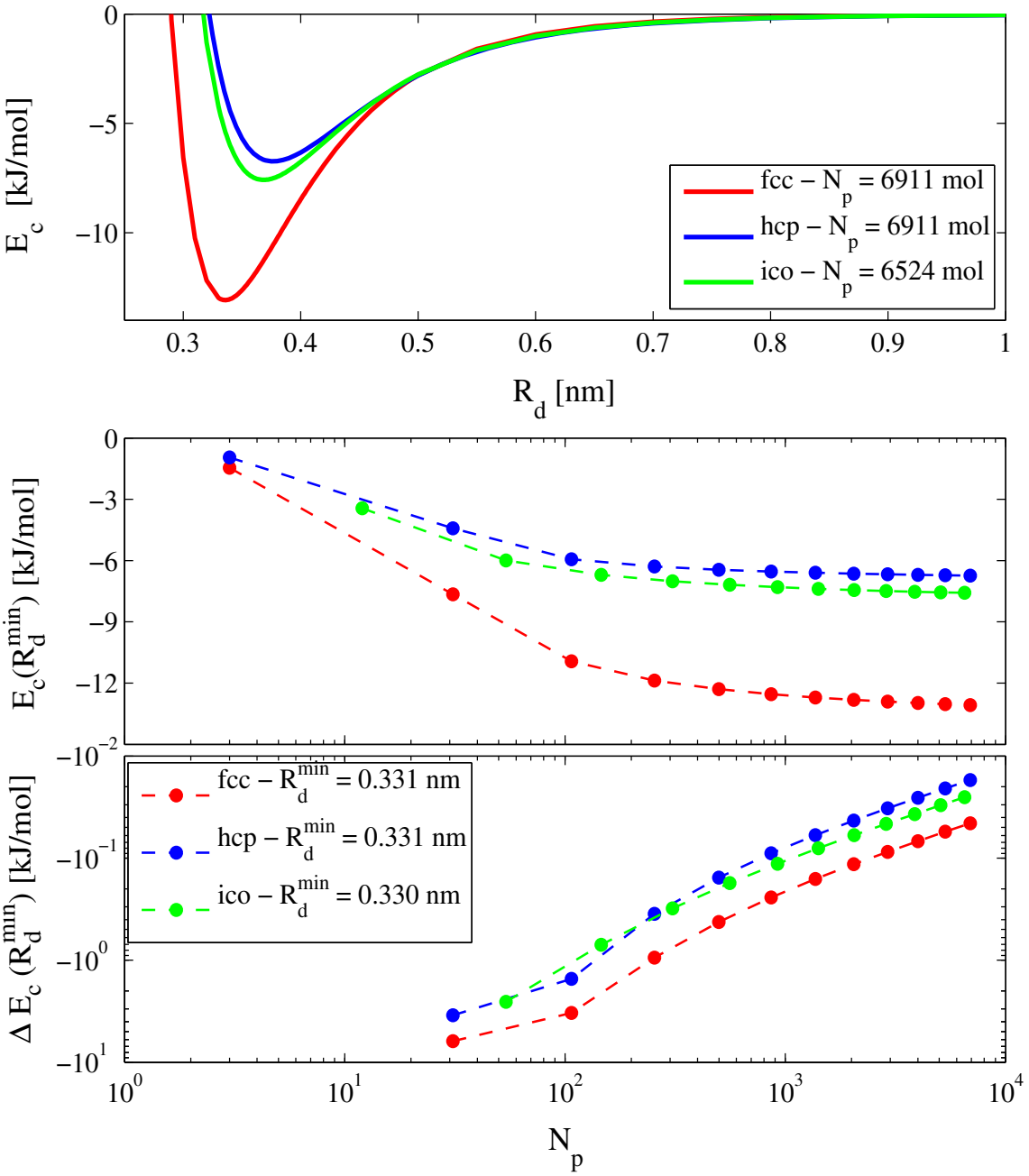

Figure 5.23: The cohesive energies per molecule, $E_c(R_d, \theta_A, \phi_A)$ from Eq. 5.56 is converged with respect to the magnitude of the simulation boxes, i.e. the number of molecules, N_p, constituting the Cl_2-doped crystals with fcc (blue curves), hcp (red curves) and ico (green curves) symmetries. The top panel shows the cohesive energies vs the NNdistance, R_d, for a simulation box made of $n_c = 10$ primitive cells per direction. The middle panel shows the convergence of the cohesive energies at the minimum NNdistance, R_d^{min}, from the top panel vs N_p. The bottom panel shows the changes in the cohesive energies increasing the magnitude of the simulation box, i.e. the number of primitive cells per direction, n_c, by steps of one unit.

Table 5.13: Nearest-neighbour equilibrium distances, $R_d^{\min}$ and corresponding cohesive energies per molecule, $E_c(R_d^{\min})$, and $E_c(R_d^{\min}, \theta_A, \phi_A)$ from Eqs. 5.55 and 5.56, respectively, of the pure pH_2 and doped $Cl_2@pH_2$ crystals with fcc, hcp and quasi-crystal with icosahedral symmetries are listed for $N_p = 4000$. All entries are given in nm and kJ/mol.

Molecular System	Symmetry	$R_d^{\min}$ [nm]	$E_c(R_d^{\text{eq}})$ [kJ/mol]
Pure pH_2	fcc	0.331	−2.36
	hcp	0.331	−2.36
	ico	0.325	−2.08
Molecular System	Symmetry	$R_d^{\min}$ [nm]	$E_c(R_d^{\text{eq}}, \theta_A, \phi_A)$ [kJ/mol]
Doped $Cl_2@pH_2$	fcc	0.331	−2.36
	hcp	0.331	−2.36
	ico	0.330	−2.07

the value expected when using the LJ-potential, that is 8.6ϵ [288]. If $\epsilon = 0.2813$ kJ/mol, i.e. the well depth of the NWB pair potential used for converging the simulation boxes, the expected cohesive energy per molecule would in fact be -2.42 kJ/mol. In the middle panels of Figs. 5.22 and 5.23 the crystal cohesive energy per molecule is now calculated by stepwise varying the crystal size, but fixing the NNd at the fixed value $R_d^{\min}$ for which the total energy of the crystal is minimized. At each step, n_c is increased by one, so that the N_p increases from $4 \times n_c^3$ to $4 \times (n_c + 1)^3$. Thus, when the cohesive energy per molecule becomes constant with respect to the crystal size, the simulation box converges, since the interaction between each molecule and the most distant ones becomes negligible. The hcp and fcc simulation boxes, when using the minimum image convention, converge faster than the icosahedral quasi-crystal, which instead suffers the surface effects, and the cohesive energy per molecule becomes almost constant for a crystal made of 4000 molecules with $n_c = 10$. This can be better seen in the bottom panels, where the changes of the cohesive energy per molecule is plotted again the crystal size. When increasing the crystal size from $n_c = 9$ to the $n_c = 10$, the change in the energy is about or even less than 1 J/mol depending on the crystal symmetry considered. Please note that the convergence of the $Cl_2@pH_2$ simulation boxes again assumes the impurity to be directed along the z-

direction for the fcc and hcp crystals and along the C_5 symmetry axis for the icosahedral quasi-crystal, as in the first-shell cluster calculations in the previous section.

The minimum of the cohesive energy per molecule for both the fcc and hcp crystal is found at the NN equilibrium distance $R_d^{\min} = 0.331$ nm, which does not fit the experimentally measured value $R_{\exp} = 0.378$ nm. Similarly, the cohesive energy per molecule $E_c(R_d^{\min}) = -2.36$ kJ/mol is more than thrice the sublimation energy value of 0.74 kJ/mol measured from experiment [289]. This is due to the strong quantum effects, which make the theoretical treatment of solid hydrogen more elaborate than that of RG crystals. Our model so far do not account for the large Zero-Point Energy (ZPE), which covers up to two thirds of the classical cohesive energy $E_c(R_d^{\min})$, confirming a rather large quantum effect.

In the next section, the EM will be applied with the aim of including the ZPE and calculating the corresponding translational wavefunctions both for a pH_2 and a Cl_2 molecule in the matrix. Summation of the ZPE to the classically calculated cohesive energies, is expected eventually to predict the experimental NNd, $R_{\exp}$, and the correct sublimation energy, E_s. Additionally, within the multi-stage adiabatic separation, the ZPEs will be later compared to the rotational energies of the pH_2 and Cl_2 molecules in order to discuss whether the rotational and translational DOFs may be, or to which degree, separable.

5.3.8 Translational and Rotational DOFs

The study of the Cl_2@pH_2 system involved so far many approximations. In the first step, the low temperature of liquid Helium ensured the safe separation of the electronic DOFs of solute and solvent from the other DOFs. In the subsequent step, where internal (vibrational) and external (rotational and translational) DOFs are separated, it is assumed that only the vibrational ground states of the two molecules are populated and, moreover, that the coupling to the rotations is negligible. It must be mentioned that this last assumption based either on the gas-phase diatomic constants or on the pair potentials calculated above, is in turn transferred to the solid-phase, which is indeed a multi-body problem, so that they have to be thoroughly considered. The internal and external DOFs of Cl_2, for example, can be safely separated on the base of gas-phase diatomic constants, since the spacing between the two first vibrational levels is three order of magnitude larger than the one between the first rotational states (see Tab. 5.1), but the situation could drastically change in the solid-phase, since the dopant is expected to show a hindered rotation or even a libration. Thus, vibrations are first neglected, but will be discussed *a posteriori* in the next sections after a model is applied for the calculation of the Cl_2 rotational/librational energy levels in the crystal. The energy difference between the first two vibrational levels of H_2 is only one order of magnitude larger than the one between the first two rotational levels in the gas-phase. The situation is expected to hold also in the solid-phase, since the narrow vibrational potential is not expected to undergo drastic changes and the rotational states are practically undistorted as we learnt from the pair potentials. Thus, conclusions

are now transferred to the solid-phase, a many-body interactions problem, on the base of just pair interactions. This is justified in the case of Cl_2, since the solvent-dopant potential describes the distortions suffered by each of the solvent molecule in the vicinity of the impurity, which, in the spirit of the pair interaction approximation, largely conserves additivity. This is not true for the $(pH_2)_2$ potential, since it describes the interaction between two individual solvent molecules, even though in the crystal each of them is actually interacting with 12 nearest-neighbours at the same time. Thus, the true distortion of the rotational levels is probably more than twelve time the distortion undergone under the presence of only one solvent molecule (less additivity), e.g. the terms of order $N > 2$ in the many-body expansion of Eq. 5.1 becomes more important. Finally, the couplings of the solvent rotations to Cl_2 internal vibrations is neglected, which introduces an error in the RA pH_2-Cl_2 pair potential with an upper limit of 8% in the linear configuration when the solvent molecules lie along the Cl_2 bond (head-on), see Sec. 5.3.4. For the same reasons just discussed, these last conclusions based on pair potentials are again safely transferred to the solid-phase.

Once the internal DOFs are adiabatically separated, still all possible non-adiabatic couplings between translational and rotational DOFs has to be disclosed. From now on, the models applied serve for the calculation of rotational and translational energy levels of molecules embedded in the crystal, so that all conclusions refer to the solid-phase. Those models suffer from the same range of errors just discussed, i.e. the neglect of the NACTs terms between solvent rotational and solute vibrations and of higher order terms of the many-body expansion, in particular the three-body term.

In general, rotational and translational DOFs of a molecule are separable only in the gas-phase, whereas in the solid-phase the situation is highly complicated by the non-adiabatic interactions with the matrix. The translations in the gas-phase, become external vibrations around the lattice nominal positions in the solid-phase[7]. Such vibrations can be analyzed in terms of collective motions, which give rise to phonon modes, the quantum-mechanical equivalent of classical vibrational normal mode. Phonon modes are coupled in different ways to the internal vibrational [290] and in particular to the rotational DOF [27,291–294] of the solvent as well as of the solute molecule.

Translational and rotational PESs can be explored simultaneously by rotating the test-molecule around its COM and by displacing it at the same time. This allows also for the calculation of the NACTs given in Eqs. 2.75 and 2.76 of Sec. 2.2.5. However, along this investigation the two DOFs are treated separately. On one side, the translational PES is explored along different crystallographic directions, on the other side, the rotational PES is explored for different lattice symmetries. In the limiting case of complete AS, no

[7] Please note that in the literature translations in the crystals are often synonymous to vibrations, since the molecules or atoms move back and forth from their nominal lattice positions. Recall that they have been called "external" vibrational DOFs in Chap. 2, in contrast to the "internal" vibrational DOFs.

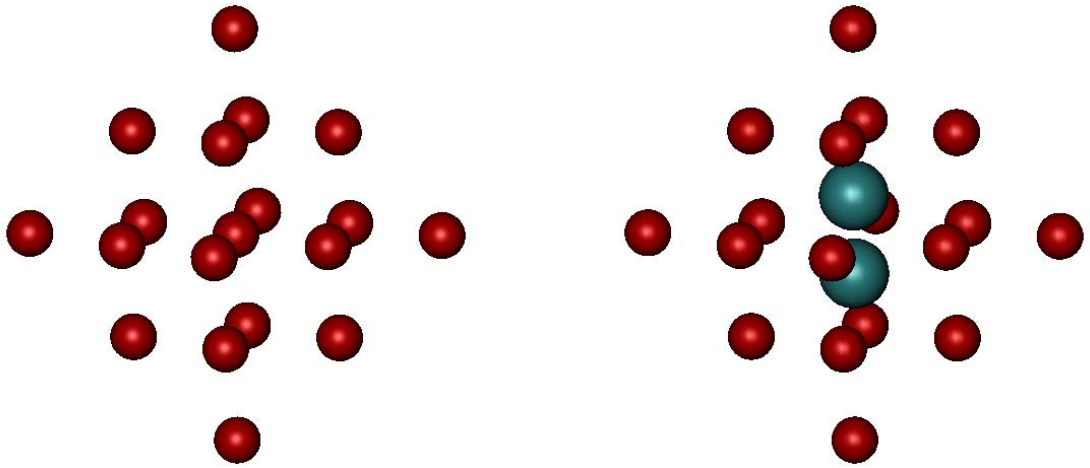

Figure 5.24: The first 12 and second 6 nearest-neighbours are shown for the pure and Cl_2-doped pH_2 crystals in the left and right panels, respectively. Their positions are optimized in the 1D and 3D non-rigid EMs.

dependence of the translational energy levels on the rotational DOFs, and vice versa, is expected to be observed. The individual PESs are evaluated by using the Einstein Model (EM) [173] and the Devonshire Model (DM) [174] for the translational and the rotational DOFs, respectively. In both models, the interaction potentials are calculated as the change in the crystal cohesive energy when only the central molecule in the lattice, also called test-molecule, is displaced from its nominal lattice position, or rotated around its COM fixed at its nominal lattice position, respectively, while keeping all other molecules frozen (classical treatment). Fig. 5.24 shows a pH_2 (left) and a Cl_2 (right) molecule, embedded in the nearest environment, i.e. the first two shells of pH_2 molecules in a fcc lattice. The PESs felt by the test-molecules are effective, since they account for also the anharmonicity of the system. Afterwards, they are inserted in the respective translational or rotational SEs in order to calculate the corresponding quantum states. However, this classical treatment is expected not to hold in the case of translational quantum crystals, because of the large quantum mechanical distribution functions and of the high anharmonicity due to the large amplitude of such translational motions. Moreover, the large lattice constant makes the solid hydrogen to be a spacious and soft lattice for guest molecules [6]. Experimental studies on doped para-hydrogen show indeed that the rotational parameters of doping species are typically about 90% of those in the gas phase and even less affected than in He droplets, see for example [295]. The inverse compressibility, called bulk modulus, was calculated in Ref. 176 to be 1.6 kbar at the zero-temperature limit. As an example, the experimental bulk modulus for solid Ne and Ar at 0K are 11.2 and 26.7 kbar, respectively [296].

Along this work we try to include the softness of the crystal by considering a non-rigid environment, which allows the molecules to move away from their nominal positions, but still treats them in a classical way, so that their quantum mechanical distribution functions

are still neglected. By means of an optimization routine, the lattice is relaxed around the central molecule trying to simulate the ability of the pH_2 molecules to partially adjust their positions and favourably lower the total energy of the crystal. Unfortunately, due to the computational costs of optimizing the position of the $N_p - 1$ molecules in the crystal, only the positions of the first two coordination shells are optimized for a total of 18 molecules, 12 from the first coordination shell and 6 from the second shell, whereas the remaining $N_p - 19$ molecules are still kept frozen. For the fcc lattice, the first two shells form the octahedrons depicted in Fig. 5.24.

All equations were implemented by using the TrajLab software [274], whereas the SEs are solved by using the WavePacket software [297].

Translational DOFs: The Einstein Model [173]

The harmonic EM has been proposed by Einstein in 1907 to solve the problem of specific heats of solids, which had not found adequate explanation in classical mechanics. It assumes all particles in the solids to be independent three-dimensional quantum harmonic oscillators vibrating at the same frequency, ω_j (in contrast to the Debye model, which considers instead collective phonon motions). The idea behind the EM can be easily traced back to the concept of adiabatic separation applied to the translational motions of particles in a solid. If they vibrate independently of each other, then the ZPE of a crystal within the EM is calculated just by summing over the ZPEs of the single oscillators.

This simple model has been successfully applied to rigid lattices, such as RG matrices, but fails when applied to translational quantum crystals. Therefore, the harmonic EM has been extended in order to include different properties. The 1D "anharmonic Einstein model" proposed by Manz *et al.* in Ref. 16 includes anharmonicity effects. Within this model the potential is evaluated by displacing a test-molecule away from its nominal lattice position, while all the other molecules are treated classically, that is for T = 0 K. Nevertheless, such potentials effectively include the anharmonicity of the system. The quantum mechanical character of solid hydrogen is in contrast included in the "quantum Einstein model" by Rościszewski and Paulus [237], who use a distribution function for describing the positions of the molecules in the lattice. They use the idea of the Self Consistent Field method (see Sec. 2.3.1) in order to average the effective potential over all the quantum mechanical distribution functions. However, they fit the obtained potential to an harmonic potential, so that possibly existing anharmonic contributions are cut out, which is in contrast with the argued anharmonicity of translations in quantum crystals. Unfortunately, an extension of the quantum EM to include anharmonicity corresponds to average over distribution functions others than Gaussians, which is expected to notably increase the already non negligible computational efforts of the Self Consistent method. An important property of translational quantum crystals, which has been neglected so far, is its high compressibility [176, 207], which implies a "soft" matrix. The anharmonic Einstein model

(EM) is therefore partially rethought in the present work in order to account for it. In practical terms, the first 2 coordination shells around the test-molecule, will be allowed to relax and move from their lattice nominal positions in order to simulate a less rigid environment. In this context, the model could be named "non-rigid anharmonic EM".

First we extend the 1D anharmonic EM [16] to a 3D model, here simply called rigid EM. The effective PESs are evaluated by implementing the following equation

$$V_{\mathrm{EM}}(\delta\vec{R}_A; R_d, [\theta_A, \phi_A]) = \frac{1}{2N_p} \sum_{j>1}^{N_p} V(\delta\vec{R}_A - \vec{R}_j; R_d, [\theta_A, \phi_A]) - E_{\mathrm{c}}(R_d, [\theta_A, \phi_A]) \ , \quad (5.57)$$

where, for A = Cl_2, the potential is evaluated at $\theta_A = \phi_A = 0$, independently of the crystal symmetry considered. Otherwise, if A = pH_2 (or oD_2), the parameters θ_A and ϕ_A can be just dropped, since they have already been averaged out in the calculation of the pair potential (doubly rotational adiabatization). $E_{\mathrm{c}}(R_d, [\theta_A, \phi_A])$ is the cohesive energy per molecule of the crystal before displacing the test-molecule (see Eqs. 5.55 and 5.56 in Sec. 5.3.7). In order to evaluate Eq. 5.57 the simulation box is reduced to $n_c = 3$ cells in each direction for a total number of molecules, $N_p = 4 \times 3^3 = 108$ without loss in the accuracy of the simulations, since systematic errors are cancelled out by the subtraction.

When the matrix is relaxed around the test-molecule, the model is called "non-rigid EM". Within this approach, Eq. 5.57 becomes:

$$\tilde{V}_{\mathrm{EM}}(\delta\vec{R}_A; R_d, [\theta_A, \phi_A]) = \min_{R_j \in [-C,C]} \left\{ \frac{1}{2} \sum_{j>1}^{N_p} V(\delta\vec{R}_A - \vec{R}_j; R_d, [\theta_A, \phi_A]) - \tilde{E}_{\mathrm{c}}(R_d, [\theta_A, \phi_A]) \right\} \quad (5.58)$$

where C is the maximum allowed displacement of the caging molecules away from their nominal lattice positions, used as a constraint in the optimization routine, and $\tilde{E}_{\mathrm{c}}(R_d, [\theta_A, \phi_A])$ corresponds to $E_{\mathrm{c}}(R_d, [\theta_A, \phi_A])$ in the non-rigid model, that is the cohesive energy of the crystal when keeping the central molecule at its nominal lattice position and relaxing the remaining molecules.

$$\tilde{E}_{\mathrm{c}}(R_d, [\theta_A, \phi_A]) = \min_{R_j \in [-C,C]} \left\{ \frac{1}{2} \sum_{j>1}^{N_p} V(\vec{R}_1 - \vec{R}_j; R_d, [\theta_A, \phi_A]) \right\} . \quad (5.59)$$

Within the non-rigid model the number of cells per direction of the simulation box is increased from $n_c = 3$ to 4, so that the total number of molecules becomes $N_p = 4 \times 4^3 = 256$.

By following the notation in Sec. 2.2.5, the translational SE is written as

$$\begin{aligned}(\hat{\mathbf{H}}_{\mathrm{tra}}(\nabla_{\delta\vec{R}_A}, \delta\vec{R}_A; R_d, [\theta_A, \phi_A]) \quad &- \quad E_0^{(n=v=0,\, k=0)}(R_d, [\theta_A, \phi_A])) \times \\ &\times \quad \Psi_{\mathrm{A}}^{(n=v=0,\, k=0)}(\delta\vec{R}_A; R_d, [\theta_A, \phi_A]) = 0 \ , \end{aligned} \tag{5.60}$$

For A = Cl_2, the latter equation closely resembles Eq. 2.70 except for the additional parameter R_d, which determines the positions of all molecules in the crystal and appears because the multi-stage adiabatic separation tool is now applied on the solid phase. The translational Hamiltonian is defined as

$$\hat{\mathbf{H}}_{\mathrm{tra}}(\vec{\nabla}_{\delta\vec{R}_A}, \delta\vec{R}_A; R_d, [\theta_A, \phi_A]) = -\frac{\hbar^2}{2M_{\mathrm{A}}}\Delta_{\delta\vec{R}_A} + W^{(n=v=0)}(\delta\vec{R}_A; R_d, [\theta_A, \phi_A]) \tag{5.61}$$

where the parameters $\{R_d, \theta_A, \phi_A\}$, the variable $\delta\vec{R}_A$ and the interaction potential $W^{(n=v=0)}$ $(R_d, [\theta_A, \phi_A])$ correspond respectively to the parameters $\{\theta, \phi\}$, the variable $\vec{R}_{\mathrm{tra}}$ and the potential $\hat{V}_{\mathrm{tra}}(\vec{R}_{\mathrm{tra}}; \theta, \phi) = W_{\mathrm{ext}}^{(n,v)}(\vec{R}_{\mathrm{ext}})$ in Eqs. 2.68. Finally, the potential $W^{(n=v=0)}(R_d,$ $[\theta_A, \phi_A])$ is one of the translational PESs, either $V_{\mathrm{EM}}(\delta\vec{R}_A; R_d, [\theta_A, \phi_A])$ or $\tilde{V}_{\mathrm{EM}}(\delta\vec{R}_A; R_d,$ $[\theta_A, \phi_A])$, within the rigid and non-rigid EMs, respectively, i.e. Eqs. 5.57 and 5.58.

The SE is solved in order to obtain the translational ground state wavefunctions and the corresponding probability densities

$$\rho_A^{(k=0)}(\delta\vec{R}_A; R_d, [\theta_A, \phi_A]) = |\Psi_A^{(n=v=0,\, k=0)}(\delta\vec{R}_A; R_d, [\theta_A, \phi_A])|^2 \ , \tag{5.62}$$

which are in many cases very close to Gaussian distributions and are, therefore, fitted to the following Gaussian function (in 1D)

$$\rho_A^{(k=0)}(\delta R_A; R_d, [\theta_A, \phi_A]) \quad \approx \quad N_0 \exp\left[-\left(\frac{\delta R_A}{\sigma}\right)^2\right] \ , \tag{5.63}$$

with σ always referring to the widths along the crystallographic direction of the fcc and the hcp crystals properly chosen case by case (for the Cartesian coordinates and the respective Miller indices refer to Fig. 5.20).

The ZPEs, $E_0^{(n=v=0,\, k=0)}(R_d, [\theta_A, \phi_A])$ are finally summed to the respective classically calculated cohesive energies $E_{\mathrm{c}}(R_d, [\theta_A, \phi_A])$ in order to find the ZPE-corrected interaction potential of a particle in the translational quantum crystal, namely:

$$V_{\mathrm{QM}}(R_d,[\theta_A,\phi_A]) = E_{\mathrm{c}}(R_d,[\theta_A,\phi_A]) + E_0^{(n=v=0,\,k=0)}(R_d,[\theta_A,\phi_A]) \ , \tag{5.64}$$

where QM stands for quantum mechanical. For the discussion, the following particular NNds are additionally defined: The NNd, R_{c}, at the minimum of the classical cohesive energy curve $E_{\mathrm{c}}(R_d,[\theta_A,\phi_A])$ from Eq. 5.55 and 5.56, the NNd, R_0, at the minimum of the ZPE curve $E_0^{(n=v=0,\,k=0)}(R_d,[\theta_A,\phi_A])$ from Eq. 5.60, and the quantum mechanical corrected NNd, R_{QM}, at the minimum of the effective ZPE-corrected curve $V_{\mathrm{QM}}(R_d,[\theta_A,\phi_A])$ from Eq. 5.64:

$$R_{\mathrm{c}} = \underset{R_d}{arg\ min}(E_{\mathrm{c}}(R_d,[\theta_A,\phi_A])) \ , \tag{5.65}$$

$$R_0 = \underset{R_d}{arg\ min}(E_0^{(n=v=0,\,k=0)}(R_d,[\theta_A,\phi_A])) \ , \tag{5.66}$$

$$R_{\mathrm{QM}} = \underset{R_d}{arg\ min}(V_{\mathrm{QM}}(R_d,[\theta_A,\phi_A])) \ , \tag{5.67}$$

where *arg min* defines the value of the argument at the minimum of the corresponding function. R_{QM} and $-V_{\mathrm{QM}}(R_{\mathrm{QM}})$ are directly compared to the experimental NN equilibrium distance, $R_{\mathrm{exp}} = 0.3789$ nm and $R_{\mathrm{exp}} = 0.3610$ nm, and to the sublimation energies, $E_{\mathrm{s}} = -V_{\mathrm{QM}}(R_{\mathrm{QM}}) = 0.74$ and 1.1 kJ/mol [289] for the pH_2@pH_2 and oD_2@oD_2 systems, respectively.

pH_2/oD_2 Translational Zero-Point Energies in the Matrix.
fcc rigid EM

In the one-dimensional EM proposed by Manz and coworkers, the test-molecule was displaced along the <100>, <110> and <111> crystallographic directions of an fcc-lattice. Thus, they used one-dimensional versions of Eqs. 5.57, 5.60 and 5.61 [176]. The effective potential $V_{\mathrm{EM}}(R_d)$ was calculated by using the NWB pair potential and the resulting ZPEs $E_0^{(n=v=0,\,k=0)}(R_d)$ approximated by the sum of the ZPEs along the three chosen directions:

$$E_0^{(n=v=0,\,k=0)}(R_d) \approx E_0^{(k=0)}(\mathbf{e}_1;R_d) + E_0^{(k=0)}(\mathbf{e}_2;R_d) + E_0^{(k=0)}(\mathbf{e}_3;R_d) \tag{5.68}$$

where $\mathbf{e}_1$, $\mathbf{e}_2$ and $\mathbf{e}_3$ are unit vectors along the <100>, <110> and <111> directions. Such approximation is based on the fact that along those crystallographic directions the probability distributions are nearly isotropic, that is the ZPEs depend weakly on the direction of the translations. This has been already proved in Ref. 176 to be the case within a certain range of R_d values including R_{exp}, but the ZPEs have in turn shown dependence

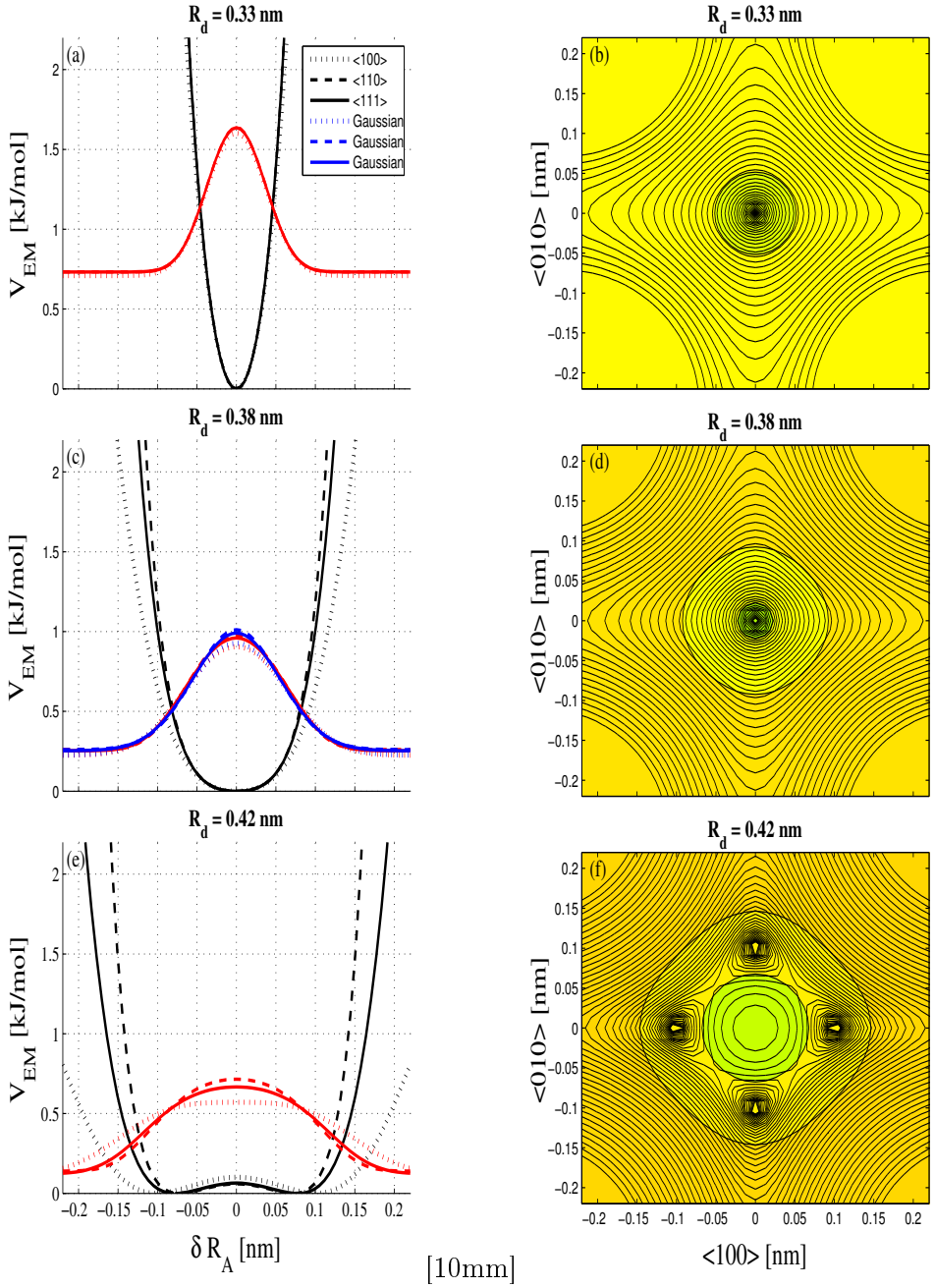

Figure 5.25: $pH_2@pH_2$ effective potentials, $V_{\rm EM}(R_d)$ in Eq. 5.57, are evaluated in the fcc crystal within the 1D rigid EM (panels (a), (c), (e)) along the $\mathbf{e}$ = <100>, <110>, <111> directions, and within the 3D rigid EM (2D cuts in panels (b), (d), (f)), along the $\{001\}$ plane at three representative NNds, $R_d = 0.33$, 0.38 and 0.42 nm (top, middle and bottom panels, respectively). Contour lines are given in a logarithmic scale by 48 steps between 0.001 and 100 kJ/mol. The corresponding ground state probability densities, $\rho_A^{(k=0)}(\delta\vec{R}_A; R_d)$ in Eq. 5.62, are superimposed. For the 1D model at the experimental NNd, $\mathrm{R}_0 = \mathrm{R}_{\rm exp} = 0.38$ nm in panel (c) the corresponding Gaussian approximations (blue curves) in Eq. 5.63 are additionally plotted.

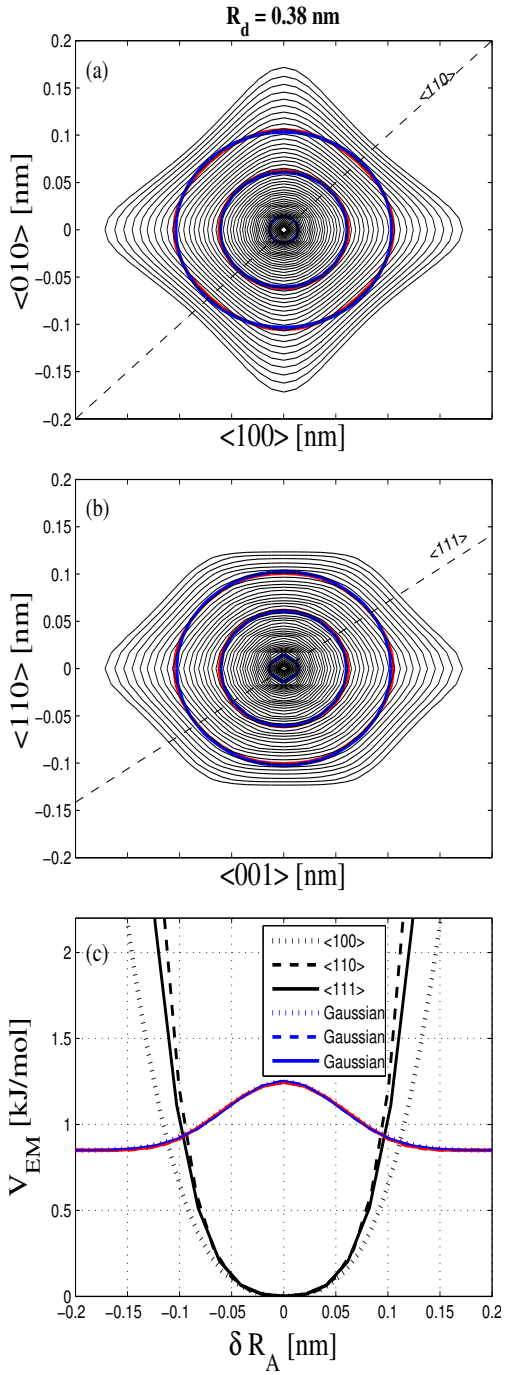

Figure 5.26: $pH_2@pH_2$ effective potentials, $V_{\mathrm{EM}}(R_d)$ in Eq. 5.57, are evaluated in the fcc crystal within the 3D rigid EM at the experimental NNd, $\mathrm{R_0} = \mathrm{R_{exp}} = 0.38$ nm. 2D cuts are plotted together with the probability densities (red curves), $\rho_A^{(k=0)}(\delta\vec{R}_A; R_d)$ in Eq. 5.62, and their approximated Gaussian functions (blue curves) in Eq. 5.63 along the {001} and {110} planes in panels (a) and (b), respectively. The 1D cuts along the <100>, <110> and <111> directions are additionally plotted in panel (c) together with their Gaussian approximations.

on the direction of displacement for larger NNds. These results are reproduced in panels (a), (c) and (e) of Fig. 5.25 and compared now to the extended three-dimensional (3D) EM in the corresponding next panels (b), (d) and (f). The 2D cuts of the 3D effective potentials $V_{\mathrm{EM}}(R_d)$ (black contour-lines) have been also obtained by using the NWB pair potential and are shown at the same three representative NNds, $R_d = 0.33$, 0.38 and 0.42 nm, respectively, in the top, middle and bottom panels. In the former case, the three one-dimensional (1D) cuts along the <100>, <110> and <111> fcc crystallographic directions are depicted, whereas in the latter 3D model, two-dimensional (2D) contour plots are shown along the {001} plane (x and y Cartesian directions defined in Fig. 5.20). Please note that due to the O_h symmetry of the fcc crystal, the (001), (100) and (010) planes are equivalent. Similarly to the 1D model, when increasing R_d from 0.30 nm to 0.42 nm, the effective potential becomes flatter (black curves), since the test-molecule has more space at disposal for translating. At the largest NNd, $R_d = 0.42$ nm, the double-well potential in panel (e) within the 1D model becomes four-well shaped in panel (f) within the 3D model. As the potential becomes flatter, the corresponding ground state probability density (PD) (red curves and green contour lines for 1D and 3D plots, respectively) broaden and the ZPE decreases. The background colour-code in panels (b), (d) and (f) corresponds to the decreasing of the ZPE when going from light to dark yellow. Only at the experimental NNd, $R_{\mathrm{exp}} = 0.38$ nm, the resulting PDs have been approximated by Gaussian distributions (see Eq. 5.63) and superimposed (blue curves) in Fig. 5.25(c) to the 1D PDs. The same is done in Figs. 5.26(a) and 5.26(b) for the 3D EM, where 2D cuts of the PDs are superimposed to their corresponding 2D Gaussian approximations, respectively along the {001} and {110} crystallographic planes. The diagonal dashed-lines in Figs. 5.26(a) and 5.26(b) indicate the <110> and the <111> directions. Finally, for better comparison with the 1D model, 1D cuts of the effective potentials and of the PDs along <100>, <110> and <111> are extracted from the 3D model and plotted in Fig. 5.26(c), the blue curves being again 1D Gaussian approximations.

In addition to the anharmonicity of the effective potentials, both the 3D and the 1D model show a notable dependence on the direction of the displacement at the largest NNd ($R_d = 0.42$ nm), where the effective potentials become double- and fourth-well shaped and the wavefunctions deviates, therefore, from Gaussian distributions. This latter case justifies the extension to an anharmonic EM. The widths of the Gaussian approximations at the experimental NNd, $R_{\mathrm{exp}} = 0.38$ nm, are listed in Tab. 5.14. The translational PDs become more similar to their Gaussian approximations, and their widths are practically independent from the crystallographic direction, in particular in the 3D EM. This is easily discovered comparing Figs. 5.25(c) and 5.26(c). In Ref. 176 the 1D Gaussian approximation is given only for the PD arithmetically averaged over the three directions, that is $\rho_{\mathrm{av}}^{(k=0)} = \frac{1}{3}\left(\rho_{<100>}^{(k=0)} + \rho_{<110>}^{(k=0)} + \rho_{<111>}^{(k=0)}\right) = 0.0876\ \mathrm{nm}^{-1}$. Thus, extension to the 3D model results in slightly narrower wavefunctions in position space and, in turn, in broader wavefunction in

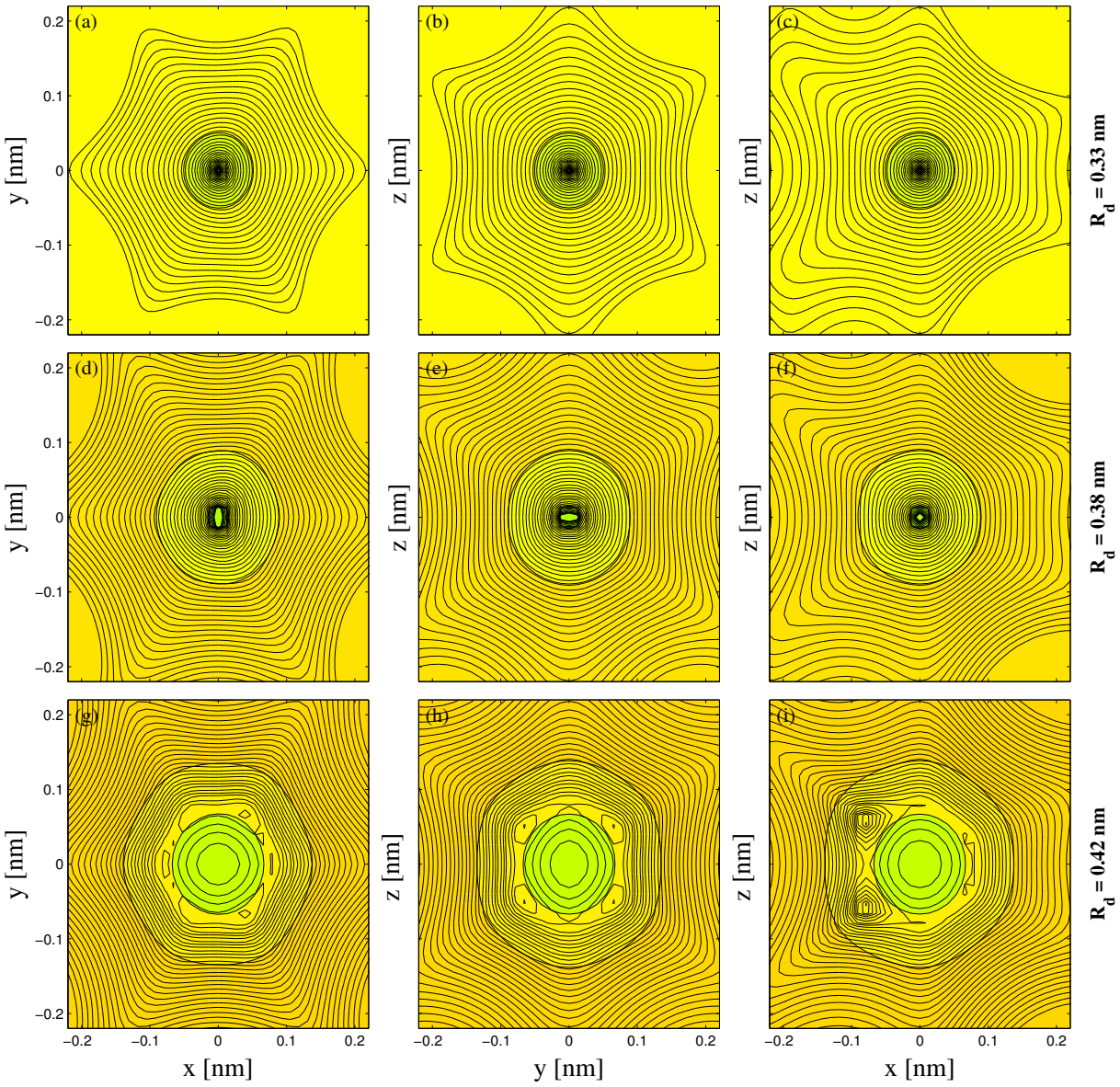

Figure 5.27: pH_2@pH_2 effective potentials, $V_{\rm EM}(R_d)$ in Eq. 5.57, are evaluated in the hcp crystal within the 3D rigid EM (2D cuts) along the xy-plane (panels (a), (d) and (g)), along the yz-plane (panels (b), (e) and (h)) and along the xz-plane (panels (c), (f) and (i)) at three representative NNds, $R_d = 0.33$, 0.38 and 0.42 nm (top, middle and bottom panels, respectively). Contour lines are given in a logarithmic scale by 48 steps between 0.001 and 100 kJ/mol. The corresponding ground state probability densities, $\rho_A^{(k=0)}(\delta\vec{R}_A; R_d)$ in Eq. 5.62, are superimposed.

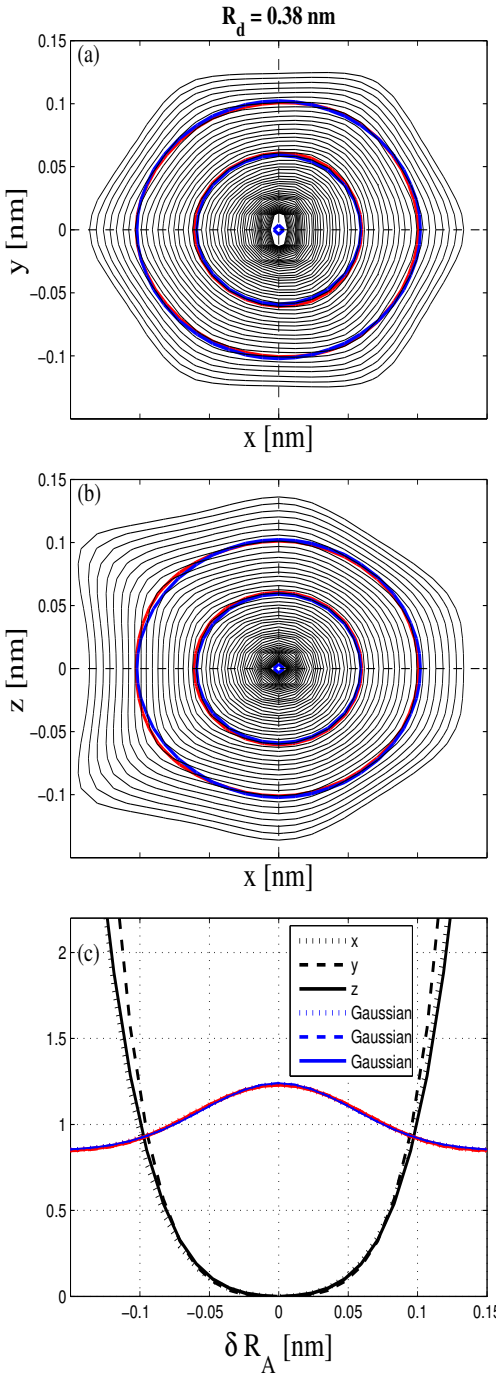

Figure 5.28: $pH_2@pH_2$ effective potentials, $V_{\rm EM}(R_d)$ in Eq. 5.57, are evaluated in the hcp crystal within the 3D rigid EM at the experimental NNd, $R_0 = R_{\rm exp} = 0.38$ nm. 2D cuts are plotted together with the probability densities (red curves), $\rho_A^{(k=0)}(\delta\vec{R}_A; R_d)$ in Eq. 5.62, and their approximated Gaussian functions (blue curves) in Eq. 5.63 along the xy and xz planes in panels (a) and (b), respectively. 1D cuts along the x, y and z directions are plotted in panel (c).

Table 5.14: The widths σ of the 1D Gaussian function defined in Eqs. 5.63 and approximated to the probability densities resulting from the 1D and 3D rigid EMs when using the $(pH_2)_2$ pair potential by NWB are listed for the fcc and hcp phases. All values are given in nm^{-1} at $R_{exp} = 0.380$ nm.

rigid Model	$\sigma^{<100>}$	$\sigma^{<110>}$	$\sigma^{<111>}$	C
1D-fcc	0.0865	0.0761	0.0788	0
3D-fcc	0.0789	0.0759	0.0763	0
non-rigid Model	$\sigma^{<100>}$	$\sigma^{<110>}$	$\sigma^{<111>}$	C
1D-fcc	0.1041	0.0849	0.0916	0.01
	0.1245	0.0918	0.1069	0.02
	0.1356	0.0983	0.1167	0.03
3D-fcc	0.0898	0.0853	0.0867	0.01
	0.0955	0.0904	0.0923	0.02
rigid Model	σ^x	σ^y	σ^z	C
3D-hcp	0.0778	0.0772	0.0775	0

momentum space, that is higher translational energies. The values of $E_0^{(n=v=0,\,k=0)}(R_{QM})$ can be compared in Tab. 5.15 both for the pH_2@pH_2 and oD_2@oD_2 systems and for both the fcc and hcp lattices, when using the $(pH_2)_2$ pair potentials of NWB, GS and from the present work. In particular, when going from the 1D to the 3D EM the ZPEs increase approximately by a 20% and 10% for the two systems, respectively, independently of the $(pH_2)_2$ pair potential used and the lattice structure considered, calling for the extension to the 3D EM. Next to the ZPEs, Tab. 5.15 additionally shows the respective values of the quantum mechanical NNd, R_{QM} (see Eq. 5.67).

hcp rigid EM

The 1D and 3D EM have also been applied to the hcp crystal. The results are presented in Figs. 5.27 and 5.28, but only for the 3D model. Since the test-molecule is displaced along the Cartesian directions x, y and z, the Miller indices are not used along this section (see

Fig. 5.20). The orthogonal x, y and z directions as well as the three xy, yz and xz planes are not equivalent as in the fcc-lattice because of the lowered symmetry. Along the xy-plane, the central molecule is at the center of the honeycomb-like hexagon typical for closed-packed lattices, which gives the regular hexagonal shapes to the effective potentials in panels (a), (d) and (g). In particular, the vertices of the hexagon correspond to displacements directed between two NNs, whereas the middle of the sides, where the potential is steeper, to displacements directed against a NN. Panels (b), (e) and (h) show the cuts along the yz-plane. The effective potential has also an hexagonal shape, but is elongated, that is shallower, along the z-direction, since the central molecule is directed against the triangular windows, whereas in the y-direction the potential is steeper, because it encounters a NN. The potential along the xz-plane in panels (c), (f) and (i) present less regular and less intuitive shapes. This irregularity is due to the fact that only two NNs lie on this plane, both in the x-positive half, where the potential is indeed steeper, whereas in the x-negative half, the NNs are all off-plane resulting in a shallower effective potential. The asymmetry of the effective potential along the x-direction is also observed in Fig. 5.28(c), where 1D cuts of the PDs at the experimental NNd, $R_{\mathrm{exp}} = 0.38$ nm, are shown together with the Gaussian approximations to them. The 2D PDs along the xy (most symmetric) and xz (least symmetric) planes are also approximated to 2D Gaussian functions and shown in Figs. 5.28(a) and 5.28(b). The resulting 1D widths have been collected in Tab. 5.14 and reveal that despite the stronger anharmonicity of the hcp effective potentials, in particular along the x-direction, the PDs are again very close to Gaussian distributions and their widths even more similar to each other, i.e. more independent from the crystallographic direction. When comparing the Gaussian widths of the two different lattice structures, fcc and hcp, one sees that the 3D wavefunctions are, very similar, as expected on the base of the environment felt by the test-molecule, which is identical for the first coordination shell.

The $V_{\mathrm{QM}}(R_d)$ (green-), $E_{\mathrm{c}}(R_d)$ (red-) and $E_0^{(n=v=0,\,k=0)}(R_d)$ (blue-)curves are shown together in Figs. 5.29 and 5.30, respectively for the pH_2@pH_2 and oD_2@oD_2 systems. The red curve is the same in all panels, since the classical cohesive energy is obtained using the NWB pair potential, which describes both the $(pH_2)_2$ and $(oD_2)_2$ interactions. $R_{\mathrm{c}} = 0.331$ nm, is highlighted by the X-marker on the red curves. In contrast, $E_0^{(n=v=0,\,k=0)}(R_d)$ and $V_{\mathrm{QM}}(R_d)$ depends on the mass and on the EM used. R_{QM} and $V_{\mathrm{QM}}(R_{\mathrm{QM}})$ are highlighted by the X-mark on the green curves and their numerical values listed in Tab. 5.15. The dot-mark shows the $V_{\mathrm{QM}}(R_{\mathrm{QM}})$ value obtained in Ref. 237 (only for the pH_2@pH_2 system) by using the quantum Einstein. Their R_{QM} value is only 0.6% shorter than the experimental one, but the sublimation energy, E_{s} is underestimated by about 26%. Finally, the cross-mark shows the experimental NNd, R_{exp}, and sublimation energy, E_{s}, given in Ref. 289. By using the 3D EM we found $R_{\mathrm{QM}} = 0.381/0.381$ nm and $0.363/0.362$ (fcc/hcp), which are only 0.5% longer than the experimental ones, and sublimation energies, $-V_{\mathrm{QM}}(R_{\mathrm{QM}})$ of about 0.85 and 1.2 kJ/mol which are only 12% and 8.3% larger than the experimental

values for the $pH_2@pH_2$ and $oD_2@oD_2$ systems, respectively. Finally, our 3D anharmonic EM reduces the classical cohesive energies by 64% and 49%, respectively and comes very close to the experimental values.

These results are in very good agreement with the experiments. Thus, in spite of all approximations introduced so far, as for example the omission of the three-body interactions, but in particular the classical treatment of the remaining N_p-1 molecules in the lattice, the three-dimensional extended rigid EM works well for translational quantum crystals. Since the quantum EM in Ref. 237 averages the effective potential over all quantum mechanical positions of the neighbouring molecules (within a cutoff distance of 1 nm), but neglects anharmonicity, by fitting the potential to a harmonic form, the two model are in some sense complementary. Unfortunately a combination of them, even if theoretical possible, is expected to be very expensive from the computational point of view, since the calculation of the effective potential within the quantum EM would involve the solution of complicated three-dimensional integrals, which in the harmonic model have been evaluated analytically.

fcc non-rigid EM

In order to calculate the ZPEs within the non-rigid EM, an optimization procedure is carried out by stepwise increasing the constraint C in Eqs. 5.58 and 5.59, which is the maximal change allowed to the three components of the displacement vectors of each molecule, so that the absolute value of the displacement vector can be larger than C. At each step the constraint C is increased by 0.01 nm and the geometries optimized in the previous step are taken as starting point and further optimized in the next step. Thus the 18^3-dimensional optimization procedure is subdivided in smaller sub-tasks diminishing the risk of remaining trapped in a local minimum. Moreover, from one step to the next, one can monitor the degree of relaxation around the central molecule until in principle the global minimum is reached and the displacements from the nominal lattice positions converge to a maximum value.

First the 1D non-rigid EM is applied. The results are presented in Fig. 5.31. In panels (a), (d) and (g) the first two solvation shells are allowed to move not more than $C = 0.01$ nm away from their position. In panels (b), (e) and (h) the constraint is enlarged to $C = 0.02$ nm and, finally, in panels (c), (f) and (i) to $C = 0.03$ nm. In the three top panels, when going from $C = 0.01$ to 0.03 nm, no significant changes are observed in the effective potentials, since the crystal is so densely packed, that the relaxation process easily converges. At the experimental NNd, R_d =0.38 nm, comparing additionally Fig. 5.25(c) ($C = 0$ nm) to Figs. 5.31(d), 5.31(e) and 5.31(f), one observes the effective potential cuts become less repulsive and the wavefunctions broader. Please note that the barrier forming the double-well effective potential appears at shorter NNds with respect to the rigid EM, since the first two solvation shells can now adjust their position creating the condition for the minimum configuration at larger displacements, δR_A. Thus, the effective potentials become double- or even quadruple-well shaped already at shorter NNds. However, as long

Table 5.15: The NNds, R_{QM} (see Eq. 5.67) and the ZPEs, $E_0^{(n=v=0,\,k=0)}(R_{\mathrm{exp}})$ and $E_0^{(n=v=0,\,k=0)}(R_{\mathrm{QM}})$, of the pH_2 and oD_2 within the 1D and 3D rigid and non-rigid EMs are compared for both the fcc and hcp lattices using the $(pH_2)_2$ potentials by NWB, GS and from the present work. $R_{\mathrm{exp}} = 0.380$ nm. Energies are given in kJ/mol.

pH_2							
Pair Pot.	Lattice	$1D+1D+1D$			$3D$		
		rigid EM					
		$E_0(R_{\mathrm{QM}})$	$E_0(R_{\mathrm{exp}})$	R_{QM}	$E_0(R_{\mathrm{QM}})$	$E_0(R_{\mathrm{exp}})$	R_{QM}
NWB	fcc	0.637	0.777	0.386	0.828	0.888	0.381
	hcp	0.694	0.813	0.384	0.838	0.885	0.381
SG	fcc	0.605	0.771	0.387	0.798	0.879	0.383
	hcp	0.667	0.806	0.386	0.807	0.876	0.382
Present Work	fcc	0.587	0.858	0.392	0.785	0.974	0.388
	hcp	0.640	0.895	0.391	0.901	0.970	0.387
		non-rigid EM					
NWB	fcc (C=0.01)	0.472	0.588	0.384	0.773	0.665	0.373
	fcc (C=0.02)	0.498	0.507	0.358	0.745	0.618	0.369
oD_2							
Pair Pot.	Lattice	$1D+1D+1D$			$3D$		
		rigid EM					
NWB	fcc	0.741	0.732	0.364	0.818	0.792	0.363
	hcp	0.762	0.751	0.364	0.817	0.788	0.362
SG	fcc	0.719	0.723	0.364	0.793	0.782	0.363
	hcp	0.738	0.741	0.364	0.793	0.778	0.363
Present Work	fcc	0.718	0.816	0.369	0.801	0.876	0.368
	hcp	0.739	0.836	0.369	0.801	0.872	0.368
		non-rigid EM					
NWB	fcc (C=0.01)	0.731	0.584	0.354	0.806	0.4637	0.353
	fcc (C=0.02)	0.681	0.565	0.356	0.750	0.576	0.353

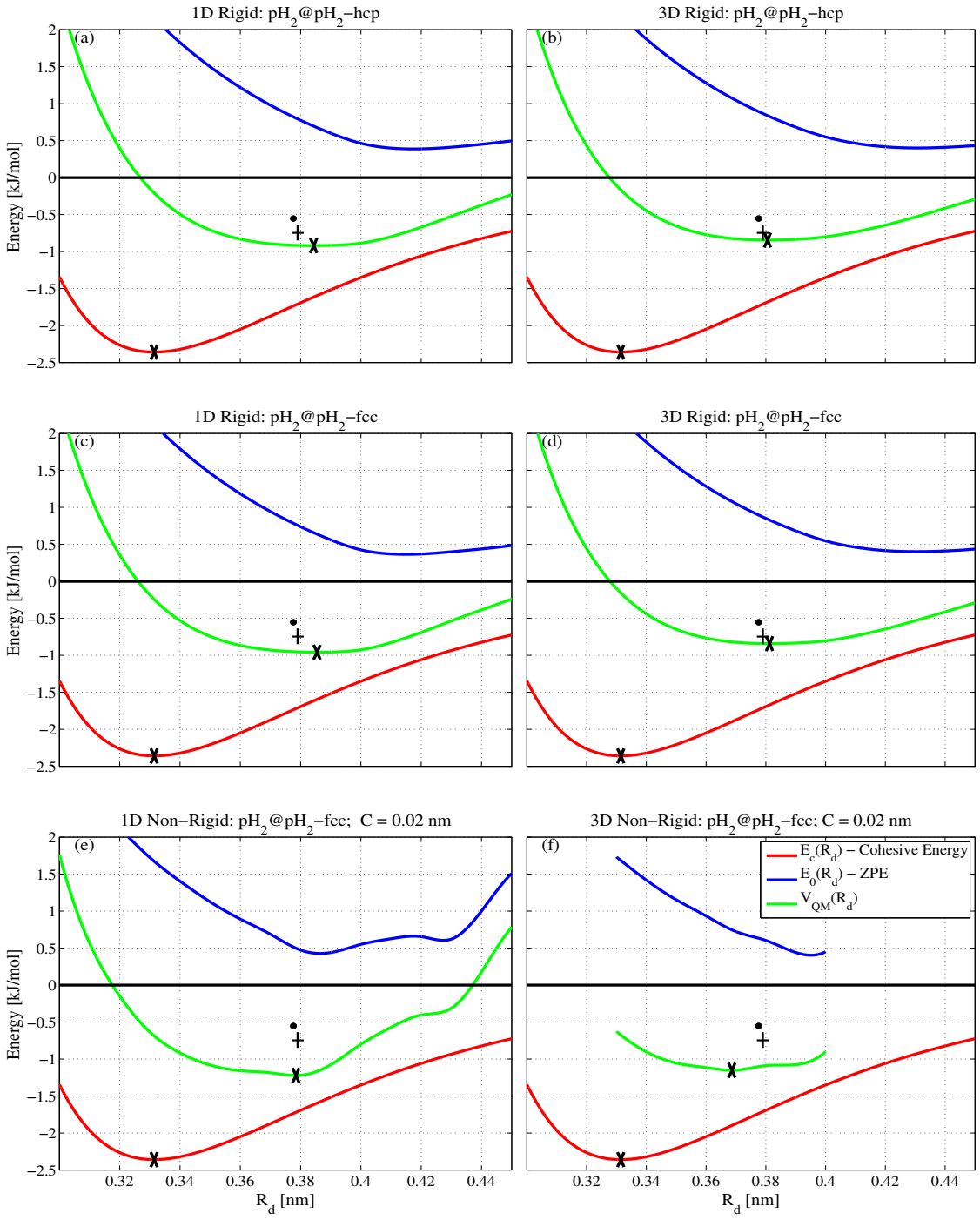

Figure 5.29: The $pH_2@pH_2$ cohesive energy, $E_c(R_d)$ (red curve) in Eq. 5.55, the ZPE, $E_0^{(n=v=0,\,k=0)}(R_d)$ (blue curve) in Eq. 5.60, and the ZPE-corrected interaction potential, $V_{\rm QM}(R_d)$ (green curve) in Eq. 5.64, evaluated in the hcp crystal within the 1D and 3D rigid EMs (panels (a) and (b), respectively), the 1D and 3D rigid and non-rigid EMs (panels (c), (d), (e), (f), respectively) using the $(pH_2)_2$ potentials by NWB are depicted in the range of $R_d = 0.30 - 0.45$ nm.

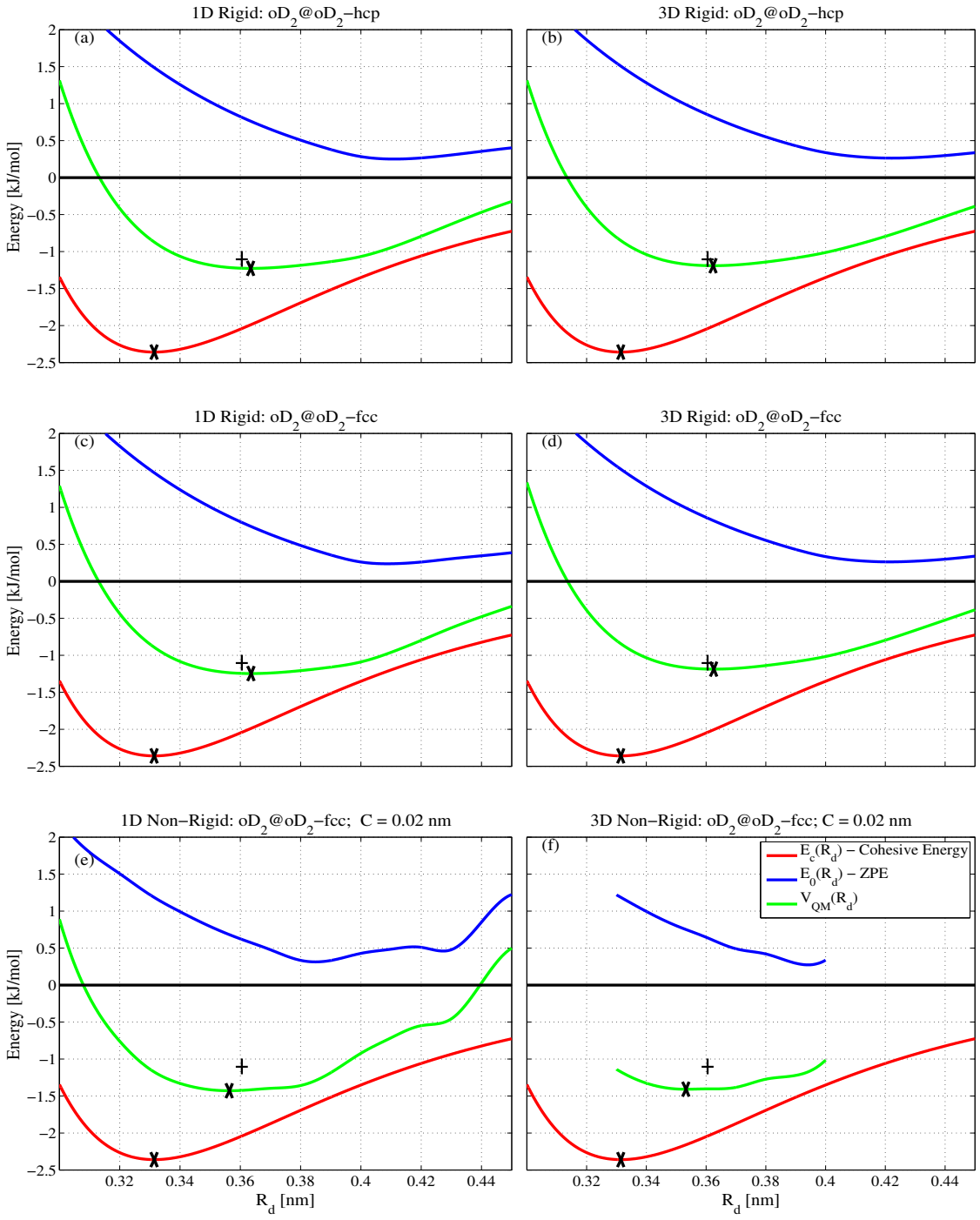

Figure 5.30: The $oD_2@oD_2$ cohesive energy, $E_c(R_d)$ (red curve) in Eq. 5.55, the ZPE, $E_0^{(n=v=0,\,k=0)}(R_d)$ (blue curve) in Eq. 5.60, and the ZPE-corrected interaction potential, $V_{QM}(R_d)$ (green curve) in Eq. 5.64, evaluated in the hcp crystal within the 1D and 3D rigid EMs (panels (a) and (b), respectively), the 1D and 3D rigid and non-rigid EMs (panels (c), (d), (e), (f), respectively) using the $(pH_2)_2$ potentials by NWB are depicted in the range of $R_d = 0.30 - 0.45$ nm.

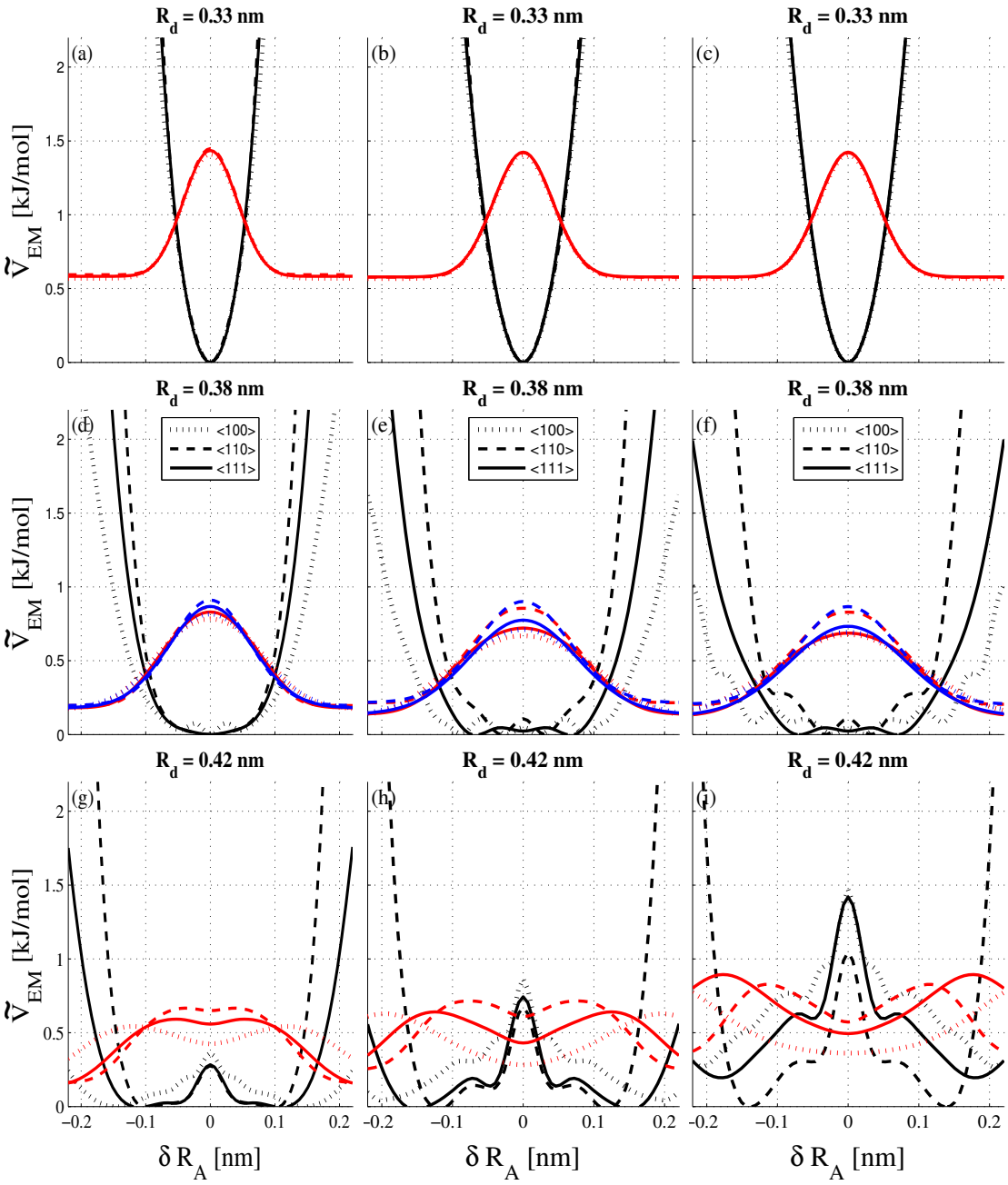

Figure 5.31: pH_2@pH_2 effective potentials, $\tilde{V}_{\rm EM}(R_d)$ in Eq. 5.58, are evaluated in the fcc crystal within the 1D non-rigid EM along the $\mathbf{e}$ = <100>, <110>, <111> directions at three representative NNds, $R_d = 0.33$, 0.38 and 0.42 nm (top, middle and bottom panels, respectively). In panels (a), (d) and (g) the constraint is set to $C = 0.01$ nm, in panels (b), (e) and (h) it is set to $C = 0.02$ nm and in panels (c), (f) and (i) it is set to $C = 0.03$ nm. The corresponding ground state probability densities (red curves), $\rho_A^{(k=0)}(\delta\vec{R}_A; R_d)$ in Eq. 5.62, are superimposed. For the 1D model at the experimental NNd, $R_0 = R_{\rm exp} = 0.38$ nm in panel (c), the corresponding Gaussian approximations (blue curves) in Eq. 5.63 are additionally plotted.

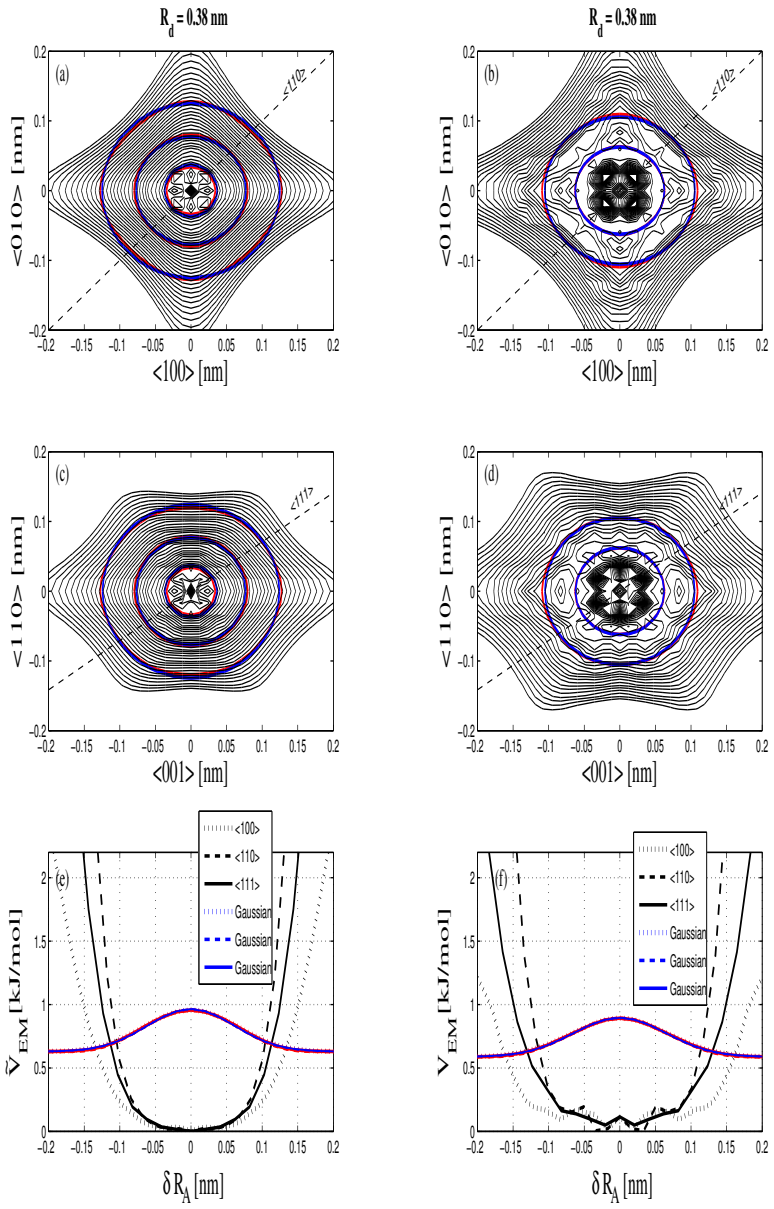

Figure 5.32: pH_2@pH_2 effective potentials, $\tilde{V}_{\rm EM}(R_d)$ in Eq. 5.58, are evaluated in the fcc crystal within the 3D non-rigid EM at the experimental NNd, $R_0 = R_{\rm exp} = 0.38$ nm. 2D cuts are plotted together with the probability densities (red curves), $\rho_A^{(k=0)}(\delta\vec{R}_A; R_d)$ in Eq. 5.62, and their approximated Gaussian functions (blue curves) in Eq. 5.63 along the {001} and {110} planes in panels (a), (b),(c),(d), respectively. The 1D cuts along the <100>, <110> and <111> directions are additionally plotted in panel (e) and (f) together with their Gaussian approximations. In panels (a), (c) and (e) the constraint is set to $C = 0.01$ nm, whereas in panels (b), (d) and (f) it is set to $C = 0.02$ nm.

as the height of the barriers is lower than or in the same order of the ZPE, the wavefunctions are still well approximated by the Gaussian distributions as depicted by the blue curves in panels (b), (e) and (h). On the contrary, at $R_d = 0.42$ nm, the barriers are energetically above the ZPEs strongly affecting the wavefunctions, which notably deviate from Gaussian distributions. Please note also that the effective potentials become so shallow that the respective wavefunctions become in some case broader than 1 nm, and the relaxation does not converge completely! Thus, if one would treat the non-rigid model in a quantum mechanical way, one would have to average the effective potential with respect to very delocalized and broad wavefunctions.

Application of the 3D non-rigid EM gives similar results as in the 1D treatment. This is already seen in Fig. 5.32, where the 2D cuts of the effective potentials are plotted along the {001} and {110} fcc crystallographic planes together with the 2D reduced PDs (red lines) and their Gaussian approximations (blue lines). Panels (a), (c) and (e) show the results for the $C = 0.01$ nm, whereas panels (b), (d) and (f) for $C = 0.02$ nm. Optimization has not been possible when setting $C = 0.03$ nm, since the potential becomes too flat and the wavefunctions tend to the particle-in-the-box ones. Panels (e) and (f), finally show the 1D cuts along the <100>, <110> and <111> fcc crystallographic directions extracted from the 3D model and fitted to 1D Gaussian functions.

The Gaussian widths at the experimental NNd, $R_{\mathrm{exp}} = 0.38$ nm from the 1D and 3D non-rigid models have been collected in Tab. 5.14 for comparison with the ones from rigid model. When increasing the constraint C, the effective potentials become shallower and the widths of the wavefunction increases. However, the PDs are still well approximated by their Gaussian fits showing that the bottom of the effective potential is still nearly harmonic. The anisotropy of the effective potentials eventually increases faster for increasing values of C in the 1D than in the more realistic 3D model, which means that the total ZPE cannot be approximated as the sum over the 1D ZPEs. The values of $E_0^{(n=v=0,\,k=0)}(R_{\mathrm{QM}})$ are summarized in Tab. 5.15 and confirm that the ZPES are slightly lowered compared to the corresponding 1D and 3D rigid EMs, however, when going from the 1D non-rigid EM to the 3D one, the ZPE again increase by about 20% and 10% for the pH_2@pH_2 and oD_2@oD_2 systems, respectively, as seen above within the rigid EMs.

The $V_{\mathrm{QM}}(R_d)$ curves obtained with the non-rigid EM are represented by the green lines in Figs. 5.29(e) and 5.29(f) and 5.30(e) and 5.30(f) respectively for the 1D and 3D cases and for the pH_2@pH_2 and oD_2@oD_2 systems. The colour code and the meanings of the marks are the same as before. In the case of the pH_2@pH_2 system the quantum mechanical NNds, R_{QM} are about 5.5% and 2.6% shorter than R_{exp} and the sublimation energies, that is $-V_{\mathrm{QM}}(R_{\mathrm{QM}})$, overestimated by about 65% and 55% by the 1D and 3D models, respectively. In the case of the oD_2@oD_2 system they are about 1.4% and 2.2% shorter than the experimental ones and the sublimations energies overestimated by about 30% and 27%, respectively. Thus, the results obtained within a 3D rigid lattice are in a much better

agreement with the experimental values than within a 3D non-rigid lattice. This may be ascribable to the time scale of the relaxation process, which is not taken into account in the optimization routine. Two opposite pictures can be proposed: In one case, the caging molecules are able to rapidly adjust their positions (non-adiabatic approximation). In the opposite case, the test-molecule is moving so rapidly that the other pH_2 molecules cannot adapt to the new configuration (adiabatic process). Reality stays somewhere in between these two extreme cases. The optimization routine certainly works in the non-adiabatic regime, since it just searches for the new global minimum on the PES after displacing the central molecule, i.e. the system has in principle an infinite time to find its new most stable configuration, whereas the real relaxation process in the pure crystal seems to be much closer to the adiabatic regime. Thus, if there would not be other sources of error, from the resulting ZPEs we could state that the rigid EM is more adequate. As a consequence, the non-rigid EM has not be applied to the hcp lattice.

Cl_2 Translational Zero-Point Energy in the Matrix

In this section the rigid and non-rigid EMs are applied to the $Cl_2@pH_2$ system. This should be considered as a preliminary step towards a more complete and realistic quantum dynamical simulation of the experiments carried out in Refs. 15, 204, where the doped $Cl_2@pH_2$ sample is grown without any annealing process, so that the crystal is expected to exhibit a mixed fcc/hcp structure [15]. In the previous quantum dynamical simulations carried out in Ref. 16, to which we refer for comparisons, an fcc lattice structure has been assumed. Moreover, the authors just assumed that the Cl_2 bond points in the direction of a vibrationally excited H_2 molecule of the surrounding cage without specifying any crystallographic direction. Following the results in Sec. 5.3.6, where small doped clusters have been grown, in the present simulations the impurity is assumed to occupy a single substitutional site at the center of an fcc lattice site. Moreover, only the <001> direction is considered (see Fig. 5.19*h*). The subsequent investigations of the Cl_2 rotating in both fcc and hcp lattices in the next section, actually show that other crystallographic directions may also be of interest for a more complete treatment.

fcc rigid EM

The results from the 1D and 3D rigid EMs are compared in Fig. 5.33. With respect to the 1D model, since the Cl_2 molecule points in the <001> crystallographic direction, the 1D cuts of the effective potential along the <100> and <010> directions are degenerate. In panels (*a*), (*d*) and (*g*), the effective potential and the corresponding probability densities (PD) are superimposed, showing that the potential is shallower along the <001> direction than along the <100>=<010> directions, since in the former case the Cl_2 points to the center of the square formed by the first NNs, easily passing through and moving to the second NN (the vertex of the octahedron), whereas in the latter case it has to pass through the lateral (equivalent to the first) square of NNs, but with the Cl_2 bond parallel to the square diagonal (see also Fig. 5.20 and 5.24), encountering more resistance. From the blue

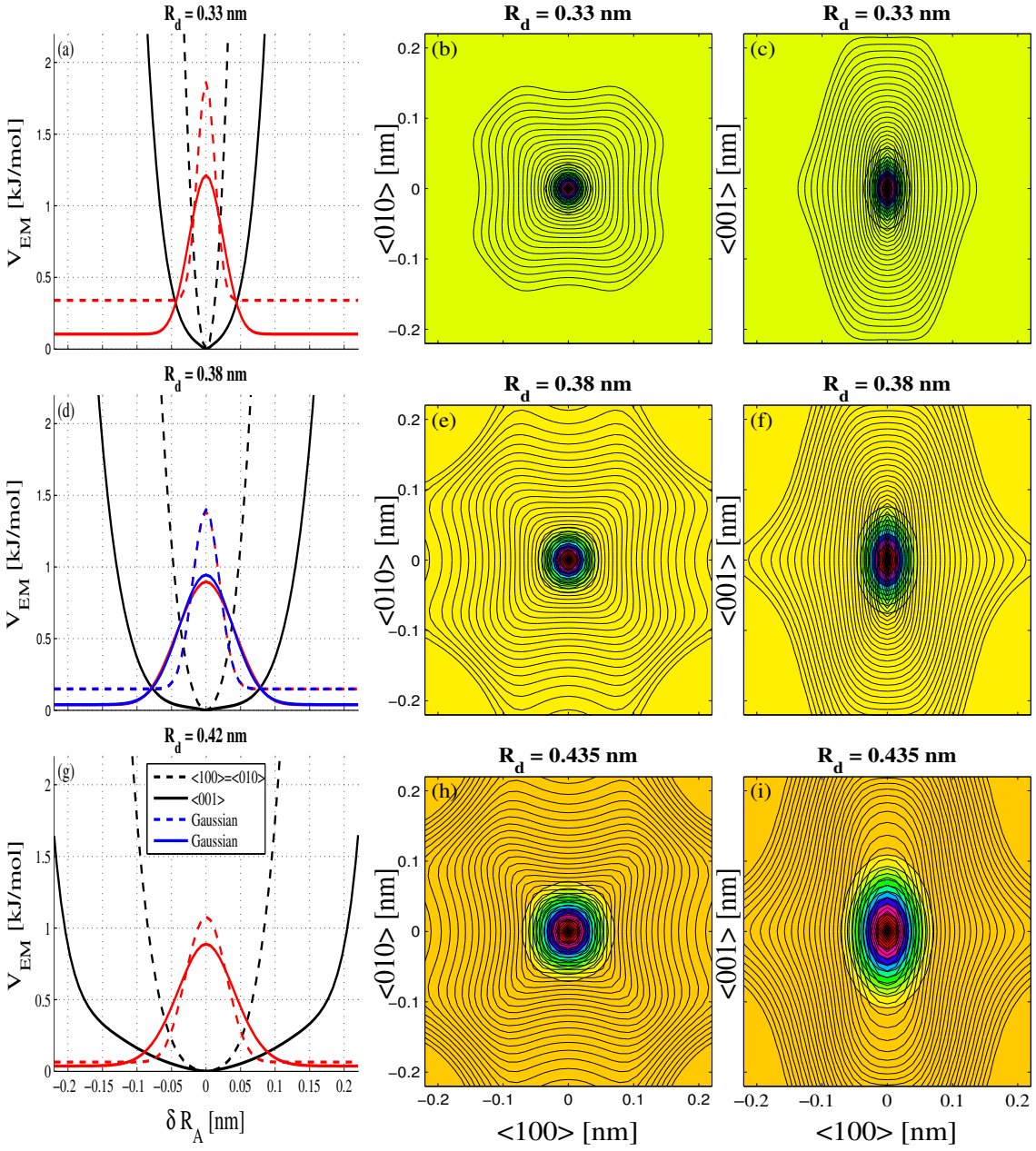

Figure 5.33: Cl_2@pH_2 effective potentials, $V_{\rm EM}(\delta\vec{R}_A; R_d, \theta_A, \phi_A)$ in Eq. 5.58, are evaluated in the fcc crystal within the 1D rigid EM (panels (a), (d), (g)) along the $<100>=<010>$ and $<001>$ directions, and within the 3D rigid EM along the $\{001\}$ plane (2D cuts in panels (b), (e), (h)) and along the $\{010\}$ plane (2D cuts in panels (c), (f), (i)) at three representative NNds, R_d = 0.33, 0.38 and 0.42 nm (top, middle and bottom panels, respectively). Contour lines are given in a logarithmic scale by 48 steps between 0.001 and 100 kJ/mol. The corresponding ground state probability densities, $\rho_A^{(k=0)}(\delta\vec{R}_A; R_d, \theta_A, \phi_A)$ in Eq. 5.62 are superimposed. For the 1D model at the experimental NNd, $R_0 = R_{\rm exp}$ = 0.38 nm in panel (c) the corresponding Gaussian approximations (blue curves) in Eq. 5.63 are additionally plotted.

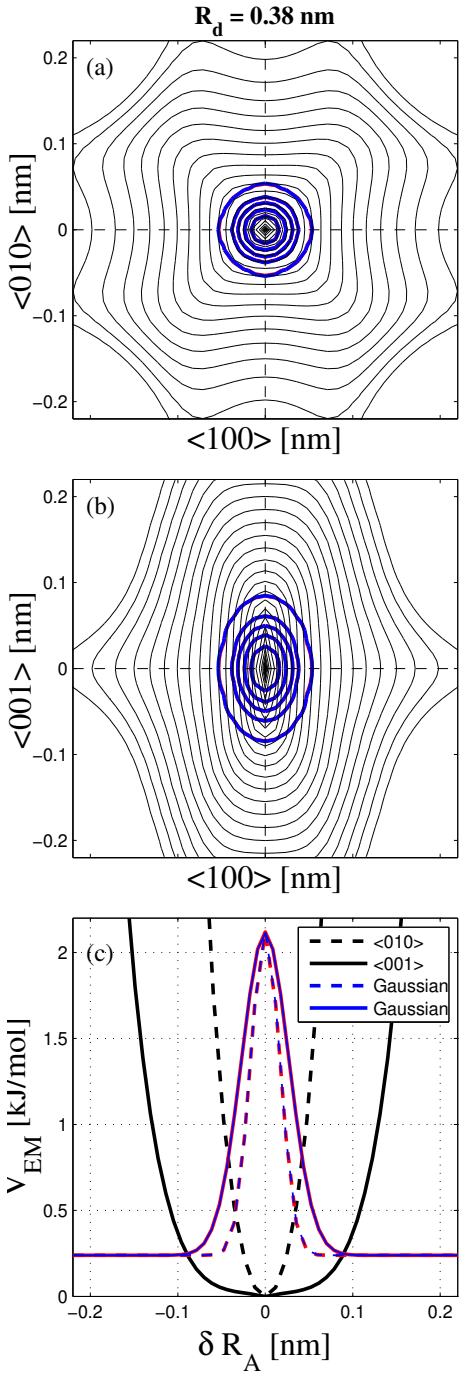

Figure 5.34: Cl_2@pH_2 effective potentials, $\tilde{V}_{\rm EM}(R_d, \theta_A, \phi_A)$ in Eq. 5.58, are evaluated in the fcc crystal within the 3D rigid EM at the experimental NNd, $R_0 = R_{\rm exp} = 0.38$ nm. 2D cuts are plotted together with the probability densities (red curves), $\rho_A^{(k=0)}(\delta\vec{R}_A; R_d, \theta_A, \phi_A)$ in Eq. 5.62, and their approximated Gaussian functions (blue curves) in Eq. 5.63 along the {001} and {100} planes in panels (a) and (b), respectively. The 1D cuts along the <010> and <001> directions are additionally plotted in panel (c) together with their Gaussian approximations.

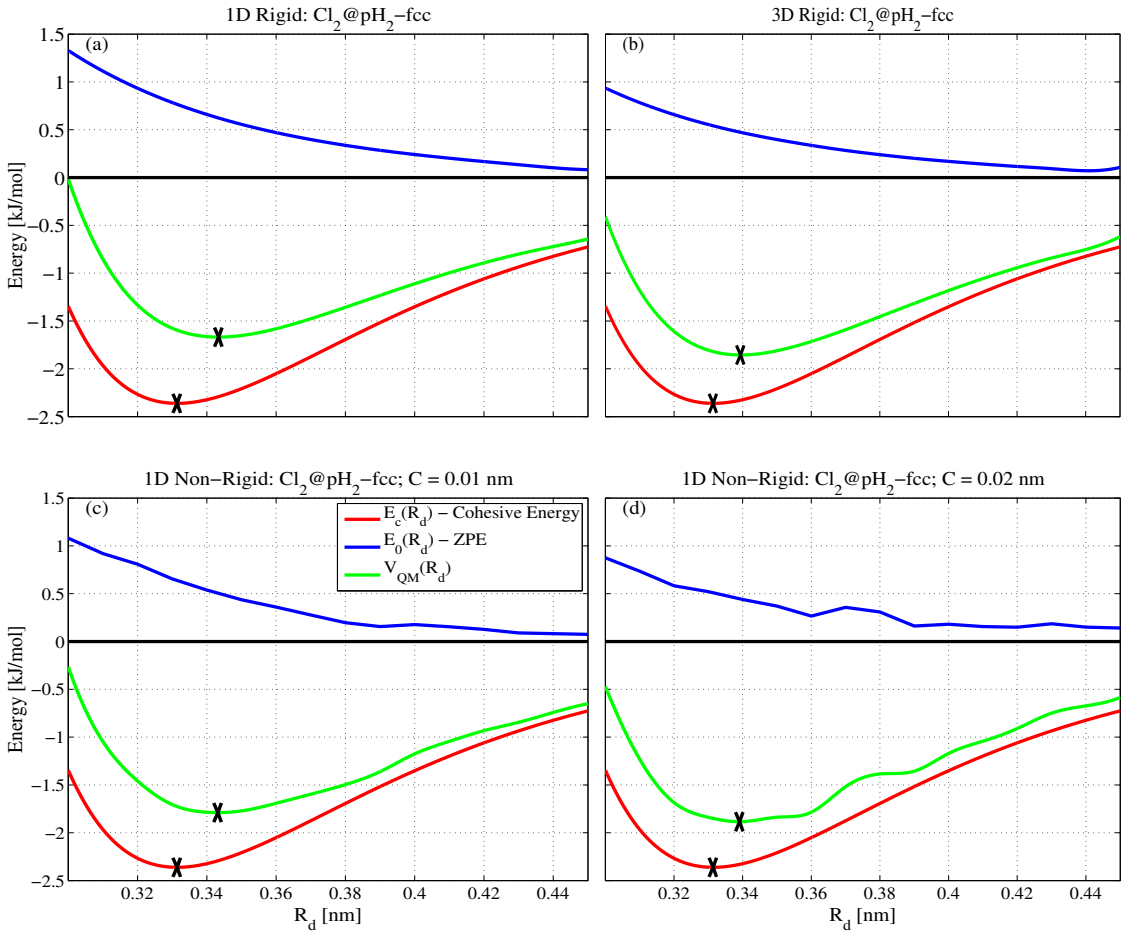

Figure 5.35: The Cl_2@pH_2 cohesive energy, $E_c(R_d, \theta_A, \phi_A)$ (red curves) in Eq. 5.55, the ZPE, $E_0^{(n=v=0,\, k=0)}(R_d, \theta_A, \phi_A)$ (blue curves) in Eq. 5.60, and the ZPE-corrected interaction potential, $V_{\rm QM}(R_d, \theta_A, \phi_A)$ (green curves) in Eq. 5.64, evaluated in the fcc crystal within the 1D and 3D rigid EMs (panels (a) and (b), respectively), the 1D non-rigid EMs (panels (c) and (d), respectively) using the $(pH_2)_2$ potentials by NWB are depicted in the range of $R_d = 0.30 - 0.45$ nm. In panels (c) and (d) the constraint values are $C = 0.01$ and 0.02 nm, respectively.

curves in panel (d) it can be seen that at the experimental NNd, $R_{\rm exp} = 0.38$ nm, the PD along the <100> direction is perfectly approximated by a Gaussian function, whereas it slightly deviates along the <001> direction. The width along the Cl_2 bond is nearly twice as broader as the one along the perpendicular direction, as shown in Tab. 5.16, where the widths of all Gaussians approximated to the 1D PDs have been collected. In panels (b), (c), (e), (f), (h) and (i), the 2D cuts of the effective potential and of the PDs from the 3D rigid EM are depicted. Similarly to the 1D model, the 2D cuts along the (100) and the (010) planes are also degenerate (suggesting two perpendicular translational modes of Cl_2), so that they are shown only once. In panels (b), (e) and (h), the potential shows an octagonal shape. The potential is more repulsive at the side centers of the octagon,

Table 5.16: The widths σ of the 1D and $\sigma_1 = \sigma_2$ of the 2D Gaussian functions are fitted to the probability densities obtained within the 1D and 3D EMs. Data are listed for the fcc and hcp phases and compared to the results from [176]. All values are given in nm for R_{exp} = 0.380 nm.

rigid EM	$\sigma^{<100>} = \sigma^{<010>}$	$\sigma^{<001>}$	C
1D-fcc	0.0271	0.0543	0
3D-fcc	0.0234	0.0385	0
non-rigid EM	$\sigma^{<100>} = \sigma^{<010>}$	$\sigma^{<001>}$	C
1D-fcc	0.0323	0.0622	0.01
	–	–	0.02

Table 5.17: The NNds, R_{QM} (see Eq. 5.66) and the ZPEs, $E_0^{(n=v=0,\,k=0)}(R_{exp})$ and $E_0^{(n=v=0,\,k=0)}(R_{QM})$, of the Cl_2 within the 1D and 3D rigid and non-rigid EMs are compared for both the fcc and hcp lattices using the $(pH_2)_2$ potentials by NWB, GS and from the present work and the pH_2-Cl_2 potential from the present work.

		Cl_2					
Pair Pot.	C	$1D+1D+1D$			$3D$		
		rigid EM					
		$E_0(R_{QM})$	$E_0(R_{exp})$	R_{QM}	$E_0(R_{QM})$	$E_0(R_{exp})$	R_{QM}
NWB	0	0.623	0.348	0.343	0.473	0.248	0.339
SG	0	0.613	0.348	0.344	0.467	0.248	0.340
Present	0	0.590	0.348	0.346	0.445	0.248	0.343
		non-rigid EM					
NWB	0.01	0.551	0.212	0.339	–	–	–
	0.02	0.454	(0.334)	0.338	–	–	–

where the test-molecule encounters more repulsion. The octagon is slightly elongated along the <010> than in the <110> direction, since in the former case the molecule encounters two of the first NNs forming the square window, whereas in the latter case it encounters only of the first NNs orthogonal to the Cl_2 bond. In panels (c), (f) and (i) the degenerate 2D cut along the (100) and (010) planes is depicted, showing both elongated effective potentials and PDs along the <001> direction. The potential is particularly shallow in the <001> direction, since this time the Cl_2 molecule passes through the square window of first NNs before encountering one of the second NNs. The background color changing from green to yellow indicates that the ZPE decreases when going from R_d = 0.33 to 0.45 nm. At the experimental distance, $R_{\rm exp}$ = 0.38, the PDs along the (001) and (100) planes have been approximated to 2D Gaussian functions (red and blue curves) in Figs. 5.34(a) and 5.34(b) showing a very good match. Actually, when looking at the corresponding 1D cuts in Fig. 5.34(c), one sees that the PD has a more Gaussian shape now also along the Cl_2 bond with respect to the PDs obtained within the 1D model. Moreover, its width is less than twice the one along the <100> or <010> directions, as shown in Tab. 5.16). Thus, as in the pure crystal, also for the Cl_2@pH_2 the 1D model predicts a larger anisotropy due to the environment than the 3D one. In contrast to the pH_2@pH_2 and oD_2@oD_2 systems, the ZPEs, $E_0^{(n=v=0,\,k=0)}(R_{\rm QM},\theta_A,\phi_A)$ and $E_0^{(n=v=0,\,k=0)}(R_{\rm exp},\theta_A,\phi_A)$ decreases (about 45%) when going to three dimensions. Thus, in the pure crystals as well as in the doped one, the 3D EM predicts ZPEs in closer agreement to the experimental values than the 1D one. Finally, it is interesting to compare the magnitude of the ZPE at $R_{\rm c}$, $E_0^{(n=v=0,\,k=0)}(R_{\rm c},\theta_A,\phi_A)$ in the 3D rigid EM, when going from the light H_2 and D_2 molecules to the heavy Cl_2. They correspond respectively to about 81%, 65% and 23% of the respective classical cohesive energies, $E_{\rm c}(R_{\rm c},[\theta_A,\phi_A])$, which reflects the high quantum nature of hydrogen and deuterium. Nevertheless, the Cl_2 ZPE in solid hydrogen is still large considering the heavy mass of about 71 amu depending probably on the larger steepness of the $V_{\rm EM}(R_{\rm c},\theta_A,\phi_A)$ potentials. For example, application of the 1D rigid EM to the Ar@Ar system results in a ZPE, which is, despite the lighter Ar mass of about 40 amu, only about 11% of the classical cohesive energy (see [176]). Thus, the big ratio between ZPE and classical cohesive energy of a Cl_2 embedded in the pH_2 matrix is to be addressed to the weaker cohesive energy of the crystal.

fcc non-rigid EM

Due to the lower symmetry of the Cl_2@pH_2 system, relaxation of the lattice around the Cl_2 impurity presented longer CPU-time and only the 1D non-rigid EM has been applied. The results are presented in Fig. 5.36 at the NNds, R_d = 0.33, 0.38 and 0.42 nm, respectively in the three top, middle and bottom panels. The constraint C is increased from 0.01 nm in panels (a), (c) and (e), to 0.02 nm in panels (b), (d) and (f). As seen previously in the pure crystals, the effective potentials become flatter when allowing the 18 caging molecules to relax. This is particularly evident at larger NNds. Moreover, the height of

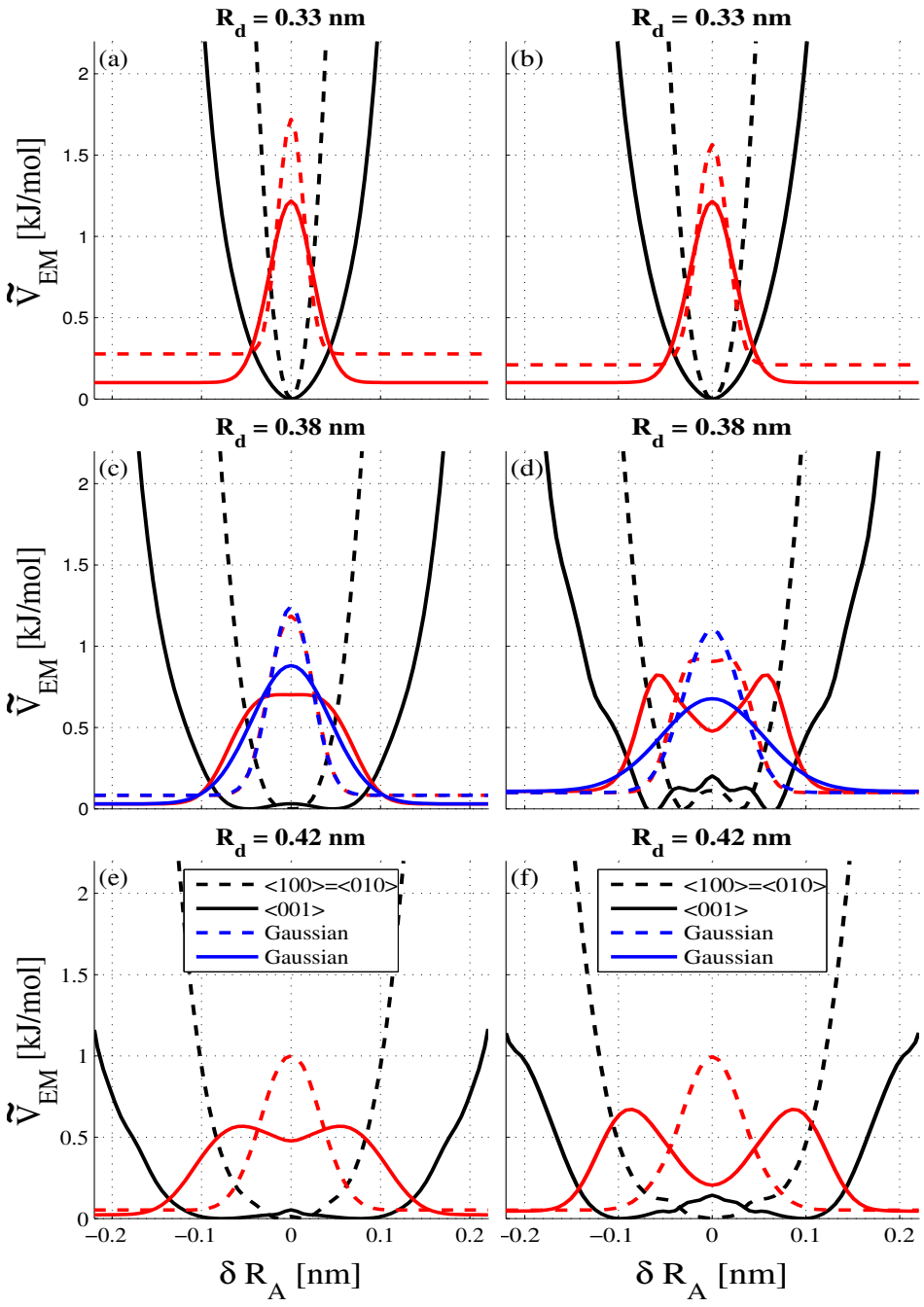

Figure 5.36: Cl_2@pH_2 effective potentials, $\tilde{V}_{\rm EM}(R_d, \theta_A, \phi_A)$ in Eq. 5.58, are evaluated in the fcc crystal within the 1D non-rigid EM along the <100>=<010> and <001> directions at three representative NNds, $R_d = 0.33$, 0.38 and 0.42 nm (top, middle and bottom panels, respectively). In panels (a), (c) and (e) the constraint is set to $C = 0.01$ nm, whereas in panels (b), (d) and (f) it is set to $C = 0.02$ nm. The corresponding ground state probability densities (red curves), $\rho_A^{(k=0)}(\delta\vec{R}_A; R_d, \theta_A, \phi_A)$ in Eq. 5.62, are superimposed. At the experimental NNd, $R_0 = R_{\rm exp} = 0.38$ nm in panels (c) and (d), the corresponding Gaussian approximations (blue curves) in Eq. 5.63 are additionally plotted.

the barrier originating at the center of the potentials also increases, influencing the shape of the corresponding wavefunctions. In particular in panel (c), along the <001> direction a double-well potential originates already for $C = 0.01$ nm, so that the corresponding PD deviates from a Gaussian distribution. The deviation is enhanced in panel (d), where also the potential along the <100>=<010> directions have now a double-well shape, so that the widths from the corresponding Gaussian approximations are not given in Tab. 5.16. To the flattening of the effective potentials corresponds a lowering of the ZPEs, as already seen for the pH_2@pH_2 and oD_2@oD_2 systems. Admittedly, the values of the dynamical energy at the experimental distance, $E_0^{(n=v=0,\,k=0)}(R_{\rm exp}, \theta_A, \phi_A)$, for $C = 0.02$ nm listed in Tab. 5.17 could be inaccurate due to an inefficient optimization at NNds, $R_d > 0.34$nm (the value is given in brackets). This is also seen in Fig. 5.35, where the static energy, $E_{\rm c}(R_d, \theta_A, \phi_A)$ (red), the dynamical energy, $E_0^{(n=v=0,\,k=0)}(R_d, \theta_A, \phi_A)$ (blue), and the total quantum mechanical energy, $V_{\rm QM}(R_d, \theta_A, \phi_A)$ (green) are plotted with respect to R_d. Thus, the three crystal systems show similar changes in the properties of the effective potentials calculated, and of the corresponding wavefunctions, when going from the 1D rigid model to the 3D one, or to the 1D non-rigid one. On this bases, we speculate that the 3D non-rigid model is expected to results in even more shallow and isotropic potentials. Correspondingly, the value of $E_0^{(n=v=0,\,k=0)}(R_{\rm exp}, \theta_A, \phi_A)$ in the 3D model is expected to be even below the value of 0.248 kJ/mol reported in Tab. 5.17. Actually, the Cl_2 ZPE, $E_0^{(n=v=0,\,k=0)}(R_{\rm exp}, \theta_A, \phi_A) = 0.212$ kJ/mol (1D non-rigid EM, $C = 0.01$ nm, NWB, fcc), is approximately one fourth of the pH_2 ZPE, $E_0^{(n=v=0,\,k=0)}(R_{\rm exp}) = 0.888$ kJ/mol (3D rigid EM, NWB, fcc), so that the caging molecules are expected to follow more easily when the Cl_2 is moving because of their higher translational frequency. In terms of the time scales mentioned above, the doped crystal probably is closer to the non-adiabatic regime than the pure crystal, that is the solvent molecules translate much more rapidly than the solute molecule, so that the non-rigid EM for Cl_2@pH_2 may be more adequate than for pH_2@pH_2.

Cl_2 Rotational DOF: The Devonshire Model [174]

The dynamics of rotating diatomic molecules trapped in crystals has been widely investigated since the 1930's in the theoretical and experimental fields of research. A first theoretical model was proposed by Pauling [298] in 1930, which takes into account the interaction of a trapped molecule in the field of a crystal of definite symmetry. The model considered the molecule rotating on a plane and was extended to the more realistic three dimensional cases by Devonshire [174] in 1936. Considering only crystals of octahedral symmetry, he connected the strength of the crystal field to the shifts and splittings of the rotational energy levels of the molecule with respect to those of a free rotor, providing a first tool for the interpretation of rovibrational spectra of diatoms embedded in RG matrices. In the Devonshire model (DM) [174] the crystal is taken to be rigid with the COM of the host as well as of the guest molecules fixed at the nominal lattice positions. This has

the advantage of describing the interaction potential as a linear combination of (totally symmetric) spherical harmonics of the lattice symmetry. In the case of fcc crystals with octahedral symmetry O_h, one just uses linear combinations of cubic harmonics. Devonshire included only the first cubic harmonic with $J = 4$ and $M = -4, 0, 4$ and multiplied the linear combination by a constant K being the strength of the solute-solvent interaction. On the one hand, if the trapped molecule interacts weakly with the environment, that means the crystal field barriers are lower than the molecular rotational constant, the molecule behaves as a slightly hindered rotor, as for example small molecules such as the hydrogen halides [3]. In the most extreme cases even as a free rotor, as for example solid molecular hydrogen, at least in a very good approximation. On the other hand, if the trapped molecule strongly interacts with the environment, that is the case if the crystal field barriers are much higher than the molecular rotational constant, the guest molecule librates around some crystallographic directions. In the most extreme case, librational quantum states are better described by a harmonic or anharmonic oscillator, which involves also an additional quantum effect, i.e. librational ZPEs. The DM was later extended to include cubic harmonics of higher orders [299–303] and other crystal symmetries [304] and it is today commonly known as crystal field theory (CFT). Nevertheless, when considering rigid lattices, one completely neglects couplings between rotational and translational (either of solute or solvent) DOFs. Thus, the DM failed to predict the fine structure of many diatoms embedded in RG matrices. In the 1960's Friedman and Kimel [26,305–307] introduced the rotation-translation coupling (RTC) model, which includes only the translational DOF of the impurity and still considers a rigid lattice. They assumed the impurity to rotate around a center of interaction not coinciding with the center of symmetry in heteronuclear molecules. This causes the center of interaction to translate (or externally vibrate) during rotation (eccentric rotation). The coupling is treated using second order perturbation theory in the distance between the impurity COM and the center of interaction expressing the strength of the perturbation. The RTC model was further generalized by Mannheim [291], who introduced the coupling to the lattice vibrations represented by Green's functions. Afterwards, many models originated and evolved including different couplings, see [292–294]. In particular, Kono and Lin [293] adiabatically separated the intramolecular vibrational DOF from the heat bath DOFs, which closely resembles the investigation in Chap. 4, where also localized matrix-solute modes are separated from the solvent modes.

Another meaningful contribution to the solute-solvent interaction was given by Manz [308] in 1980, who extended the DM including a more realistic non-rigid host lattice. The molecules in the vicinity of the impurity are relaxed to new equilibrium positions, so that the cage assumes the form of the guest linear molecule and an ellipsoidal deformation is induced. Thus, when the impurity is rotating, the molecules undergo small deviations from their nominal lattice positions. The final effect is called pseudorotation and couples the guest rotational to the host translational DOFs. A further consequence of the pseu-

dorotation is an effective increase of the total moment of inertia of the guest molecule corresponding to a decreasing of the rotational constant, the detection of which has been documented in spectroscopy [301, 309–316].

In the present work, effective rotational PESs are obtained first within the CFT, namely considering a rigid DM, afterwards by relaxing the first two solvation shells around the impurity, namely considering a non-rigid DM, in close connection to the rigid and non-rigid EMs from the previous section. In the same way the rotational PESs are calculated as the change in the crystal cohesive energy when rotating the Cl_2 molecule in the matrix,

$$V_{\mathrm{DM}}(f(\delta\theta_A, \delta\phi_A); R_{\mathrm{exp}}) = \frac{1}{2}\sum_{j>1}^{N_p} V(f(\delta\theta_A, \delta\phi_A) - \vec{R}_j; R_{\mathrm{exp}}) - E_{\mathrm{c}}(R_{\mathrm{exp}}) \tag{5.69}$$

where $f(\delta\theta_A, \delta\phi_A)$ simply transforms the spherical coordinates into the corresponding Cartesian coordinates of the Cl atoms. Similarly, if the two solvation shells are relaxed the previous equation becomes

$$\tilde{V}_{\mathrm{DM}}(f(\delta\theta_A, \delta\phi_A); R_{\mathrm{exp}}) = \min_{R_j \in [-C,C]} \quad \frac{1}{2}\sum_{j>1}^{N_p} V(f(\delta\theta_A, \delta\phi_A) - \vec{R}_j; R_{\mathrm{exp}}) - \tilde{E}_{\mathrm{c}}(R_{\mathrm{exp}}) \tag{5.70}$$

These potentials are used in order to calculate the rotational energy levels, when imposing an fcc and hcp symmetry to the lattice, that is changing the positions $\vec{R}_j$. This is achieved by setting equations very similar to Eqs. 2.61 and 2.55, respectively. The SE to be solved is

$$(\hat{\mathbf{H}}_{\mathrm{rot}}(\nabla_{\theta_A}, \theta_A, \nabla_{\phi_A}, \phi_A; R_{\mathrm{exp}}) - E_{\mathrm{rot}}^{(n=v=0,\,l)}(R_{\mathrm{exp}})) \times \psi_{\mathrm{Cl_2}}^{(n=v=0,\,l)}(\theta_A, \phi_A; R_{\mathrm{exp}}) = 0 \tag{5.71}$$

where the rotational Hamiltonian $\hat{\mathbf{H}}_{\mathrm{rot}}$ is defined by following the notation in Sec. 2.2.5

$$\hat{\mathbf{H}}_{\mathrm{rot}}(\nabla_{\theta_A}, \theta_A, \nabla_{\phi_A}, \phi_A; R_{\mathrm{exp}}) = B^A \hat{j}_A^2 + W_{\mathrm{Cl_2}}^{(n=v=0)}(\theta_A, \phi_A; R_{\mathrm{exp}}) \ , \tag{5.72}$$

and the variables $\{\theta_A, \phi_A\}$, the parameter R_{exp} and the potential $W_{\mathrm{Cl_2}}^{(n=v=0)}(\theta_A, \phi_A; R_{\mathrm{exp}})$ correspond respectively to the variable $\{\theta, \phi\}$, the parameter $\vec{R}_{\mathrm{tra}}$ and the interaction potential $\hat{V}_{\mathrm{rot}}(\phi, \theta; \vec{R}_{\mathrm{tra}}) = W_{\mathrm{ext}}^{(n,v)}(\vec{R}_{\mathrm{ext}})$ in Eq. 2.59.

The effective potential $W_{\mathrm{Cl_2}}^{(n=v=0)}(\theta_A, \phi_A; R_{\mathrm{exp}})$ is evaluated on a 73×37 grid for equidistant points in the range $[0 - 180°]$ and $[0 - 360°]$ for the θ_A and ϕ_A coordinates, respectively, implementing Eqs. 5.69 and 5.70 within the TrajLab software [274] for the rigid and non-rigid DMs, respectively. The SE is solved by using the WavePacket software [297]. The quantum numbers given as superscript in the potential term, $W_{\mathrm{Cl_2}}^{(n=v=0)}(\theta_A, \phi_A; R_{\mathrm{exp}})$, means that the Cl_2 molecule lies in its electronic and vibrational ground states, whereas the translational DOFs are neglected, since the positions of the molecules are described classically (no distribution functions). These quantum numbers come from the multi-stage AS applied to the system, see Sec. 2.2.5. Please recall that the classical approximation is additionally imposed for Cl_2 internal vibrations by using the ground state vibrationally averaged equilibrium bond distance, $\tilde{r}_{\mathrm{Cl_2}}$, even though the vibrational dynamics could couple the rotational eigenfunctions, and vice versa, as already seen for the H_2 rotational wavefunctions. We also recall that the Cl_2 translational and rotational DOFs in the present models are treated separately. On one side, the rotational SE is solved at only one value of $\vec{R}_A$ (determined directly by R_{exp}), that is with the guest molecule COM fixed at the nominal lattice position, on the other side the Cl_2 translational energies were calculated in the previous section for only one angular orientation, i.e. the <001> fcc crystallographic direction.

The rotational wavefunction $\psi_{\mathrm{Cl_2}}^{(n=v=0,\,l)}(\theta_A, \phi_A; R_{\mathrm{exp}})$ is again expanded in SHs, but since the rotational constant is now much smaller, the Cl_2 free rotor energy levels are more dense and energetically expected to be in the same or even lower order than the barriers of the potential, $W_{\mathrm{Cl_2}}^{(n=v=0)}(\theta_A, \phi_A; R_{\mathrm{exp}})$. Actually, the rotational wavefunctions are so strongly coupled by the potential, that they must be expanded up to the SH with maximum angular momentum $J_{\mathrm{max}} = 80$. Please note that for the rotational adiabatization of H_2, the wavefunction was expanded just up to $J_{\mathrm{max}} = 5$ (see Sec. 5.3.4). On the other hand, the mass ratio between the two species is approximately 35.17, and the ratio of the two momenta of inertia is 249! Since the accuracy of the adiabatization depends strongly on how accurate the computation of the SHs is, a denser DVR grid is needed. This means that the potentials V_{DM} and $\tilde{V}_{\mathrm{DM}}$ in Eqs. 5.69 and 5.70 must be also fitted to the new grid before the SE can be treated numerically as in Eq. 5.27. The new grid is conveniently taken at the Gauss-Legendre DVR points in order to apply the GQ scheme with $G_{\theta_A} = 512$ and $G_{\phi_A} = 256$, see Sec. 5.3.3.

The effective potentials felt by Cl_2 rotating in the crystal are shown in Figs. 5.37 (panels (a), (c) and (e)) and 5.38, respectively for the fcc and hcp lattices. Figs. 5.37(a) and 5.38(a) show the crystal field potentials felt by the impurity rotating in the rigid lattice with $C = 0$ nm. Correspondingly, Figs. 5.37(c) and 5.38(e) show the rotational PESs when letting the first two coordination shells relax around the impurity with constrained maximum displacement $C = 0.06$ nm away from the lattice nominal position in all directions. The corresponding displacement vectors when relaxing the matrix are depicted by the blue

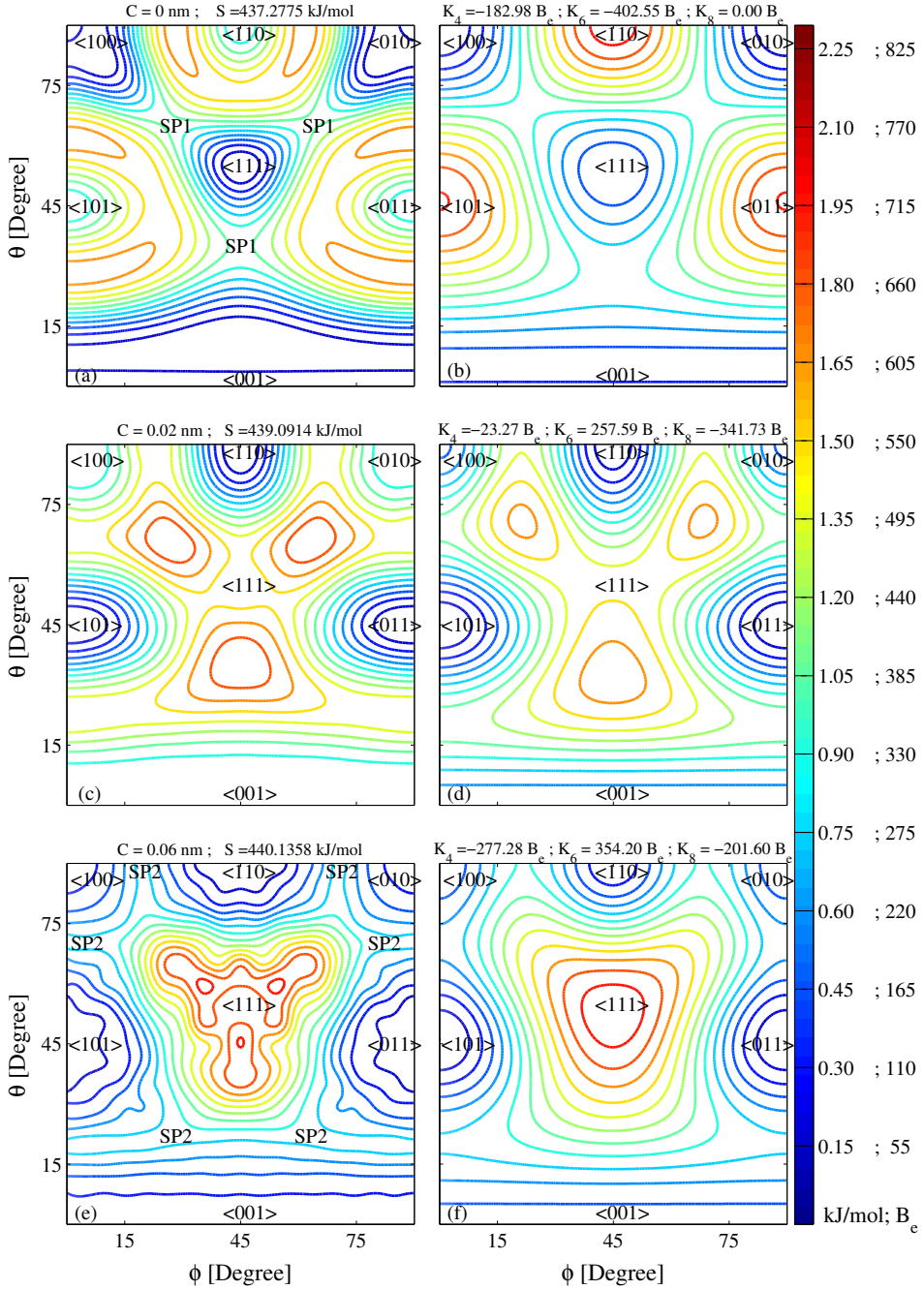

Figure 5.37: Cl_2@pH_2 effective rotational PESs, $W^{(n=v=0)}_{Cl_2}(\theta_A, \phi_A; \vec{R}_A)$ in Eq. 5.72, are evaluated in a fcc crystal within the rigid (panel (a)) and non-rigid DM (panels (c) and (e)). By relaxing the caging molecules the constraint values are $C = 0.02$ and 0.06 nm, respectively. Panels (b), (d) and (f) are the corresponding PESs obtained by fitting the linear combination of cubic harmonics given in Eq. 5.73. Contour lines are given in the same range of energies in units of kJ/mol, i.e. [0 - 2.25] and steps of 15.0, and in units of B_e in the range [0 - 825] and steps of 55, where B_e is the Cl_2 rotational constant in the gas-phase.

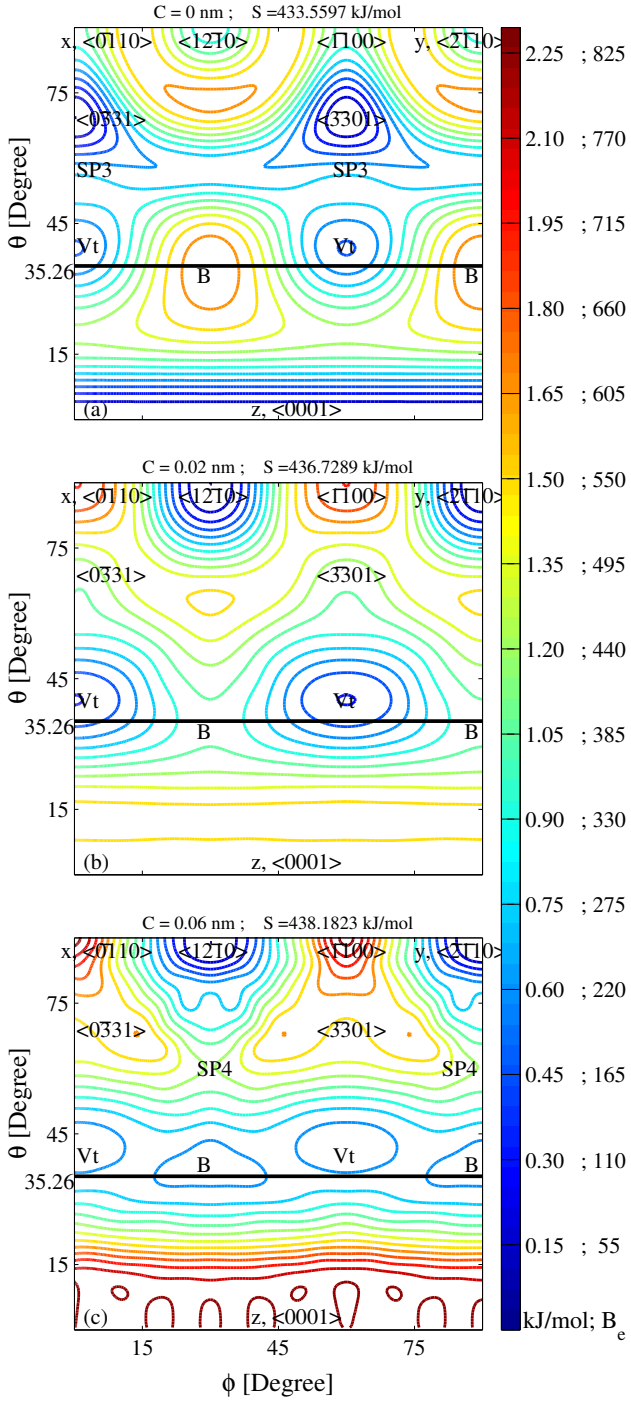

Figure 5.38: Cl_2@pH_2 effective rotational PESs, $W^{(n=v=0)}_{Cl_2}(\theta_A, \phi_A; \vec{R}_A)$ in Eq. 5.72, are evaluated in the a hcp crystal within the rigid (panel (a)) and non-rigid DM (panels (b) and (c)). By relaxing the caging molecules the constraint values are $C = 0.02$ and 0.06 nm, respectively. Contour lines are given in the same range of energies in units of kJ/mol, i.e. [0 - 2.25] and steps of 15.0, and in units of B_e in the range [0 - 825] and steps of 55, where B_e is the Cl_2 rotational constant in the gas-phase.

Table 5.18: The equilibrium distances of the caging molecules from the Cl_2 COM obtained by relaxing the first two coordination shells around the impurity within the fcc non-rigid model are compared to the equilibrium distances of the solvent molecules for the $Cl_2(pH_2)_{14}$ cluster obtained in Sec. 5.3.6.

Cage molecule numbers		$Cl_2(pH_2)_{14}$ cluster	$Cl_2@pH_2$ (C = 0.06)
5,6,7,8	(belt ring)	0.244 nm	0.295 nm
1,2,3,4 and 9,10,11,12	(square windows)	0.362 nm	0.370 nm
13,14	(head-ons)	0.471 nm	0.510 nm

arrows in Figs. 5.39, 5.40 and 5.41 for the fcc lattice and in Figs. 5.42, 5.43 and 5.44 for the hcp lattice, respectively, and their corresponding absolute values are listed in Tab. 5.19. Finally, intermediate situations with $C = 0.02$ nm are shown in Figs. 5.37(b) and 5.38(c) for comparison. All rotational potentials have been shifted to have their global minima at zero for easier comparison. The magnitude of the shifts S is given on top of each panel next to the constraint C. All figures are plotted within the same energy range [0 - 2.2995] kJ/mol with regularly spaced contour lines at intervals of 0.1503 kJ/mol. Such interval exactly corresponds to 55 B_e and their values are also given in units of B_e next to the kJ/mol units as [kJ/mol ; B_e]. This should help the reader to readily discriminate whether the impurity dynamics lies in the hindered rotor (B_e much larger than the rotational potential barriers) or in the librational (B_e much smaller than the rotational potential barriers) regime. For both lattice symmetries considered, the absolute energy decreases when relaxing the caging molecules as inferred from the magnitude of the shifts S when comparing respectively panels (a), (c) and (e) of Fig. 5.37 and the corresponding panels (a), (b) and (c) of Fig. 5.38. The absolute energy scale of the rotational PESs depends on the magnitude of the simulation box used, thus the larger the box the lower the energy (pair interaction are summed up), so that relative energies are more appropriate for comparisons. Generally, one expects the energy difference between global maximum and global minimum to decrease upon relaxation of the molecular system, as well. An optimized interaction between the molecules in the crystal should in fact flatten the respective rotational barriers. This is not seen here since the pH_2-Cl_2 interactions are about 7 (T-shaped) and 10 (linear) times larger than the respective $(pH_2)_2$ ones, which particularly affects the first two coordination shells included in the optimization code. They prefer to stay closer to the impurity, instead of mediating between the impurity and the

outer shells, so that to consider the remaining lattice molecules as rigid, finally stabilizes the minimum geometries more than the maximum ones. Thus, these energy differences increase oppositely from 1.73 to 2.01 kJ/mol and from 1.78 to 2.30 kJ/mol when considering the fcc and hcp lattices, respectively. This systematic error could not be avoided because of CPU time limits and must be added to the already long list of approximations involved in the model. However, it is reasonable to think that the model slightly enhances the barriers without losing its overall topology, since the PESs are strongly affected by the relaxation process. In all cases, those energy differences are small, i.e. in the order of 2 kJ/mol, which is due to the softness of the crystal. Nevertheless, such a small barrier is still very large compared to the rotational constant $B_e = 2.733 \times 10^{-3}$ kJ/mol, so that the Cl_2 molecule is eventually expected to librate in the matrix.

In Fig. 5.37(a), the global minimum is found in the <100> crystallographic direction, where the Cl_2 is pointing to the center of the square window and to the second nearest-neighbour, see Fig. 5.39. A local minimum is found in the <111> direction, where the impurity is pointing to the center of the triangular window, see Fig. 5.41. The energy difference between the two minima is only 0.0147 kJ/mol and the saddle point (SP1) between them lies at 1.03 kJ/mol. A second local minimum with the very peculiar form of a volcano is finally visible along the <110> direction, where the Cl_2 is pointing to one of the first nearest-neighbour, see Fig. 5.40. The volcano minimum becomes the global one in Fig. 5.37(e) after relaxation. The displacement vectors in Fig. 5.40 show that the head-on nearest-neighbours are pushed away to the minimum equilibrium distance dictated by the pH_2-Cl_2 pair potential. The other 16 caging molecules also adjust their positions to lower the total cohesive energy of the system. The minimum along the <111> direction becomes the global maximum after relaxation. In reality, the absolute cohesive energy is lowering upon relaxation, see Fig. 5.41, but the relative energy with respect to the global minimum increases. Finally, the minimum along <001> turns in a local minimum lying at 0.225 kJ/mol with a saddle point (SP2 in Fig. 5.37(e)) to the global minimum at 0.792 kJ/mol. Again the absolute cohesive energy of the system is lowered upon relaxation, whereas the relative one increases.

For the rigid lattice in Fig. 5.38(a) global minima are found along the z or <0001> and along the $<0\bar{3}31>$ crystallographic directions. In the former case the impurity points in both directions to the triangular windows lying on the top and bottom parallel honeycomb sheets formed by the molecules numbered respectively 1,2,3 and 10,11,12 in Figs. 5.42, 5.43 and 5.44, whereas in the latter case, the Cl_2 bond points on one end to the center of the a lateral triangular window formed for example by the molecules numbered 1,4,5 or 4,5,10, and on the other end to an opposite square window (not shown) [8]. These two

[8] Please note that now the Miller indices are used in order to indicate the hcp crystallographic directions. For the hcp symmetry two equivalent conventions exist: The three indices <hkl> one, as for fcc, and the four indices <hkil> one, which is used along this section. For the equivalence between the conventions please refer to [287].

crystallographic directions are not equivalent. Nevertheless, the energy difference of the minima along them is practically negligible. Two local minima are found on the PES. The first one when the Cl_2 bond points almost to one of the three vertices of the top (or bottom) triangular windows, see Fig. 5.44, the energy of which is 0.437 kJ/mol. The direction pointing exactly to one of such vertices is the $<0\bar{2}21>$ crystallographic direction with $\theta_A = 35.26°$ (or $180° - 35.26° = 144,74°$), which is indicated in the three panels of Fig. 5.38 by the black solid line. Since the minimum is found at slightly larger angles than $35.26°$ (or slightly smaller than $144,74°$), this direction is labeled as "Vt" in Fig. 5.38. The global maximum is found between each of the Vt local minima (not shown) and is simply labeled with a "B" in Fig. 5.38. Finally, the saddle points between the Vt local minimum and the global minimum along the $<0\bar{3}31>$ (labeled SP3 in Fig. 5.38(a)) is 0.816 kJ/mol and between the same local minimum and the global minimum along z or $<0001>$ (not labeled in Fig. 5.38(a)) is 1.23 kJ/mol. Similarly to the fcc lattice, a volcano minimum is found along the $<1\bar{2}10>$ crystallographic direction (the equivalent $<2\bar{1}\bar{1}0>$ corresponds to the y Cartesian direction) in Fig. 5.38(a), when the Cl_2 is pointing to one of the equatorial nearest-neighbours (see top panel in Fig. 5.43). Please note that as in the fcc lattice, the volcano minima become global minima in Fig. 5.38(c) upon relaxation. As seen before for fcc, the head-on nearest-neighbours are pushed away to the minimum equilibrium distance dictated by the pH_2-Cl_2 pair potential, see Fig. 5.43, and the other 16 cage molecules adjust their positions to lower the total cohesive energy of the system. Upon relaxation, the global minimum along the $<0\bar{3}31>$ direction simply disappears, whereas the global minimum along the z or $<0001>$ direction becomes a maximum, confirming that their near degeneracy before relaxation was just incidental. The Vt remains a local minimum and the maximum B becomes a local minimum nearly degenerate to the Vt ones. Finally, the saddle point (SP4 in Fig 5.38(c)) between global and local B minimum is 1.20 kJ/mol, and between the two local minima (not labeled in Fig. 5.38(c)), Vt and B 0.68 kJ/mol.

Convergence of the optimization routine was difficult to check. In fact, since only the first two shells are relaxed in the present model, the optimization routine is mostly driven by the pH_2-Cl_2 pair potential, as already mentioned above, so that the caging molecules eventually move even closer to the impurity for larger values of the constraint, $C > 0.06$ nm, resulting in slightly artificial rotational PESs. Therefore, we compare the subsystem shown in Fig. 5.39 with the impurity along the $<001>$ to the $Cl_2(pH_2)_{14}$ minimum cluster structure shown in Fig. 5.19(g) of Sec. 5.3.6. The equilibrium distances of the caging molecules numbered from 1 to 14 after relaxation of the non-rigid fcc lattice and those optimized within the cluster growth are listed in Tab. 5.19 in the first and second columns, respectively. In the second column of Tab. 5.18 the distances are larger, since the solvent molecules are slightly attracted by the molecules of the outer shells in the matrix. This effect is stronger on the molecules in the belt ring than on those forming the square windows. The cohesive energy of the $Cl_2(pH_2)_{14}$ cluster has been recalculated by using

these larger distances resulting in a slightly more stable cluster of -25.15 kJ/mol against -24.88 kJ/mol of the optimized cluster $Cl_2(pH_2)_{14}$. The comparison confirms that the structure optimized is very close to the equilibrium structures, so that we believe that the optimization was stopped before entering the artificial regime.

Finally, please note that in all bottom panels of Figs. 5.39, 5.40 and 5.41 for the fcc lattice and to Figs. 5.42, 5.42 and 5.44 for the hcp lattice, the first two shells of solvent molecules after relaxation assume as expected an ellipsoidal form around the impurity. Nevertheless, when using the Manz's model [308] for pseudorotation, even by taking the largest displacement from Tab. 5.19, that is 0.085 nm as the average displacement, the increase in the moment of inertia due to pseudorotation is still less than 1.0% (upper limit) because of the very light mass of molecular hydrogen. Thus, pseudorotation is easily taking place, but the influence on the rotational constant and, consequently, on the rotational energy levels is negligible. Thus, coupling due to pseudorotation does not give rise to notable displacements in the vibrational frequencies or splitting in the rotational frequencies in the rovibrational spectrum, as suggested by Manz also for the CO@Ar cryogenic system.

Fit of the fcc Rotational PESs

The top panel of Figs. 5.39, 5.40 and 5.41 for the fcc lattice and to Figs. 5.42, 5.43 and 5.44 for the hcp lattice all represent the geometrical system configurations at different points of the rigid rotational PESs in Figs. 5.37(a) and 5.38(a), respectively. When rotating the impurity the O_h and D_{3h} symmetries of the fcc and hcp lattices are locally broken. However the overall symmetry is still conserved due to the rigid character of the outer molecules of the lattice considered. The bottom panels of Figs. 5.39, 5.40 and 5.41 for the fcc lattice and of Figs. 5.42, 5.43 and 5.44 for the hcp lattice, respectively, show the changes in the positions of the molecules in the first two solvation shells after relaxation ($C = 0.06$ nm). Similarly to the rigid DM, the O_h and D_{3h} symmetries are locally lost. For example, in Fig. 5.39 the symmetry of the $Cl_2(pH_2)_{18}$ subsystem is lowered from O_h to D_{4h}. Nevertheless, the overall symmetry of the rotational PESs is again preserved as before, since the environment is still taken to be rigid. Consequently, all rotational PESs can be still approximated by linear combinations of spherical harmonics as done by Devonshire. Equations are given here only for the O_h (fcc) symmetry by summing up linearly combined cubic harmonics up to the angular momentum $J = 8$,

$$W_{Cl_2}^{(0,0,0)}(\theta_A, \phi_A; \vec{R}_A) = K_0 V_0(\theta_A, \phi_A) + K_4 V_4(\theta_A, \phi_A) + K_6 V_6(\theta_A, \phi_A) + K_8 V_8(\theta_A, \phi_A) \quad (5.73)$$

where the coefficient K_0 corresponds to the shift parameter S, the coefficients K_4, K_6 and K_8 are given in Fig. 5.37 on top of the corresponding panel, terms $V_{J=0,4,6,8}$ are the

symmetry adapted spherical harmonics (SASH) of order J [301,302,317,318]

$$\begin{aligned} V_0(\theta_A,\phi_A) &= a_0 \times Y_{0,0} \\ V_4(\theta_A,\phi_A) &= a_4^4 \times Y_{4,4} + a_4{}^\circ \times Y_{4,0} + a_4^{-4} \times Y_{4,-4} \\ V_6(\theta_A,\phi_A) &= a_6^4 \times Y_{6,4} + a_6{}^\circ \times Y_{6,0} + a_6^{-4} \times Y_{6,-4} \\ V_8(\theta_A,\phi_A) &= a_8^8 \times Y_{8,8} + a_8^4 \times Y_{8,4} + a_8{}^\circ \times Y_{8,0} + a_8^{-4} \times Y_{8,-4} + a_8^{-8} \times Y_{8,-8} \end{aligned} \quad (5.74)$$

where the coefficients a_J^M determine the linear combinations of SHs and are found in Table I(a) of Ref. 319 as well as in Table I of Ref. 317. Similar equations can be written also for the hcp lattice, even though this is slightly more laborious, see for example [320]. Eq. 5.73 was used here in order to fit the rotational PESs with the K_J coefficients being the fitting parameters. This is very convenient for dynamical simulations since the potential energy matrix elements become just product of three spherical harmonics, for which analytical solutions are known. In order to fit the rotational PES in Fig. 5.37(a), Eq. 5.73 was expanded only to $K = 6$. The resulting potential already predicts the right landscape, except for the volcano shaped maxima for which cubic harmonics of order $J > 8$ are needed, but not implemented. The fitted values are K_4 = -182.98 kJ/mol and K_6 = -402.55 kJ/mol. The appearance of particular combinations of minima and maxima in octahedral crystal fields was connected to the signs of the K_4 and K_6 values already by Smith [300] in 1977 and are correctly predicted in Fig. 5.37(b), where both of them are negative. In Figs. 5.37(d) and 5.37(f) the connection between the signs of the K_4 and K_6 and the positions of minima and maxima on the PESs foreseen in Ref. 300 is instead broken, due to the inclusion of the K_8 parameter.

Cl_2 Librational Energy Levels in the Matrix

The rotational PESs, $W_{\mathrm{Cl_2}}^{(n=v=0)}(\theta_A,\phi_A;R_{\mathrm{exp}})$, within the fcc rigid and non-rigid lattice in Figs. 5.37(a) and 5.37(e) and within the hcp rigid and non-rigid lattice in Figs. 5.38(a) and 5.38(c), have been inserted in the SE given in Eq. 5.71 in order to calculate the respective rotational energy levels. The results are depicted in the spectrum-like Fig. 5.45, where they are also compared with the free rotor quantum levels. The energies are again given in the double scale units [kJ/mol ; B_e], as for the effective rotational PESs. Before entering the many information contained in this figure, the reader should note that for each of the models, the saddle point energies SP1, SP2, SP3, SP4 from Figs. 5.37 and 5.38 are represented by the respective green lines. These energies have to be understood as the respective barriers hindering the Cl_2 rotation within the crystal and must be compared to the free rotor energy levels depicted on the left side of the figure. The green lines are found between the rotational levels $J = 16$ and $J = 21$, which is roughly between 275 and 440 B_e units. Thus, referring to the DM, the Cl_2@pH_2 molecular system resides at one of

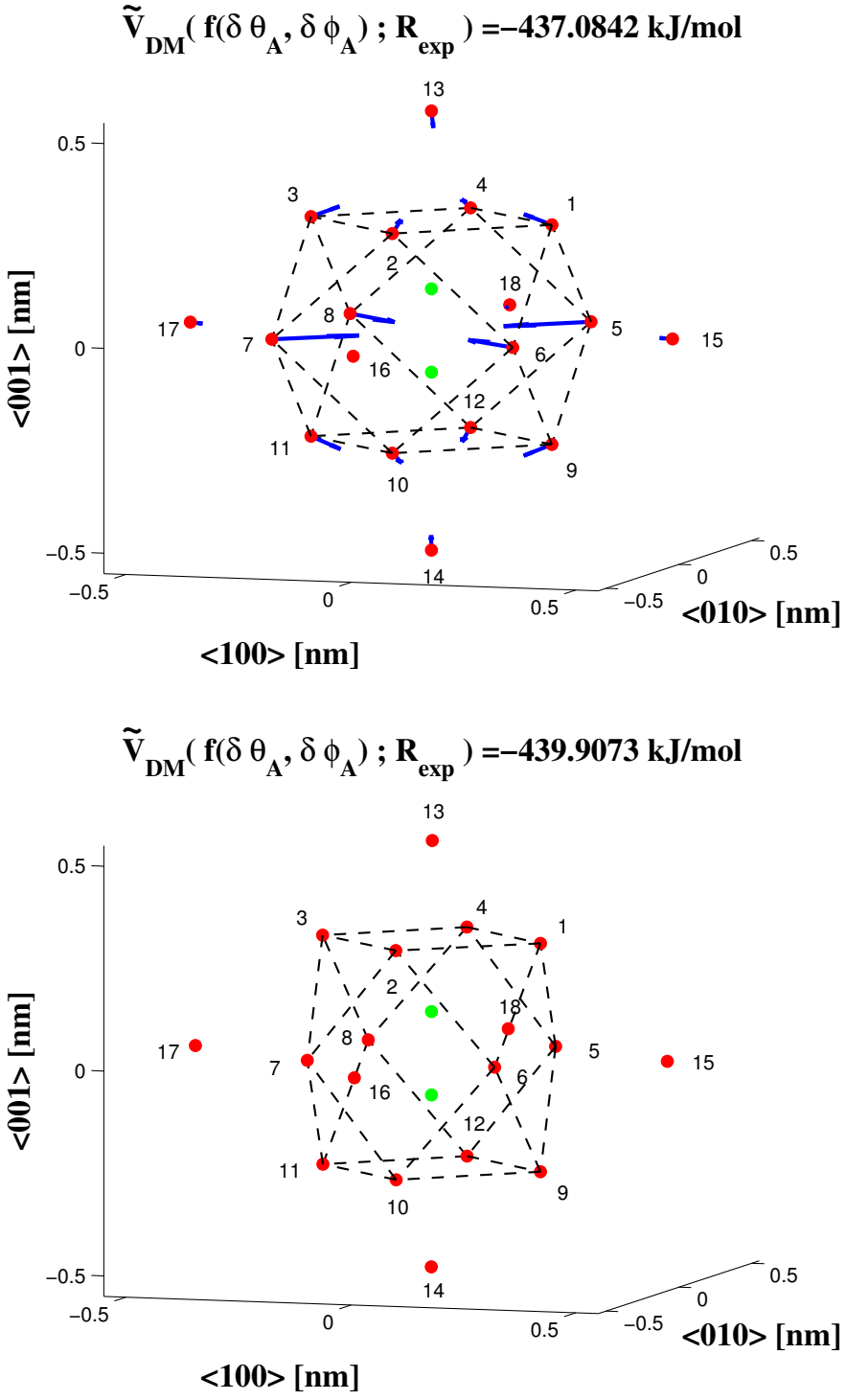

Figure 5.39: The position of the caging molecules is shown before (top panel) and after (bottom panel) relaxing ($C = 0.06$ nm) an fcc crystal around the Cl_2 molecule lying along the <001> direction. The motion is depicted by the blue arrows. The corresponding energies, $V_{\rm DM}(f(\delta\theta_A, \delta\phi_A); R_{\rm exp})$ and $\tilde{V}_{\rm DM}(f(\delta\theta_A, \delta\phi_A); R_{\rm exp})$ in Eqs. 5.69 and 5.70 are also given.

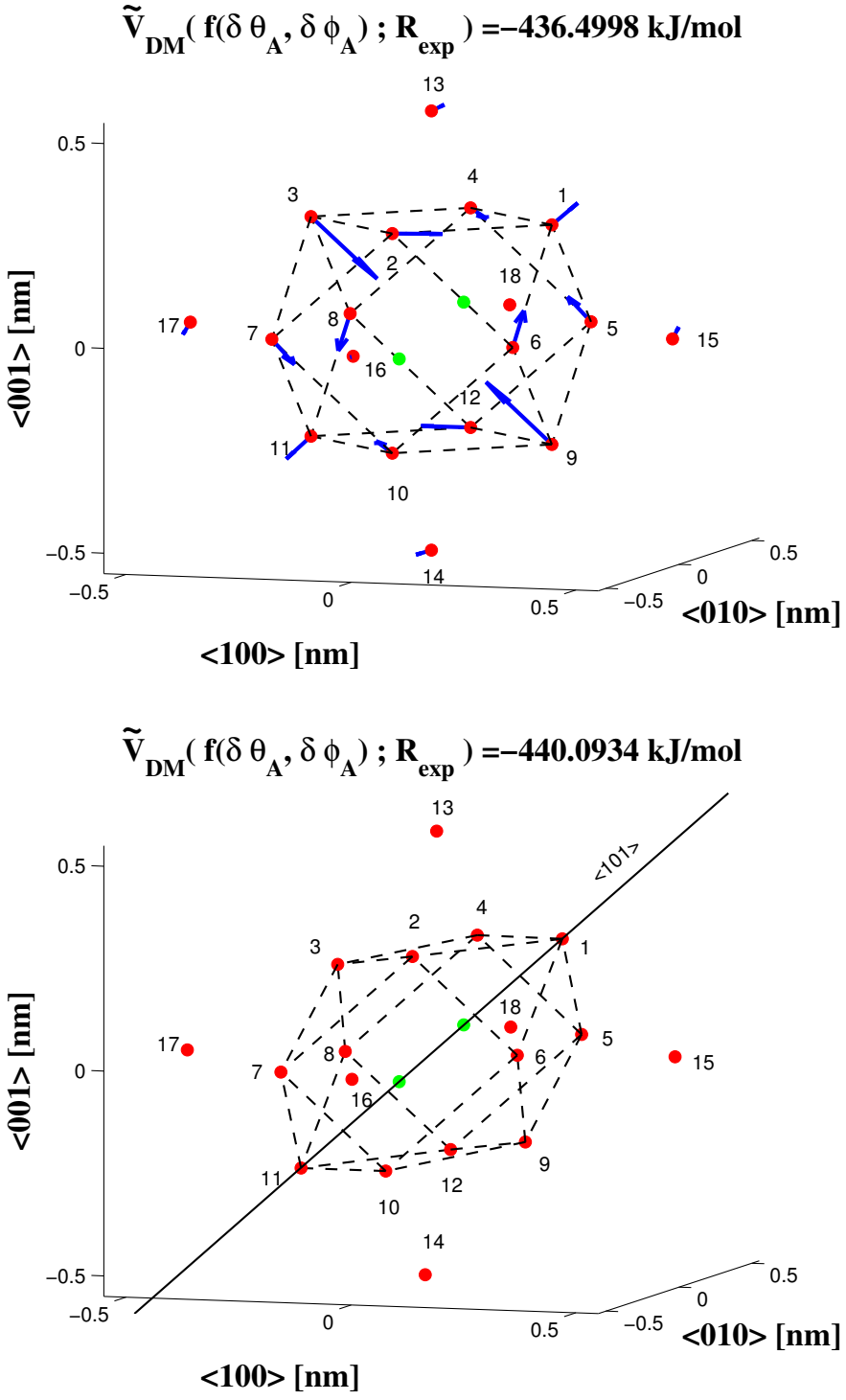

Figure 5.40: The position of the caging molecules is shown before (top panel) and after (bottom panel) relaxing ($C = 0.06$ nm) an fcc crystal around the Cl_2 molecule lying along the <101> direction. The motion is depicted by the blue arrows. The corresponding energies, $V_{\rm DM}(f(\delta\theta_A, \delta\phi_A); R_{\rm exp})$ and $\tilde{V}_{\rm DM}(f(\delta\theta_A, \delta\phi_A); R_{\rm exp})$ in Eqs. 5.69 and 5.70 are also given.

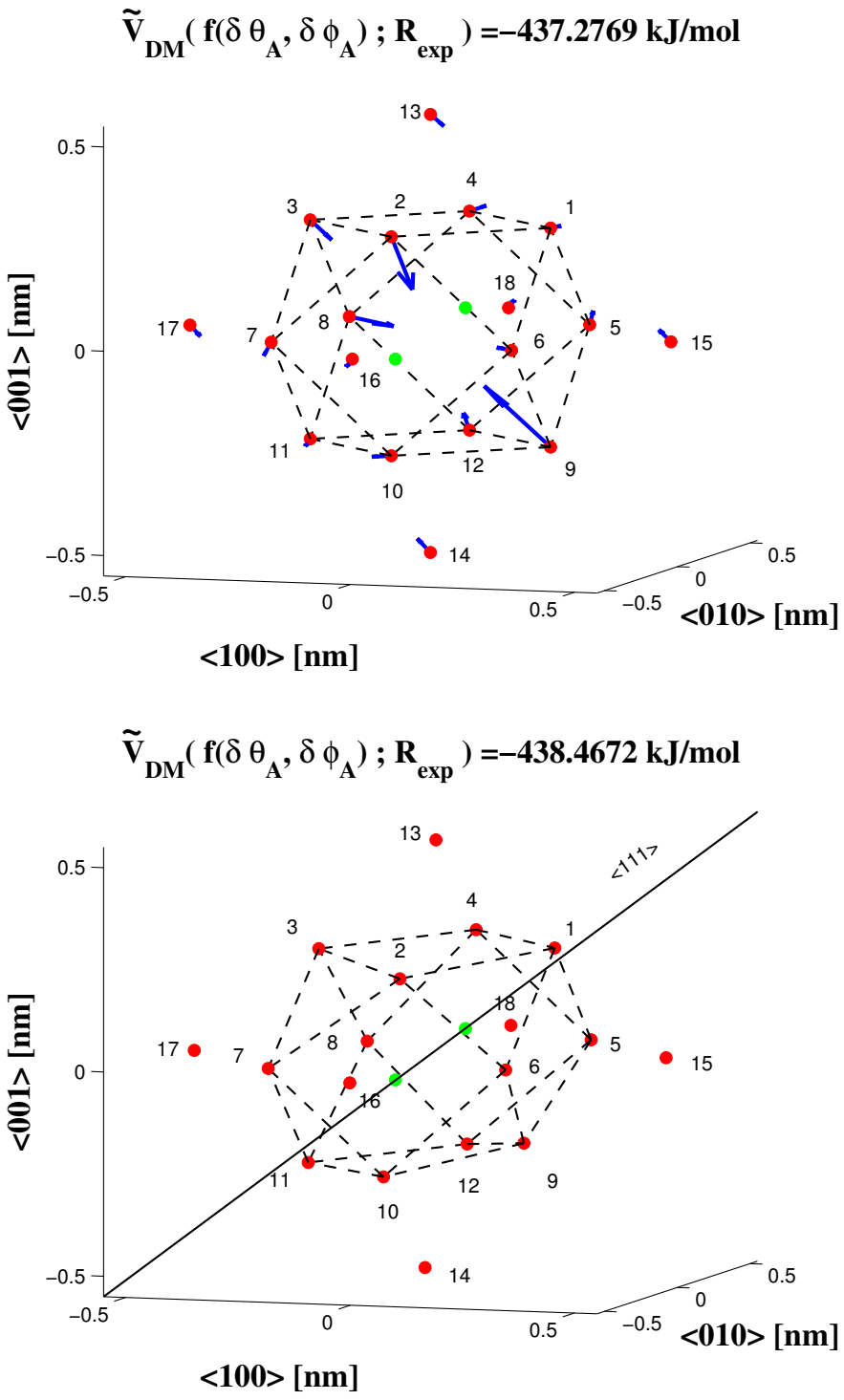

Figure 5.41: The position of the caging molecules is shown before (top panel) and after (bottom panel) relaxing ($C = 0.06$ nm) an fcc crystal around the Cl_2 molecule lying along the <111> direction. The motion is depicted by the blue arrows. The corresponding energies, $V_{\rm DM}(f(\delta\theta_A, \delta\phi_A); R_{\rm exp})$ and $\tilde{V}_{\rm DM}(f(\delta\theta_A, \delta\phi_A); R_{\rm exp})$ in Eqs. 5.69 and 5.70 are also given.

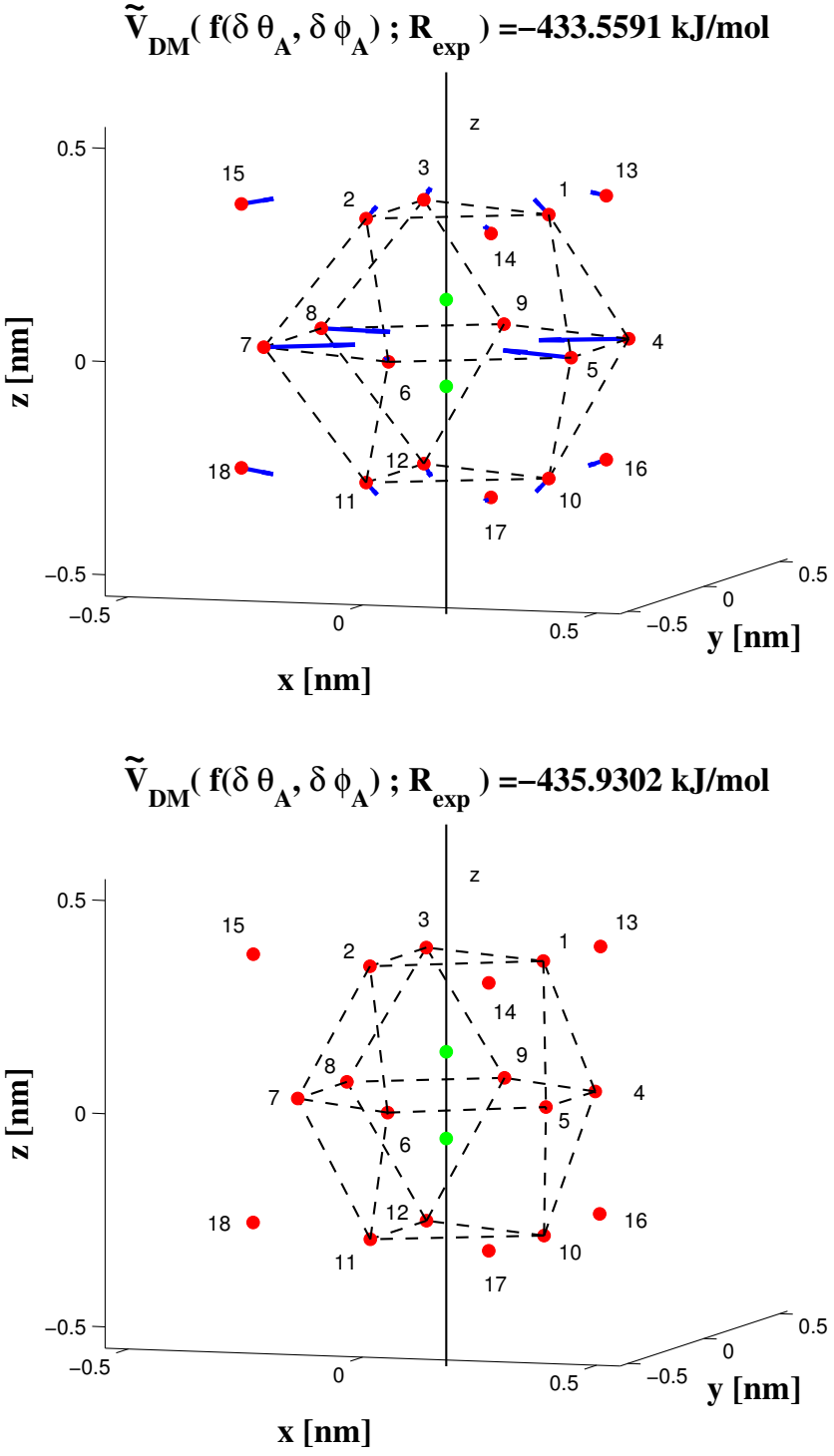

Figure 5.42: The position of the caging molecules is shown before (top panel) and after (bottom panel) relaxing ($C = 0.06$ nm) an hcp crystal around the Cl_2 molecule lying along the <0001> (or z) direction. The motion is depicted by the blue arrows. The corresponding energies, $V_{\rm DM}(f(\delta\theta_A, \delta\phi_A); R_{\rm exp})$ and $\tilde{V}_{\rm DM}(f(\delta\theta_A, \delta\phi_A); R_{\rm exp})$ in Eqs. 5.69 and 5.70 are also given.

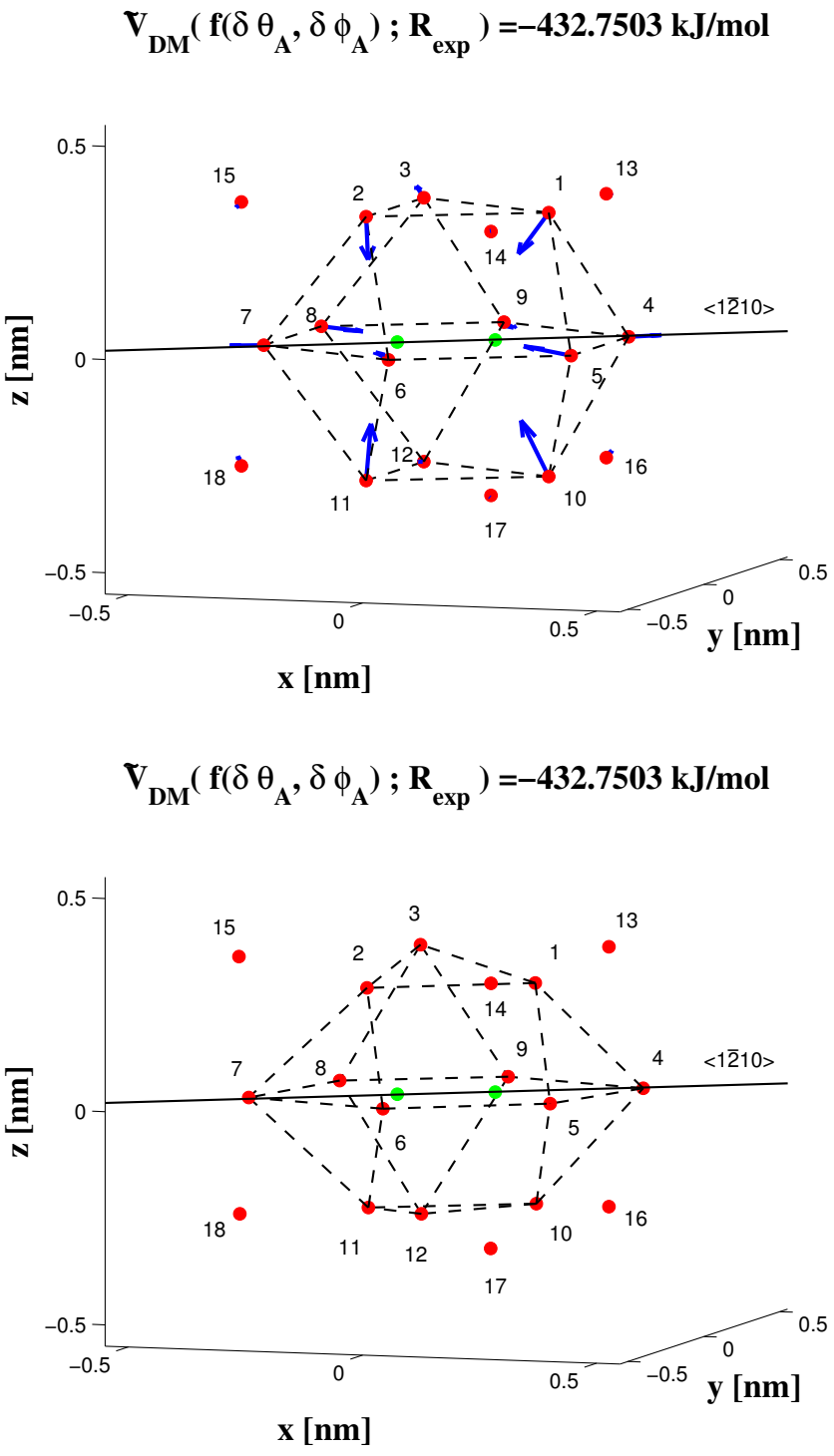

Figure 5.43: The position of the caging molecules is shown before (top panel) and after (bottom panel) relaxing ($C = 0.06$ nm) an hcp crystal around the Cl_2 molecule lying along the $<1\bar{2}10>$ direction. The motion is depicted by the blue arrows. The corresponding energies, $V_{\rm DM}(f(\delta\theta_A, \delta\phi_A); R_{\rm exp})$ and $\tilde{V}_{\rm DM}(f(\delta\theta_A, \delta\phi_A); R_{\rm exp})$ in Eqs. 5.69 and 5.70 are also given.

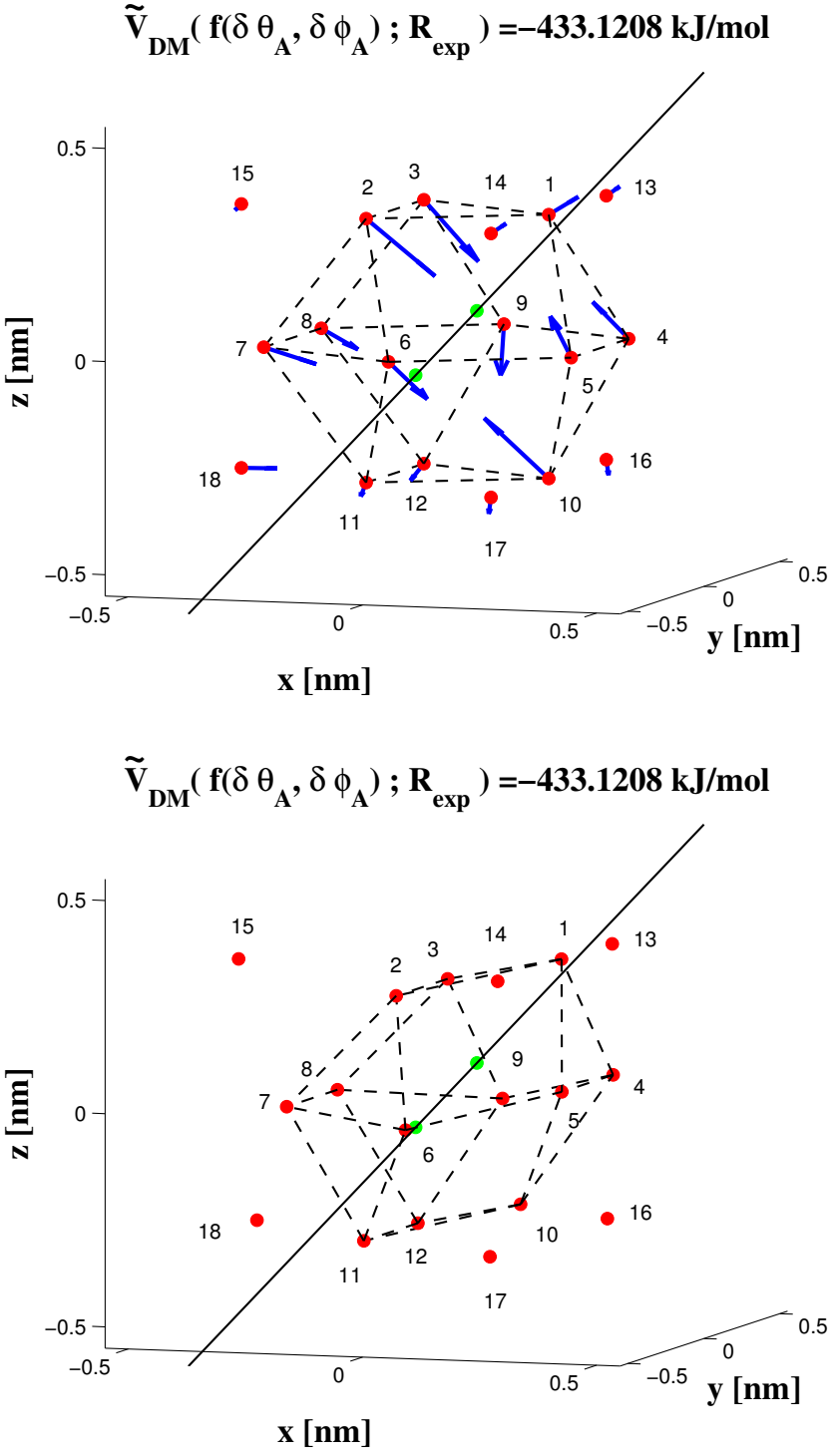

Figure 5.44: The position of the caging molecules is shown before (top panel) and after (bottom panel) relaxing ($C = 0.06$ nm) an hcp crystal around the Cl_2 molecule lying along the Vt direction. The motion is depicted by the blue arrows. The corresponding energies, $V_{\mathrm{DM}}(f(\delta\theta_A, \delta\phi_A); R_{\mathrm{exp}})$ and $\tilde{V}_{\mathrm{DM}}(f(\delta\theta_A, \delta\phi_A); R_{\mathrm{exp}})$ in Eqs. 5.69 and 5.70 are also given.

Table 5.19: The absolute values of the displacement vectors due to relaxation ($C = 0.06$ nm) of the molecules in the first two solvation shells are listed for Cl_2 lying along the <001>, <101> and <111> of the fcc matrix, and along the <0001> (or z), <$1\bar{2}10$> (or y) and Vt directions of the hcp matrix are listed.

Molecule Number	$< 001 > [pm]$	$< 101 > [pm]$	$< 111 > [pm]$
1	27	32	15
2	29	56	83
3	28	84	27
4	28	56	16
5	85	55	14
6	85	57	27
7	85	57	15
8	85	57	84
9	29	84	83
10	30	55	17
11	29	32	15
12	29	56	27
13	17	13	18
14	15	14	20
15	11	13	20
16	12	5	19
17	11	14	18
18	12	7	21
Molecule Number	$< 0001 >, z\,[pm]$	$< 1\bar{2}10 >, y\,[pm]$	$Vt\,[pm]$
1	15	83	84
2	14	27	22
3	14	78	20
4	7	30	52
5	17	86	34
6	15	29	85
7	22	66	76
8	22	57	76
9	61	71	53
10	14	78	85
11	61	74	50
12	72	31	50
13	19	15	17
14	17	12	17
15	25	13	34
16	19	16	17
17	15	13	17
18	25	12	10

the far ends of the Devonshire [174] diagram for large absolute values of K and, therefore, definitely in the librational regime.

Molecular librations around main crystallographic directions can be described within 2D anharmonic oscillators (AO). Since the results are going to be discussed only qualitatively, let us for simplicity consider a non-degenerate 2D HO approximated by the sum of two 1D HOs along each of the two dimensions. Moreover, let us already distinguish between global and local minima by considering two of them:

$$E_{Cl_2}^{(\Lambda_1;\Lambda_2)}(\vec{R}_A) = \hbar\omega_1\left(\Lambda_1+\frac{1}{2}\right)+\hbar\omega_2\left(\Lambda_2+\frac{1}{2}\right) \quad (5.75)$$

$$E_{Cl_2}^{(\Lambda_3;\Lambda_4)}(\vec{R}_A) = \hbar\omega_3\left(\Lambda_3+\frac{1}{2}\right)+\hbar\omega_4\left(\Lambda_4+\frac{1}{2}\right) \quad (5.76)$$

where the first couple of quantum numbers, $(\Lambda_1;\,\Lambda_2)$ will be always referred to the global minimum wells and the second couple of quantum numbers $(\Lambda_3;\,\Lambda_4)$ to the local minimum wells. In the most simple case of degenerate 1D HOs, that is the case if $\omega_1=\omega_2$ and $\omega_3=\omega_4$, the previous equations reduce to the even more simple form of the 2D HOs

$$E_{Cl_2}^{(\Lambda_g)}(\vec{R}_A) = \hbar\omega_g\,(\Lambda_g+1) \quad (5.77)$$

$$E_{Cl_2}^{(\Lambda_l)}(\vec{R}_A) = \hbar\omega_l\,(\Lambda_l+1) \quad (5.78)$$

with $\omega_g=\omega_1=\omega_2$, $\omega_l=\omega_3=\omega_4$ and $\Lambda_g=\Lambda_1+\Lambda_2$ and $\Lambda_l=\Lambda_3+\Lambda_4$. To recall the 2D HO model at this point is useful, since it helps in reading the features in Fig. 5.45. In a 2D HO the first eigenvector with quantum number $\Lambda_g=0$ has no nodes and is singly degenerate. The next eigenvector can either have one node along the first dimension, that is $(\Lambda_1=1;\,\Lambda_2=0)$, or along the second one, that is $(\Lambda_1=0;\,\Lambda_2=1)$, but since the sum of the two quantum numbers is $\Lambda_g=1$ in both cases, the eigenvector is doubly degenerate. Similarly, the eigenvector with $\Lambda_g=2$ is triply degenerate, since the following three combinations of couples of quantum numbers $(\Lambda_1=2;\,\Lambda_2=0)$, $(\Lambda_1=0;\,\Lambda_2=2)$ and $(\Lambda_1=1;\,\Lambda_2=1)$ are possible and so on. Finally, the eigenvectors present (Λ_g+1)-fold or, equivalently, (Λ_l+1)-fold degeneracy.

The different librational states could be recognized on the base of the number of the nodes along the θ_A or the ϕ_A dimensions of the respective two dimensional eigenvectors, at least as long as the eigenvalues lie below the respective saddle points SP1, SP2, SP3 and SP4 between global and local minima. Above such limit, that is above the green lines, the wavefunctions from the different wells begin to mix and the assignment of the right quantum numbers to the eigenvectors becomes too difficult. These mixed states are

represented by the black lines up to the arbitrary energy value of 1.5 kJ/mol, whereas below such threshold the red and blue lines are always the librational levels localized respectively in the global and local minimum wells. Please note that in the former two "spectra" (fcc), the green lines are between black lines, whereas in the latter two "spectra" (hcp), they are still between red and/or blue lines. This may depend on how important tunneling effects between minimum wells are, since they can anticipate the mixing of eigenvectors already below the respective energy barriers.

Please note that when solving the SE in Eq. 5.71, all rotational PESs are evaluated in the range $\theta_A = 0 - 180°$ and $\phi_A = 0 - 360°$, so that the property of homonuclear molecules to exist in their para and ortho species, proper also to Cl_2, similarly to H_2 and D_2, was neglected. In fact, half of the rotational PESs is found by just inverting the position of the chlorine atoms. Thus, the SE is solved as the impurity would be the $Cl^{35}Cl^{37}$ heteronuclear molecule.

The number n of minimum wells found on the potential dictates the degeneracy of the eigenvalues, since this corresponds to consider an ensemble of n 2D HOs. Finally, in the ideal case of n independent 2D HOs, one expects therefore $n_g \times (\Lambda_g + 1)$ and $n_l \times (\Lambda_l + 1)$ degenerate eigenvalues. Since the oscillators are neither harmonic, nor independent, such degeneracy is definitively lifted in Fig. 5.45, but nonetheless the $d_g = n_g \times (\Lambda_g + 1)$-fold and $d_l = n_l \times (\Lambda_l + 1)$-fold librational energy levels, $E_{Cl_2}^{(\Lambda_g)}$ and $E_{Cl_2}^{(\Lambda_l)}$ of the ideally six uncoupled 2D HOs are calculated as the arithmetic mean values of the corresponding non-degenerate eigenvalues $E_{Cl_2}^{(\Lambda_1;\Lambda_2)}$ and $E_{Cl_2}^{(\Lambda_3;\Lambda_4)}$ with $\Lambda_1 + \Lambda_2 = \Lambda_g$ and $\Lambda_3 + \Lambda_4 = \Lambda_l$, respectively. The quantum numbers $(\Lambda_1; \Lambda_2)$, $(\Lambda_3; \Lambda_4)$, Λ_g and Λ_l, as well as the degeneracies (d_g) and (d_l) are given in Fig. 5.45.

fcc Rigid DM

Global Minima (red librational energy levels). Let us consider the librational quantum levels obtained within the fcc rigid lattice model in more detail. The corresponding rotational PES shows six global minimum wells along the <001> crystallographic direction corresponding to the three couples of spherical angles $\{\theta_A; \phi_A\} = \{0°; \infty\}, \{90°; 0°\}, \{90°; 90°\}$, respectively. The spherical coordinates corresponding to the other three minima are found by inverting the position of the two chlorine atoms, they are $\{\theta_A; \phi_A\} = \{180°; \infty\}$, $\{90°; 180°\}, \{90°; 270°\}$. The first six eigenvectors present no nodes and the corresponding eigenvalues are $d_g = 6$-fold (nearly) degenerate, so that the system is well approximated by an ensemble of six uncoupled 2D HOs with quantum number $\Lambda_g = \Lambda_1 + \Lambda_2 = 0$, with ideal first librational eigenvalue $E_{Cl_2}^{(\Lambda_g=0)} = \frac{1}{2}\hbar\omega_g = 0.24$ kJ/mol (see Eq. 5.77 for $\Lambda_g = 0$). Please note that this is the librational ZPE of the system within the harmonic approximation considered here. The degeneracy is slightly lifted by tunneling effects between the six potential wells coupling the oscillators. The next twelve eigenvectors have either a node along the first dimension ϕ_A or along the second dimension θ_A, so that the correspond-

ing quantum numbers are ($\Lambda_1 = 1$; $\Lambda_2 = 0$) or ($\Lambda_1 = 0$; $\Lambda_2 = 1$), both corresponding to $\Lambda_g = \Lambda_1 + \Lambda_2 = 1$ in the ideal case of six uncoupled 2D HOs. The degeneracy is completely lifted by tunneling effects, which indeed increase for higher eigenvalues, and additionally by the anharmonicity of the oscillators, i.e. two different frequencies ω_1 and ω_2 along the two dimensions. From the eigenvectors and the corresponding eigenvalues, it could be argued that the potential well is narrower, i.e. steeper, along the second coordinate, θ_A, than along the first one, ϕ_A. and therefore $\omega_2 > \omega_1$. Finally, the second librational level of the ideal ensemble of 2D HOs has energy $E_{Cl_2}^{(\Lambda_g=1)} = 0.42$ kJ/mol with $\Delta E_{\Lambda_g=1\leftarrow 0} = 0.18$ kJ/mol. Following this line of reasoning, we can assign also the next 18 eigenvectors to the three following combinations of quantum numbers ($\Lambda_1 = 0$; $\Lambda_2 = 2$), ($\Lambda_1 = 1$; $\Lambda_2 = 1$) and ($\Lambda_1 = 2$; $\Lambda_2 = 0$) and corresponding ideally to the quantum number $\Lambda_g = \Lambda_1 + \Lambda_2 = 2$. The degeneracy of the $d_g = 18$ eigenvalues is again lifted by an even increased anharmonicity of the oscillators and by strong tunnel effects coupling them. The third librational level of the ideal ensemble of 2D HOs has energy $E_{Cl_2}^{(\Lambda_g=2)} = 0.68$ kJ/mol with $\Delta E_{\Lambda_g=2\leftarrow 1} = 0.26$ kJ/mol. The fourth and last group of librational levels comprises the 12 eigenvectors with quantum numbers ($\Lambda_1 = 1$, $\Lambda_2 = 2$) and ($\Lambda_1 = 2$, $\Lambda_2 = 1$), so that those with quantum numbers ($\Lambda_1 = 0$, $\Lambda_2 = 3$) and ($\Lambda_1 = 3$, $\Lambda_2 = 0$) ideally corresponding to the $\Lambda_g = \Lambda_1 + \Lambda_2 = 3$, as well, are already mixing with the eigenvectors from the local minimum wells. The eigenvalue of the ideal ensemble of 2D HO oscillators is $E_{Cl_2}^{(\Lambda_g=3)} = 0.85$ kJ/mol with $\Delta E_{\Lambda_g=3\leftarrow 2} = 0.17$ kJ/mol.

Local Minima (blue librational energy levels). Eight local minima are found in the rotational PES along the <111> crystallographic direction to which the following spherical coordinates correspond: $\{\theta_A;\phi_A\} = \{54.7°; 45° + n \times 90°\}, \{125.3°; 45° + n \times 90°\}$ with $n = 0, 1, 2, 3$. The first eight eigenvectors do not have any nodes, i.e. with quantum numbers $\Lambda_l = \Lambda_3 + \Lambda_4 = 0$. They present complete $d_l = 8$ degeneracy, so that the librations is well described by eight independent 2D HOs with librational ZPE $E_{Cl_2}^{(\Lambda_l=0)} = \frac{1}{2}\hbar\omega_l = 0.54$ kJ/mol (see Eq. 5.78 for $\Lambda_l = 0$). Please note that the librational ZPE is calculated from the bottom of the local minimum well at 0.0147 kJ/mol indicated in Fig. 5.45 by the blue dotted horizontal line. Since the local minimum wells are much steeper and narrower than the global minimum wells, the higher eigenvalues are already above the saddle point SP2 in the upper part of the figure, where the corresponding eigenvectors mix with those localized in the global minimum (black lines).

fcc Non-rigid DM

Global Minima (red librational energy levels). The same reasoning can now be repeated for each of the other DMs. The fcc non-rigid lattice results in a rotational PES with 12 global minimum well along the <101> corresponding to the following spherical coordinates $\{\theta_A;\phi_A\} = \{45°; 0+n\times 90°\}, \{90°; 45°+n\times 90°\}$ and $\{135°; 0°+n\times 90°\}$, respectively with $n = 0, 1, 2, 3$. Along this crystallographic direction the impurity points to one of the 12 first NNs. The first 12 eigenvectors do not have any nodes and the corresponding eigenvalues

are $d_g = 12$-fold (nearly) degenerate, so that the system is still well approximated by an ensemble of 12 uncoupled 2D HOs with quantum number $\Lambda_g = \Lambda_1 + \Lambda_2 = 0$, the librational ZPE of which is $E_{Cl_2}^{(\Lambda_g=0)} = \frac{1}{2}\hbar\omega_g = 0.29$ kJ/mol (see Eq. 5.77 for $\Lambda_g = 0$). The next 24 eigenvectors have either one node along ϕ_A or along θ_A, i.e. their quantum numbers are ($\Lambda_1 = 1$ $\Lambda_2 = 0$) or ($\Lambda_1 = 0$; $\Lambda_2 = 1$) both corresponding ideally to $\Lambda_g = \Lambda_1 + \Lambda_2 = 1$. The ideal $d_g = 24$-fold degeneracy is now completely lifted. Since the potential well has similar steepness along the two dimensions, i.e. the frequencies ω_1 and ω_2 are similar, we argue that the anharmonicity effects are small and that the degeneracy is lifted principally because of tunneling effects between global and local minima. The approximation to an ideal system of 12 uncoupled 2D HOs gives a librational energy level at $E_{Cl_2}^{(\Lambda_g=1)} = 0.55$ kJ/mol with $\Delta E_{\Lambda_g=1\leftarrow 0} = 0.26$ kJ/mol, which is indeed energetically close to the saddle point (SP2) between global and local minima. This is also proved by the fact that the eigenvectors at higher energies already mix with those in the local minimum wells even though they lie still below the saddle point energy SP2.

Local Minima (blue librational energy levels). When relaxing the fcc lattice, the global minima within the fcc rigid DM become now local minima. They are therefore located along the same crystallographic direction. The first 6 eigenvectors do not have any nodes and the corresponding $d_l = 6$ librational energy levels are nearly degenerate. The approximation to an ensemble of six ideally uncoupled 2D HOs with quantum number $\Lambda_l = \Lambda_3 + \Lambda_4 = 0$ results in the ideal librational ZPE $E_{Cl_2}^{(\Lambda_l=0)} = \frac{1}{2}\hbar\omega_l = 0.23$ kJ/mol (see Eq. 5.78 for $\Lambda_l = 0$), where the bottom of the local minimum well at 0.2252 kJ/mol is indicated in Fig. 5.45 by the blue dotted horizontal line. The next 12 eigenvectors have either one node along ϕ_A or along θ_A so that their quantum numbers are ($\Lambda_3 = 1$; $\Lambda_4 = 0$) and ($\Lambda_3 = 0$; $\Lambda_4 = 1$) both corresponding ideally to $\Lambda_l = \Lambda_3 + \Lambda_4 = 1$. The approximation to an ideal system of six uncoupled 2D HOs results in the second librational energy level, $E_{Cl_2}^{(\Lambda_l=1)} = 0.45$ kJ/mol with $\Delta E_{\Lambda_l=1\leftarrow 0} = 0.22$ kJ/mol. As in the global minima, the ideal $d_l = 6$-fold and $d_l = 12$-fold degeneracies for $\Lambda_l = 0$ and $\Lambda_l = 1$ are lifted by small tunneling effects. It is interesting to note that the minimum wells in the <001> direction, even though they became local minima upon relaxation, remain almost unchanged, in particular the bottoms. This is inferred by comparing the librational ZPE and the first librational quantum in the global minima of the fcc rigid DM and in the local minima of the fcc non-rigid DM, that is $E_{Cl_2}^{(\Lambda_g=0)} = \frac{1}{2}\hbar\omega_g = 0.24$ kJ/mol and $\Delta E_{\Lambda_g=1\leftarrow 0} = 0.18$ kJ/mol against $E_{Cl_2}^{(\Lambda_l=0)} = \frac{1}{2}\hbar\omega_l = 0.23$ kJ/mol and $\Delta E_{\Lambda_l=1\leftarrow 0} = 0.22$ kJ/mol, respectively. What effectively changes upon relaxation are indeed the relative stabilities of the system along the <111> and the <101> directions: The former destabilized to a maximum, the latter stabilized to a global minimum. Finally, with respect to the fcc rigid DM, the librational frequencies are all in the same order or, equivalently, the walls in the respective wells have similar steepness. With respect to the fcc rigid DM within the non-rigid fcc DM broader wells are favoured upon relaxation.

hcp Rigid DM

Global Minima (red librational energy levels). In the hcp rigid model, librational states could be assigned only to the 12 global minimum wells along the $<0\bar{3}31>$ direction, to which correspond the spherical coordinates $\{\theta_A;\phi_A\} = \{71.8°; 0° + n \times 60°\}$ and $\{180° - 71.8°; 0° + n \times 60°\}$ with $n = 0, 1, 2, 3, 4, 5$, and to the nearly degenerate couple of minima along the $<0001>$ (or z) direction to which correspond the spherical coordinates $\{\theta_A;\phi_A\} = \{0°;\infty\}$ and $\{180°;\infty\}$, respectively. There is a set of 14 lowest eigenvalues with quantum number $\Lambda_g = \Lambda_1 + \Lambda_2 = 0$. To the twelve eigenvectors localized in the wells along the $<0\bar{3}31>$ direction correspond $d_g = 12$-fold (nearly) degenerate eigenvalues, whereas to the two eigenvectors localized in the wells along the $<0001>$ (or z) direction correspond two degenerate eigenvalues at a slightly higher energy. From this we deduce that the latter wells are steeper compared to the former one. The two crystallographic directions are indeed not equivalent, as already mentioned above in Sec. 5.3.8. Nevertheless, the system is approximated by an ensemble of 14 uncoupled 2D HOs with ideal librational ZPE $E_{Cl_2}^{(\Lambda_g=0)} = \frac{1}{2}\hbar\omega_g = 0.49$ kJ/mol (see Eq. 5.77 for $\Lambda_g = 0$). The degeneracy within the ideally $d_g = 12$-fold degenerate eigenvalues is principally lifted due to tunneling effects between the global minimum wells ($<0\bar{3}31>$), and to the anharmonicity of the oscillators (triangular shape of the well). The next 24 eigenvectors with quantum numbers $(\Lambda_1 = 1; \Lambda_2 = 0)$ and $(\Lambda_1 = 0; \Lambda_2 = 1)$ are localized in the potential wells along the $<0\bar{3}31>$ direction only. The ideal $d_g = 24$-fold degeneracy of the corresponding eigenvalues is lifted again due to tunneling effects, but in particular to the more evident anharmonicity effects. From the eigenvectors and the corresponding eigenvalues, it could be argued that the potential well is narrower, i.e. steeper, along the second coordinate θ_A, than along the first one, ϕ_A, i.e. $\omega_2 > \omega_1$. The librational energy levels of the approximated system of 12 uncoupled 2D HOs finally results in $E_{Cl_2}^{(\Lambda_g=1)} = 0.82$ kJ/mol with $\Delta E_{\Lambda_g=1\leftarrow 0} = 0.33$ kJ/mol. Higher eigenvectors are difficult to assign, since they lie energetically above the saddle point SP3 energy (black levels) mixing with the one from the local minimum wells. However, in contrast to the fcc non-rigid DM, the 24 eigenvectors ideally with $\Lambda_g = \Lambda_1 + \Lambda_2 = 1$ could be still correctly assigned, even though some of them also lie energetically above the saddle point. This is due to the fact that the bottom of the local minimum wells (Vt) lie at the high energy of 0.4373 kJ/mol (see blue dotted line in Fig. 5.45) and the respective eigenvectors well above the saddle point.

Local Minima (blue librational energy levels). No librational states could be assigned exclusively to the local minimum wells. Compared to both the fcc rigid and non-rigid DMs, the librational quanta between librational levels slightly increases because of narrower and steeper walls of the global minimum wells.

hcp Non-rigid DM

Global Minima (red librational energy levels). Upon relaxation in the hcp matrix the 6 volcano minima along the $<1\bar{2}10>$ (or y) direction become global minima, to which cor-

respond the following spherical coordinates: $\{\theta_A;\phi_A\} = \{90°;30° + n \times 60°\}$, respectively for $n = 0,1,2,3,4,5$. The first six eigenvectors do not have any nodes and have therefore quantum numbers $\Lambda_g = \Lambda_1 + \Lambda_2 = 0$. To them correspond $d_g = 6$ degenerate librational eigenvalues, so that the system behaves as an ensemble of six uncoupled 2D HOs with librational ZPE $E_{Cl_2}^{(\Lambda_g=0)} = \frac{1}{2}\hbar\omega_g = 0.40$ kJ/mol. Tunneling effects are absent, since the global minimum wells are separated by the global maxima along the $<0\bar{1}10>$ (or y) direction (about 2.3 kJ/mol) and the librational ZPE lies well below the bottom of the local minimum wells. Moreover, 12 eigenvectors with quantum numbers $\Lambda_g = 1$ could be assigned easily. To the 6 eigenvectors with quantum numbers ($\Lambda_1 = 0$; $\Lambda_2 = 1$) and and to those with quantum numbers ($\Lambda_1 = 1$; $\Lambda_2 = 0$) correspond to two groups of 6 degenerate eigenvalues. Thus, the ideally $d_g = 12$ degenerate eigenvalues are split in two groups. This proves that there are no tunneling effects between the minimum wells, but only anharmonicity effects due to different steepnesses along the two dimensions θ_A and ϕ_A, respectively. In particular, we could argue that $\omega_2 > \omega_1$. The second librational level of the ideal ensemble of 2D HOs is found at $E_{Cl_2}^{(\Lambda_g=1)} = 0.79$ kJ/mol with $\Delta E_{\Lambda_g=1\leftarrow 0} = 0.39$ kJ/mol. A third series of eigenvectors with quantum numbers $\Lambda_g = \Lambda_1 + \Lambda_2 = 2$ is localized in the global wells. The degeneracy of the corresponding $d_g = 18$ librational energies is now lifted also by tunneling effects between global and local minima. Nevertheless, those effects are still small, since the eigenvectors could be assigned easily even though they lie energetically above the saddle point SP4. Approximation of the system to an ensemble of six uncoupled 2D HOs gives the librational energy $E_{Cl_2}^{(\Lambda_g=2)} = 1.16$ kJ/mol with $\Delta E_{\Lambda_g=2\leftarrow 1} = 0.37$ kJ/mol. The higher eigenvectors lie well above the saddle point SP4, where the eigenvectors from global and local wells are mixing. The librational quanta in the global minimum well are again larger than in both the fcc rigid and non-rigid DMs.

Local Minima (blue librational energy levels). The local minima along the Vt and $<0\bar{3}31>$ directions are practically degenerate and the barrier between them is only 0.13 kJ/mol. As a consequence, the eigenvectors in the 24 wells mix already at low energies and the degeneracies d_l of the corresponding eigenvalues are completely lifted (the levels are spread out in Fig. 5.45). In other words, the approximation to the ensemble of 2D HOs is rather poor. Nevertheless, due to the high energy of the saddle point SP4, the eigenvectors from local and global minima mix only late and at least the sequences of eigenvalues are easily assigned. Two series of 24 and 48 eigenvalues are assigned to the librational ground state and to first excited librational energies, respectively. Considering an ideal ensemble of six uncoupled 2D HOs the librational ZPE is $E_{Cl_2}^{(\Lambda_l=0)} = \frac{1}{2}\hbar\omega_l = 0.29$ kJ/mol and the energy of second librational level is $E_{Cl_2}^{(\Lambda_l=1)} = 1.10$ kJ/mol with $\Delta E_{\Lambda_l=1\leftarrow 0} = 0.31$ kJ/mol. Finally, the librational quanta in the local minimum wells are comparable to those in both the fcc rigid and non-rigid DMs.

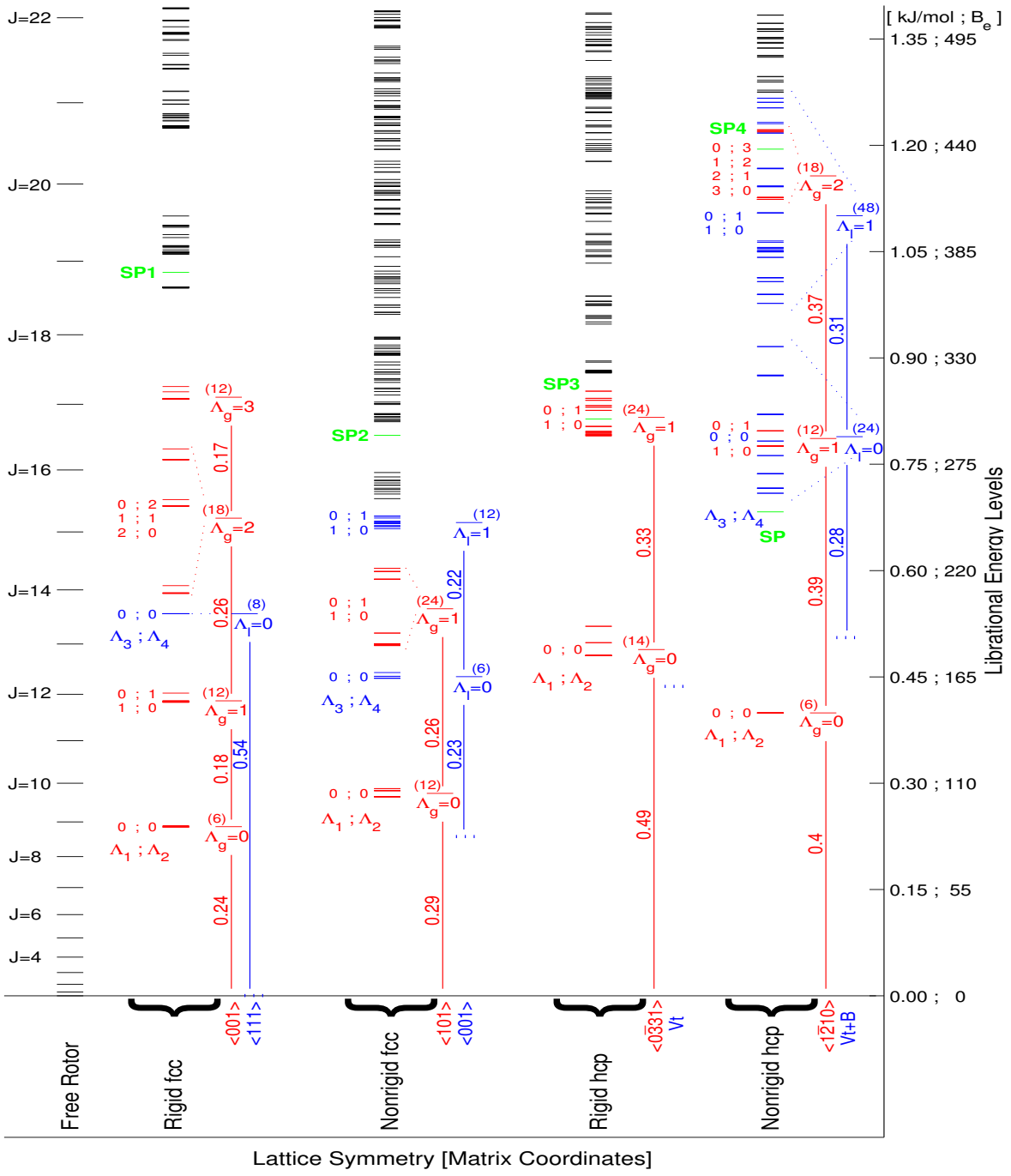

Figure 5.45: Librational energy levels of Cl_2 embedded in the pH_2 crystal are evaluated within the rigid and non-rigid DMs by solving Eq. 5.71 when considering fcc and hcp lattices. The corresponding eigenvalues localizes in the global (red) and local (blue) minima are depicted as long as the corresponding eigenvectors are not mixing. The mixed eigenvalues are depicted in black up 1.4 kJ/mol. The corresponding quantum numbers, $(\Lambda_1\ ;\ \Lambda_2\ )$ and $(\Lambda_3\ ;\ \Lambda_4\ )$ in Eqs. 5.75 and 5.76 are indicated respectively in red and blue for the global and local minima. Arithmetically averaged librational energy levels (harmonic approximation) of eigenvectors with the same quantum numbers $\Lambda_g = \Lambda_1 + \Lambda_2$ and $\Lambda_l = \Lambda_3 + \Lambda_4$ in Eqs. 5.77 and 5.78 are also given in order to qualitatively interpret the results in terms of uncoupled ensembles of 2D harmonic oscillators. The degeneracy of the eigenvectors in the 2D harmonic approximation is given in brackets next to the eigenvalues with quantum numbers Λ_g and Λ_l. The vertical solid lines indicate the energies between two consecutive librational levels in the 2D harmonic approximation.

General Remarks. In conclusion, comparison of the librational energy levels in Fig. 5.45 for the four different cases within the harmonic approximation given in Eqs. 5.77 and 5.78, tells that the librational quanta are slightly higher within the hcp lattices than within the fcc ones, but definitively in the same order. When changing the lattice symmetry or relaxing the environment, the librational ZPEs are still in a narrow range, namely [0.23 - 0.54] kJ/mol. Except for the hcp rigid DM, the impurity can librate in the cage around two different crystallographic directions corresponding to the global and local minima of the corresponding rotational PES. Nevertheless, at 0 K the Cl_2 molecule is expected to librate trapped along the crystallographic direction with the lowest possible eigenstate, since all rotational barriers are still in the order of hundreds of B_e units and tunneling effects should be negligible.

It is very interesting to note that similarly to the translational DOFs, the librational ZPEs are large compared to the depths of the corresponding minimum wells. For the fcc rigid DM the ZPEs are about one fourth and one half of the saddle point SP1 along the <001> and <111> directions, respectively. For the hcp rigid DM this ratio becomes even more than one half.

Referring to the application of the EMs to the Cl_2 molecule, we have to admit that it was restrictive to consider the impurity aligned only along the <001> direction just in the fcc lattice, since librations are also expected along the <111> and <101> directions in the case of rigid and non-rigid fcc lattice models, respectively, and also along the $<0\bar{3}31>$, Vt and $<1\bar{2}10>$ (or y) directions in the case of an rigid and non-rigid hcp lattice. It would be interesting in fact to compare translational and rotational fundamental quanta between the corresponding lattice models, instead of just rigid fcc with the Cl_2 aligned exclusively along the <001> direction.

Adiabatic Separability of Internal and External DOFs.

In the previous sections the pH_2 and Cl_2 translational and Cl_2 librational DOFs were investigated in the matrix. Adiabatic separability of internal and external DOFs as well of translational and rotational DOFs was assumed. Therefore, it is interesting to compare *a posteriori* the energies of fundamental vibrational, translational and rotational/librational quanta listed in Tab. 5.20. The vibrational and free rotor energies are just reported from Tab. 5.1. It is known that for RG as well as pH_2 matrices, the vibrational levels shift very little from the gas to the solid-phase. The translational and librational energies are taken in the harmonic approximation by just doubling their respective ZPEs. The vibrational harmonic energies are circa 30 - 40 times larger for the pure $pH_2@pH_2$ and 20 - 30 times larger for the pure $oD_2@oD_2$ crystals than the corresponding translational ones depending on the lattice model applied. The Cl_2 internal vibrational frequency is between 13 and 16 times larger than the translational ones in the rigid and non-rigid EMs, and between 12 and 28 times larger than the librational frequencies in the four DMs, respectively. Thus,

Table 5.20: Vibrational (gas phase), rotational (gas phase), translational and librational (solid phase, i.e. 3D Einstein and Devonshire models, respectively) energies are compared. Please note that vibrational, translational and librational energies are given in the harmonic approximation. The subscripts g and l stand for the global and local minimum of the respective rotational PESs. (* = 1D Einstein model)

DOF	matrix or specie	fcc lattice[kJ/mol]		hcp lattice [kJ/mol]	
		rigid	non-rigid	rigid	non-rigid
Librational	Cl_2@pH_2	0.239_g	0.286_g	0.490_g	0.400_g
		0.540_l	0.230_l	–	0.280_l
Translational	pH_2@pH_2	1.776	1.236	1.770	–
	oD_2@oD_2	1.584	1.152	1.576	–
	Cl_2@pH_2	0.500	0.420*	–	–
Free Rotor	pH_2	4.087			
	oD_2	2.099			
	Cl_2	5.4×10^{-3}			
Vibrational *gas phase*	H_2	49.75			
	D_2	35.79			
	Cl_2	6.632			

vibrational-translational and vibrational-librational couplings are probably small, but still not entirely negligible. Finally, the AS of translational and rotational/librational DOFs in the matrix is more troublesome, since the corresponding harmonic quanta lie in the same energetic order of magnitude. Therefore, more advanced models should simultaneously treat these DOFs and accurately evaluate the NACTs.

5.4 Conclusion

An extensive theoretical investigation is carried out on a Cl_2 molecule embedded in a H_2 crystal at cryogenic temperatures. Beside the many fascinating features of solid hydrogen pointed out along this work, mostly connected to the translational and quantum nature of the crystal, the energetics and structure of the doped crystal are characterized with the aim of providing the initial state for quantum dynamics simulations of the Cl + H_2 $\rightarrow$ HCl + H reaction experimentally observed in the system upon simultaneous UV+IR irradiation [15, 204].

The multi-body system is completely treated in a pairwise fashion. The multi-dimensional PES of a hydrogen molecule interacting with a chlorine molecule is calculated by using ab-initio methods at the MP2:aug-cc-pVQZ level of theory. Later verifications on a subpart of the PES shows that the results extrapolated from the CCSD(T):aug-cc-pVQZ and CCSD(T):aug-cc-pV5Z levels of theory to the complete basis-set are comparable. The multi-dimensional PES of two interacting hydrogen molecules is calculated extrapolating the results from the CCSD(T):aug-cc-pVQZ and CCSD(T):aug-cc-pV5Z levels of theory to the complete basis-set limit. On the way, the electrostatic interactions between closed-shell linear molecules, such as H_2 and Cl_2, are discussed on the base of the classical static quadrupole-quadrupole interaction.

For the calculation of the multi-dimensional *ab-initio* H_2-H_2 and H_2-Cl_2 potential interactions, all intramolecular bond lengths are fixed at their $v = 0$ vibrationally averaged values, $\tilde{r} = \langle r \rangle_{v=0}$. This is referred through the thesis as "classical approximation", since practically an infinitely narrow delta function centered at the equilibrium bond distance is considered instead of the ground state vibrational distribution function. The ab-initio PESs are numerically averaged over the spherical coordinates of the fast rotating hydrogen molecules in order to obtain the rotationally adiabatic (RA) pH_2-pH_2, pH_2-Cl_2 (ground state, $l = 0$) and three oH_2-Cl_2 (excited states, $l = 1, 2, 3$) pair potentials. This procedure is based on the multi-stage adiabatic separation tool described in Chap. 2. The corresponding RA interaction potentials with D_2 instead of H_2 are obtained as well, even though they are based on the same *ab-initio* PESs, that is with the deuterium intramolecular bond fixed at the $\tilde{r}_{H_2}$ bond length. However, since the $v = 0$ vibrationally averaged D_2 bond length, $\tilde{r}_{D_2}$ is only 0.005% shorter than $\tilde{r}_{H_2}$ distance, this is expected to introduce negligible errors. This is also confirmed by Hinde, who calculated similar (but not identical)

vibrationally averaged multipole dispersion coefficients [197]. The classical approximation applied on the rotating H_2 molecules, corresponding in the rotational adiabatization to the rigid-rotor approximation, does not introduce a considerable systematic error in the pair potentials. This is proved by the comparison to the vibrationally averaged $(pH_2)_2$ pair potential by Hinde [190], i.e. not in the rigid-rotor approximation, and to the already mentioned $(pH_2)_2$ vibrationally averaged multipole dispersion coefficients [197]. The $(pH_2)_2$ pair potential is also compared to the *ab-initio* curve by Li, Le Roy and Roy (LLR) [240] at a higher level of theory and to the semi-empirical curves by Norman, Watts and Buck (NWB) [193], Silvera-Goldmann [13] and to the Lennard-Jones potential based on Michels' results [255]. No remarkably differences between all these curves are eventually found. In contrast, the "classical approximation" applied on the Cl_2 molecule introduces a systematic error in the ($l = 0$) pH_2-Cl_2 and oD_2-Cl_2 potentials, which is estimated to be circa 8% of the dissociation energies at the intermolecular equilibrium distances, R_{AB}, and at the collinear geometry, $\theta_A = 0°$. Since at the latter configuration the H_2 or D_2 COMs lie along the Cl_2 bond, the solvent rotational coupling to the solute vibrations is the strongest and the systematic error of 8% an upper limit. All H_2-Cl_2 and D_2-Cl_2 pair potentials with $l = 0, 1, 2$ present a global and a local minimum at $\theta_A = 0°$ (collinear configuration) and $\theta_A = 90°$ (perpendicular configuration), whereas for the corresponding pair potentials with $l = 3$ the situation is reversed. A saddle point is always found between $\theta_A = 45°$ and 56°. In general, all pairpotentials are highly anisotropic, with the intermolecular distance, R_{AB}, being much shorter at the perpendicular than at the collinear configuration. It is interesting to note that the rotationally excited oH_2-Cl_2 and pD_2-Cl_2 pair potentials with quantum number $l = 1, 2$ present both at the local and global minima larger dissociation energies than in their respective rotational ground states with $l = 0$. This is due to the additional electrostatic quadrupole moment of oH_2 and pD_2 molecules interacting with the Cl_2 molecule. More in general, this supports the experimentally observed clustering of residual oH_2 molecules present in parahydrogen crystal around impurities with permanent multipoles [7].

All RA potentials are fitted to HFD-functions and the resulting parameters found in Sec. 5.3.5 and App. 6.4. Two main topics are investigated on the base of these pair potentials: The growth of small pure $(pH_2)_N$ and doped $Cl_2(pH_2)_N$ global minimum cluster structures out of N dimensional PESs, and the calculation of translational and rotational PESs of solvent and solute molecules in the matrix. Please note that all codes implement the NWB-$(pH_2)_2$ fitting parameters, since the one from the present work was obtained in a later stage, and that a systematic error is introduced by neglecting the three-body terms, which in the case of pure parahydrogen cover up to a 10% of the crystal cohesive energy.

The cluster sequences are grown by means of classical molecular dynamics and does not involve temperature. The growing process of the pure clusters closely follows the Farges's series of interpenetrating icosahedrons [268] and could be easily compared to the

cluster growing processes found in the literature in particular when using Lennard-Jones potentials, see for example [267]. The latter ones, in fact, shares with the HFD-functions the R^{-6} term in the attractive part of the potential. The growing process of the doped clusters is essentially dominated by the solute-solvent interaction until completion of the first coordination shell at $N = 14$. The structures of the first 14 clusters mirror the high anisotropy of the H_2-Cl_2 pair potentials, showing a strong preference (when possible) to coordinate the solvent molecules along the Cl_2 bond. The $Cl_2(pH_2)_{14}$ cluster presents a distorted fcc symmetry with the solute lying along the <001> crystallographic direction in a single substitutional site. In particular, the head-on molecules are slightly pushed away by the impurity, and the equatorial ones are slightly attracted, so that the symmetry is lowered from O_h to D_{4h}. In the larger clusters with $N > 14$, the growing process is dominated by the solvent-solvent interactions and an icosahedral phase forms leaving the nearly fcc structure at the surface. The growing process could not be compared to other investigations, since none was found in the literature, but interesting comparisons are made with the RG systems Cl_2He_N and Cl_2Ar_N.

The pair potentials are also used to investigate the energetics of $(pH_2)_{13}$ and $Cl_2(pH_2)_{12}$ first-shell clusters when imposing the fcc, hcp and icosahedral symmetries, since they all coordinate 12 solvent molecules in their first shell. The results from the previous optimized cluster structures are confirmed. The most stable pure first-shell cluster has icosahedral symmetry. The pure fcc and hcp first-shell clusters are found to have almost identical energies supporting the possibility for the large icosahedral quasi-crystal (no translational symmetry) to switch either to fcc or hcp according to the literature. In the doped first-shell clusters, the Cl_2 prefers to be surrounded by an fcc cage. By comparing the fcc pure and doped first-shell clusters it is found that the crystal does not need to expand in order to accommodate the Cl_2 molecule in the single substitutional site, so that the elongated D_{4h} symmetry of the previous optimized $Cl_2(pH_2)_{14}$ cluster is exclusively due to the high anisotropy of the pH_2-Cl_2 pair potential.

In the subsequent stage, the simulation boxes for the fcc and hcp pure and doped crystals are converged. The minimum image convention is used to calculate the cohesive energy per molecule against the increasing sizes of the crystals. In all cases, a simulation box of at least 4000 molecules is needed in order to have negligible surface effects at the boundaries. This is in agreement with previous investigations [176]. The convergences show a negligible preference for the fcc crystal structure.

In the last part of this work, two models are used for investigating the translational and rotational DOFs of the Cl_2 molecule embedded in the matrix as well as the translational DOF of pH_2 and oD_2 in their respective pure crystals, separately: The Einstein [173] and the Devonshire [174] models, respectively. They allow for the calculation of the effective translational or rotational PESs felt by a molecule in the crystal and are further developed in order to include non-rigid lattices. Relaxation of the matrix around hosting and

guest molecules tries to simulate the softness of translational quantum crystals, which is connected to their typical high compressibility. However, only the positions of the first two shells of solvent molecules are optimized, since the relaxation of the whole simulation boxes would have been too expensive from the CPU-time point of view. Afterwards, the PESs obtained within these models are inserted in the respective Schrödinger equations in order to calculate the respective translational and rotational eigenvalues and eigenstates. Translational eigenstates are calculated for the pH_2@pH_2, oD_2@oD_2 and Cl_2@pH_2 crystals. For the doped crystal only the fcc crystal structure is taken into account with the impurity lying along the <001> direction. It is observed that the simulation of a non-rigid lattice may be more adequate for the doped crystal, whereas the pure crystals are still better described by the rigid lattice approximation. This is explained on the base of the different translational frequencies of heavy solute and light solvent: The relaxing time-scale of the hydrogen or deuterium molecules is, in fact, comparable to the slow translational motions of Cl_2, that is the solvent molecules are able to readily adapt to a new configuration (non-adiabaticity), whereas they cannot follow the fast pH_2 or oD_2 translations (adiabaticity). Rigid and non-rigid lattices are considered for the calculation of the Cl_2 rotational eigenstates in the matrix, as well. It is disclosed that, despite the softness of the crystal, the Cl_2 is not free to rotate in the matrix, but librates along one or two crystallographic directions depending on the lattice model considered. In fact, after relaxation of the lattice the topology of the rotational PESs changes favouring a different main direction for the librations. In general, the librational ZPEs calculated are large with respect to the depth of the minimum wells found on the rotational PESs. The librational eigenvalues lie in a similar range of energies independently of the lattice model simulated, which implies they are not strongly coupled to the relative positions of the host molecules, that is to the translational modes of the solvent molecules. A comparison of the solute librational and solvent translational ZPEs let us suppose that upon lattice relaxation the pH_2 molecules easily adjust their positions around the rotating Cl_2 (non-adiabaticity).

The present investigation involves a long sequence of adiabatic separations in order to investigate the several DOFs individually, even though approximately, which is called "multi-stage adiabatic separation" through the thesis (please refer to Fig. 2.1). *Stage* $m = 1$: The gas phase diatomic constants listed in Tab. 5.1 show that the electronically excited states lie energetically high enough to consider the Born-Oppenheimer approximation safe for both the H_2 and Cl_2 molecules. *Stage* $m = 2$: By assuming that the vibrational frequencies are not shifted from the gas to the solid phase, the subsequent adiabatic separation between internal (vibrations) and external (rotations and translations) DOFs for the individual species is safe only for the Cl_2 molecule, whereas for the solvent molecules the vibrationally excited states lie only one order of magnitude (or less than) higher in energy than the corresponding rotational excited states (see Tab. 5.1), that is the solvent rotational eigenstates may be coupled to the vibrational ones. Nevertheless, this stage of

the multi-stage adiabatic separation is considered, *a priori*, to be valid. *A posteriori*, the comparison of the pH_2-pH_2 potential curve from this work to the vibrationally averaged one by Hinde suggests only small couplings. Comparison of the energies listed in Tab. 5.20 suggests that the vibrational and translational DOFs of solvent and solute are instead coupled when embedded in the matrix. The H_2-Cl_2 and D_2-Cl_2 pair potentials eventually suggest that the Cl_2 vibrational DOFs couple the H_2 and D_2 rotational DOFs. *Stage* $m = 3$: Translational and rotational/librational (solvent/solute molecules) eigenvectors are also coupled, since the respective eigenvalues listed in Tab. 5.20 are in the same order of magnitude.

Hence, the model could be improved by implementing also three-body interactions, which are important for the description of systems interacting in the van der Waals regime, such as closed-shell molecules. Furthermore, the $(H_2)_2$ and H_2-Cl_2 pair potentials could be also averaged with respect to the vibrational DOFs of H_2 (as already done by Hinde [190]) as well as of Cl_2. Upon improved description of the crystal energy interactions, translational and rotational DOFs of the guest molecule in the crystal could be trated simultaneously and include the respective NACTs. The 5D (2 rotational and 3 translational coordinates) effective PES could be eventually treated in the MCTDH approximation using DVR in order to simulate the laser driven quantum dynamics of the solvent-solute reaction. For the treatment of vibrational-translational, vibrational-rotational and vibrational-librational couplings different methods must eventually be implemented.

6 Appendix

6.1 Kinematics of three-body Collisions X+Y_2 [16]

From the laboratory frame to the center of mass frame.

Consider a molecular system, as depicted in Fig. 6.1, at the time t=t_i, before collision.

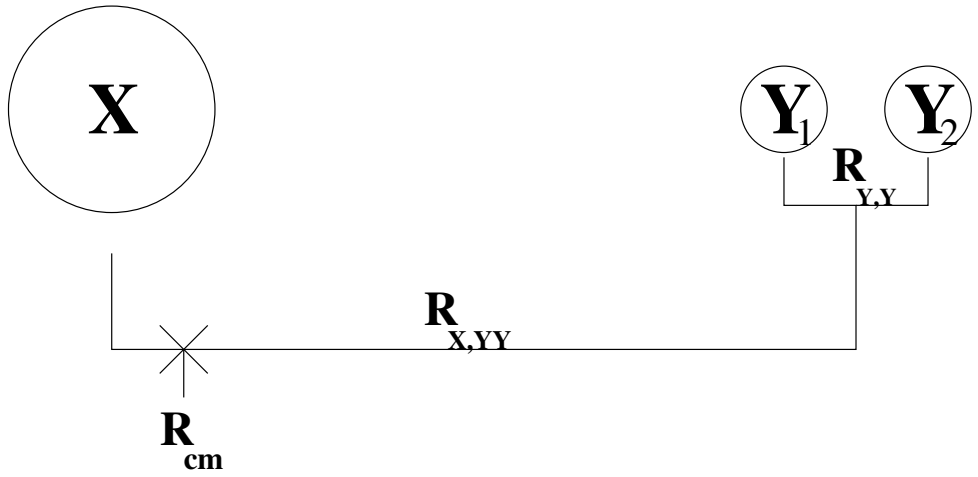

The total kinetic energy of the molecular system in the laboratory frame is:

$$T = \frac{P_{\mathrm{X}}^2}{2M_{\mathrm{X}}} + \frac{P_{\mathrm{Y}_1}^2}{2M_{\mathrm{Y}}} + \frac{P_{\mathrm{Y}_2}^2}{2M_{\mathrm{Y}}} = T_{\mathrm{X}} + T_{\mathrm{Y}_1} + T_{\mathrm{Y}_2} \tag{6.1}$$

In order to describe the kinematics of a three-body collision, the expression of the kinetic energy with respect to the center of mass frame needs to be calculated. This involves a transformation from the laboratory frame to the center of mass frame coordinate system. In matrix notation:

$$\begin{pmatrix} q_1 \\ q_2 \\ q_3 \end{pmatrix} = \begin{pmatrix} R_{\mathrm{Y,Y}} \\ R_{\mathrm{X,YY}} \\ R_{\mathrm{cm}} \end{pmatrix} = \begin{pmatrix} 0 & -1 & 1 \\ -1 & \frac{1}{2} & \frac{1}{2} \\ c_{\mathrm{X}} & c_{\mathrm{Y}} & c_{\mathrm{Y}} \end{pmatrix} \cdot \begin{pmatrix} R_{\mathrm{X}} \\ R_{\mathrm{Y}_1} \\ R_{\mathrm{Y}_2} \end{pmatrix} \tag{6.2}$$

or, in a more general notation:

$$q = R_{\mathrm{CF}} = T \cdot R_{\mathrm{LF}} \tag{6.3}$$

where CF means Center of mass Frame and LF means Laboratory Frame.

The coefficients in the matrix are correlated to the masses involved in the collision. In particular, $c_{\mathrm{X}} = \frac{M_{\mathrm{X}}}{M_{\mathrm{tot}}}$ and $c_{\mathrm{Y}} = \frac{M_{\mathrm{Y}}}{M_{\mathrm{tot}}}$, where $M_{\mathrm{tot}} = M_{\mathrm{X}} + 2M_{\mathrm{Y}}$ is the total mass of the system. Finally, since these coefficients are the ratios of the single masses with respect to the total one, it also holds $c_{\mathrm{X}} + 2c_{\mathrm{Y}} = 1$.

From coordinate space to momentum space

In the laboratory frame the momentum is given as:

$$P_{\mathrm{X}} = -i\hbar\frac{\partial}{\partial R_{\mathrm{X}}}, \qquad P_{\mathrm{Y}_1} = -i\hbar\frac{\partial}{\partial R_{\mathrm{Y}_1}} \qquad \text{and} \qquad P_{\mathrm{Y}_2} = -i\hbar\frac{\partial}{\partial R_{\mathrm{Y}_2}} \tag{6.4}$$

In contrast, in the center of mass frame:

$$P_{\mathrm{CF,l}} = p_l = -i\hbar\frac{\partial}{\partial q_l} \qquad \text{with l=1,2,3} \tag{6.5}$$

Applying the chain rule one obtains:

$$\begin{aligned} P_{\mathrm{X}} &= -i\hbar\sum_{l=1}^{3}\frac{\partial q_l}{\partial R_{\mathrm{X}}}\frac{\partial}{\partial q_l} \\ P_{\mathrm{Y}_1} &= -i\hbar\sum_{l=1}^{3}\frac{\partial q_l}{\partial R_{\mathrm{Y}_1}}\frac{\partial}{\partial q_l} \\ P_{\mathrm{Y}_2} &= -i\hbar\sum_{l=1}^{3}\frac{\partial q_l}{\partial R_{\mathrm{Y}_2}}\frac{\partial}{\partial q_l} \end{aligned} \tag{6.6}$$

The relation between the momenta in the two frames is found to be the transposed of the matrix T of Eq. 6.2, namely

$$P_{\mathrm{LF}} = T^T \cdot P_{\mathrm{CF}} \tag{6.7}$$

with

$$T^T = \begin{pmatrix} 0 & -1 & c_{\mathrm{X}} \\ -1 & \frac{1}{2} & c_{\mathrm{Y}} \\ 1 & \frac{1}{2} & c_{\mathrm{Y}} \end{pmatrix} \tag{6.8}$$

As a consequence, the inverse of the transposed matrix T relates the new momenta in the center of mass frame to the momenta in the laboratory frame,

$$P_{\mathrm{CF}} = (T^T)^{-1} \cdot P_{\mathrm{LF}} \tag{6.9}$$

with

$$(T^T)^{-1} = \begin{pmatrix} 0 & -\frac{1}{2} & \frac{1}{2} \\ -2c_{\mathrm{Y}} & c_{\mathrm{X}} & c_{\mathrm{X}} \\ 1 & 1 & 1 \end{pmatrix} \tag{6.10}$$

Thus, the general solutions for the new momenta are:

$$\begin{aligned} p_1 &= -\frac{1}{2}P_{\mathrm{Y}_1} + \frac{1}{2}P_{\mathrm{Y}_2} \\ p_2 &= -2c_{\mathrm{Y}}P_{\mathrm{X}} + c_{\mathrm{X}}P_{\mathrm{Y}_1} + c_{\mathrm{X}}P_{\mathrm{Y}_2} \\ p_3 &= P_{\mathrm{X}} + P_{\mathrm{Y}_1} + P_{\mathrm{Y}_2} \end{aligned} \tag{6.11}$$

Substituting Eqs. 6.6 in the expression of the kinetic energy Eq. 6.1, after some calculation, one arrives at the following very simple equation for the kinetic energy in the center of mass frame:

$$T = \frac{p_1^2}{2\mu_{\mathrm{Y,Y}}} + \frac{p_2^2}{2\mu_{\mathrm{X,YY}}} + \frac{p_3^2}{2M_{\mathrm{tot}}} = T_{\mathrm{Y,Y}} + T_{\mathrm{X,YY}} + T_{\mathrm{cm}} \tag{6.12}$$

where $\mu_{\mathrm{Y,Y}}$ indicates the reduced mass of the molecule Y_2, and $\mu_{\mathrm{X,YY}}$ indicates the reduced mass of the molecular system, the halogen atom X and the mass of the molecule Y_2.

Special case: Photodissociation

Let us now consider a special scenario, in which the initial Y_2 molecule is at rest in the laboratory frame, i.e. $P_{\mathrm{Y}_1} = P_{\mathrm{Y}_2} = 0$, and X has a momentum P_{X} due to a photodissociation process. The corresponding total energy of the system is therefore given by (see Eq. 6.1):

$$T = \frac{P_{\mathrm{X}}^2}{2M_{\mathrm{X}}} \tag{6.13}$$

Applying Eq. 6.11, the resulting momenta in the center of mass frame are

$$\begin{pmatrix} p_1 \\ p_2 \\ p_3 \end{pmatrix} = \begin{pmatrix} 0 \\ -\frac{2M_{\mathrm{Y}}}{M_{\mathrm{tot}}}P_{\mathrm{X}} \\ P_{\mathrm{X}} \end{pmatrix} \tag{6.14}$$

From this result, one concludes that:

1. The momentum for the two atoms Y with respect to their center of mass is zero.
2. The momentum for the halogen atom X with respect to the center of mass of the molecule Y_2 is $-\frac{2M_{\mathrm{Y}}}{M_{\mathrm{tot}}}$ times the momentum of the halogen atom. The magnitude of this factor depends on the masses of the atoms X and Y involved.

3. The momentum for the center of mass of the system is the same as P_{X}.

Finally, the fraction of kinetic energy available for reaction is calculated as the ratio of the kinetic energy of the center of mass and the initial total one,

$$\frac{T_{\mathrm{X,YY}}}{T_{\mathrm{X}}} = \frac{\frac{p_2^2}{2\mu_{\mathrm{X,YY}}}}{\frac{P_{\mathrm{X}}^2}{2M_{\mathrm{X}}}} = \frac{\frac{(2c_{\mathrm{Y}})^2}{2\mu_{\mathrm{X,YY}}}}{\frac{1}{2M_{\mathrm{X}}}} = \frac{2M_{\mathrm{Y}}}{M_{\mathrm{tot}}} \tag{6.15}$$

If one now considers the photodissociated atom X being the halogen atom, Cl, and the molecule Y_2 being H_2 or D_2, these equations demonstrate that the quantity of energy, which is really available for the reaction for this kind of three-body system, is just a small fraction of the total energy at disposal.

In particular:

$$\frac{T_{\mathrm{Cl,HH}}}{T_{\mathrm{X}}} = \frac{2M_{\mathrm{H}}}{M_{\mathrm{Cl}} + 2M_{\mathrm{H}}} \approx 5.4\%$$

$$\frac{T_{\mathrm{CL,DD}}}{T_{\mathrm{X}}} = \frac{2M_{\mathrm{D}}}{M_{\mathrm{Cl}} + 2M_{\mathrm{D}}} \approx 10\%$$

where $M_{\mathrm{Cl}} = 34.968852$ a.m.u. , $M_{\mathrm{H}} = 1.00794$ a.m.u. and $M_{\mathrm{D}} = 2.01355$ a.m.u.

6.2 The Gaussian Quadrature [321]

In numerical analysis, numerical quadrature is practically a synonym for numerical integration. They are often called quadrature methods or just quadrature. There is a very broad family of algorithms for calculating the numerical value of a definite integral.

$$\int_a^b f(x)dx \tag{6.16}$$

If $f(x)$ is a smooth well-behaved function with bounded limits of integration, a and b, there are many quadrature methods for approximating the integral with an arbitrary precision. In a very general fashion, quadrature methods can be described as a weighted sum of integrand evaluations at a finite set of points (integration points) in order to approximate the integral. The integration points and weights depend merely on the method used and the accuracy desired.

The probably largest class of quadrature rules consist in the use of polynomials as interpolating functions, since they are easy to integrate. The simplest of these quadratures is the midpoint or rectangle rule, where the interpolating function is a polynomial of degree zero passing through the middle points ($(a+b)/2$, $f((a+b)/2)$).

$$\int_a^b f(x)dx \approx f\left(\frac{a+b}{2}\right) \cdot (b-a) \tag{6.17}$$

The interpolating function could be an affine function, which means a polynomial of degree one, passing through the integration points. This is called the trapezoidal rule.

$$\int_a^b f(x)dx \approx \frac{f(a)+f(b)}{2} \cdot (b-a) \tag{6.18}$$

For both of these methods, higher accuracy is reached by dividing the intervals $[a, b]$ into an arbitrary number n of subintervals (*nesting* property). Quadrature methods based on equidistant integration points belong to the more general Newton-Cotes formulas. In contrast, if one allows the space intervals between the interpolation points to vary, the quadrature methods are called Gaussian Quadrature formulas (GQ) and are typically more accurate than a Newton-Cotes rules which requires the same number of function evaluations. The two points GQ formula can be seen as an extension of the trapezoidal rule, where the arguments of the function are not predetermined as a and b, but are the unknowns (not equidistant anymore) x_1 and x_2, so that with the coefficients there are altogether four unknowns.

$$\int_a^b \omega(x)f(x)dx = \omega_1 f(x_1) + \omega_2 f(x_2) \tag{6.19}$$

Table 6.1: Different kind of polynomials used in the Gaussian Quadrature methods listed together with their properties [321].

Interval	**Weighting Function** $\omega(x)$	Orthogonal Polynomials
$[-1,1]$	1	Legendre Polynomials
$(-1,1)$	$(1-x)^{\alpha}(1+x)^{\beta}$, with $\alpha,\beta>-1$	Jacobi Polynomials
$(-1,1)$	$\frac{1}{\sqrt{1-x^2}}$	Chebyshev Polynomials of first kind
$[-1,1]$	$\sqrt{1-x^2}$	Chebyshev Polynomials of second kind
$[0,+\infty)$	e^{-x}	Laguerre Polynomials
$(-\infty,+\infty)$	e^{-x^2}	Hermite Polynomials

The general n-points GQ is thus defined as:

$$\int_a^b \omega(x)f(x)dx = \sum_{\alpha=1}^{n} \omega_\alpha f(x_\alpha) \tag{6.20}$$

The fundamental theorem of GQ states that, chosen an orthogonal polynomial $q(x)$ of order n, whose n roots are the integration points x_α, for some set of ω_α, Eq. 6.20 is exact, if $f(x)$ is a polynomial of degree $< 2n$. It is well known, that one always can fit an $n-1$ degree polynomial to a set of n points. For example, 2 points define a line, 3 points a parabola, etc. The GQ theorem practically says that by carefully choosing the integration points and weights, one can exactly fit a polynomial $q(x)$ of degree $n-1$ to a polynomials of degree $< 2n$, which is computationally not expensive and very accurate. Depending on the integral to be evaluated the best suited polynomial should be chosen, corresponding to a different class of GQ. Table 6.1 lists the most common polynomials used together with the respective weighting function and interval of validity. The Chebyshev polynomials form the one dimensional particle-in-the-box basis set functions [30]. They give equally spaced integration points centered at $x = \cos^{-1}(\theta)$. The Legendre and associated Legendre polynomials with $x = \cos(\theta)$ are appropriate for angular functions and are closely related to the Spherical Harmonics (SH) basis-set [30]. The Hermite polynomials form the one dimensional Harmonic Oscillator basis set functions apart from a constant multiplication factor [30]. After the polynomials chosen for the integration, these quadrature are respectively called Chebyshev-Gauss, Legendre-Gauss, Gauss-Hermite quadratures, respectively [30].

6.3 Quadrupole-Quadrupole Interactions

The quadrupole is the lowest non-vanishing electrostatic momentum possessed by a linear molecule belonging to the $D_{\infty h}$ symmetry point group, as for instance the H_2 and Cl_2 molecules. As a consequence, when considering a molecular system composed of two linear molecules, the lowest possible electrostatic interaction is the Quadrupole-Quadrupole (QQ) one. The higher electrostatic terms, like the Hexadecapole-Quadrupole and Hexadecapole-Hexadecapole interactions, are not considered here, but are also present in such systems.

In the following appendix the QQ-interaction between the chlorine molecule A fixed in the space and the rotating hydrogen molecule B will be explicitly calculated with the aim of showing that for molecules with spherical rotational distributions, such as pH_2 and oD_2, the quadrupolar (actually all) electrostatic momentum vanishes, whereas for molecules with a non spherical rotational distribution, such as oH_2 and pD_2, it does not.

In more mathematical term, this is shown by integrating the QQ-interaction formula over the absolute value of the respective spherical harmonics, $|Y_{L,M}(\theta_B, \phi_B)|^2$.

$$\int_0^{\pi} \int_0^{2\pi} Q_A Q_B \cdot |Y_{L,M}(\theta_B, \phi_B)|^2 \sin\theta_B d\theta_B d\phi_B \tag{6.21}$$

where $Q_A Q_B$ is the QQ-interaction formula and is given in the next equation.

$$\begin{aligned} Q_A Q_B \;=\; & \underbrace{1}_{I} - \underbrace{5\cos^2\theta_A}_{II} - \underbrace{5\cos^2\theta_B}_{III} + \underbrace{17\cos^2\theta_A\cos^2\theta_B}_{IV} + \\ & + \underbrace{2\sin^2\theta_A\sin^2\theta_B\cos^2\phi_A\cos^2\phi_B}_{V} + \underbrace{2\sin^2\theta_A\sin^2\theta_B\sin^2\phi_A\sin^2\phi_B}_{VI} + \\ & + \underbrace{4\sin^2\theta_A\sin^2\theta_B\cos\phi_A\cos\phi_B\sin\phi_A\sin\phi_B}_{VII} + \\ & - \underbrace{16\sin\theta_A\sin\theta_B\cos\theta_A\cos\theta_B\cos\phi_A\cos\phi_B}_{VIII} + \\ & - \underbrace{16\sin\theta_A\sin\theta_B\cos\theta_A\cos\theta_B\sin\phi_A\sin\phi_B}_{IX} \end{aligned} \tag{6.22}$$

Inserting Eq. 6.23 into Eq. 6.21, for each of the addends of the QQ-interaction formula enumerated with the roman numbers, a different integral has to be solved. For each species considered, a different spherical harmonic has to be integrated. The spherical harmonic, $Y_{L=0,M=0}$, for an isolated pH_2 or oD_2 molecule and the spherical harmonics, $Y_{L=1,M=-1,0,1}$ for an isolated oH_2 or pD_2 molecule. These four spherical harmonics are given below together with their absolute values:

$$
\begin{aligned}
Y_{0,0}(\theta_B,\phi_B) &= \sqrt{\frac{1}{4\pi}} && \Rightarrow |Y_{0,0}(\theta_B,\phi_B)|^2 = \frac{1}{4\pi} \\
Y_{1,\mp1}(\theta_B,\phi_B) &= \sqrt{\frac{3}{8\pi}}\sin\theta_B e^{\mp i\phi} && \Rightarrow |Y_{1,\mp1}(\theta_B,\phi_B)|^2 = \frac{3}{8\pi}\sin^2\theta_B \\
Y_{1,0}(\theta_B,\phi_B) &= \sqrt{\frac{3}{4\pi}}\cos\theta_B && \Rightarrow |Y_{1,0}(\theta_B,\phi_B)|^2 = \frac{3}{4\pi}\cos^2\theta_B
\end{aligned}
$$

The list of integrals needed for solving the integrals have been taken in [321] and are listed below:

$$
\begin{aligned}
A: &\quad \int \sin cx dx = -\frac{1}{c}\cos cx \\
B: &\quad \int \sin cx \cos^n cx dx = -\frac{1}{c(n+1)}\cos^{n+1} cx \\
C: &\quad \int \cos^2 cx dx = \frac{\cos cx \sin cx}{2} + \frac{1}{2}x \\
D: &\quad \int \sin^2 cx dx = -\frac{\sin cx \cos cx}{2} + \frac{1}{2}x \\
E: &\quad \int \cos^n cx dx = \frac{\cos^{n-1} cx \sin cx}{nc} + \frac{n-1}{n}\int \cos^{n-2} cx dx \quad (for\ n>0) \\
F: &\quad \int \sin^n cx dx = -\frac{\sin^{n-1} cx \cos cx}{nc} + \frac{n-1}{n}\int \sin^{n-2} cx dx \quad (for\ n>0) \\
G: &\quad \int \sin cx \cos cx = \frac{1}{2c}\sin^2 cx \\
H: &\quad \int \cos cx dx = \frac{1}{c}\sin cx \\
I: &\quad \int \sin^n cx \cos^m cx dx = -\frac{\sin^{n-1} cx \cos m+1 cx}{c(n+m)} \\
&\qquad + \frac{n-1}{n+m}\int \sin^{n-2} cx \cos^m cx dx \quad (for\ m,n>0)
\end{aligned}
$$

Integration over $Y_{0,0}(\theta_B, \phi_B)$ ($\mathbf{pH_2}$ and $\mathbf{oD_2}$ rotational ground states):

$$
\begin{aligned}
I &= \frac{1}{4\pi} \underbrace{\int_0^{2\pi} d\phi_B}_{=2\pi} \underbrace{\int_0^{\pi} \sin\theta_B d\theta_B}_{=2 \text{ because of A}} \cdot 1 = 1 \\
II &= -5\cos^2\theta_A \cdot \frac{1}{4\pi} \underbrace{\int_0^{2\pi} d\phi_B}_{=2\pi} \underbrace{\int_0^{\pi} \sin\theta_B d\theta_B}_{=2 \text{ because of A}} = -5\cos^2\theta_A \\
III &= -5 \cdot \frac{1}{4\pi} \underbrace{\int_0^{2\pi} d\phi_B}_{=2\pi} \underbrace{\int_0^{\pi} \cos^2\theta_B \sin\theta_B d\theta_B}_{\frac{2}{3} \text{ because of B}} = -\frac{5}{3} \\
IV &= 17\cos^2\theta_A \cdot \frac{1}{4\pi} \underbrace{\int_0^{2\pi} d\phi_B}_{=2\pi} \underbrace{\int_0^{\pi} \cos^2\theta_B \sin\theta_B d\theta_B}_{\frac{2}{3} \text{ because of B}} = \frac{17}{3}\cos^2\theta_A \\
V &= 2\sin^2\theta_A \cos^2\phi_A \cdot \frac{1}{4\pi} \underbrace{\int_0^{2\pi} \cos^2\phi_B d\phi_B}_{=\pi \text{ because of C}} \underbrace{\int_0^{\pi} \sin^3\theta_B d\theta_B}_{\frac{4}{3} \text{ because of F+A}} = \frac{1}{3}\sin^2\theta_A \cos^2\phi_A \\
VI &= 2\sin^2\theta_A \sin^2\phi_A \cdot \frac{1}{4\pi} \underbrace{\int_0^{2\pi} \sin^2\phi_B d\phi_B}_{=\pi \text{ because of D}} \underbrace{\int_0^{\pi} \sin^3\theta_B d\theta_B}_{\frac{4}{3} \text{ because of F+A}} = \frac{1}{3}\sin^2\theta_A \sin^2\phi_A \\
VII &= 4\sin^2\theta_A \cos\phi_A \sin\phi_A \cdot \frac{1}{4\pi} \underbrace{\int_0^{2\pi} \sin\phi_B \cos\phi_B d\phi_B}_{=0 \text{ because of G}} \underbrace{\int_0^{\pi} \sin^3\theta_B d\theta_B}_{\frac{2}{3} \text{ because of F+A}} = 0 \\
VIII &= -16\sin\theta_A \cos\theta_A \cos\phi_A \cdot \frac{1}{4\pi} \underbrace{\int_0^{2\pi} \cos\phi_B d\phi_B}_{=0 \text{ because of H}} \int_0^{\pi} \sin^2\theta_B \cos\theta_B d\theta_B = 0 \\
IX &= -16\sin\theta_A \cos\theta_A \sin\phi_A \cdot \frac{1}{4\pi} \underbrace{\int_0^{2\pi} \sin\phi_B d\phi_B}_{=0 \text{ because of A}} \int_0^{\pi} \sin\theta_B \cos\theta_B d\theta_B = 0
\end{aligned}
$$

Finally, summing up all non-vanishing terms:

$$
\begin{aligned}
\int_0^{\pi}\int_0^{2\pi} Q_A Q_B \quad &\cdot \quad |Y_{0,0}(\theta_B, \phi_B)|^2 \sin\theta_B d\theta_B d\phi_B \\
&= 1 - 5\cos^2\theta_A - \frac{5}{3} + \frac{17}{3}\cos^2\theta_A + \frac{2}{3}\sin^2\theta_A \underbrace{\cos^2\phi_A}_{1-\sin^2\phi_A} + \frac{2}{3}\pi \sin^2\theta_A \sin^2\phi_A \\
&= -\frac{2}{3} + \frac{2}{3}\cos^2\theta_A + \frac{2}{3}\sin^2\theta_A = \frac{2}{3} + \frac{2}{3} = 0
\end{aligned}
$$

Integration over $Y_{1,\pm1}(\theta_B,\phi_B)$ (oH_2 and pD_2 rotational ground states):

$$
\begin{aligned}
I &= \frac{3}{8\pi}\underbrace{\int_0^{2\pi} d\phi_B}_{=2\pi}\ \underbrace{\int_0^{\pi}\sin^3\theta_B d\theta_B}_{\frac{4}{3}\text{ because of F+A}} = 1\\
II &= -5\cos^2\theta_A \cdot I = -5\cos^2\theta_A\\
III &= -5\cdot\frac{3}{8\pi}\underbrace{\int_0^{2\pi} d\phi_B}_{=2\pi}\underbrace{\int_0^{\pi}\cos^2\theta_B\sin^3\theta_B d\theta_B}_{\frac{4}{15}\text{ because of I}} = \frac{1}{5}\\
IV &= III\cdot\frac{1}{-5}\cdot 17\cos^2\theta_A = -\frac{17}{25}\cos^2\theta_A\\
V &= \frac{3}{8\pi}\cdot 2\sin^2\theta_A\cos^2\phi_A\underbrace{\int_0^{2\pi}\cos^2\phi_B d\phi_B}_{=\pi\text{ because of C}}\ \underbrace{\int_0^{\pi}\sin^5\theta_B d\theta_B}_{\frac{16}{15}\text{ because of F+F}} = \frac{4}{5}\sin^2\theta_A\cos^2\phi_A\\
VI &= \frac{3}{8\pi}\cdot 2\sin^2\theta_A\sin^2\phi_A\underbrace{\int_0^{2\pi}\sin^2\phi_B d\phi_B}_{=\pi\text{ because of D}}\ \underbrace{\int_0^{\pi}\sin^5\theta_B d\theta_B}_{\frac{16}{15}\text{ because of F+F}} = \frac{4}{5}\sin^2\theta_A\sin^2\phi_A\\
VII &= \frac{3}{8\pi}\cdot 4\sin^2\theta_A\cos\phi_A\sin\phi_A\underbrace{\int_0^{2\pi}\sin\phi_B\cos\phi_B d\phi_B}_{=0\text{ because of G}}\int_0^{\pi}\sin^5\theta_B d\theta_B = 0\\
VIII &= \frac{3}{8\pi}\cdot -16\sin\theta_A\cos\theta_A\cos\phi_A\underbrace{\int_0^{2\pi}\cos\phi_B d\phi_B}_{=0\text{ because of H}}\int_0^{\pi}\sin^4\theta_B\cos\theta_B d\theta_B = 0\\
IX &= \frac{3}{8\pi}\cdot -16\sin\theta_A\cos\theta_A\sin\phi_A\underbrace{\int_0^{2\pi}\sin\phi_B d\phi_B}_{=0\text{ because of A}}\int_0^{\pi}\sin\theta_B\cos\theta_B d\theta_B = 0
\end{aligned}
$$

Finally, summing up all non-vanishing terms:

$$
\begin{aligned}
\int_0^{\pi}\int_0^{2\pi} Q_A Q_B \quad &\cdot \quad |Y_{1,\pm}(\theta_B,\phi_B)|^2\sin\theta_B d\theta_B d\phi_B\\
&= 1 - 5\cos^2\theta_A + \frac{1}{5} - \frac{17}{25}\cos^2\theta_A + \frac{4}{5}\sin^2\theta_A\underbrace{\cos^2\phi_A}_{1-\sin^2\phi_A} + \frac{4}{5}\sin^2\theta_A\sin^2\phi_A\\
&= \frac{6}{5} - \frac{42}{25}\cos^2\theta_A + \frac{4}{5}\sin^2\theta_A\\
&= \frac{6}{5} + \frac{20}{25}\sin^2\theta_A + \frac{20}{25}\cos^2\theta_A - \frac{62}{25}\sin^2\theta_A\\
&= \frac{30}{25} + \frac{20}{25} - \frac{62}{25}\cos^2\theta_A = 2 - \frac{62}{25}\cos^2\theta_A
\end{aligned}
$$

Integration over $Y_{1,0}(\theta_B, \phi_B)$ (oH_2 and pD_2 rotational ground states):

$$
\begin{aligned}
I &= \frac{3}{4\pi} \underbrace{\int_0^{2\pi} d\phi_B}_{=2\pi} \underbrace{\int_0^{\pi} \cos^2\theta_B \sin\theta_B d\theta_B}_{\frac{2}{3} \text{ because of B}} = 1 \\
II &= -5\cos^2\theta_A \cdot I = -5\cos^2\theta_A \\
III &= -5 \cdot \frac{3}{4\pi} \underbrace{\int_0^{2\pi} d\phi_B}_{=2\pi} \underbrace{\int_0^{\pi} \cos^4\theta_B \sin\theta_B d\theta_B}_{\frac{2}{5} \text{ because of B}} = -3 \\
IV &= III \cdot \frac{1}{-5} \cdot 17\cos^2\theta_A = \frac{51}{5}\cos^2\theta_A \\
V &= \frac{3}{4\pi} \cdot 2\sin^2\theta_A \cos^2\phi_A \underbrace{\int_0^{2\pi} \cos^2\phi_B d\phi_B}_{=\pi \text{ because of C}} \underbrace{\int_0^{\pi} \sin^3\theta_B \cos^2\theta_B d\theta_B}_{\frac{4}{15} \text{ because of I+B}} = \frac{2}{5}\sin^2\theta_A \cos^2\phi_A \\
VI &= V \cdot \frac{\sin^2\phi_A}{\cos^2\phi_A} = \frac{2}{5}\sin^2\theta_A \sin^2\phi_A \\
VII &= \frac{3}{4\pi} \cdot 4\sin^2\theta_A \cos\phi_A \sin\phi_A \underbrace{\int_0^{2\pi} \sin\phi_B \cos\phi_B d\phi_B}_{=0 \text{ because of G}} \int_0^{\pi} \sin^3\theta_B \cos^2\theta_B d\theta_B = 0 \\
VIII &= \frac{3}{4\pi} \cdot -16\sin\theta_A \cos\theta_A \cos\phi_A \underbrace{\int_0^{2\pi} \cos\phi_B d\phi_B}_{=0 \text{ because of H}} \int_0^{\pi} \sin^2\theta_B \cos^3\theta_B d\theta_B = 0 \\
IX &= \frac{3}{4\pi} \cdot -16\sin\theta_A \cos\theta_A \sin\phi_A \underbrace{\int_0^{2\pi} \sin\phi_B d\phi_B}_{=0 \text{ because of A}} \int_0^{\pi} \sin^2\theta_B \cos^3\theta_B d\theta_B = 0
\end{aligned}
$$

Finally, summing up all non-vanishing terms:

$$
\begin{aligned}
\int_0^{\pi}\int_0^{2\pi} Q_A Q_B \quad &\cdot \quad |Y_{1,0}(\theta_B, \phi_B)|^2 \sin\theta_B d\theta_B d\phi_B \\
&= 1 - 5\cos^2\theta_A - 3 + \frac{51}{5}\cos^2\theta_A + \frac{2}{5}\sin^2\theta_A \underbrace{\cos^2\phi_A}_{1-\sin^2\phi_A} + \frac{2}{5}\sin^2\theta_A \sin^2\phi_A \\
&= -2 + \frac{26}{5}\cos^2\theta_A + \frac{2}{5}\sin^2\theta_A \\
&= -2 + \frac{24}{5}\cos^2\theta_A + \frac{2}{5}\cos^2\theta_A + \frac{2}{5}\sin^2\theta_A \\
&= -\frac{8}{5} + \frac{24}{5}\cos^2\theta_A
\end{aligned}
$$

6.4 RA-PES Fitted Legendre Polynomials Expansion Coefficients

Table 6.2: Coefficients for the expansion in the first three even Legendre Polynomials, $P_{n=0,2,4}(\theta_A)$, of the 8 angular dependent parameters in the HFD-function, $V_{AB}^{(l)}(R_{AB},\theta_A)$ in Eq. 5.29, fitting the two-dimensional RA-PESs, $W_{pH_2-Cl_2}^{(n=v=0,\ l=0)}(R_{AB},\theta_A)$ and $W_{oD_2-Cl_2}^{(n=v=0,\ l=0)}(R_{AB},\theta_A)$, are given in a.u. respectively in the left and right columns of the table.

	$\times P_0(\theta_A)$	$\times P_2(\theta_A)$	$\times P_4(\theta_A)$	$\times P_0(\theta_A)$	$\times P_2(\theta_A)$	$\times P_4(\theta_A)$
$V^{(l=0)}$		pH_2-Cl_2			oD_2-Cl_2	
$R_p(\theta_A)$	6.546083	2.457239	−0.961604	7.463068	2.376177	−1.238354
$p(\theta_A)$	8.342770	10.81063	5.339028	4.235626	1.179803	3.617177
$\log a(\theta_A)$	0.123888	−0.1575050	0.1006369	0.312947	−0.342894	0.1995624
$b(\theta_A)$	0.227439	0.2124749	−0.448644	0.987746	−0.7396689	0.242461
$c(\theta_A)$	0.1137108	−0.1481077	0.1166428	−0.005826	0.015604	−0.0000019
$C_6(\theta_A)$	40.46230	127.8287	58.22363	139.1351	373.1690	164.2687
$C_8(\theta_A)$	1136.867	1496.881	185.1981	625.5885	754.4154	−710.9507
$C_{10}(\theta_A)$	4827.163	2567.031	−1152.398	4816.229	2553.961	−1373.243

Table 6.3: Coefficients for the expansion in the first three even Legendre Polynomials, $P_{n=0,2,4}(\theta_A)$, of the 8 angular dependent parameters in the HFD-function, $V_{AB}^{(l)}(R_{AB},\theta_A)$ in Eq. 5.29, fitting the two-dimensional RA-PESs, $W_{pH_2-Cl_2}^{(n=v=0,\ l=1)}(R_{AB},\theta_A)$ and $W_{oD_2-Cl_2}^{(n=v=0,\ l=1)}(R_{AB},\theta_A)$, are given in a.u. respectively in the left and right columns of the table.

	$\times P_0(\theta_A)$	$\times P_2(\theta_A)$	$\times P_4(\theta_A)$	$\times P_0(\theta_A)$	$\times P_2(\theta_A)$	$\times P_4(\theta_A)$
$V^{(l=1)}$		oH_2-Cl_2			pD_2-Cl_2	
$R_p(\theta_A)$	7.272212	2.457591	−1.132996	7.082789	2.580084	−1.198885
$p(\theta_A)$	5.600052	1.155076	4.941181	5.628994	1.141327	5.068411
$\log a(\theta_A)$	0.153863	−0.173002	0.103477	0.222301	−0.252485	0.150700
$b(\theta_A)$	0.873880	−0.698060	0.266102	0.955018	−0.773104	0.277703
$c(\theta_A)$	0.005791	0.004250	0.01814	−0.001737	0.015031	−0.000332
$C_6(\theta_A)$	107.4460	283.5249	133.6542	120.0814	308.5875	130.9678
$C_8(\theta_A)$	533.6362	804.6727	−748.2995	404.4496	622.6149	−301.0167
$C_{10}(\theta_A)$	3182.611	1451.915	1340.984	2019.258	3997.051	−1.339907

Table 6.4: Coefficients for the expansion in the first three even Legendre Polynomials, $P_{n=0,2,4}(\theta_A)$, of the 8 angular dependent parameters in the HFD-function, $V_{AB}^{(l)}(R_{AB},\theta_A)$ in Eq. 5.29, fitting the two-dimensional RA-PESs, $W_{pH_2-Cl_2}^{(n=v=0,\ l=2)}(R_{AB},\theta_A)$ and $W_{oD_2-Cl_2}^{(n=v=0,\ l=2)}(R_{AB},\theta_A)$, are given in a.u. respectively in the left and right columns of the table.

	$\times P_0(\theta_A)$	$\times P_2(\theta_A)$	$\times P_4(\theta_A)$	$\times P_0(\theta_A)$	$\times P_2(\theta_A)$	$\times P_4(\theta_A)$
$V^{(l=2)}$		oH_2-Cl_2			pD_2-Cl_2	
$R_p(\theta_A)$	7.887075	2.241792	−1.066878	7.761789	0.018946	0.260517
$p(\theta_A)$	3.789988	1.746207	2.585752	7.523380	15.02365	4.229105
$\log a(\theta_A)$	0.030453	−0.030127	0.018277	0.081839	−0.078861	0.002692
$b(\theta_A)$	0.2851373	−0.4098456	0.195429	0.5533672	−0.538118	−0.657567
$c(\theta_A)$	0.037022	−0.011143	0.001354	0.034101	0.016519	0.079221
$C_6(\theta_A)$	176.8759	443.7729	161.1696	37.75205	122.9202	68.46941
$C_8(\theta_A)$	721.6169	413.5156	−607.2996	1626.125	506.7775	−352.6596
$C_{10}(\theta_A)$	4788.124	2572.646	−1399.737	3226.777	1447.586	1298.371

Table 6.5: Coefficients for the expansion in the first three even Legendre Polynomials, $P_{n=0,2,4}(\theta_A)$, of the 8 angular dependent parameters in the HFD-function, $V_{AB}^{(l)}(R_{AB},\theta_A)$ in Eq. 5.29, fitting the two-dimensional RA-PESs, $W_{pH_2-Cl_2}^{(n=v=0,\ l=3)}(R_{AB},\theta_A)$ and $W_{oD_2-Cl_2}^{(n=v=0,\ l=3)}(R_{AB},\theta_A)$, are given in a.u. respectively in the left and right columns of the table.

	$\times P_0(\theta_A)$	$\times P_2(\theta_A)$	$\times P_4(\theta_A)$	$\times P_0(\theta_A)$	$\times P_2(\theta_A)$	$\times P_4(\theta_A)$
$V^{(l=3)}$	oH_2-Cl_2			pD_2-Cl_2		
$R_p(\theta_A)$	7.659767	2.484850	−0.732845	7.053535	2.492342	−0.788342
$p(\theta_A)$	4.181904	1.528093	2.288791	6.382567	1.797911	5.305201
$\log a(\theta_A)$	0.027879	−0.026671	0.014598	0.257607	−0.272980	0.164915
$b(\theta_A)$	0.246792	−0.409352	0.220119	0.102531	−0.679282	0.290446
$c(\theta_A)$	0.038907	−0.009858	−0.003952	−0.005042	0.008230	−0.004256
$C_6(\theta_A)$	190.5950	462.1301	168.0032	91.2944	233.7369	104.4669
$C_8(\theta_A)$	507.4645	599.0433	−341.9357	351.1368	542.6530	−526.6093
$C_{10}(\theta_A)$	4607.373	1142.824	−2738.211	3001.648	−3.794078	23.36125

6.5 Einstein Model Computational Details

This Appendix gives information about the computational technicalities in order to set up the Einstein models. The effective potentials $V_{EM}(R_0)$ have been calculated at 16 different Nearest-Neighbour distances (NNd), R_d between 0.30 and 0.45 nm with steps δR_d =0.01 nm. For the non-rigid Einstein model, eventually, this grid has been reduced discarding few of the shorter and larger NNds, because of the computational cost. The models have been generally applied to both the fcc and the hcp lattices except for the non-rigid Einstein model, which has been applied only to the fcc lattice again because of the computational cost. The simulation boxes are constituted by a number of cells n_c =3 and 4 for each dimension for the rigid and non-rigid Einstein model, respectively. The effective potential are very little influenced by the magnitude of the simulation box, since by subtracting the fcc cohesive energy per molecule, $E_{\mathrm{c}}(R_d)$, in Eq. 5.54, the systematic errors are cancelled out. The test-molecule at the center of the slab is displaced along chosen directions, which are indicated by Miller indices for which we refer to Tab. 6.6. The number of grid points N_g has been chosen case by case. The initial and final points are always $-R_d$ and R_d and the relative spacing δd between them is simply $\delta d = \frac{2R_d}{(N_g-1)}$. In the case of the 1D rigid model N_g was independent from the value of R_d and always equal to 121. The 1D effective potentials, V_{EM}, have been fitted to 128 grid points by a spline interpolation, before calculating the ZPEs. In the case of the 1D non-rigid Einstein model, N_g has been made dependent from the NNd, R_d, of the lattice. It has been varied for increasing values of R_d between 21 to 51 and from 39 to 69 for the pH_2/oD_2 and the Cl_2 systems, respectively, with a step, δg, of 2 points. The total number of grid points needed to be drastically decreased with respect to the rigid Einstein model, since the optimization routine for the relaxation of the cage around the central molecule was highly CPU-consuming. In contrast, the spacing, δd, does not increase drastically at large values of R_d, as in the rigid Einstein model, such that the fit of the effective potentials, V_{EM}, to 128 points by the spline interpolation is still accurate. In the 3D rigid and non-rigid Einstein model N_g has been varied from 31^3 to 61^3 for both the fcc and the hcp lattices with a step, δg, of 2 points. The effective potentials, V_{EM}, have been fitted to a 64^3 grid by using an spline interpolation before evaluating the ZPEs. All parameters are summarized again in Tab. 6.6.

Table 6.6: The table summarizes the simulation box size in terms of number of primitive cells, n_c, the number of grid points, N_g, along the crystallographic directions of displacements and the step size, δg, of the number of grid points used in the different Einstein models and lattice symmetry used. The minimum and maximum displacements are always -R_d and R_d.

pH_2/oD_2					
Einstein Model	Lattice	n_c	N_g	δg	Directions
1D rigid	fcc	3	121	0	$< 100 >$ $< 011 >$ $< 111 >$
1D rigid	hcp	3	121	0	$< 100 >$ $< 010 >$ $< 001 >$
1D non-rigid	fcc	4	$[21 - 51]$	2	$< 100 >$ $< 110 >$ $< 111 >$
1D non-rigid	hcp	4	$[21 - 51]$	2	$< 100 >$ $< 010 >$ $< 001 >$
3D rigid	fcc/hcp	3	$[31^3 - 61^3]$	2	$< 100 >$ $< 010 >$ $< 001 >$
3D non-rigid	fcc	4	$[31^3 - 61^3]$	2	$< 100 >$ $< 010 >$ $< 001 >$
Cl_2					
Einstein Model	Lattice	n_c	N_g	δg	Directions
1D rigid	fcc/hcp	3	87	0	$< 100 >$ $< 010 >$ $< 001 >$
1D non-rigid	fcc	4	$[39 - 69]$	2	$< 100 >$ $< 010 >$ $< 001 >$
3D rigid	fcc/hcp	3	$[31^3 - 61^3]$	2	$< 100 >$ $< 010 >$ $< 001 >$
3D non-rigid	fcc	4	$[31^3 - 61^3]$	2	$< 100 >$ $< 010 >$ $< 001 >$

Bibliography

[1] D. N. Betchelder, *Rare Gas Solids*, vol. II, Academic Press, New York, 1977. 1, 5.1.3

[2] S. Leutwyler and J. Bösiger *Chem. Rev.* **90**, pp. 489–507, 1990. 1

[3] V. A. Apkarian and N. Schwentner, "Molecular Photodynamics in Rare Gas Solid," *Chem. Rev.* **6**, p. 1481, 1999. 1, 4.1, 5.1.2, 5.3.8

[4] M. Bargheer, A. Borowski, A. Cohen, M. Fushitani, R. B. Gerber, M. Gühr, P. Hamm, H. Ibrahim, T. Kiljunen, M. V. Korolkov, O. Kühn, J. Manz, B. Schmidt, M. Schröder, and N. Schwentner, "Coherence and control of molecular dynamics in rare gas matrices," in *Analysis and Control of Ultrafast Photoinduced Reactions*, *Springer Series in Chemical Physics Vol. 87*, pp. 257–385, Springer, (Heidelberg), 2007. 1, 4.1

[5] T. Oka, "High-Resolution Spectroscopy of Solid Hydrogen," *Annu. Rev. Phys. Chem.* **44**, p. 299, 1993. 1, 5.1.3

[6] T. Momose, M. Fushitani, and H. Hoshina, "Chemical Reactions in Quantum Crystals," *Int. Rev. Phys. Chem.* **24**, p. 533, 2005. 1, 5.1.3, 5.3.8

[7] K. Yoshioka, P. L. Raston, and D. T. Anderson, "Infrared Spectroscopy of Chemically Doped Solid Parahydrogen," *Int. Rev. in Phys. Chem.* **25**, p. 469, 2006. 1, 5.1.3, 5.3.4, 5.4

[8] K. Huber and G. Herzberg, "Constants of Diatomic Molecules," in *NIST Chemistry WebBook, NIST Standard Reference Database Number 69*, Eds. P.J. Linstrom and W.G. Mallard, National Institute of Standards and Technology, (Gaithersburg MD, 20899, http://webbook.nist.gov/chemistry), August 2012. 1, 5.1, 5.2

[9] M. Born and R. Oppenheimer, "Zur Quantentheorie der Molekeln," *Ann. Phys.* **84**, p. 457, 1927. 1, 2.2.1

[10] W. Domcke, D. Yarkony, and H. Köppel, "Conical Intersections: Electronic Structure, Dynamics and Spectroscopy.," *Advanced Series in Physical Chemistry, Vol. 15*, World Scientific Publishing Co., (Singapore), 2004. 1, 2.2.1, 2.2.1, 2.2.2, 2.2.3, 4.1

[11] W. Domcke, D. Yarkony, and H. Köppel, "Conical Intersections: Theory, Computation and Experiment," *Advanced Series in Physical Chemistry, Vol. 17*, World Scientific Publishing Co., (Singapore), 2011. 1, 2.2.3, 4.1

[12] M. Baer, "Beyond Born-Oppenheimer: Electronic Nonadiabatic Coupling Terms and Conical Intersections," John Wiley and Sons, Inc., (New Jersey), 2006. 1, 2.2.1, 2.2.1, 2.2.2

[13] I. F. Silvera, "The solid Molecular Hydrogen in the Condensed Phase: Fundamentals and Static Properties," *Rev. Mod. Phys.* **52**, p. 393, 1980. 1, 5.1.1, 5.1.2, 5.1.2, 5.3.5, 5.14, 5.6, 5.7, 5.3.6, 5.3.6, 5.4

[14] J. V. Kranendonk, *Solid Hydrogen: Theory of the Properties of Solid H_2, HD and D_2*, Plenum Publishing Corporation, 1983. 1, 5.1.2, 5.1.3, 5.16

[15] P. L. Raston and D. T. Anderson, "Infrared-Induced Reaction of Cl Atoms Trapped in Solid Parahydrogen," *Phys. Chem. Chem. Phys.* **8**, p. 3124, 2006. 1, 5.1, 5.1.3, 5.3.8, 5.4

[16] M. V. Korolkov, J. Manz, and A. Schild, "The Cl + H_2 → HCl + H Reaction Induced by IR + UV Irradiation of Cl_2 in Solid para-H_2: Quantum Model Simulation [1]," *J. Phys. Chem. A* **113**, p. 7630, 2009. (document), 1, 5.1.3, 5.3.6, 5.3.8, 5.3.8, 6.1

[17] A. Borowski and O. Kühn, "Tailoring Model Hamiltonians for Dihalogen-Rare Gas Matrix Problems: A Diatomic-In-Molecules Study of Br_2 in Solid Ar," *Theor. Chem. Acc.* **117**, p. 521, 2007. 2.2.3, 4.1

[18] J. Manz and J. Römelt, "On the Collinear I+HI and I+MuI Reactions," *Chem. Phys. Lett.* **81**, p. 179, 1981. 2.2.4, 2.2.4

[19] J. Manz, R. Meyer, E. Pollak, and J. Römelt, "A New Possibility of Chemical Bonding: Vibrational Stabilization of IHI," *Chem. Phys. Lett.* **83**, p. 184, 1982. 2.2.4, 2.2.4

[20] J. Manz, R. Meyer, and J. Römelt, "On Vibrational Bonding of IHI," *Chem. Phys. Lett.* **96**, p. 607, 1983. 2.2.4, 2.2.4

[21] I. Navrotskaya, A. V. Soudackov, and S. Hammes-Schiffer, "Model System-Bath Hamiltonian and Nonadiabatic Rate Constants for Proton-Coupled Electron Transfer at Electrode-Solution interfaces," *J. Chem. Phys.* **128**, p. 244712, 2008. 2.2.4

[1] Please note that the back-reference labeled "(document)" appears whenever a citation occurs in the title of a chapter or a section and is, therefore, collected in the table of contents.

[22] S. Hammes-Schiffer and A. V. Soudackov, "Proton-Coupled Electron Transfer in Solution, Proteins, and Electrochemistry," *J. Phys. Chem. B* **112**, p. 14108, 2008. 2.2.4

[23] D. K. Chakravorty, A. V. Soudackov, and S. Hammes-Schiffer, "Hybrid Quantum/Classical Molecular Dynamics Simulations of the Proton Transfer Reactions Catalyzed by Ketosteroid Isomerase: Analysis of Hydrogen Bonding, Conformational Motions, and Electrostatics," *Biochemistry* **48**, p. 10608, 2009. 2.2.4

[24] A. D. Bandrauk, J. Manz, and M. Vrakking, "Attosecond Molecular Dynamics," *Chem. Phys.* **366**, pp. 1–150, 2009. 2.2.4, 3.2

[25] G. Herzberg, *Molecular Spectra and Molecular Structure. I. Spectra of Diatomic Molecules*, Van Nostrand Reinhold Company, New York, 1950. 2.2.5, 4.1

[26] H. Friedmann and S. Kimel, "Theory of Shifts of Vibration-Rotation Lines of Diatomic Molecules in Noble-Gas Matrices. Intermolecular Forces in Crystals," *J. Chem. Phys.* **43**, p. 3925, 1965. 2.2.5, 5.3.8

[27] T. Yildirim and A. B. Harris, "Rotational and Vibrational Dynamics of Interstitial Molecular Hydrogen," *Phys. Rev. B* **66**, p. 214301, 2002. 2.2.5, 5.3.8

[28] J. C. Light, I. P. Hamilton, and J. V. Lill, "Generalized Discrete Variable Approximation in Quantum Mechanics," *J. Chem. Phys.* **82**, p. 1400, 1985. 2.2.5, 2.4.1, 4.2

[29] R. G. Littlejohn, M. Cargo, J. T. Carrington, and K. A. M. B. Poirier, "A General Framework for Discrete Variable Representation Basis Sets," *J. Chem. Phys.* **116**, p. 8691, 2002. 2.2.5, 2.4.1, 4.2

[30] J. C. Light and T. Carrington, "Discrete-Variable Representations and their Utilization," *Advances in Chemical Physics, Vol. 114*, Eds. I. Prigogine and S. A. Rice. John Wiley and Sons, Inc., 2007. 2.2.5, 2.4.1, 4.2, 6.2

[31] N. Makri and W. H. Miller, "Time-Dependent Self-Consistent Field (TDSCF) Approximation for a Reaction Coordinate Coupled to a Harmonic Bath: Single and Multiple Configuration Treatments," *J. Chem. Phys.* **87**, p. 5781, 1987. 2.2.5, 2.4.1, 4.1

[32] H.-D. Meyer, U. Manthe, and L. S. Cederbaum, "The Multi-Configurational Time-Dependent Hartree Approach," *Chem. Phys. Lett.* **165**, p. 73, 1990. 2.2.5, 2.4.1

[33] U. Manthe, H.-D. Meyer, and L. S. Cederbaum, "Wave-Packet Dynamics within the Multiconfiguration Hartree Framework: General Aspects and Application to NOCl," *J. Chem. Phys.* **97**, p. 3199, 1992. 2.2.5, 2.4.1

[34] M. H. Beck and H.-D. Meyer, "An Efficient and Robust Integration Scheme for the Equations of Motion of the Multiconfiguration Time-Dependent Hartree (MCTDH) Method," *Z. Physik D: At., Mol. Clusters* **42**, p. 113, 1997. 2.2.5, 2.4.1, 2.4.1, 2.4.1

[35] G. A. Worth, H.-D. Meyer, and L. S. Cederbaum, "Relaxation of a System with a Conical Intersection Coupled to a Bath: A Benchmark 24-Dimensional Wave Packet Study Treating the Environment Explicitly," *J. Chem. Phys.* **109**, p. 3518, 1998. 2.2.5, 2.4.1, 2.4.1

[36] M. H. Beck, A. Jäckle, G. A. Worth, and H.-D. Meyer, "The Multiconfiguration Time-Dependent Hartree Method: A Highly Efficient Algorithm for Propagating Wavepackets," *Phys. Rep.* **324**, p. 1, 2000. 2.2.5, 2.4.1, 2.4.1, 2.4.1, 2.4.1, 2.4.1, 2.4.1, 2.4.1, 3.2, 3.2

[37] H.-D. Meyer and G. A. Worth, "Quantum Molecular Dynamics: Propagating Wavepackets and Density Operators Using the Multiconfiguration Time-Dependent Hartree (MCTDH) method," *Theor. Chem. Acc.* **109**, p. 251, 2003. 2.2.5, 2.4.1, 2.4.1, 2.4.1

[38] A. Szabo and N. S. Ostlund, *Modern Quantum Chemistry: Introduction to Advanced Electronic Structure Theory*, Macmillan, New York, 1982. 2.3, 2.3.1, 2.3.1, 2.3.1, 2.3.3, 2.3.3, 2.3.3

[39] F. Jensen, *Introduction to Computational Chemistry*, John Wiley and Sons, Inc., Chichester, 1999. 2.3, 2.3.1, 2.3.1, 2.3.1, 2.3.2, 2.3.4, 2.3.4, 2.3.4, 2.2, 2.3.4

[40] C. C. J. Roothaan, "New Developments in Molecular Orbital Theory," *Rev. Mod. Phys.* **23**, p. 69, 1951. 2.3.2

[41] G. G. Hall, "The Molecular Orbital Theory of Chemical Valency. VIII A Method of Calculating Ionization Potentials.," *Proc. R. Soc. Lond. A* **205**, p. 541, 1951. 2.3.2

[42] T. H. Dunning, "Gaussian Basis Sets for Use in Correlated Molecular Calculations. I. The Atoms Boron Through Neon and Hydrogen," *J. Chem. Phys.* **90**, p. 1007, 1989. 2.3.2

[43] T. Helgaker, P. Jorgensen, and J. Olsen, *Molecular Electronic Structure Theory*, John Wiley and Sons, Inc., Chichester, 2000. 2.3.2

[44] D. O. Harris, G. G. Engerholm, and W. D. Gwinn, "Calculation of Matrix Elements for One-Dimensional Quantum-Mechanical Problems and the Application to Anharmonic Oscillators," *J. Chem. Phys.* **43**, p. 1515, 1965. 2.4.1, 4.2

[45] A. S. Dickinson and P. R. Certain, "Calculation of Matrix Elements for One-Dimensional Quantum-Mechanical Problems," *J. Chem. Phys.* **49**, p. 4209, 1968. 2.4.1, 4.2

[46] H.-D. Meyer, U. Manthe, and L. S. Cederbaum, "The Multi-Configurational Time-Dependent Hartree Approach," *Chem. Phys. Lett.* **165**, p. 73, 1990. 2.4.1

[47] A. Jäckle and H.-D. Meyer, "Product Representation of Potential Energy Surfaces," *J. Chem. Phys.* **104**, p. 7974, 1996. 2.4.1

[48] A. Jäckle and H.-D. Meyer, "Product Representation of Potential Energy Surfaces II," *J. Chem. Phys.* **109**, p. 3772, 1998. 2.4.1

[49] R. Kosloff and H. Tal-Ezer, "A Direct Relaxation Method for Calculating Eigenfunction and Eigenvalues of the Schrödinger Equation on a Grid," *Chem. Phys. Lett.* **127**, p. 223, 1986. 2.4.1

[50] J.-Y. Fang and H. Guo, "Multiconfiguration Time-Dependent Hartree Studies of the CH_3I/MgO Photodissociation Dynamics," *J. Chem. Phys.* **101**, p. 5831, 1994. 2.4.1

[51] G. A. Worth, H.-D. Meyer, and L. S. Cederbaum, "The Effect of a Model Environment on the S_2 Absorption Spectrum of Pyrazine: A Wave Packet Study Treating all 24 Vibrational Modes," *J. Chem. Phys.* **105**, p. 4412, 1996. 2.4.1, 2.4.1

[52] G. A. Worth, H.-D. Meyer, L. S. Cederbaum, W. Domcke, D. Yarkony, and H. Köppel, "Multidimensional Dynamics Involving a Conical Intersection: Wavepacket Calculations Using the MCTDH Method," in *Conical Intersections: Electronic structure, dynamics and spectroscopy*, *Advanced Series in Physical Chemistry, Vol. 15*, p. 583, World Scientific Publishing Co, (Singapore), 2004. 2.4.1

[53] G. A. Worth, M. H. Beck, A. Jäckle, and H.-D. Meyer. The MCTDH Package, Version 8.4, (2007). See http://www.pci.uni-heidelberg.de/tc/usr/mctdh/. 2.4.1, 2.4.2, 3.2, 3.2

[54] A. P. Pierce, M. A. Dahleh, and H. Rabitz, "Optimal Control of Quantum-Mechanical Systems: Existence, Numerical Approximation, and Applications," *Phys. Rev. A* **37**, p. 4950, 1988. 2.4.2

[55] R. Kosloff, S. A. Rice, P. Gaspard, S. Tersigni, and D. J. Tannor, "Wavepacket Dancing: Achieving Chemical Selectivity by Shaping Light Pulses ," *Chem. Phys.* **139**, p. 201, 1989. 2.4.2

[56] L. Wang, H.-D. Meyer, and V. May, "Femtosecond Laser Pulse Control of Multidimensional Vibrational Dynamics: Computational Studies on the Pyrazine Molecule," *J. Chem. Phys.* **125**, p. 14102, 2006. 2.4.2, 2.4.2, 2.4.2, 2.4.2

[57] M. Schröder, J.-L. Carreon-Macedo, and A. Brown, "Implementation of an Iterative Algorithm for Optimal Control of Molecular Dynamics into MCTDH," *Phys. Chem. Chem. Phys.* **10**, p. 850, 2007. 2.4.2, 4.8, 4.3.2, 4.3.2

[58] D. J. Tannor, *Introduction to Quantum Mechanics: A Time Dependent Perspective*, University Science Books, USA, 2007. 2.4.2, 3.4

[59] J. Manz, K. Sundermann, and R. de Vivie-Riedle, "Quantum Optimal Control Strategies for Photoisomerization Via Electronically Excited States," *Chem. Phys. Lett.* **290**, p. 415, 1998. 2.4.2

[60] J. Waluk, "Tautomerization in porphycenes," in *Hydrogen Transfer Reactions, Vol. 1*, p. 245, eds. J. T. Hynes, J. P. Klinman, H.-H. Limbach and R. L. Schowen, Wiley-VCH, (Weinheim), 2007. (document), 3, 3.1

[61] M. J. S. Dewar, S. Olivella, and J. J. P. Stewart, "Mechanism of the Diels-Alder Reaction: Reactions of Butadiene with Ethylene and Cyanoethylenes," *J. Am. Chem. Soc.* **108**, p. 5771, 1986. 3.1

[62] S. Pedersen, J. L. Herek, and A. H. Zewail, "The Validity of the "Diradical" Hypothesis: Direct Femtosecond Studies of the Transition-State Structures," *Science* **266**, p. 1359, 1994. 3.1

[63] R. A. Marcus, "Global Potential Energy Contour Plots for Chemical Reactions. Stepwise vs Concerted 2 + 2 Cycloaddition," *J. Am. Chem. Soc.* **117**, p. 4683, 1995. 3.1

[64] H. Lischka, E. Ventura, and M. Dallos, "The Diels-Alder Reaction of Ethene and 1,3-Butadiene: An Extended Multireference ab initio Investigation," *ChemPhysChem* **5**, p. 1365, 2004. 3.1

[65] L. Xu, C. E. Doubleday, and K. N. Houk, "Dynamics of 1,3-Dipolar Cycloaddition Reactions of Diazonium Betaines to Acetylene and Ethylene: Bending Vibrations Facilitate Reaction," *Angew. Chem. Int. Ed.* **48**, p. 2746, 2009. 3.1

[66] L. Xu, C. E. Doubleday, and K. N. Houk, "Dynamics of 1,3-Dipolar Cycloaddition: Energy Partitioning of Reactants and Quantitation of Synchronicity," *J. Am. Chem. Soc.* **132**, p. 3029, 2010. 3.1, 3.5

[67] V. A. Mozhayskiy, J. D. Savee, J. E. Mann, R. E. Continetti, and A. I. Krylov, "Conical for Stepwise, Glancing for Concerted: The Role of the Excited-State Topology in the Three-Body Dissociation of sym-Triazine," *J. Phys. Chem. A* **112**, p. 12345, 2008. 3.1

[68] Z. Smedarchina, W. Siebrand, and F. Zerbetto, "Comparison of Synchronous and Asynchronous Hydrogen Transfer Mechanism in Free-Base Porphyrins," *Chem. Phys.* **136**, p. 285, 1989. 3.1

[69] Z. Smedarchina, W. Siebrand, and A. Fernández-Ramos, "Correlated Double-Proton Transfer. I. Theory," *J. Chem. Phys.* **127**, p. 174513, 2007. 3.1, 3.1, 3.1, 3.2, 3.2, 3.2

[70] L. Meschede and H.-H. Limbach, "Dynamic NMR of the Kinetic HH/HD/DD Isotope Effects on the Double Proton Transfer in Ciclyc Bis(p-fluorophenyl)formamidine Dimers," *J. Phys. Chem.* **95**, p. 19267, 1991. 3.1

[71] M. F. Shibl, M. Pietrzak, H.-H. Limbach, and O. Kühn, "Geometric H/D Isotope Effects and Cooperativity of the Hydrogen Bonds in Porphycene," *ChemPhysChem* **8**, p. 315, 2007. 3.1

[72] J. M. L. del Amo, U. Langer, V. Torres, M. Pietrzak, G. Buntkowsky, H.-M. Vieth, M. F. Shibl, O. Kühn, M. Bröring, and H.-H. Limbach, "Isotope and Phase Effects on the Proton Tautomerism in Polycrystalline Porphycene Revealed by NMR," *J. Phys. Chem. A* **113**, p. 2193, 2009. 3.1

[73] H. Ushiyama and Takatsuka, "Successive Mechanism of Double-Proton Transfer in Formic Acid Dimer: A Classical Study," *J. Chem. Phys.* **115**, p. 5903, 2001. 3.1, 3.5

[74] A. Douhal, S. K. Kim, and A. H. Zewail, "Femtosecond Molecular Dynamics of Tautomerization in Model Base Pairs," *Nature* **378**, p. 260, 1995. 3.1

[75] O.-H. Kwon and A. H. Zewail, "Double Proton Transfer Dynamics of Model DNA Base Pairs in the Condensed Phase," *Proc. Natl. Acad. Sci. U.S.A.* **104**, p. 8703, 2007. 3.1

[76] K. Sakota, C. Okabe, N. Nishi, and H. Sekiya, "Excited-State Double-Proton Transfer in the 7-Azaindole Dimer in the Gas Phase. 3.Reaction Mechanism Studied by Picosecond Time-Resolved REMPI Spectroscopy," *J. Phys. Chem. A* **109**, p. 5245, 2005. 3.1

[77] H. Sekiya and K. Sakota, "Excited-State Double-Proton Transfer in the 7-Azaindole Dimer in the Gas Phase. Resolution of the Stepwise versus Concerted Mechanism Controversy and a New Paradigm," *Bull. Chem. Soc. Jpn.* **79**, p. 373, 2006. 3.1

[78] Z. Smedarchina, W. Siebrand, and A. Fernández-Ramos, "Multiple Proton Transfer: From Stepwise to Concerted," in *Hydrogen Transfer Reactions, Vol. 2*, p. 895, eds. J. T. Hynes, J. P. Klinman, H.-H. Limbach and R. L. Schowen, Wiley-VCH, (Weinheim), 2007. 3.1

[79] Z. Smedarchina, W. Siebrand, A. Fernández-Ramos, and R. Meana-Pañeda, "Mechanism of Double Proton Transfer. Theory and Applications," *Z. Phys. Chemie* **222**, p. 1291, 2008. 3.1

[80] S. Schweiger, B. Hartke, and G. Rauhut, "Double Proton Transfer Reactions at the Transition from a Concerted to a Stepwise Mechanism: A Comparative *ab initio* Study," *Phys. Chem. Chem. Phys.* **7**, p. 493, 2005. 3.1

[81] S. Schweiger, B. Hartke, and G. Rauhut, "Analysis and Dynamics of Unusual Double Proton Transfer Reactions Based on the Reaction Path Hamiltonian," *Phys. Chem. Chem. Phys.* **6**, p. 3341, 2004. 3.1

[82] H. F. von Horsten, G. Rauhut, and B. Hartke, "Fingerprints of Delocalized Transition States in Quantum Dynamics," *J. Phys. Chem. A* **110**, p. 13014, 2006. 3.1

[83] H. F. von Horsten and B. Hartke, "Links Between Potential Energy Structures and Quantum Cumulative Reaction Probabilities of Double Proton Transfer Reactions," *Chem. Phys.* **338**, p. 160, 2007. 3.1, 3.3

[84] B. Engels and M. Christl, "What Controls the Reactivity of 1,3-Dipolar Cycloadditions?," *Angew. Chem. Int. Ed.* **48**, p. 7968, 2009. 3.1

[85] G. L. Barnes and W. L. Hase, "Bent Out of Shape," *Nature Chem.* **1**, p. 103, 2009. 3.1

[86] J. C. Polanyi, "Concepts in Reaction Dynamics," *Acc. Chem. Res.* **5**, p. 161, 1972. 3.1, 5.1.3

[87] M. K. Abdel-Latif and O. Kühn, "Infrared Laser Control of Double Proton Transfer Reactions," *Chem. Phys.* **368**, p. 76, 2010. 3.1

[88] L. Walewski, J. Waluk, and B. Lesyng, "Car-Parrinello Molecular Dynamics Study of the Intramolecular Vibrational Mode-Sensitive Double Proton Transfer Mechanism in Porphycene," *J. Phys. Chem. A* **114**, p. 2313, 2010. 3.2

[89] T. J. Butenhoff, R. S. Chuck, H.-H. Limbach, and C. B. Moore, "Vibrational Photochemistry of Porphine Imbedded in a *n*-Hexane-d_{14} Shpol'skii Matrix," *J. Phys. Chem.* **94**, p. 7847, 1990. 3.2, 3.2

[90] T. J. Butenhoff and C. B. Moore, "Hydrogen Atom Tunneling in the Thermal Tautomerism of Porphine Imbedded in a *n*-Hexane Matrix," *J. Am. Chem. Soc.* **110**, p. 8336, 1988. 3.2, 3.2

[91] J. Braun, M. Schlabach, B. Wehrle, H.-H. Limbach, and E. Vogel, "NMR Study of the Tautomerism of Porphyrin Including the Kinetic HH/HD/DD Isotope Effects in the Liquid and the Solid State," *J. Am. Chem. Soc.* **116**, p. 6593, 1994. 3.2, 3.2

[92] J. Braun, H.-H. Limbach, P. G. Williams, H. Morimoto, and D. E. Wemmer, "Observation of Kinetic Tritium Isotope Effects by Dynamics NMR. The Tautomerism of Porphyrin," *J. Am. Chem. Soc.* **118**, p. 7231, 1996. 3.2, 3.2

[93] Z. Smedarchina, M. Z. Zgierski, W. Siebrand, and P. M. Kozlowski, "Dynamics of Tautomerism in Porphine: An Instanton Approach," *J. Chem. Phys.* **109**, p. 1014, 1998. 3.2

[94] D. J. Tannor and S. A. Rice, "Control of Selectivity of Chemical Reaction Via Control of Wave Packet Evolution," *J. Chem. Phys.* **83**, p. 5013, 1985. 3.2

[95] D. J. Tannor, R. Kosloff, and S. A. Rice, "Coherent Pulse Sequence Induced Control of Selectivity of Reactions: Exact Quantum Mechanical Calculations," *J. Phys. Chem.* **85**, p. 5805, 1986. 3.2, 4.3.2

[96] S. A. Rice and M. Zhao, *Optimal Control of Molecular Dynamics*, Wiley-VCH, New York, 2001. 3.2

[97] M. Shapiro and P. W. Brumer, *Principles of the Quantum Control of Molecular Processes*, Wiley-VCH, New York, 2003. 3.2

[98] W. Li, X. Zhou, R. Lock, S. Patchkovskii, A. Stolow, H. C. Kapteyn, and M. M. Murnane, "Time-Resolved Dynamics in N_2O_4 Probed Using High Harmonic Generation," *Science* **322**, p. 1207, 2008. 3.2

[99] A. Jäckle and H.-D. Meyer, "Time-Dependent Calculation of Reactive Flux Employing Complex Adsorbing Potentials: General Aspects and Application within the Multiconfigurational Time-Dependent Hartree Wave Approach," *J. Chem. Phys.* **105**, p. 6778, 1996. 3.3

[100] A. Kenfack, G. K. Paramonov, I. Barth, C. Lasser, and B. Paulus, "Initial-State Dependence of Coupled Electronic and Nuclear Fluxes in Molecules," *Phys. Rev. A* **81**, p. 52502, 2010. 3.4, 3.5

[101] R. B. Gerber, M. V. Korolkov, J. Manz, M. Y. Niv, and B. Schmidt, "A Reflection Principle for the Control of Molecular Photodissociation in Solids: Model Simulation for F_2 in Ar," *Chem. Phys. Lett.* **327**, p. 76, 2000. 3.4, 4.1

[102] M. V. Korolkov and J. Manz, "Quantum Simulations of Wave Packet Dynamics in Reduced Dimensionality: From Analysis to Coherent Spin Control," in *Analysis and Control of Ultrafast Photoinduced Reactions*, *Springer Series in Chemical Physics, Vol. 87*, pp. 328–374, Springer, (Heidelberg), 2007. 3.4

[103] I. Barth, H.-C. Hege, H. Ikeda, A. Kenfack, M. Koppitz, J. Manz, F. Marquardt, and G. K. Paramonov, "Concerted Quantum Effects of Electronic and Nuclear Fluxes in Molecules," *Chem. Phys. Lett.* **481**, p. 118, 2009. 3.5

[104] P. Baum, J. Manz, and A. Schild, "Quantum Model Simulations of Attosecond Electron Diffraction," *Science in China G* **53**, p. 987, 2010. 3.5

[105] I. Barth and J. Manz, "Periodic Electron Circulation Induced by Circularly Polarized Laser Pulses: Quantum Model Simulations for Mg Porphyrin," *Angew. Chem. Int. Ed.* **45**, p. 2962, 2006. 3.5

[106] I. Barth, J. Manz, Y. Shigeta, and K. Yagi, "Unidirectional Electronic Ring Current Driven by a Few Cycle Circularly Polarized Laser Pulse: Quantum Model Simulations for Mg-Porphyrin," *J. Am. Chem. Soc.* **128**, p. 7043, 2006. 3.5

[107] I. Barth, J. Manz, and P. Sebald, "Spinning a Pseudorotating Molecular Top by Means of a Circularly Polarized Infrared Laser Pulse: Quantum Simulations for $^{114}CdH_2$," *Chem. Phys.* **346**, p. 89, 2008. 3.5

[108] I. Barth and J. Manz, "Quantum Switching of Magnetic Fields by Circularly Polarized Re-Optimized π Laser Pulses: From One-Electron Atomic Ions to Molecules," in *Progress in Ultrafast Intense Laser Science VI*, *Springer Series in Chemical Physics Vol. 99*, pp. 21–44, Eds. K. Yamanouchi and G. Gerber and A. D. Bandrauk, (Berlin, 2010). 3.5

[109] K. Hoki, M. Yamaki, S. Koseki, and Y. Fujimura, "Molecular Motors Driven by Laser Pulses: Role of Molecular Chirality and Photon Helicity," *J. Chem. Phys.* **118**, p. 497, 2008. 3.5

[110] K. P. Huber and G. Herzberg, *Molecular Spectra and Molecular Structure. IV. Constants of Diatomic Molecules*, Van Nostrand Reinhold, New York, 1979. 4.1

[111] H. Lefebvre-Brion and R. W. Field, *The Spectra and Dynamics of Diatomic Molecules*, Elsevier Academic Press, San Diego, 2004. 4.1

[112] Y. Fujii, N. A. Lurie, R. Pynn, and G. Shirane, "Inelastic Neutron Scattering from Solid ^{36}Ar," *Phys. Rev. B* **10**, p. 3647, 1974. 4.1

[113] P. Jungwirth and R. B. Gerber, "Quantum Dynamics of Ultrafast Processes in Large Polyatomic Systems," *Chem. Rev.* **99**, p. 1583, 1999. 4.1

[114] M. Gühr and N. Schwentner, "Effective Chromophore Potential, Dissipative Trajectories, and Vibrational Energy Relaxation: Br_2 in Ar Matrix," *J. Chem. Phys.* **123**, p. 244506, 2005. 4.1

[115] M. Bargheer, M. Y. Niv, R. B. Gerber, and N. Schwentner, "Ultrafast Solvent-Induced Spin-Flip and Nonadiabatic Coupling: ClF in Argon Solids," *Phys. Rev. Lett.* **89**, p. 108301, 2002. 4.1

[116] M. Bargheer, R. B. Gerber, M. V. Korolkov, O. Kühn, J. Manz, M. Schröder, and N. Schwentner, "Subpicosecond Spin-Flip Induced by the Photodissociation Dynamics of ClF in an Ar Matrix," *Phys. Chem. Chem. Phys.* **4**, p. 5554, 2002. 4.1

[117] M. Bargheer, A. Cohen, R. B. Gerber, M. Gühr, M. V. Korolkov, J. Manz, M. Y. Niv, M. Schröder, and N. Schwentner, "Dynamics of Electronic States and Spin-Flip for Photodissociation of Dihalogens in Matrices: Experiment and Semiclassical Surface-Hopping and Quantum Model Simulations for F_2 and ClF in Solid Ar," *J. Phys. Chem. A* **111**, p. 9573, 2007. 4.1

[118] A. Cohen and R. B. Gerber, "A 1 fs Spin-Flip in a Chemical Reaction: Photodissociation of HF in Solid Ar ," *Chem. Phys. Lett.* **441**, p. 48, 2007. 4.1

[119] A. Borowski and O. Kühn, "Nonadiabatic Quantum Dynamics of Br_2 in Solid Ar: A Four-Dimensional Study of the B to C State Predissociation," *Chem. Phys.* **347**, p. 523, 2008. (document), 4.1, 4.2, 4.2, 4.2, 4.2, 4.3, 4.2, 4.2, 4.3.1, 4.4

[120] A. Borowski, *Non-Adiabatic Multi-Dimensional Quantum Dynamics of Br_2 in Solid Argon*. PhD thesis, Fachbereich Chemie - Freie Universität Berlin, 2008. (document), 4.1, 4.2, 4.2, 4.1, 4.2, 4.2, 4.2, 4.3, 4.2, 4.2, 4.3.1, 4.4, 5.11

[121] M. C. Heaven, "Fluorescence Decay Dynamics of the Halogens and Interhalogens," *Chem. Soc. Rev.* **15**, p. 405, 1986. 4.1

[122] C. Lienau and A. H. Zewail, "Femtochemistry at High Pressures: Solvent Effect in the Gas-to-Liquid Transition Region.," *Chem. Phys. Lett.* **222**, p. 224, 1994. 4.1

[123] H. Ibrahim, M. Gühr, and N. Schwentner, "Valence Transitions of Br_2 in Ar Matrices: Interaction with the Lattice, Phonon Sidebands and Predissociation," *J. Chem. Phys.* **128**, p. 064504, 2008. 4.1

[124] M. Y. Niv, M. Bargheer, and R. B. Gerber, "Photodissociation and Recombination of F_2 Molecule in Ar_{54} Cluster: Nonadiabatic Molecular Dynamics Simulations," *J. Chem. Phys.* **113**, p. 6660, 2000. 4.1

[125] M. Fushitani, N. Schwentner, M. Schröder, and O. Kühn, "Cage Motions Induced by Electronic and Vibrational Excitations: Cl_2 in Ar," *J. Chem. Phys.* **124**, p. 24505, 2006. 4.1

[126] M. Gühr, M. Bargheer, and N. Schwentner, "Generation of Coherent Zone Boundary Phonons by Impulsive Excitation of Molecules," *Phys. Rev. Lett.* **91**, p. 085504, 2003. 4.1

[127] M. Gühr and N. Schwentner, "Coherent Phonon Dynamics: Br_2 in Solid Ar," *Phys. Chem. Chem. Phys.* **7**, p. 760, 2005. 4.1

[128] M. Fushitani, M. Bargheer, M. Gühr, and N. Schwentner, "Pump-Probe Spectroscopy with Phase-Locked Pulses in the Condensed Phase: Decoherence and Control of Vibrational Wavepackets," *Phys. Chem. Chem. Phys.* **7**, p. 3143, 2005. 4.1

[129] M. Gühr, H. Ibrahim, and N. Schwentner, "Controlling Vibrational Wave Packet Revivals in Condensed Phase: Dispersion and Coherence for Br_2 in Solid Ar," *Phys. Chem. Chem. Phys.* **6**, p. 5353, 2004. 4.1

[130] M. Fushitani, M. Bargheer, M. Gühr, H. Ibrahim, and N. Schwentner, "Control of Chromophore to Bath Coupling by Interferometry," *J. Phys. B* **41**, p. 74013, 2008. 4.1

[131] I. Last and T. F. George, "Electronic States of the Xe-HCl Systems in Gas and Condensed Phases," *J. Chem. Phys.* **89**, p. 3071, 1988. 4.1

[132] B. L. Grigorenko, A. V. Nemukhin, and V. A. Apkarian, "Many-Body Potentials and Dynamics Based on Diatomics-In-Molecules: Vibrational Frequency Shifts in Ar_nHF (n=1-12,62) Clusters," *J. Chem. Phys.* **104**, p. 5510, 1996. 4.1

[133] F. O. Ellison, "A Method of Diatomics in Molecules. I. General Theory and Application to H_2O," *J. Am. Chem. Soc.* **85**, p. 3540, 1963. 4.1

[134] F. O. Ellison, N. T. Huff, and J. C. Patel, "A Method of Diatomics in Molecules. II. H_3 and H_3^+," *J. Am. Chem. Soc.* **85**, p. 3544, 1963. 4.1

[135] J. C. Tully and R. K. Preston, "Trajectory Surface Hopping Approach to Nonadiabatic Molecular Collisions: The Reaction of H^+ with D_2," *J. Chem. Phys.* **55**, p. 562, 1971. 4.1

[136] J. C. Tully, "Diatomics-in-molecules Potential Energy Surfaces. I. First-row Triatomic Hydrides," *J. Chem. Phys.* **58**, p. 1396, 1973. 4.1

[137] J. C. Tully, "Diatomics-in-molecules Potential Energy Surfaces. II. Nonadiabatic and Spin-Orbit Interactions," *J. Chem. Phys.* **59**, p. 5122, 1973. 4.1

[138] I. H. Gersonde and H. Gabriel, "Molecular Dynamics of Photodissociation in Matrices Including Nonadiabatic Processes," *J. Chem. Phys.* **98**, p. 2094, 1993. 4.1

[139] I. H. Gersonde, S. Hennig, and H. Gabriel, "Nonadiabatic Transitions in the Photodissociation of HCl," *J. Chem. Phys.* **101**, p. 9558, 1994. 4.1

[140] W. G. Lawrence and V. A. Apkarian, "Many-Body Potentials of an Open Shell Atom: Spectroscopy of Spin-Orbit Transitions of Iodine in Crystalline Xe and Kr," *J. Chem. Phys.* **101**, p. 1820, 1994. 4.1

[141] V. S. Batista and D. F. Coker, "Nonadiabatic Molecular Dynamics Simulation of Photodissociation and Geminate Recombination of I_2 in Liquid Xenon," *J. Chem. Phys.* **105**, p. 4033, 1996. 4.1

[142] V. S. Batista and D. F. Coker, "Nonadiabatic Molecular Dynamics Simulation of Ultrafast Pump-Probe Experiments on I_2 in Solid Rare Gases," *J. Chem. Phys.* **106**, p. 6923, 1997. 4.1

[143] V. S. Batista and D. F. Coker, "Nonadiabatic Molecular Dynamics Simulations of the Photofragmentation and Geminate Recombination Dynamics in Size-Selected $I_2^- \cdot Ar_n$ Cluster Ions," *J. Chem. Phys.* **106**, p. 7102, 1997. 4.1

[144] A. I. Krylov and R. B. Gerber, "Photodissociation Dynamics of HCl in Solid Ar: Cage Exit, Nonadiabatic Transitions, and Recombination," *J. Chem. Phys.* **106**, p. 6574, 1997. 4.1

[145] M. Y. Niv, A. I. Krylov, and R. B. Gerber, "Photodissociation, Electronic Relaxation and Recombination of HCl in Ar_n(HCl) Clusters," *Faraday Discuss.* **108**, p. 243, 1997. 4.1

[146] M. Y. Niv, A. I. Krylov, and R. B. Gerber, "Photodissociation of HCl Adsorbed on the Surface of an Ar_{12} Cluster: Nonadiabatic Molecular Dynamics Simulations," *J. Chem. Phys.* **110**, p. 11047, 1999. 4.1

[147] B. L. Grigorenko, A. V. Nemukhin, A. A. Buchachenko, N. F. Stepanov, and S. Y. Umanskii, "Diatomics-in-molecules Description of the Rg-Hal_2 Rare Gas-Halogen Van der Waals Complexes with Applications to He-Cl_2," *J. Chem. Phys.* **106**, p. 4575, 1997. 4.1

[148] A. A. Buchachenko and N. F. Stepanov, "Ar-I_2 Interactions: The Models Based on the Diatomics-In-Molecule Approach," *J. Chem. Phys.* **104**, p. 9913, 1996. 4.1

[149] A. A. Buchachenko and N. F. Stepanov, "Structure and Interaction Energies of the $Ar\cdots Cl_2$ Complex. Application of First-Order Intermolecular Potentials," *Chem. Phys. Lett.* **261**, p. 591, 1996. 4.1

[150] A. A. Buchachenko, "Predissociation of the Rg$\cdots$I$_2$(B) (Rg=Ne, Ar, Kr) Complexes: Simulations based on the First-Order Diatomics-In-Molecule Perturbation Theory," *Chem. Phys. Lett.* **292**, p. 273, 1998. 4.1

[151] C. J. Margulis and D. F. Coker, "Applying Diatomic-In-Molecules in Excited Electronic State Calculations for Flexible Polyatomic Molecules. The I_3 Molecule," *J. Chem. Phys.* **113**, p. 6113, 2000. 4.1

[152] G. Chaban, R. B. Gerber, M. V. Korolkov, J. Manz, M. Y. Niv, and B. Schmidt, "Photodissociation Dynamics of Molecular Fluorine in an Argon Matrix Induced by Ultrashort Laser Pulses," *J. Phys. Chem. A* **105**, p. 2770, 2001. 4.1

[153] M. V. Korolkov and J. Manz, "Initial Processes of Laser Induced Diatomic Molecular Photodissociation in Matrices: Quantum Simulations for F_2 in Ar in Reduced Dimensionality," *Z. Phys. Chemie* **217**, p. 115, 2003. 4.1

[154] A. B. Alekseyev, M. V. Korolkov, O. Kühn, J. Manz, and M. Schröder, "Model Simulation of Coherent Laser Control of the Ultrafast Spin-Flip Dynamics of Matrix-Isolated Cl_2," *J. Photochem. and Photobiol. A* **180**, p. 262, 2006. 4.1, 4.3.2

[155] M. V. Korolkov and J. Manz, "Design of UV Laser Pulses for the Preparation of Matrix Isolated Homonuclear Diatomic Molecules in Selective Vibrational Superposition States," *J. Chem. Phys.* **126**, p. 174306, 2007. 4.1, 4.3.2

[156] M. V. Korolkov and J. Manz, "Coherent Spin Control of Matrix Isolated Molecules by IR + UV Laser Pulses: Quantum Simulations for ClF in Ar," *J. Chem. Phys.* **120**, p. 11522, 2004. 4.1

[157] M. V. Korolkov and J. Manz, "Cage Exit Supported by Spin-Orbit Coupling: Quantum Model Simulations for ClF in an Ar Matrix," *J. Chem. Phys.* **393**, p. 44, 2004. 4.1

[158] A. Borowski and O. Kühn, "Towards a Quantum Mechanical Description of the Photochemistry of Dihalogens in Rare Gas Matrices," *J. Photochem. and Photobiol. A* **190**, p. 169, 2007. (document), 4.1, 4.2, 4.2, 4.2, 4.2, 4.4

[159] W. H. Miller, N. C. Handy, and J. E. Adams, "Reaction Path Hamiltonian for Polyatomic Molecules," *J. Chem. Phys.* **72**, p. 99, 1980. 4.1

[160] T. Carrington Jr. and W. H. Miller, "Reaction Surface Hamiltonian for the Dynamics of Reactions in Polyatomic Systems," *J. Chem. Phys.* **81**, p. 3942, 1984. 4.1

[161] N. Makri and W. H. Miller, "Basis Set Methods for Describing the Quantum Mechanics of a 'System' Interacting with a Harmonic 'Bath'," *J. Chem. Phys.* **86**, p. 1451, 1987. 4.1

[162] H. Köppel, W. Domcke, and L. S. Cederbaum, "Multimode Molecular Dynamics Beyond the Born-Oppenheimer Approximation," *Adv. Chem. Phys.* **57**, p. 59, 1984. 4.1, 4.2

[163] L. S. Cederbaum, W. Domcke, H. Köppel, and W. von Niessen, "Strong Vibronic Coupling Effects in Ionization Spectra: The Mystery Band of Butatriene," *Chem. Phys.* **26**, p. 126, 1977. 4.1

[164] L. S. Cederbaum and W. Domcke, "Theoretical Aspects of Ionization Potentials and Photoelectron Spectroscopy: A Many-Body Approach," *Adv. Chem. Phys.* **36**, p. 205, 1977. 4.1

[165] J. Tellinghuisen, "Erratum: "Transition Strengths and Potential Curves for the Valence Transitions in Br_2 from a Reanalysis of the Ultraviolet-Visible Absorption at Low Resolution"," *J. Chem. Phys.* **118**, p. 1573, 2003. 4.2

[166] L. D. Landau, "On the Theory of Transfer of Energy at Collisions II," *Phys. Z. Sov.* **2**, p. 46, 1932. 4.3.1

[167] C. Zener, "Non-adiabatic crossings of energy levels," *Proc. R. Soc. Lond. A* **137**, p. 696, 1932. 4.3.1

[168] N. Rosen and C. Zener, "Double Stern-Gerlach experiment and related collision phenomena," *Phys. Rev.* **40**, p. 502, 1932. 4.3.1

[169] V. Berghof and N. Schwentner, "Selective Dissociation of HCl in Kr from Vibrational Overtones," *J. Chem. Phys.* **117**, p. 8256, 2002. 4.3.2

[170] R. Pausch, M. Heid, T. Chen, H. Schwoerer, and W. Kiefer, "Quantum Control by Stimulated Raman Scattering," *J. Raman Spectrosc.* **31**, p. 7, 2000. 4.3.2

[171] U. Banin, A. Bartana, S. Ruhman, and R. Kosloff, "Impulsive Excitation of Coherent Vibrational Motion Ground Surface Dynamics Induced by Intense Short Pulses," *J. Chem. Phys.* **101**, p. 8461, 1994. 4.3.2

[172] O. Kühn, D. Malzahn, and V. May, "Theoretical Description of Dissipative Vibrational Dynamics Using the Density Matrix in the State Representation," *Int. J. Quantum Chem.* **57**, p. 343, 1996. 4.3.2

[173] A. Einstein, "Die Plancksche Theorie der Strahlung und die Theorie der Spezifischen Wärme," *Annalen der Physik* **22**, p. 180, 1907. (document), 5.1, 5.3.8, 5.3.8, 5.4

[174] A. F. Devonshire, "The Rotation of Molecules in Fields of Octahedral Symmetry," *Proc. Roy. Soc. A* **153**, p. 601, 1936. (document), 5.1, 5.1.3, 5.3.8, 5.3.8, 5.3.8, 5.4

[175] A. Bondi, "Van der Waals Volumes and Radii," *J. Chem. Phys.* **68**, p. 441, 1964. 5.1.1, 5.3.1

[176] O. Kühn, J. Manz, and A. Schild, "Quantum Effects on Translational Motions in Solid para-Hydrogen and ortho-Deuterium: Anharmonic Extension of the Einstein Model," *J. Phys.: Condens. Matter* **22**, p. 135401, 2010. 5.1.1, 5.1.3, 5.1.3, 5.3.8, 5.3.8, 5.3.8, 5.3.8, 5.3.8, 5.16, 5.3.8, 5.4

[177] D. R. Linde, *CRC Handbook of Chemistry and Physics*, CRC Press, USA, West Palm Beach, 87, 2006. 5.1.1

[178] B. M. Axilrod and E. Teller, "Interaction of the van der Waals Type Between Three Atoms," *J. Chem. Phys.* **11**, p. 299, 1943. 5.1.2

[179] J. A. Barker, R. O. Watts, J. K. Lee, T. P. Schafer, and Y. T. Lee, "Interatomic Potentials for Krypton and Xenon," *J. Chem. Phys.* **61**, p. 3081, 1974. 5.1.2

[180] G. A. Gallup, "Electron Tunneling, Charge Transfer, and the Intermolecular Forces between two H_2 Molecules," *J. Chem. Phys.* **66**, p. 2252, 1977. 5.1.2, 5.1.2

[181] J. Schaefer and W. Meyer, "Theoretical Studies of H_2-H_2 Collisions. I. Elastic Scattering of Ground State para- and ortho-H_2 in the Rigid Rotor Approximation," *J. Chem. Phys.* **70**, p. 344, 1979. 5.1.2

[182] J. Schaefer and R. O. Watts, "The Equation of State of Hydrogen from an *ab initio* Potential Surface," *Mol. Phys.* **47**, p. 933, 1982. 5.1.2

[183] P. Wind and I. Roeggen, "A Theoretical Study of the $(H_2)_2$ Dimer. II. The Potential Energy Surface," *Chem. Phys.* **167**, p. 263, 1992. 5.1.2

[184] P. Wind and I. Roeggen, "A Theoretical Study of the $(H_2)_2$ Dimer. III. The Isotropic Potential," *Chem. Phys.* **174**, p. 345, 1993. 5.1.2

[185] P. Wind and I. Roeggen, "Ab Initio Calculation of the Three-Body Interaction in the $(H_2)_3$ Trimer.," *Chem. Phys.* **211**, p. 179, 1996. 5.1.2

[186] P. Diep and J. K. Johnson, "An Accurate H_2-H_2 Interaction Potential from First Principles," *J. Chem. Phys.* **112**, p. 4465, 2000. 5.1.2, 5.1.2

[187] A. I. Boothroyd, P. G. Martin, W. J. Keogh, and M. J. Peterson, "An Accurate Analytic H_4 Potential Energy Surface," *J. Chem. Phys.* **116**, p. 666, 2002. 5.1.2

[188] K. Patkowski, W. Cencek, P. Jankowski, K. Szalewicz, J. B. Mehl, G. Garberoglio, and A. H. Harvey, "Potential Energy Surface for Interaction between two Hydrogen Molecules," *J. Chem. Phys.* **129**, p. 94304, 2008. 5.1.2, 5.1.2, 5.3.5, 5.14

[189] R. J. Hinde, "Dependence of the H_2-H_2 Interaction of the Monomer Bond Lengths: Steps Towards an Accurate *ab initio* Estimate," *Few-Body System* **38**, p. 187, 2006. 5.1.2, 5.3.5

[190] R. J. Hinde, "A Six-Dimensional H_2-H_2 Potential Energy Surface for Bound State Spectroscopy," *J. Chem. Phys.* **128**, p. 154308, 2008. 5.1.2, 5.14, 5.7, 5.4

[191] R. J. Hinde, "Three-Body Interactions in Solid Parahydrogen," *Chem. Phys. Lett.* **460**, pp. 141–145, 2008. 5.1.2, 5.1.2, 5.3.5

[192] I. F. Silvera and V. V. Goldmann, "The Isotropic Intermolecular Potential for H_2 and D_2 in the Solid and Gas Phase," *J. Chem. Phys.* **69**, p. 4209, 1978. 5.1.2

[193] M. J. Norman, R. O. Watts, and U. Buck, "A Spherical Potential for Hydrogen from Solid State Scattering Data," *J. Chem. Phys.* **81**, p. 3500, 1984. 5.1.2, 5.3.5, 5.14, 5.6, 5.7, 5.4

[194] R. Ahlrichs, R. Penco, and G. Scoles, "Intermolecular Forces in Simple Systems," *Chem. Phys.* **19**, p. 119, 1977. 5.1.2, 5.3.4

[195] A. J. Stone, *The Theory of Intermolecular Forces*, Oxford University Press, USA, Oxford, 1997. 5.1.2, 5.3.1, 5.3.1

[196] W. Meyer, "Dynamic Multipole Polarizabilities of H_2 and He and Long-Range Interaction Coefficients for H_2-H_2, H_2-He and He-He," *Chem. Phys.* **17**, p. 27, 1976. 5.1.2

[197] T. C. Lillestolen and R. J. Hinde, "Vibrationally Averaged Isotropic Dispersion Energy Coefficients of the Parahydrogen Dimer," *J. Chem. Phys.* **136**, p. 204303, 2012. 5.1.2, 5.2, 5.3.5, 5.6, 5.4

[198] G. N. Lewis, D. Lipkin, and T. T. Magel, "Reversible Photochemical Processes in Rigid Media. A Study of the Phosphorescent State," *J. Am. Chem. Soc.* **63**, p. 3005, 1941. 5.1.3

[199] P. Jungwirth and R. B. Gerber, "Quantum Molecular Dynamics of Ultrafast Processes in Large Polyatomic Systems," *Chem. Rev.* **99**, p. 1583, 1999. 5.1.3

[200] D. P. Weliky, K. E. Kerr, T. J. Byers, Y. Zhang, and T. Momose, "High-Resolution Infrared Spectroscopy of Isotopic Impurity $Q_1(0)$ Transitions in Solid Parahydrogen," *J. Chem. Phys.* **105**, p. 4461, 1996. 5.1.3

[201] M. Miki, T. Wakabayashi, T. Momose, and T. Shida, "Infrared Spectroscopy Studies of Carbon Clusters Trapped in Solid Parahydrogen," *J. Phys. Chem.* **100**, p. 12135, 1996. 5.1.3

[202] D. T. Anderson, R. J. Hinde, S. Tam, and M. E. Fajardo, "High-Resolution Spectroscopy of HCl and DCl Isolated in Solid Parahydrogen: Direct, Induced and Cooperative Infrared Transitions in a Molecular Quantum Solid," *J. Chem. Phys.* **116**, p. 594, 2002. 5.1.3

[203] M. E. Fajardo, S. Tam, and M. E. DeRose, "Matrix Isolation Spectroscopy of H_2O, D_2O and HDO in Solid Parahydrogen," *J. Mol. Struc.(Theochem)* **695-696**, p. 111, 2004. 5.1.3

[204] S. C. Kettwich, P. L. Raston, and D. T. Anderson, "The Cl+H_2 $\rightarrow$ HCl+H Reaction Induced by IR+UV Irradiation of Cl_2 in Solid para-H_2: Experiment," *J. Phys. Chem. A* **113**, p. 7621, 2009. 5.1.3, 5.3.8, 5.4

[205] L. O. Paulson and D. T. Anderson, "High-Resolution Vibrational Spectroscopy of *trans*-Formic Acid in Solid Parahydrogen," *J. Phys. Chem. A* **113**, p. 1770, 2009. 5.1.3, 5.3.4

[206] M. Bahou and Y.-P. Lee, "Diminished Cage Effect in Solid p-H_2: Infrared Absorption of CH_3S Observed from Photolysis *in situ* of CH_3SH, CH_3SCH_3, or CH_3SSCH_3 Isolated in p-H_2 Matrices," *J. Chem. Phys.* **113**, p. 164316, 2010. 5.1.3

[207] M. S. Anderson and C. A. Swenson, "Experimental Compressions for Normal Hydrogen and Normal Deuterium to 25 kbar at 4.2 K," *Phys. Rev. B* **10**, p. 5184, 1974. 5.1.3, 5.1.3, 5.3.8

[208] F. Königsmann, *Femtosecond Spectroscopy of Solid Hydrogen: Long Lived Coherences in a Molecular Quantum Crystal.* PhD thesis, Fachbereich Physik - Freie Universität Berlin, 2012. 5.1.3

[209] M. Fajardo and S. Tam, "Observation of the Cyclic Water Hexamer in Solid Parahydrogen," *J. Chem. Phys.* **115**, p. 6807, 2001. 5.1.3

[210] M. E. Fajardo, S. Tam, T. L. Thompson, and M. E. Cordonnier, "Spectroscopy and Reactive Dynamics of Atoms Trapped in Molecular Hydrogen Matrices," *Chem. Phys.* **189**, p. 351, 1994. 5.1.3

[211] S. Grebenev, B. Sartakov, J. P. Toennies, and A. F. Vilesov, "Evidence for Superfluidity in para-Hydrogen Clusters Inside Helium-4 Droplets at 0.15 Kelvin," *Science* **289**, p. 1532, 2000. 5.1.3

[212] S. Grebenev, B. Sartakov, J. P. Toennies, and A. F. Vilesov, "Effect of the Symmetry of H_2 Molecules on their Rotations around an OCS Molecule in Superfluid ^{4}He Droplets," *Phys. Rev. Lett.* **89**, p. 225301, 2002. 5.1.3

[213] Y. Kwon and K. B. Whaley, "Microscopic Two-Fluid Theory of Rotational Constants of the OCS-H_2 Complex in ^{4}He Droplets," *J. Chem. Phys.* **119**, p. 1986, 2003. 5.1.3

[214] D. E. Bernholdt, S.-Y. Liu, and C. E. Dykstra, "A Theoretical Study of the Structure, Bonding, and Vibrational Frequency Shifts of the H_2-HF Complex," *J. Chem. Phys.* **85**, p. 5120, 1986. 5.1.3

[215] D. C. Clary and P. J. Knowles, "Calculation of van der Waals spectra for H_2HF, D_2HF, and H_2DF," *J. Chem. Phys.* **93**, p. 6334, 1990. 5.1.3

[216] D. C. Clary, "Vibrational Predissociation in D_2HF," *J. Chem. Phys.* **96**, p. 90, 1992. 5.1.3

[217] D. H. Zhang and J. Z. H. Zhang, "An Efficient Time-Dependent Golden Rule Treatment for Three-Dimensional Vibrational Predissociation of Helium Diiodide," *J. Phys. Chem.* **96**, p. 1575, 1992. 5.1.3

[218] D. H. Zhang, J. Z. H. Zhang, and Z. Bačić, "Mode-Specific Decay Widths in Vibrational Predissociation of D_2HF," *Chem. Phys. Lett.* **194**, p. 313, 1992. 5.1.3

[219] D. H. Zhang, J. Z. H. Zhang, and Z. Bačić, "A Time-Dependent Calculation for Vibrational Predissociation of H_2HF," *J. Chem. Phys.* **97**, p. 3149, 1992. 5.1.3

[220] P. J. Krause and D. C. Clary, "Vibrational Predissociation of D_2HF and H_2HF with a New Potential Energy Surface," *Mol. Phys.* **93**, p. 619, 1998. 5.1.3

[221] S. Moroni, M. Botti, S. D. Paolo, and A. R. W. McKellar, "Small *para*-Hydrogen Clusters Doped with Carbon Monoxide: Quantum Monte Carlo Simulations and Observed Infrared Spectra," *J. Chem. Phys.* **122**, p. 94314, 205. 5.1.3, 5.2, 5.3.6

[222] S. Manzhos, K. Nakaia, and K. Yamashita, "Three-Body Interactions in Clusters CO- $(pH_2)_n$," *Chem. Phys. Lett.* **493**, p. 229, 2010. 5.1.3

[223] Z. Li and V. A. Apkarian, "Impurity Rotations in Quantum versus Classical Solids: O_2 in Solid Hydrogens," *J. Chem. Phys.* **107**, p. 1544, 1997. 5.1.3

[224] H. Zhu and D. Xie, "N_2O in Small *para*-Hydrogen Clusters: Structures and Energetics," *J. Comput. Chem.* **30**, p. 841, 2009. 5.1.3, 5.2

[225] D. Li and G. A. Voth, "A Path Integral Einstein Model for Characterizing the Equilibrium States of Low Temperature Solids," *J. Chem. Phys.* **96**, p. 5340, 1992. 5.1.3

[226] M. Sterling, Z. Li, and V. A. Apkarian, "Simulations of Quantum Crystals by Classical Dynamics," *J. Chem. Phys.* **103**, p. 5679, 1995. 5.1.3

[227] D. Scharf, G. J. Martyna, D. Li, G. A. Voth, and M. L. Klein, "Nature of Lithium Trapping Sites in the Quantum Solids *para*-Hydrogen and *ortho*-Deuterium," *J. Chem. Phys.* **99**, p. 9013, 1993. 5.1.3

[228] K. Kinugawa, P. B. Moore, and M. L. Klein, "Centroid Path Integral Molecular Dynamics Simulation of Lithium para-Hydrogen Clusters," *J. Chem. Phys.* **106**, p. 1154, 1997. 5.1.3

[229] S. Jang and G. A. Voth, "Lithium Impurity Recombination in Solid para-Hydrogen: A Path Integral Quantum Transition State Theory Study," *J. Chem. Phys.* **108**, p. 4098, 1998. 5.1.3

[230] S. Jang, S. Jang, and G. A. Voth, "Quantum Molecular Dynamics Simulations of Low-Temperature High Energy Density Matter: Solid p-H_2/Li and p-H_2/B," *J. Phys. Chem. A* **103**, p. 9512, 1999. 5.1.3

[231] I. Røeggen, H. R. Skullerud, T. H. I. Løvaas, and D. K. Dysthe, "The Li^+-H_2 System in a Rigid-Rotor Approximation: Potential Energy Surface and Transport Coefficients," *J. Phys. B: At. Mol. Opt. Phys.* **35**, p. 1707, 2002. 5.1.3

[232] V. P. Bulychev, K. M. Bulanin, and M. O. Bulanin, "Theoretical Study of the Spectral and Structural Parameters of the van der Waals Complexes of the Li^+ Cation with the H_2, D_2, and T_2 Isotopomers of the Hydrogen Molecule," *Optics and Spectroscopy* **96**, p. 205, 2004. 5.1.3

[233] Z. Li, V. A. Apkarian, and L. B. Harding, "A Theoretical Study of Solid Hydrogens Doped with Atomic Oxygen," *J. Chem. Phys.* **106**, p. 942, 1997. 5.1.3

[234] J. R. Krumrine, S. Jang, M. H. Alexander, and G. A. Voth, "Quantum Molecular Dynamics and Spectral Simulation of a Boron Impurity in Solid *para*-Hydrogen," *J. Chem. Phys.* **113**, p. 9079, 2000. 5.1.3, 5.2

[235] M. Alagia, N. Balucani, L. Cartechini, P. Casavecchia, G. G. Volpi, F. J. Aoiz, L. Banares, T. C. Allison, S. L. Mielke, and D. G. Truhlar, "Dynamics of the Cl+H_2/D_2 Reaction: A Comparison of Crossed Molecular Beam Experiments with Quasiclassical Trajectory and Quantum Mechanical Calculations," *Phys. Chem. Chem. Phys.* **2**, p. 599, 2000. 5.1.3

[236] G. Capecchi and H. J. Werner, "Ab initio Calculations of Coupled Potential Energy Surfaces for the Cl($^2P_{3/2}$,$^2P_{1/2}$) + H_2 Reaction," *Phys. Chem. Chem. Phys.* **6**, p. 4975, 2004. 5.1.3, 5.1.3

[237] K. Rościszewski and B. Paulus, "The Zero-Point Energy in the Molecular Hydrogen Crystal," *Mol. Phys.* **108**, p. 2147, 2010. 5.1.3, 5.3.8, 5.3.8, 5.3.8

[238] D. T. Moore, M. Ishiguro, and R. E. Miller, "Binary Complexes of HCN with H_2, HD, and D_2 Formed in Helium Nanodroplets," *J. Chem. Phys.* **115**, p. 5144, 2001. 5.2

[239] F. Paesani and K. B. Whaley, "Potential Energy Surface and Infrared Spectra of OCS-Hydrogen Complexes," *Mol. Phys.* **104**, p. 61, 2006. 5.2

[240] H. Li, P.-N. Roy, and R. J. L. Roy, "An "Adiabatic-Hindered-Rotor" Treatment Allows *para*-H_2 to be Treated as if it were Spherical," *J. Chem. Phys.* **133**, p. 104305, 2010. 5.2, 5.3.4, 5.3.5, 5.14, 5.7, 5.4

[241] W. H. Press, S. Teukolsk, W. Vetterling, and B. Flannery, *Numerical Recipes. The Art of Scientific Computing, 3rd Edition*, Cambridge University Press, Cambridge, 2007. 5.2, 5.2

[242] H.-J. Werner, P. J. Knowles, F. R. Manby, M. Schütz, P. Celani, G. Knizia, T. Korona, R. Lindh, A. Mitrushenkov, G. Rauhut, T. B. Adler, R. D. Amos, A. Bernhardsson, A. Berning, D. L. Cooper, M. J. O. Deegan, A. J. Dobbyn, F. Eckert, E. Goll, C. Hampel, A. Hesselmann, G. Hetzer, T. Hrenar, G. Jansen, C. Köppl, Y. Liu, A. W. Lloyd, R. A. Mata, A. J. May, S. J. McNicholas, W. Meyer, M. E. Mura, A. Nicklass, P. Palmieri, K. Pflüger, R. Pitzer, M. Reiher, T. Shiozaki, H. Stoll, A. J. Stone, R. Tarroni, T. Thorsteinsson, M. Wang, and A. Wolf, "Molpro, version 2010.1, a package of ab initio programs," 2010. see http://www.molpro.net. 5.3

[243] P. J. Knowles and N. C. Handy, "A New Determinant-based Full Configuration Interaction Method," *Chem. Phys. Letters* **111**, pp. 315–321, 1984. 5.3

[244] H.-J. Werner and P. J. Knowles, "A Second Order MCSCF Method with Optimum Convergence," *J. Chem. Phys.* **82**, p. 5053, 1985. 5.3

[245] P. J. Knowles and H.-J. Werner, "An Efficient Second Order MCSCF Method for Long Configuration Expansions," *Chem. Phys. Letters* **115**, pp. 259–267, 1985. 5.3

[246] H.-J. Werner and P. J. Knowles, "An Efficient Internally Contracted Multiconfiguration Reference CI Method," *J. Chem. Phys.* **89**, pp. 5803–5814, 1988. 5.3

[247] P. J. Knowles and H.-J. Werner, "An Efficient Method for the Evaluation of Coupling Coefficients in Configuration Interaction Calculations," *Chem. Phys. Letters* **145**, pp. 514–522, 1988. 5.3

[248] R. D. Amos, J. S. Andrews, N. C. Handy, and P. J. Knowles, "Open Shell Møller–Plesset Perturbation Theory," *Chem. Phys. Letters* **185**, pp. 256–264, 1991. 5.3

[249] P. J. Knowles, J. S. Andrews, R. D. Amos, N. C. Handy, and J. A. Pople, "Restricted Møller–Plesset Theory for Open Shell Molecules," *Chem. Phys. Letters* **186**, pp. 130–136, 1991. 5.3

[250] P. J. Knowles and H.-J. Werner, "Internally Contracted Multiconfiguration Reference Configuration Interaction Calculations for Excited States," 1992. 5.3

[251] P. J. Knowles, C. Hampel, and H.-J. Werner, "Coupled Cluster Theory for High Spin Open Shell Reference Wavefunctions," *J. Chem. Phys.* **99**, pp. 5219–5227, 1993. 5.3

[252] P. J. Knowles and N. C. Handy, "A Determinant Based Full Configuration Interaction Program," *Comput. Phys. Commun.* **54**, pp. 75–83, 1989. 5.3

[253] S. F. Boys and F. Bernardi, "The Calculation of Small Molecular Interactions by the Differences of Separate Total Energies. Some Procedures with Reduced Errors," *Mol. Phys.* **19**, p. 553, 1970. 5.3

[254] J. Williams, A. Rohrbacher, D. Djahandideh, K. C. Janda, A. Jamka, F.-M. Tao, and N. Halberstadt, "Are Rare-Gas Cl_2 van der Waals Molecules Linear or T-Shaped?," *Mol. Phys.* **91**, pp. 573–588, 1997. 5.3.4, 5.11, 5.3.6

[255] A. Michels, W. D. Graff, and C. A. T. Seldam, "Virial Coefficients of Hydrogen and Deuterium at Temperatures between -175^{o}C and +150^{o}C. Conclusions from the Second Virial Coefficient with Regards to the Intermolecular Potential," *Physica* **26**, p. 393, 1960. 5.3.5, 5.14, 5.7, 5.4

[256] L. Pacioli, *De divina proportione*, Luca Paganinem de Paganinus de Brescia (Antonio Capella), Venice, 1509. 5.16, 5.3.6

[257] A. Bravais, "Mémoire sur les Systèmes formés par des Points Distribués Régulièrement sur un Plan ou Dans l'Espace," *J. Ecole Polytech* **19**, pp. 1–128, 1949. 5.3.6, 5.3.6

[258] W. Miehle, O. Kandler, T. Leisner, and O. Echt, "Mass Spectrometric Evidence for Icosahedral Structure in Large Rare Gas Clusters: Ar, Kr, Xe," *J. Chem. Phys.* **91**, p. 5940, 1989. 5.3.6

[259] D. Shechtman, I. Blech, D. Gratias, and J. Cahn, "Metallic Phase with Long-Range Orientational Order and no Translational Symmetry," *Phys. Rev. Lett.* **53**, pp. 1951–1953, 1984. 5.3.6

[260] G. Tejeda, J. M. Fernandez, S. Montero, D. Blume, and J. P. Toennies, "Raman Spectroscopy of Small para-H_2 Clusters Formed in Cryogenic Free Jets," *Phys. Rev. Lett.* **92**, p. 223401, 2004. 5.3.6

[261] F. Mezzacapo and M. Boninsegni, "Structure, Superfluidity, and Quantum Melting of Hydrogen Clusters," *Phys. Rev. A* **75**, p. 33201, 2007. 5.3.6, 5.3.6

[262] F. Mezzacapo and M. Boninsegni, "Superfluidity of Isotopically Doped Parahydrogen Clusters," *Phys. Rev. A* **76**, p. 21201, 2007. 5.3.6, 5.3.6

[263] S. A. Khairallah, M. B. Sevryuk, D. M. Ceperley, and J. P. Toennies, "Interplay Between Magic Number Stabilities and Superfluidity of Small Parahydrogen Clusters," *Phys. Rev. Lett.* **98**, p. 183401, 2007. 5.3.6, 5.3.6

[264] J. Navarro and R. Guardiola, "Thermal Effects on Small para-Hydrogen Clusters," *International Journal of Quantum Chemistry* **111**, pp. 463–471, 2011. 5.3.6, 5.3.6

[265] J. E. Cuervo and P.-N. Roy, "Path Integral Ground State Study of Finite-Size Systems: Application to Small (Parahydrogen)$_N$($N = 2-20$) Clusters," *J. Chem. Phys.* **125**, p. 124314, 2006. 5.3.6, 5.3.6

[266] S. Warnecke, M. B. Sevryuk, D. M. Ceperley, J. P. Toennies, R. Guardiola, and J. Navarro, "The Structure of para-Hydrogen Clusters," *The European Physical Journal D* **56**, pp. 353–358, 2010. 5.3.6

[267] A. L. Mackay, "A Dense Non-Crystallographic Packing of Equal Spheres," *Acta Cryst.* **15**, p. 916, 1962. 5.3.6, 5.3.6, 5.4

[268] J. Farges, M. F. D. Feraudy, B. Raoult, and G. Torchet, "Cluster Models Made of Double Icosahedral Units," *Surface Science* **156**, pp. 370–378, 1985. 5.3.6, 5.3.6, 5.4

[269] J. P. K. Doye and F. Calvo, "Entropic Effects on the Structure of Lennard-Jones Clusters," *J. Chem. Phys.* **116**, p. 8307, 2002. 5.3.6, 5.3.6

[270] D. J. Wales, *Energy Landscapes* , Cambridge University Press, Cambridge, 2003. 5.3.6

[271] F. Ding, J.-L. Wang, W.-F. Shen, B.-L. Wang, H. Li, and G.-H. Wang, "The Stability of Icosahedral Cluster and the Range of Interaction Potential," *Commun. Theor. Phys.* **36**, pp. 459–462, 2001. 5.3.6

[272] J. P. K. Doye, M. A. Miller, and D. J. Wales, "Evolution of the Potential Energy Surface with Size for Lennard-Jones Clusters," *J. Chem. Phys.* **111**, p. 8417, 1999. 5.3.6

[273] B. Hartke, "Global Geometry Optimization of Clusters using a Growth Strategy Optimized by a Genetic Algorithm," *Chem. Phys. Lett.* **240**, p. 560, 1995. 5.3.6

[274] B. Schmidt. TrajLab, Version 0.8: A Program Package for Classical Trajectories and Metastability Analysis. Available via http://trajlab.sourceforge.net (2011). 5.3.6, 5.3.8, 5.3.8

[275] N. J. A. Sloane and B. K. Teo, "Theta Series and Magic Numbers for Close-Packed Spherical Clusters," *J. Chem. Phys.* **83**, p. 6520, 1985. 5.3.6

[276] O. M. Becker and M. Karplus, "The Topology of Multidimensional Potential Energy Surfaces: Theory and Application to Peptide Structure and Kinetics ," *J. Chem. Phys.* **106**, p. 1495, 1997. 5.3.6, 5.18

[277] J. H. V. Lenthe, R. Vov, J. V. D.-V. de Rijdt, and F. V. Duijneveldt, "An Accurate ab initio Calculation of the He_2 Potential Curve," *Chem. Phys. Lett.* **143**, p. 435, 1988. 5.11

[278] V. M. Akimov, L. I. Kolesnikova, L. Y. Rusin, M. B. Sevryuk, and J. P. Toennies, "Structure of Small Hydrogen Nanoclusters Containing ortho-Molecules," *Russian Journal of Physical Chemistry B* **3**, pp. 743–752, 2009. 5.3.6

[279] J. Choo and Y. Kwon, "Magic Number Stabilities of Small para-H_2 Clusters Doped by a Single ortho-D_2," *J. Low Temp. Phys.* **150**, pp. 358–363, 2008. 5.3.6

[280] F. Paesani and K. B. Wahley, "Vibrational Shifts of OCS in Mixed Clusters of Parahydrogen and Helium," *J. Chem. Phys.* **124**, p. 234310, 2006. 5.3.6

[281] H. Li, R. J. L. Roy, P.-N. Roy, and A. R. W. McKellar, "Molecular Superfluid: Nonclassical Rotations in Doped *para*-Hydrogen Clusters," *Phys. Rev. Lett.* **105**, p. 133401, 2010. 5.3.6

[282] J. Tang and A. R. W. McKellar, "Infrared Spectra of Seeded Hydrogen Clusters: (para-H2)$_N$-N_2O and (ortho-H2)$_N$-N_2O, N=2-13," *J. Chem. Phys.* **123**, p. 114314, 2005. 5.3.6

[283] M. A. McMahon and K. B. Whaley, "Quantum Monte Carlo Studies of Anisotropy and Rotational States in He_NCl_2," *J. Chem. Phys.* **103**, p. 2561, 1995. 5.3.6

[284] F. Y. Naumkin and D. J. Wales, "Influence of the Atom-Atom Interaction Anisotropy on the Structure and Stability of Ar_nCl_2 Clusters ," *Chem. Phys. Lett.* **290**, pp. 164–170, 1998. 5.3.6

[285] M. Buchholz, C.-M. Goletz, F. Grossmann, B. Schmidt, J. Heyda, and P. Jungwirth, "Semiclassical Hybrid Approach to Condensed Phase Molecular Dynamics: Application to the I_2Kr_{17} Cluster ," *J. Phys. Chem. A* **in press**, 2012. 5.3.6

[286] S. Grebenev, M. Hartmann, M. Havenith, B. Sartakov, J. P. Toennies, and A. F. Vilesov, "The Rotational Spectrum of Single OCS Molecules in Liquid ^{4}He droplets," *J. Chem. Phys.* **112**, p. 4485, 2000. 5.3.6

[287] W. H. Miller, *Historical Atlas of Crystallography*, Kluwer Academic Publishers, Dordrecht, Dordrecht, 1990. 5.20, 6, 8

[288] N. W. Ashcroft and N. D. Mermin, *Solid State Physics*, Holt-Saunders International Editions, Saunders College West Washington Square Philadelphia, PA 19105, 1981. 5.3.7

[289] O. Schnepp, "One-Phonon Excited States of Solid H_2 and D_2 in the Ordered Phase," *Phys. Rev. A* **2**, p. 2574, 1970. 5.3.7, 5.3.8, 5.3.8

[290] E. Blaisten-Barojas and M. Allavena, "An Application of Green's Functions to the Study of the Vibration-Translation Coupling of Trapped Oscillators in a Linear Chain," *Int. J. Quantum Chem.* **7**, p. 195, 1973. 5.3.8

[291] P. D. Mannheim and H. Friedmann, "Theory of Optical Absorption by Diatomic Molecules Embedded in Rare Gas Crystals," *phys. stat. sol.* **39**, p. 409, 1970. 5.3.8, 5.3.8

[292] M. Allavena, H. Chakroun, and D. White, "Role of Phonon Coupling in the Broadening of Rotational Lines of Diatomics Trapped in Rare Gas Matrices. A Model Calculation for HCl in Ar.," *J. Chem. Phys.* **77**, p. 1757, 1982. 5.3.8, 5.3.8

[293] H. Kono and S. H. Lin, "Spectroscopic Properties and Relaxation Processes of Impurity Molecules in Solids. I. Rotational Spectra," *J. Chem. Phys.* **78**, p. 2607, 1983. 5.3.8, 5.3.8

[294] I. L. Garzón and E. Blaisten-Barojas, "Libron-Phonon Coupling Effects on the Infrared Absorption Spectra of Molecules Trapped in Matrices," *J. Chem. Phys.* **83**, p. 4311, 1985. 5.3.8, 5.3.8

[295] Y.-P. Lee, Y.-J. Wu, R. M. Lees, L.-H. Xu, and J. T. Hougen, "Internal Rotation and Spin Conversion of CH_3OH in Solid para-Hydrogen," *Science* **311**, p. 365, 2006. 5.3.8

[296] A. O. Urvas, D. L. Losee, and R. O. Simmons, "The Compressibility of Krypton, Argon, and Other Noble Gas Solids," *Journal of Physics and Chemistry of Solids* , p. 2269, 1967. 5.3.8

[297] B. Schmidt. WavePacket, Version 4.8: A Program Package for Numerical Simulations of Quantum-Mechanical Wavepacket Dynamics. Available via http://wavepacket.sourceforge.net/ (2012). 5.3.8, 5.3.8

[298] L. Pauling, "The Rotational Motion of Molecules in Crystals," *Phys. Rep.* **36**, p. 430, 1930. 5.3.8

[299] H. U. Beyeler, "Vibration-Rotation Absorption Spectra of a Rotator Hindered by Fields of Cubic Symmetry," *J. Chem. Phys.* **60**, p. 4123, 1974. 5.3.8

[300] D. Smith, "Hindered Rotational Energy Levels of a Linear Ion in Octahedral and Tetrahedral Crystalline Fields," *J. Chem. Phys.* **68**, p. 3222, 1978. 5.3.8, 5.3.8

[301] V. Berghof, M. Martins, B. Schmidt, and N. Schwentner, "Vibrational Overtones and Rotational Structure of HCl in Rare Gas Matrices," *J. Chem. Phys.* **116**, p. 9364, 2002. 5.3.8, 5.3.8

[302] T. Kiljunen, B. Schmidt, and N. Schwentner, "Intense-Field Alignment of Molecules Confined in Octahedral Fields," *Phys. Rev. Lett.* **94**, p. 123003, 2005. 5.3.8, 5.3.8

[303] M. E. Fajardo, C. M. Lindsay, and T. Momose, "Crystal Field Theory Analysis of Rovibrational Spectra of Carbon Monoxide Monomers Isolated in Solid Parahydrogen," *J. Chem. Phys.* **130**, p. 244508, 2009. 5.3.8

[304] M. T. Bowers and W. H. Flygare, "Vibration-Rotation Spectra of Monomeric HCl, DCl, HBr, DBr, and HI in the Rare-Gas Lattices and N_2-Doping Experiments in the Rare-Gas Lattices.," *J. Chem. Phys.* **44**, p. 1389, 1966. 5.3.8

[305] L. F. Keyser and G. W. Robinson, "Infrared Spectra of HCl and DCl in Solid Rare Gases. I. Monomers," *J. Chem. Phys.* **44**, p. 3225, 1966. 5.3.8

[306] H. Friedmann and S. Kimel, "Rotation-Translation-Coupling Effect in Noble-Gas Crystals Containing Molecular Impurities," *J. Chem. Phys.* **47**, p. 3589, 1967. 5.3.8

[307] H. Friedmann, A. Shalom, and S. Kimel, "Rotation-Translation Levels of a Tetrahedral Molecule in an Octahedral Cell," *J. Chem. Phys.* **50**, p. 2496, 1969. 5.3.8

[308] J. Manz, "Rotating Molecules Trapped in Pseudorotating Cages," *J. Am. Chem. Soc.* **102**, p. 1801, 1980. 5.3.8, 5.3.8

[309] B. Laroui, O. Damak, O. Maillard, and C. Girardet, "HCl-Rare Gas van der Waals Dimers Trapped in Rare Gas Matrix: Interpretation of the Vibration-Orientation Spectrum," *J. Chem. Phys.* **97**, p. 2359, 1992. 5.3.8

[310] B. Laroui, J. P. Perchard, and C. Girardet, "Rotational Hindering for $H^{35}Cl$ Trapped in Binary Rare Gas Matrices. I. Experimental Evidence from Fouriertransform Infrared Spectroscopy," *J. Chem. Phys.* **97**, p. 2347, 1992. 5.3.8

[311] Z. Bačić and R. E. Miller, "Molecular Clusters: Structure and Dynamics of Weakly Bound Systems," *J. Phys. Chem.* **100**, p. 12945, 1996. 5.3.8

[312] A. N. Aleksandrovskii, V. G. Manzhelii, V. B. Esel'son, and B. G. Udovidchenko, "Influence of Rotational Motion of Nitrogen Molecules on the Thermal Expansion of Solid Solutions of Ar-Nz: A New Effect," *Journal of Low Temperature Physics* **108**, p. 297, 1997. 5.3.8

[313] K. Nauta and R. E. Miller, "Solvent Mediated Vibrational Relaxation: Superfluid Helium Droplet Spectroscopy of HCN Dimer," **111**, p. 3426, 1999. 5.3.8

[314] T. Momose, H. Hoshina, M. Fushitani, and H. Katsuki, "High-Resolution Spectroscopy and its Analysis of Ro-Vibrational Transitions of Molecules in Solid Parahydrogen," *Vib. Spectrosc.* **34**, p. 95, 2004. 5.3.8

[315] E. Popov, T. Kiljunen, H. Kunttu, and J. Eloranta, "Rotation of Methyl Radicals in a Solid Argon Matrix," *J. Chem. Phys.* **126**, p. 134504, 2007. 5.3.8

[316] E. Popov, T. Kiljunen, H. Kunttu, and J. Eloranta, "Rotation of Methyl Radicals in a Solid Krypton Matrix," *J. Chem. Phys.* **130**, p. 164504, 2009. 5.3.8

[317] B. Schmidt and P. Zdanska, "Solution of the Time-Dependent Schrödinger Equation for Highly Symmetric Potentials," *Comp. Phys. Comm.* **127**, p. 290, 2000. 5.3.8, 5.3.8

[318] T. Kiljunen, B. Schmidt, and N. Schwentner, "Aligning and Orientating Molecules Trapped in Octahedral Crystal Fields," *Phys. Rev. A* **72**, p. 53415, 2005. 5.3.8

[319] S. L. Altmann and A. P. Cracknell, "Lattice Harmonics I. Cubic Groups," *Rev. Mod. Phys.* **37**, p. 19, 1965. 5.3.8

[320] S. L. Altmann and C. J. Bradley, "Lattice Harmonics II. Hexagonal Close-Packed Lattice," *Rev. Mod. Phys.* **37**, p. 33, 1965. 5.3.8

[321] M. Abramowitz and I. Stegun, *Handbook of Mathematical Functions with Formulas, Graphs, and Mathematical Tables*, Dover Publications, New York, 1972. (document), 6.2, 6.1, 6.3

Acknowledgements

These acknowledgements may become too long if I would thank all people, who in different ways aided me to reach this very important life goal. Ultimately, this PhD is the result of the joint effort of many persons besides myself. My first thank goes to my "Doktorvater", Prof. Dr. J. Manz, who took me into his group, provided and supported the different interesting topics worked out along these years. I would like to thank all the members of the group, past and present, for being always polite and ready to help when needed, as well as enjoyable during the coffee breaks and birthday parties. A special thanks to Prof. Dr. Oliver Kühn, who supervised the first part of my PhD, when I, still as a novice, had to struggle between English, German and of course research. I thank him for his patience, his support and his guidance. From the same period, I thank my first two office colleagues, Dr. Mikhail Korolkov and in particular my predecessor Dr. Alexander Borowski, who introduced me to the contents of his doctorate. A special thanks again to Prof. Dr. J. Manz, with whom I had very nice talks on the fluxes subject during the second part of my PhD, and to my colleague Ingo Barth, who helped me programming this part. A special thanks to Priv. Doz. Dr. Burkhard Schmidt, who supervised the third and final part of my PhD. I thank him for being a pleasant person, a great scientist, for sitting next to me many hours and for teaching me how to use Matlab.

For his assistance with computer problems I want to thank Dr. Holger Naundorf. For the bureaucratic administration many thanks to Julija Djordjevic, who managed the very nice group activities. I also would like to thank Priv. Doz. Dr. Monika Leibscher, who patiently helped me through my first lessons on Quantum Reaction Dynamics. For reading part of the first chapter on Quantum Chemistry and for being king by giving me back my office in the last sprint of my writing I would like to thank Prof. Dr. Beate Paulus, to whom I also wish a successful research and good luck in leading her workgroup. For giving me CPU time I would like to thank the workgroup of Prof. Dr. Schütte from the department for mathematics and also the ZEDAT institute of the Free University of Berlin.

I also want to thank many friends, who supported me during these years. Guillermo for being a sincere friend, the "Mensakumpeln" Antje, Caroline, Joanjo, Nina, Santiago, Wiebke for the nice and amusing lunch breaks. I would like to thank Isla, with who I shared the most part of my time as a PhD student, for supporting me through my long backache period and along my doctorate. For these and many other reasons I deeply thank her. Finally, I express my deepest thanks to my parents for educating me, for supporting my studies in Bologna, which brought me to this point, and to my sister for being always there.

For financial support I thank the Sonderforschungsbereich 450 der Deutschen Forschungsgemeinschaft.

Publications

A DFT Computational Study of the Mechanism of Butadiene Carbonylation Catalyzed by Palladium Complexes.
M. A. Carvajal and G. P. Miscione and A. Accardi and J. J. Novoa and A. Bottoni
Molecular Physics, Vol. 104, pp. 805-831 (2006)

Nonadiabatic Quantum Dynamics and Laser Control of Br_2 in Solid Argon
A. Accardi and A. Borowski and O. Kühn
Journal of Physical Chemistry A, Vol. 113, pp. 7491-7498 (2009)

From Synchronous to Sequential Double Proton Transfer: Quantum Dynamics Simulations for the Model Porphine
A. Accardi and I. Barth and O. Kühn and J. Manz
Journal of Physical Chemistry A, Vol. 114, pp. 11252-11262 (2009)

Lebenslauf

Der Lebenslauf ist in der Online-Version aus Gründen des Datenschutzes nicht enthalten.

December 18, 2012

Erklärung

Hiermit erkläre ich, dass ich die vorliegende Arbeit mit den angegebenen Hilfsmitteln selbständig angefertigt habe.

Berlin, 2012